Contribution to the study of fission products release from nuclear fuels in severe accident conditions : effect of the pO2 on Cs, Mo and Ba speciation

Claire Le Gall

Communauté
UNIVERSITÉ Grenoble Alpes

THÈSE

Pour obtenir le grade de

**DOCTEUR DE LA
COMMUNAUTE UNIVERSITE GRENOBLE ALPES**

Spécialité : Physique de la Matière Condensée et du Rayonnement

Arrêté ministériel : 25 mai 2016

Présentée par

Claire LE GALL

Thèse dirigée par **Jean-Louis HAZEMANN**
et encadrée par **Fabienne AUDUBERT, Yves PONTILLON** et **Jacques LECHELLE**

préparée au sein du **Laboratoire d'Analyse de la Migration des radioéléments** au CEA de Cadarache
dans **l'École Doctorale de Physique (ED n°47)**

Contribution à l'étude du relâchement des produits de fission hors de combustibles nucléaires en situation d'accident grave : effet de la pO_2 sur la spéciation du Cs, Mo et Ba

Contribution to the study of fission products release from nuclear fuels in severe accident conditions : effect of the pO_2 on Cs, Mo and ba speciation

Thèse soutenue publiquement le **16 Novembre 2018**,
devant le jury composé de :

Monsieur Luc SALVO
Professeur à l'Université de Grenoble, Président
Monsieur René GUINEBRETIERE
Professeur à l'Université de Limoges, Rapporteur
Monsieur Yann LE PETITCORPS
Professeur à l'Université de Bordeaux, Rapporteur
Monsieur Dario MANARA
Ingénieur de recherche au JRC-Karlsruhe, Examinateur
Madame Anne-Cécile GREGOIRE
Ingénieure de recherche à l'IRSN, Examinatrice

A ma sœur,

Ce petit bout de femme au courage et à la volonté de fer

A mes parents,

Mes modèles de toujours

Ce travail a été réalisé dans le cadre d'un contrat de formation par la recherche au CEA de Cadarache. J'exprime ma sincère reconnaissance à l'ensemble des membres du jury d'avoir accepté de le juger : à Yann Le Petitcorps et René Guinebretière pour avoir rapporté de mon travail et pour vos questions et remarques pertinentes, à Luc Salvo pour avoir présidé et animé les discussions, à Anne-Cécile Grégoire et Dario Manara pour les échanges autour des perspectives et de l'impact de ce travail dans la communauté du nucléaire.

Merci à la direction, du SA3C, devenu SA3E en 2018, pour l'aide qu'elle nous a apporté tout au long de la thèse. En particulier, je remercie Oliver Dugne pour ses conseils avisés lors de la relecture des articles sur VERDON-1 et le duo formé par Béatrice Teisseire et Chrystelle Nonon-Solaro notamment pour leur réactivité lors de la lecture des rapports de stage et leur patience. Corine, un immense merci pour l'aide que tu m'as apportée en toutes circonstances toujours avec le sourire et beaucoup de bienveillance.

Je remercie aussi Eric Hanus et Isabelle Moysan-Lavoine, successivement chefs du LAMIR. Un grand merci à toi Isabelle pour ton humanité et l'attention que tu portes à tous les membres du labo !

Ma gratitude va aussi à Jacques Royer et Pascal Bros successivement responsables du projet TERPF, pour leur soutien concret et l'intérêt qu'ils ont porté à ma thèse.

Je tiens à remercier EDF, qui a financé une partie de mon travail de thèse. Particulièrement, merci à Bruno Tourniaire et Hadrien Perron pour leur relecture, leur patience et leur aide, notamment lors de la publication des articles VERDON-1 !

Je souhaite aussi dire merci au personnel de l'exploitation du labo UO_2 (Catherine Collavoli, Sébastien Lefèvre, Vincent Moutte) et du SPR (Karine Burbaud et David Gravier) pour leur aide, leurs conseils et leur bienveillance. En particulier, merci à Christophe Bertrand pour nous avoir sauvés la vie avec les derniers transports de matière !

Un immense merci à tous ceux avec qui j'ai eu le plaisir de travailler que ce soit au CEA ou en dehors car sans eux, ce travail n'aurait pas été si riche. Je vous remercie tous pour l'intérêt que vous m'avez témoigné, tant du point de vue personnel que professionnel.

Merci aux personnes du LARC avec qui j'ai pu travailler pendant mon stage et re-solliciter pendant la thèse, Alexandre Labet, Serge Pontremolli, Christophe Winckelmann, Mathieu Aubert et Maitë Bertaux. Alexandre, merci pour tes explications très claires et tout le temps que tu m'as accordé.

Merci à une grosse partie du LEMCI devenu LCPC : Laurent Fayette, Stéphane Reboul, Karine Hanifi, Isabelle Félines, Isabelle Zacharie-Aubrun, Thierry Blay, Philippe Bienvenu, Ingrid Roure, Jean Noirot et Virginie Basini. Travailler avec vous sur les échantillons VERDON a été extrêmement enrichissant. Je vous remercie pour votre patience, votre gentillesse et votre aide sur l'interprétation des résultats.

Merci à Pierre Matheron, Florent Garel, Mathias Soulon, Andréa Sanchez, Catherine Tanguy et Joseph Sanchez (tous deux à la retraite) du LCU pour m'avoir formée et aidée à de multiples reprises au labo, toujours dans la bonne humeur ! Je remercie aussi Xavière Iltis, Nicolas Tarisien, Hélène Rouquette, Joël Raynal de m'avoir accordée du temps sur le MEB et

la DRX. Un immense merci à Doris Drouan pour son temps sur le MEB, son aide précieuse lors des transports, son efficacité redoutable et sa bonne humeur. Je garderai un très bon souvenir des nombreuses journées MEB à guetter « Momo l'escargot » et à voir de la nourriture dans les SIMFuels à midi ! C'était un réel plaisir de travailler avec toi. Merci aussi pour le temps que tu as accordé à Camille et Valentin au labo.

Merci à Vincent Klosek pour son aide sur le traitement et l'interprétation des données XAS ainsi que pour avoir mis « de la vraie musique » sur les lignes de l'ESRF ou de SOLEIL =P

Merci à Chantal Martial pour m'avoir formée à l'utilisation de Factsage avec une pédagogie à toute épreuve. J'ai été très heureuse de travailler avec toi et te remercie aussi pour le travail que tu as fait avec Valentin. Merci à Christine Guéneau du DPC à Saclay pour son aide sur les calculs thermochimiques avec ThermoCalc et le temps que nous avons passé au téléphone ! Merci pour ta patience et ta bonne humeur =D

Un grand merci à Philippe Valenza du LIEN pour son travail sur la conception du porte-échantillon pour l'ESRF, et à Philippe Martin sans qui je ne serai peut-être pas partie en Allemagne.

Sans oublier tout le LAMIR, pour m'avoir accueillie et intégré dès mon arrivée en stage. Merci à tous pour l'ambiance, souvent festive, et pour votre gentillesse. Je souhaite notamment remercier Jean-Christophe (eh oui, tu ne pourras pas dire que je t'ai oublié hein ! =D) et Frédéric Martin pour les TT sur DURANCE. A mes trois petits scarabées Camille Thouzellier, Pierre Taupin et Valentin Muharem, un grand merci car vous m'avez beaucoup apporté (des résultats bien sûr, mais pas seulement !). J'espère avoir été à la hauteur au niveau de votre encadrement et vous avoir au moins appris que les animations dans les Power Point… C'est la base !

J'adresse aussi tous mes remerciements au personnel des lignes MARS au synchrotron SOLEIL et FAME / FAME-UHD de l'ESRF. Myrtille, Denis et Pier-Lorenzo, merci pour l'accueil sur MARS, pour votre aide sans faille lors des manips et votre disponibilité. Quelle belle surprise de te voir à la soutenance Myrtille ! De même, Olivier, Mauro, Eric, William et Antonio, merci pour votre réactivité, vos conseils et votre aide, notamment pour la mise en place de la 1ère manip en température sur FAME-UHD !! Votre bonne humeur à toute épreuve a rendu nos séjours à Grenoble très sympas ! Merci aussi à Patrick Colomp pour son aide précieuse sur la préparation du dossier sécurité / sûreté de l'expérience XANES en température.

Last but not least, I would like to express my deep and sincere gratitude to the ones who welcomed me at the JRC-Karlsruhe. Thanks to Dario Manara, responsible for the Gentle project and Rudy Konings head of the Nuclear Fuel Safety service for having accepted my application. Marco, Michael, Herwin, Co and Karin, thank you for having integrated me so quickly in your team, it was such a pleasure to work with you! I learnt a lot during these two months and not only how to drive in the right direction =P Thank you very much also for the work you did with Pierre. Big up to Concettina, Emanuele, Luca, Jean-François, Wen-Jie and all the football team =D

Un grand merci à tous les thésards, stagiaires et apprentis dont j'ai croisé la route et qui ont contribué à la bonne ambiance de ces 3 ans (Marie, Adrien, Mariem, Yue, Ahmed, Mira, les Jerems…). Tout particulièrement, merci à :

Chico Ernesto, mon premier co-bureau, par où commencer sinon par dire que tu m'as tout appris ? J'ai eu beaucoup de chance de partager ton bureau pendant quasiment 1 an. J'admire beaucoup ta pédagogie, ta patience et ta gentillesse. Merci de m'avoir mis le pied à l'étrier au tout début, de m'avoir guidée, conseillée et bien sûr formée lors de mon passage à Saclay. Merci aussi pour tous les bons moments que nous avons passé au CEA et en dehors !

Manon et Marion, je suis ravie de vous avoir rencontrées. Tous ces déjeuners que nous avons partagés, ces potins que nous nous sommes (ou plutôt que vous m'avez) racontés et tous les moments passés ensemble hors du CEA restent de très bons souvenirs. Marion, merci pour ces beaux voyage en Sicile et en Egypte (je n'en reviens toujours pas !) =D

Bernardo « Chic », merci pour toutes les aventures que nous avons vécues au bureau : ces batailles pour fermer la porte, pour ouvrir la fenêtre ou allumer la clim ha ha ha ! Merci pour ces grandes discussions sur le sens de la vie ou sur nos sujets de thèse respectifs et surtout, surtout, pour ta patience avec moi tous les matins jusqu'à 9h depuis plus d'un an et demi XD Gracias también por todos los lindos momentos que hemos pasado juntos, por el apoyo que me das en cualquier circunstancia y por tu paciencia en general (guiño guiño). Le agradezco al CEA y al destino por ponerte a mi lado.

Merci infiniment à mon directeur et à mes encadrants de thèse :

Jean-Louis, merci pour ta confiance, ta patience et tes conseils avisés tout au long de la thèse. Un grand merci aussi pour le temps que tu nous as accordé sur FAME et FAME-UHD.

Yves, merci pour le temps que tu as dégagé pour moi pendant 3 ans. Toutes ces entrevues joviales et optimistes desquelles je sortais en ayant oublié le stress ont été des bols d'air frais ! Je te remercie aussi pour ton aide dans l'interprétation des résultats expérimentaux ainsi que pour l'attention que tu as porté à mon bien-être pendant la thèse.

Jacques, merci pour le temps que tu as consacré à cette thèse, sur synchrotron et pour la conception et la préparation de l'expérience XANES en température. J'ai eu beaucoup de chance de pouvoir travailler avec toi et j'ai beaucoup appris. Ta gentillesse, ton humilité, ta bonne humeur constante et toutes les connaissances que tu centralises sont des atouts majeurs pour le CEA !!

Fabienne, la fermeture du LEFCA a été un des plus beaux cadeaux que m'a fait le CEA. Le soutien que tu m'as apporté tant sur les plans technique, logistique qu'humain a été un facteur décisif dans la réussite de cette thèse. Je l'ai vécu comme un vrai travail d'équipe et je garderai un superbe souvenir de ces 3 ans malgré des périodes de stress ultime ! Merci pour tout ce que tu m'as enseigné et par-dessus tout pour m'avoir accordé ta confiance.

Louise, mes Roeus (Anabou et Ik), malgré la distance qui nous sépare, vous avez toujours été là pour moi. Merci pour votre soutien dans les moments difficiles de ces 3 dernières années et vive les aventures ANACLAAFI ! Gaugau, merci d'être venu, c'était génial de te voir arriver à l'INSTN (Merci

Fabienne et Maman pour la surprise !). Guillaume merci à toi aussi d'avoir été à mes côtés pour la soutenance =D

Enfin, un grand merci à toute ma famille. Papa, Maman, Marie, cette thèse c'est aussi à vous que je la dois ! Je crois que je vous en ai tellement parlé pendant ces 3 ans que vous auriez pu l'écrire ! Merci infiniment pour le soutien sans faille que vous m'avez apporté depuis toujours, pour la force que vous m'avez communiquée dans les moments de doute et de panique et pour la confiance que vous m'accordez tous les jours. Sans vous, je n'aurais pas franchi la ligne d'arrivée.

LIST OF ABBREVIATIONS

BSE: Back Scattered Electrons

ECD: Equivalent Circle Diameter

EDX: Energy Dispersive X-ray Spectroscopy

EPMA: Electron Probe Microanalysis

ESRF: European Synchrotron Radiation Facility

FBR: Fast Breeder Reactor

FP: Fission Products

HERFD: High Energy Resolution Fluorescence Detection

HBS: High Burn-up Structure

ICP-AES: Inductive Coupled Plasma-Atomic Emission Spectroscopy

ICP-MS: Inductive Coupled Plasma-Mass Spectrometry

JRC: Joint Research Center

LCU: Laboratoire du Combustible Uranium

LWR : Light Water Reactors

OM: Optical Microscopy

PWR: Pressurized Water Reactor

SA: Severe Accident

SE: Secondary Electrons

SEM: Scanning Electron Microscopy

SIMS: Secondary Ion Mass Spectrometry

SPS: Spark Plasma Sintering

XANES: X-ray Absorption Near-Edge Structure

XAS: X-ray Absorption Spectroscopy

XRD: X-ray Diffraction

TABLE OF CONTENT

GENERAL INTRODUCTION

Nuclear energy, which is one of the least CO_2-emitting sources of energy, is used to produce around 12% of the world's electricity [1]. Concerns about climate change and CO_2 emissions are mounting as the world's population continues to grow and thus its energy needs with it. For this reason, nuclear power is destined to develop further across the world in the coming decades. From this perspective, guaranteeing the safety and security of the nuclear facilities is paramount.

When the first nuclear power plants were designed in the early 60s, the risk of a severe accident was not considered because the safety systems were believed to be robust enough to prevent accident conditions [2]. In 1979, however, a series of events triggered an accident at the Three-Mile Island power plant in the US, leading to the meltdown of almost half of the core in one of its two reactors. This event proved that a severe accident was possible and highlighted the need to better understand the phenomena involved in core meltdowns and radioactive material releases (e.g. fission products and other radionuclides).

Many research programmes were therefore launched across the world in the wake of Three Mile Island, including:

- Integral or in-pile tests representative of severe accident conditions occurring in small-scale nuclear power plants
- Analytical or out-of-pile tests to focus on certain phenomena or on the effect of specific parameters on the progress of the accident
- Development of models and calculation codes used to simulate severe accident sequences and predict their consequences. These models and codes were then validated on the basis of experimental data provided through integral or analytical tests.

With these programmes, the scientific community was able to gain a better understanding of the development of a severe accident, particularly with respect to:

- Final temperatures reached during a severe accident, which can range between 2300°C and 2600°C
- Atmosphere in the core, which can be strongly impacted by the oxidation of structural materials, the emergency safety measures (e.g. core reflooding), and the behaviour of the containment (its failure can lead to air ingress in the core)
- Oxidation process of the fuel cladding, which leads to H_2 production
- Interactions between the fuel and structural materials, leading to early fuel melting
- Effect of several parameters such as temperature, oxygen potential and type of fuel on the chemical state of fission products, which strongly impact their release and volatility.

The nuclear accidents at the Chernobyl (Ukraine, 1986) and Fukushima-Daiichi (Japan, 2011) power plants again revealed that some scenarios provoked specific phenomena had yet to be considered in safety studies. Both accidents resulted in massive contamination of the environment and once again highlighted the current limits of our ability to predict the consequences of a severe accident. The need to continue research to improve severe accident management measures for the current and future nuclear reactors has since been further consolidated. Research and development on reactor safety has led, for example, to consider the implementation of a corium recovery system in the new European Pressurized Reactors (EPR) systems or to develop accident-tolerant fuels thanks to the improved cladding behavior of new fuel cladding geometries in the case of steam oxidation [3].

The research priorities for light-water reactor (LWR) severe accidents are regularly assessed within the framework of the Severe Accident Research Network of excellence (SARNET). Their objective is to reduce uncertainties on simulation tools, to investigate phenomena that have yet to be considered or examined in detail, and to improve the current severe accident management measures. In 2014, these priorities concerned [4]:

- Phenomena occurring during in-vessel accidents
- Phenomena that could lead to early or late containment failure
- Phenomena linked to the release and transport of fission products (FP).

One of the key priorities is the impact of an oxidising environment on the source term in the case of high burn-up UO_2 and MOX fuels (covered in the three topics described above). This subject concerns the characterization and quantification of fission product releases, especially volatile elements. The current lack of experimental data greatly limits the validation of theoretical models used in calculation codes. Yet another topic of medium priority is the assessment of thermodynamic databases, which are one of the main sources of errors when calculating a severe accident sequence involving molten fuel.

In this context, the present work addresses the effect of the oxygen potential on MOX fuel behaviour and FP speciation (i.e. chemical reactions involving FP), more precisely in the case of Cs, Mo and Ba. Experimental data are provided in reducing and oxidizing atmospheres on irradiated and simulated fuels at different stages of a severe accident sequence. They are intended to be used for assessing the accuracy of the models used in calculation codes like MFPR [5] and thermodynamic databases such as the TAF-ID currently developed by the OECD-NEA [6].

This manuscript has been divided into four parts:

The first chapter of this thesis provides a literature review of nuclear fuel behavior and FP speciation in normal through to accident conditions in a PWR. The phenomenology of severe nuclear accidents is then presented after a brief description of PWR operating conditions focusing on the parameters that most affect nuclear fuel changes. The changes in nuclear fuel observed experimentally in severe accident conditions are then highlighted, as is the behaviour of three fission products, Cs, Mo and Ba. This chapter also discusses a mechanism that has been proposed in the literature to explain the release of these three FP. The main assumptions on which this mechanism is based are then detailed.

The second chapter is devoted to the study of irradiated fuels. Fuel samples were treated at very high temperatures (at 2300°C and 2530°C) in a reducing or oxidizing atmosphere, corresponding to different severe accident scenarios. Post-test characterizations were then performed and highlighted the effect of the atmosphere on fuel degradation mechanisms and FP behavior.

Due to their complexity and cost, the tests performed on these samples made it difficult to study FP speciation during the intermediate stages of the severe accident sequence. Given the insignificant volume of fission products produced by fission in the fuel, characterizing their speciation also proved challenging using the range of techniques available to now to analye irradiated samples. Hence, simulant materials called SIMFuel were used for their low radioactivity and representativeness in terms of FP chemistry.

The third chapter deals with the fabrication, thermal treatment and characterizations of SIMFuel samples produced by high-temperature sintering. Thermal treatments were performed in reducing and oxidizing conditions up to 1700°C to understand the effect of the atmosphere on FP speciation in the intermediate stages of a severe accident.

Due to the high-temperature sintering stage, however, volatile FPs could not be incorporated into these SIMFuel samples. The fabrication of SIMFuel based on low-temperature sintering was therefore investigated in order to study the speciation of Cs.

The fourth and last chapter of this study covers the development of a synthesis process to obtain dense UO_2 samples containing Cs, Mo and Ba.

The main findings of this study are summarised in the conclusion, together with future prospects for studies that could enable us to delve further into understanding FP speciation.

REFERENCES

[1] Observ'ER, "Quinzième inventaire / Fifteenth inventory: La production d'électricité d'origine renouvelable dans le monde / Worldwide electricity production from renewable energy sources - Edition 2013," 2013. [Online]. Available: http://www.energies-renouvelables.org/electricite_renouvelable.asp. [Accessed: 14-Sep-2018].

[2] D. Jacquemain, *Les accidents de fusion du coeur des réacteurs nucléaires de puissance - Etat des connaissances*, IRSN. edp sciences, 2013.

[3] S. J. Zinkle, K. A. Terrani, J. C. Gehin, L. J. Ott, and L. L. Snead, "Accident tolerant fuels for LWRs: A perspective," *J. Nucl. Mater.*, vol. 448, no. 1, pp. 374–379, May 2014.

[4] W. Klein-Heßling *et al.*, "Conclusions on severe accident research priorities," *Ann. Nucl. Energy*, vol. 74, pp. 4–11, Dec. 2014.

[5] M. S. Veshchunov, V. D. Ozrin, V. E. Shestak, V. I. Tarasov, R. Dubourg, and G. Nicaise, "Development of the mechanistic code MFPR for modelling fission product release from irradiated UO2 fuel," *Nucl. Eng. Des.*, vol. 236, no. 2, pp. 179–200, 2006.

[6] "OECD NEA/NSC: Thermodynamics of Advanced Fuels – International Database (TAF-ID) - working version of january 2018." [Online]. Available: https://www.oecd-nea.org/science/taf-id/. [Accessed: 25-Aug-2016].

Chapter I:

LITTERATURE REVIEW

TABLE OF CONTENT

I.1 INTRODUCTION

During irradiation cycles of nuclear fuel in the reactor, Fission Products (FP) are created and retained in the fuel, modifying its microstructure and properties (thermal conductivity, creep behavior…). Among them, Cs, Mo and Ba are of prior interest as they are produced in high quantity during fission and are able to interact with other elements (like FP or the fuel itself) modifying their volatility. They have also a huge radiological impact, being poisons for living organisms in the mid to long term.

In case of a severe accident, FP can be released from the fuel in the environment. Their chemical nature and the quantities released (called source term) strongly depend on the scenario and the accidental conditions involved (temperature, type of fuel, burn-up[1], oxygen potential…). A deep understanding of FP release mechanisms out of the fuel is thus essential in order to get a realistic estimation of the source term of the accident and hence to be able to better predict its consequences whatever the scenario can be.

Many research programs have started worldwide to this end, leading to a better understanding of FP release during temperature transients under a controlled atmosphere. However, to develop realistic models for FP behavior, getting experimental data on their speciation and on fuel microstructure evolution, and confronting them to thermodynamics predictions is mandatory.

The main objective of this chapter is to provide a summary of the current knowledge concerning:

- The state of the fuel and FP in normal Pressurized Water Reactor (PWR) operating conditions.
- The basics of nuclear severe accidents phenomenology and the results of several integral and analytical programs concerning the evolution of the fuel and FP in such a situation.
- The hypotheses taken in mechanistic calculations, which have led to the elaboration of FP release mechanisms based on FP speciation in the fuel.

The positioning of this thesis as well as the method used to answer its objectives are exposed in the last part of this chapter.

[1] The burn-up enables the quantification of the amount of fuel consumed during fission. It is usually expressed in gigawatt-day per ton of heavy metals, which is a measure of the energy released by the fission of one heavy nucleus.

I.2 PRESSURIZED WATER REACTORS

I.2.1 General principle

I.2.1.1 Fission reaction

PWR represent 65% of the nuclear power plants existing in the world and produce 70% of the electricity provided by nuclear power. Most particularly, these reactors constitute the entire nuclear fleet operated by EDF in France. They operate the thermal energy produced by the fission of nuclear fuel to produce electricity.

In a PWR, fission within the fuel occurs when a thermal neutron (with an energy of 25 meV) is captured by a heavy nuclide such as ^{235}U or ^{239}Pu. During this reaction, these nuclides are split in two smaller ones called FP, several fast neutrons and gamma rays are also released as shown in **Figure I-1**. The kinetic energy released during the fission of one ^{235}U or ^{239}Pu nucleus (around 200 MeV [1]) causes thermal agitation within the fuel producing heat.

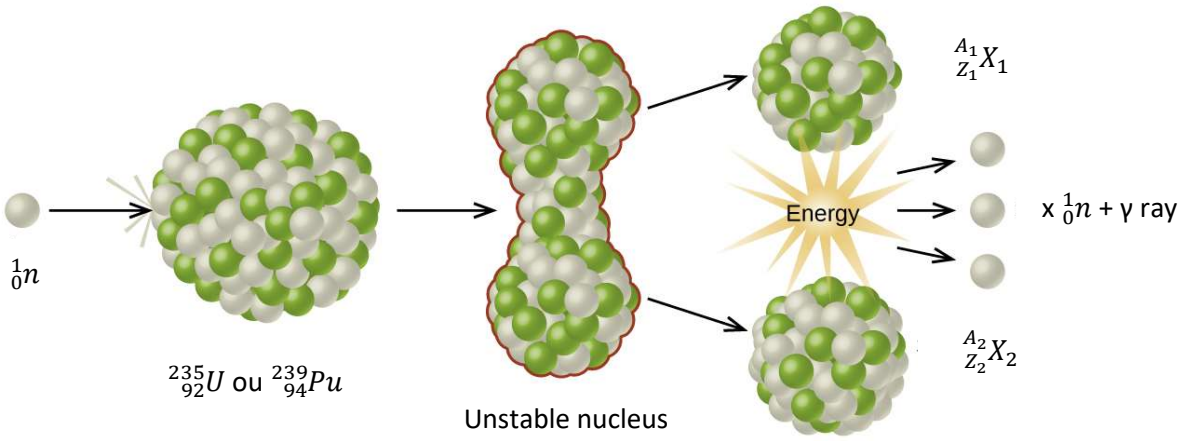

Figure I-1: Schematic illustration of the fission reaction after neutron capture [2].

The statistical mass distributions of the FP created during the thermal fission of ^{235}U and ^{239}Pu are bimodal (**Figure I-2**). The maximum FP yields occur at 95 amu and 138 amu in the case of ^{235}U. The first peak corresponding to the lighter FP created is displaced to higher mass and centered around 99 amu in the case of ^{239}Pu whereas the second peak is not appreciably displaced.

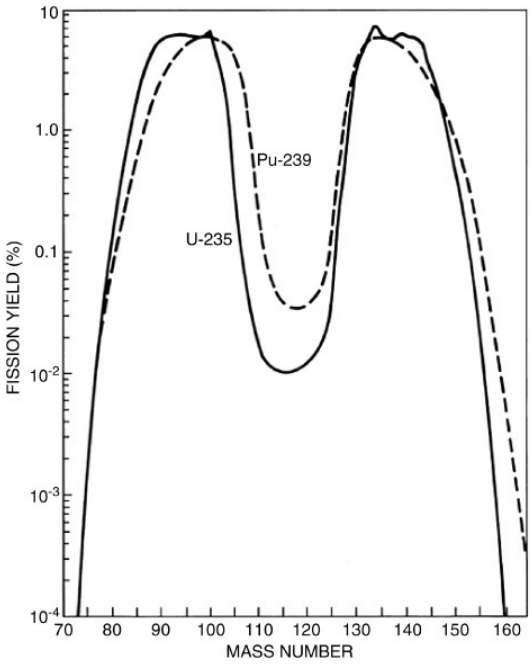

Figure I-2: Yield distribution of radioisotopes as a function of atomic mass from the thermal fission of ^{235}U (solid curve) and ^{239}Pu (dashed curve) extracted from [3].

I.2.1.2 Main features of a PWR

I.2.1.2.1 Coolant

PWR are part of the reactors that operates light water as a coolant in the primary circuit. This water is maintained in liquid state in order to ensure efficient transfer of the heat produced in the core. Its usual operating temperature is 300°C and it is pressurized at 155 bars [4]. The primary water is also used as moderator in order to control neutrons energy.

The heat removed from the core is then transferred to the water contained in the secondary circuit through the steam generator. The steam produced in the secondary circuit passes through a turbine coupled to an alternator enabling thermal energy to be converted in electricity.

I.2.1.2.2 Fuel assembly

As shown in **Figure I-3**, the fuel assembly of a PWR consists in 17 x 17 fuel rods maintained together thanks to nozzles at both ends and spacing grids placed regularly lengthwise [4]. The fuel rods are composed of Zr alloy tubes called fuel cladding and of fuel pellets.

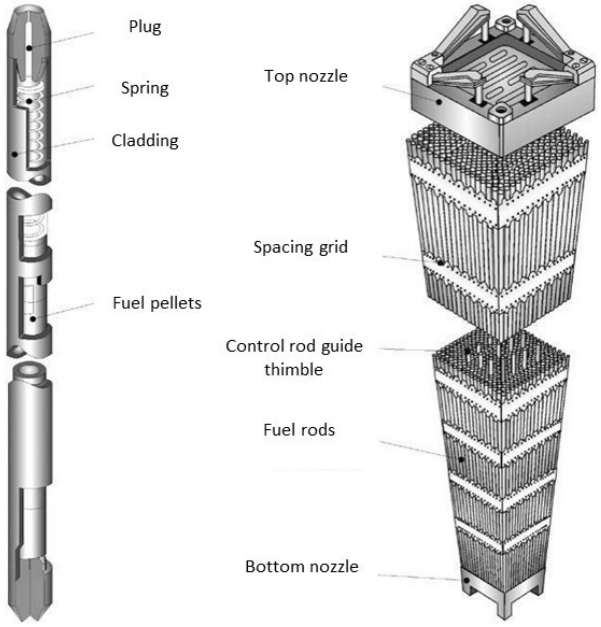

Figure I-3: Schematic of a fuel rod (left) and a PWR fuel assembly (right) extracted from [4].

Fuel cladding

Two main types of cladding materials are used in the actual French PWR, as shown in **Table I-1**. Zr has been chosen to be the main alloying element because of its transparence to thermal neutrons, its creep strength and its rather good resistance to corrosion in humid atmosphere [5].

In the case of Zyrcaloy-4, Sn is used to enhance Zr mechanical behavior and Fe and Cr improve the corrosion resistance. The M5^{TM} main alloying element is Nb, it offers a better resistance to corrosion and hydride blisters formation. Impurities of O are added to strengthen the both types of cladding [6].

Table I-1: Compositions of the two main cladding alloys used in PWR (wt%, the difference to 100% is due to the Zr content).

Alloying elements (wt%)	Zircaloy-4	M5^{TM}
Sn	1.3	-
Fe	0.2	0.025
Cr	0.1	-
Nb	-	1
O	1200	1250

Fuel

Within these cladding tubes, fuel pellets of around 8.2 mm in diameter and 13.5 mm in height, composed of uranium dioxide (UO_2) enriched with 3 to 5 % of ^{235}U or mixed oxide (MOX, $(U, Pu)O_2$) are stacked on approximately 4 m and blocked thanks to a string and two plugs (**Figure I-3**). A gap needed to stack the pellets is present between the fuel and the cladding and connected to the plenum (space left between the top plug and the first fuel pellet in the rod). This free volume enables

to accommodate fuel swelling and gaseous FP released during fuel irradiation cycles. It is initially filled in He and pressurized at 10-30 bars in order to improve its thermal conductivity [7], [8].

The fuel pellets are produced by sintering at 1700°C during 4h under H_2. The initial density of the fuel pellets is set to 95 % d_{th} and the initial grain size is about 7-10 µm [5], [9]. In the case of MOX fuels, Pu from the recycling of spent UO_2 is added to fresh UO_2. Classically, the ratio of Pu/(U+Pu) ranges between 5 and 10%. The fabrication process used in the case of LWR MOX fuels is the MIMAS (Micronized MasterBlend) one [10]. It results fuel pellets with inhomogeneous microstructure shown in **Figure I-4** and composed of:

- PuO_2-rich agglomerates with a size ranging from 100 to 200 µm.
- UO_2-rich phase called matrix.
- Coating phase containing intermediate Pu content.

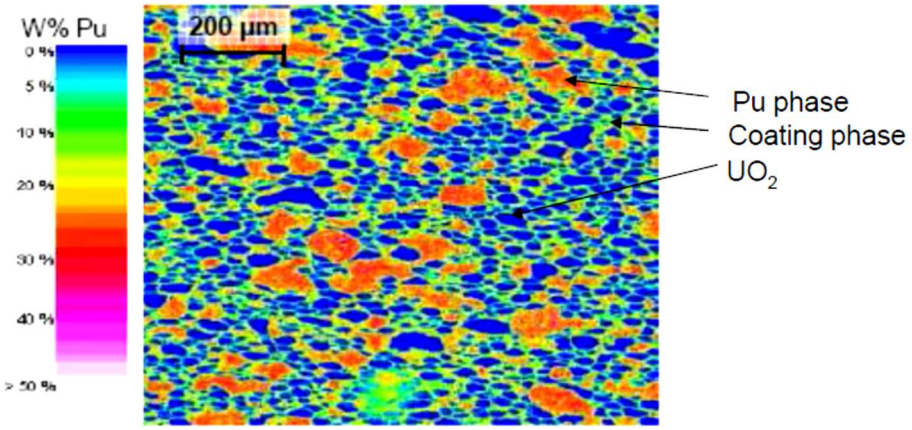

Figure I-4: Pu X-ray map showing the heterogeneous microstructure of MOX fuels

As shown in **Figure I-5**, UO_2 has a high melting temperature of 2852°C [11] and is able to accommodate a certain range of stoichiometry which varies with temperature (yellow region of the phase diagram) [12].

The Pu-O phase diagram assessed in the TAF-ID database [13], [14] on the basis of the Pu-O phase diagram proposed in [15] integrating the experimental data of [16] and [17] is presented in **Figure I-6**. The melting temperature of stoichiometric PuO_2 was measured by direct laser heating measurements to be around 2740°C [17].

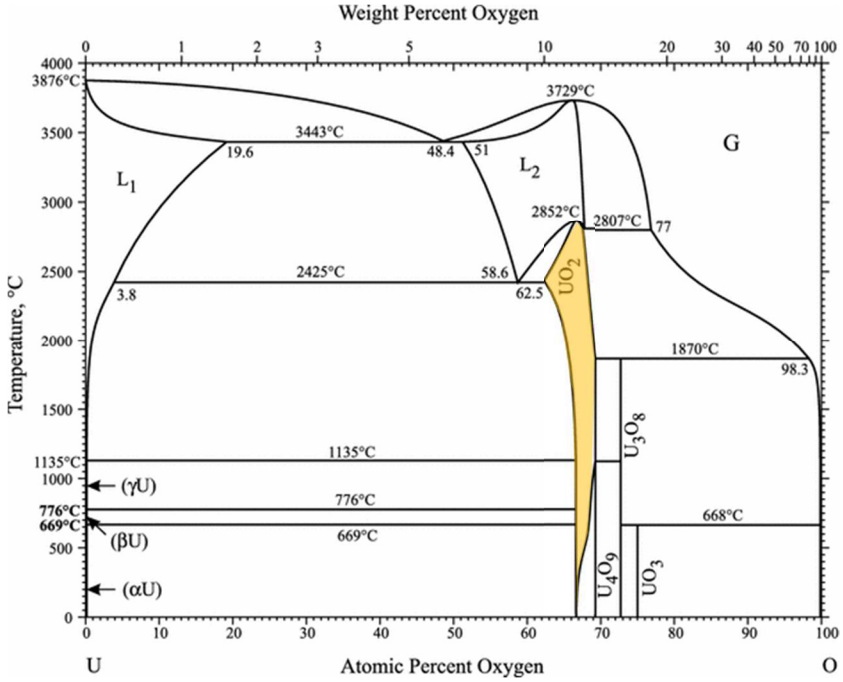

Figure I-5: U-O phase diagram extracted from [11].

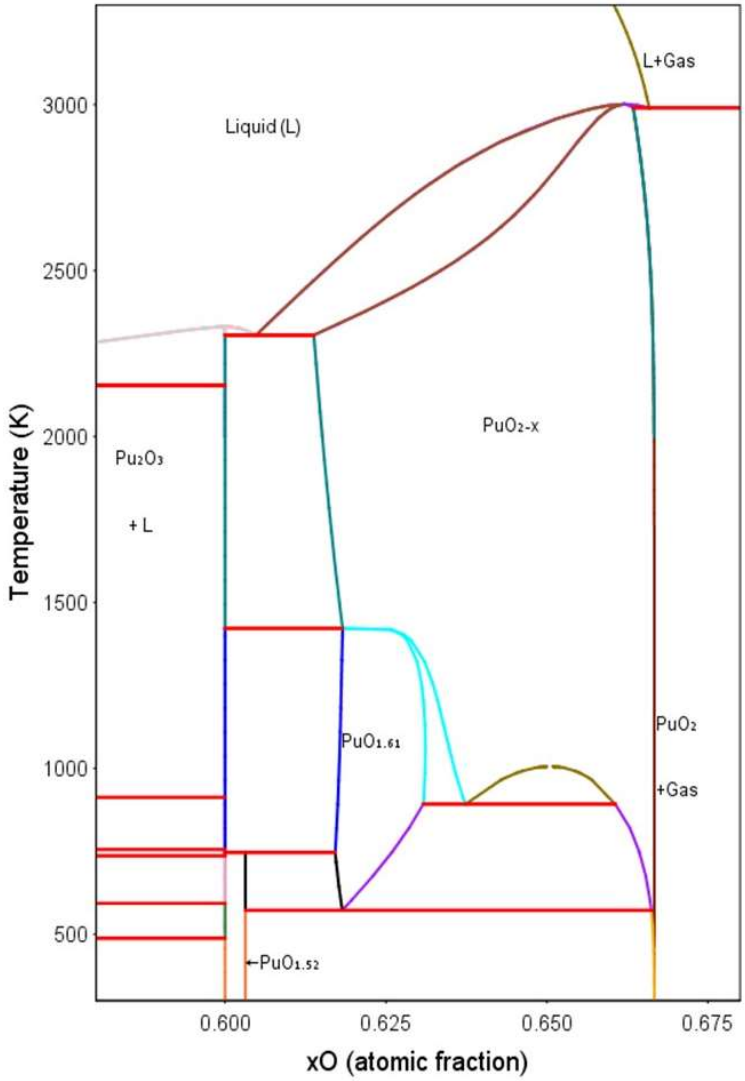

Figure I-6: Pu-O phase diagram from 58 to 68 at% O calculated using ThermoCalc [18] and the TAF-ID [13].

Stoichiometric U and Pu dioxides have a fluorine crystallographic structure (space group Fm-3m). As shown in **Figure I-7**, the metallic cations (U^{4+} and Pu^{4+}) are involved in the face centered cubic lattice in which the O^{2-} anions occupies the tetrahedral sites.

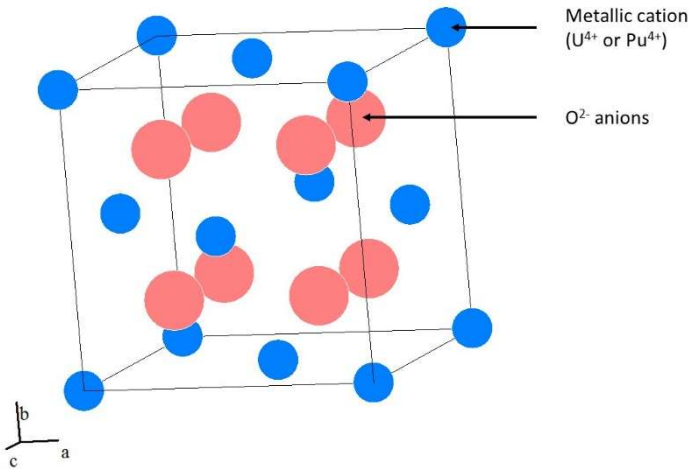

Figure I-7: Fluorine structure of the stoichiometric UO_2 and PuO_2 oxides

As the atomic radius of U and Pu are close, they can be substituted in the cationic structure and form solid solutions composed of $U_{1-y}Pu_yO_{2\pm x}$ (MOX) on a wild range of Pu content, as shown in the pseudo-binary diagram of **Figure I-8**. The minimum melting temperature for the system UO_2-PuO_2 has been measured by laser heating to be 2630-2730°C for a composition between 0.4 and 0.7 mol% of PuO_2 in [19].

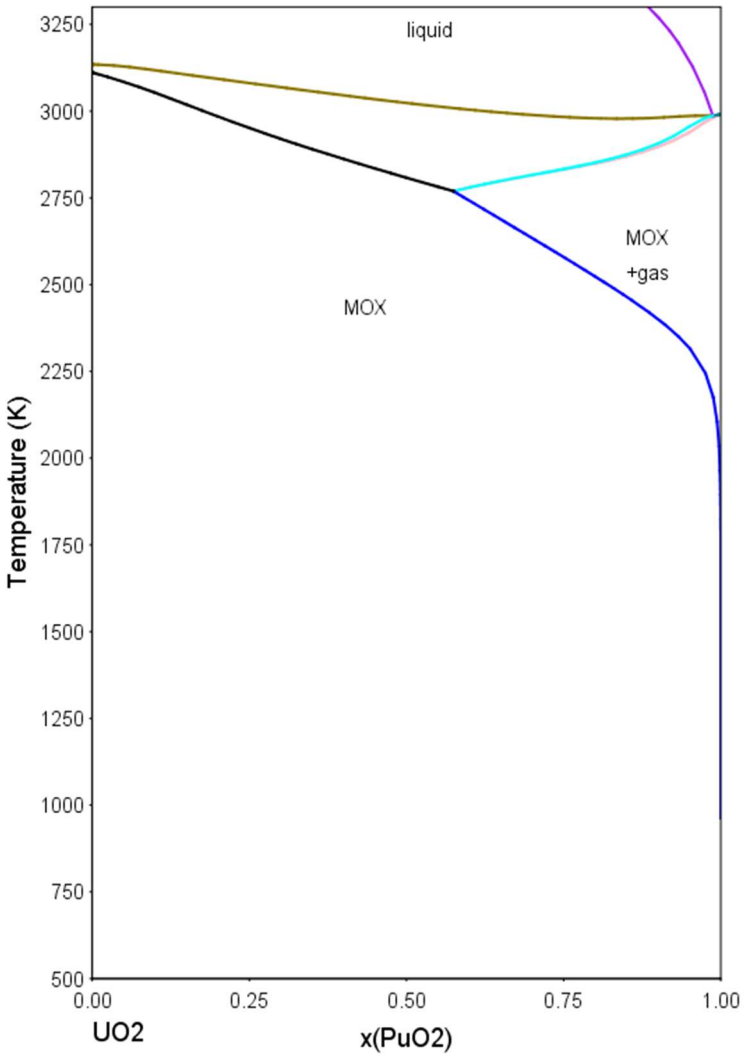

Figure I-8: Pseudo-binary diagram of the UO_2-PuO_2 system calculated using ThermoCalc [18] coupled with the TAF-ID [13].

I.2.2 Fuel evolution in normal operating conditions

I.2.2.1 Thermal evolution

Due to the poor thermal conductivity of UO_2 and MOX fuels [20], [21], a radial temperature gradient appears in the fuel pellet. Indeed, its periphery, closer to the coolant, is cooled more efficiently than the center of the pellet. In the typical range of linear power in a PWR (180 to 270 $W.cm^{-1}$), the temperature in the center of the fuel thus ranges from 900 to 1300°C whereas it is 500-600°C at the periphery of the pellets, as shown in **Figure I-9** [5]. The temperature difference observed between the inner face of the cladding and the periphery of the pellet is mainly due to the different nature of the materials (oxide / metal) and the gap filled in He.

During the irradiation cycles, the fuel undergoes chemical and physical evolutions, which can modify the temperature profile within the pellets. Moreover, in contact with water, a ZrO_2 layer is formed at the surface of the cladding, reducing its thermal conductivity. The gap between the fuel and cladding also tends to close during irradiation (swelling of the materials, pressure of the coolant on the fuel rods…).

The strong thermal gradients imposed to the fuel coupled to the defects induced by irradiation lead to the fracturing of the pellets in the first cycles of irradiation. They are also a driving force for the diffusion of elements within the fuel pellets, which can lead to gaseous FP release in PWR normal operating conditions [5].

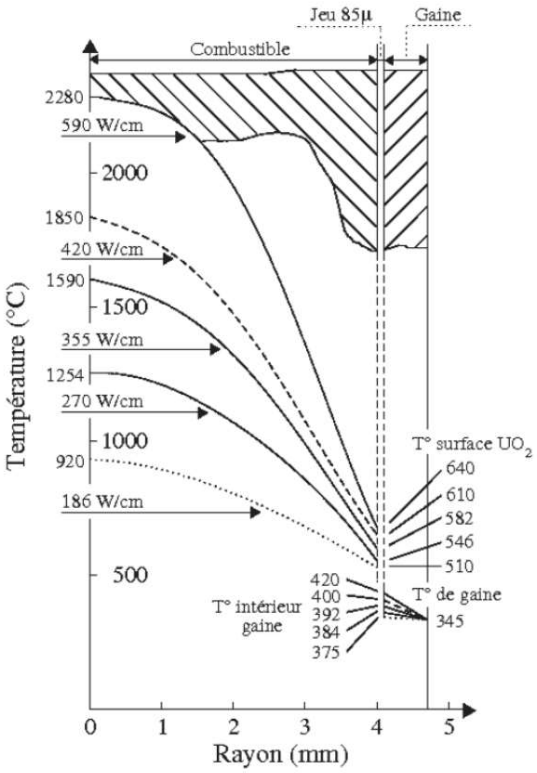

Figure I-9: Radial temperature profiles observed in a PWR fuel rod as a function of the linear power, extracted from [5].

I.2.2.2 Mechanical evolution

The thermal gradient applied on the fuel pellets leads to differential dilatation between the center and the periphery. This phenomenon induces tangential traction stresses on the pellet and given the fragile behavior of the fuel at the temperatures considered, axial cracking occurs in the first cycle of irradiation [22].

A densification occurs in the pellet which adopts a diabolo shape. Simultaneously, fission induces swelling of the fuel. Below 15 GWd.t_{HM}^{-1}, these effects combine and cause a contraction of the fuel. Above, the swelling of the fuel coupled to the irradiation creep of the cladding and the pressure of the coolant lead to the progressive closure of the fuel-cladding gap, which is almost complete for a burn-up of 30 GWd.t_{HM}^{-1}. These different phenomena are represented in **Figure I-10**.

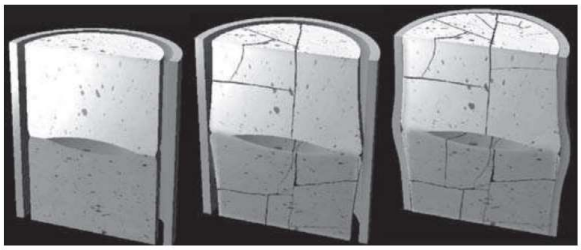

Figure I-10: Evolution of the fuel rod during irradiation extracted from [4]: cracking of the fuel pellets, appearance of the diabolo shape and closure of the fuel-cladding gap. The space observed between two pellets is due to the dishing applied at the top and bottom surfaces of each pellets during their fabrication.

I.2.2.3 Microstructural evolution

I.2.2.3.1 High Burn-up Structure

Non fissile elements such as ^{238}U composing the main part of the fuel pellets are fertile elements. Given the neutron energy spectrum of a PWR, they are able to capture an epithermal neutron and turn into a fissile nucleus (i.e. ^{239}Pu) [23], [24]. This reaction has a higher probability to occur at the pellets periphery because of spatial self-shielding effect of the rods. As, ^{239}Pu has a higher probability to undergo fission compared to ^{235}U [25], the local burn-up in the periphery of the pellet or in the Pu agglomerates can be two to three times higher than in the rest of the pellet.

As soon as a threshold local burn-up of 50 $GWd.t_{HM}^{-1}$ has been reached at temperatures below 1100°C, the fuel undergoes restructuring [26]. The structure appearing is called High Burn-up Structure (HBS) and was characterized experimentally in LWR fuels in several studies [27]–[35]. The main characteristics of this HBS region are:

- High porosity (up to 20 %) linked to a high density of fission gas bubbles.
- High FP content and notably a high density of metallic precipitates composed of Mo, Ru, Rh, Pd and Tc.
- Grain subdivision resulting in submicronic grains of two types [32]: the polyhedral subgrains observed in the bulk of the HBS region have a size up to 0.8 µm and round subgrains with a size around 0.1 µm are surrounding by gas bubbles and open surfaces.

In LWR UO_2 fuels, the HBS extends in the very periphery of the pellets on several µm at 40 $GWd.t_{HM}^{-1}$, up to more than 1 mm beyond 100 $GWd.t_{HM}^{-1}$ [35]. A picture of the periphery of a PWR UO_2 fuel pellet irradiated up to a burn up of 70 $GWd.t_{HM}^{-1}$ is shown in **Figure I-11**.

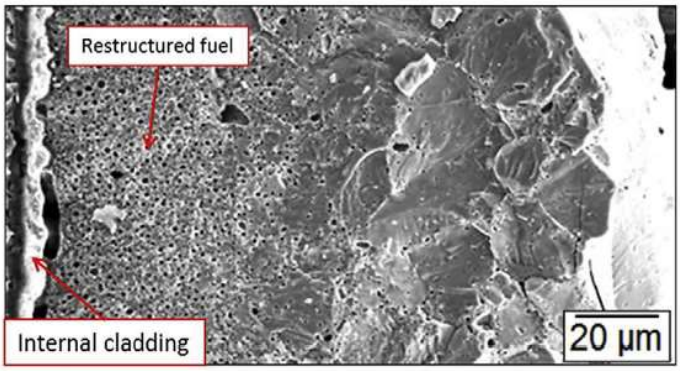

Figure I-11: Fractography of the periphery of a PWR UO_2 fuel irradiated up to a burn-up of 70 $GWd.t_{HM}^{-1}$ [36].

The behavior of MOX fuel is more complex than UO_2. Indeed, typical HBS develops only in the Pu agglomerates where the local burn-up overcomes the HBS formation threshold (up to mid pellet radius). These agglomerates appear as dark phases in Optical Microscopy (OM), due to their high porosity. The restructuration limit in LWR irradiated MOX pellets is usually set around 0.5 R (where R is the pellet radius). Pu agglomerates in the center of the pellet are hardly distinguishable as few porosity is present [33], [34]. Moreover, the size of fission gas bubbles and subgrains increase in the higher temperature region of the fuel (towards the center of the pellet) [27].

This restructuration of the pellet induces a decrease of the thermal conductivity as well as softening of the fuel in the HBS region [26].

I.2.2.4 Chemical evolution

I.2.2.4.1 Oxygen potential

Due to the fission reaction, the fuel chemistry is also strongly impacted. Indeed, several new elements are created in the fuel and can react with it. The majority of these elements have an oxidation state inferior to U or Pu in the fuel which globally implies an increase of the oxygen on metal ratio (O/M [2]) in the pellet.

This O/M value enables to calculate the oxygen potential[3] in the fuel, which plays a major role on the reactivity of the different FP, the fuel and the cladding. Indeed, as shown in **Figure I-12**, an element M having a Gibbs energy below the fuel oxygen potential is able to react with O and form an oxide (MO_x). Conversely, if the Gibbs energy of the reaction M + x/2 O_2 → MO_x is over the fuel oxygen potential, it stays as an element in the fuel matrix as a metal for example.

As the equilibrium oxygen potential of Zr/ZrO_2 is below the ones of U/UO_2 and Pu/PuO_2, the internal part of the cladding will thus oxidize as soon as a fuel-cladding contact is set, enabling O to diffuse. This reaction would consume the excess of oxygen available at the periphery of the fuel leading to a decrease of the O/M ratio at the periphery of the fuel.

[2] The O/M ratio is defined as the total amount of O on the sum of the amount of elements found as oxides (U, Pu and all the oxide FP dissolved or not).

[3] The oxygen potential is defined as $\Delta G_{O2} = RT \ln p_{O2}$ where R is the ideal gas constant, T is the temperature and p_{O2} is the oxygen partial pressure.

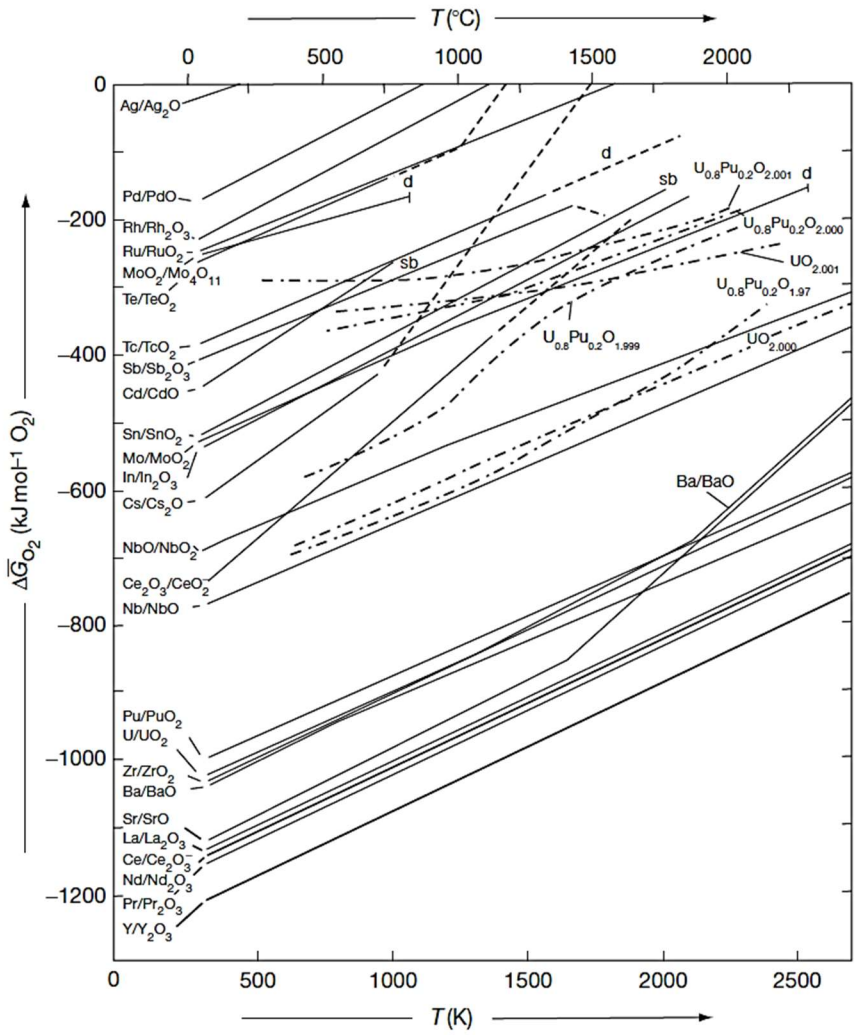

Figure I-12: Ellingham diagram describing the relative partial molar Gibbs free energies of oxygen of the fission product oxides, $UO_{2\pm x}$ and $U_{0.8}Pu_{0.2}O_{2\pm x}$ extracted from [37].

Finally, due to the radial thermal gradient and O concentration gradient present in the fuel pellet, the oxygen can diffuse from the center (hottest area) to the periphery (coolest area). This oxygen redistribution thus contributes to an increase of the oxygen potential in the periphery of the pellet, which will still stay inferior to the oxygen potential in the center of the pellet.

According to the work of [38]–[40], the oxygen potential in UO_2 LWR fuels with burn-ups from 30 to 75 GWd.t_{HM}^{-1} would range from -440 kJ.mol_{O2}^{-1} in the periphery of the pellets to -340 kJ.mol_{O2}^{-1} in the center. As shown in **Figure I-13**, this range of oxygen potential at the temperature of the fuel is close to the oxidation of Mo in MoO_2. Oxygen buffering of the fuel by the Mo/MoO_2 couple thus maintains the oxygen potential of the fuel quasi-constant (around -450 kJ.mol_{O2}^{-1} at 750°C in the periphery) in normal operating conditions [38], [39].

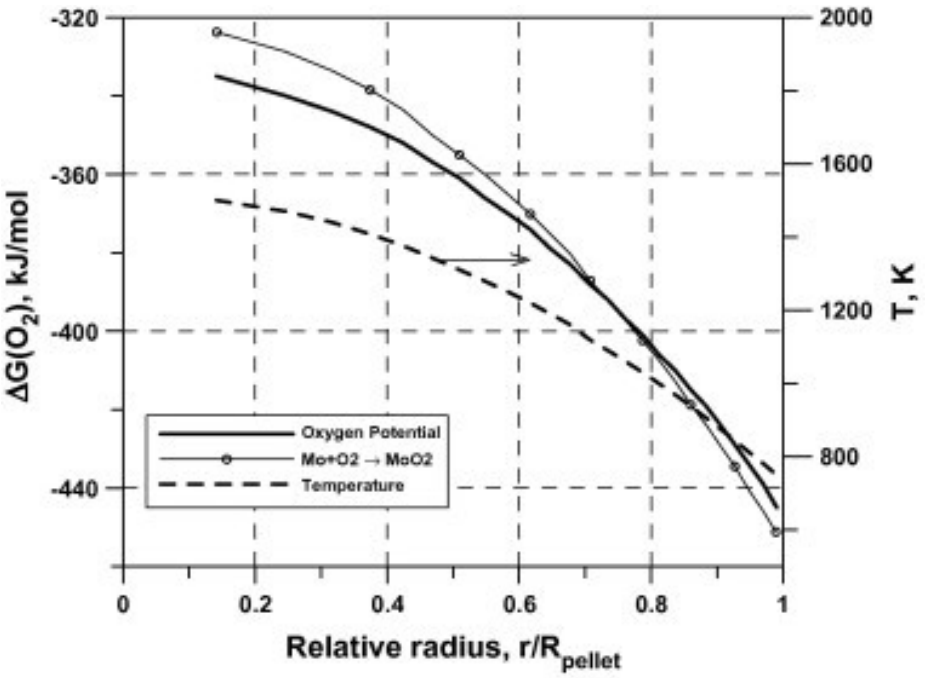

Figure I-13: Temperature profile and calculated oxygen potential as a function of the radial position in the high burn-up region, extracted from [40].

As shown in **Figure I-12**, the equilibrium oxygen potential of stoichiometric UO_2 is slightly lower than the one of stoichiometric $U_{0.8}Pu_{0.2}O_{2.00}$ in the nominal temperature range of a PWR. Thus, the oxygen potential in stoichiometric MOX fuel is slightly higher than in stoichiometric $UO_{2.00}$. Thus, at 1000°C for a LWR MOX fuel with a burn-up of 100 $GWd.t_{HM}^{-1}$, the stoichiometry is reached for an oxygen potential of -400 $kJ.mol^{-1}$ (about 80 $kJ.mol^{-1}$ above $UO_{2.00}$) [41]. The oxygen potential in MOX fuels decreases with O/M and Pu content [42], [43].

I.2.2.4.2 Fuel-Cladding Interaction

As stated in the previous paragraph, the oxygen potential equilibrium of Zr/ZrO_2 is under the ones of U/UO_2 and Pu/PuO_2 (**Figure I-12**) inducing the formation of an oxide layer in the inner surface of the cladding during in-pile irradiation.

Post-irradiation observation performed on LWR fuels highlighted the presence of a bonding layer resulting of the interpenetration of the HBS region of the fuel pellet and the ZrO_2 layer of the cladding. The thickness of this layer depends on the burn-up of the fuel and is typically in the range of 10 to 15 µm in the burn-up range 40-70 $GWd.t_{HM}^{-1}$ [27], [30].

LWR MOX fuels with a burn-up of 42 $GWd.t_{HM}^{-1}$ and a composition UO_2 + 5% PuO_2 obtained by a co-milling process were analyzed in the work of [33]. The size of the Pu agglomerates were 100 µm in average. The bonding layer of the Zircaloy-4 cladding near these agglomerates was two times thicker than near the UO_2 matrix. This was inferred to the higher oxygen potential in the Pu agglomerates due to the higher yield of Pu fission compared to U.

RAMAN spectroscopy and Electron Probe Micro-Analyses (EPMA) characterizations performed in [44], [45] on PWR UO_2 fuel irradiated up to 58.7 $GWd.t_{HM}^{-1}$ in its Zircaloy-4 cladding revealed three different crystallographic layers in the inner oxide layer of the cladding. Near the fuel pellet, a tetragonal ZrO_2 structure, probably stabilized by irradiation and FP implantation and corresponding

to the bonding layer was observed. Then a monoclinic ZrO_2 structure followed by a "damaged tetragonal" ZrO_2 structure were observed. The latter may have been stabilized by compressive stresses or hypostoichiometry close to the metal-oxide interface. Tests realized on model materials revealed no effect of the type of cladding on the fuel-cladding interactions. Nevertheless, hyperstoichiometric fuel induced more rapid Zr-U interdiffusion leading to the quicker growth of the bonding layer.

I.2.3 Fission products chemical state in normal PWR operating conditions

During their formation by fission, the FP are implanted in the fuel in an elemental form. Thanks to the radial temperature and oxygen potential gradients present in the fuel pellet, they are then able to diffuse and react chemically with the surrounding elements (fuel, cladding or other FP). These chemical reactions can occur depending on FP solubility, temperature, burn-up, oxygen potential, type of fuel and the decay channel of FP... Kleykamp proposed a classification of the FP according to their reactivity in [46]:

1- Gases and volatile FP (Xe, Kr, Br and I).
2- Metallic precipitates (Mo, Tc, Ru, Rh, Pd, Te, Ag, Cd, In, Sn and Sb).
3- Oxide precipitates (Ba, Cs, Zr, Nb, Mo, Te and Rb).
4- Dissolved in the fuel matrix (Sr, Zr, Nb, Y, La, Ce, Pr, Nd…).

Continuous transitions occur between group 2, 3 and 4 mainly depending on temperature, oxygen potential and burn-up.

The typical metallic precipitates observed in irradiated fuels are composed of Mo-Ru-Rh-Pd-Tc and known as white inclusions due to their color in OM observations. These elements have a very low solubility in the fuel (e.g. Mo which has a maximum solubility of 0.002 wt% in UO_2 at 2173 K and 0.02 wt% in $U_{0.8}Pu_{0.2}O_2$) [47].

The ones observed in the center of the pellets generally have a size in the range of 10 µm whereas they are smaller in the periphery (HBS, around 1 µm) [34]. This is probably due to the higher temperature in the center of the fuel, enhancing the migration of the small precipitates formed by the accumulation of metallic FP.

In [33], metallic FP were characterized at the center and at the periphery of a LWR MOX fuel pellet containing 5 % of Pu (burn-up of 44 $Gwd.t_{HM}^{-1}$). Almost all the precipitates analyzed were in the hcp domain of the quinary Mo-Ru-Rh-Pd-Tc system. The Mo content was shown to decrease in these metallic phases toward the periphery (Mo/Ru ≈ 0.5 compared to 1 in the center). This is consistent with the oxygen potential in the HBS region in the periphery of the pellet, which becomes higher than the equilibrium free energy of Mo/MoO_2 (**Figure I-13**) enabling Mo to be oxidized.

In the study by [47], the maximum solubility of Cs in UO_2 was measured to be 0.07 wt% at 1900°C. Some submicronic precipitates containing Cs were observed all over the pellet radius but no particular association with other elements was detected [33]. Cs has also been found with I but only

on the inner surface of the cladding, which have been attributed to a recoil effect[4] rather than to a reaction between Cs and I.

The maximum solubility of Ba in UO_2 fuel has been measured to be 0.3 wt% at 2173 K and 0.6 wt% in $U_{0.8}Pu_{0.2}O_2$ [47]. In PWR fuels, no association between Ba and other elements have been observed in normal operating conditions. Ba is only found dissolved in the fuel or in submicronic BaO precipitates [31], [36].

Thus, in PWR fuels in normal operating conditions, the main phases that can be identified are the metallic precipitates, also known as white inclusions, and the fission gas bubbles [26], [30], [36], [46], [48]–[50]. Other FP such as Cs or Ba are found in undefined phases in the fuel.

[4] FP can be implanted at several µm from the point where they were created because of the energy freed during the fission process

I.3 NUCLEAR SEVERE ACCIDENT

I.3.1 Phenomenology

A severe accident is a hypothetical scenario implying fuel degradation with the meltdown of at least part of the core of the reactor. This situation can only take place if an accumulation of malfunctions or failure appears. If the accident cannot be stopped in the vessel of the reactor by cooling the core, this can lead to the radiological barriers failure and to radioactive materials release in the environment. To be able to set up the appropriate safety systems during the design of a reactor in order to avoid this type of situation or to mitigate the consequences of the accident in case it happens, the issue is to:

- Identify all the physical phenomena occurring during the development of the accident.
- Determine the different scenarii leading to this situation.

The main phenomena taking place during a severe accident progress are detailed hereafter [4].

I.3.1.1 Core uncovery

The first event supposed to take place in the severe accident phenomenology is the loss of coolant around the core. The initiating event can be a Loss of Coolant Accident (LOCA), which suppose a breach in the wall of the primary circuit leading to its depressurization and to the vaporization of the water around the core.

In a PWR, several safety systems are available to control the core reactivity, maintain the cooling of the rods and evacuate the residual heat. Indeed, the reactor will automatically stop thanks to the insertion of the control rods, the security water injection (containing neutron poisons) as well as a water spraying system will also start. The severe accident scenarii imply the failure of at least one of these systems enabling the core temperature to rise.

The duration of this phase (from few tens of minutes to several days) mainly depends on the initiating event.

I.3.1.2 Fuel rods damaging

Because the core cannot be cooled anymore, the temperature of the fuel rods will rise, causing cladding deformation around 700 to 900°C.

Moreover, due to the depressurization of the primary circuit, the water is vaporized leading to rapid oxidation of the fuel cladding according to the reaction (1). This reaction is enhanced around 1200°C and even further at 1500°C, as oxygen diffusion is improved in the tetragonal and cubic zirconia.

$$Zr_{(s)} + 2H_2O_{(g)} \rightarrow ZrO_{2\,(s)} + 2H_{2\,(g)} \qquad (1)$$

The production of H_2 during the Zr oxidation modifies the H_2O/H_2 ratio around the fuel. The oxygen potential imposed by the gas phase on the fuel-cladding system changes from an oxidizing steam atmosphere to a more reducing one. This H_2 can also be transported out of the primary circuit in the containment and trigger explosions.

Moreover, this highly exothermic reaction causes additional increase of temperature in the core and embrittlement of the cladding as ZrO_2 is formed. In parallel, as the temperature increases, FP release

from the fuel pellets is enhanced. From 1200°C, the cladding can fail leading to FP release in the primary circuit.

I.3.1.3 Core meltdown

Schematically, from 900°C to 1800°C, the metallic component of the core will melt or vaporize. Interactions between metallic and oxide elements may result in eutectic formation and cause early melting of the fuel (before 2800°C).

The core meltdown results in a complex liquid solution called corium which is kept in the liquid state because of the residual heat produced by the radioactive decay of FP trapped in it. This corium will then relocate in the lower vessel wall which may fail in few tens of minutes.

At this stage, reflooding the damaged core with water is needed to stop the progressing corium and prevent its possible interaction with the concrete composing the containment. However, this may enhance the oxidation of the corium leading to H_2 and further heat production. FP release can also be impacted as thermal shock could cause debris bed formation.

I.3.1.4 Containment failure

If the corium comes in contact with the concrete walls of the containment, concrete-corium interaction takes place leading to the massive production of gas. This phenomenon will increase the pressure in the containment. Coupled to other event such as steam or H_2 explosion, it can thus trigger containment failure and radioactive materials (e.g. FP) release in the environment.

I.3.2 Classification

The radiological consequences of a severe accident are linked to the source term. This concept is related to the nature, quantity and kinetics of the radioactive emissions of a nuclear installation. Three types of source terms have been defined depending on their severity:

- S1: failure of the containment at short term (within few hours after the accident started).
- S2: direct release in the atmosphere due to the failure of the containment several days after the accident started.
- S3: indirect and delayed release in the atmosphere after filtration and retention of FP.

In order to make it simpler for people to understand the severity of nuclear accidents, the INES (International Nuclear and radiological Event Scale) has been created by the International Atomic Energy Agency and Organization for Economic Cooperation and Development/Nuclear Energy Agency. It consists in 8 layers from 0 (being termed as deviation from normal operating conditions) to 7 (being a major accident) as shown in **Figure I-14** [51]. It is based on three criteria:

- The consequences of the event outside the nuclear site over people and the environment (radioactive release in the environment).
- The consequences inside the nuclear site on the radiological barriers and control.
- The impact on the in-depth defense in case of events in which several measures aiming at preventing the accident did not work as expected.

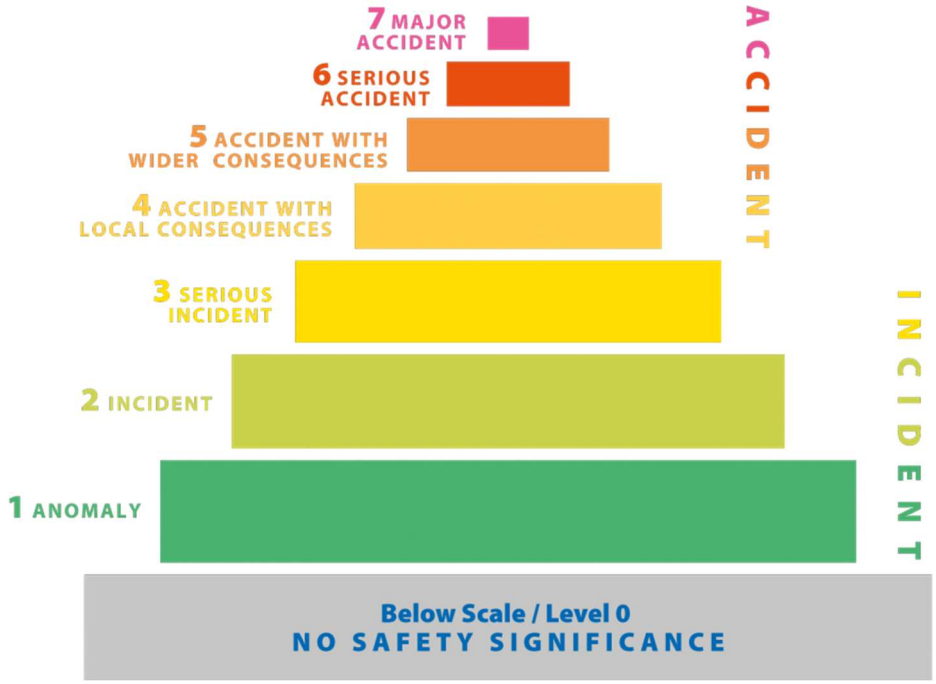

Figure I-14: INES scale extracted from [51].

I.3.3 Main severe accidents in history

Three main severe accidents occurred on LWR from the beginning of the civilian nuclear power history. In 1979 in the USA an accident rated 5 on the INES scale happened in the Three Mile Island (TMI) power plant. In 1986 in Ukraine, the Tchernobyl accident was classified as level 7 (major accident) as the Fukushima-Daiichi event that occurred in 2011 in Japan.

I.3.3.1 Three Mile Island

The TMI station was composed of two reactors. The accident occurred in the second one (TMI-2) which had a power of 800 MWe. It started with a failure in the water supply of the steam generators which prevented heat removal from the core leading to a temperature and pressure increase in the primary circuit. Then, a combination between operators' mistakes and a failure of security elements led to a LOCA type accident. 16h after the beginning of the accident, core cooling could be restored.

Despite the fact that 45 % of the core melted during the accident, the containment resisted limiting the source term. Indeed, more than half of the gaseous and volatile FP were released in the primary circuit and the containment but only 0.01 % of the initial FP core inventory was released in the environment.

This first nuclear severe accident triggered deep analyses and reflections on the nuclear risks as such a situation had never been considered before. The power plant's instrumentation, examinations of the core debris and calculation codes provided information on the final state of the core and on the accident scenario. This event raises also a lot of questions concerning the accidents phenomenology, notably on the behavior of the core during the accident and during reflooding with water [4].

I.3.3.2 Tchernobyl

The Tchernobyl station was composed of four RBMK (Reactor Bochoï Molchnasti Kanlnyi). These Boiling Water Reactors (BWR) are moderated with graphite and closed by a concrete block. The

accident occurred on the reactor number 4 which had a power of 1000 MWe during a test aiming at testing the circulating pumps of the reactor in case of a loss of external electrical power supply. The non-compliance with the safety procedures and the conditions of the test led to a Reactivity Induced Accident (RIA) and steam explosion.

Fragmentation and later on melting of the fuel occurred as well as the destruction of the containment leading to huge release of radioactive materials in the environment. Indeed, 1/3 of the release took place at the time of the accident (mainly gaseous and volatile FP) and 2/3 took place on the 10 following days, as the core temperature increased. Finally, almost 100 % of the gaseous FP, 50-60 % of I, 20-40 % of Cs and 3-6 % of other elements were released in the environment.

This accident is the most severe towards the environmental contamination. The way authorities managed the crisis led to questioning about transparency concerning the information about civilian nuclear activities (e.g. INES scale). It also reinforced the need for research on the reactor components behavior in severe accident conditions and raised also the issue on the possible long term effects of a such an event [4].

I.3.3.3 Fukushima-Daiichi

The Fukushima-Daiichi station was composed of six BWR (1 to 6). The units 1 (460 MWe), 2 (784 MWe) and 3 (784 MWe) were running at full power whereas the 4 (784 MWe), 5 (784 MWe) and 6 (1100 MWe) were shut down for maintenance. First, an earthquake of magnitude 9 on the Richter scale occurred triggering automatic shutdown of the reactors 1 to 3. An hour later, a Tsunami hit the station leading to the loss of internal cooling systems and provoking a station blackout. The reactors 1 to 3 thus underwent a LOCA. Hydrogen explosions occurred in units 1, 3 and 4 leading to the failure of the containment and to radioactive materials release.

Up to now, the release are estimated to be around 25 % of the Tchernobyl ones concerning I, 45 % concerning Cs and 0.01 to 0.1 % for the other elements. Concerning the gaseous FP, 100 % of the initial inventory of the units 1 to 3 cores would have been released. Besides the atmospheric releases, a significant amount of FP passed in the groundwater and ocean through contaminated water discharges during the accident.

The analysis of this accident is far from being complete. However, even if the global phenomenology of this severe accident is rather well understood nowadays, some uncertainties remain on the complete scenario of the Fukushima-Daiichi accident. Several techniques have thus been developed in order to be able to have access to the state of the core (robots, laser cutting… [52]) which will provide the information needed to understand the accidental sequence. This event also pushed the French nuclear power plants owners to design safety systems that guarantee water, air and electrical power supply whatever the situation.

I.3.4 Prediction of the consequences in term of contamination

These three severe accidents, and particularly the first one (TMI-II accident), stressed out the need to understand the physical phenomena occurring, the scenario of the accidental sequence as well as to predict accurately the radiological consequences in such conditions. Several tools have thus been developed in order to be able to understand the behavior of a nuclear facility in case of a severe accident and accurately assess the source term, depending on the accidental scenario.

Among them, many research programs were initiated all over the world to understand the behavior of the fuel, FP and structural materials thanks to integral (STEP [53], ACRR [54], [55], PBF [56]–[59], LOFT-FP [60], PHEBUS-FP [61]…) or analytical tests (ORNL tests [62], CRL tests [63], VEGA [64], HEVA [65], VERCORS [66] or VERDON [67], COLOSS [68]…). The integral tests enabled to determine the main parameters influencing the degradation of the core and the release of FP. The effects of these parameters were then studied in analytical or separate-effects tests.

As shown in **Figure I-15**, the results of both types of tests were used to build physical models and to develop integral (MAAP [69], [70], MELCOR [71], THALES [72], ASTEC [73]…) and mechanistic codes [74]. These codes also need to be validated. First, the physical models are checked using specific analytical tests which can be performed on irradiated or simulated fuels. The codes are then qualified using the results of integral tests to check the coupling between the different physical phenomena.

Finally, these codes enable to simulate a whole accident or specific phenomena of the accidental sequence. They are used as tools in the safety design of the reactors, to check the dimensioning of the facilities and to help managing the crisis during a real accident (e.g. predict the consequences in term of contamination, understand the accidental scenario). Therefore, these codes need to give accurate results, notably when it comes to the source term of a real accident.

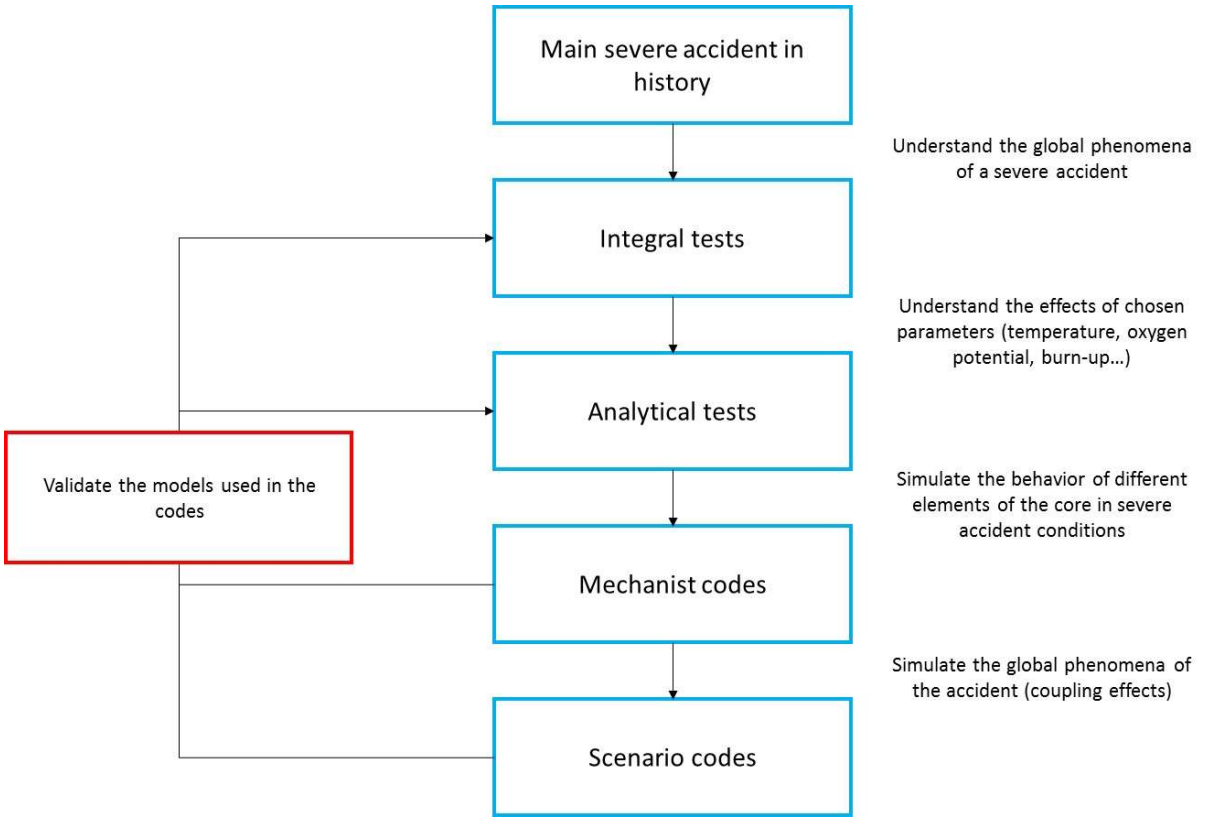

Figure I-15: Global method to understand the development of a severe accident and predict its consequences in term of contamination.

These different tools highlighted that FP release from the fuel was highly impacted by their chemical reactions in the fuel (i.e. the speciation of FP as already mentioned in **section I.2.3**) according to four main parameters:

- The temperature enhancing diffusion of FP in the fuel.

- The oxygen potential, namely the H_2O/H_2 ratio around the fuel during the accidental sequence. It plays a role on the release kinetics (volatile FP) as well as on the final quantity of FP released (notably in the case of the semi and low volatile FP).
- The type of fuel (UO_2, MOX, burn-up) modifying the creation ratios between the FP and the microstructure of the fuel (heterogeneous in the case of MOX fuels).
- The state of the fuel (debris bed, liquid…) providing more or less paths for FP diffusion or migration out of the fuel.

Thus, to understand the FP release mechanism, it is important to understand the fuel behavior during the accidental sequence and the chemical reactions that can involve FP. In the following subsections, a literature review of the available post-tests characterizations concerning the evolution of the state of the fuel and FP in temperature and oxygen potential is given. Special attention has been paid on the behavior of Cs, Mo and Ba because of:

- Their fission yield. As shown in **section I.2.1**, Cs, Ba and Mo are among the most abundant FP to be created during the thermal fission of ^{235}U and ^{239}Pu.
- Their radiological impact in case of release in the environment depends on their half-lives and the nature of the radiation they emit during decay. For example, ^{137}Cs has long term consequences on human health [75].
- Their contribution to the residual heat generated in the fuel or in the corium. This is particularly the case for ^{140}Ba which significantly contributes to the residual power through its decay to ^{140}La [76].
- Their chemical reactivity which can strongly impact their volatility. This mainly the case of Mo, which can be easily oxidized to MoO_2 in normal PWR operating conditions, acting as an oxygen potential buffer. Moreover, Mo is able to react with many other elements such as Cs, Ba, Ru…

Even though, Cs is known to form very stable compounds with I (CsI [37], [46], [77], [78]), its fission yield is approximately ten times higher than the one of I in the type of fuels considered here. Moreover, I chemistry constitutes a whole subject in itself. Thus, **the interactions between Cs and I will not be considered in this study**.

I.4 EXPERIMENTAL RESULTS CONCERNING THE FUEL AND FP EVOLUTION IN SEVERE ACCIDENT CONDITIONS

I.4.1 Irradiated fuels studies

Post-test characterization campaigns were performed on the fuel after some integral and analytical tests in order to understand the phenomena involved in the loss of integrity of the core and FP speciation. The main experimental results obtained on irradiated fuels and available on these two topics are summarized in this section.

I.4.1.1 TMI-2 accident

The corium coming from the damaged core of the TMI-2 reactor was analyzed [79], [80] and three main types of solid solutions involving Zr and U were identified:

- Cubic solid solution (fluorite) represented the majority of the sample (up to 90 vol%).
- Monoclinic solid solution was attributed to $U_{1-x}Zr_xO_2$ with x = 0.9.
- Tetragonal solid solution was attributed to $U_{1-x}Zr_xO_2$ with x = 0.75.

The last phase does not exist at thermodynamic equilibrium and can be explained by a diffusion-less transformation of the cubic phase below 2100°C as already observed by [81]. In the study by [80], the same trend is reported for prototypical PWR corium composed of 80 wt% UO_2 and 20 wt% ZrO_2 heated up to 2700°C in the VULCANO facility of the PLINIUS plateform [82]. They ended up with a two phase system with a cubic solid solution and a tetragonal one with a composition of $U_{0.4}Zr_{0.6}O_2$ and proposed a meta-stable phase diagram accounting for the tetragonal meta-stable region in the $UO_2 – ZrO_2$ system.

I.4.1.2 PHEBUS-FP integral tests

The objective of the PHEBUS FP program was to study the different phenomena occurring in severe accident conditions. More precisely, this program addressed:

- The fuel degradation phenomena until the formation of a molten phase.
- The production of H_2 through the oxidation of the cladding tubes.
- FP release from the core and their transport through the primary circuit and containment, the physics of aerosols and the chemistry of I.

Five in-pile tests were thus carried out in the Phébus reactor on a fuel assembly composed of 20 fuel rods and 1 control rod of around 1 m high except the FPT-4 test, which was performed with a UO_2/ZrO_2 debris bed. The steam generator was simulated by a U-inverted tube and the containment by a 10 m^3 tank containing water and gas. This facility was representative of a PWR of 900 MWe with a scale of 1/5000 (**Figure I-16**). Different conditions of atmosphere, fuels and temperatures were tested as extensively described in [61], [83] and summarized in **Table I-2**. Extensive on-line and off-line instrumentation was used on each test as described in [84].

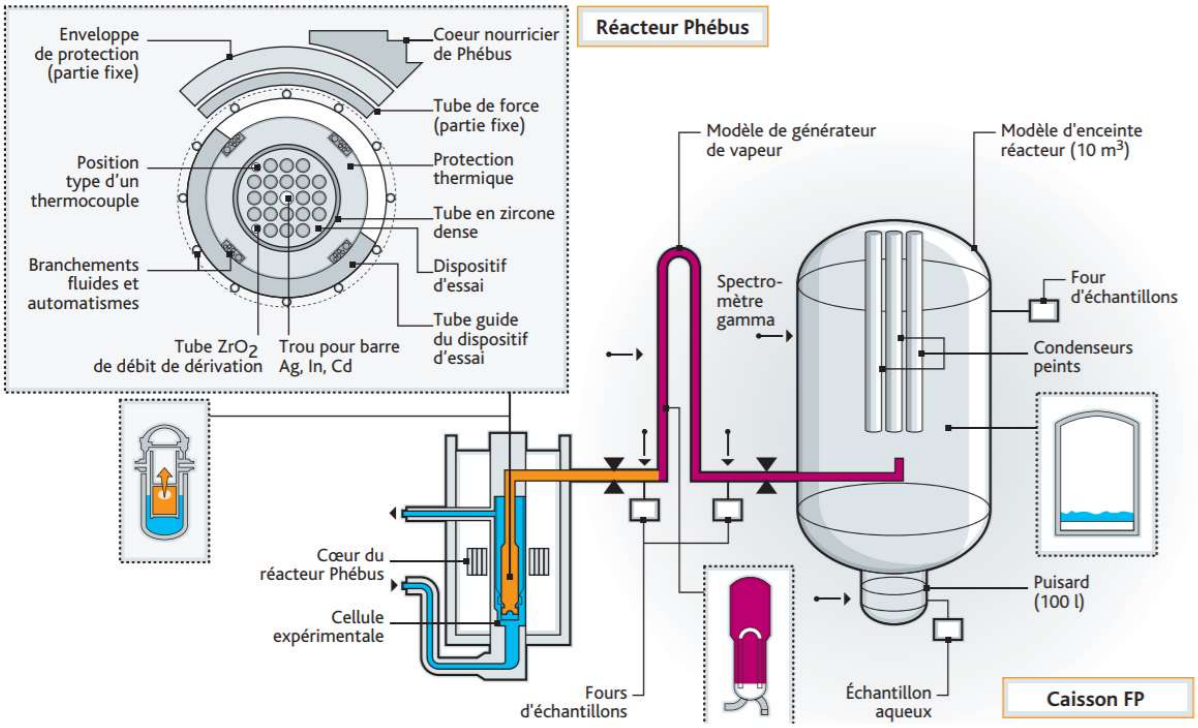

Figure I-16: Schematic view of the Phébus-FP experimental core and facility extracted from [4].

Table I-2: Phebus FP program test grid

Test	Fuel type	Temperature (°C)	Atmosphere	Date	Reference
FPT-0	Fresh UO_2 fuel pre irradiated Zircaloy-4 cladding Ag-In-Cd rod	455 to 2600°C	Mixture H_2O/H_2 rich in steam	12/1993	[85], [86]
FPT-1	UO_2 fuel with a burn-up of 23 $GWd.t_{HM}^{-1}$ Reirradiation Zircaloy-4 cladding Ag-In-Cd rod	455 to 2230°C	As FPT-0	07/1996	[86], [87]
FPT-2	As FPT-1	625 to 2225°C	Poor steam conditions (-400 to -135 $kJ.mol^{-1}$)	10/2000	[86], [87]
FPT-3	As FPT-1 B_4C rod	614 to 2000°C	As FPT-2	11/2004	[86], [88]
FPT-4	Debris bed UO_2/ZrO_2 Burn-up of 38 $GWd.t_{HM}^{-1}$ No reirradiation	400 to 2500°C	Steam	07/1999	[86], [89]

Globally, the Phébus-FP program enabled to progress on the understanding of the interactions between the fuel and other materials [90], [91] on FP release and transport and on the cladding oxidation phenomenon [92] leading to major improvement of the calculation codes.

Besides the instrumentation used during the tests, fuel samples were recovered after the tests and characterized mainly through OM, Scanning Electron Microscopy (SEM), X-ray tomography and EPMA. The results of post-test characterizations performed in the case of the FPT-0, 1 and 2 tests are summarized below.

The PHEBUS FPT-0 and FPT-1 tests were conducted on UO_2 up to 2600°C and 2230°C respectively in rich steam atmosphere. At the end of the tests, X-ray tomography analyses showed that respectively 50% and 70% of the fuel remained as pellets. Relocation and melting of the fuel happened in both cases, leading to a corium phase characterized by EPMA and composed of $U_{0.51}Zr_{0.46}O_{2\pm x}$ in the case of FPT-0 and $U_{0.48}Zr_{0.48}O_{2\pm x}$ in the case of FPT-1 with 1 to 2 % of Fe coming from the structural materials.

SEM observations combined with X-ray mapping showed that the periphery of the pellets located in the upper part of the bundle exhibited interconnected intergranular porosity and large bubbles up to 10 µm in diameter. At the center, partly interconnected intergranular pores and small (< 0.1 µm) intragranular pores were observed.

In the center of the pellets located at mid-height of the bundle, intergranular porosity interconnection was observed. At the periphery, highly porous (up to 80% porosity) foamy regions composed of U and Zr were found, corresponding to fuel-cladding interaction zones and liquid formation [93], [94].

The FPT-2 test was performed under poor steam conditions with a pure steam phase at the very end of the test, up to 2225°C on UO_2 fuel with a mean burn-up of 32 $GWd.t_{HM}^{-1}$. The oxygen potential was calculated to vary from -400 to -135 $kJ.mol^{-1}$ during the test.

During the cladding oxidation phase, the melting temperature of metallic Zr has been exceeded in the inner hotter rods of the bundle whereas the full oxidation of the cladding in the outer rods limited the fuel-cladding interaction.

The rods exhibited very small intragranular pores as well as poorly interconnected intergranular ones in the center of the pellets. In the periphery, foamy zones corresponding to molten regions of the fuel were also observed. These zones were more extended in the hotter rods. The corium composition has been determined by EPMA to be $U_yZr_{1-y}O_{2\pm x}$ with $0.6 < y < 0.7$.

In the center of the hottest pellets of the Phebus FPT-2 test, metallic precipitates containing Ru and Tc but no Mo were found as well as some phases containing Ba and Mo but not as precipitates. In the periphery, some precipitates containing both Ba and Mo were found as well as metallic inclusions composed of Ru, Tc, Rh and Pd without Mo. Cs release has been measured to be twice higher in the periphery compared to the center of the pellets [95], [96].

I.4.1.3 COLOSS analytical tests

The Core Loss of Geometry program [68] (COLOSS) took place from 2000 to 2003. Large-scale experiments in VVER and PWR configurations were performed on fresh and irradiated fuels. They had for objectives:

- Study the effects of B_4C on the gas production after oxidation and on the volatile FP behavior in severe accident conditions.
- Study irradiated and fresh fuel dissolution and fuel liquefaction, mainly on MOX fuel.
- Study the oxidation of the U-Zr-O system and the resulting production of H_2, particularly during core reflooding.

This program demonstrated that a phase separation appeared in the (U, Zr)O_2 mixture on cooling, leading to a U-rich phase containing 11 wt% of Zr and a Zr-rich phase containing 8 wt% of U and metallic Zr. Moreover, on the rod scale, different fuel dissolution states were observed, contrary to crucible tests. Locally, stronger fuel-cladding interactions were noticed, corresponding to areas where the pellet-cladding gap was narrower.

They also showed that the behavior of MOX and UO_2 fuels towards the fuel-cladding interactions at high temperature was similar. However, a considerable accelerating effect of irradiation on the fuel dissolution process was demonstrated. Two factors enhanced this dissolution:

- The thermal cracking enables melt penetration and assists fuel break-up.
- The fission gas release may enlarge the grain boundaries, may cause bubbles in the molten corium and more generally may enhance the contacts within the melt.

I.4.1.4 HEVA-VERCORS analytical tests

I.4.1.4.1 HEVA program

The HEVA program was launched at the CEA between 1983 and 1989 [65] and consisted in 8 tests aiming at studying the FP release in severe accident conditions. An induction furnace enabled heating three irradiated PWR fuel pellets in their original cladding up to 1630 to 2100°C under a gas mixture of H_2O/H_2. The burn-up range investigated was 19.4 to 36.7 GWd.t_{HM}^{-1}. Control rods materials (Ag-In-Cd) were also used. On-line gamma spectrometry as well as aerosols collections device were implemented in the experimental facility installed in a shielded cell (**Figure I-17**).

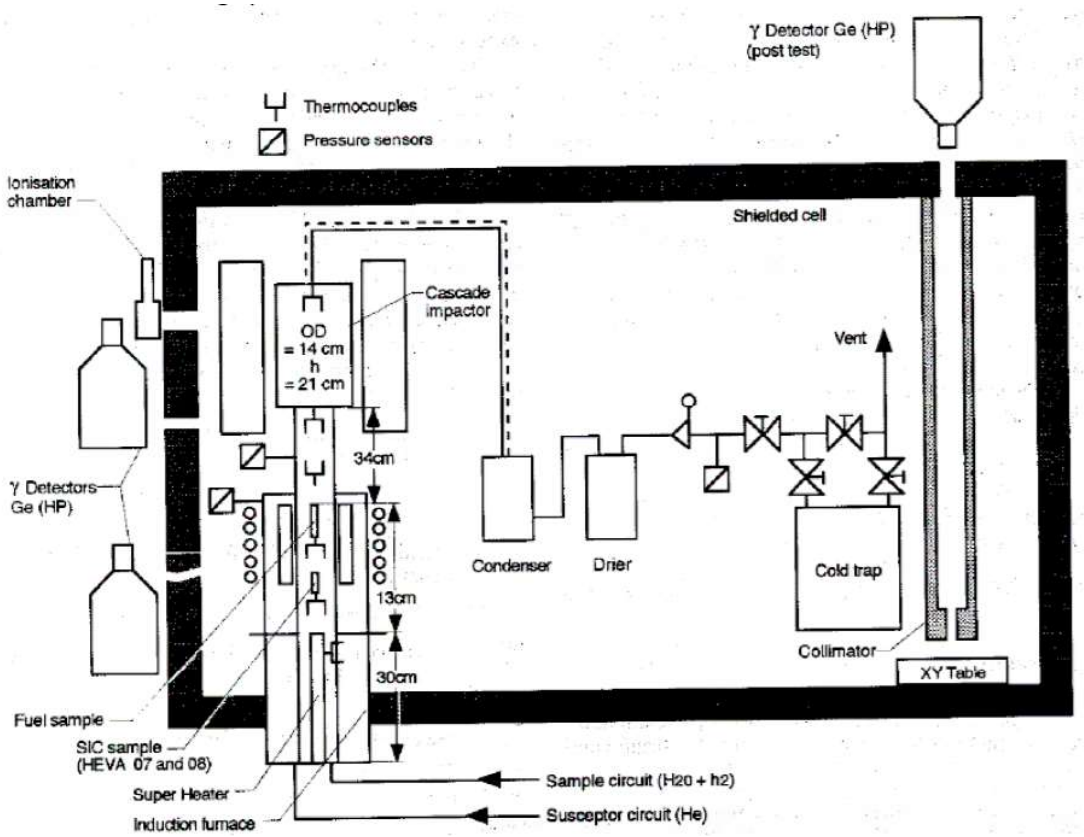

Figure I-17: Schematic view of the HEVA experimental loop, extracted from [65].

Post-test characterizations by means of OM, X-ray tomography and gamma tomography of the fuels showed that the Zircaloy cladding was completely oxidized in the tests performed under steam atmosphere (HEVA-03 to 05 and HEVA-08). A strong fuel-cladding interaction occurs in these tests. Under pure H_2 (HEVA-06), the metallic cladding melted and interacted with the fuel, penetrating in the cracks of the pellets. Ba was observed to remain trapped in the molten cladding.

I.4.1.4.2 VERCORS program

The VERCORS program was launched after the HEVA one at the CEA from 1989 to 1994 [66], [97]. The experimental loop can be seen in **Figure I-17**. The samples were composed of 3 PWR irradiated pellets in their original cladding, reirradiated at low linear power to recreate short half-lives FP. The induction furnace is composed of a separate ZrO_2 and ThO_2 internal circuit allowing the oxygen potential to vary around the fuel without oxidizing the furnace. The conditions of the six tests carried out are summarized in **Table I-3**. An oxidation plateau was performed around 1500°C in VERCORS thermal sequences in order to fully oxidize the cladding. Typical VERCORS thermal sequence was composed of different stages:

- Initial state corresponding to a LWR fuel in normal operating conditions (350 to 800°C),
- Temperature ramp up to 1500°C,
- Oxidation plateau around 1500°C,
- Temperature ramp up to 2300°C,
- High temperature plateau at temperature above 2300°C.

The first stage is performed in neutral conditions (He) whereas the second and third ones are performed under oxidizing H_2O/H_2 atmosphere. The last two ones are performed under varying

H_2O/H_2 conditions (reducing or oxidizing) in order to be representative of a severe accident scenario with core reflooding, excessive production of H_2, air ingress in the core…

The objective of the VERCORS program was to study the fuel and FP behavior up to maximum temperatures of 2350°C.

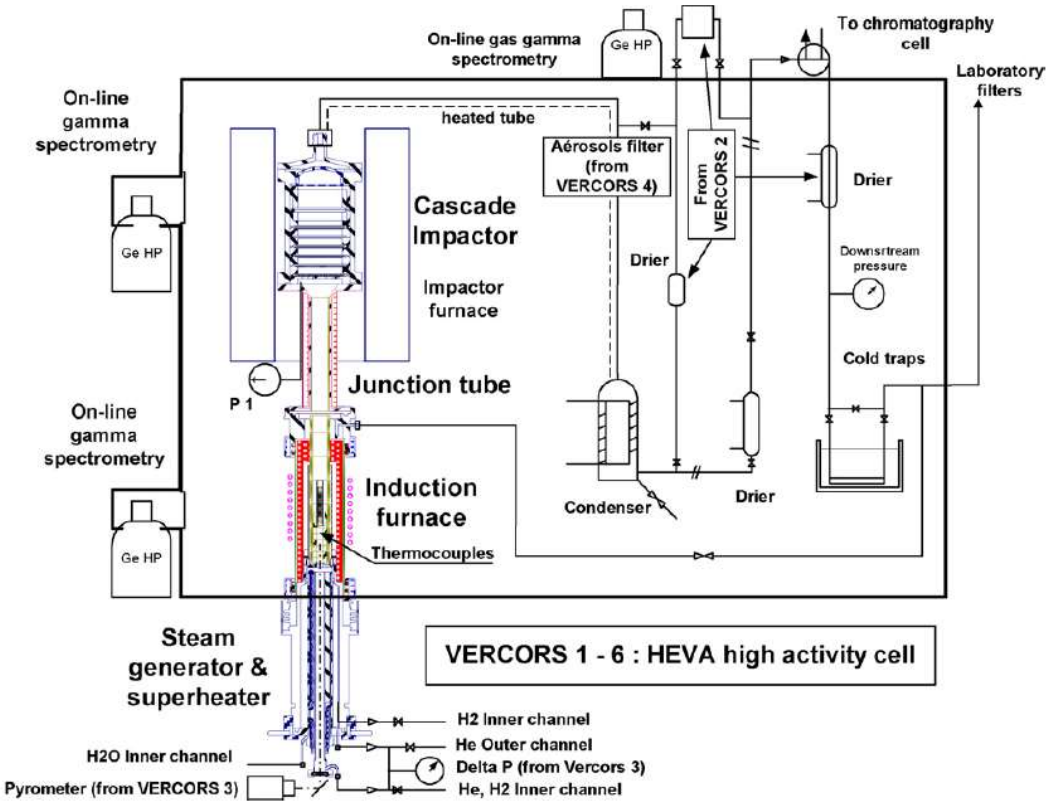

Figure I-18: Schematic view of the VERCORS experimental loop, extracted from [97].

Table I-3: VERCORS tests grid

Test	Fuel type	Temperature (°C)	Atmosphere at the end of the test
VERCORS-1	UO_2 with a burn-up of 42.9 $GWd.t_{HM}^{-1}$ Zircaloy-4 cladding	1860°C	Mixture H_2O/H_2
VERCORS-2	UO_2 with a burn-up of 38.3 $GWd.t_{HM}^{-1}$ Zircaloy-4 cladding	1880°C	Mixture H_2O/H_2
VERCORS-3	UO_2 with a burn-up of 38.3 $GWd.t_{HM}^{-1}$ Zircaloy-4 cladding	2300°C	Mixture H_2O/H_2
VERCORS-4	UO_2 with a burn-up of 38.3 $GWd.t_{HM}^{-1}$ Zircaloy-4 cladding	2300°C	H_2
VERCORS-5	UO_2 with a burn-up of 38.3 $GWd.t_{HM}^{-1}$ Zircaloy-4 cladding	2300°C	H_2O
VERCORS-6	UO_2 with a burn-up of 60 $GWd.t_{HM}^{-1}$ Zircaloy-4 cladding	2350°C	Mixture H_2O/H_2

From 1996 to 2002, the VERCORS HT (High Temperature, **Figure I-19**) and RT (Release of Transuranians, **Figure I-20**) series of tests were initiated at the CEA. In the HT experimental loop, Thermal gradient tubes were added in order to study FP transport and their interactions with the main component of the primary circuit of a PWR.

These two types of tests aimed at enlarging the database on FP release and actinides behavior in severe accident conditions until the melting of the fuel [97]–[100]. The conditions of these two types of tests are given in **Table I-4**.

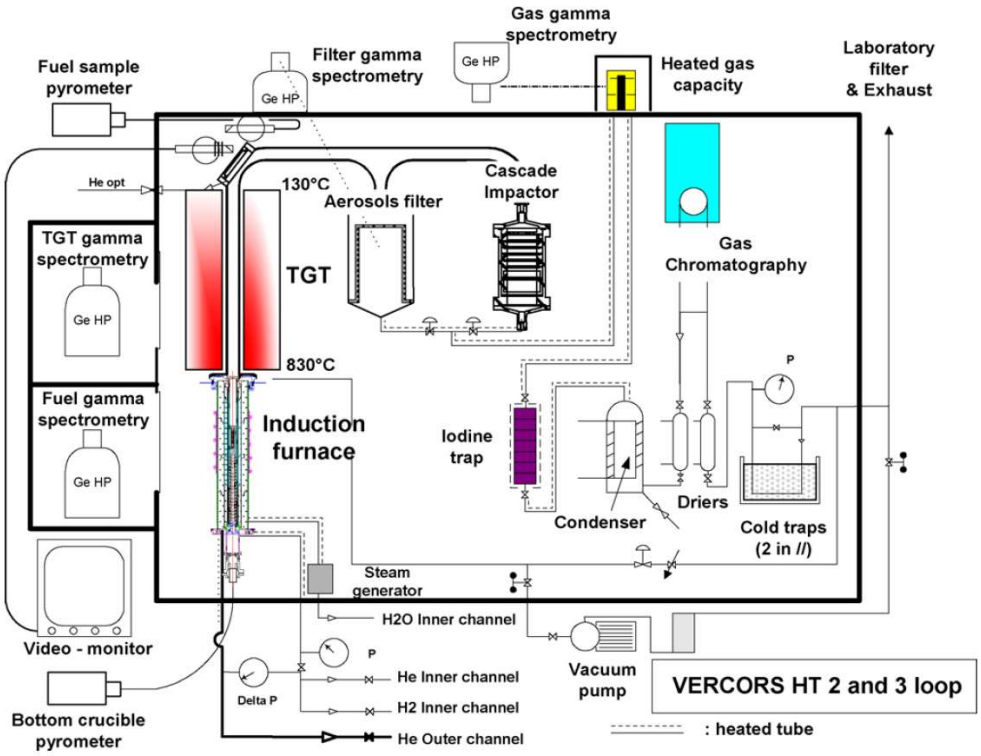

Figure I-19: Schematic view of the VERCORS HT experimental loop, extracted from [97].

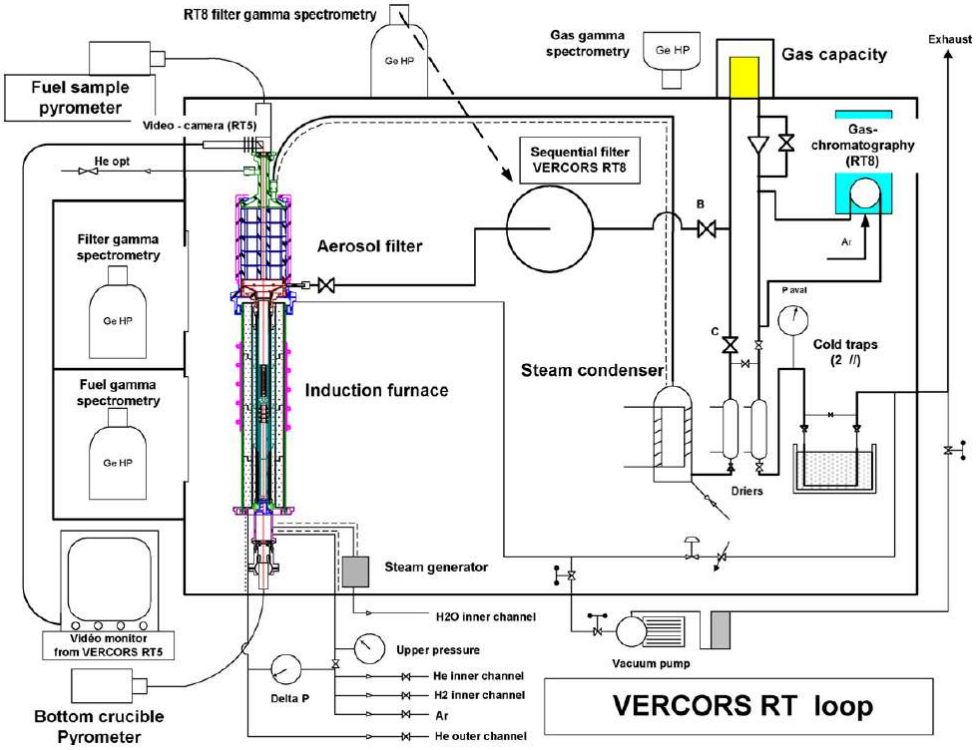

Figure I-20: Schematic view of the VERCORS RT experimental loop, extracted from [97].

Table I-4: VERCORS HT and RT tests grid

Test	Fuel type	Temperature (°C)	Atmosphere at the end of the test
VERCOR HT1	UO_2 with a burn-up of 49.4 $GWd.t_{HM}^{-1}$ Zircaloy-4 cladding	2630°C	H_2
VERCORS HT2	UO_2 with a burn-up of 47.7 $GWd.t_{HM}^{-1}$ Zircaloy-4 cladding	2150°C	H_2O
VERCORS HT3	UO_2 with a burn-up of 49.3 $GWd.t_{HM}^{-1}$ Zircaloy-4 cladding	2410°C	H_2
VERCORS RT1	UO_2 with a burn-up of 47.3 $GWd.t_{HM}^{-1}$ Zircaloy-4 cladding	2300°C	Mixture $H_2O > H_2$
VERCORS RT2	MOX with a burn-up of 45.6 $GWd.t_{HM}^{-1}$ Zircaloy-4 cladding	2170°C	Mixture $H_2O > H_2$
VERCORS RT3	UO_2 debris bed with a burn-up of 39 $GWd.t_{HM}^{-1}$ Zircaloy-4 cladding	2700°C	Mixture $H_2O < H_2$
VERCORS RT4	UO_2/ZrO_2 debris bed with a burn-up of 37.6 $GWd.t_{HM}^{-1}$ Zircaloy-4 cladding	2250°C	Mixture $H_2O > H_2$
VERCORS RT6	UO_2 with a burn-up of 71.8 $GWd.t_{HM}^{-1}$ Zircaloy-4 cladding	2200°C	Mixture $H_2O > H_2$
VERCORS RT7	MOX with a burn-up of 43 $GWd.t_{HM}^{-1}$ Zircaloy-4 cladding	2620°C	H_2
VERCORS RT8	UO_2 with a burn-up of 70 $GWd.t_{HM}^{-1}$ Zircaloy-4 cladding	2380°C	Mixture He/ 10 % air

Extensive post-test characterizations were performed after the tests mainly thanks to OM, X-ray tomography and gamma tomography. These tests highlighted the full oxidation of the fuel cladding up to 1300°C even in presence of H_2.The fuel relocation was shown to occur between 2150 and 2350°C independently of the burn-up. However, the atmosphere had a strong impact on the relocation temperature, which was lowered in oxidizing conditions. This phenomenon was inferred to higher fuel-cladding interaction when the cladding is fully oxidized ($UO_2 – ZrO_2$).

In the case of the VERCORS-5 test, the molten phase penetrated in the pellets along the cracks. The hypothesis made to explain this behavior was that the cladding was not fully oxidized during the oxidation phase and thus, the metallic cladding could interact with UO_2 by solid state diffusion [66], [97]–[101].

A comparison between the Phébus-FP tests and the VERCORS series showed that Ba release was higher in the case of analytical tests. This behavior was inferred to an interaction between Ba and structural materials (cladding tubes and control rods), which is much more severe in the case of Phébus-FP tests than in the VERCORS series. The vapor pressure of Ba would thus decrease because of the formation of compounds such as $BaZrO_3$.

This was also confirmed by the FPT-4 test performed on UO_2-ZrO_2 debris bed. Indeed, as long as the materials remained solid, Ba release was high but as soon as liquid started to form, Ba release decreased [102].

In term of FP, the main contribution of these HEVA and VERCORS programs was the classification of FP in 4 categories of volatility depending on their behavior with temperature and oxygen potential [97]–[100]:

- Volatile elements (Xe, Kr, I, Cs, Sb, Te, Cd, Rb, Ag) exhibit a nearly complete release at temperature around 2300°C. Their release kinetics can be affected by the experimental conditions such as the oxygen potential.
- Semi-volatile elements (Mo, Rh, Ba, Pd, Tc) are released in high quantity but their behavior is strongly dependent on the oxygen potential.
- Low volatile elements (Ru, Nb, Sr, Y, La, Ce, Eu) have a generally low release fraction but it can reach 20 to 60% depending on the experimental conditions (mostly on the oxygen potential).
- Non-volatile elements (Zr, Nb, Pr) are released in too low quantity to be quantified, even after fuel melting.

I.4.1.5 VERDON analytical tests

The VERDON program started in 2011 at the CEA within the frame of the International Source Term Program (ISTP), in collaboration with the US-NRC, IRSN, EDF, PSI, European Commission, EACL, KAERI and JAEA. The VERDON furnace (**Figure I-21**) is based on induction technology and has been extensively described in [103], [67], [104]. The samples are made of two irradiated fuel pellets in their original cladding blocked at the two extremities by half-depleted UO_2 pellets. As for the VERCORS tests, the samples were reirradiated at low linear power. They are placed in a crucible made of hafnia. The temperature of the samples is measured thanks to a pyrometer sighting under the crucible and to three thermocouples placed underneath the samples and in front of it. FP release kinetics are measured using on-line gamma spectrometry stations (sighting in the center of the sample, in the aerosol filter and in the may-pack filter) and a micro gas chromatograph. The VERDON experimental loop can be used in two different configurations: the Release and the Transport circuits (**Figure I-22**). The main difference between these two circuits lays in the thermal gradients tubes, enabling the study of FP behavior in a PWR primary circuit conditions.

Four VERDON tests were launched aiming at quantifying the FP release and studying the fuel behavior in the case of UO_2 and MOX LWR fuels. The conditions of the different tests are given in

Table I-5 [103], [67], [104], [105]. The VERDON-1, 3 and 4 tests were performed in the Release configuration of the VERDON experimental loop whereas the VERDON-2 test was performed using the Transport configuration. The typical thermal sequence was very similar to the VERCORS one.

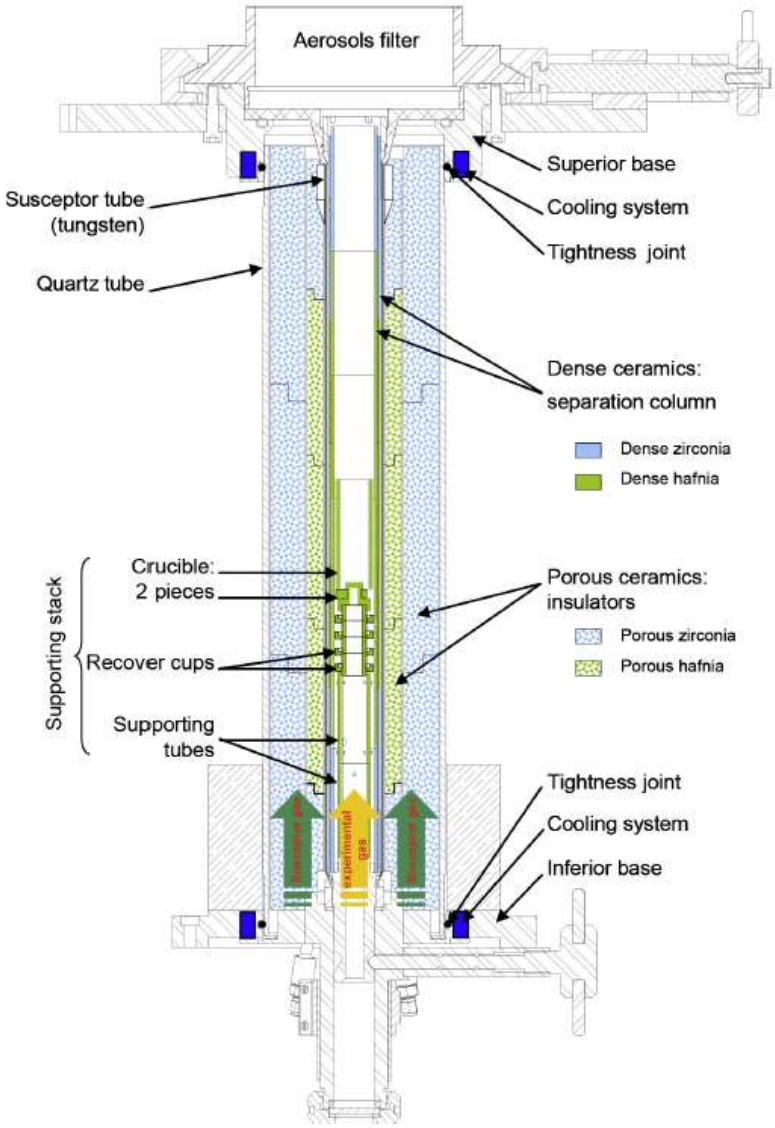

Figure I-21: The VERDON furnace, extracted from [104].

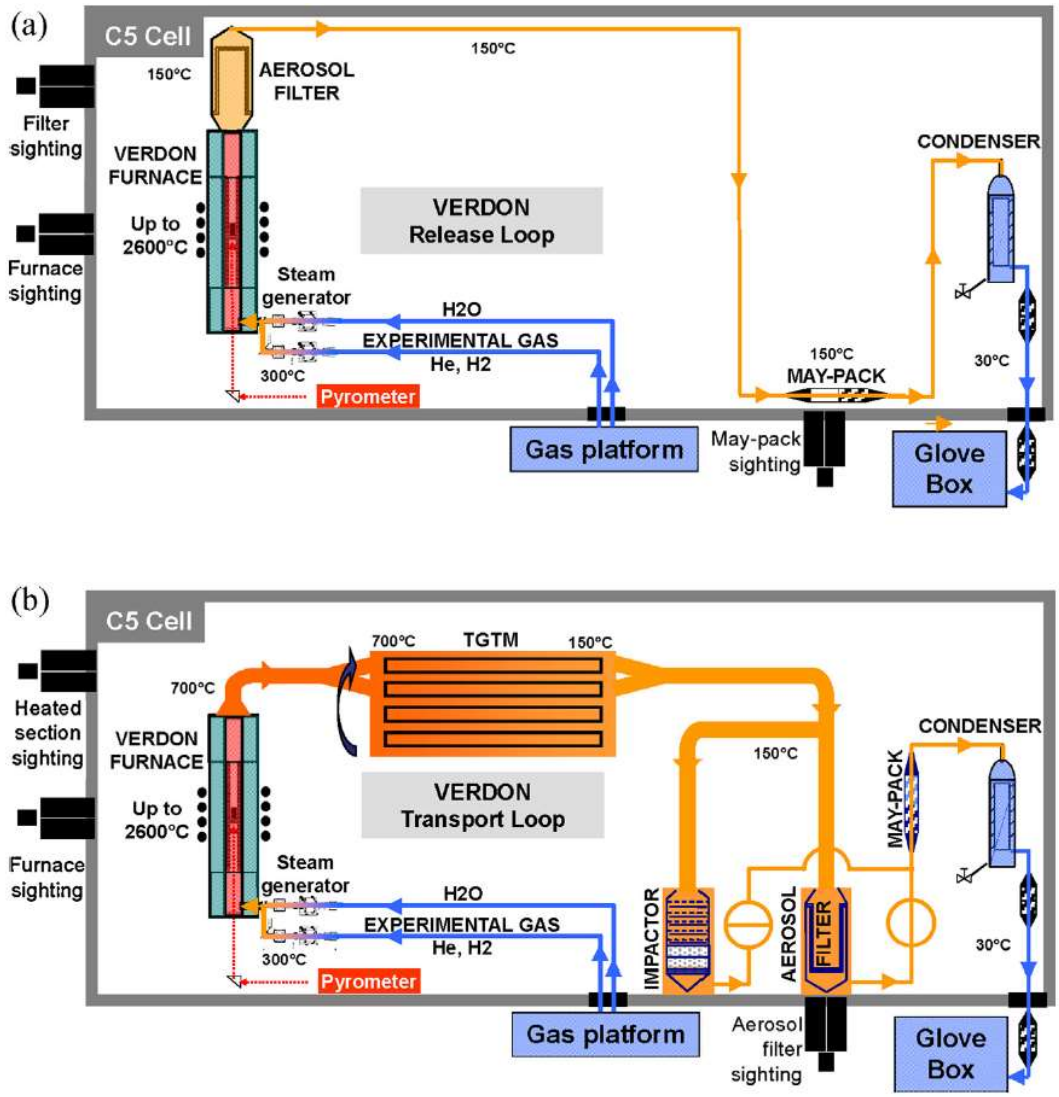

Figure I-22: The Release (a) and Transport (b) circuits of the VERDON experimental loop, extracted from [105].

Table I-5: VERDON ISTP tests grid

Test	Fuel type	Temperature (°C)	Atmosphere at the end of the test	Dates
VERDON-1	UO_2 with a burn-up of 72 $GWd.t_{HM}^{-1}$ M-5 cladding	2610°C	Mixture H_2O/H_2 = 1/10	09/2011
VERDON-2	MOX with a burn-up of 60 $GWd.t_{HM}^{-1}$ M-5 cladding	2100°C	Mixture H_2O/air = 1/2	06/2012
VERDON-3	MOX with a burn-up of 60 $GWd.t_{HM}^{-1}$ M-5 cladding	2300°C	Pure H_2O	04/2013
VERDON-4	MOX with a burn-up of 60 $GWd.t_{HM}^{-1}$ M-5 cladding	2530°C	Pure H_2	10/2014

The VERDON-1 test was performed on UO_2 pellets with a high burn-up whereas the VERDON-2, 3 and 4 tests were performed on the same MOX fuel. The main findings in these tests were [105]:

- The fastening effect of MOX fuel on the release kinetics of volatile and semi-volatile FP during the oxidizing phase, observed in the case of the VERDON-2 and 3 tests.
- A peculiar behavior of Ba was observed in the VERDON-2 and 4 tests. Indeed, the Ba final released fraction was surprisingly high at the end of the VERDON-2 test despite the strongly oxidizing nature of the atmosphere (> 80 % of the initial inventory). During the VERDON-3 test, the release of Ba was lower than the one of Mo, consistently with the oxidizing character of the atmosphere. During the VERDON-4 test, the Ba released fraction is higher than Mo one but surprisingly low with slow kinetics compared to VERDON-1.
- A specific behavior of Ru in MOX fuel, with low release and slow kinetics in oxidizing conditions (VERDON-2 and 3 tests) was observed.

Post-tests characterizations performed on the VERDON-1 samples clearly showed that melting of the fuel occurred well below the UO_2 melting temperature, after a fuel-cladding interaction. The molten phase penetrated through the cracks of the pellet consistently with the observations made in the HEVA-VERCORS programs. The composition of this phase was analyzed to be $U_{0.48}Zr_{0.52}O_2$. A Zr concentration gradient was observed between the center of the molten regions and the periphery, indicating that the $(U, Zr)O_2$ original melt may have dissolved more UO_2 on its way through the cracks [36], [50], [104], [106], [107].

These observations concerning the fuel cladding interaction and melting are also consistent with the ones made in other experiments (VEGA [64], [108], ACRR [54], LOFT-FP [109]) but no result of post-test characterizations was available in the open literature, to our best knowledge.

Two types of metallic inclusions were found at the end of the VERDON-1 test [36]. Both contained Ru, Mo, Rh and Tc but the Mo and Ru concentrations varied from 23.6 and 45.4 wt% to 10.5 and 52.8 wt% respectively. Some very large inclusions (with diameters up to 160 µm compared to the 1.1 µm in the rest of the sample) were found in the molten areas of the fuel. This was explained by the coalescence of the small precipitates due to their improved diffusivity in the molten $(U,Zr)O_2$ phase.

A few precipitates containing Ba were found in the HBS region of the father rod and in the porous regions of the VERDON-1 sample but no association with other FP was noticed. This has been explained by the low temperature of the fuel during normal PWR operating conditions. At the final temperature of the VERDON-1 test, the oxide precipitates (if they existed before) may have dissociated [36], [50], [104], [106], [107].

I.4.1.6 Other analytical studies

I.4.1.6.1 Knudsen Cell measurements

In the study of [110], MOX MIMAS fuel with a burn-up of 44.5 $GWd.t_{HM}^{-1}$ and containing Pu agglomerates with a size of up to 200 µm was analyzed. The temperature at the center of the sample was 1300°C and 580°C at the periphery. The sample, without cladding, was heated under vacuum up to 2330°C in a tungsten Knudsen cell[5] combined with a quadrupole mass spectrometer. The cell was

[5] The Knudsen effusion mass spectrometry consists in recording the mass spectra of the species effusing from a sample through the orifice of the Knudsen cell. Thermodynamic equilibrium within

heated through induction and the temperature was measured by a pyrometer. The ionization energy was set at 40 eV.

From 1200°C, the grain boundaries started to open and thermal etching occurs. At 1330°C, densification of the Pu agglomerates started and around 1500°C, interconnection of the pores began in the UO_2 matrix. Around 1800°C, vaporization of the UO_2 matrix has started and re-sintering of the Pu agglomerates has occurred leaving intragranular large bubbles and many metallic precipitates in them.

The same kind of study was performed in the work of [111] on UO_2 fuel with a burn-up of 102 $GWd.t_{HM}^{-1}$. Post-test observations were performed and showed the presence of complex oxide precipitates with a composition of $Ba(U, Pu, Zr)O_3$ at 1530°C. Metallic precipitates containing Mo, Ru, Rh, Tc and Pd were observed and characterized. It was observed that Mo content was higher in the region with higher burn-up. It was also detected as oxide in the gas phase at the same temperature as Cs, Rb, I and Te, which could indicate its participation to complex phases containing these elements (e.g. Cs_2MoO_4). Once again, sintering, grain growth and pore interconnection were observed around 1500°C.

I.4.1.6.2 Observations performed on Fast Breeder Reactors fuels

Extensive characterizations have been performed on Fast Breeder Reactors (FBR) irradiated fuels. The temperatures reached within a FBR fuel are much higher than the ones of a PWR (more than 2000°C in the central void[6]), the oxygen potential and thermal gradients within the pellets differ also. This will thus modify the kinetics of chemical reaction and the diffusion of species.

However, the same type of elements are present in the fuels (U, Pu, O and FP). Thus, on the pure chemical aspect, the phases observed in FBR fuels can thus be extrapolated to the ones expected to form in a PWR fuel during a severe accident. As already introduced in **section I.2.3**, FP can be classified in different groups depending on the type of chemical phases they can form in the fuel.

Metallic precipitates (Mo-Ru-Rh-Pd-Tc)

These precipitates can melt between 1800 and 2000°C depending on the Pd content. They can form eutectic with the fuel leading to melting at 2000°C. Migration of metallic precipitates and coalescence has been observed in FBR fuels, in which very large metallic ingots were found in the central void of the pellet [112]–[114]. One of them was mechanically extracted and analyzed through EPMA and XRD. The Mo/Ru ratio was 1.5 and the structure of the inclusion was hcp with lattice parameters of a = 2.73 ± 0.02 Å and c = 4.44 ± 0.04 Å. At the interface between the precipitate and the fuel, Pu, U, Pd, Rh and Ru were detected with a fcc structure (a = 4.127 ± 0.002 Å) [113]. Metallic inclusions of up to 5 µm in diameter were chemically extracted from the same fuel sample. Only one hcp phase was detected with a Mo/Ru ratio of 1 and lattice parameters of a = 2.756 ± 0.001 Å and c =

---

the cell is reached and cannot be disturbed by the orifice given its very small diameter (0.5 to 2 mm) compared to the surface of the effusing sample. Thanks to this method, the identification of gaseous species in the vapor phase is possible as well as equilibrium partial pressures determination.

[6] Due to the high power density applied on the fuel pellets composing FBR pins, pore migration occurs towards high temperature region of the pellets, forming a central void.

4.426 ± 0.002 Å, in good agreement with the large inclusion found in the central void [114]. These inclusions were all in the hcp (ε-phase) domain of the quinary Mo-Ru-Rh-Pd phase diagram.

At low oxygen potential, when the Mo content increases, two phases can be formed. A bcc (β) phase has been observed at temperature below 1900°C and a tetragonal (σ) phase can form at temperature above 1900°C.

A third bcc (α) phase can be formed at high burn-up in Pd-enriched and Mo-depleted precipitates [115]–[118].

Under strongly reducing conditions (defective FBR fuels), a cubic two phases system composed of $(Rh, Pd)_3(U,Pu)$ has been observed [46], [114], [119], [120].

Oxide phases

In FBR fuels, a reaction layer involving the fuel, the cladding and FP such as Cs, Mo, Ba and Pd, called fuel-to-clad joint (JOG), has also been observed in several studies [121], [122]. Some Cs uranates, plutonates or molybdates have been observed in the cooler regions of the pellets (fuel side of the fuel-cladding gap). This region has a temperature which roughly corresponds to the center of a PWR fuel pellet. However, the oxygen potential is higher than in the center of a PWR fuel [123] which may explain why such phases were never observed in PWR fuels under normal operating conditions.

The maximum solubility of Ba in UO_2 fuel has been measured to be 0.3 wt% at 2173 K and 0.6 wt% in $U_{0.8}Pu_{0.2}O_2$ [47]. Given this low solubility, Ba has been observed to precipitate as BaO [124]–[126], or as multicomponent complex phases with a composition $(Ba_{1-x-y}Sr_xCs_y)(U, Pu, Zr, Mo, RE)O_3$ (where RE stands for Rare Earths) [46], [119], [125], [127]. These last phases, also called grey phases or perovskites due to their crystallographic structures, have been observed in the hottest zones of FBR fuels with $BaZrO_3$ and $BaUO_3$ as the main components [37], [46], [119], [128], [129]. The RE are usually observed in this phase at high burn-up except in the case of Ce which is always present. Nevertheless, the decay channel of ^{140}Ba ends up with stable ^{140}Ce, which could explain the systematic presence of Ce in the grey phase [130] but the study of the $BaO\text{-}CeO_2$ system [131] showed the existence of a $BaCeO_3$ phase, which is stable until 1440°C. Finally, the amount of Mo in the grey phase depends on the oxygen potential: the Mo content increases with the oxygen potential. Nevertheless, $BaMoO_3$ has low solubility in $BaZrO_3$ and tends to form a separate phase [46].

Near the central void of FBR fuel (burn-up of 7 at%), $[Ba_{0.9}(Sr,Cs)_{0.1}][(U_{0.5}Pu_{0.2}RE_{0.05})Zr_{0.25}]O_3$ phase with a cubic structure (a = 4.33 Å) was observed by [46], [129].

Oxides containing both Ba and Zr were observed from the mid-radius region to the periphery of FBR fuels with a burn up of 13.3 at%. At lower burn-up, precipitates containing Ba without Zr were found near the central void [125].

I.4.2 Non-irradiated fuels studies

Analytical studies were also performed on non-irradiated materials composed of non-irradiated fuel pellets or of more complex materials produced by mixing, doping or implanting fresh UO_2 fuel with other elements such as Zr, Mo... in order to study the fuel and simulated FP chemistry.

Thermal treatments followed by post-test characterization campaigns were performed on the different types of samples in order to understand the phenomena involved in the loss of integrity of the core and FP speciation.

The advantages of this approach are that it enables easier handling, transportation and characterization of the samples, as they are far less radioactive than irradiated fuels. Moreover, it gives access to a wider range of characterization techniques allowing speciation studies.

The main experimental results obtained on non-irradiated fuels and available on fuel-cladding interaction and FP speciation are summarized in this section.

I.4.2.1 CODEX tests

The CODEX (Core Degradation Experiment) integral test program was launched in 1995-2001 at the KFKI Atomic Energy Agency Research Institute (Hungary) [132]. The main objective was to investigate the core degradation in VVER reactors as well as the interaction between fresh UO_2 and Zr-1 % Nb cladding.

Seven fuel rods were organized in an hexagonal lattice and heated on 600 mm thanks to resistive W heating device. The main components of the CODEX facility can be seen in **Figure I-23**.

The main findings of this program were:

- The general interactions between UO_2 and cladding tubes made out of Zr-1 % Nb are globally the same compared to Zircaloy except that the kinetics of reaction is different.
- An important oxide layer on the cladding has a protective effect towards fast temperature rising in case of reflooding of the damaged core.
- Aerosols formation could be correlated to the oxidation process of the fuel rods.

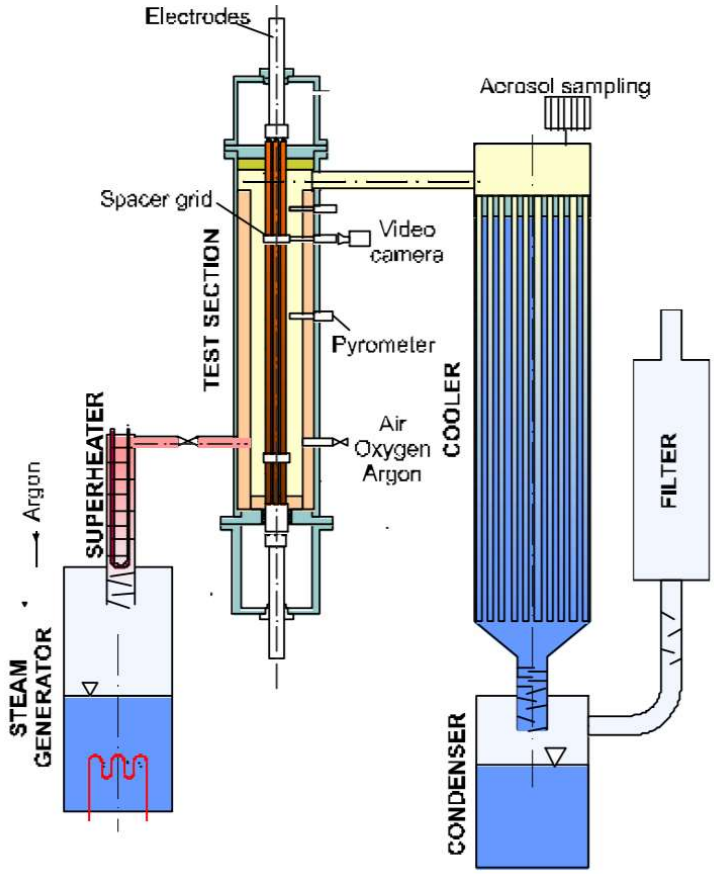

Figure I-23: Main components of the CODEX facility, extracted from [132].

I.4.2.2 CORA analytical tests

The CORA (Complex Out-of-Pile bundle Assembly) program took place from 1987 to 1993 at the Joint Research Center of Karlsruhe within the frame of the Severe Fuel Damage program. 19 tests were performed in order to provide experimental data to understand the phenomena involved in a severe accident and leading to the melting of the core (interactions between the fuel and structural materials, absorbants, cladding…) [133], [134].

In the CORA facility, 57 fuel rods of 2 m in length composed of UO_2 and Zircaloy cladding can be studied. Control rods made of Ag-In-Cd or B_4C, Zircaloy or Inconel grids can also be inserted. The CORA facility (**Figure I-24**) is composed of a high temperature section, a power supply, a heated steam circuit, a quenching device and a containment. Important instrumentation and visualization apparatus were also deployed.

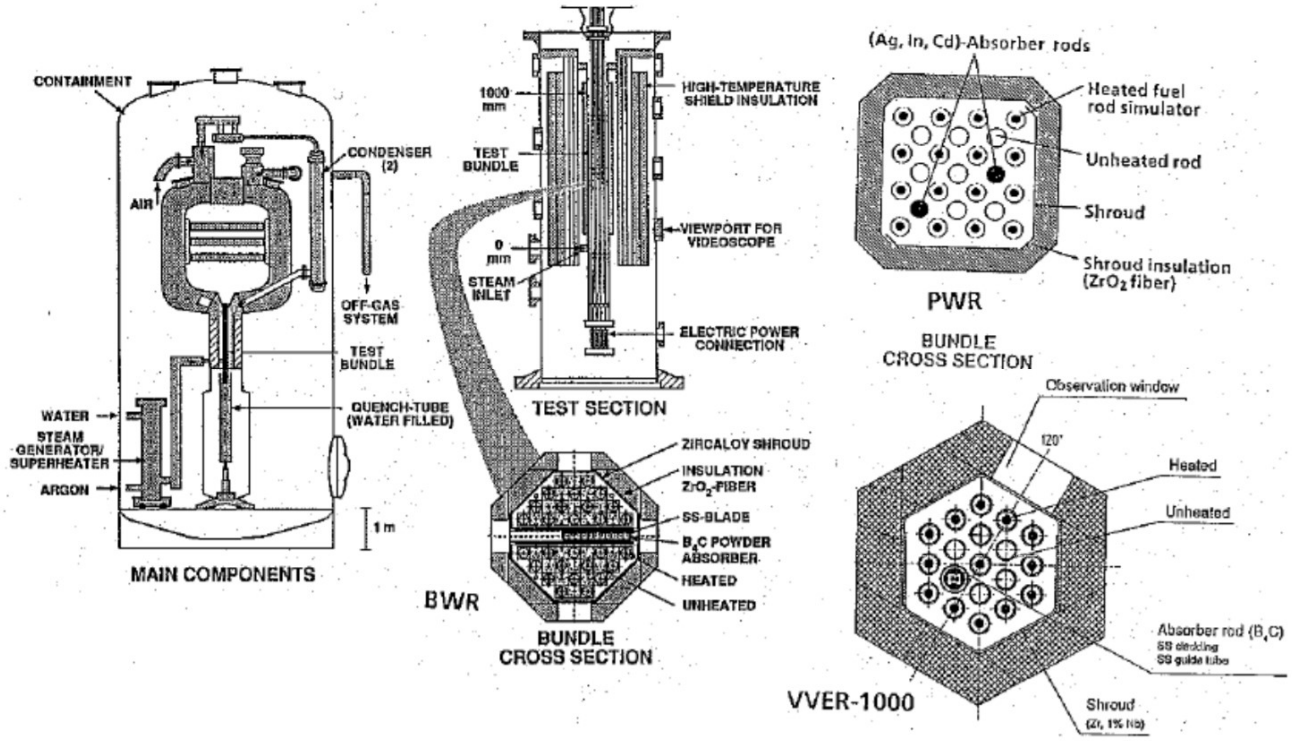

Figure I-24: Schematic view of the CORA facility with the PWR, BWR and VVER assembly that can be studies, extracted from [134].

The main findings of this program were described in [135] and summarized here:

- As soon as the melting point of metallic Zr is reached, the metal can flow and penetrate the superficial oxide layer areas.
- Eutectics can be reached by the interactions between the Zircaloy and the stainless steel, Inconel or absorbent rods, leading to liquid formation at 1300°C.
- The composition of the corium varies with time and temperature due to the numerous interactions between the different materials composing the core.
- The H_2 formation depends on the heating rate and the availability of the Zircaloy and steam. Reflooding of a damaged core can thus trigger rapid oxidation of the corium and a rise in temperature with a fast H_2 production.
- The analysis of the CORA tests enabled to define three stages in a severe accident scenario depending on the initial oxidation state of the cladding and the temperature reached. The first one corresponds to a localized degradation of the core (around 1500°C). Then a second phase occurs up to 2100°C with an extended degradation of the core. Finally beyond 2600°C total destruction of the core can be reached.

In the CORA W1 and W2 tests, the bundles were composed of UO_2 fuel with Zr-1%Nb cladding coming from VVER-1000 Russian type reactors. They were submitted to maximum temperatures of 1900-2400°C under steam atmosphere. No radial U and Zr concentration profile in the molten regions was observed but an axial profile in the rods, with lower U content at lower position of the rod. A mechanism was proposed to explain this concentration profile based on the competition between a dissolution process and Zr oxidation. First a saturation stage where Zr dissolves UO_2 and ZrO_2 simultaneously takes place. Then, a precipitation stage occurs due to the O flux arising from

ZrO_2 and the atmosphere of the tests: the oxidation of Zr and the dissolution of ZrO_2 lead to the precipitation of the $U_{1-y}Zr_yO_{2-x}$ phase [109], [136], [137].

I.4.2.3 Model materials studies

To better understand the chemical interaction between the different elements present in and around the fuel (U, Pu, Zr, FP…) in severe accident conditions, specific studies using simplified systems (model materials) are used. The data available in the literature and the TAF-ID database [13] have been used to calculate the phase diagrams presented hereafter.

I.4.2.3.1 Studies of the U-Zr-O and Pu-U-Zr-O systems

In the study of [138], fresh UO_2-ZrO_2 mixed oxide pellets with ZrO_2 content from 0 to 100 mol% were sintered during 6h at 1650°C under Ar/H_2, to ensure the production of stoichiometric UO_2.

Melting temperature was obtained thanks to laser heating technique. The minimum temperature was recorded to be 2525°C under pure Ar for compositions between $U_{0.5}Zr_{0.5}O_2$ and $U_{0.3}Zr_{0.7}O_2$, consistently with the phase diagram proposed in **Figure I-25**. Some tetragonal crystallites were observed in the Zr-rich part of the melt which is consistent with the observations made on the TMI-2, Phebus and VERCORS corium.

Under air, the melting of the systems happened around 2230°C. XANES measurements helped determining the O/M ratio which was 2.16. The phases observed in the system after quenching these samples were a cubic phase and a Zr-rich tetragonal phase. Traces of monoclinic zirconia were also observed.

When the amount of Zr in the mixture was below 0.8, two phases are systematically observed with different amount of ZrO_2: a Zr-rich phase mainly tetragonal and a cubic phase. The presence of these two phases may be explained by a diffusion-less transformation occurring on cooling. These observations are consistent with **Figure I-25**, the study of [81] and the metastable tetragonal zone proposed by [80] in the UO_2-ZrO_2 phase diagram.

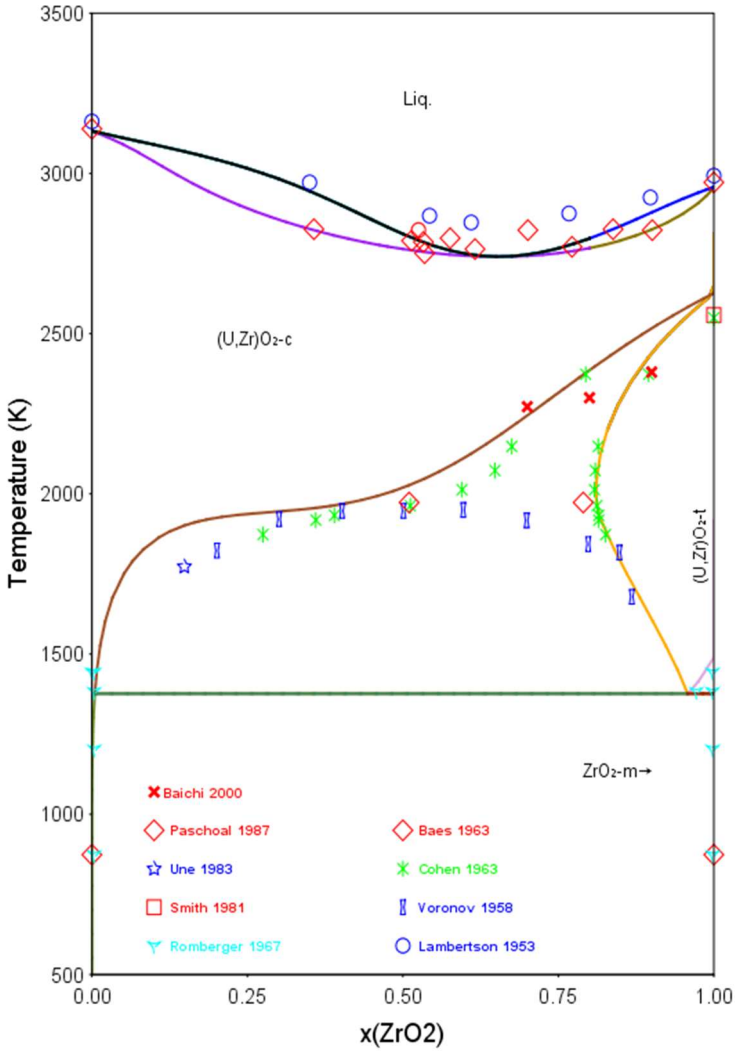

Figure I-25: Pseudo-binary phase diagram of the system UO_2-ZrO_2 calculated using ThermoCalc [18] coupled with the TAF-ID [13].

Investigations of the PuO_2-UO_2-ZrO_2 system at high temperature was carried thanks to laser melting technique in the study of [139]. The samples used were prepared by mixing ZrO_2, UO_2 and PuO_2 powders in different concentrations in the range $(PuO_2)_{0.5}(ZrO_2)_{0.5}UO_2$ and $(UO_2)_{0.5}(ZrO_2)_{0.5}PuO_2$. Sintering was then performed at 1600°C for 6h under Ar/H_2 to ensure a O/M as close as possible to 2.

Minimum melting temperature of 2500°C was registered for the system $(UO_2)_{0.15}(PuO_2)_{0.5}(ZrO_2)_{0.35}$, which is quite close from the minimum melting temperature of the UO_2-ZrO_2 system. It was also shown that high UO_2 content samples are stabilized to O/M = 2 in reducing conditions whereas low UO_2 content samples are stabilized to the stoichiometry in oxidizing conditions.

I.4.2.3.2 Studies of FP chemistry

As described in **Section I.2.3**, interactions between the three FP of interest (Cs, Mo and Ba) and the fuel (U, Pu), cladding material (Zr) or other FP (Ru, Rh, Pd) can take place. In this part, the main results concerning the systems involving Cs, Mo, Ba, Ru, Rh, Pd, Zr, U and O are described.

Metallic precipitates

The work of [116], [140] provided experimental data on the Mo-Rh-Ru-Pd alloys and established the ternary phase diagrams at different temperatures presented in **Figure I-26**. Mo and Ru being the main components of the metallic FP encountered in irradiated nuclear fuel (except Tc which cannot be simulated by another element), the binary phase diagram of the system Mo-Ru is presented in **Figure I-27**. The samples were produced whether by arc melting of a powder mixture containing Mo, Ru, Rh and Pd [116], or by induction melting in high vacuum [140] of a powder mixture containing Mo, Ru, Rh and Pd and (U, Pu)O_2.

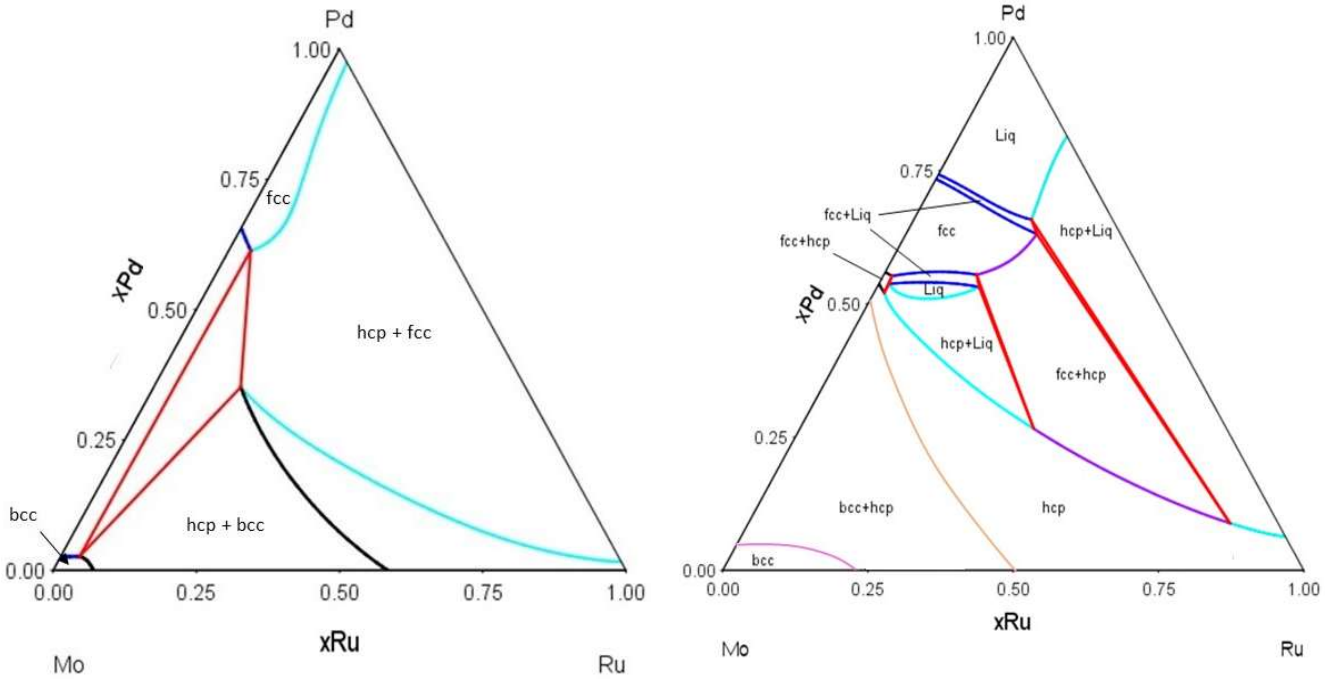

Figure I-26: Ternary diagram of the system Mo-Ru-Pd calculated at 1000°C (left) and 1700°C (right) using ThermoCalc [18] coupled with the TAF-ID [13].

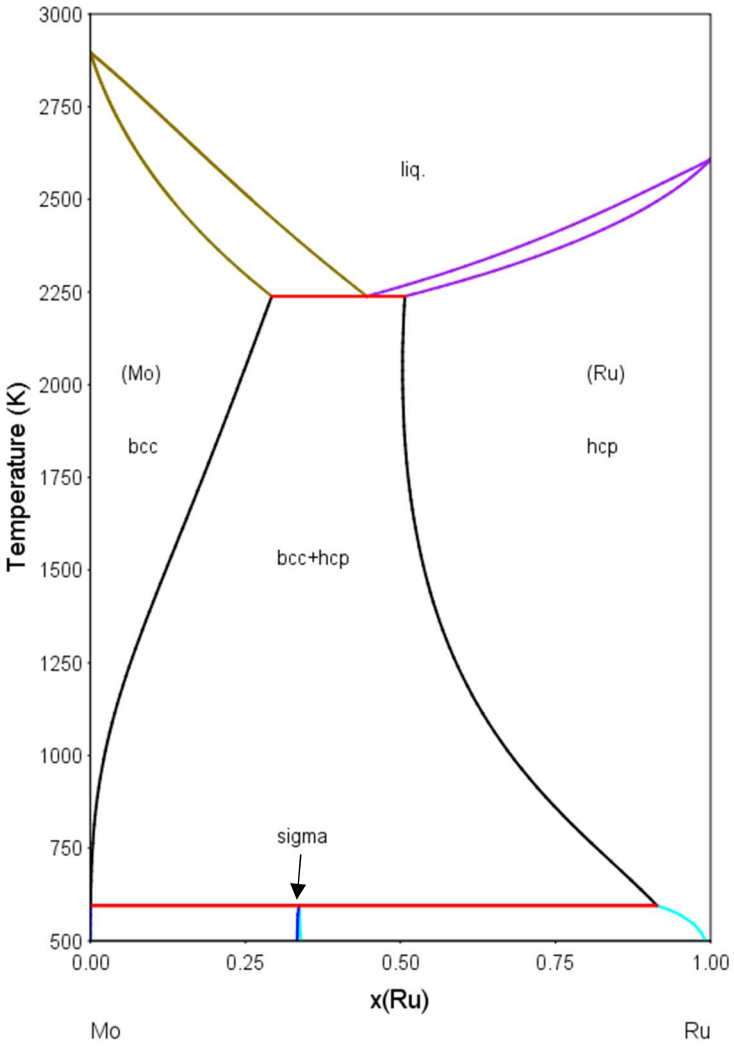

Figure I-27: Binary phase diagram of the system Ru-Mo calculated using ThermoCalc [18] coupled with the TAF-ID [13].

In the study by [141] Mo was implanted in fresh UO_2 pellets. Its chemical state was then studied through XANES analyses. They proved the existence of a correlation between the chemical form of Mo and the oxidation state of the fuel. Mo is in oxidation states +IV and 0 confirming the buffer role of the couple MoO_2/Mo proposed by [39]. However the Mo +IV ions do not form inclusions but are inserted in the cationic sites of the UO_2 lattice.

Oxide phases

Cs is a component of the perovskite phase $(Ba_{1-x}Sr_x)(U, Pu, Zr, Mo, RE)O_3$ observed in FBR fuels. In the studies of [142]–[146], the interactions between Cs, U and O were investigated.

The thermal stability of Cs uranates was first assessed in the work of [146]. They showed that Cs_2UO_4 and $Cs_2U_2O_7$ coexisted up to 650°C. At this temperature, Cs_2UO_4 decomposition took place according to the following reaction:

$$2\ Cs_2UO_4 \rightarrow Cs_2U_2O_7 + Cs_2O$$

However, later studies of [147] showed that humidity during heating strongly influenced the decomposition temperature of Cs_2UO_4, which appeared at 950°C under dry atmosphere.

A pseudo-binary Cs_2MoO_4-MoO_3 phase diagram was proposed in [148] and shown in **Figure I-28**. A eutectic is present at 458°C leading to a liquid composed of 45 mol% MoO_3. The melting point of Cs_2MoO_4 was also determined to be 940°C which is in agreement with the value reported by [149].

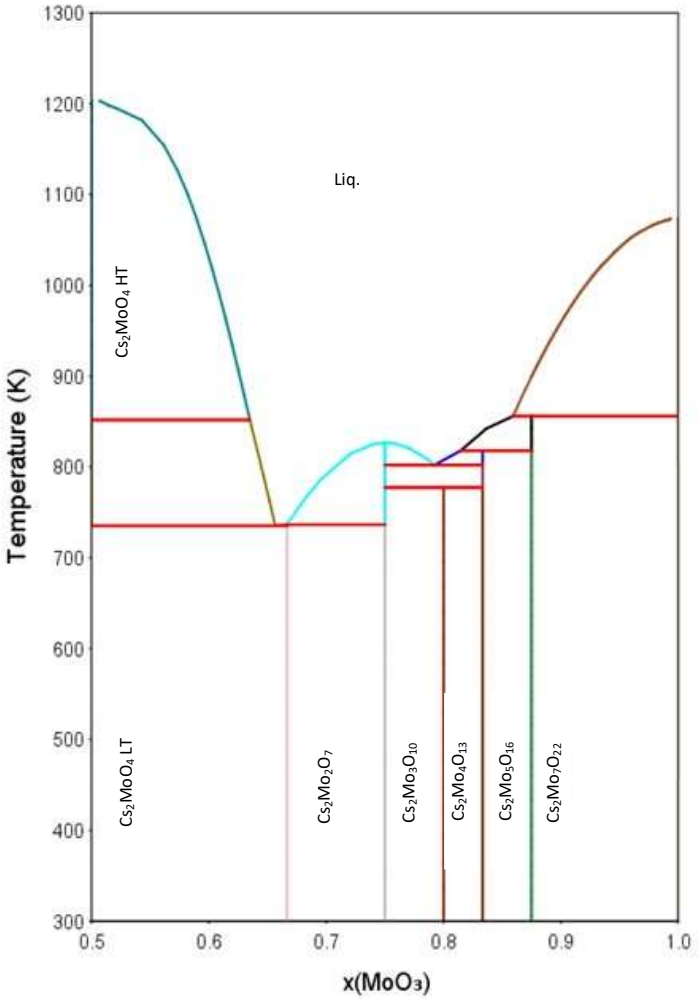

Figure I-28: Pseudo-binary phase diagram of the system Cs_2MoO_4-MoO_3 calculated using ThermoCalc [18] coupled with the TAF-ID [13].

In the work of [129], the interactions between UO_2, BaO, MoO_2 and ZrO_2 were investigated. The Bao-ZrO_2 pseudo-binary phase diagram is presented in **Figure I-29**. As shown in this diagram, the solubility of BaO increases in the tetragonal and cubic ZrO_2. $BaZrO_3$ melting was shown to occur congruently at 2705°C [150].

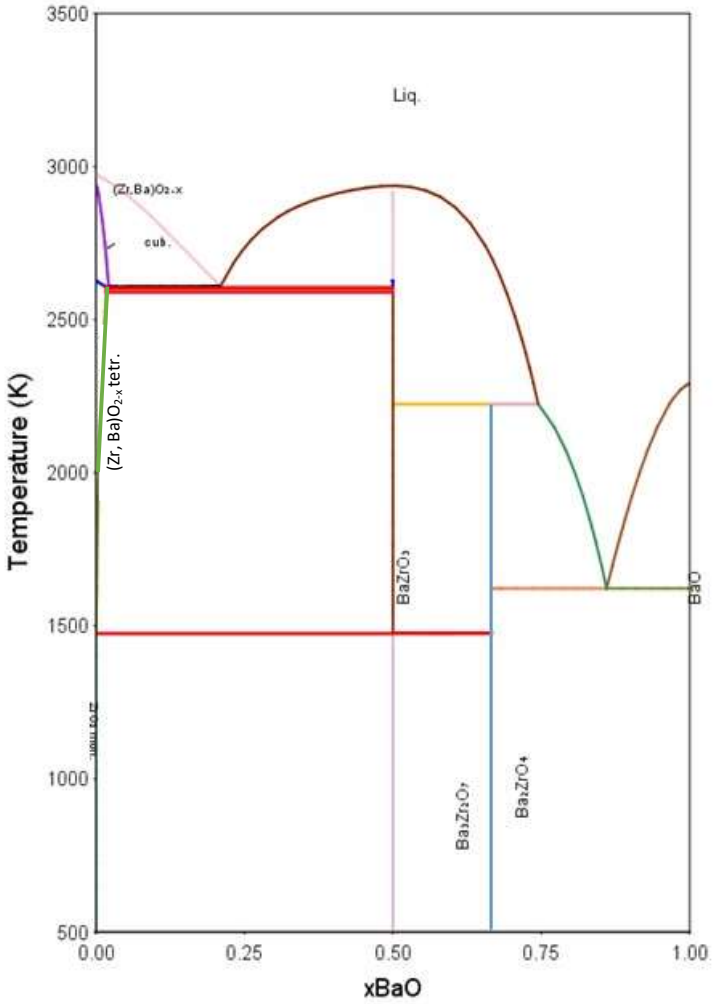

Figure I-29: Pseudo-binary phase diagram of the system ZrO_2-BaO calculated using ThermoCalc [18] coupled with the TAF-ID [13].

The phase diagram of the BaO-UO_2 system (**Figure I-30**) is characterized by the occurrence of a ternary oxide $BaUO_3$ which melts congruently at 2450°C according to [150]. This compound is completely miscible in $BaZrO_3$.

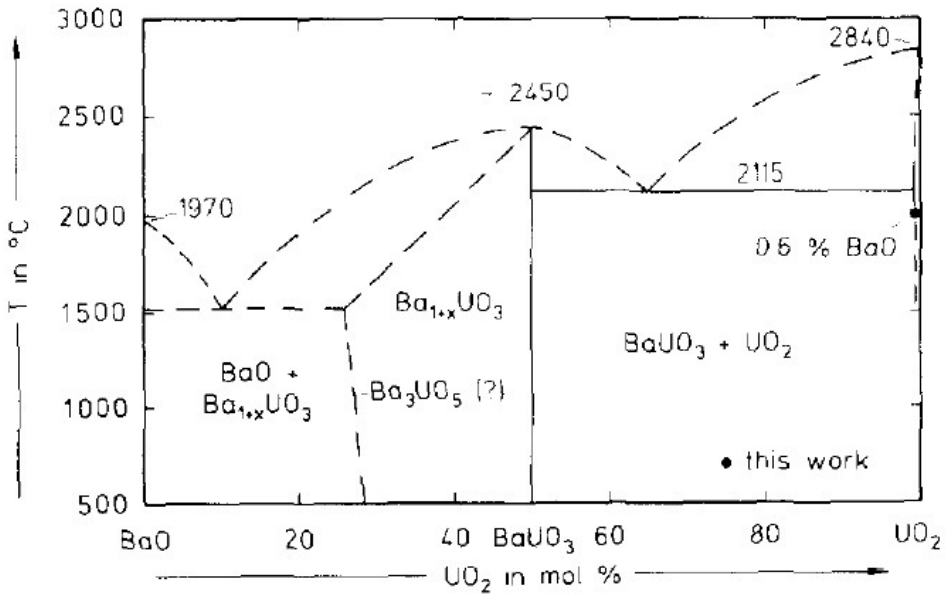

Figure I-30: Pseudo-binary phase diagram of the system UO_2-BaO, extracted from [129].

Concerning the BaO-MoO_2 system, [150] showed that a ternary oxide $BaMoO_3$ could crystallize in a perovskite structure in a restricted range of oxygen potential. This compound was observed to decompose at 1380°C into $BaMoO_4$, Mo and BaO under Ar or He atmosphere. This decomposition causes limited solubility of $BaMoO_3$ in the Ba(U, Zr)O_3 phase. As far as enough oxygen is available, the BaO-MoO_3 pseudo-binary system is considered (**Figure I-31**). The $BaMoO_4$ compound has a congruent melting point of 1457°C.

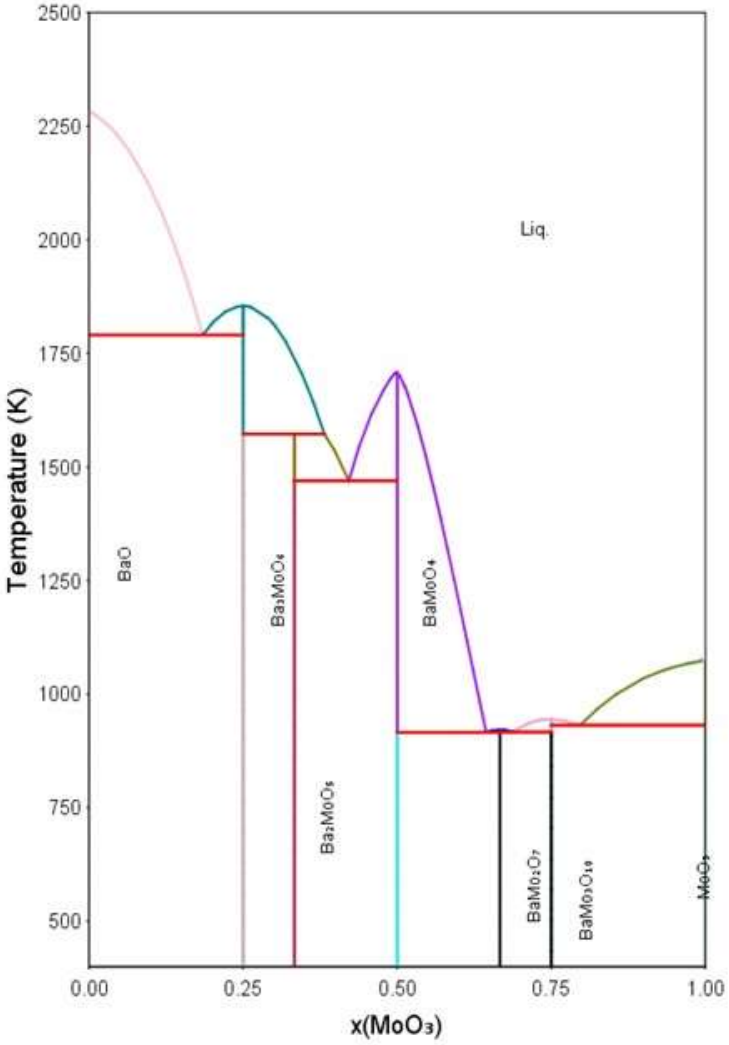

Figure I-31: Pseudo-binary phase diagram of the system BaO-MoO_3 calculated using ThermoCalc [18] coupled with the TAF-ID [13].

More complex materials were produced in the work of [151] in order to study the behavior of 12 FP in a chemical state representative of a FBR. These samples after sintering at 1700°C during 4 h contained three main phases: the perovskite phase ($(Ba_{1-x}Sr_x)(U, Zr, Mo, RE)O_3$), the metallic inclusions (Mo-Rh-Ru-Pd) and dissolved elements in the fuel matrix (Nd, La…). These kinds of SIMFuel samples have been used to perform different studies on FP behavior in PWR or spent nuclear fuels [50], [152]–[155] or on the HBS thanks to ion irradiation [156].

In the work of [157], fresh UO_2 and MOX pellets were doped with Mo, Ru, Rh, Pd, Ba and Zr to study the behavior of Mo in different atmosphere and temperatures conditions. A thermal gradient was set between the periphery (up to 1600°C) and the center (up to 2700°C) of the pellets. They showed that in oxidizing conditions, a reaction between Ba and Mo took place, which was inferred to the reaction between Mo oxide vapor and BaO. The liquid phase formed in the samples was observed in the high-temperature regions of the fuel and slightly richer in Ba.

The evolution of the complex oxide phase containing Ba was also observed in the work of [50] who performed XANES measurements on SIMFuel samples to determine the speciation of Mo and Ba. They showed that an interaction between $BaZrO_3$ (stable in reducing

conditions) and Mo, which consumes the entire Ba available took place in oxidizing conditions. Two different phases containing Mo, Ba and O were observed with two different Ba/Mo ratios (around 1 and 0.2). According to the pseudo-binary phase diagram proposed in **Figure I-31**, these observations could be explained by a decomposition of $BaMoO_4$ in BaO and MoO_3. However, no oxidized Mo precipitates could be observed in the samples, which could be explained by the release of Mo during the tests.

I.5 REMAINING QUESTIONS AND OBJECTIVES OF THE THESIS

I.5.1 Proposed FP release mechanisms

In order to interpret the experimental results obtained on irradiated fuels and using the thermodynamic experimental data presented in the previous section, calculations were performed using the Mechanism of Fission Products Release code (MFPR).

This code is based on the resolution of equations in the grain [74], [158], [159]. The latter is considered as a tetrakaidecahedron (TDK) having 7 faces, 12 edges and 6 corners. The evolution of various defects and interactions with gas atoms and bubbles migrating out of the grains is taken into account.

For fission gas, the model has three steps:

- Grain surface saturation,
- Interlinkage of bubbles to form channels towards the grain edges and channels,
- Interconnection of the pores leading to tunnels and open porosity.

The transport of the gas is intragranular until they reach the grain boundaries. They form precipitates or bubbles in the grains and can accumulate in the intergranular pores before being release through interconnected pores. As far as the gas has reached the open porosity, it is considered by the code as released from the system.

A chemical solver based on the minimization of global Gibb's free energy of the system is used to solve the coupled transport/mass action equations for all the chemically active FP. These FP can be found in five phases in MFPR: the solid solutions and separate phases, the ternary compounds, the metallic phases and CsI. The cladding is not represented in the code. The chemistry of the fuel-FP system is based on diffusion and solubility data: the FP can precipitate or be dissolved in the fuel matrix. The precipitates can form only on the grain faces, at the interface with the gas bubbles. The oxidation of the fuel is also calculated.

Based on this type of calculation, on the experimental observations performed on irradiated fuels and model materials and on the thermodynamic data presented in the previous section, a mechanism for FP release has thus been proposed in the literature [153], [159]. This mechanism is adapted to a typical VERCORS/VERDON thermal sequence described in **section I.4.1.4.2**.

At the initial state Cs is calculated to be under $Cs_2U_xO_y$ (the simplest being Cs_2UO_4), Ba and Mo as BaO and MoO_2 respectively in solid solution with the fuel matrix as none of these oxides exist as precipitate in the code. Part of the Mo is also found in metallic precipitates.

Around 1000°C MoO_2 migration takes place to the grain boundaries and condensation occurs in the intergranular porosity of the cold regions of the fuel. The size of intergranular pores increases due to gas mobility and accumulation in the bubbles enhanced by temperature. Cs_2MoO_4 can be formed according to eq. 1, consistently with observations performed at the periphery of FBR MOX fuels.

$$MoO_{2(s)} + Cs_2UO_{4(s)} \rightarrow Cs_2MoO_{4(s)} + UO_{2(s)} \qquad \text{eq. 1}$$

During the oxidation plateau, part of the cesium uranates is destroyed and gaseous Cs migrates to intergranular porosity, increasing the pressure in the pores which begin to interconnect. This leads to

a first release of Cs according to eq. 2 (if the oxygen potential is between -400 and -300 kJ.mol^{-1}). The remaining Cs is still found in the fuel as Cs_2MoO_4 which can be destroyed or vaporized according to eq. 3 and 4. In the same time, the Zr cladding starts to oxidize in ZrO_2.

$$Cs_2UO_{4(s)} \rightarrow 2\ Cs_{(g)} + UO_{2(s)} + O_{2(g)} \qquad \text{eq. 2}$$

According to the experimental observations of [50], $BaZrO_3$ would be formed during the oxidation plateau and could react with MoO_2 to form $BaMoO_4$ in oxidizing conditions according to equation 2'. These observations are also supported by the characterization of the Phebus FPT-0, FPT-1 and FPT-2 fuel rods [93], [95] and several studies performed on FBR fuels [121], [125], [130] presented in **sections I.4.1.2** and **I.4.1.6.2**.

$$BaZrO_{3(s)} + MoO_{2(g)} + ½\ O_{2(g)} \rightarrow BaMoO_{4(s)} + ZrO_{2(s)} \qquad \text{eq. 2'}$$

During the temperature ramp up to 2300°C, simultaneous Ba, Cs and Mo releases occur according to reactions 2 and 3 (if the oxygen potential is below -300 kJ.mol^{-1}), 4 and 5 (above 1700°C for oxygen potential between -400 and -200 kJ.mol^{-1}). BaO is partially retained in the cladding as $BaZrO_3$ (eq. 6). Depending on the atmosphere of the test, MoO_2 can be reduced returning in the metallic precipitates which limit its release (eq. 7).

$$Cs_2MoO_{4(s)} \rightarrow 2Cs_{(g)} + MoO_{2(g)} + O_{2(g)} \qquad \text{eq.3}$$

$$Cs_2MoO_{4(s)} \rightarrow Cs_2MoO_{4(g)} \qquad \text{eq.4}$$

$$BaO_{(s)} \rightarrow Ba_{(g)} + ½\ O_{2(g)} \qquad \text{eq. 5}$$

$$BaO_{(s)} + ZrO_{2(s)} \rightarrow BaZrO_{3(s)} \qquad \text{eq. 6}$$

$$MoO_{2(s)} + 2H_{2(g)} \rightarrow Mo_{(s)} + H_2O_{(g)} \qquad \text{eq. 7}$$

In the last high temperature phase (up to 2000°C), $BaZrO_3$ is destroyed leading to the release of Ba according to equation 8.

$$BaZrO_{3(s)} \rightarrow Ba_{(g)} + ½\ O_{2(g)} + ZrO_{2(s)} \qquad \text{eq. 8}$$

Two different release mechanisms were proposed in [50] to account for the effect of the atmosphere in the final stages of the VERCORS/VERDON tests:

- **In reducing atmosphere** (**Figure I-32**), all the remaining MoO_2 is reduced and Mo returns to the metallic inclusions. The $BaMoO_4$ formed during the oxidation plateau would be destroyed leading to the release of Ba according to eq. 9.

$$BaMoO_{4(s)} + 4H_{2(g)} \rightarrow Ba_{(g)} + Mo_{(s)} + 4H_2O_{(g)} \qquad \text{eq. 9}$$

- **In oxidizing atmosphere** (**Figure I-33**), full oxidation of the Mo contained in the metallic precipitates would occur leading to massive Mo release as MoO_2. The volatilization and destruction of the Ba and Cs molybdates would also enhance Mo and Cs release. Ba would be found as BaO in precipitates or dissolved in the matrix at the end of the sequence according to eq. 10.

$$BaMoO_{4(s)} \rightarrow BaO_{(s)} + MoO_{2(s)} + ½\ O_{2(g)} \qquad \text{eq. 10}$$

These two mechanisms are presented in **Figure I-32** and **Figure I-33**:

- The blue boxes correspond to the steps resulting from the MFPR calculations.
- The purple boxes correspond to the steps observed experimentally on PWR irradiated fuels.
- The yellow boxes correspond to the compounds observed experimentally on model materials.

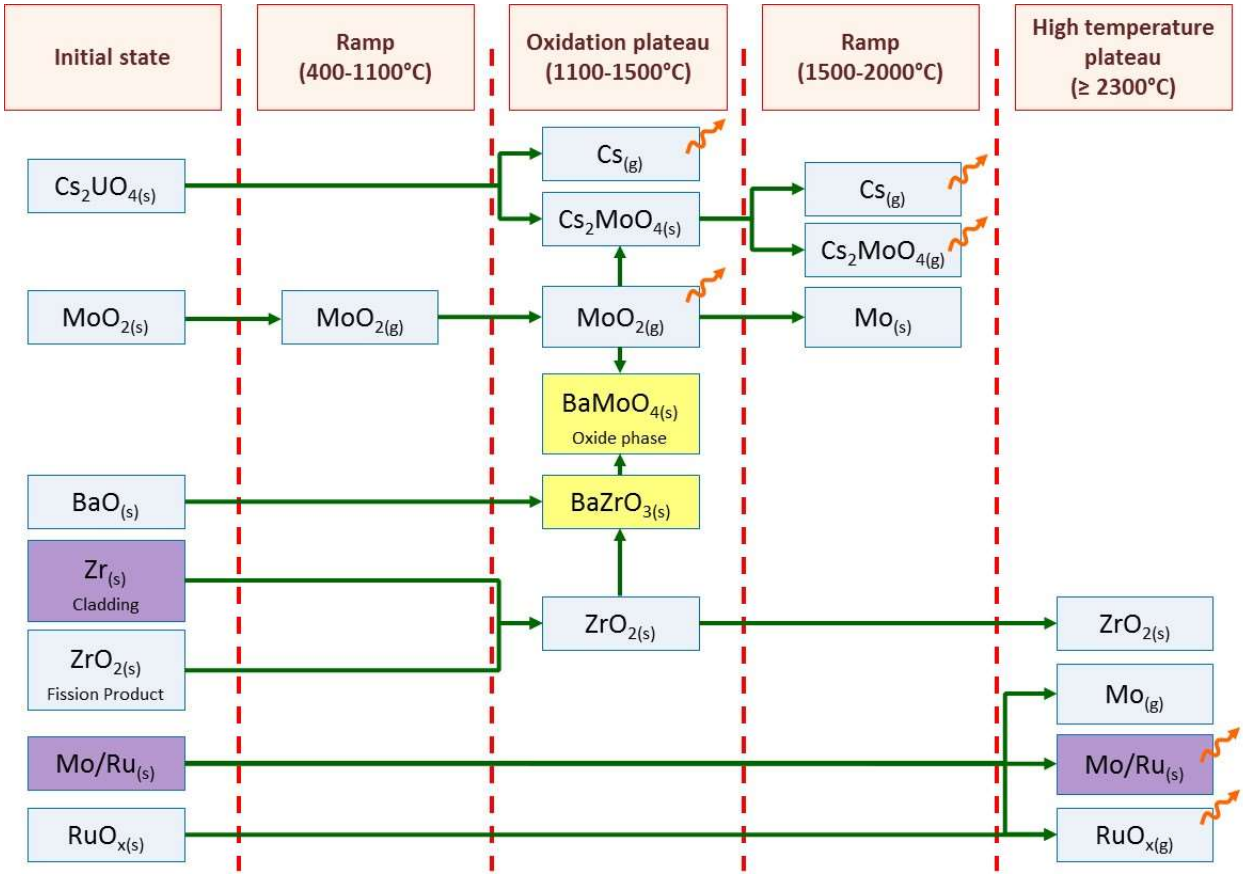

Figure I-32: Release mechanism proposed in [50] for the last two stages in reducing conditions

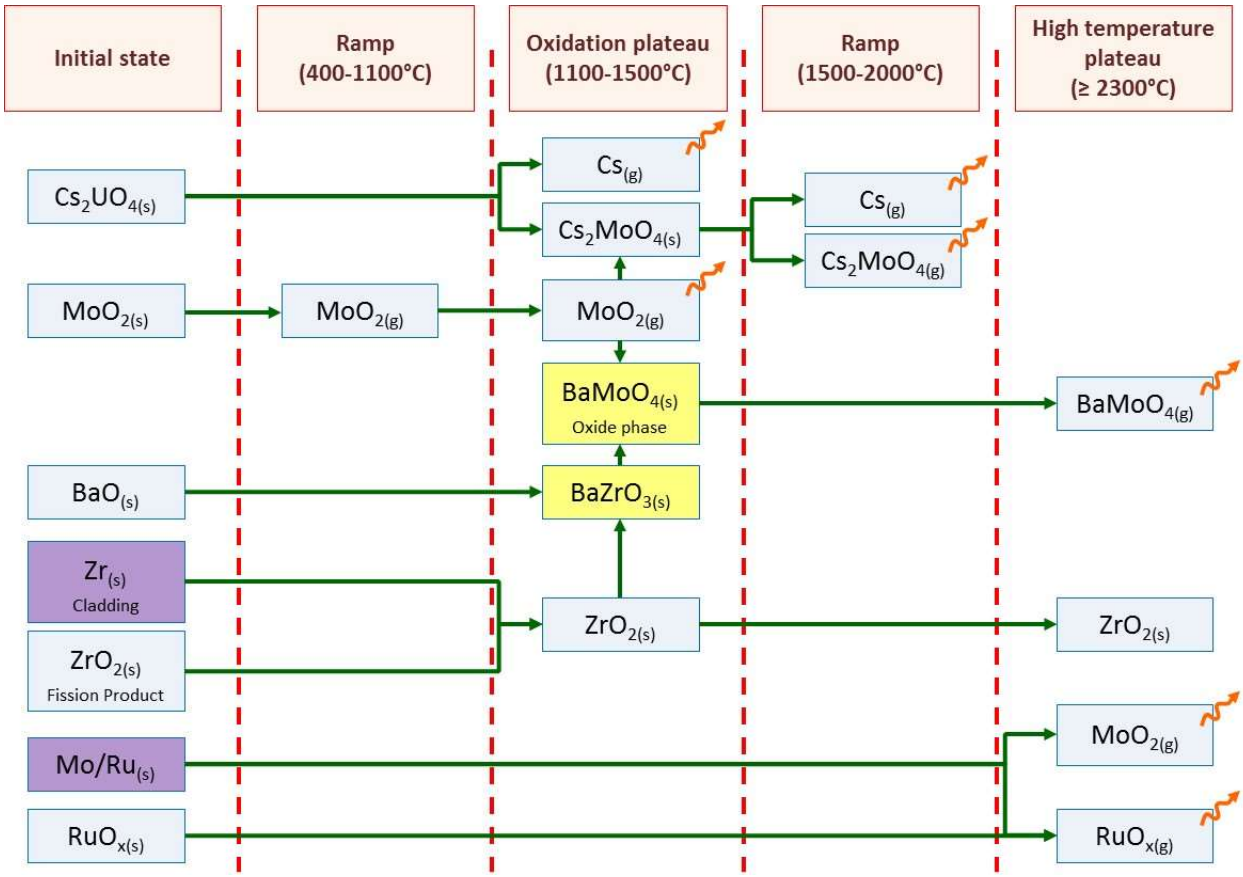

Figure I-33: Release mechanism proposed in [50] for the last two stages in oxidizing conditions

I.5.2 Thesis objectives and methodology

As explained throughout this chapter, the uncertainties remaining on the different systems involving the fuel, cladding and FP elements have repercussions on the calculated release of FP in severe accident conditions. This highly limits the prediction capacities of the actual release models and thus the accuracy of the source term estimation in case of nuclear severe accident. The different hypotheses made in the scenario or mechanistic software and used to build the FP release mechanisms presented in the previous subsection thus need to be validated and completed.

This can be made through the production of experimental data thanks to integral or analytical tests on nuclear fuels in order to study the different phenomena occurring in a severe accident. The interpretations of these tests is then based on the physical and chemical transformations of the fuel and the FP release dependence on temperature, oxygen potential and burn-up. Microanalyses thus need to be performed on fuel samples after different tests to provide experimental data on the FP distribution and speciation in the fuel.

In this context, the present work aims at studying the effect of temperature and oxygen potential on the fuel and FP behavior. More especially, the behavior of Cs, Mo and Ba is emphasized. This work has thus been built thanks to two main tools: an experimental materials study and thermodynamic calculation, enabling the interpretation of the experimental results and their confrontation to two databases (the SGPS [160], [161] and the TAF-ID [13]). The main objectives were:

- To provide experimental data on the behavior of irradiated MOX fuel submitted to severe accident conditions as well as on the relative distribution and chemical forms of FP.

- To study the distribution and chemical evolution of the FP of interest in intermediate stages of a severe accident, notably the evolution of the oxide/grey phase with the oxygen potential.
- To assess the validity of the proposed release mechanisms described in the previous subsection.

To this end, three work axes were investigated:

1. An irradiated fuels study: two irradiated MOX samples recovered after the VERDON-3 and VERDON-4 tests were characterized in detail in the LECA-STAR facility. The objective was here to investigate the effect of the oxygen potential on the fuel and FP behavior.

2. A model materials study: SIMFuel samples were first produced in the UO_2 Laboratory of the CEA Cadarache. Thermal treatments in conditions representative of the intermediate stages of a severe accident were performed. The objective was again to investigate the effect of the oxygen potential of the tests on FP speciation thanks to XANES analyses.

3. A fabrication development: Spark Plasma Sintering (SPS) was used to produce SIMFuel samples at rather low temperature compared to conventional UO_2 sintering. The objective was to produce dense UO_2 samples containing Cs, Mo and Ba in order to study their speciation in intermediate stages of a severe accident. The samples' manufacturing was performed using the SPS device available at the Joint Reasearch Center of Karlsruhe, Germany.

I.6 REFERENCES

[1] M. F. James, “Energy released in fission,” *J. Nucl. Energy*, vol. 23, no. 9, pp. 517–536, Nov. 1969.

[2] “Nuclear Fission and Fusion,” *Chemistry LibreTexts*, 12-Jul-2016. [Online]. Available: https://chem.libretexts.org/LibreTexts/Heartland_Community_College/HCC%3A_Chem_162/21%3A_Nuclear_Chemistry/21.7%3A_Nuclear_Fission_and_Fusion. [Accessed: 17-Sep-2018].

[3] C. C. Lin, *Radiochemistry in Nuclear Power Reactors*. National Academies, 1996.

[4] D. Jacquemain, *Les accidents de fusion du coeur des réacteurs nucléaires de puissance - Etat des connaissances*, IRSN. edp sciences, 2013.

[5] C. Lemaignan, *Science des matériaux pour le nucléaire*. EDP Sciences, 2004.

[6] *Les matériaux du nucléaire : Modélisation et simulation des matériaux de structure*, Le Moniteur. CEA Saclay: Groupe Moniteur, 2016.

[7] D. R. Olander and A. Motta, *Light Water Reactor Materials*, vol. 1. ANS, 2009.

[8] H. Bailly, C. Prunier, and D. Ménessier, *The Nuclear Fuel of Pressurized Water Reactors and Fast Neutron Reactors: Design and Behaviour*. Intercept Limited, 1999.

[9] E. Supko, “13 - Nuclear fuel fabrication,” in *Uranium for Nuclear Power*, I. Hore-Lacy, Ed. Woodhead Publishing, 2016, pp. 353–382.

[10] H. Bernard, “Advanced fuel fabrication,” *J. Nucl. Mater.*, vol. 166, no. 1, pp. 105–111, Jul. 1989.

[11] H. Okamoto, “O-U (Oxygen-Uranium),” *J. Phase Equilibria Diffus.*, vol. 28, no. 5, pp. 497–497, Oct. 2007.

[12] J. D. Higgs, W. T. Thompson, B. J. Lewis, and S. C. Vogel, “Kinetics of precipitation of U4O9 from hyperstoichiometric UO2+x,” *J. Nucl. Mater.*, vol. 366, no. 3, pp. 297–305, Jul. 2007.

[13] “OECD NEA/NSC: Thermodynamics of Advanced Fuels – International Database (TAF-ID) - working version of january 2018.” [Online]. Available: https://www.oecd-nea.org/science/taf-id/. [Accessed: 25-Aug-2016].

[14] C. Guéneau *et al.*, “Thermodynamic modelling of advanced oxide and carbide nuclear fuels: Description of the U–Pu–O–C systems,” *J. Nucl. Mater.*, vol. 419, no. 1, pp. 145–167, Dec. 2011.

[15] H. A. Wriedt, “The O-Pu (Oxygen-Plutonium) system,” *Bull. Alloy Phase Diagr.*, vol. 11, no. 2, pp. 184–202.

[16] M. Kato, K. Morimoto, H. Sugata, K. Konashi, M. Kashimura, and T. Abe, “Solidus and liquidus of plutonium and uranium mixed oxide,” *J. Alloys Compd.*, vol. 452, no. 1, pp. 48–53, Mar. 2008.

[17] F. De Bruycker, K. Boboridis, D. Manara, P. Pöml, M. Rini, and R. J. M. Konings, “Reassessing the melting temperature of PuO2,” *Mater. Today*, vol. 13, no. 11, pp. 52–55, Nov. 2010.

[18] J.-O. Andersson, T. Helander, L. Höglund, P. Shi, and B. Sundman, “Thermo-Calc & DICTRA, computational tools for materials science,” *Calphad*, vol. 26, no. 2, pp. 273–312, 2002.

[19] R. Böhler *et al.*, “Recent advances in the study of the UO2–PuO2 phase diagram at high temperatures,” *J. Nucl. Mater.*, vol. 448, no. 1–3, pp. 330–339, May 2014.

[20] D. Staicu, “2.17 - Thermal Properties of Irradiated UO2 and MOX A2 - Konings, Rudy J.M.,” in *Comprehensive Nuclear Materials*, Oxford: Elsevier, 2012, pp. 439–464.

[21] D. Staicu and M. Barker, “Thermal conductivity of heterogeneous LWR MOX fuels,” *J. Nucl. Mater.*, vol. 442, no. 1–3, pp. 46–52, Nov. 2013.

[22] J.-L. Guillet, Y. Guérin, and B. Bonin, *Combustibles nucléaires*, Le Moniteur. CEA Saclay: Groupe Moniteur, 2008.

[23] P. D’hondt, C. Wagemans, A. Emsallem, and R. Brissot, “Measurement of the thermal-neutron-induced fission cross-section of 238U,” *Ann. Nucl. Energy*, vol. 11, no. 10, pp. 485–488, Jan. 1984.

[24] H. I. Liou and R. E. Chrien, “Epithermal Neutron Capture in Uranium-238,” *Nucl. Sci. Eng.*, vol. 62, no. 3, pp. 463–478, Mar. 1977.

[25] M. C. Davis, G. F. Knoll, J. C. Robertson, and D. M. Gilliam, “Absolute measurements of 235U and 239Pu fission cross-sections with photoneutron sources,” *Ann. Nucl. Energy*, vol. 5, no. 11, pp. 569–581, Jan. 1978.
[26] V. V. Rondinella and T. Wiss, “The high burn-up structure in nuclear fuel,” *Mater. Today*, vol. 13, no. 12, pp. 24–32, Dec. 2010.
[27] J. Spino, K. Vennix, and M. Coquerelle, “Detailed characterisation of the rim microstructure in PWR fuels in the burn-up range 40–67 GWd/tM,” *J. Nucl. Mater.*, vol. 231, no. 3, pp. 179–190, 1996.
[28] J. Spino and D. Papaioannou, “Lattice parameter changes associated with the rim-structure formation in high burn-up UO2 fuels by micro X-ray diffraction,” *J. Nucl. Mater.*, vol. 281, no. 2–3, pp. 146–162, 2000.
[29] H. Matzke and J. Spino, “Formation of the rim structure in high burnup fuel,” *J. Nucl. Mater.*, vol. 248, pp. 170–179, 1997.
[30] J. Noirot, L. Desgranges, and J. Lamontagne, “Detailed characterisations of high burn-up structures in oxide fuels,” *J. Nucl. Mater.*, vol. 372, no. 2–3, pp. 318–339, 2008.
[31] L. E. Thomas, C. E. Beyer, and L. A. Chariot, “Microstructural analysis of LWR spent fuels at high burnup,” *J. Nucl. Mater.*, vol. 188, pp. 80–89, Jun. 1992.
[32] N. Lozano, L. Desgranges, D. Aymes, and J. C. Niepce, “High magnification SEM observations for two types of granularity in a high burnup PWR fuel rim,” *J. Nucl. Mater.*, vol. 257, no. 1, pp. 78–87, Sep. 1998.
[33] H. Kleykamp, “Post-irradiation studies on LWR-MOX fuel fabricated by the optimized co-milling process,” *J. Nucl. Mater.*, vol. 324, no. 2–3, pp. 198–202, 2004.
[34] Y. Guérin, J. Noirot, C. Struzik, P. Garcia, P. Blanpain, and G. Chaigne, “Microstructure evolution and in-reactor behaviour of MOX fuel,” presented at the Proc. ANS Topical Meeting on Light Water Reactor Fuel Performance, Park City, Utah (USA), 2000.
[35] R. Manzel and C. T. Walker, “EPMA and SEM of fuel samples from PWR rods with an average burn-up of around 100 MWd/kgHM,” *J. Nucl. Mater.*, vol. 301, no. 2, pp. 170–182, Mar. 2002.
[36] E. Geiger *et al.*, “Fission products and nuclear fuel behaviour under severe accident conditions part 2: Fuel behaviour in the VERDON-1 sample,” *J. Nucl. Mater.*, vol. 495, no. Supplement C, pp. 49–57, 2017.
[37] B. J. Lewis, W. T. Thompson, and F. C. Iglesias, “2.20 - Fission Product Chemistry in Oxide Fuels,” in *Comprehensive Nuclear Materials*, R. J. M. Konings, Ed. Oxford: Elsevier, 2012, pp. 515–546.
[38] H. Matzke, “Oxygen potential in the rim region of high burnup UO2 fuel,” *J. Nucl. Mater.*, vol. 208, no. 1, pp. 18–26, Jan. 1994.
[39] H. Matzke, “Oxygen potential measurements in high burnup LWR U02 fuel,” *J. Nucl. Mater.*, vol. 223, no. 1, pp. 1–5, May 1995.
[40] V. D. Ozrin, “A model for evolution of oxygen potential and stoichiometry deviation in irradiated UO2 fuel,” *J. Nucl. Mater.*, vol. 419, no. 1, pp. 371–377, Dec. 2011.
[41] J. Spino and P. Peerani, “Oxygen stoichiometry shift of irradiated LWR-fuels at high burn-ups: Review of data and alternative interpretation of recently published results,” *J. Nucl. Mater.*, vol. 375, no. 1, pp. 8–25, Mar. 2008.
[42] M. Kato, K. Takeuchi, T. Uchida, T. Sunaoshi, and K. Konashi, “Oxygen potential of (U0.88Pu0.12)O2±x and (U0.7Pu0.3)O2±x at high temperatures of 1673–1873K,” *J. Nucl. Mater.*, vol. 414, no. 2, pp. 120–125, Jul. 2011.
[43] T. M. Besmann and T. B. Lindemer, “Chemical thermodynamic representations of 〈PuO2−x〉 and 〈U1−zPuzOw〉,” *J. Nucl. Mater.*, vol. 130, pp. 489–504, Feb. 1985.
[44] C. Ciszak *et al.*, “Micro-Raman analysis of the fuel-cladding interface in a high burnup PWR fuel rod,” *J. Nucl. Mater.*, vol. 495, pp. 392–404, Nov. 2017.
[45] C. Ciszak, “Etude de l’accrochage pastille/gaine des crayons combustibles des réacteurs à eau pressurisée,” thesis, Bourgogne Franche-Comté, 2017.

[46] H. Kleykamp, “The chemical state of the fission products in oxide fuels,” *J. Nucl. Mater.*, vol. 131, no. 2–3, pp. 221–246, 1985.
[47] H. Kleykamp, “The solubility of selected fission products in UO2 and (U, Pu)O2,” *J. Nucl. Mater.*, vol. 206, no. 1, pp. 82–86, 1993.
[48] J. Noirot *et al.*, “Fission Gas Inventory in PWR high burnup fuel: Experimental Characterisation and Modelling,” in *PWR Fuel Performance*, Orlando - Florida, USA, 2004.
[49] J. Noirot, I. Zacharie-Aubrun, and T. Blay, “FIB/SEM Examination of High Burn-Up UO2 in the Center of a Pellet,” *Nucl. Eng. Technol.*
[50] E. Geiger, “Study of fission products (Cs, Ba, Mo, Ru) behaviour in irradiated and simulated nuclear fuels during severe accidents using X-ray absorption spectroscopy, SIMS and EPMA,” PhD Thesis, Paris-Saclay, CEA Cadarache, 2016.
[51] “International Nuclear and Radiological Event Scale (INES),” 22-Nov-2017. [Online]. Available: https://www.iaea.org/topics/emergency-preparedness-and-response-epr/international-nuclear-radiological-event-scale-ines. [Accessed: 17-Sep-2018].
[52] C. Journeau, D. Roulet, E. Porcheron, P. Piluso, and C. Chagnot, “Fukushima Daiichi fuel debris simulant materials for the development of cutting and collection technologies,” *J. Nucl. Sci. Technol.*, vol. 55, no. 9, pp. 985–995, Sep. 2018.
[53] L. J. Baker, J. K. Fink, R. Simms, B. J. Schlenger, and J. E. Herceg, “Source Term Experiments Project (STEP): A summary: Final report,” Argonne National Lab., IL (USA), EPRI-NP-5753M, Mar. 1988.
[54] P. Royl, W. Breitung, E. A. Fischer, G. Schumacher, R. O. Gauntt, and S. A. Wright, “Contributions from the ACRR in-pile experiments to the understanding of key phenomena influencing unprotected loss of flow accident simulations in LMFBRs,” *Nucl. Eng. Des.*, vol. 100, no. 3, pp. 387–408, Mar. 1987.
[55] M. D. Allen, H. W. Stockman, K. O. Reil, A. J. Grimley, and W. J. Camp, “ACRR Fission Product Release Tests ST-1 and ST-2,” in *Proceedings*, Avignon, France, 1988.
[56] Z. R. Martinson, D. A. Petti, and B. A. Cook, “PBF (Power Burst Facility) severe fuel damage test 1-1: Volume 2, Test results report, Appendices A through I,” EG and G Idaho, Inc., Idaho Falls (USA), NUREG/CR-4684-Vol.2; EGG-2463-Vol.2, Oct. 1986.
[57] A. D. Knipe, S. A. Ploger, and D. J. Osetek, “PBF severe fuel damage scoping test. Test results report,” EG and G Idaho, Inc., Idaho Falls (USA), NUREG/CR-4683; EGG-2413, Aug. 1986.
[58] Z. R. Martinson *et al.*, “PBF (Power Burst Facility) severe fuel damage test 1--3 test results report,” Nuclear Regulatory Commission, Washington, DC (USA). Div. of Systems Research; EG and G Idaho, Inc., Idaho Falls, ID (USA), NUREG/CR-5354; EGG-2565, Oct. 1989.
[59] D. A. Petti *et al.*, “Power Burst Facility (PBF) severe fuel damage test 1-4 test results report,” Nuclear Regulatory Commission, Washington, DC (USA). Div. of Systems Research; EG and G Idaho, Inc., Idaho Falls, ID (USA), NUREG/CR-5163; EGG-2542, Apr. 1989.
[60] E. W. Coryell, “Summary of important results and SCDAP/RELAP5 Analysis for OECD LOFT Experiment LP-FP-2,” EGG Idaho, NUREG/CR-6160 NEA-CSNI-R(94)3 EGG-2721, 1994.
[61] P. von der Hardt and A. Tattegrain, “The phebus fission product project,” *J. Nucl. Mater.*, vol. 188, pp. 115–130, Jun. 1992.
[62] R. A. Lorenz and M. F. Osborne, “A summary of ORNL fission product release tests with recommended release rates and diffusion coefficients,” Nuclear Regulatory Commission, Oak Ridge National Lab., NUREG/CR--6261, 1995.
[63] Z. Lui, D. S. Cox, R. S. Dickson, and P. Elder, “A summary of CRL fission product release measurements from UO2 samples during post-irradiation annealing (1983-1992),” COG-92-377, 1994.
[64] T. Kudo, T. Fuketa, and A. Hidaka, “VEGA: An experimental study of radionuclides release from fuel under severe accident conditions,” in *Proceedings of 2005 Water Reactor Fuel Performance Meeting*, Kyoto, Japan, 2005.
[65] J. P. Leveque, B. Andre, G. Ducros, G. Le Marois, and G. Lhiaubet, “The HEVA experimental program,” *Nucl. Technol.*, vol. 108, no. 1, pp. 33–44, 1994.

[66] G. Ducros, P. P. Malgouyres, M. Kissane, D. Boulaud, and M. Durin, “Fission product release under severe accidental conditions: general presentation of the program and synthesis of VERCORS 1–6 results,” *Nucl. Eng. Des.*, vol. 208, no. 2, pp. 191–203, 2001.
[67] A. Gallais-During, “Overview of the VERDON-ISTP Program and main insights from the VERDON-2 air ingress test,” presented at the 7th European Review Meeting on Severe Accident Research, Marseille, 24-Mar-2015.
[68] B. Adroguer *et al.*, “Core loss during a severe accident (COLOSS),” *Nucl. Eng. Des.*, vol. 235, no. 2, pp. 173–198, Feb. 2005.
[69] J. R. Gabor and R. E. Henry, “The MAAP-BWR severe accident analysis code,” *Light Water React. Sev. Accid. Eval.*, 1983.
[70] R. Hiwatari, S. Nishimura, M. Furuya, and Y. Nishi, “Severe accident analysis of PWR with MAAP code. Primary large LOCA and secondary small LOCA.”
[71] R. M. Summers, R. K. J. Cole, E. A. Boucheron, M. K. Carmel, S. E. Dingman, and J. E. Kelly, “MELCOR 1.8.0: A computer code for nuclear reactor severe accident source term and risk assessment analyses,” Nuclear Regulatory Commission, Sandia National Labs., NUREG/CR--5531, 1991.
[72] K. Abe, N. Watanabe, M. Ida, M. Nishi, and T. Noguchi, “Overview of development and application of THALES code system for analyzing progression of core meltdown accident of LWR’s,” *Proc. Second Int. Top. Meet. Nucl. Power Plant Therm. Hydraul. Oper.*, 1986.
[73] L. Cantrel, F. Cousin, L. Bosland, K. Chevalier-Jabet, and C. Marchetto, “ASTEC V2 severe accident integral code: Fission product modelling and validation,” *Nucl. Eng. Des.*, vol. 272, pp. 195–206, Jun. 2014.
[74] M. S. Veshchunov, V. D. Ozrin, V. E. Shestak, V. I. Tarasov, R. Dubourg, and G. Nicaise, “Development of the mechanistic code MFPR for modelling fission product release from irradiated UO2 fuel,” *Nucl. Eng. Des.*, vol. 236, no. 2, pp. 179–200, 2006.
[75] D. J. Alpert, D. I. Chanin, and L. T. Ritchie, “Relative importance of individual elements to reactor accident consequences assuming equal release fractions,” Sandia National Labs., Albuquerque, NM (USA), NUREG/CR-4467; SAND-85-2575, Mar. 1986.
[76] M. Baichi, “Contribution à l’étude du corium d’un réacteur nucléaire accidenté : aspects puissance résiduelle et thermodynamique des systèmes U-UO2 et UO2-ZrO2,” PhD Thesis, INPG, Grenoble, 2001.
[77] E. Walle, P. Perrot, J. Foct, and M. Parise, “Evaluation of the Cs–Mo–I–O and Cs–U–I–O diagrams and determination of iodine and oxygen partial pressure in spent nuclear fuel rods,” *J. Phys. Chem. Solids*, vol. 66, no. 2–4, pp. 655–664, Feb. 2005.
[78] F. G. Di Lemma, J. Y. Colle, O. Beneš, and R. J. M. Konings, “A separate effect study of the influence of metallic fission products on CsI radioactive release from nuclear fuel,” *J. Nucl. Mater.*, vol. 465, pp. 499–508, Oct. 2015.
[79] A. Brown, G. J. McIntyre, C. Gr&#x00E4, and slund, “Analysis of Crystalline Phases in Core Bore Materials from Three Mile Island Unit 2,” *Nucl. Technol.*, vol. 87, no. 1, pp. 137–145, Aug. 1989.
[80] P. Piluso, G. Trillon, and C. Journeau, “The UO2–ZrO2 system at high temperature (T > 2000 K): importance of the meta-stable phases under severe accident conditions,” *J. Nucl. Mater.*, vol. 344, no. 1–3, pp. 259–264, 2005.
[81] I. Cohen and B. E. Schaner, “A metallographic and X-ray study of the UO2-ZrO2 system,” *J. Nucl. Mater.*, vol. 9, no. 1, pp. 18–52, 1963.
[82] P. Piluso *et al.*, “Severe accident experiments on PLINIUS platform. Results of first experiments on COLIMA facility related to VVER-440. Presentation of planned VULCANO and KROTOS tests.”
[83] M. Schwarz, G. Hache, and P. von der Hardt, “PHEBUS FP: a severe accident research programme for current and advanced light water reactors,” *Nucl. Eng. Des.*, vol. 187, no. 1, pp. 47–69, 1999.

[84] P. March and B. Simondi-Teisseire, “Overview of the facility and experiments performed in Phébus FP,” *Ann. Nucl. Energy*, vol. 61, pp. 11–22, Nov. 2013.
[85] B. Clément *et al.*, “LWR severe accident simulation: synthesis of the results and interpretation of the first Phebus FP experiment FPT0,” *Nucl. Eng. Des.*, vol. 226, no. 1, pp. 5–82, Nov. 2003.
[86] B. Clément and R. Zeyen, “The objectives of the Phébus FP experimental programme and main findings,” *Ann. Nucl. Energy*, vol. 61, pp. 4–10, Nov. 2013.
[87] L. E. Herranz, M. Vela-García, J. Fontanet, and C. L. del Prá, “Experimental interpretation and code validation based on the PHEBUS-FP programme: Lessons learnt from the analysis of the containment scenario of FPT1 and FPT2 tests,” *Nucl. Eng. Des.*, vol. 237, no. 23, pp. 2210–2218, Dec. 2007.
[88] T. Haste *et al.*, “Phébus FPT3: Overview of main results concerning the behaviour of fission products and structural materials in the containment,” *Nucl. Eng. Des.*, vol. 261, pp. 333–345, Aug. 2013.
[89] Dickinson *et al.*, “Synthesis of IPSN Pre-Test Analysis for FPT0, the First Test of the PHEBUS FP Programme,” Jun. 1994.
[90] P. Hofmann, “Current knowledge on core degradation phenomena, a review,” *J. Nucl. Mater.*, vol. 270, no. 1, pp. 194–211, Apr. 1999.
[91] O. de Luze, T. Haste, M. Barrachin, and G. Repetto, “Early phase fuel degradation in Phébus FP: Initiating phenomena of degradation in fuel bundle tests,” *Ann. Nucl. Energy*, vol. 61, pp. 23–35, Nov. 2013.
[92] P. Chatelard, J. Fleurot, O. Marchand, and P. Drai, “Assessment of ICARE/CATHARE V1 Severe Accident Code,” pp. 145–154, Jan. 2006.
[93] R. Dubourg, H. Faure-Geors, G. Nicaise, and M. Barrachin, “Fission product release in the first two PHEBUS tests FPT0 and FPT1,” *Nucl. Eng. Des.*, vol. 235, no. 20, pp. 2183–2208, Sep. 2005.
[94] P. D. W. Bottomley, A. D. Stalios, J.-P. Glatz, B. Sätmark, and C. T. Walker, “Examination of melted fuel rods and released core material from the first Phebus-FP reactor accident experiment,” *J. Nucl. Mater.*, vol. 278, no. 2, pp. 136–148, Apr. 2000.
[95] M. Barrachin, D. Gavillet, R. Dubourg, and A. De Bremaecker, “Fuel and fission product behaviour in early phases of a severe accident. Part I: Experimental results of the PHEBUS FPT2 test,” *J. Nucl. Mater.*, vol. 453, no. 1, pp. 340–354, Oct. 2014.
[96] R. Dubourg, M. Barrachin, R. Ducher, D. Gavillet, and A. De Bremaecker, “Fuel and fission product behaviour in early phases of a severe accident. Part II: Interpretation of the experimental results of the PHEBUS FPT2 test,” *J. Nucl. Mater.*, vol. 453, no. 1, pp. 355–374, Oct. 2014.
[97] Y. Pontillon, G. Ducros, and P. P. Malgouyres, “Behaviour of fission products under severe PWR accident conditions VERCORS experimental programme—Part 1: General description of the programme,” *Nucl. Eng. Des.*, vol. 240, no. 7, pp. 1843–1852, 2010.
[98] Y. Pontillon and G. Ducros, “Behaviour of fission products under severe PWR accident conditions: The VERCORS experimental programme—Part 2: Release and transport of fission gases and volatile fission products,” *Nucl. Eng. Des.*, vol. 240, no. 7, pp. 1853–1866, 2010.
[99] Y. Pontillon and G. Ducros, “Behaviour of fission products under severe PWR accident conditions. The VERCORS experimental programme—Part 3: Release of low-volatile fission products and actinides,” *Nucl. Eng. Des.*, vol. 240, no. 7, pp. 1867–1881, 2010.
[100] G. Ducros, Y. Pontillon, and P. P. Malgouyres, “Synthesis of the VERCORS experimental programme: Separate-effect experiments on Fission Product release, in support of the PHEBUS-FP programme,” *Ann. Nucl. Energy*, vol. 61, pp. 75–87, Nov. 2013.
[101] Y. Pontillon *et al.*, “Lessons learnt from VERCORS tests.: Study of the active role played by UO2–ZrO2–FP interactions on irradiated fuel collapse temperature,” *J. Nucl. Mater.*, vol. 344, no. 1–3, pp. 265–273, 2005.
[102] R. Dubourg and P. Taylor, “A qualitative comparison of barium behaviour in the PHEBUS FPT0 test and analytical tests,” *J. Nucl. Mater.*, vol. 294, no. 1, pp. 32–38, Apr. 2001.

[103] A. Gallais-During *et al.*, “VERDON Laboratory : Performances of the Experimental LWR Severe Accident Device and Fisrt Results of Fission Products Release on High Burn-up UO2 fuel,” presented at the 21st International Conference Nuclear Energy for New Europe, Ljubjana, 2012.
[104] Y. Pontillon *et al.*, “Fission products and nuclear fuel behaviour under severe accident conditions part 1: Main lessons learnt from the first VERDON test,” *J. Nucl. Mater.*, vol. 495, no. Supplement C, pp. 363–384, 2017.
[105] A. Gallais-During *et al.*, “Performance and first results of fission product release and transport provided by the VERDON facility,” *Nucl. Eng. Des.*, vol. 277, pp. 117–123, 2014.
[106] C. Le Gall *et al.*, “Fission products and nuclear fuel behaviour under severe accident conditions part 3: Speciation of fission products in the VERDON-1 sample,” *J. Nucl. Mater.*, vol. 495, no. Supplement C, pp. 291–298, Nov. 2017.
[107] A. Gallais-During *et al.*, “Nuclear fuel behaviour at high temperature: new insights from post-test examinations on the VERDON-1 sample,” in *LWR fuels with enhanced safety and performance*, Idaho, USA, 2016.
[108] A. Hidaka, “Outcome of VEGA Program on Radionuclide Release from Irradiated Fuel under Severe Accident Conditions,” *J. Nucl. Sci. Technol.*, vol. 48, no. 1, pp. 85–102, 2011.
[109] B. J. Lewis, R. Dickson, F. C. Iglesias, G. Ducros, and T. Kudo, “Overview of experimental programs on core melt progression and fission product release behaviour,” *J. Nucl. Mater.*, vol. 380, no. 1–3, pp. 126–143, 2008.
[110] J.-Y. Colle *et al.*, “Fission product release and microstructure changes of irradiated MOX fuel at high temperatures,” *J. Nucl. Mater.*, vol. 442, no. 1–3, pp. 330–340, Nov. 2013.
[111] J.-P. Hiernaut *et al.*, “Fission product release and microstructure changes during laboratory annealing of a very high burn-up fuel specimen,” *J. Nucl. Mater.*, vol. 377, no. 2, pp. 313–324, Jul. 2008.
[112] B. T. Bradbury, J. T. Demant, P. M. Martin, and D. M. Poole, “Electron probe micro-analysis of irradiated UO2,” *J. Nucl. Mater.*, vol. 17, no. 3, pp. 227–236, Nov. 1965.
[113] B. M. Jeffery, “Microanalysis of inclusions in irradiated UO2,” *J. Nucl. Mater.*, vol. 22, no. 1, pp. 33–40, Apr. 1967.
[114] J. I. Bramman, R. M. Sharpe, D. Thom, and G. Yates, “Metallic fission-product inclusions in irradiated oxide fuels,” *J. Nucl. Mater.*, vol. 25, no. 2, pp. 201–215, Feb. 1968.
[115] H. Kleykamp, “The Chemical State of Fission Products in Oxide Fuels at Different Stages of the Nuclear Fuel Cycle,” *Nucl. Technol.*, vol. 80, no. 3, pp. 412–422, Mar. 1988.
[116] H. Kleykamp, “Constitution and thermodynamics of the Mo-Ru, Mo-Pd, Ru-Pd and Mo-Ru-Pd systems,” *J. Nucl. Mater.*, vol. 167, pp. 49–63, Sep. 1989.
[117] J. O. A. Paschoal, H. Kleykamp, and F. Thümmler, “The constitution of the Ru□Rh system,” *J. Common Met.*, vol. 98, no. 2, pp. 279–284, Apr. 1984.
[118] M. H. Kaye, B. J. Lewis, and W. T. Thompson, “Thermodynamic treatment of noble metal fission products in nuclear fuel,” *J. Nucl. Mater.*, vol. 366, no. 1, pp. 8–27, Jun. 2007.
[119] H. Kleykamp, J. O. Paschoal, R. Pejsa, and F. Thümmler, “Composition and structure of fission product precipitates in irradiated oxide fuels: Correlation with phase studies in the Mo-Ru-Rh-Pd and BaO-UO2-ZrO2-MoO2 Systems,” *J. Nucl. Mater.*, vol. 130, pp. 426–433, 1985.
[120] M. Kaye and L. Wang, “U-Ru-Rh-Pd QUATERNARY SYSTEM: THERMODYNAMIC CALCULATIONS AND EXPERIMENTAL EXPLORATIONS,” 2016.
[121] M. Tourasse, M. Boidron, and B. Pasquet, “Fission product behaviour in phenix fuel pins at high burnup,” *J. Nucl. Mater.*, vol. 188, pp. 49–57, Jun. 1992.
[122] J.-C. Dumas, *Etude des conditions de formation du joint oxyde-gaine dans les combustibles des réacteurs à neutrons rapides : observations et proposition d’un modèle de comportement des produits de fission volatils*. Grenoble INPG, 1995.
[123] I. Johnson, C. E. Johnson, C. E. Crouthamel, and C. A. Seils, “Oxygen potential of irradiated urania-plutonia fuel pins,” *J. Nucl. Mater.*, vol. 48, no. 1, pp. 21–34, Aug. 1973.

[124] C. T. Walker, C. Bagger, and M. Mogensen, “Migration of fission product barium in UO2 fuel under transient conditions,” *J. Nucl. Mater.*, vol. 173, no. 1, pp. 14–25, Sep. 1990.
[125] I. Sato, H. FURUYA, T. ARIMA, K. IDEMITSU, and K. YAMAMOTO, “Behavior of Fission Products Zirconium and Barium in Fast Reactor Fuel Irradiated to High Burnup,” *J. Nucl. Sci. Technol.*, vol. 36, no. 9, pp. 775–780, Sep. 1999.
[126] W. H. Hocking, A. M. Duclos, and L. H. Johnson, “Study of fission-product segregation in used CANDU fuel by X-ray photoelectron spectroscopy (XPS) II,” *J. Nucl. Mater.*, vol. 209, no. 1, pp. 1–26, 1994.
[127] C. Sari, C. T. Walker, and G. Schumacher, “Solubility and migration of fission product barium in oxide fuel,” *J. Nucl. Mater.*, vol. 79, no. 1, pp. 255–259, Jan. 1979.
[128] F. T. Ewart, R. G. Taylor, J. M. Horspool, and G. James, “The chemical effects of composition changes in irradiated oxide fuel materials II-Fission product segregation and chemical equilibria,” *J. Nucl. Mater.*, vol. 61, no. 3, pp. 254–270, Sep. 1976.
[129] J. O. A. Paschoal, H. Kleykamp, and F. Thümmler, “Phase equilibria in the pseudoquaternary BaO-UO2-ZrO2-MoO2 system,” *J. Nucl. Mater.*, vol. 151, no. 1, pp. 10–21, 1987.
[130] D. R. O’boyle, F. L. Brown, and J. E. Sanecki, “Solid fission product behavior in uranium-plutonium oxide fuel irradiated in a fast neutron flux,” *J. Nucl. Mater.*, vol. 29, no. 1, pp. 27–42, Jan. 1969.
[131] J. P. Guha and D. Kolar, “Phase equilibria in the system BaO-CeO2,” *J. Mater. Sci.*, vol. 6, no. 9, pp. 1174–1177.
[132] Z. Hozer, L. Maroti, B. Toth, and P. Windberg, “VVER-440 core degradation experiment,” *Eighth Int. Top. Meet. Nucl. React. Therm.-Hydraul.*, 1997.
[133] S. Hagen, L. Sepold, P. Hofmann, and G. Schanz, “CORA experiments on the behaviour of LWR fuel rod bundles under severe fuel damage conditions,” *Kerntechnik*, vol. 53, no. 1, pp. 15–20, 1988.
[134] W. Hering and P. Hofmann, “Material interactions during severe LWR accidents. Summary of separate-effects test results,” 1994.
[135] P. Hofmann, S. J. L. Hagen, V. Noack, G. Schanz, and L. K. Sepold, “Chemical-Physical Behavior of Light Water Reactor Core Components Tested Under Severe Reactor Accident Conditions in the CORA Facility,” *Nucl. Technol.*, vol. 118, no. 3, pp. 200–224, Jun. 1997.
[136] M. S. Veshchunov and A. V. Berdyshev, “Modeling of chemical interactions of fuel rod materials at high temperatures I. Simultaneous dissolution of UO2 and ZrO2 by molten Zr in an oxidizing atmosphere,” *J. Nucl. Mater.*, vol. 252, no. 1, pp. 98–109, Jan. 1998.
[137] N. E. Agency, “International standard problem ISP36. Cora-W2 experiment on severe fuel damage for a Russian type PWR,” Nuclear Energy Agency, NEA-CSNI-R--95-20, 1996.
[138] S. Mastromarino *et al.*, “Assessment of solid/liquid equilibria in the (U, Zr)O2+y system,” *J. Nucl. Mater.*, vol. 494, no. Supplement C, pp. 368–379, Oct. 2017.
[139] A. Quaini *et al.*, “High temperature investigation of the solid/liquid transition in the PuO2–UO2–ZrO2 system,” *J. Nucl. Mater.*, vol. 467, Part 2, pp. 660–676, 2015.
[140] S. Yamanaka and K. Kurosaki, “Thermophysical properties of Mo–Ru–Rh–Pd alloys,” *J. Alloys Compd.*, vol. 353, no. 1–2, pp. 269–273, 2003.
[141] P. Martin, M. Ripert, G. Carlot, P. Parent, and C. Laffon, “A study of molybdenum behaviour in UO2 by X-ray absorption spectroscopy,” *J. Nucl. Mater.*, vol. 326, no. 2, pp. 132–143, Mar. 2004.
[142] D. C. Fee and C. E. Johnson, “Cesium thermomigration and reaction in nuclear fuels,” *J. Nucl. Mater.*, vol. 96, no. 1, pp. 71–79, Jan. 1981.
[143] D. C. Fee and C. E. Johnson, “Cesium-uranium-oxygen chemistry in uranium-plutonium oxide fast reactor fuel pins,” *J. Nucl. Mater.*, vol. 99, no. 1, pp. 107–116, Jul. 1981.
[144] D. C. Fee and C. E. Johnson, “The interaction of cesium with urania in uranium-plutonium oxide fast reactor fuel pins,” *J. Nucl. Mater.*, vol. 78, no. 1, pp. 219–224, Nov. 1978.
[145] D. C. Fee and C. E. Johnson, “Phase equilibria in the Cs□U□O system in the temperature range from 873 to 1273 K,” *J. Inorg. Nucl. Chem.*, vol. 40, no. 7, pp. 1375–1381, 1978.

[146] E. H. P. Cordfunke, A. B. Van Egmond, and G. Van Voorst, “Investigations on cesium uranates—I: Characterization of the phases in the Cs□U□O system,” *J. Inorg. Nucl. Chem.*, vol. 37, no. 6, pp. 1433–1436, Jun. 1975.
[147] S. R. Dharwadkar, M. Shyamala, G. Chattopadhyay, and M. S. Chandrasekharaiah, “Thermal stability of Cs2UO4 phase at high temperature,” *Trans. Indian Inst. Met.*, vol. 36, pp. 295–297, 1983.
[148] P. A. G. O’Hare and H. R. Hoekstra, “Thermochemistry of molybdates I. Standard enthalpy of formation of cesium molybdate (Cs2MoO4),” *J. Chem. Thermodyn.*, vol. 5, no. 6, pp. 851–856, Nov. 1973.
[149] R. J. M. Konings and E. H. P. Cordfunke, “The thermochemical properties of cesium molybdate, CS2MoO4, from 298.15 to 1500 K,” *Thermochim. Acta*, vol. 124, pp. 157–162, 1988.
[150] M. G. Adamson, E. A. Aitken, and R. W. Caputi, “Experimental and thermodynamic evaluation of the melting behavior of irradiated oxide fuels,” *J. Nucl. Mater.*, vol. 130, pp. 349–365, Feb. 1985.
[151] P. G. Lucuta, R. A. Verrall, H. Matzke, and B. J. Palmer, “Microstructural features of SIMFUEL — Simulated high-burnup UO2-based nuclear fuel,” *J. Nucl. Mater.*, vol. 178, no. 1, pp. 48–60, 1991.
[152] E. Geiger, R. Bès, P. Martin, Y. Pontillon, P. L. Solari, and M. Salome, “Fission products behaviour in UO 2 submitted to nuclear severe accident conditions,” *J. Phys. Conf. Ser.*, vol. 712, no. 1, p. 012098, 2016.
[153] E. Geiger, R. Bès, P. Martin, Y. Pontillon, G. Ducros, and P. L. Solari, “Insights on fission products behaviour in nuclear severe accident conditions by X-ray absorption spectroscopy,” *J. Nucl. Mater.*, vol. 471, pp. 25–33, 2016.
[154] J. Cobos, D. Papaioannou, J. Spino, and M. Coquerelle, “Phase characterisation of simulated high burn-up UO2 fuel,” *J. Alloys Compd.*, vol. 271–273, pp. 610–615, Jun. 1998.
[155] Z. Hiezl, “Processing and microstructural characterisation of UO2-based simulated spent nuclear fuel ceramics for the UK`s advanced gas-cooled reactors,” Aug. 2015.
[156] V. G. Baranov, A. V. Lunev, V. F. Reutov, A. V. Tenishev, M. G. Isaenkova, and A. V. Khlunov, “An attempt to reproduce high burn-up structure by ion irradiation of SIMFUEL,” *J. Nucl. Mater.*, vol. 452, no. 1–3, pp. 147–157, Sep. 2014.
[157] G. Giacchetti and C. Sari, “Behavior of Molybdenum in Mixed-Oxide Fuel,” *Nucl. Technol.*, vol. 31, no. 1, pp. 62–69, Oct. 1976.
[158] G. Nicaise, R. Dubourg, and P. Taylor, “Analyse d’essais de séquences accidentales et interprétation du relâchement des produits de fission : interdépendance de relâchement du Cs, du Mo, et du Ba,” presented at the 11th Symposium on Thermodynamics of Nuclear Materials, Karlsruhe, Germany, 2004.
[159] G. Nicaise, “Note Technique DPAM/SEMIC n° 2004/37 - Interprétation du relâchement de Cs, Mo, Ba, I, Ru dans les essais VERCORS, VERCORS HT et VERCORS RT.” 2004.
[160] C. W. Bale *et al.*, “FactSage thermochemical software and databases,” *Calphad*, vol. 26, no. 2, pp. 189–228, 2002.
[161] C. W. Bale *et al.*, “FactSage thermochemical software and databases — recent developments,” *Calphad*, vol. 33, no. 2, pp. 295–311, 2009.

Chapter II:

CHARACTERIZATION OF MOX IRRADIATED FUELS TREATED AT VERY HIGH TEMPERATURE

TABLE OF CONTENT

II.1 INTRODUCTION

As discussed in the first chapter, the release mechanisms of FP are strongly linked to their speciation in the fuel and to the microstructure evolution of the fuel pellets during the different stages of a nuclear severe accident. These two parameters are strongly impacted by the atmosphere (i.e. the oxygen potential) during an accidental scenario. A deep understanding of the FP speciation dependence on oxygen potential is thus essential to better predict the consequences of a nuclear severe accident.

Among the research programs launched to this end, the VERDON program are performed on different types of fuel (UO_2 and MOX), burn-ups, geometries (pellets or debris bed) and oxygen potential conditions (reducing or oxidizing) and enable to:

- Quantify FP release and study their transportation through the experimental loop thanks to on-line γ spectrometry measurements and gas chromatography.
- Study the fuel and FP chemistry before and after the tests thanks to the characterization techniques available in the dedicated hot laboratory of the LECA-STAR facility (CEA Cadarache).

The objective of this second chapter is to provide experimental data on MOX fuel and FP behavior at high temperature in oxygen potential conditions representative of a nuclear severe accident. More precisely, the effect of the oxygen potential on the fuel-cladding interaction phenomena and Cs, Mo and Ba speciation are investigated in a temperature range corresponding to the last phase of a VERDON test.

To this end, the samples recovered after two complementary VERDON tests performed on fuel pellets originated from the same father rod and treated under oxidizing (VERDON-3) or reducing conditions (VERDON-4 tests) were characterized in detail. These results were compared to the characterizations performed on the father rod in order to conclude about the oxygen potential effect on the chemical evolution of the phases containing Cs, Mo and Ba.

OM and SEM observations enabled to study the microstructure and porosity of the samples. SIMS isotope mapping and X-ray maps enabled to determine FP location and associations in the fuel samples. Mass spectra were also recorded on different regions of the samples mainly to discriminate Zr coming from the cladding and Zr produced by fission within the fuel. EPMA was used in order to quantify the amount of the different elements present in the fuel samples.

Thermodynamic calculations were used in support to the interpretation of experimental data. They notably helped to establish a scenario explaining the main phenomena that took place during the VERDON-3 and 4 tests.

Finally, the results obtained were used to assess the validity of the initial and final steps of the FP speciation mechanisms proposed in the literature [1]–[3] and shown in **Figure I-32** and **Figure I-33**.

II.2 CHARACTERISTICS OF IRRADIATED FUEL SAMPLES

II.2.1 Father Rod characteristics

The three samples studied in this part were extracted from the FXP2CC-B05 father rod which consisted in MOX-E fuel irradiated 4 cycles in a PWR operated by EDF. It was prepared according to the MIMAS/ADU process using a RESTCH screening machine during the powder preparation step. The Pu content is higher than for classical MOX fuels. The characteristics of the father rod are presented in **Table II-1**. The local burn-up of the segment where the three samples were taken from was around 60 GWd.t_{HM}^{-1}.

Table II-1:FXP2CC-B05 rod fabrication characteristics

Position in assembly FXP2CC	B05
Cladding material	M5
Rod length (mm)	3851.7
Outer diameter of the clad (mm)	9.5
Inner diameter of the clad (mm)	8.36
Fuel type	MOX-E
Pu/(U+Pu+^{241}Am)	7.245
Mean pellet height (mm)	11.5
Mean pellet diameter (mm)	8.192
Mean burn-up (GWd.t_{HM}^{-1})	55.6
Average linear power during the 4th cycle (W.cm^{-1})	180
Reactor	Chinon B3

The sample B05 consisted in a pellet and its original M5 cladding embedded in a metallic alloy (Bi/Sn) after its extraction from the father rod. It was characterized thanks to OM and EPMA [4], [5]. The chemical state of this sample is representative of the fuel behavior in normal PWR operating conditions which constitutes the initial state of the FP release mechanisms.

II.2.2 VERDON-3 and 4 samples characteristics

Four other irradiated pellets and their claddings were extracted from this rod to form the VERDON-3 and VERDON-4 samples, composed each of two pellets. Two half-pellets of depleted and un-irradiated uranium dioxide were placed at each end of the samples and maintained by crimping the cladding. The cladding was not fully sealed to enable interactions between the samples and the surrounding atmosphere during the tests as shown in **Figure II-1**.

Before the VERDON experiments, the samples were re-irradiated at low linear power (17 W.cm^{-1} for VERDON-3 and 20 W.cm^{-1} for VERDON-4) in the OSIRIS Material Testing Reactor for nine days to recreate the short half-life FP without any in-pile release. As a consequence, these FP (i.e. ^{99}Mo, ^{132}Te, ^{133}I, ^{131}I, ^{140}Ba…) known for their radiological effects were measurable by using online gamma spectrometry during the experiment.

The samples were placed vertically in a hafnia crucible in the VERDON furnace, described in detail in **Chapter I**, **section I.4.1.5**. The VERDON-3 and 4 tests took place respectively in April 2013 and October 2014 in the VERDON laboratory of the LECA-STAR facility. They were part of the VERDON-

ISTP program that aimed at studying the fuel and FP behavior in severe accident conditions [6]. The main objective of these two complementary tests was the study of MOX fuel behavior and FP release under oxidizing (VERDON-3) and reducing (VERDON-4) conditions at very high temperature (> 2300°C).

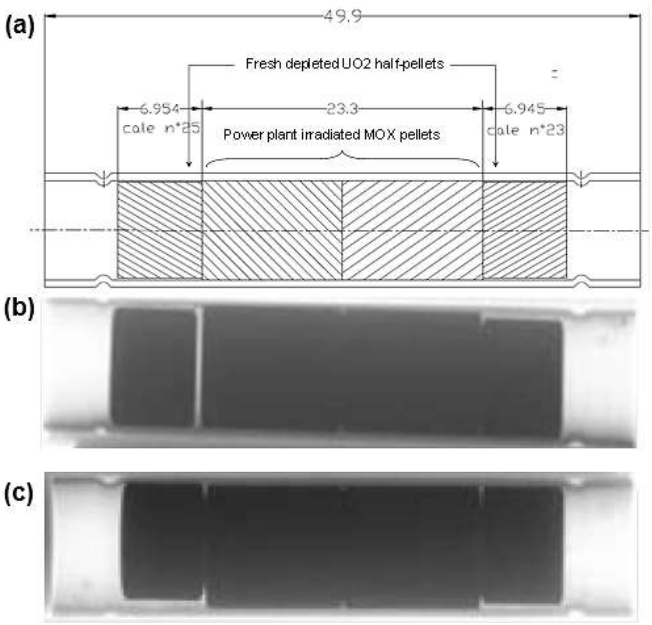

Figure II-1: Schematic dimensions in mm (a) and radiography of the VERDON-3 (b) and VERDON-4 (c) samples.

II.2.2.1 VERDON-3 test

The VERDON-3 thermal sequence consisted in three stages as shown in **Figure II-2**:

- The first stage consisted in a temperature ramp (0.1°C.min^{-1}) up to 400°C followed by a dwell at this temperature, under pure He.
- The second stage (stage 2) was carried up to 1500°C with a dwell of 10 minutes. The heating rate was set at 0.2°C.min^{-1} and a temperature plateau was performed at 1200°C to study FP release in LOCA conditions. The atmosphere during the test was imposed by the equilibrium of H_2O/H_2.
- The final stage (stage 3) was carried under pure steam up to 2300°C. The heating rate was set at 0.2°C.min^{-1} and successive plateau of 10 minutes were performed every 100°C from 1900°C to the maximum temperature.

The evolution of the oxygen potential during stages 2 and 3 has been calculated from the H_2O/H_2 system by integration of the whole quantity of gas injected during the step considered (**Figure II-3**). Thermodynamic equilibrium is also supposed. The jump observed at 1500°C is the consequence of these two hypotheses: the change in the atmosphere between stage 2 and 3 does not account for the initial dilution of the gas injected in stage 3 by the one present in stage 2.

The cooling stage was performed by shutting down the induction furnace and can be seen as a quench for the sample.

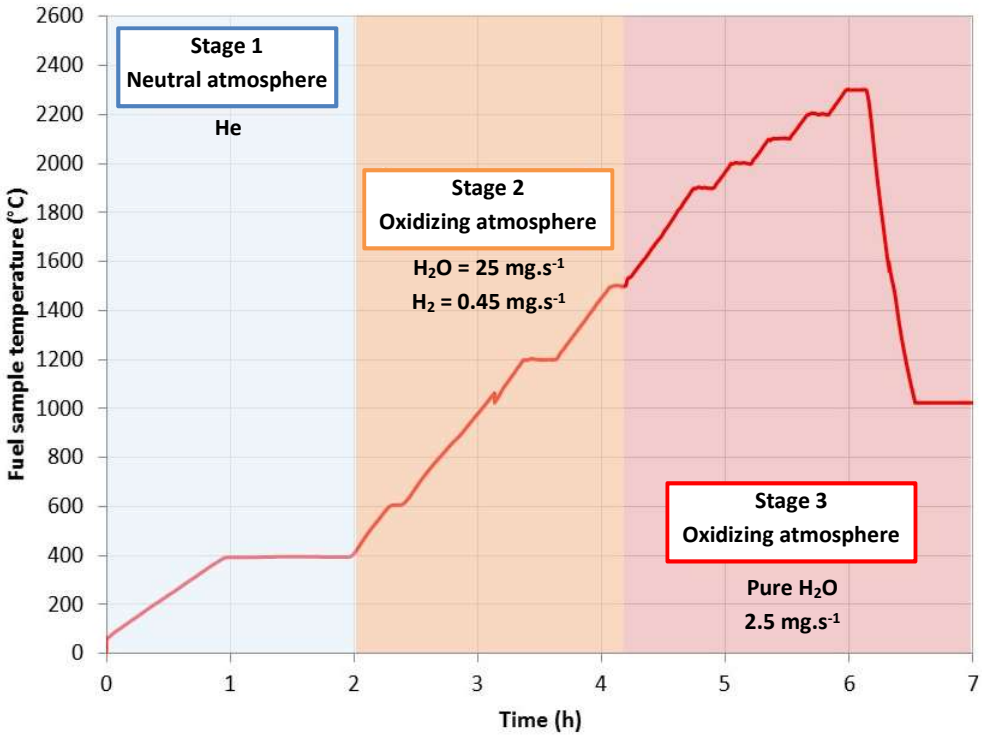

Figure II-2: Thermal sequence of the VERDON-3 test

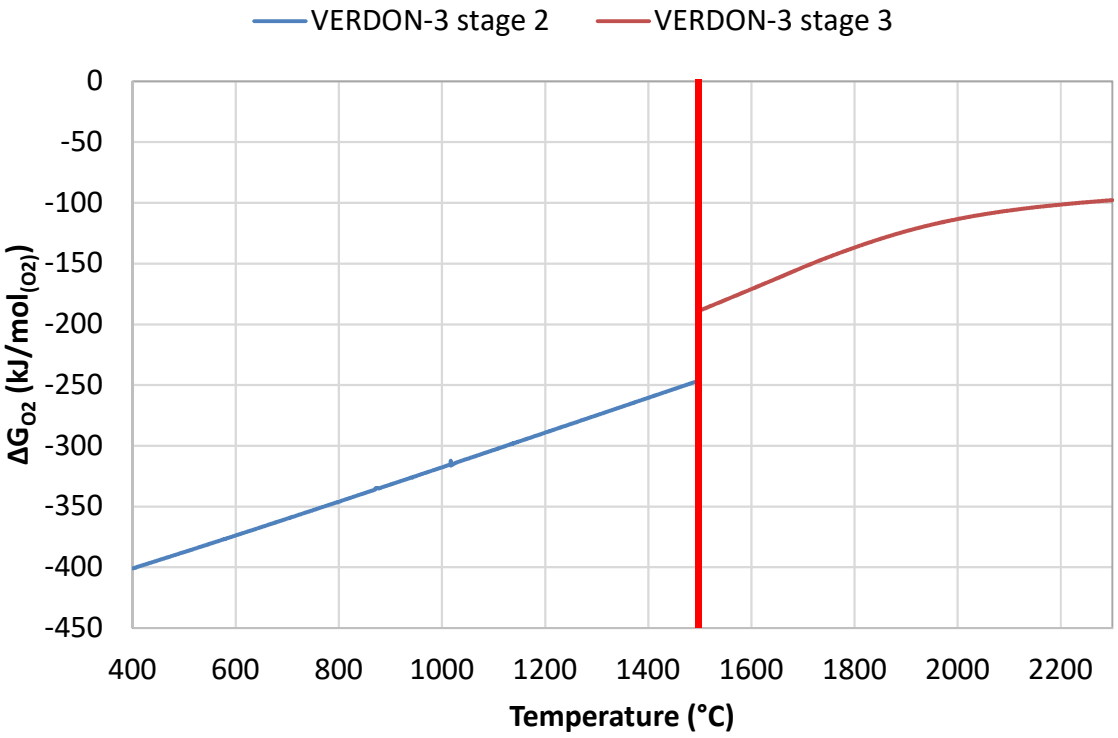

Figure II-3: Evolution of the oxygen potential during the stage 2 and 3 of the VERDON-3 test, calculated from the H_2O/H_2 system using Thermo-Calc [7] coupled with the TAF-ID [8]

II.2.2.2 VERDON-4 sample characteristics

The VERDON-4 thermal sequence consisted in three stages as shown in **Figure II-4**:

- The first phase consisted in a temperature ramp (0.1°C.min^{-1}) up to 400°C followed by a dwell at this temperature, under pure He.
- The second phase (stage 2) was carried under pure steam up to 1500°C with a dwell of 10 minutes. The heating rate was set at 0.2°C.min^{-1} and a temperature plateau was performed at 1200°C to study FP release in LOCA conditions.
- The final stage (stage 3) was carried under pure H_2 up to 2300°C. The heating rate was set at 0.2°C.min^{-1} and successive plateau of 10 minutes were performed every 100°C from 1900°C to the maximum temperature.

The atmosphere during the test was imposed by the equilibrium of H_2O/H_2. The evolution of the oxygen potential during stages 2 and 3 has been calculated from the H_2O/H_2 system by integration of the whole quantity of gas injected during the step considered (**Figure II-5**). Thermodynamic equilibrium is also supposed. The jump observed at 1500°C is the consequence of these two hypotheses, just like in the case of VERDON-3. Compared to VERDON-3, the second stage of the VERDON-4 test was performed in more oxidizing conditions (pure H_2O) whereas stage 3 was carried in reducing conditions (pure H_2).

The cooling stage was performed by shutting down the induction furnace and can be seen as a quench for the sample.

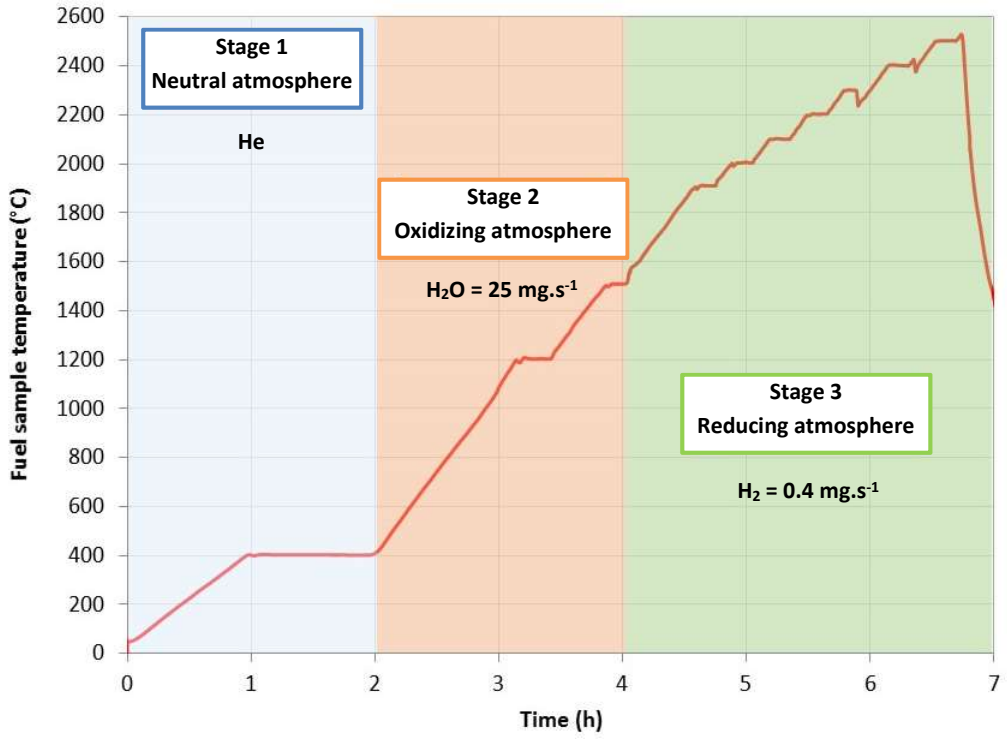

Figure II-4: Thermal sequence of the VERDON-4 test

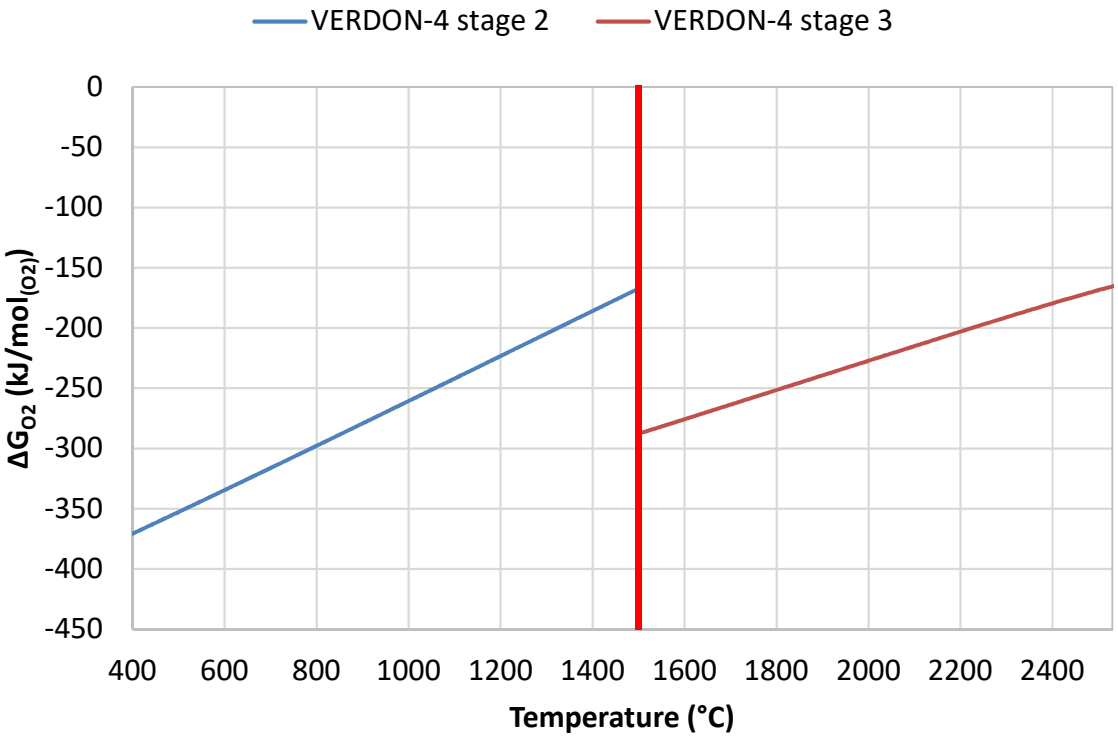

Figure II-5: Evolution of the oxygen potential during the stage 2 and 3 of the VERDON-4 test, calculated using Thermo-Calc [7] coupled with the TAF-ID [8]

II.3 SAMPLES CHARACTERIZATION

Detailed characterizations were performed on the B05 sample (taken from the father rod) and the samples retrieved after the VERDON-3 and 4 tests. The objective was to study the evolution of the different phases observed in the fuel. A special emphasis was made on the behavior of Mo, Cs and Ba.

OM and SEM observations enabled to study the microstructure and porosity of the samples. SIMS isotope mapping and X-ray maps enabled to determine FP location and associations in the fuel samples. Mass spectra were also recorded on different regions of the samples mainly to discriminate Zr coming from the cladding and Zr produced by fission within the fuel. EPMA quantitative profiles helped quantifying the amount of the different elements present in the fuel samples. These characterizations were performed in different locations of the samples. For the sake of clarity, the regions analyzed will be located on the radius of the pellet, 0R being the center and 1R the periphery.

Thermodynamic calculations were performed using the Thermo-Calc [7] software coupled with the TAF-ID database [8] in the conditions of stages 2 and 3 of the VERDON-3 and 4 tests. The objective was to help interpreting the experimental data and to assess the TAF-ID performances in the case of calculations on irradiated fuels. No calculations were performed on the first stage of the VERDON tests because the sample is not at thermodynamic equilibrium.

The experimental conditions in which the characterizations were performed are described in **Appendix 1.1**. The method and main hypotheses made in the thermodynamic calculations are presented in **Appendix 1.2**. The macro files used to calculate the VERDON-3 and 4 tests are given in **Appendix 1.3**.

II.3.1 B05 sample (father rod)

The characterizations presented here have been performed in 2009 and 2010 on the B05 sample [4], [5]. A summary of the main results is given hereafter.

II.3.1.1 Fuel behavior

A micrograph of the B05 sample is given in **Figure II-6**. Several cracks typically observed in irradiated fuels at 4 cycles are present in the sample. This MOX fuel is composed of three main phases organized in a filamentary network as can be seen on the Pu X-ray map presented in **Figure II-7**. These three regions differ from one another by their Pu content as shown in the quantitative profiles performed along Line 1 and 2 (**Figure II-8** and **Figure II-10**):

- Several Pu-rich agglomerates appearing in white in the Pu X-ray map contain around 5 at% of Pu (corresponding to 18 % of Pu/(U+Pu)).
- A coating phase with intermediate Pu content of 3 at% (10 % of Pu/(U+Pu)) appears in light grey in the Pu X-ray map.
- A UO_2-rich phase, called UO_2 matrix, appearing in dark grey in the Pu X-ray map contains 0.5 at% Pu (1.6 to 2.0 % of Pu/(U+Pu)).

The O content in the sample is constant and around 66.0 at% which leads to a O/M [1] ratio of around 2.0 ± 0.1 in the UO_2 matrix and 2.2 ± 0.2 in the Pu-agglomerates.

In the Zr X-ray map of **Figure II-7**, a piece of cladding can be observed at the periphery of the sample. The interface between the fuel and the cladding is wavy indicating a bonding between the cladding and the fuel on approximately 5 µm according to **Figure II-8**. This is consistent with the usual thickness of the "bonding layer" reported in the literature [9]–[12].

Lots of porous agglomerates can be noticed from the periphery of the sample (1R) until 0.4R (dashed red circle on **Figure II-6**). This zone corresponds to the limit of the HBS region. Indeed, during the first cycles of irradiation, the Pu agglomerates undergo massive fission leading to gas and fission metallic fission products precipitation and grain restructuration. In the center of the sample, the Pu agglomerates are hardly visible by OM as they are less porous than in the periphery. Nevertheless, they are revealed thanks to X-ray mapping as shown in **Figure II-9**.

In the HBS region at 1R, the grain size in the Pu agglomerates is lower than 1 µm. It increases gradually towards the center from 2-3 µm at 0.5R up to 10 µm in the center of the sample which corresponds to the Pu grain size before irradiation.

A lot of fine bubbles of a few microns are observed in the agglomerates at the periphery of the pellet as shown in **Figure II-7**. Their number decreases towards the center but their size increases. At 0R, several agglomerates present large bubbles as it is the case for the agglomerate presented in **Figure II-9**.

The local burn-up in the Pu agglomerates has been determined thanks to Nd quantitative analyses to be 210 $GWd.t_{HM}^{-1}$ at the center of the agglomerates located at 1R, 170 $GWd.t_{HM}^{-1}$ at 0.5R and 150 $GWd.t_{HM}^{-1}$ at 0R.

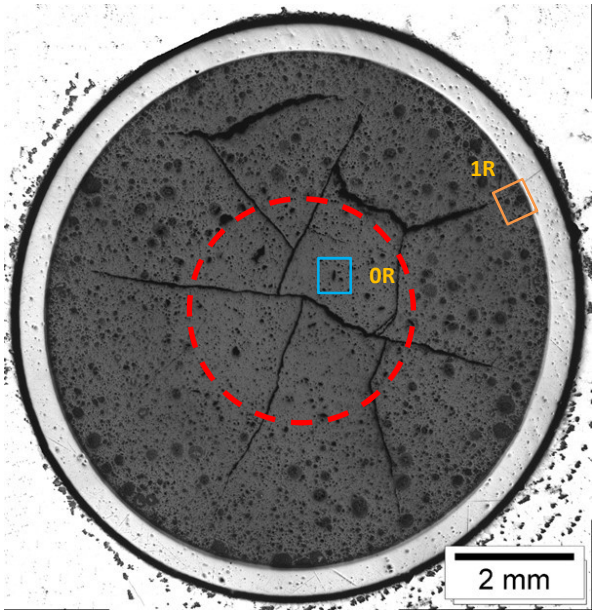

Figure II-6: Micrographs of the B05 sample after preparation

[1] M corresponds to the sum of Ba, Ce, Nd, Zr, Pu and U amounts (elements present in solid solution in (U, Pu)O_2) measured through EPMA. Several elements dissolved in the fuel could not be quantified during the analyses (Sr, La, Y…). Thus, the value calculated in this study may be slightly overestimated.

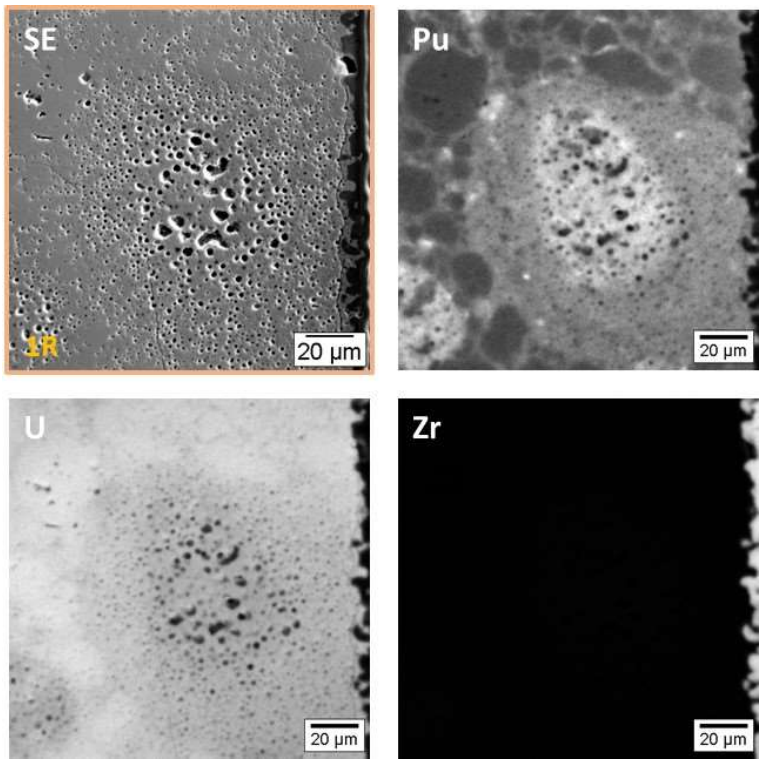

Figure II-7: SEM-SE and Pu, U and Zr X-ray maps acquired at 1R on the B05 sample

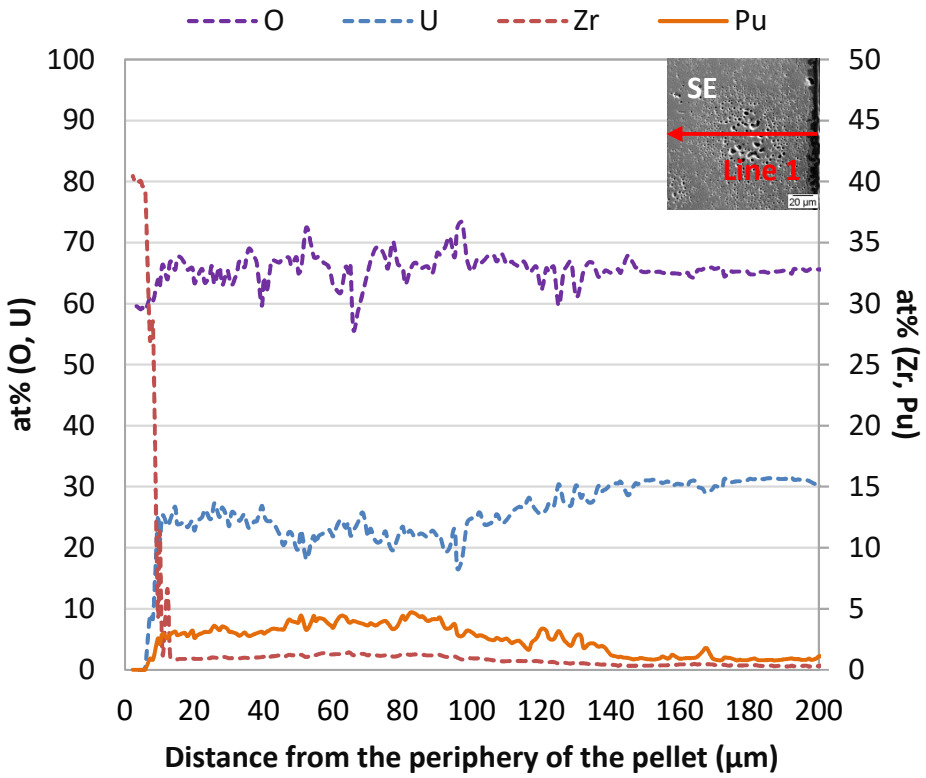

Figure II-8: O, U, Zr and Pu quantitative profiles along Line 1, B05 sample (1R)

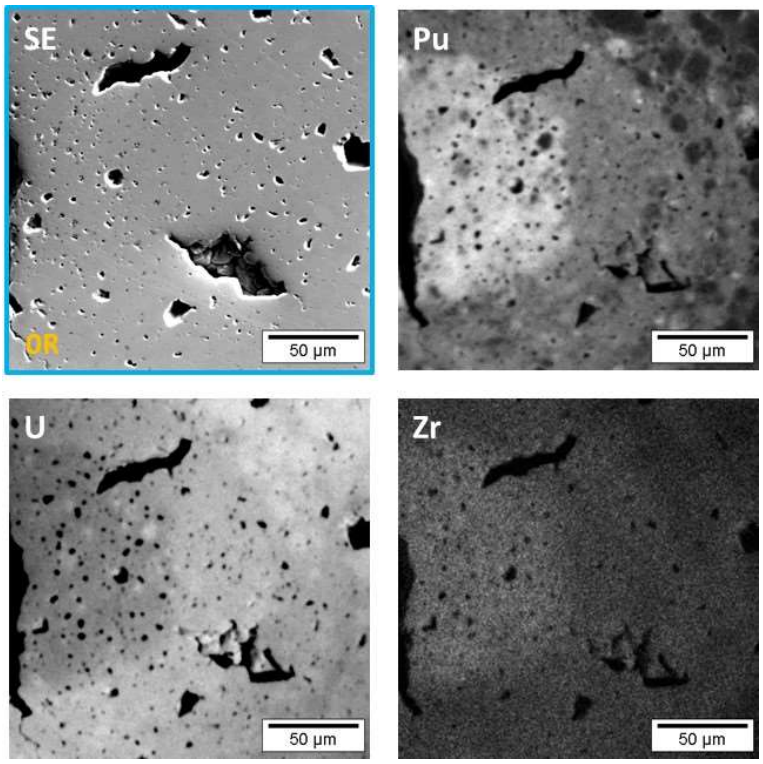

Figure II-9: SEM-SE and Pu, U and Zr X-ray maps acquired at 0R on the B05 sample

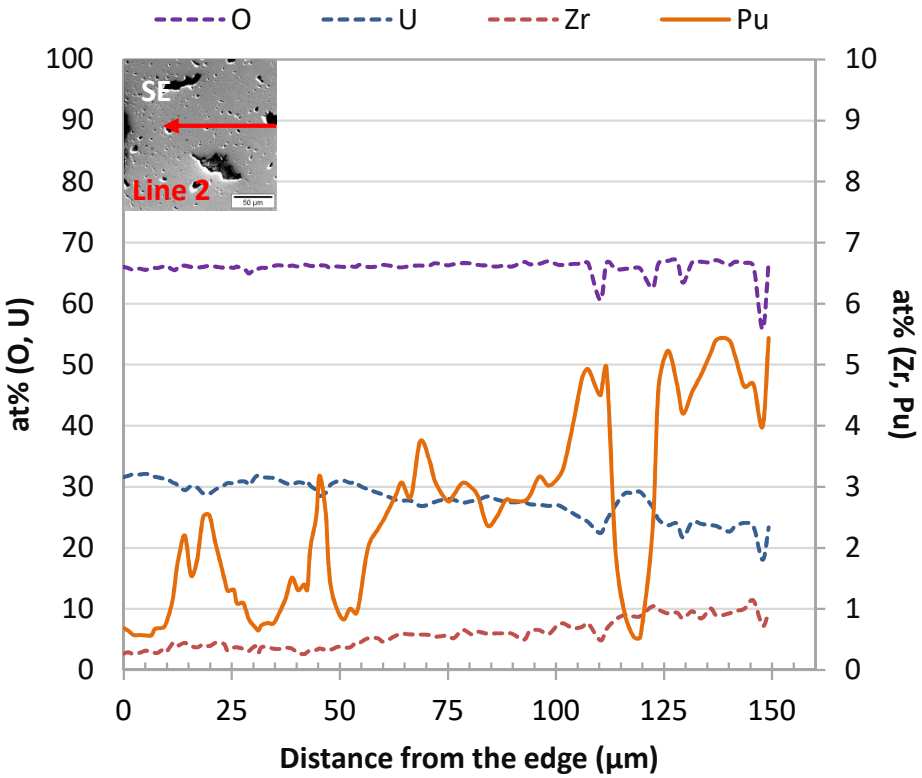

Figure II-10: O, U, Zr and Pd quantitative profiles along Line 2, B05 sample (0R)

II.3.1.2 Metallic precipitates

At the periphery of the sample, metallic precipitates with an Equivalent Circle Diameter (ECD) of 2-3 µm are observed in the Pu agglomerates (**Figure II-11**). Submicronic precipitates are also found in the coating phase. In the metallic precipitates of the restructured areas, the Mo content is almost twice inferior to the Ru one. Indeed, the mean ratio Ru/Mo is 1.8 ± 0.1 %. On the contrary, the amount of Mo dissolved in the agglomerate (0.9 at%) is three times larger than for Ru (0.3 at%) (**Figure II-12**). In the UO_2 matrix the concentrations in Mo (0.4 at%) and Ru (0.3 at%) correspond to the creation ratios between these two FP calculated by the CESAR code to be 0.87 [13]. However, these values are way higher than the solubility limits for Mo and Ru in both UO_2 and $U_{0.85}Pu_{0.15}O_2$ reported in the literature [14], [15]. This could be explained by the presence of submicrometric precipitates (metallic or oxide such as MoO_2) non observable by the techniques employed in this study.

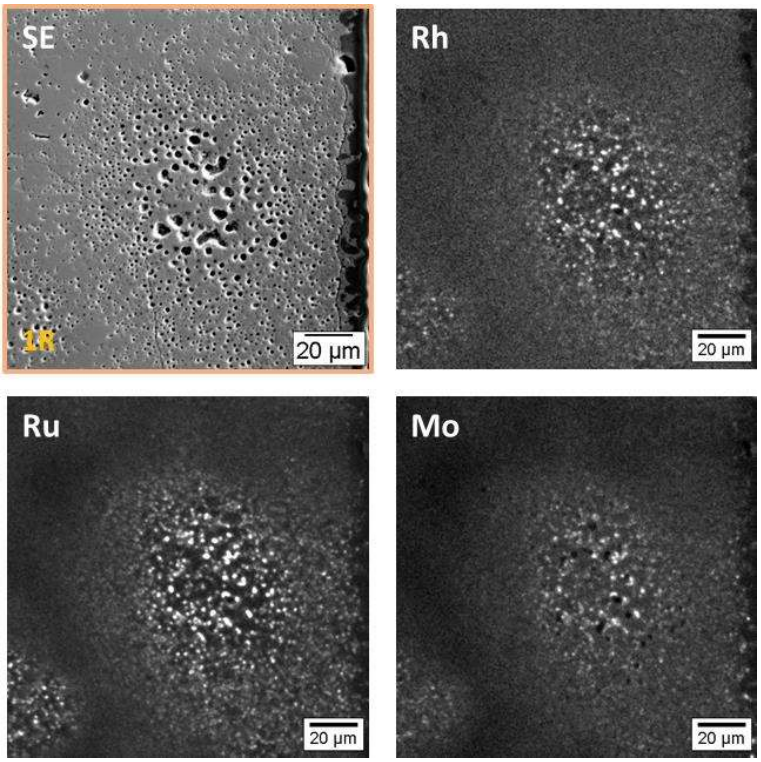

Figure II-11: SEM-SE and Ru, Mo and Rh X-ray maps acquired at 1R on the B05 sample

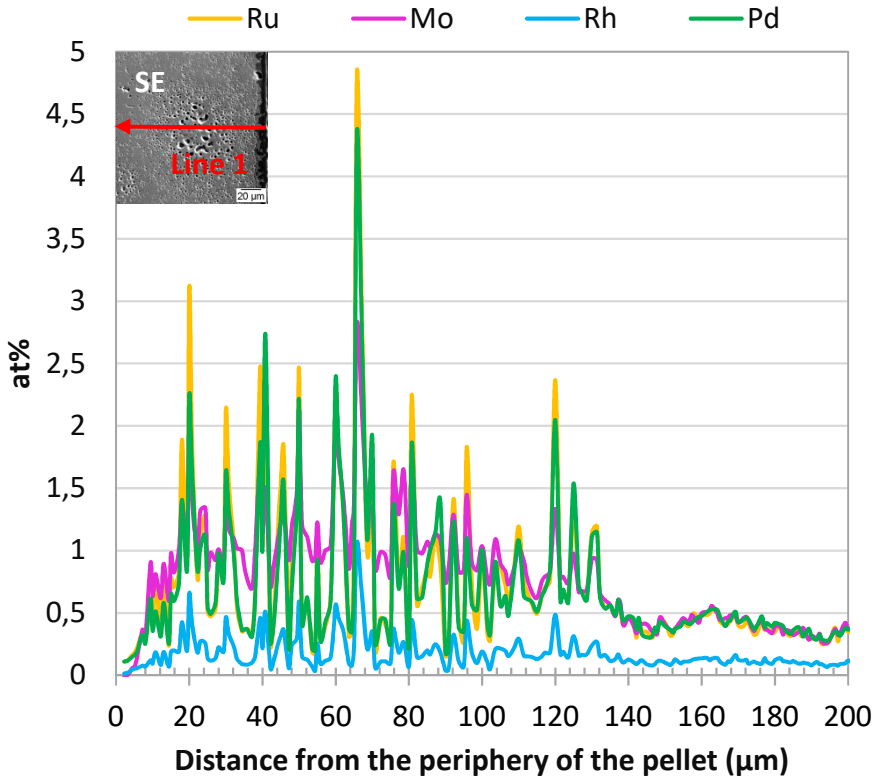

Figure II-12: Ru, Mo, Rh and Pd quantitative profiles along Line 1, B05 sample (1R)

The size of metallic precipitates in the agglomerates and the coating phase increases up to 4-5 µm and 1-2 µm respectively in the center of the sample (**Figure II-13**). At 0.5R, in the metallic precipitates the amount of Mo is inferior to Ru. In the UO_2 matrix at 0.5R as well as in the three zones of the center, the Ru/Mo ratio (with 0.9 ± 0.1 %) is consistent with the creation ratios (**Figure II-14**).

Pd and Rh are also contained in these precipitates as described in the literature. The ratio Pd/Rh is constant in the metallic precipitates all over the sample (3.8 ± 0.4 %) as well as the ratio Ru/Rh (4.3 ± 0.3 %). This is again consistent with the creation ratio between Ru and Rh calculated to be 4.11 for the father rod.

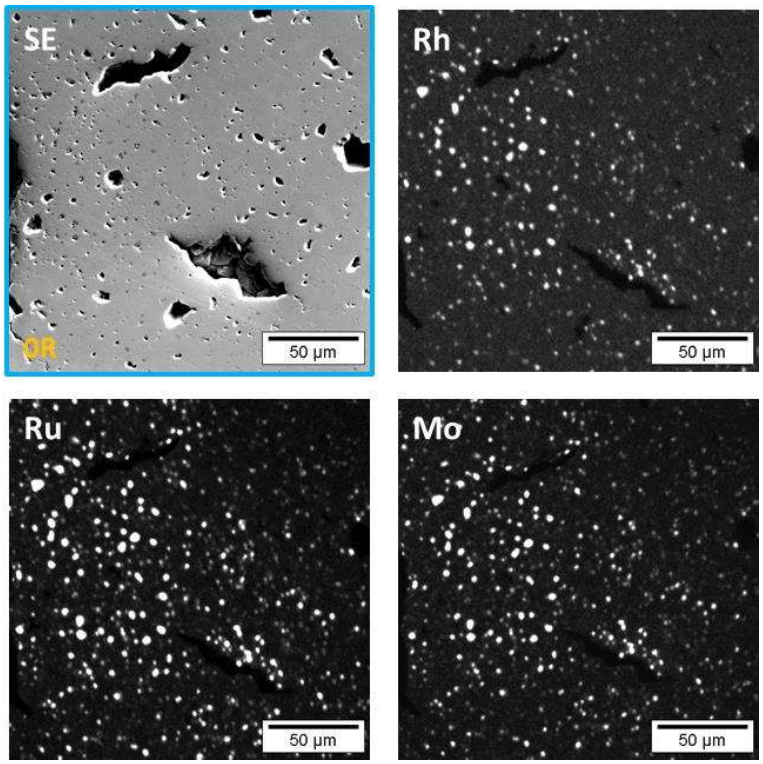

Figure II-13: SEM-SE and Ru, Mo and Rh X-ray maps acquired at 0R on the B05 sample

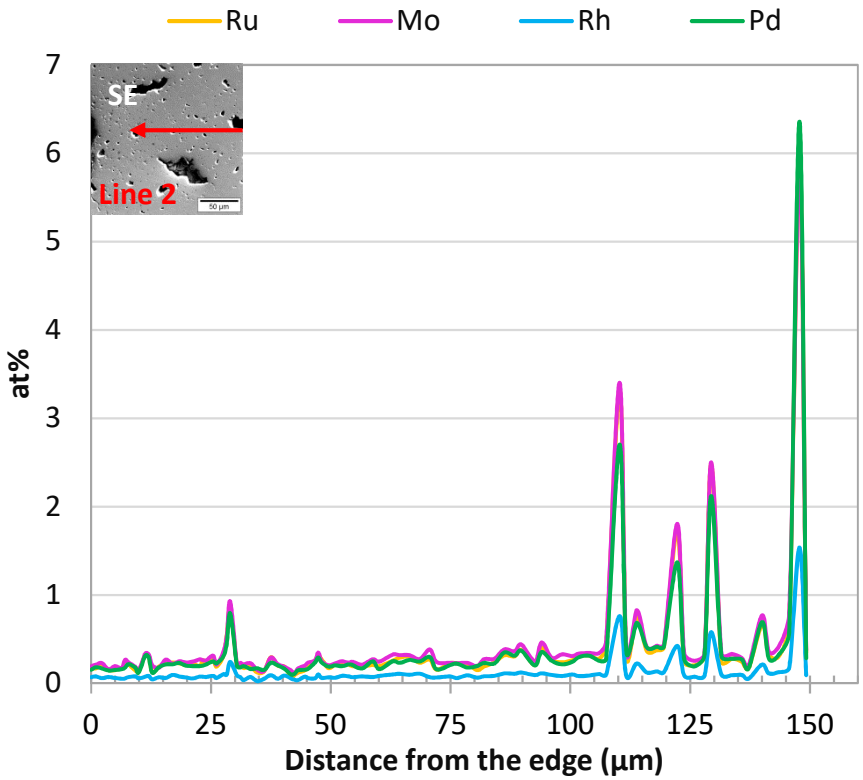

Figure II-14: Ru, Mo, Rh and Pd quantitative profiles along Line 2, B05 sample (0R)

II.3.1.3 Dissolved FP: special emphasis on Ba and Cs behavior

Ba and Cs quantitative profiles at the periphery and in the center of the sample are given in **Figure II-15** and **Figure II-16** respectively, along with the profiles of Xe and Ce. The corresponding Zr quantitative profiles are given in **Figure II-8** and **Figure II-10**. These FP are usually found dissolved in the fuel or in gas bubbles in the case of Xe and Cs. Except Xe which is chemically inert, they can react with each other and with the fuel elements to form the grey phase at high temperature [14] as described in **Chapter I**.

An increase in the Ba, Ce, Cs and Zr contents can be observed in the Pu agglomerate everywhere in the sample. This is particularly visible at 1R due to the HBS effect. Indeed, at 1R the concentrations of Ba and Cs in the agglomerate (0.6 at% and 0.7 at% respectively) are 3 times higher than in the UO_2 matrix (0.2 at% in both cases). Concerning Zr and Ce, their concentrations increase from 0.2 at% in the UO_2 matrix up to 1.3 at% and 0.8 at% respectively in the agglomerates. The Xe content drops in the Pu agglomerate from around 0.5 at% in the UO_2 matrix to less than 0.1 at%.

In the center of the pellet, the Ba and Cs contents are twice higher in the agglomerates (around 0.4 at%) than in the UO_2 matrix (around 0.2 at%). The Ce and Zr contents increase from 0.4 at% and 0.2 at% respectively in the UO_2 matrix up to 0.9 at% and 0.5 at% in the agglomerates. Concerning Xe, its concentration slightly increases in the Pu agglomerate (from 0.2 at% in the UO_2 matrix up to 0.3 at%). Some bubbles can also be noticed with Xe content reaching up to 0.7 at%.

According to [11], [16], [17] in normal operating conditions and high burn-up fuel, Ba would be a component of the oxide or grey phase (Ba, Cs, Sr)(Mo, Zr, Pu, U, RE)O_3. No such precipitates are observed in the B05 sample even in the agglomerates where the burn-up can reach 210 GWd.t_{HM}^{-1}. Nevertheless, submicronic precipitates not observed at the scales used for observations could exist, such as BaO or Cs_2O. The oxygen content in the Pu-agglomerates is higher than in the UO_2 matrix, which could encourage the formation of this phase. However, the maximum solubilities of these FP in $U_{0.8}Pu_{0.2}O_2$ given in [14], [18] are not reached in the agglomerates according to the quantitative profiles.

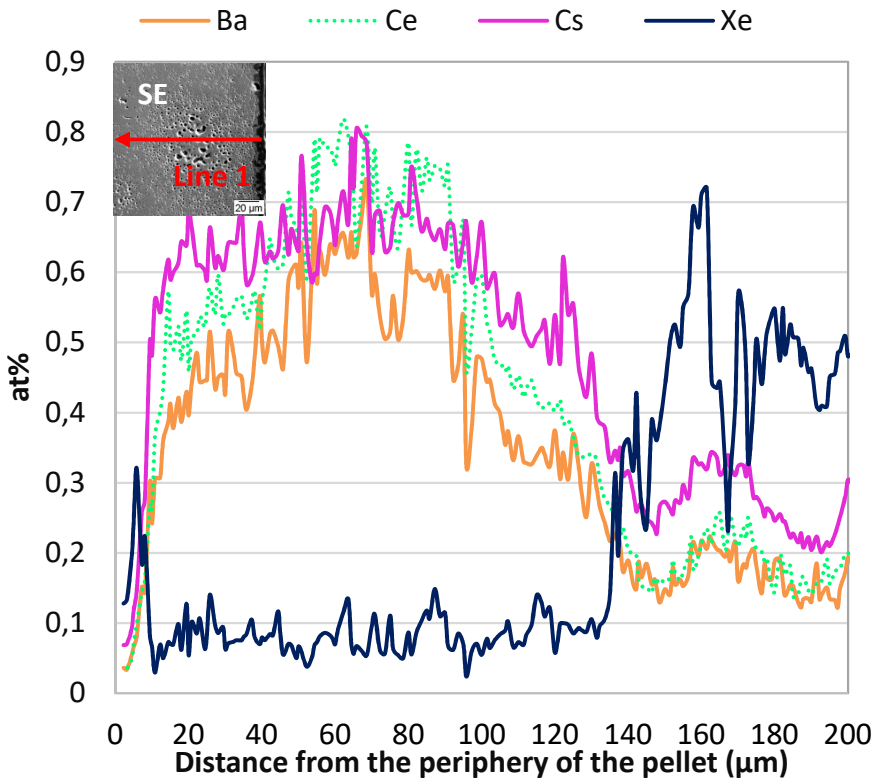

Figure II-15: Ba, Ce, Cs and Xe quantitative profiles along Line 1, B05 sample (1R)

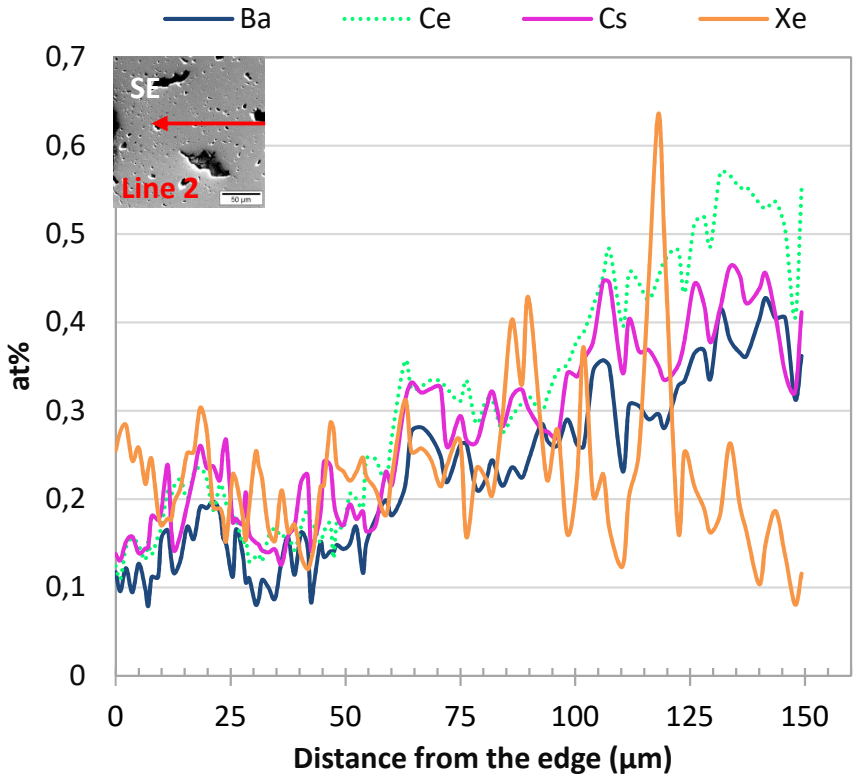

Figure II-16: Ba, Ce, Cs and Xe quantitative profiles along Line 2, B05 sample (0R)

II.3.1.4 Summary of the observations made in the father rod sample

The post-irradiation characterizations performed on the sample extracted from the father rod showed that it is a heterogeneous material in terms of composition. Indeed, three main phases with different Pu content have been highlighted, which is typical of MOX MIMAS fuels:

- The UO_2 matrix with up to 0.5 at% of Pu.
- The coating phase with up to 3 at% of Pu.
- The Pu agglomerates with up to 5 at% of Pu.

The Pu agglomerates were observed thanks to OM only from 0.4 R to 1R, in the restructured area of the fuel, because of the high porosity they exhibit. Moreover, the Pu agglomerates are richer in FP compared to the UO_2 matrix, because ^{239}Pu has a higher probability to undergo fission than ^{235}U.

Only one type of secondary phase could be clearly identified in the B05 sample: the metallic precipitates composed of Mo, Ru, Tc, Rh and Pd. Two types of population were found: one richer in Ru and the other one richer in Mo. The Ru/Mo ratio varied between 0.75 in the UO_2 matrix and 1.8 in the agglomerates.

The other FP such as Cs and Ba were found dissolved in the fuel. However their exact chemical form was difficult to identify using the set of techniques available on irradiated fuels.

An interaction between the fuel and cladding was observed at the periphery of the sample on 5 µm.

II.3.2 VERDON-3 samples

The debris recovered after the VERDON-3 test are shown in **Figure II-17**. The two fresh half pellets were easily identified from their size and integrity (**Figure II-18**) but it was harder to recognize the two MOX pellets as their shape was modified during the test (**Figure II-19**). These two pellets were very fragile and had a tendency to crumble. Therefore, no measurements could be done to determine their diameter and their length.

The elements recovered were prepared for observations and chemical analyses. One of the two VERDON-3 irradiated pellets (V-3E sample) was embedded in an epoxy resin (araldite) and the second one (V-3M sample) was embedded in a metallic alloy (Bi/Sn). Both pellets were axially polished up to half of their diameter.

Figure II-17: VERDON-3 pellets and debris recovered from the case

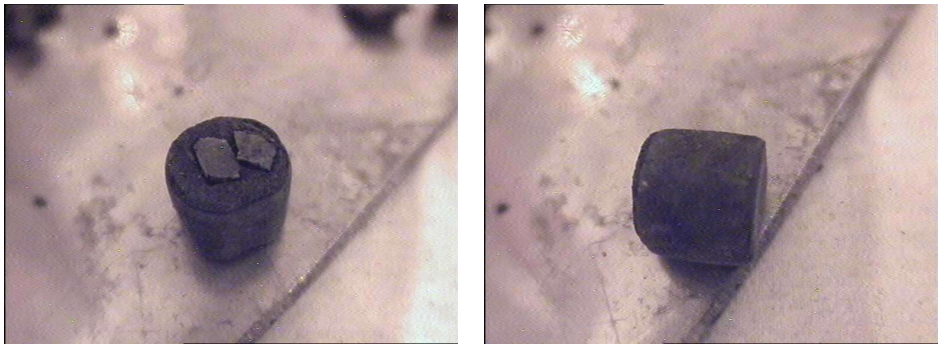

Figure II-18: The two fresh half pellets recovered after the VERDON-3 tests

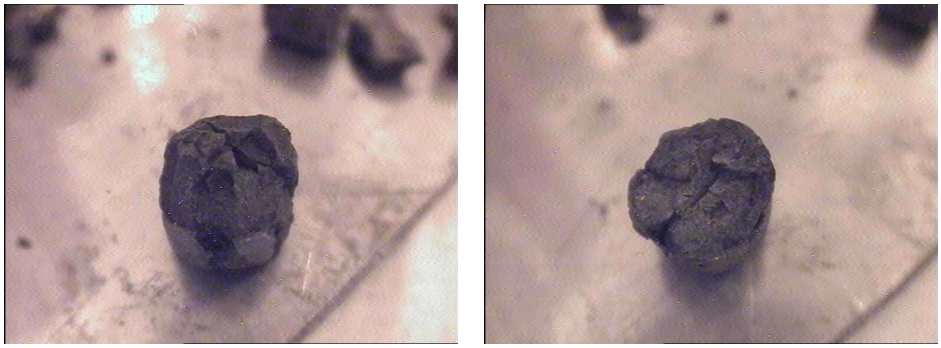

Figure II-19: The two MOX pellets recovered after the VERDON-3 test: sample V-3E on the left and V-3M on the right

II.3.2.1 Fuel behavior

II.3.2.1.1 Microstructure analysis

Optical micrographs of the V-3E and V-3M samples are presented in **Figure II-20**. A complete metallographic analysis was performed on the sample V-3M due to its better conservation status compared to the V-3E sample. Despite the advanced state of degradation they exhibit, three main features can be observed on both pellets:

- Light grey agglomerates (orange frames in **Figure II-20**) homogeneously distributed all over the pellets present a reduce porosity composed of spherical pores as shown in **Figure II-21** (0R and 0.75R zones).
- A porous matrix (green frames in **Figure II-20**) with an elevated pore interconnection degree and smaller spherical pores can be seen in **Figure II-21** (0.25R and 0.5R zones).
- A continuous flaked light grey strip (blue frames in **Figure II-20**) can be seen on the left edge of the V-3E sample and has been attributed to a remaining piece of cladding. It is even more visible on the right side of the V-3M sample, separated from the porous matrix by a longitudinal crack. This area also presents some spherical pores and several cracks (**Figure II-21**, 1R zone).

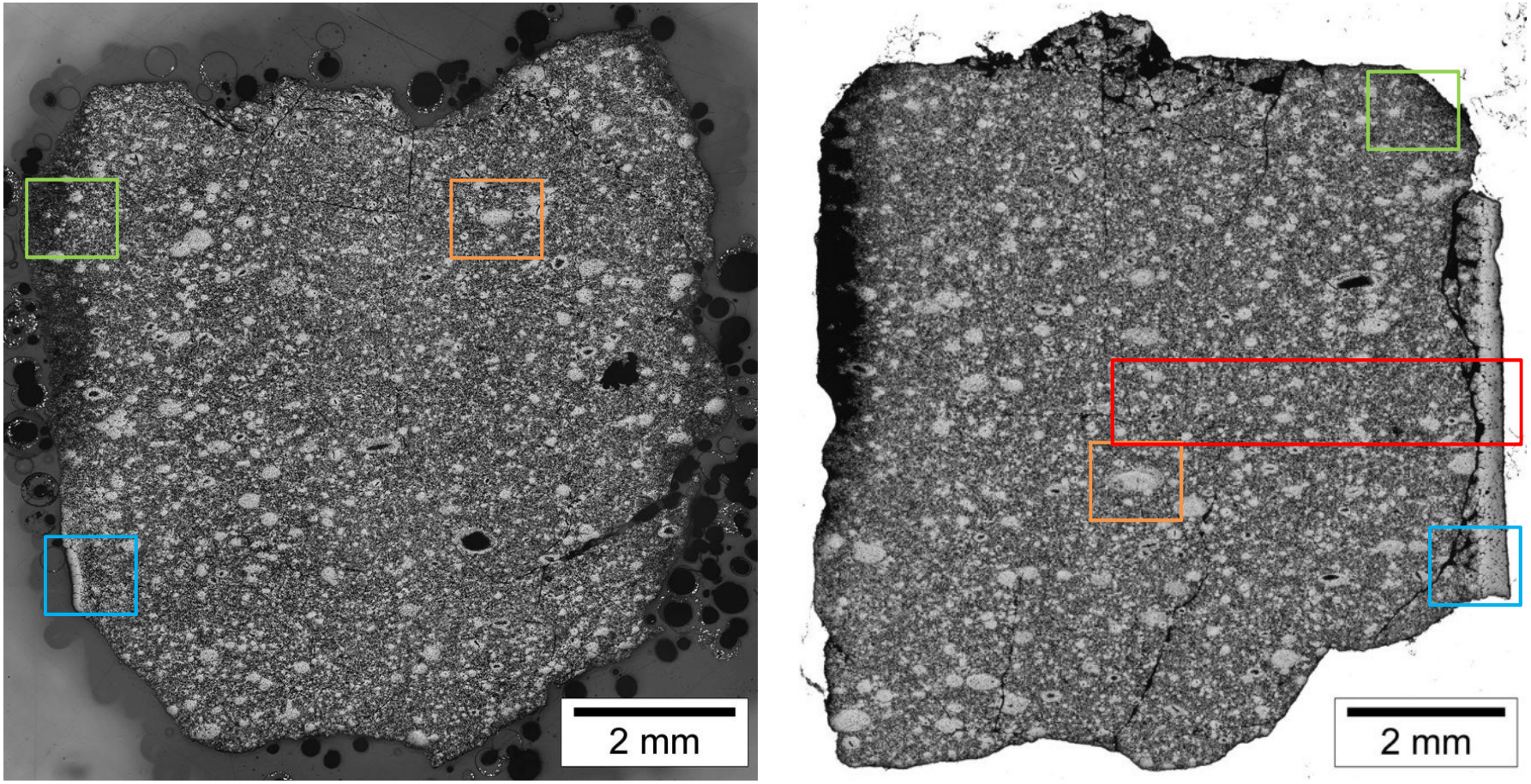

Figure II-20: Micrographs of the V-3E (left) and V-3M (right) samples after preparation

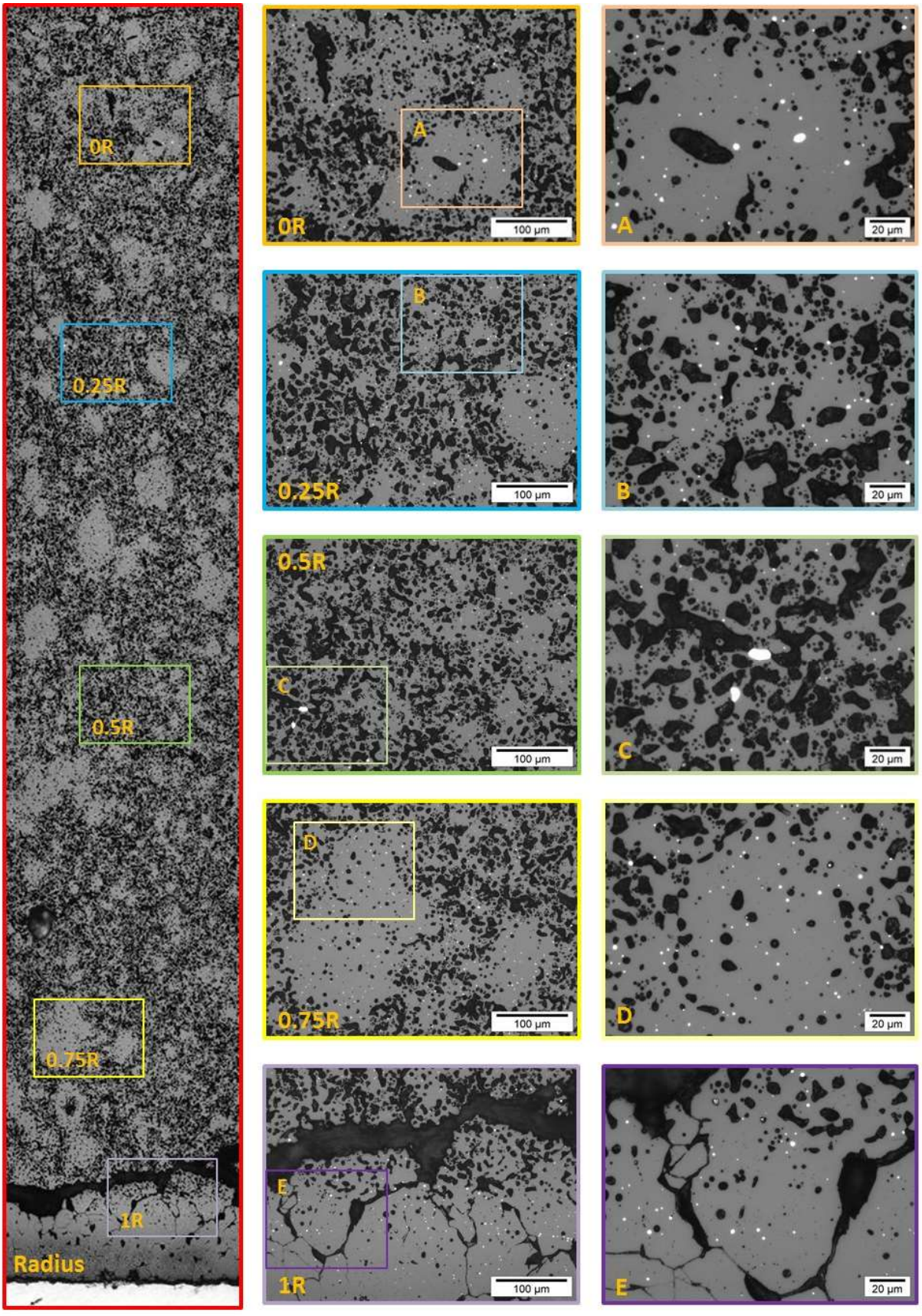

Figure II-21: Detailed radius analysis of sample V-3M

Histograms of the pore size distribution[2] in the agglomerates and in the porous matrix are presented in **Figure II-22**. Two main types of pores can be found in these two regions of the sample. The number of pores with an ECD around 1.7 µm in average is more than two times higher than the number of pores with a mean ECD of 7 to 8 µm. Features larger than 40 µm are found in the porous matrix and correspond to interconnected pores.

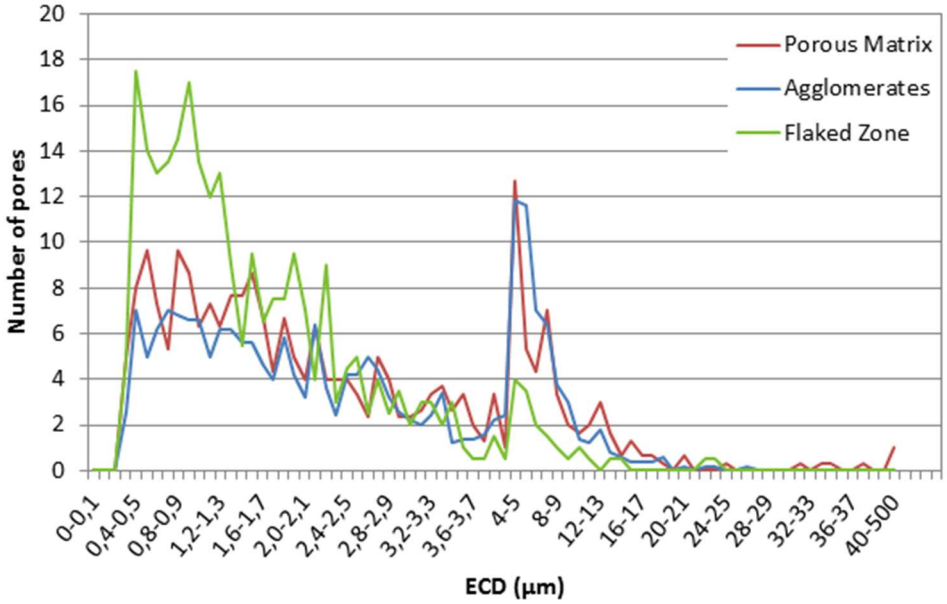

Figure II-22: Histogram of the pore size distribution in the different zones of the V-3M sample

As shown in **Figure II-23**, the surface contribution of pores in the porous matrix is two times higher than the one of the agglomerates (35% compared to 17% respectively). Concerning the flaked peripheral zone, the main type of pores has a size inferior to 4 µm with a mean pore ECD of 1.3 µm. The surface contribution of the pores in this zone is also four times inferior compared to the porous matrix.

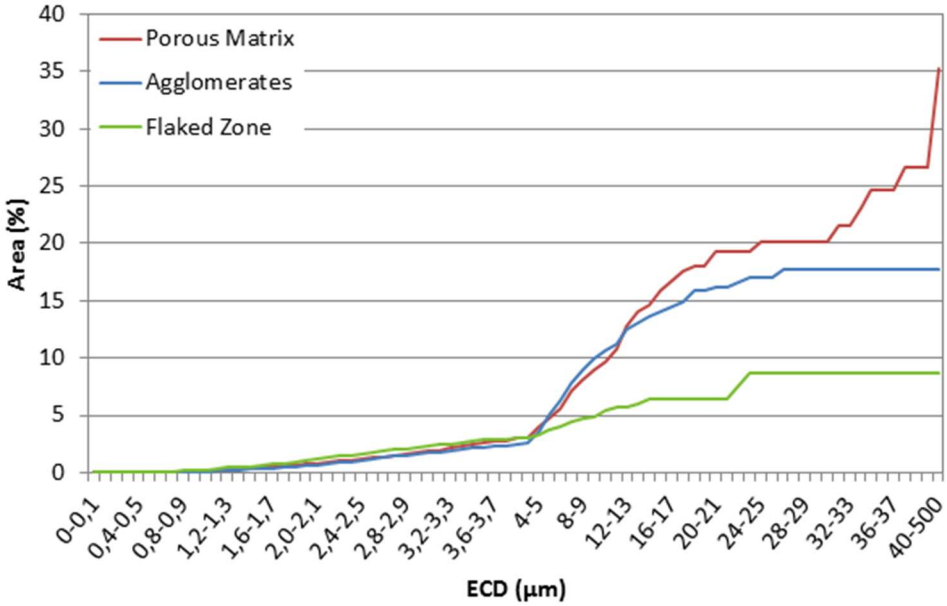

Figure II-23: Integrated pore surface contribution in the different zones of the V-3M sample

[2] Five images of 170 x 130 µm² were used to determine the number and surface contribution of the pores in each zone.

II.3.2.1.2 Chemical analyses

Chemical analyses have been performed in the different zones defined in **Figure II-21**.

Agglomerates

The agglomerates present in the sample (as presented for example **Figure II-24**) are richer in Pu compared to the porous matrix, which is consistent with the Pu agglomerates already observed in the father rod. Nevertheless, quantitative analyses performed on the radius of the V-3M sample point out that the concentration of Pu decreases compared with the father rod agglomerates (**Figure II-29**). Indeed, the Pu content varies from 1.3 at% in the matrix up to 1.8 at% in the agglomerates (3.9 % to 6.1% for Pu/(U+Pu)) compared respectively to 0.5 at% and 5 at% in the B05 sample (2% to 18% for Pu/(U+Pu)) indicating that Pu diffusion took place during the test from the agglomerates to the UO_2 matrix. The O/M[3] measured in the V-3M sample is almost constant in the whole sample (2.1 ± 0.4).

The agglomerates in the V-3M sample are dense even in the periphery while they were highly porous in the B05 sample. Thus, re-sintering may have occurred during the VERDON-3 test, probably around 1600-1800°C as observed in [19], [20].

Moreover, as shown in the micrograph of **Figure II-20**, the agglomerates are distributed homogeneously in the samples whereas they were only observed from 1R until 0.4 R in the B05 sample. This is possibly due to a higher U volatilization compared to Pu during the test which would have revealed the Pu agglomerate in the center of the sample.

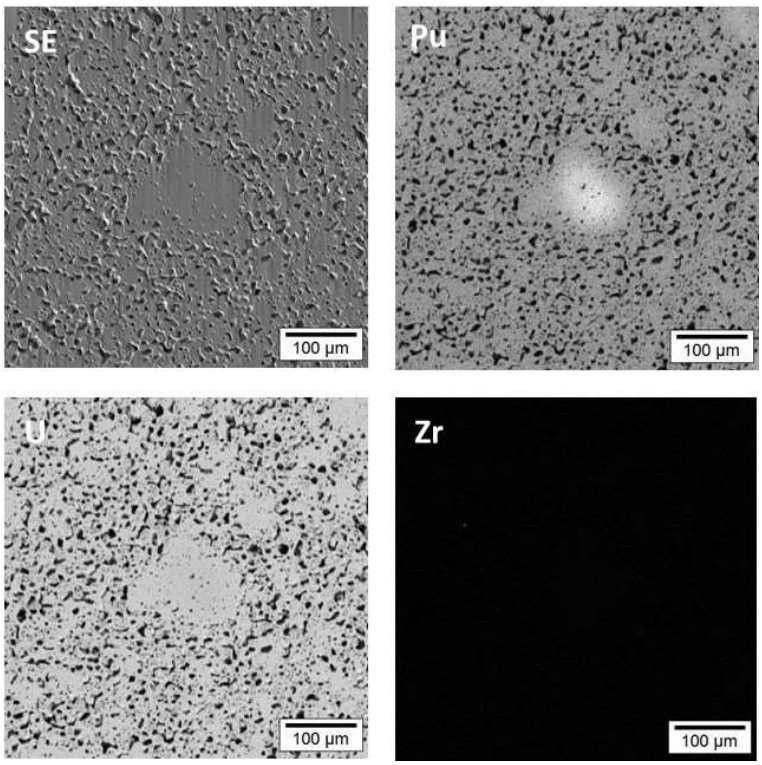

Figure II-24: SEM-SE and U, Zr and Pu X-ray maps acquired at 0.25R on sample V-3M

[3] M represents the amount of all the elements found dissolved in the fuel that have been quantified in this study (U, Pu, Zr, Nd, Ce, Nb, Cs and Ba)

Fuel-cladding interaction

As shown in **Figure II-25**, the periphery of the sample corresponding to the flaked zone (cladding, 1R) is charging due to its low electronic conductivity indicating that it is probably a part of oxidized cladding which remained attached to the pellet. Isotope mapping (**Figure II-26**) as well as X-ray mapping (**Figure II-28**) of the flaked zone indicate the presence of Zr. The mass spectrum (from 85 to 105 amu) of this zone is presented in **Figure II-27**. Five main peaks can be observed, the more intense being at 90 amu followed by the ones at 92 and 94 amu, then by the peak at 91 amu and finally by the small peak at 96 amu. This isotopic distribution is consistent with the one of natural Zr. Moreover, a small peak is present at the mass 93 amu indicating the presence of Nb in this region. The Nb amount was quantified by EPMA to be around 0.40 at.% in the area enriched in Zr (**Figure II-29**) which is consistent with the composition of the M5 alloy used to produce the cladding tube of the father rod. These observations confirm that the analyzed area corresponds to a piece of cladding.

The O/M measured in this region is lower than the one in that of the fuel (1.8 ± 0.2).

In the area located between the crack and the charging zone (1R' in **Figure II-25**), the concentration of Zr gradually decreases on approximately 70 µm when the ones of U and Pu increase towards the fuel, as shown in **Figure II-26**. The concentration gradient of Zr (**Figure II-29**) from the very periphery (35.7 at%) to the longitudinal crack observed in the pellet (0.3 at%) confirms that fuel-cladding interaction was enhanced during the VERDON-3 test leading to the formation of a $U_yZr_{1-y}O_{2\pm x}$ phase. This interaction most probably happened by interdiffusion of Zr and U during the test.

SEM observations performed on the 1R' zone in BSE mode show some lighter patterns forming lines ranging from 0.1 to 0.6 µm in thickness (**Figure II-25**). These lines display different orientations which seem to follow the grains orientations. These lines could be due to a phase separation that may have occurred in the $U_yZr_{1-y}O_{2\pm x}$ phase on cooling.

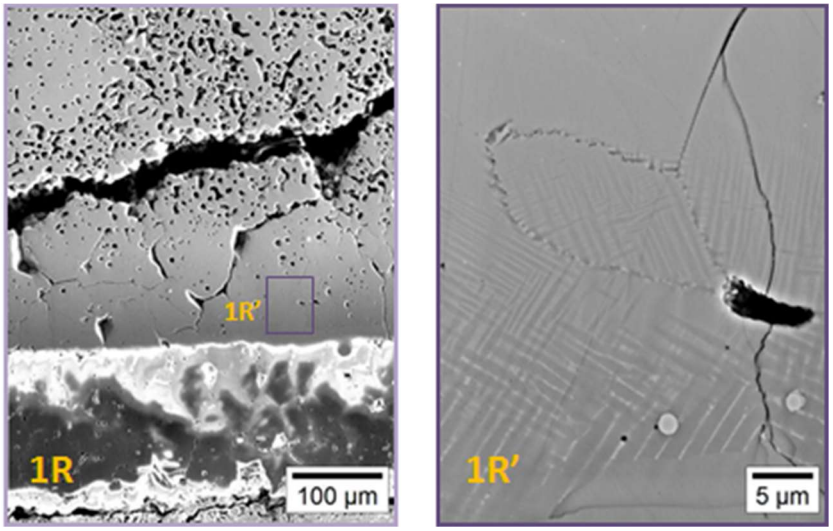

Figure II-25: SEM-SE image of the flaked light grey zone (cladding) at 1R (left) and SEM-BSE image of zone 1R'

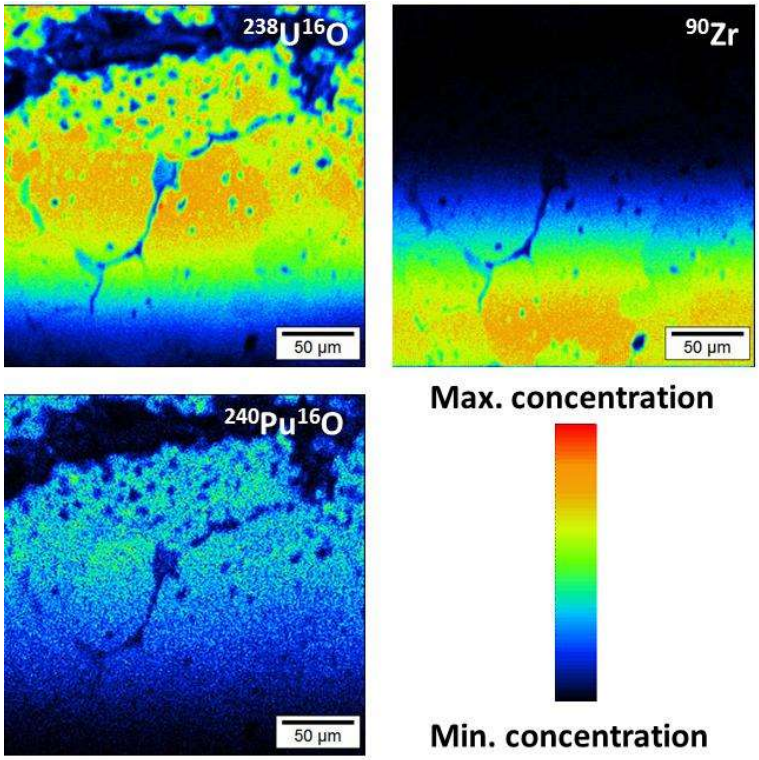

Figure II-26: SIMS isotope mapping performed at 254, 90 and 256 amu, acquired at 1R on sample V-3M. The black zones correspond to regions of the sample poor in the isotope measured whereas red areas are rich in this isotope.

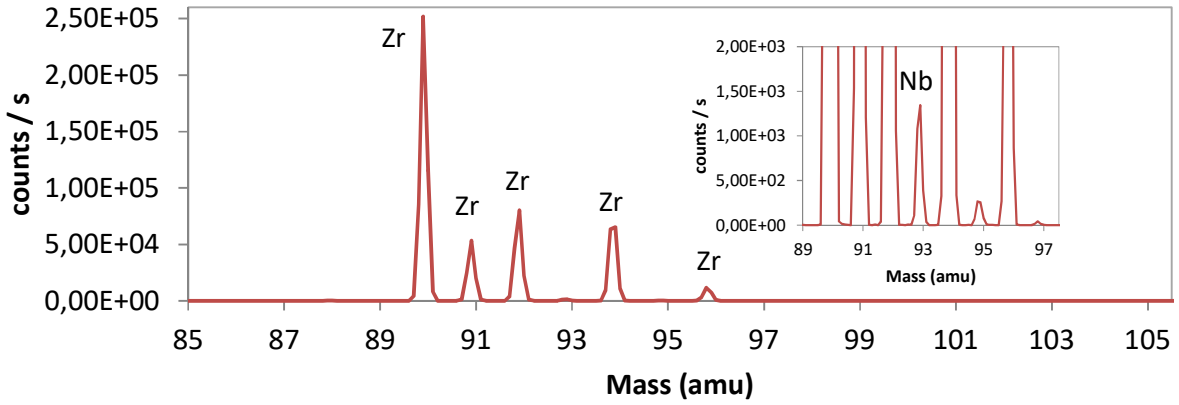

Figure II-27: Mass spectrum ranging from 85 to 105 amu acquired at 1R on sample V-3M. The peak intensities are typical of natural Zr.

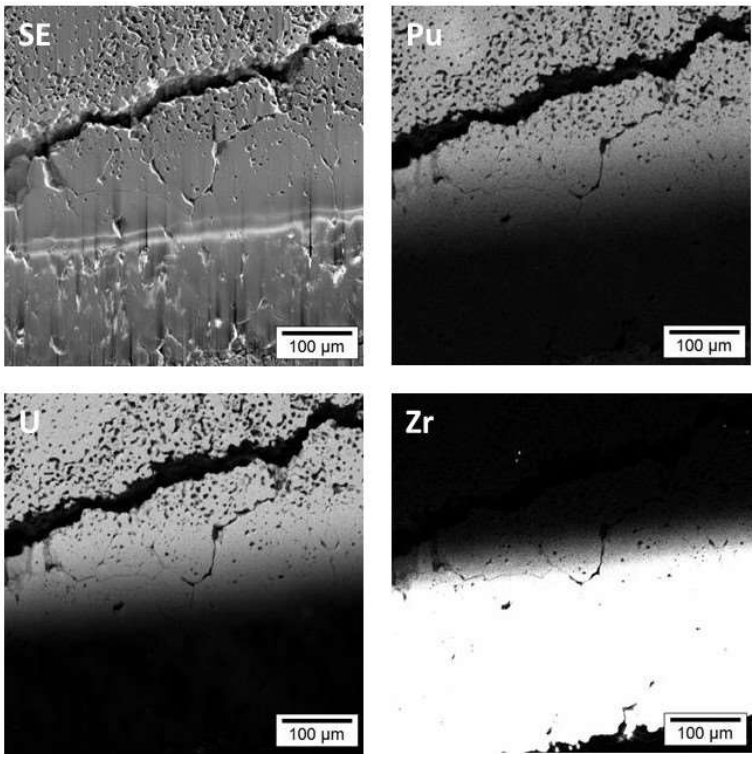

Figure II-28: SEM-SE and U, Zr and Pu X-ray maps acquired at 1R on sample V-3M

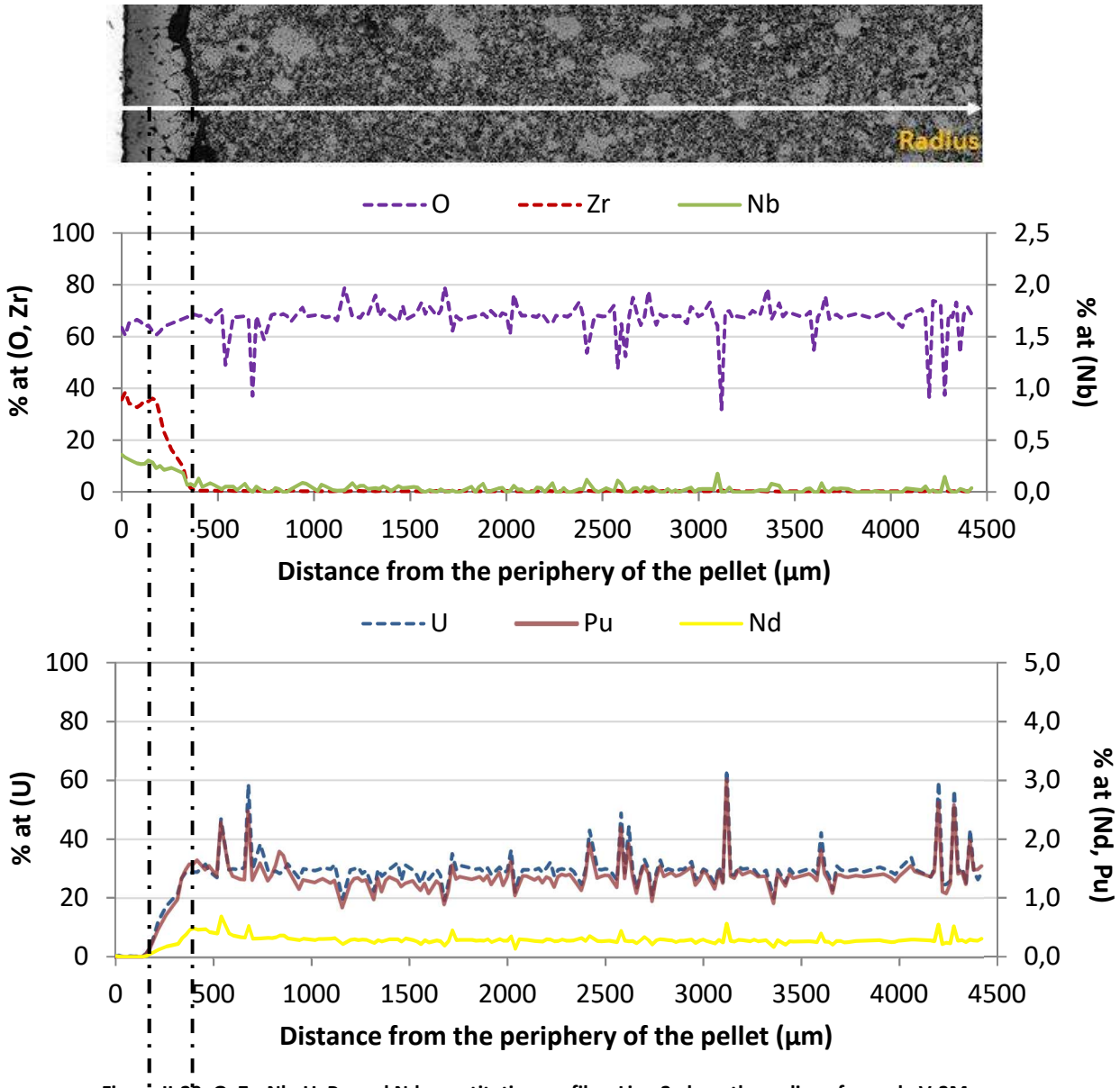

Figure II-29: O, Zr, Nb, U, Pu and Nd quantitative profiles, Line 3 along the radius of sample V-3M

II.3.2.1.3 Thermodynamic calculations

The evolution of the main phases observed in the fuel sample has been calculated during the heating phases of stages 2 and 3 of the VERDON-3 test using the Thermo-Calc [7] software coupled with the TAF-ID [8]. The oxygen potential of stages 2 and 3 have been calculated supposing thermodynamic equilibrium and by integration of the whole quantity of gas injected during the stage considered (**section II.2.2**). The transition between the two stages at 1500°C is thus discontinuous.

As shown in **Figure II-30**, these phases are composed of monoclinic ZrO_2 (ZrO2_Mono), tetragonal ZrO_2 (ZrO2_TETR), the fuel mixed oxide composed of (U, Pu)O_2 and another mixed oxide corresponding to the fuel-cladding interaction ((U, Zr)O_2).

According to the calculation, at the beginning of stage 2 monoclinic ZrO_2 and (U, Pu)O_2 are present, which is in agreement with the cladding and the fuel matrix observed experimentally in the father rod. A phase transition occurs around 1100°C from monoclinic to tetragonal ZrO_2. As soon as the tetragonal ZrO_2 is formed, the amount of (U, Pu)O_2 starts to decrease.

As shown in **Figure II-30**, during stage 3, the tetragonal ZrO_2 and the (U, Pu)O_2 phases are consumed to form the (U, Zr)O_2 mixed oxide. At 1750°C, all the ZrO_2 is in the (U, Zr)O_2 phase whereas the amount of (U, Pu)O_2 slightly decreases up to the end of the test. From 2000°C, the amount of (U, Zr)O_2 decreases because of the vaporization of 27 % of U mainly as UO_3, as shown in **Figure II-31**.

The U and Zr behavior during the stages 2 and 3 of VERDON-3 test is given in **Figure II-31** and **Figure II-32**. According to these calculations, mutual dissolution of Zr contained in ZrO_2 into the (U, Pu)O_2 phase and U from the (U, Pu)O_2 into ZrO_2 occurs as soon as the tetragonal ZrO_2 is formed.

The amount of U in (U, Pu)O_2 and tetragonal ZrO_2 decreases when (U, Zr)O_2 starts to form. At 1750°C, almost 16 % of U remains in the (U, Pu)O_2 phase whereas the U initially contained in tetragonal ZrO_2 has entirely been consumed.

Concerning Zr (**Figure II-32**), up to 12 % is dissolved in the (U, Pu)O_2 phase around 1650°C and 88 % is found in tetragonal ZrO_2. Then, the whole amount of Zr is dissolved and remains in the (U, Zr)O_2 phase until the end of the test.

At the end of the test, the composition of the (U, Zr)O_2 phase is $U_{0.46}Zr_{0.54}O_{2.05}$. However, during the cooling stage of the VERDON-3 test, part of Zr contained in this phase can return to tetragonal ZrO_2 at 1740°C and even to monoclinic ZrO_2 at lower temperature (around 1100°C). This phase separation may explain the lines observed experimentally in the fuel-cladding interaction zone of the VERDON-3 sample (**Figure II-25**).

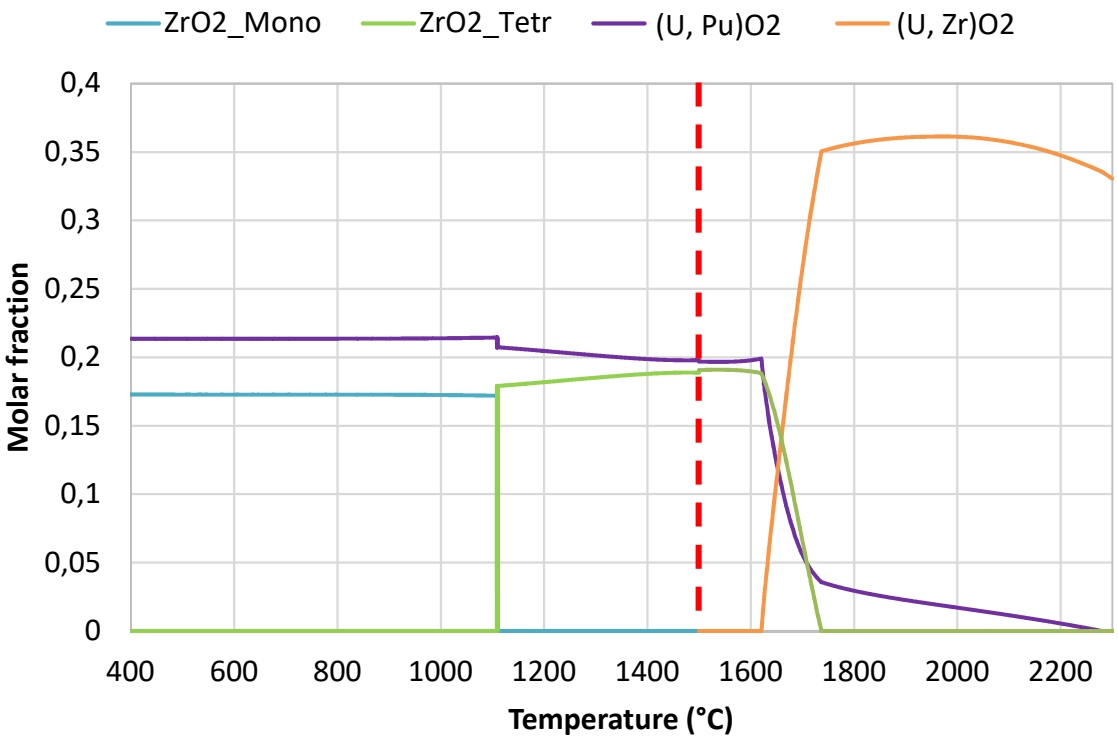

Figure II-30: Evolution of the fuel matrix and cladding during the stages 2 and 3 of the VERDON-3 test, calculated using Thermo-Calc [7] coupled with the TAF-ID [8]

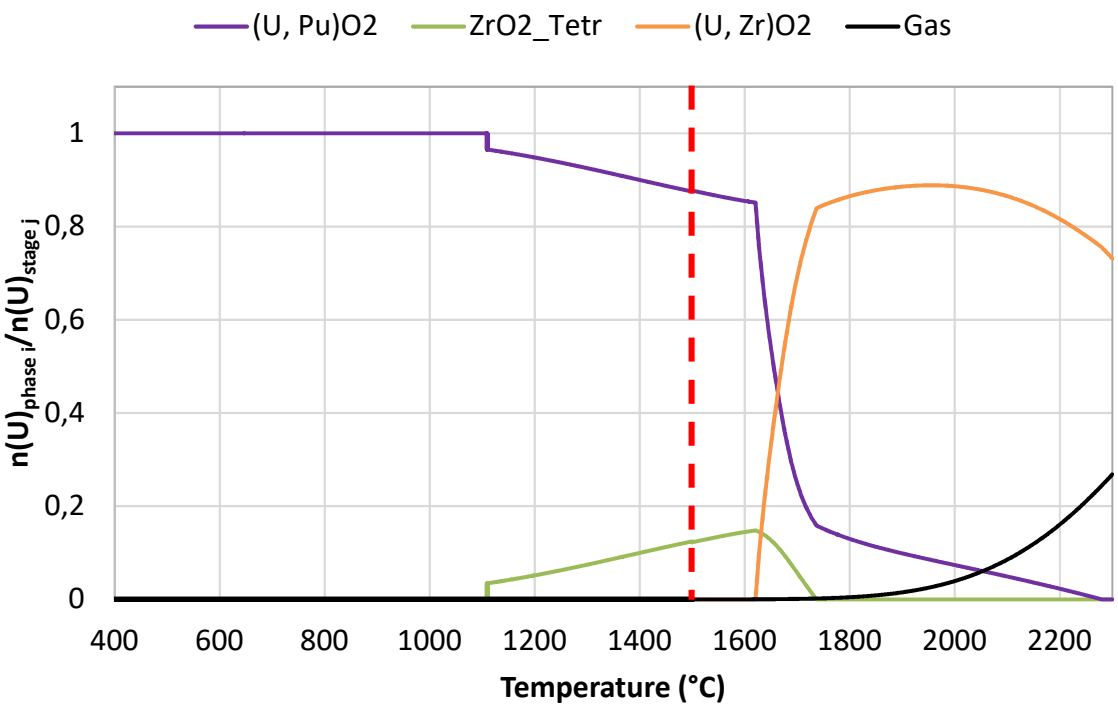

Figure II-31: U behavior during the stages 2 and 3 of the VERDON-3 test, calculated using Thermo-Calc [7] coupled with the TAF-ID [8]

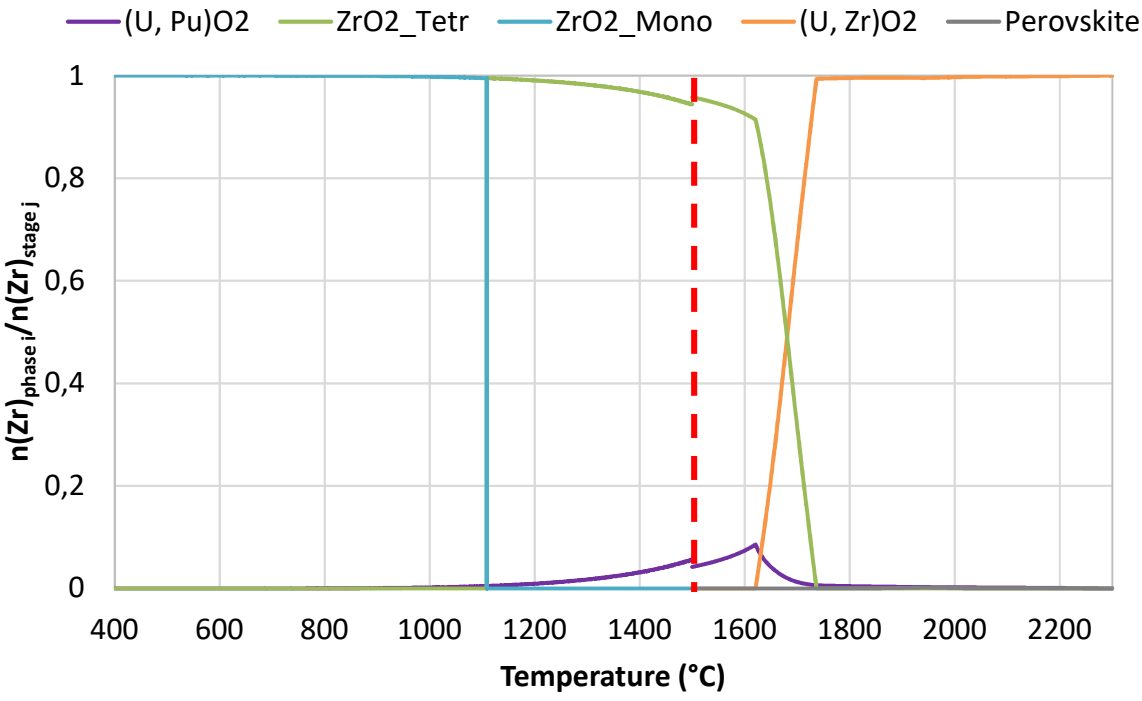

Figure II-32: Zr behavior during the stages 2 and 3 of VERDON-3 test, calculated using Thermo-Calc [7] coupled with the TAF-ID [8]

II.3.2.2 Metallic precipitates

II.3.2.2.1 Microstructure analysis

The number of white precipitates tends to decrease in the remaining piece of cladding, after the longitudinal crack until they disappear at approximately 1/3 of the cladding (**Figure II-21** zone 1R). In

the agglomerates, the white precipitates exhibit a mean ECD of 1.3 µm which is similar compared to the size of the ones found in the porous matrix (1.2 µm), as shown in **Figure II-33**[4]. The number of these precipitates as well as their contribution to the total surface analyzed (**Figure II-34**) is similar between the porous matrix and the agglomerates which is confirmed by their distribution in **Figure II-38**. In the B05 sample, metallic precipitates were found in majority within the agglomerates, indicating that migration of these precipitates occurred during the VERDON-3 test.

SEM images representative of the five different regions observed in OM on sample V-3M (1R, 1R', 0.75R, 0.5R and 0R) are presented in **Figure II-35**, **Figure II-36** and **Figure II-25**. Small round dark-grey precipitates corresponding to the white ones observed by OM are observed in BSE mode in the agglomerates as shown in **Figure II-35**. The precipitates located at the grain boundaries can be observed in the biggest pores of the porous matrix and the agglomerates (**Figure II-36**).

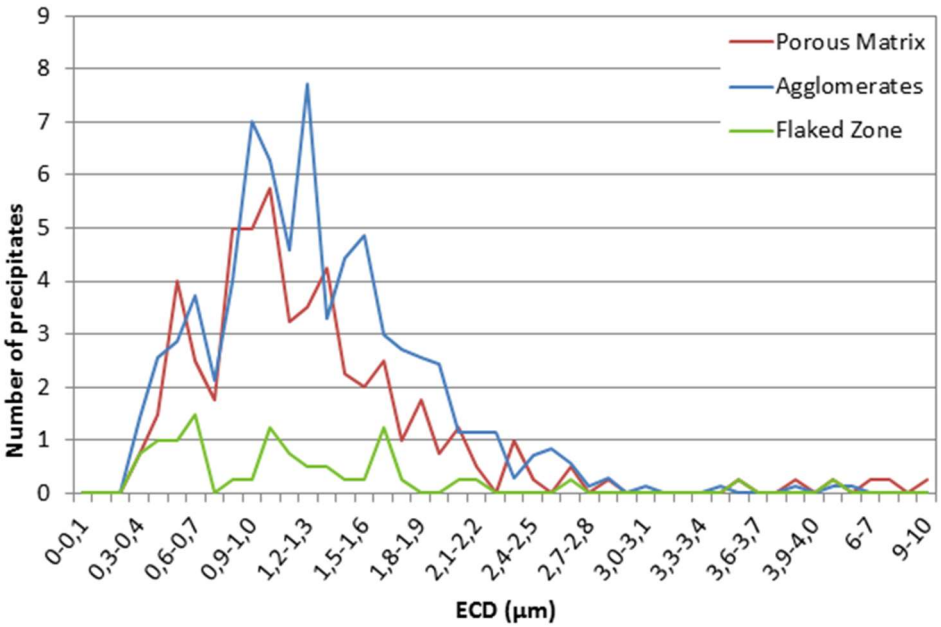

Figure II-33: Histogram of the white inclusions size distribution in the different zones of the V-3M sample

[4] Five images of 170 x 130 µm² were used to determine the number and surface contribution of the white precipitates in each zone.

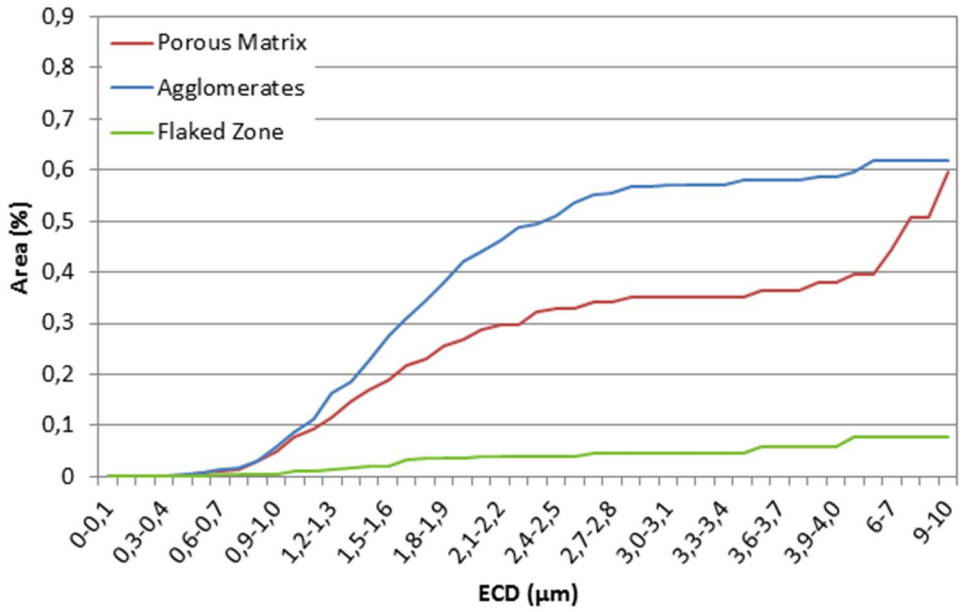

Figure II-34: Integrated white inclusions surface contribution in the different zones of the V-3M sample

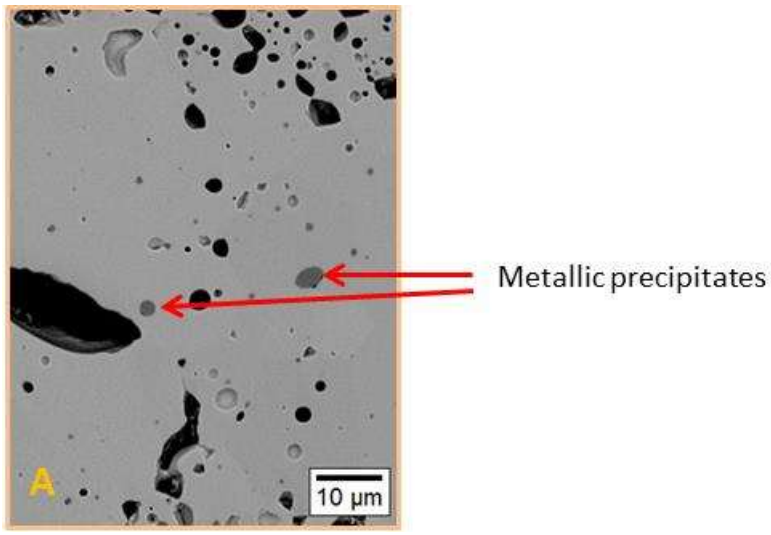

Figure II-35: SEM-BSE image of the agglomerate seen in zone A (0R)

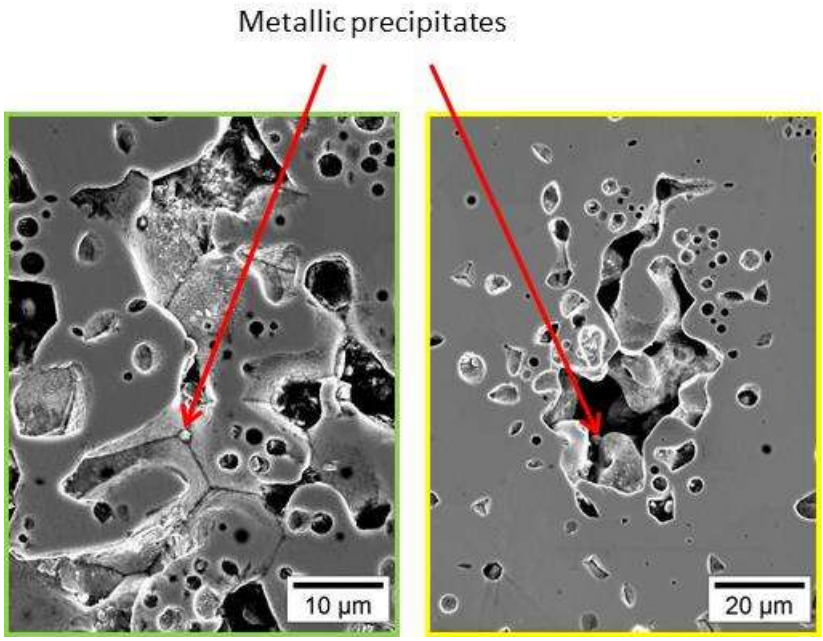

Figure II-36: SEM-SE image taken in the porous matrix region at 0.5R (left) and in an agglomerate at 0.75R (right)

II.3.2.2.2 Chemical analyses

As shown in **Figure II-37**, these precipitates are composed of Ru, Rh and Tc. Neither Mo nor Pd are present contrary to the precipitates contained in the B05 sample. The residual signal observed in the Mo isotope map may be due to interference between the isotope ^{100}Mo and ^{100}Ru which is confirmed by the absence of Mo on the X-ray map (**Figure II-38**). However, the presence of Tc, clearly evidenced from SIMS analyses, could not be identified thanks to X-ray mapping due to the interference of the $L_{\alpha 1}$ line of Tc at 2.4231 keV with the $M_{\alpha 1}$ line of Bi at 2.4177 keV contained in the embedding Bi/Sn metallic alloy. In the same way, the $L_{\alpha 1}$ line of Pd (2.8378 keV) interferes with the $L_{\beta 1}$ of Rh (2.8341 keV) and the $L_{\beta 2}$ Ru (2.8360 keV) which are the main components of the precipitates according to the quantitative profiles. Thus, the X-ray maps of Tc and Pd are not presented here.

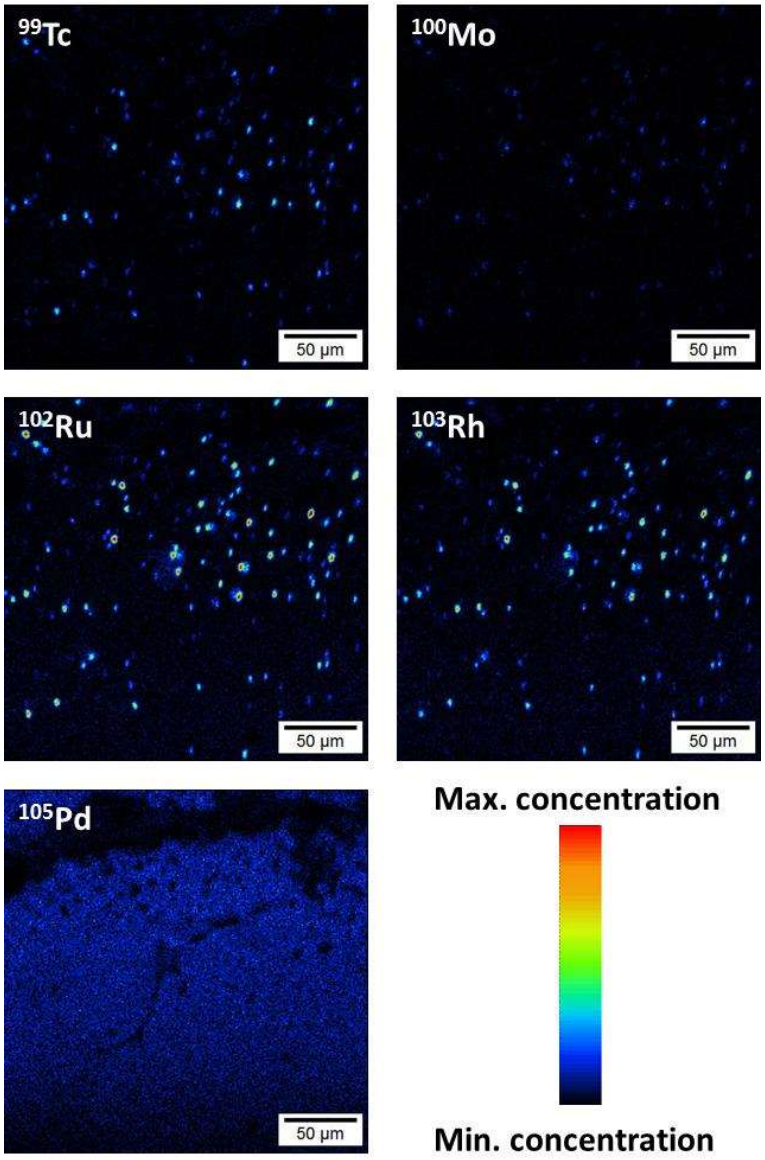

Figure II-37: SIMS isotope mapping performed at 99, 100, 102 and 103 and 105 amu, acquired at 1R on sample V-3M. The black zones correspond to regions of the sample poor in the isotope measured whereas red areas are rich in this isotope.

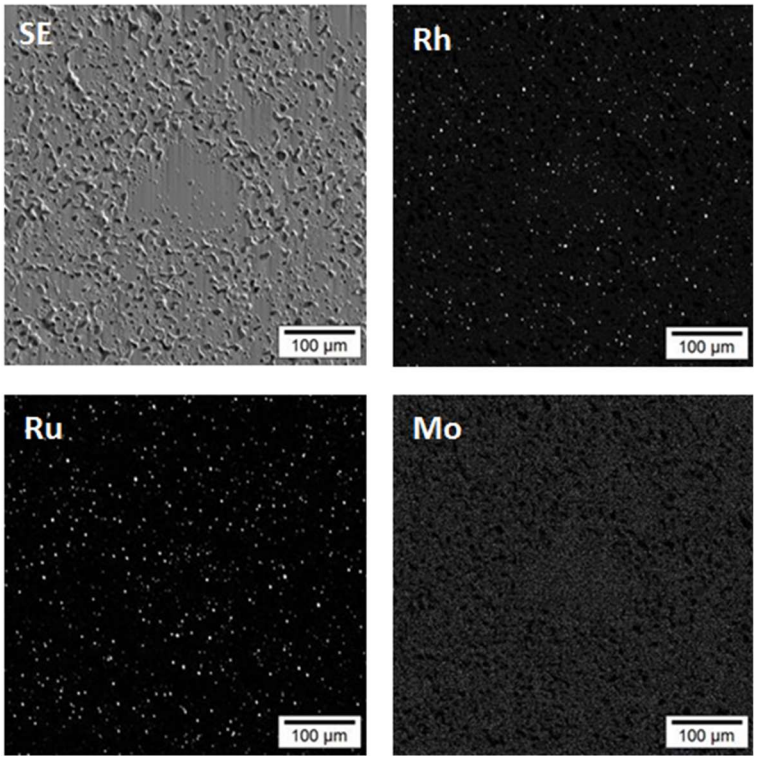

Figure II-38: SEM-SE and Rh, Ru and Mo X-ray maps acquired at 0.25R on sample V-3M

The radial quantitative profiles shown in **Figure II-39** as well as some point analyses in several precipitates located at different positions in the V-3M sample confirm that these are metallic precipitates. The Ru/Rh ratio is 3.5 ± 0.1 in the whole sample which is inferior to the ratio of 4.3 ± 0.3 measured in the B05 sample. However, some point analyses performed in the fuel-cladding interaction zone show that the Ru/Rh ratio rises up to 4.1 ± 0.3. This indicates that Ru has probably migrated from the center of the fuel towards the periphery. Mo and Pd concentrations are below the detection limit of EPMA (0.1 wt%) which is consistent with the absence of signal for these two FP in SIMS isotope maps and X-ray maps. Unfortunately, Tc could not be quantified due to the lack of reference sample available.

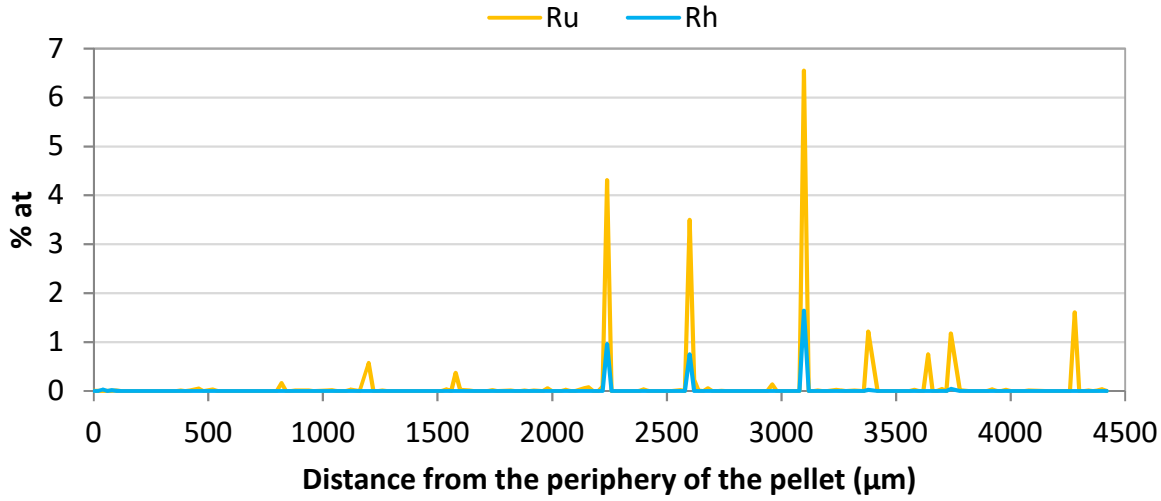

Figure II-39: Ru and Rh quantitative profiles, Line 3 along the radius of sample V-3M

II.3.2.2.3 Thermodynamic calculations

The calculated evolution of the metallic phases formed by the interactions between Mo, Ru, Rh, Pd and Tc is shown in **Figure II-40**. The oxygen potential of stages 2 and 3 have been calculated supposing thermodynamic equilibrium and by integration of the whole quantity of gas injected during the stage considered (**section II.2.2**). The transition between the two stages at 1500°C is thus discontinuous. An emphasis is made on the behavior of Mo in this part.

Initially, three types of phases are present in the fuel: a fcc metallic phase, a hcp one both composed of Tc, Ru, Rh, Pd and Mo and $MoRh_3$. At around 1100°C, the $MoRh_3$ phase is decomposed in fcc and hcp phases. At the end of stage 2, the only metallic precipitates present in the fuel have a hcp structure and contain up to 12% of the Mo in the system (**Figure II-41**).

At the beginning of stage 2, Mo can be mainly found in Cs_2MoO_4, $BaMoO_4$, $MoRh_3$ and MoO_2. Around 800°C, melting of the molybdate phases occurs and a decomposition of the Cs_2MoO_4 and the vaporization of MoO_2 explain the presence of Mo in the gas phase. The decomposition of $MoRh_3$ leads to an increase of Mo amount in the fcc and hcp phases. Around 1450°C, the whole amount of Mo contained in the fcc metallic phase goes in the hcp one.

According to the calculation, during stage 3, the metallic precipitates remaining in the fuel would melt around 2120°C (Liquid Metal. in **Figure II-40**). Their final composition would be 47.5 at% of Tc, 38.5 at% of Ru and 12.6 at% of Rh leading to a Ru/Rh ratio of 3.1, quite close to the one measured by EPMA (3.5 ± 0.1). This melting could explain the spherical shape and the migration of the metallic precipitates from the agglomerates (where they were located in the father rod) to the whole sample after the VERDON-3 test.

The switch of atmosphere between stage 2 and 3 leads to a brutal Mo depletion in the metallic precipitates. Part of Mo contained in the gas phase (mainly as MoO_2) at the end of stage 2 is condensed in the Liquid#2 composed of molybdate phases. A total volatilization of Mo occurs around 2000°C, which is consistent with the absence of Mo in the fuel after the VERDON-3 test.

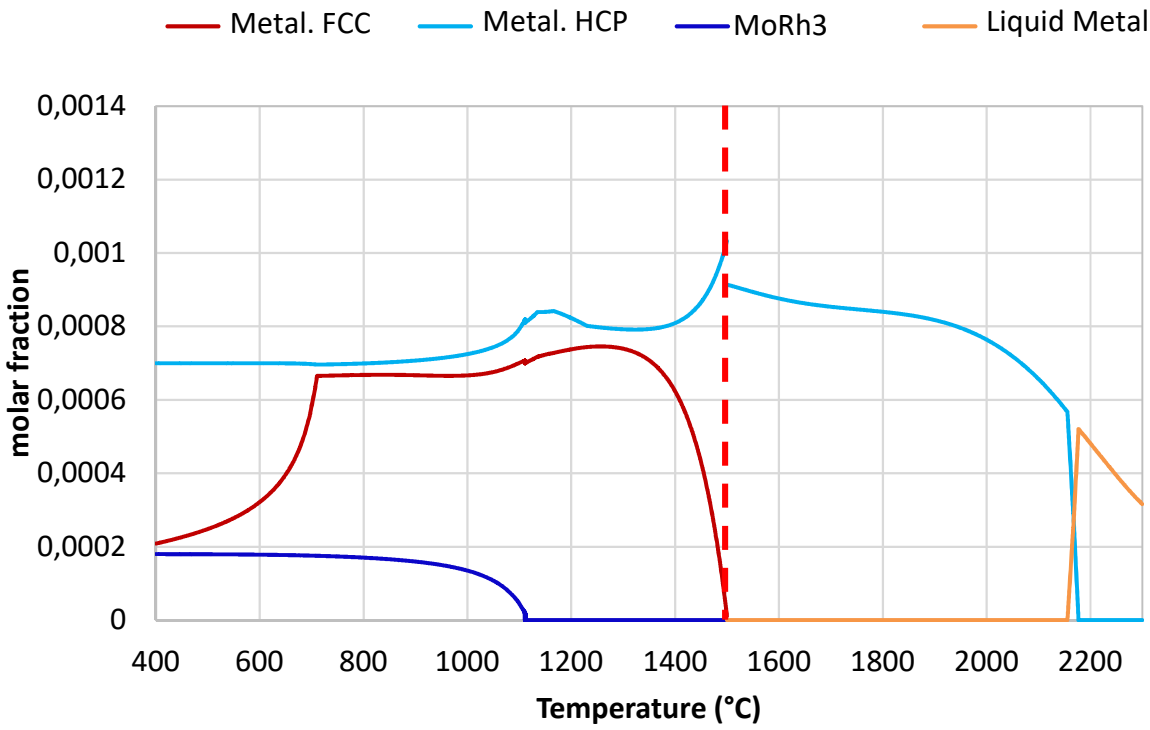

Figure II-40: Evolution of the metallic phases during the stages 2 and 3 of the VERDON-3 test, calculated using Thermo-Calc [7] coupled with the TAF-ID [8]

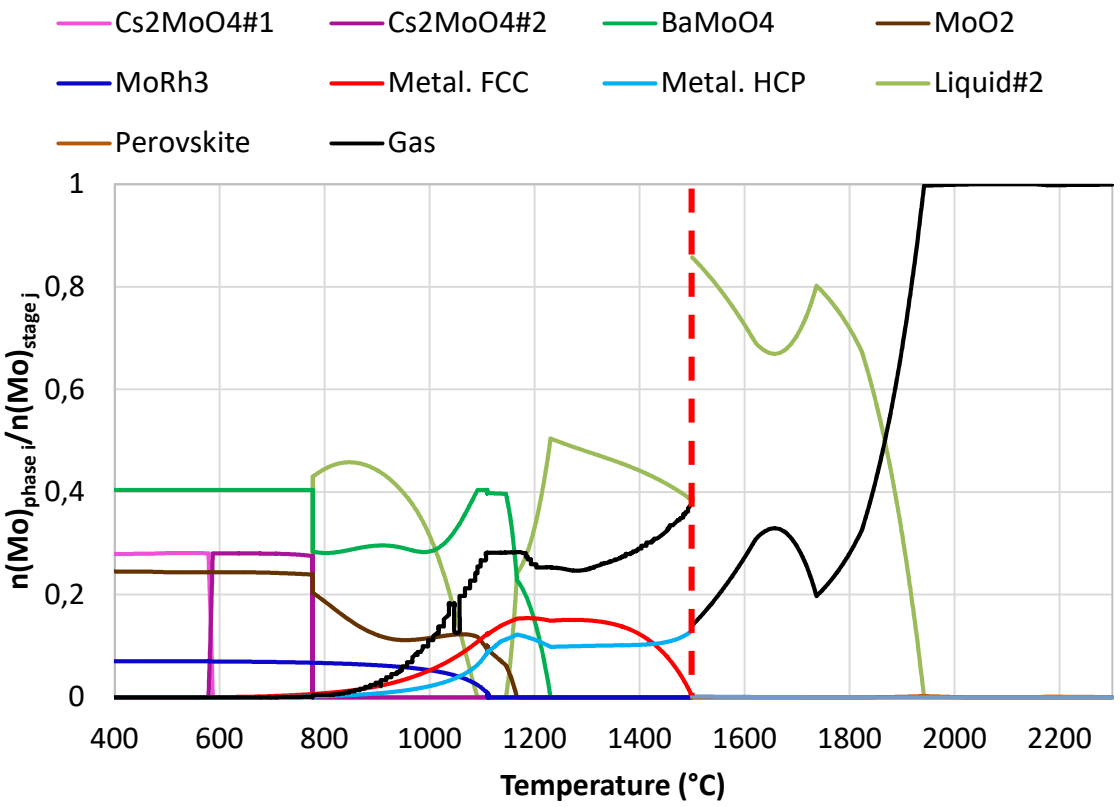

Figure II-41: Mo behavior during the stages 2 and 3 of the VERDON-3 test, calculated using Thermo-Calc [7] coupled with the TAF-ID [8]

II.3.2.3 Dissolved FP: special emphasis on Ba and Cs behavior

II.3.2.3.1 Chemical analyses

Ba and Cs are found in precipitates along with Ce at 0.5R as shown **Figure II-42**. Others precipitates containing only Cs and Zr can also be observed. This kind of precipitates is always observed in the porous matrix and not in the agglomerates. Precipitates of Ba or Cs apparently not associated to other elements can also be observed at 0.25R.

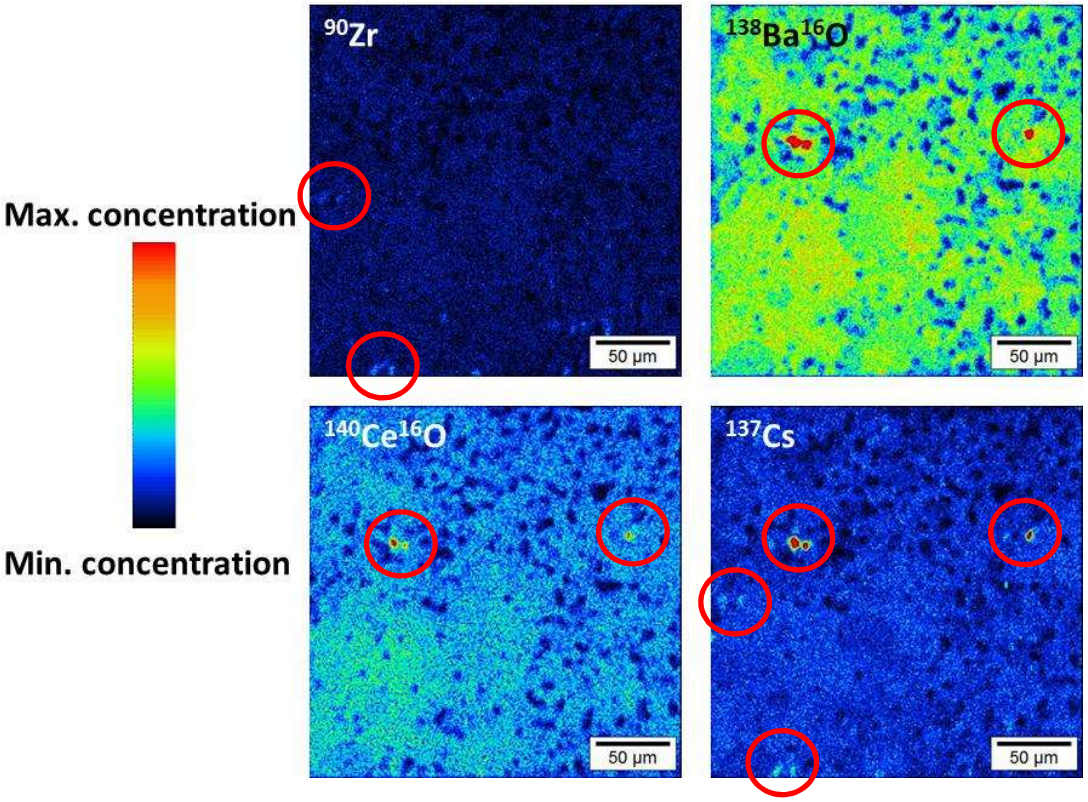

Figure II-42: SIMS isotope mapping performed at 90, 156, 154 and 137 amu, acquired at 0.5R on sample V-3M. The black zones correspond to regions of the sample poor in the isotope measured whereas red areas are rich in this isotope.

At 3720 µm from the center of the sample (**Figure II-44**), an increase in the concentration of Zr (0.8 at%), Ce (0.3 at%) and Ba (0.2 at%) at the same time indicates the presence of a precipitate containing these three FP.

The quasi-systematic presence of Ce at the same location as Ba could be due to radioactive decay of ^{140}Ba in ^{140}Ce as already observed in [21]. However, the study by [22] showed that $BaCeO_3$ can also exist but it is vaporized at much lower temperature compared to the one reached at the end of the VERDON-3 test.

Compared to the B05 sample, the amount of Ba has dropped and homogenizes. Within the whole V-3-R sample, the amount of Ba in the matrix is rather constant (0.1 at% in average) and a decrease of the Ba concentration is observed in the fuel-cladding interaction zone. Some rare bubbles containing up to 0.14 at% of Xe and around 0.04 at% [5] of Cs are still present in the sample as observed in **Figure II-43**. This is consistent with the thermodynamic calculation indicating that Cs was totally volatilized at around 1900°C (**Figure II-46**).

[5] Corresponding to 0.2 wt% for Xe and 0.15 wt% for Cs which is higher than the detection limit of the EPMA (0.1 wt%).

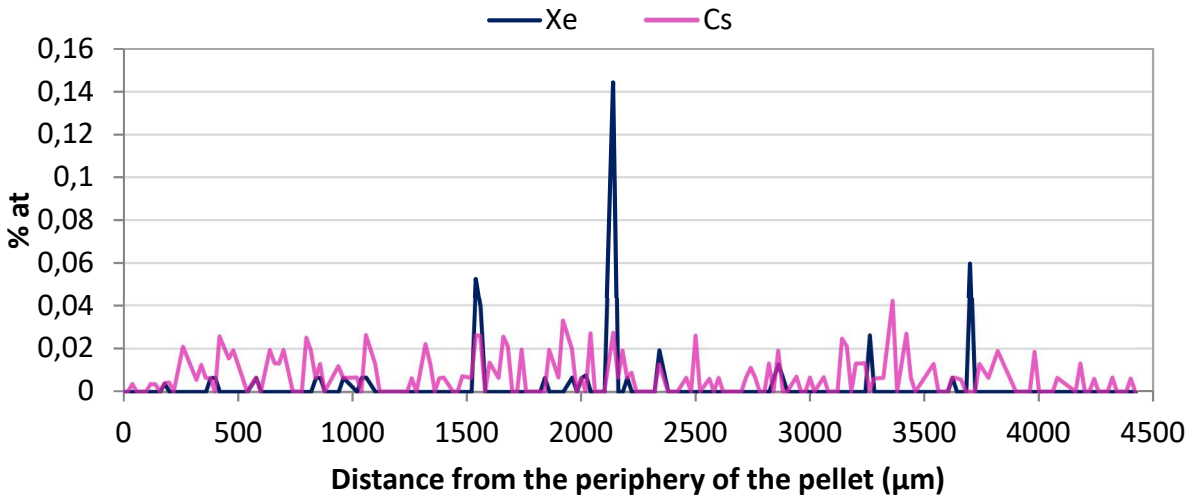

Figure II-43: Xe and Cs quantitative profiles, Line 3 along the radius of sample V-3M

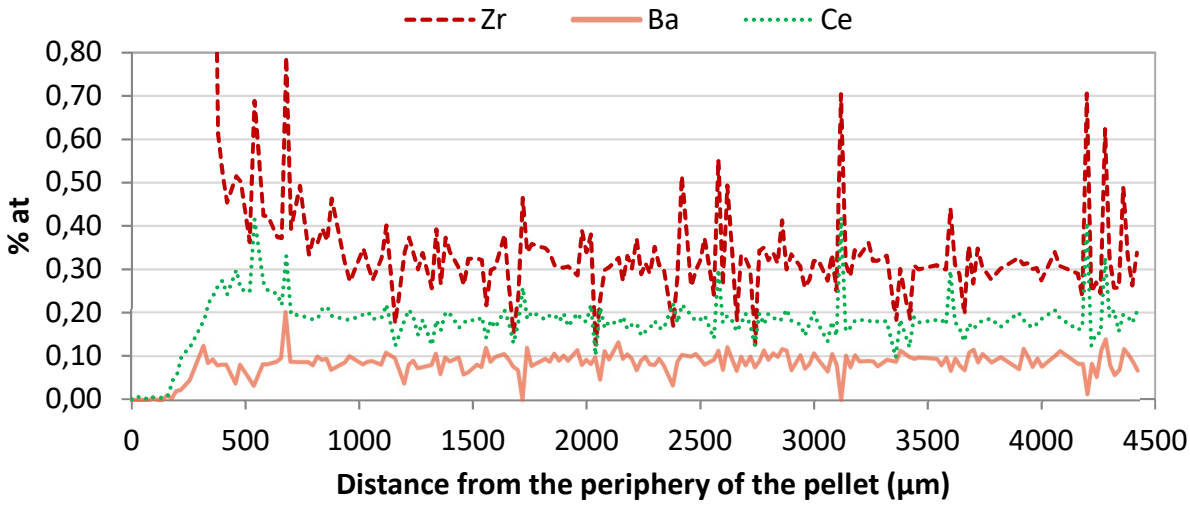

Figure II-44: Zr, Ba and Ce quantitative profiles, Line 3 along the radius of sample V-3M

II.3.2.3.2 Thermodynamic calculations

The calculated evolution of the phases containing Ba and Cs is shown in **Figure II-45**. The oxygen potential of stages 2 and 3 have been calculated supposing thermodynamic equilibrium and by integration of the whole quantity of gas injected during the stage considered (**section II.2.2**). The transition between the two stages at 1500°C is thus discontinuous. An emphasis is made on the behavior of Cs, Mo and Ba in this part.

Initially, four phases are calculated to be present in the sample: CsI, MoO_2, Cs2MoO_4 and $BaMoO_4$.

- CsI is totally vaporized at 500°C leading to an increase of the Cs amount in the gas phase, as shown in **Figure II-46**.
- Cs_2MoO_4 melts around 790°C leading to the formation of the Liquid#2 and to the vaporization of Cs and Mo as Cs_2MoO_4, as shown in **Figure II-46**.
- Part of $BaMoO_4$ also melts in the same time (Liquid#2) and a re-solidification is observed at 1020°C. At this point, part of $BaMoO_4$ is decomposed leading to Ba dissolution in the tetragonal ZrO_2 phase (**Figure II-47**) and MoO_2 vaporization (**Figure II-41**). Another liquefaction of the remaining amount of $BaMoO_4$ is calculated to appear at 1150°C.

As shown in **Figure II-45**, at the beginning of stage 3, liquid (Ba, Cs)MoO_4 is still present. It starts to decompose around 1820°C leading to the formation of the perovskite phase containing also Zr, Ce, Sr etc. The very rare precipitates containing Cs, Ba, Ce and Zr observed in the samples could correspond to the perovskite (Ba, Cs, Sr)(Zr, RE)O_3 phase. This phase is calculated to disappear at 2050°C.

As shown in **Figure II-46**, Cs is totally vaporized from the liquid molybdate phase (Liquid#2) at 1950°C.

Concerning Ba, at the beginning of stage 3 (**Figure II-47**), it found in the liquid molybdate phase and dissolved in the tetragonal ZrO_2. Around 1730°C, part of Ba contained in the tetragonal ZrO_2 returns in the liquid molybdate phase, another small part goes in the (U, Zr)O_2 phase and Ba starts to be vaporized. At the end of the sequence, Ba is only found in the (U, Zr)O_2 phase and 97% of Ba has been vaporized.

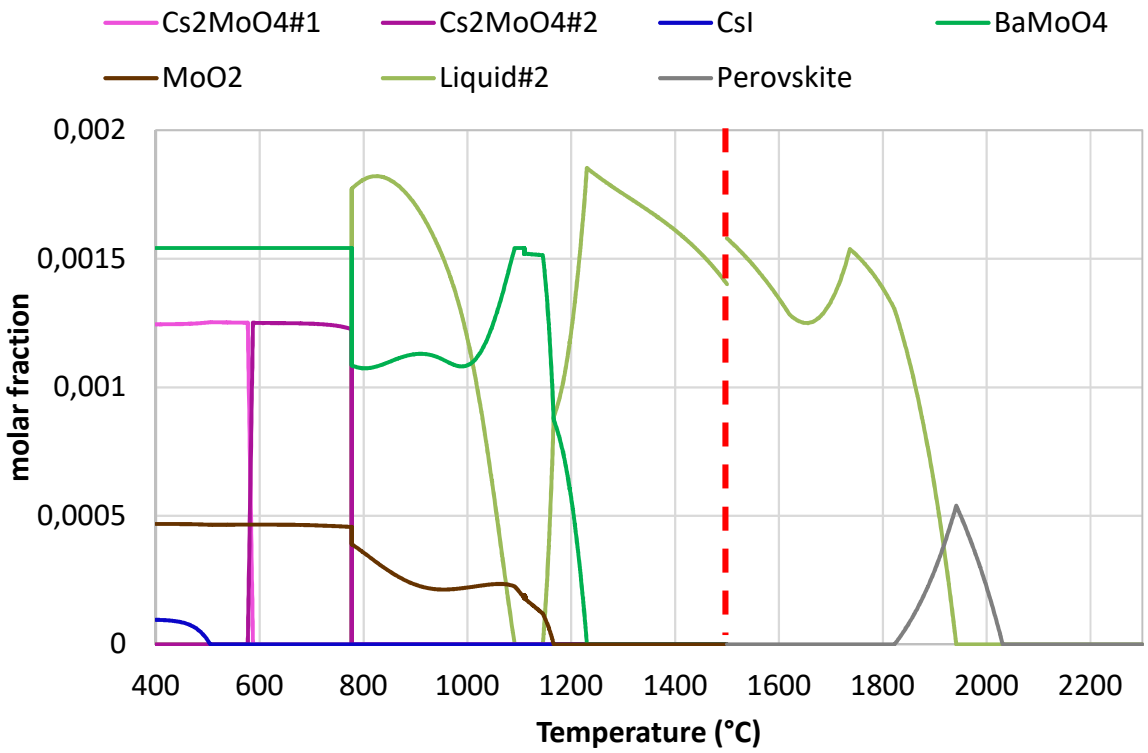

Figure II-45: Evolution of the oxide phases during the stages 2 and 3 of the VERDON-3 test, calculated using Thermo-Calc [7] coupled with the TAF-ID [8][20]

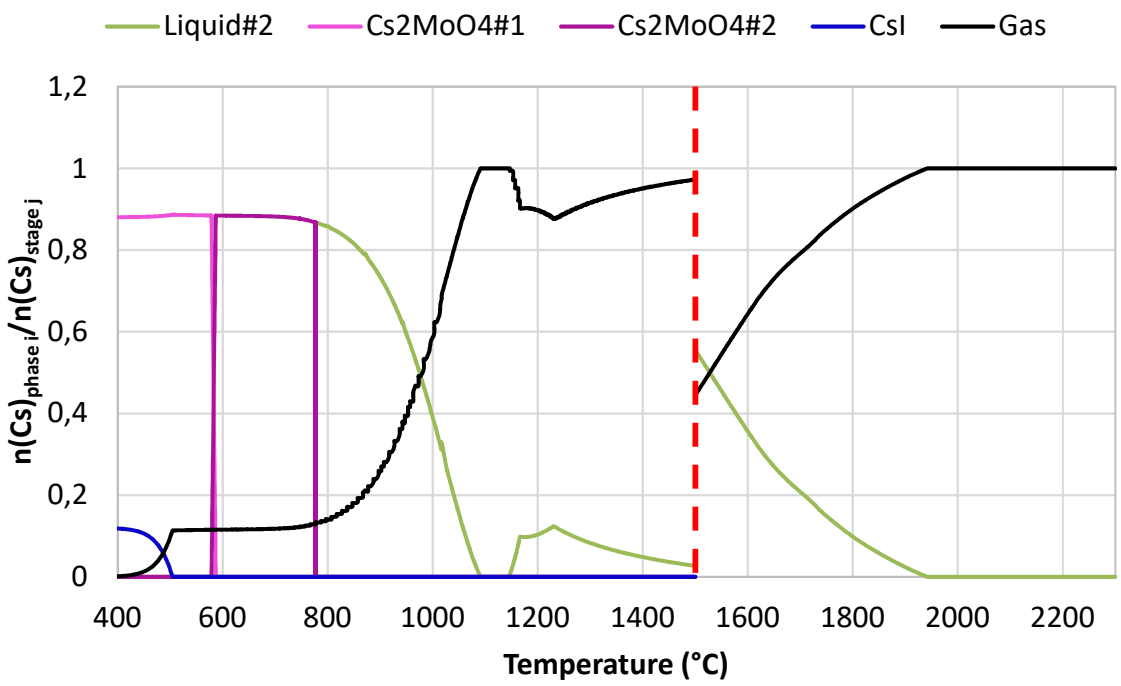

Figure II-46: Cs behavior during the stages 2 and 3 of the VERDON-3 test, calculated using Thermo-Calc [7] coupled with the TAF-ID [8]

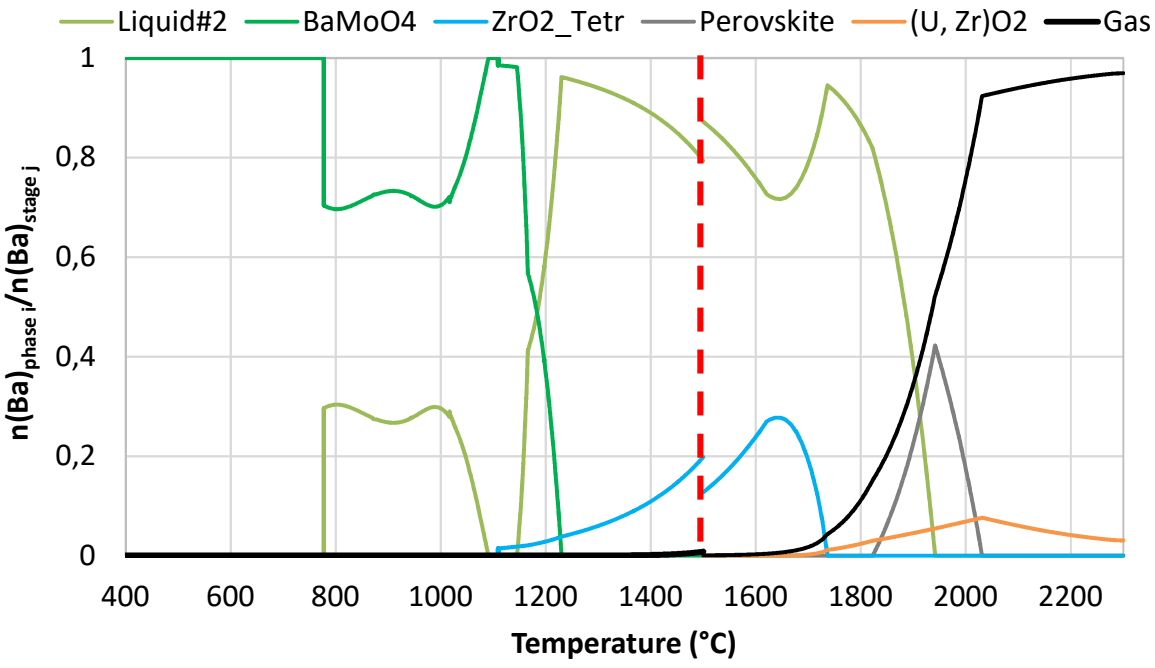

Figure II-47: Ba behavior during the stages 2 and 3 of the VERDON-3 test, calculated using Thermo-Calc [7] coupled with the TAF-ID [8]

II.3.2.4 Summary of the observations made in the VERDON-3 sample

A summary of the results obtained through experimental characterizations of the VERDON-3 sample and thermodynamic calculations is given in **Table II.2**.

Table II-2: Summary of the phases observed experimentally and calculated using Thermo-Calc [7] coupled with the TAF-ID [8] after the VERDON-3 test, and their main characteristics

	Experimentations	Calculations
Fuel-cladding interaction	Presence of a $U_yZr_{1-y}O_{2\pm x}$ phase on 70 µm at the interface of the fuel and cladding O/M ≈ 1.80 ± 0.20 No melting of the $U_yZr_{1-y}O_{2\pm x}$ phase observed at 2300°C	Presence of a $U_yZr_{1-y}O_{2\pm x}$ phase in the whole pellet at 2300°C O/M ≈ 2.05 No liquid $U_yZr_{1-y}O_{2\pm x}$ phase predicted before 2420°C
Metallic precipitates	No Mo observed in the sample Ru/Rh = 3.5 ± 0.1 Rounded shaped precipitates observed all over the sample	Total volatilization of Mo predicted Ru/Rh = 3.1 Melting of the metallic inclusion predicted at 2120°C
Dissolved phases (Ba and Cs)	Ba homogeneously distributed all over the sample, its concentration decreases in the $U_yZr_{1-y}O_{2\pm x}$ phase Very few Cs bubbles observed	Ba located in the $U_yZr_{1-y}O_{2\pm x}$ phase Total volatilization of Cs predicted

III.3.2.4.1 Fuel-cladding interaction

The thermodynamic calculations performed in this part enable a global understanding of the local fuel-cladding interaction phenomenon that takes place in the fuel pellet during the VERDON-3 sample. Indeed, this interaction takes place on 70 µm at the fuel-cladding interface in the sample whereas it is predicted to extend all over the pellet in the calculations. This is due to the hypotheses made in the calculations:

- All the initial input species are mixed and considered as a homogeneous mixture composed of (U, Pu)O_2, Zr and FP. Thus, the heterogeneity of the initial fuel sample (Pu agglomerates, UO_2 matrix, coating phase or cladding at the periphery) is not taken into account.
- Thermodynamic equilibrium is supposed.

The O/M calculated in the fuel-cladding interaction zone by EPMA is lower than that predicted by the calculations. This may be related to the uncertainty linked to O measurement by EPMA.

No melting of the mixed oxide $U_yZr_{1-y}O_{2\pm x}$ could be observed experimentally, in agreement with thermodynamics. Indeed, melting of this phase is predicted at a temperature of 2420°C, which is higher than the maximum temperature reached during the VERDON-3 test (2300°C).

III.3.2.4.2 Metallic precipitates

The experimental composition of the metallic precipitates after the VERDON-3 test is in good agreement with the thermodynamic calculations. Indeed, in both cases Mo is totally released from the sample. The calculated and experimental Ru/Rh ratios in the remaining precipitates in the sample are also consistent.

Melting of these precipitates is predicted at 2120°C by thermodynamics. This could be consistent with the rounded shape of the precipitates observed in the sample and with their mobility during the

VERDON test. Indeed, they were found to be mainly located in the Pu agglomerates in the father rod (B05 sample), whereas they were homogeneously distributed in the VERDON-3 fuel sample.

III.3.2.4.3 Cs and Ba behavior

The experimental observations concerning Cs are in agreement with thermodynamic calculations, as Cs has been released from the sample during the test. Very few Cs is indeed observed in the VERDON-3 sample.

Concerning Ba, its concentration was measured to be constant all over the sample except in the fuel-cladding interaction zone, where it decreased. This is not in agreement with the behavior of Ba predicted by thermodynamics. Indeed, Ba has been calculated to be located in the $U_yZr_{1-y}O_{2\pm x}$ phase. In this case again, this can due to the hypotheses of thermodynamic equilibrium and to the homogeneous mixture of (U, Pu)O_2, Zr and FP supposed in the calculations.

Globally, a homogenization of the fuel composition has been observed after the VERDON-3 test compared to the as-irradiated father rod, and can be attributed to the enhanced element mobility in the test conditions:

- **The fuel-cladding interaction zone progressed from 5 µm in the father rod up to 70 µm in the VERDON-3 sample.**
- **The Pu concentration has decreased in the observed agglomerates, to become constant all over the VERDON-3 sample (1.5 at% compared to 5 at% in the Pu agglomerates of the father rod and 0.5 at% in the UO_2 matrix).**
- **The metallic precipitates have been observed to be distributed homogeneously between the agglomerates and the UO_2 matrix, whereas they were hardly observed in the UO_2 matrix in the father rod.**
- **The concentrations of other FP such as Ba have also been measured to be constant all over the VERDON-3 sample, whereas their concentrations were clearly higher in the Pu agglomerates in the father rod.**

II.3.3 VERDON-4 samples

The length of the two pellets recovered after the VERDON-4 test is 24 mm with a diameter of 8.17 mm as shown in **Figure II-48**. As observed in **Figure II-49**, melting of at least the cladding took place during the test and covered the fuel elements and one of the fresh half UO_2 pellet (most probably the lower one).

The elements recovered were then prepared for observations and chemical analyses. The two VERDON-4 irradiated pellets were separated and embedded in an epoxy resin (araldite, **Figure II-50**). Given the fragility of the sample, the bigger pellet broke in two pieces. They were reunited and polished axially up to half their diameter (V-4A sample). The smaller pellet was radially polished up to half its height (V-4R sample). A gold coating was performed on the V-4R sample in order to perform SEM, EPMA and SIMS analyses.

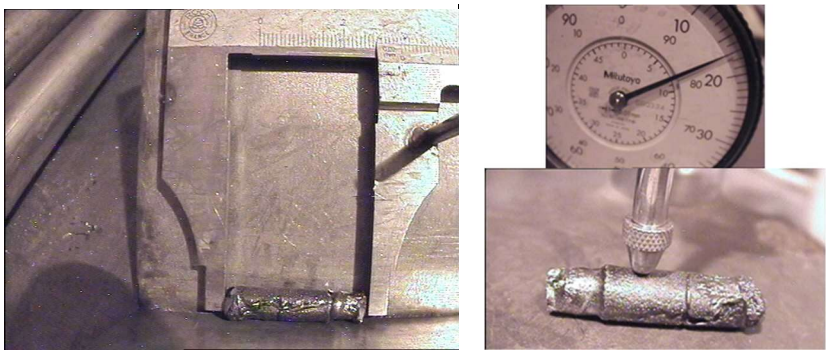

Figure II-48: Measurements of the height and diameter of the fuel elements recovered after the VERDON-4 test

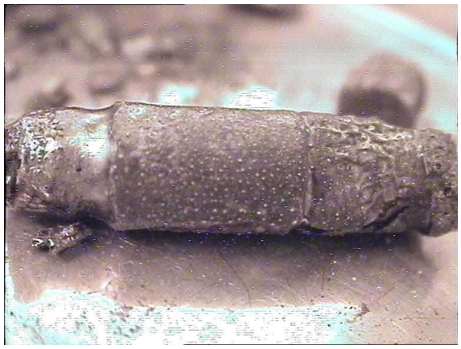

Figure II-49: VERDON-4 fuel elements recovered after the VERDON-4 test

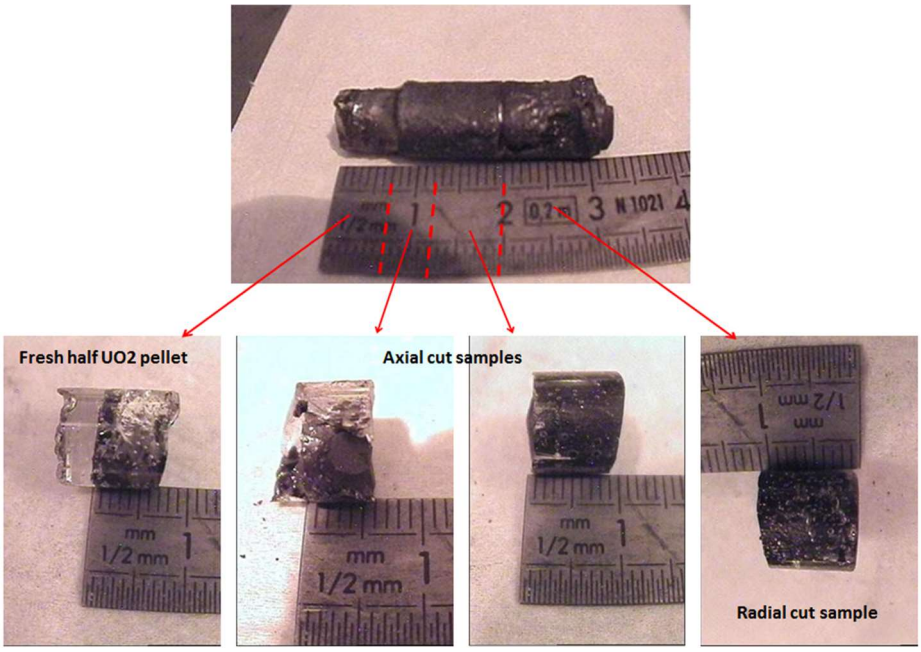

Figure II-50: Preparation of the V-4A (center) and V-4R (right) samples

II.3.3.1 Fuel behavior

II.3.3.1.1 Microstructure analysis

Optical micrographs of the V-4A and V-4R samples are presented in **Figure II-51**. Three main zones could be observed on both samples:

- Reduce porosity areas (blue frames at 0.75R in **Figure II-51**) starting from the periphery of the pellet can be observed more in detail in **Figure II-52** (0.75R).
- A porous matrix (green frames at 0R in **Figure II-51**) with elevated pore interconnection degree and small spherical pores can be seen more in detail in **Figure II-52** (0R).
- Light grey agglomerates (orange frames at 0.5R in **Figure II-51**) appearing from the periphery of the pellets (1R) to 0.4R exhibit a moderate porosity as detailed in **Figure II-52** (0.5R).

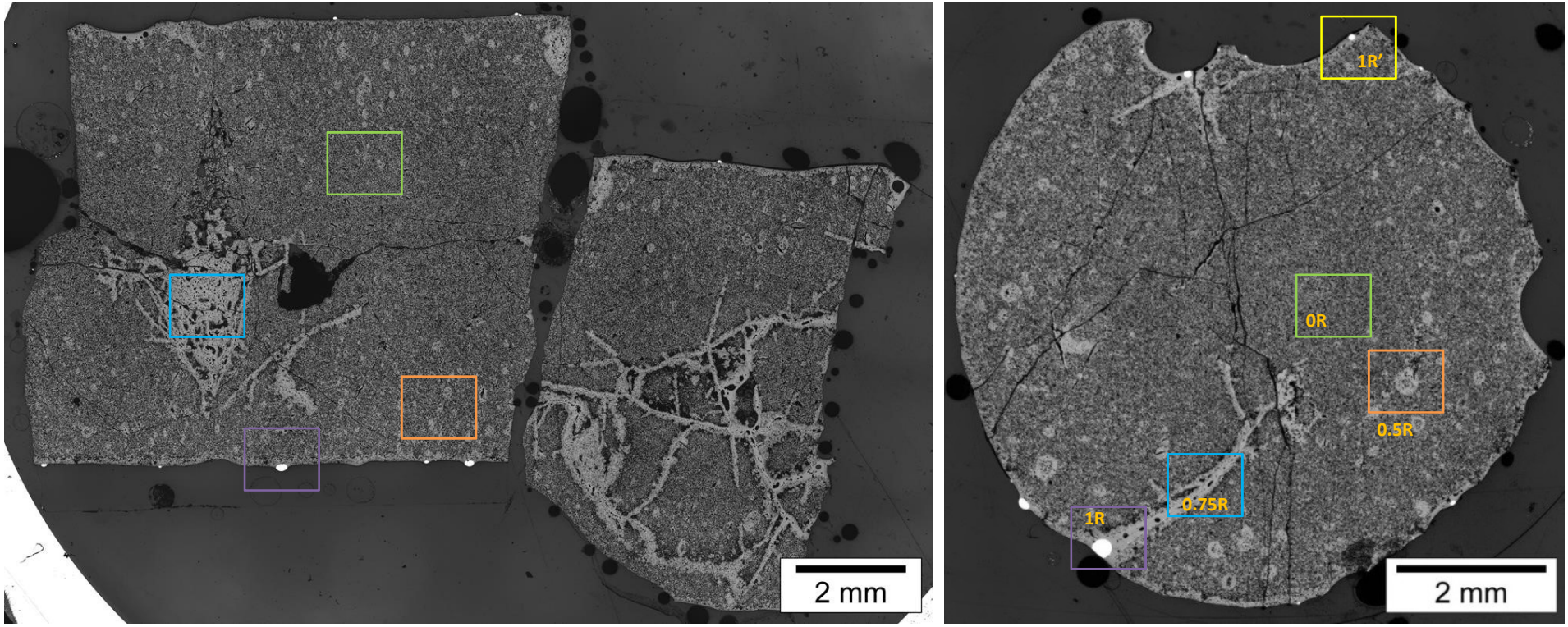

Figure II-51: Micrographs of the V-4A (left) and V-4R (right) samples after preparation

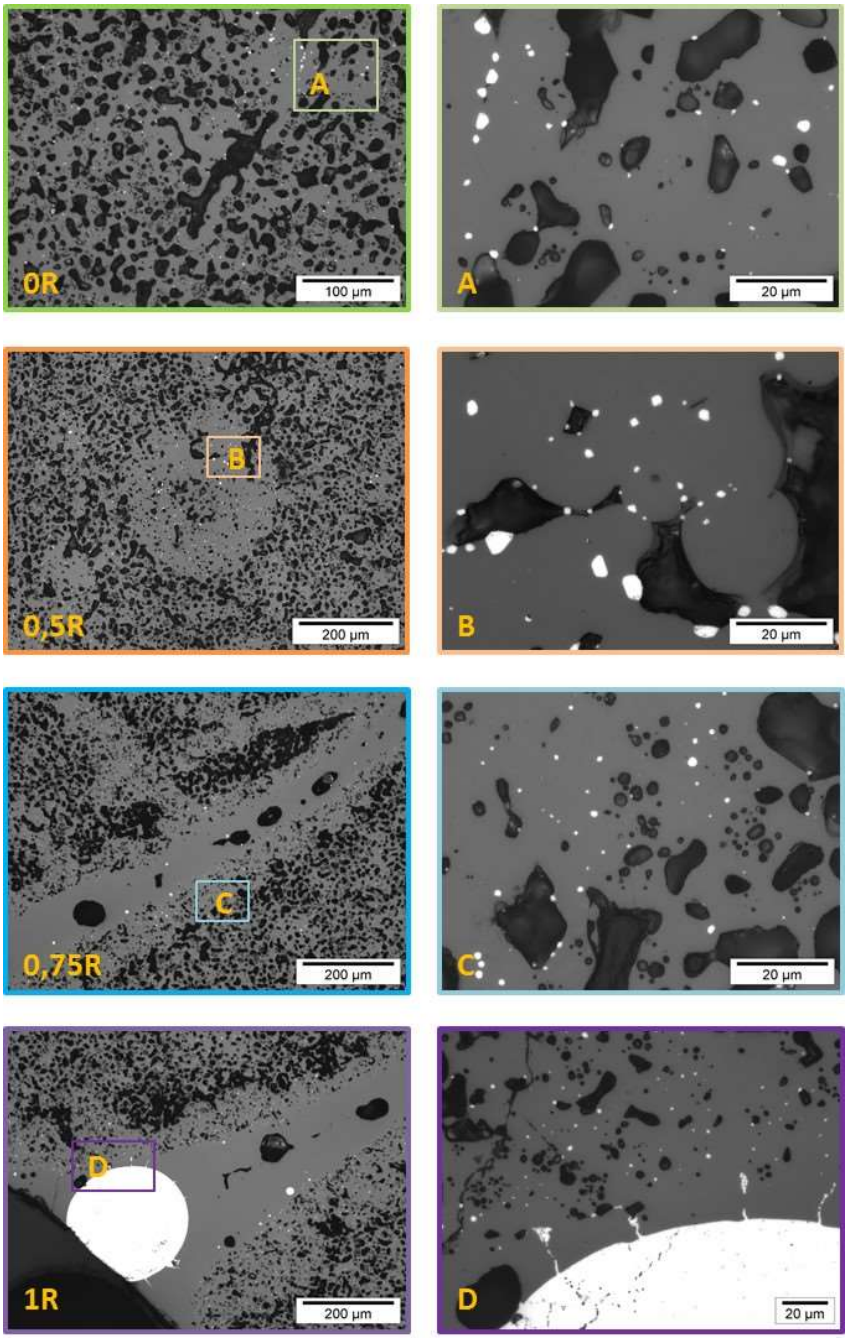

Figure II-52: Detailed analysis of the four zones identified on sample V-4R

Histograms of the pore size distribution[6] in these zones are presented in **Figure II-53**. In the reduce porosity zones, almost all the pores are smaller than 4 µm and the maximum number of pores are found to have an ECD of 0.5-0.6 µm. The larger ones have a mean ECD of 7.0 ± 0.6 µm. The number of pores with a size inferior to 4 µm found in the porous matrix is more than two times higher than in the agglomerates. However, the number of pores with a size superior to 4 µm are similar in both regions. Features larger than 40 µm have been observed only in the porous matrix due to pore

[6] Ten images of 170 x 130 µm² of the three first zones were used to determine the number and surface contribution of the pores.

interconnection. As shown in **Figure II-54**, the total surface contribution of the pores in the porous matrix is three times higher compared to the agglomerates and 11 times higher than in the reduce porosity area. In the porous matrix, the surface contribution of the pores larger than 40 µm is twice the one of pores smaller than 40 µm.

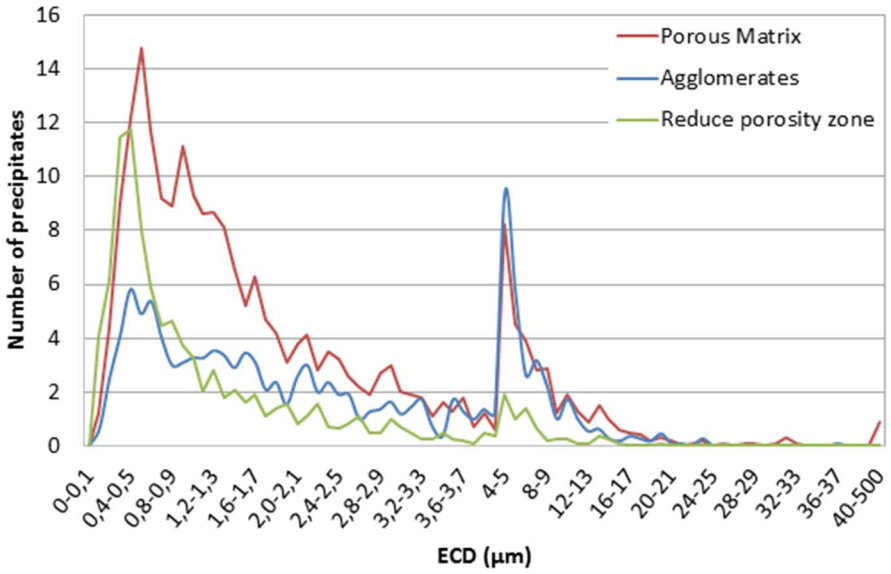

Figure II-53: Histogram of the pore size distribution in the different zones of the V-4R sample

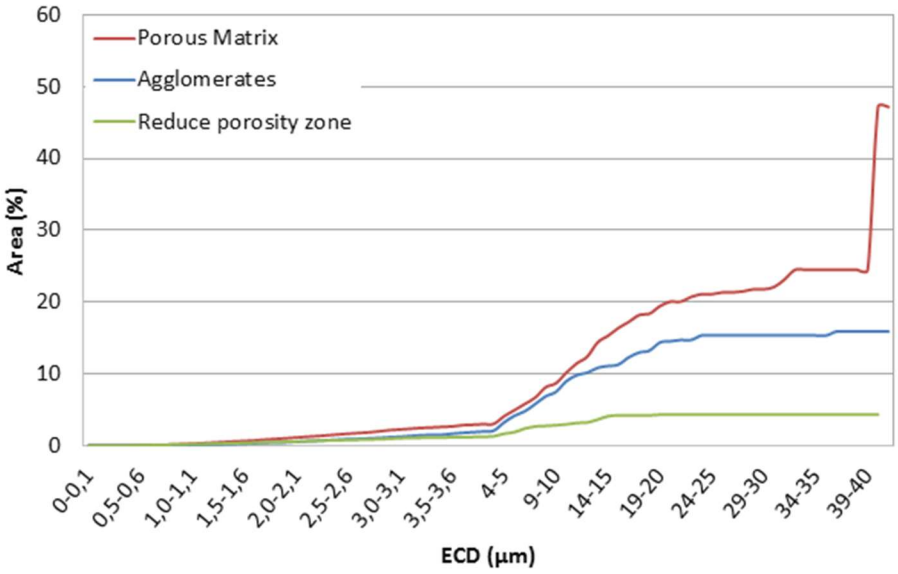

Figure II-54: Integrated pore surface contribution in the different zones of the V-4R sample

II.3.3.1.2 Chemical analyses

Agglomerates

The agglomerates observed in the micrographs of the V-4R samples are richer in Pu than the porous matrix as shown in **Figure II-55**. The U content decreases from 35.2 at% in the porous matrix down to 31.3 at% in the agglomerates when the Pu content rises from 1.6 at% up to 4.5 at% (4.3% to 12.5 % for Pu/(U+Pu)) in the center of the agglomerate (**Figure II-56**). The amount of Pu in the UO_2 matrix is higher than in the B05 sample whereas the Pu content in the agglomerates is lower. This may indicate that Pu diffusion took place during the test from the agglomerates to the UO_2 matrix.

Nevertheless, this diffusion is not as efficient as in the V-3M sample where the Pu content was almost homogeneous. The O/M ratio in the matrix is similar to that measured in the agglomerates and is 1.6 ± 0.3. These two values are way smaller than the ones measured in the B05 and V-3M sample confirming the strong reducing conditions of the VERDON-4 test.

The moderated porosity observed in the V-4R sample's agglomerates indicates that re-sintering took place during the VERDON-4 test as it was the case in the VERDON-3 test.

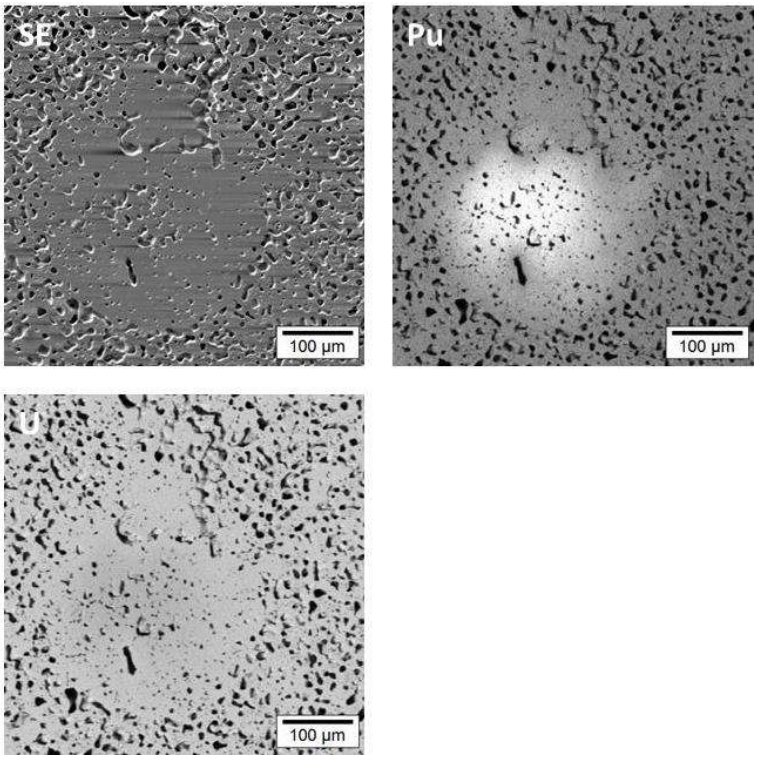

Figure II-55: SEM-SE and O, U and Pu X-ray maps acquired at 0.5R on sample V-4R

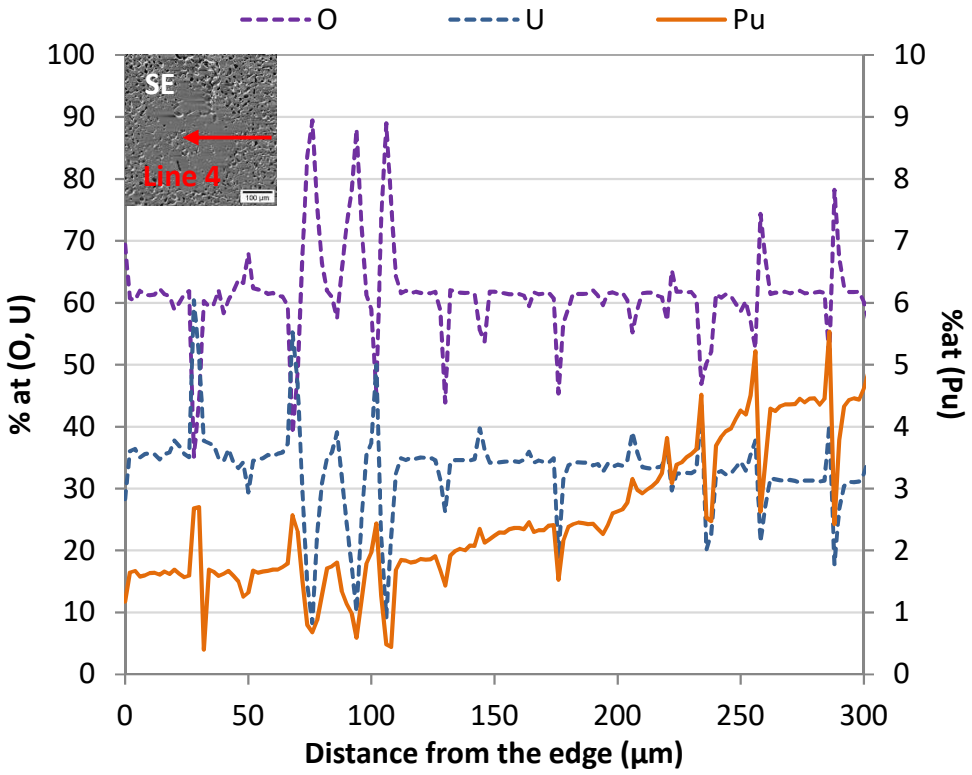

Figure II-56: O, U and Pu quantitative profiles along Line 4, 0.5R on sample V-4R

Fuel-cladding interaction

Isotope mapping and X-ray mapping of the reduce porosity area at 0.75R (**Figure II-57** and **Figure II-58**) indicate that it is mainly composed of U and Zr. As presented in **Figure II-59**, the isotopic distribution of Zr corresponds to natural Zr as already observed in the case of V-3M sample (**Figure II-27**). Once again, a peak is present at the mass 93 amu which may indicate the presence of Nb in this region. These observations indicate that this area consists in a mix of the M5 cladding tube originally surrounding the fuel pellet and the pellet itself.

The amount of U and Pu decreases as the concentration of Zr increases. This trend is clearly seen in the quantitative profiles performed along Line 5 (**Figure II-60**). According to these results, the Zr concentration increases from around 0.5 at% in the porous matrix up to 19.4 at% in the center of the reduce porosity region. On the contrary, the U and Pu contents decrease from 35.4 at% and 1.8 at% down to 19.3 at% and 1.3 at% respectively. Regarding O, its concentration slightly decreases from 60.6 at% down to 58.8 at% at the center of the reduce porosity region. Thus at the center of the crack the molten phase has a composition close to $U_{0.50}Zr_{0.50}O_{1.51}$.

Quantitative profiles performed in the reduce porosity areas located at the periphery of the pellet near the large precipitate observed in **Figure II-61**, indicate that the amount of Zr is slightly higher (22.0 at%) whereas the U content is lower (16.6 at%). The O and Pu contents are constant with 58.8 at% and 1.3 at% respectively. Thus the composition of the molten zone observed in the very periphery is $U_{0.43}Zr_{0.57}O_{1.71}$. As observed on the graph, the Zr concentration rapidly decreases when the amount of U increases in direction of the porous matrix.

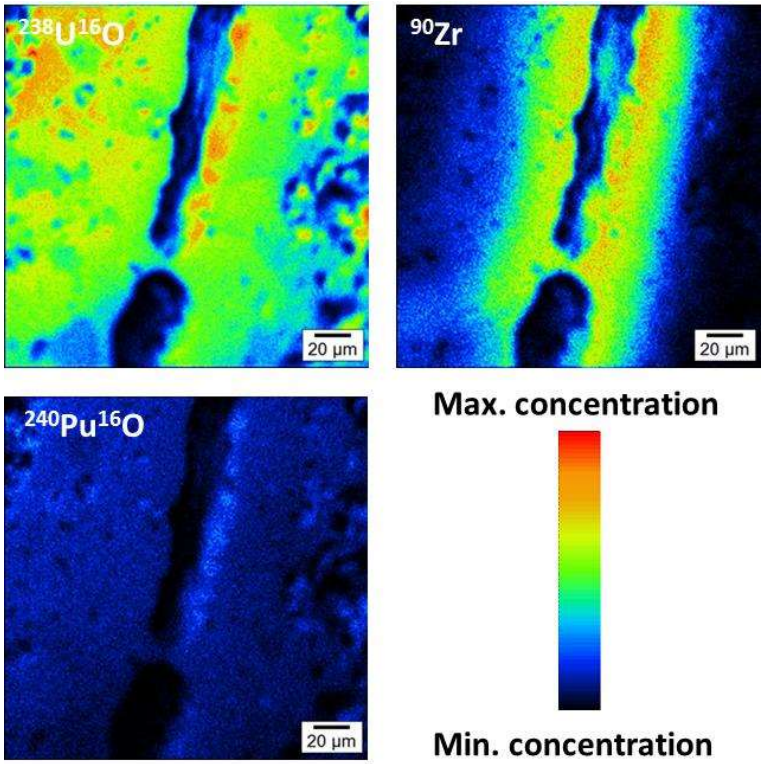

Figure II-57: SIMS isotope mapping performed at 254, 90 and 256 amu acquired at 0.75R on sample V-4R. The black zones correspond to regions of the sample poor in the isotope measured whereas red areas are rich in this isotope.

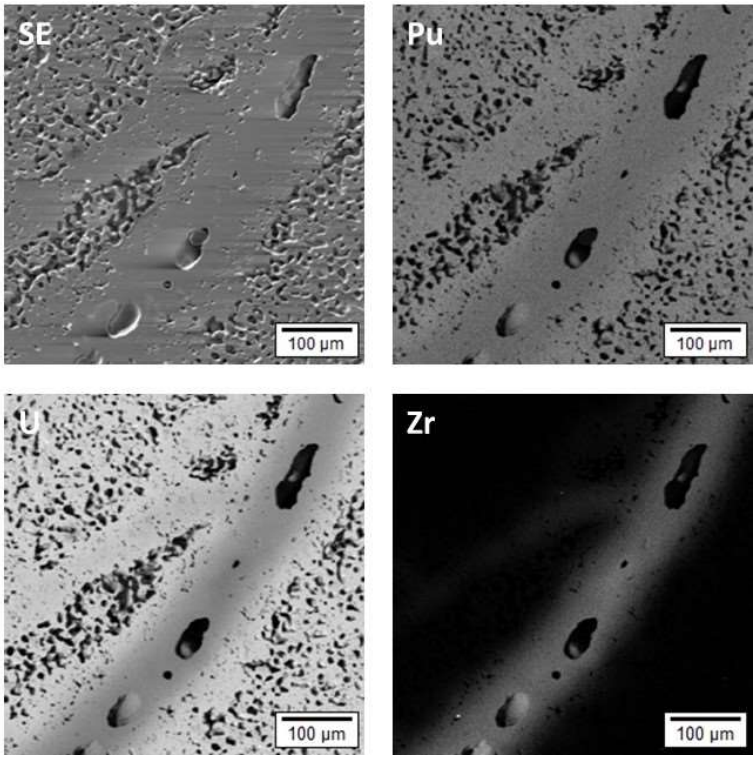

Figure II-58: SEM-SE and O, U, Zr, Pu, Ba, Ce and Cs X-ray maps acquired at 0.75R on sample V-4R

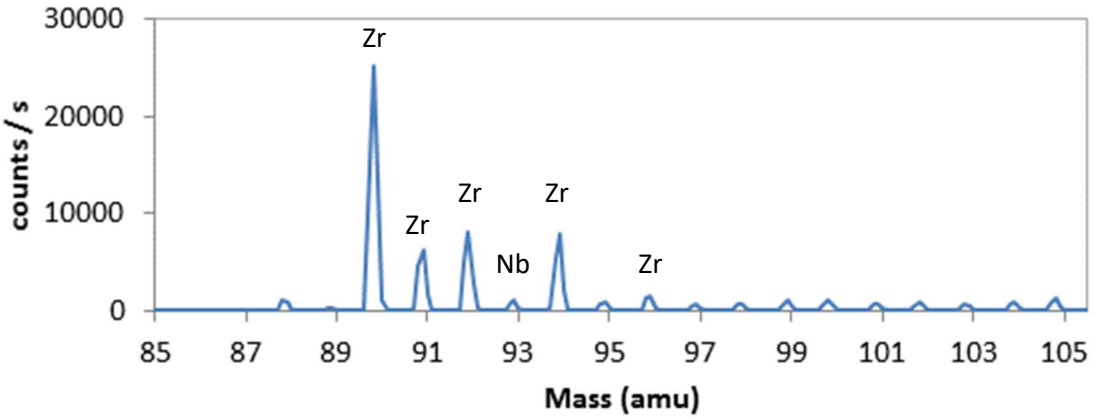

Figure II-59: Mass spectrum ranging from 85 to 105 amu acquired at 0.75R on sample V-4R, the peaks intensities are typical of natural Zr

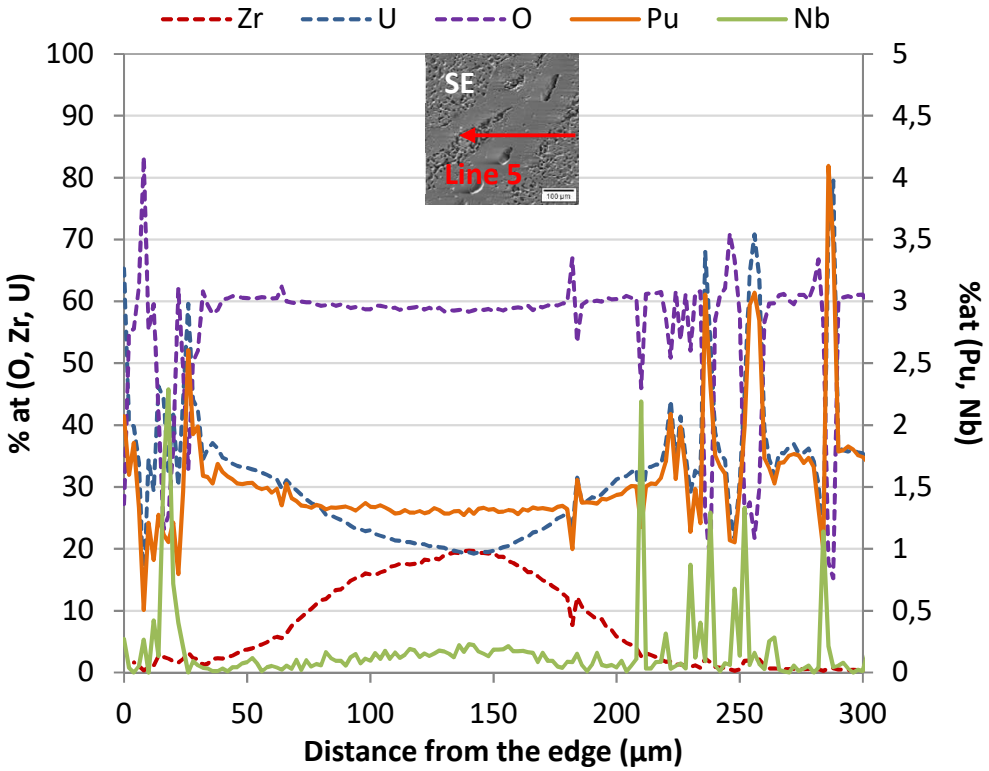

Figure II-60: O, Zr, U, Pu and Nb quantitative profiles along Line 5, 0.75R on sample V-4R

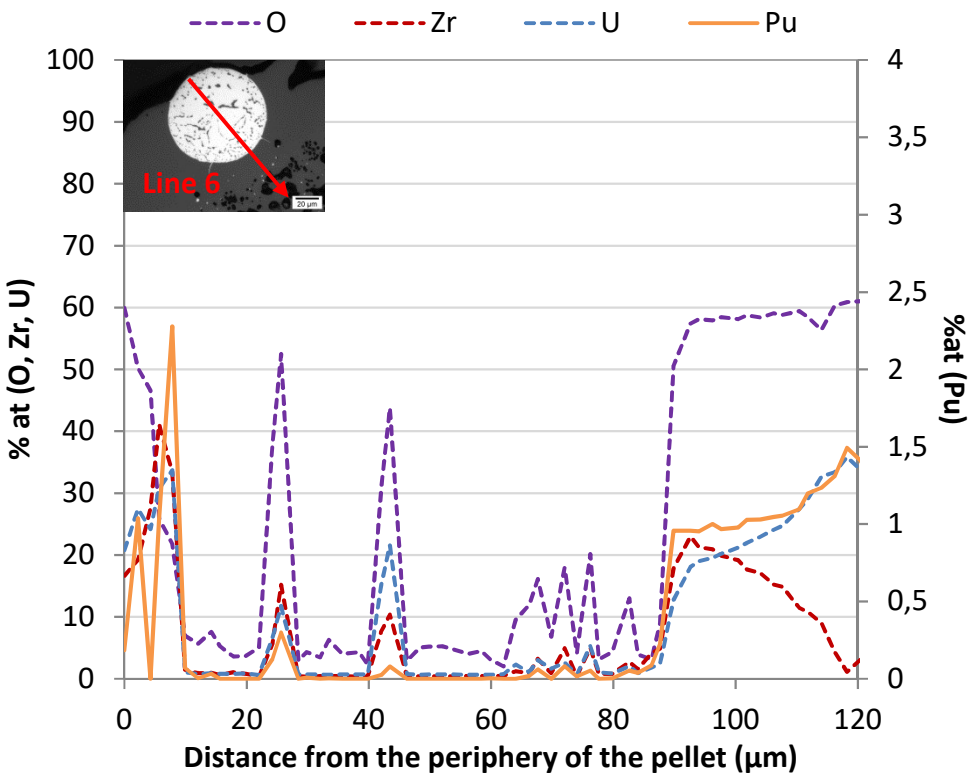

Figure II-61: O, Zr, U and Pu quantitative profiles along Line 6, 1R' on sample V-4R

This behavior has already been observed in reducing conditions notably during the COLOSS [23], HEVA-06 [24], VERCORS-5 [25]–[27] and VERDON-1 tests [28], [29]. The final composition of the liquid phase measured experimentally in the periphery of the V-4R sample (close to the cladding), at the fuel matrix close to the crack found at 0.75 R (**Figure II-58**), in its periphery and in its center have been reported on the diagram presented in **Figure II-62** calculated using the TAF-ID. As indicated in this diagram, the composition measured in these points are consistent with the tie lines orientation. Moreover, a Zr enrichment is observed as the compositions This confirms the hypothesis of the progressive dissolution of UO_2 coming from the fuel matrix by the liquid $U_yZr_{1-y}O_{2\pm x}$ phase originally formed at the periphery when temperature increased.

These VERDON-4 experimental compositions of the $U_yZr_{1-y}O_{2\pm x}$ phase are also consistent with experimental data available on the corium solutions analyzed after the Phebus FPT-0, -1 and -2 ($U_{0.51}Zr_{0.46}O_2$, $U_{0.65}Zr_{0.35}O_2$ and $U_{0.4}Zr_{0.6}O_2$ respectively) [30]–[32] and the analytical study by [33] ($U_{0.4}Zr_{0.6}O_2$). However, no phase separation could be clearly identified within the molten phase after cooling the VERDON-4 sample as it was the case in the TMI-2 corium described in **Chapter I**, **section I.4.1.1** (tetragonal and monoclinic solid solutions [33]). This could be attributed to the fast cooling rate of the VERDON tests which prevented the formation of such phases.

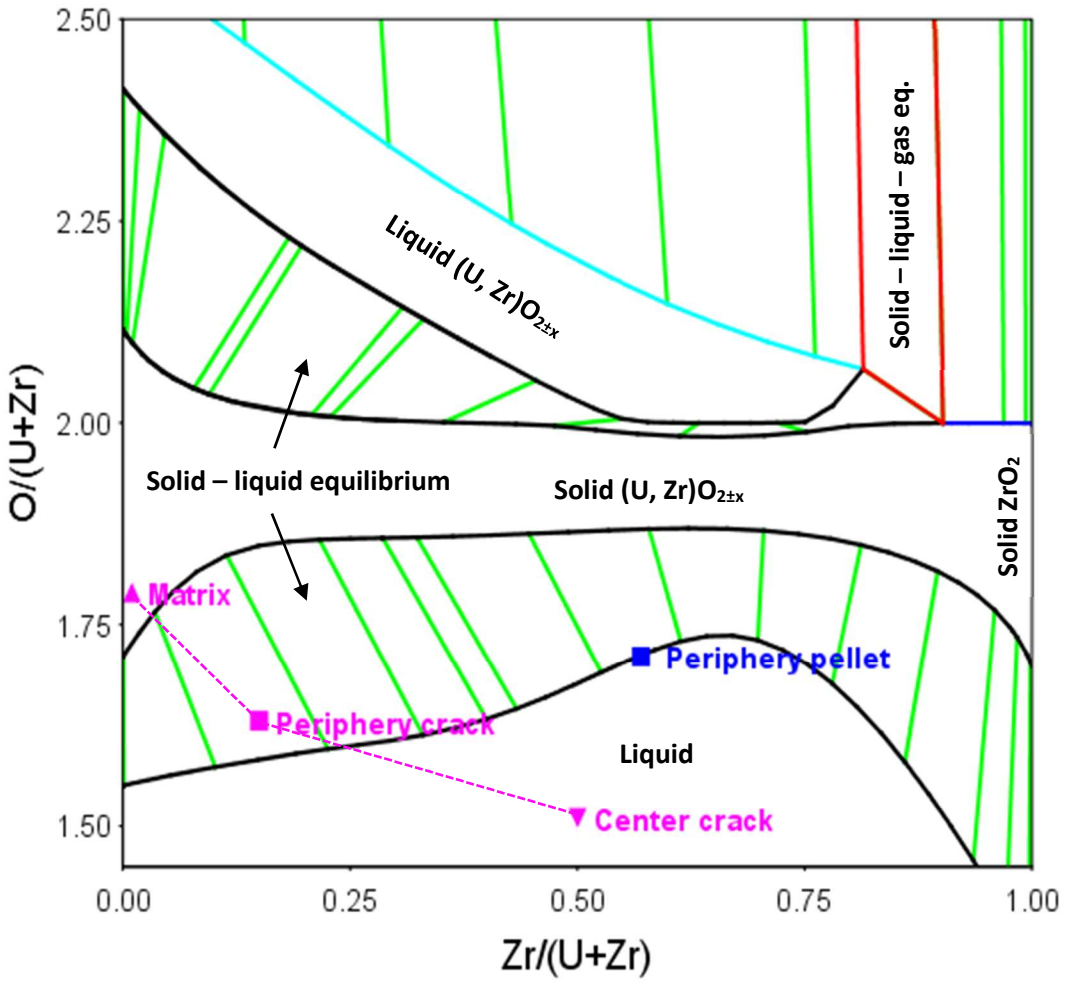

Figure II-62: Calculated isotherm diagram of the Zr/(U+Zr) content as a function of O/(U+Zr) at 2530°C where the experimental data obtained in the molten regions at the periphery of the sample and in the the crack found at 0.75R of the VERDON-4 samples are reported, calculated using Thermo-Calc [7] coupled with the TAF-ID [8]

II.3.3.1.3 Thermodynamic calculations

The evolution of the main phases observed in the fuel sample has been calculated during the heating phases of stages 2 and 3 of the VERDON-4 test using the Thermo-Calc [7] software coupled with the TAF-ID [8]. The oxygen potential of stages 2 and 3 have been calculated supposing thermodynamic equilibrium and by integration of the whole quantity of gas injected during the stage considered (**section I.2.2**). The transition between the two stages at 1500°C is thus discontinuous.

As shown in **Figure II-63**, these phases are composed of monoclinic ZrO_2 (ZrO2_Mono), tetragonal ZrO_2 (ZrO2_Tetr), the fuel mixed oxide composed of (U, Pu)O_2 and another mixed oxide corresponding to the fuel-cladding interaction ((U, Zr)O_2).

According to the calculations, at the beginning of stage 2 monoclinic ZrO_2 and (U, Pu)O_2 are present, which is in agreement with the limited interaction layer observed experimentally between the cladding and the fuel pellet in the father rod. A phase transition occurs around 1100°C from monoclinic to tetragonal ZrO_2. As soon as the tetragonal ZrO_2 is formed, the amount of (U, Pu)O_2 starts to decrease.

During stage 3, the tetragonal ZrO_2 and the (U, Pu)O_2 phases are consumed to form the (U, Zr)O_2 mixed oxide. At 1750°C, all the ZrO_2 is in the (U, Zr)O_2 phase whereas the amount of (U, Pu)O_2 slightly decreases up to the end of the test. From 2000°C, the amount of (U, Zr)O_2 decreases because of the vaporization of 25 % of U mainly as UO_3, as shown in **Figure II-64**.

The U and Zr behavior during stages 2 and 3 of VERDON-4 test is given in **Figure II-64** and **Figure II-65**. According to these calculations, dissolution of Zr contained in ZrO_2 into the (U, Pu)O_2 phase and occurs as well as a dissolution of U from the (U, Pu)O_2 into ZrO_2, as soon as the tetragonal ZrO_2 is formed.

The amount of U in (U, Pu)O_2 and tetragonal ZrO_2 decreases when (U, Zr)O_2 is formed. At 1750°C, almost 16 % of U remains in the (U, Pu)O_2 phase whereas the U initially contained in tetragonal ZrO_2 has entirely been consumed. At 2480°C, the (U, Zr)O_2 phase starts to melt consistently with experimental observations. At the end of the test, the composition of the (U, Zr)O_2 phase is $U_{0.43}Zr_{0.57}O_{2.03}$ which is very consistent with the experimental observations performed at the periphery of the VERDON-4 sample $U_{0.43}Zr_{0.57}O_{1.71}$ (except concerning the O content).

Concerning Zr (**Figure II-65**), up to 14 % is dissolved in the (U, Pu)O_2 phase around 1650°C and 86 % is found in tetragonal ZrO_2. Then, the whole amount of Zr is dissolved and remains in the (U, Zr)O_2 phase until the end of the test.

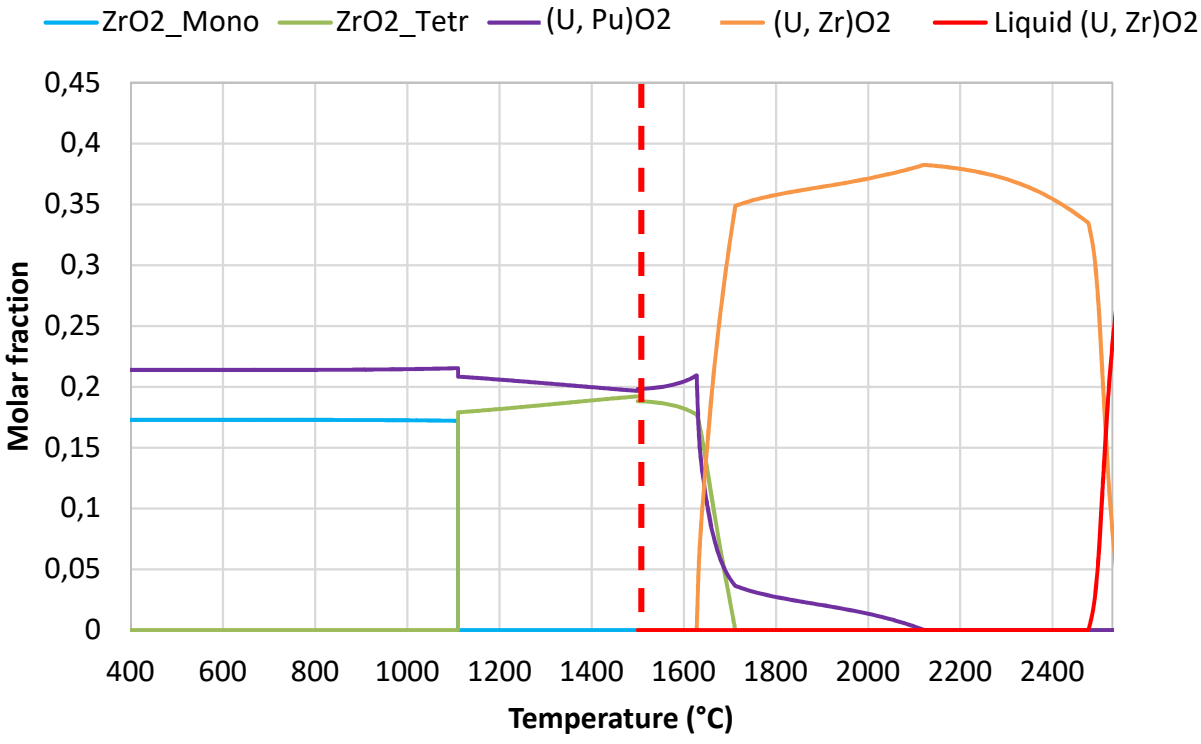

Figure II-63: Evolution of the fuel matrix and cladding during the stages 2 and 3 of the VERDON-4 test, calculated using Thermo-Calc [7] coupled with the TAF-ID [8]

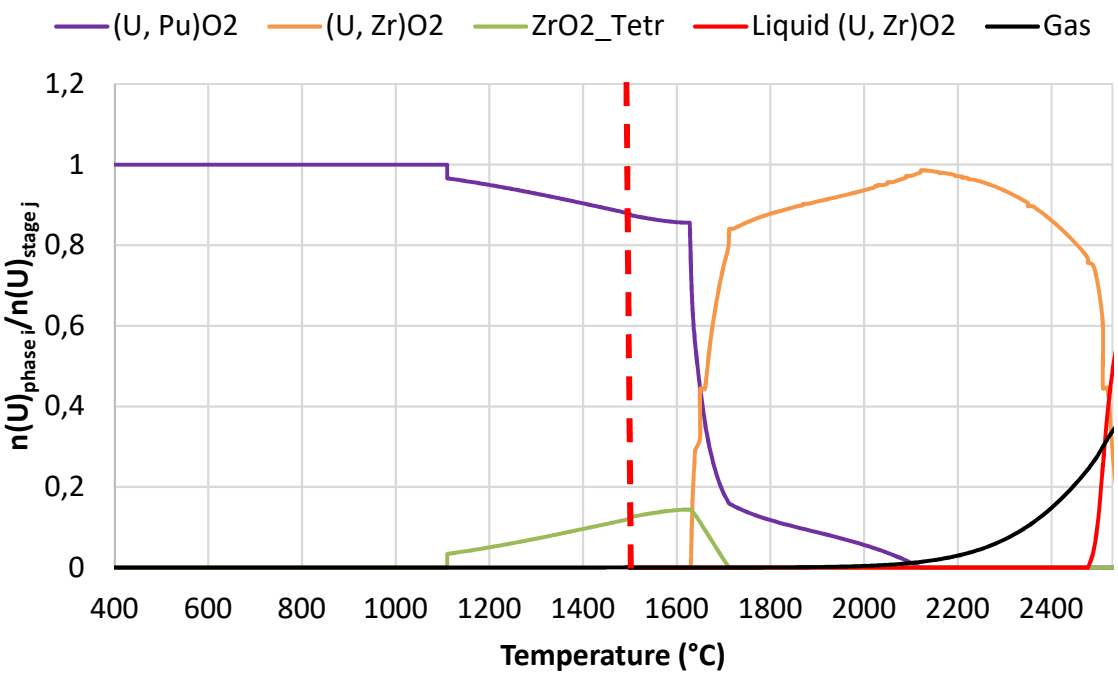

Figure II-64: U behavior during the stages 2 and 3 of the VERDON-4 test, calculated using Thermo-Calc [7] coupled with the TAF-ID [8]

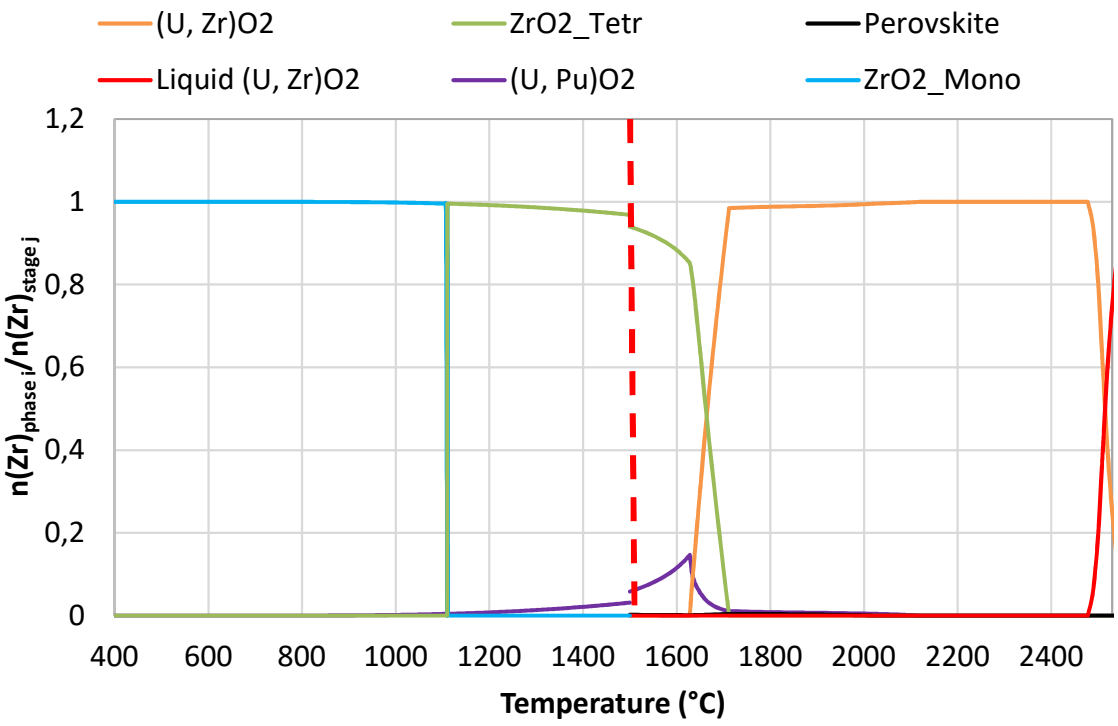

Figure II-65: Zr behavior during the stages 2 and 3 of the VERDON-4 test, calculated using Thermo-Calc [7] coupled with the TAF-ID [8]

II.3.3.2 Metallic precipitates

II.3.3.2.1 Microstructure analysis

Large white precipitates have been found at the very periphery of the VERDON-4 sample as shown in **Figure II-51** (purple frames at 1R) and in detail in **Figure II-52** (1R). Smaller ones, mainly located in the agglomerates, have also been observed (**Figure II-66**).

In the agglomerates, the white precipitates are more numerous and larger than in the porous matrix as shown in **Figure II-67**[7]. This is particularly visible at 0.5R in **Figure II-66**. Their mean ECD is 1.6 ± 0.2 µm whereas they measure in average 1.2 ± 0.3 µm in the porous matrix. Some small precipitates with a mean ECD of 1.4 ± 0.3 µm along with very large ones (up to 200 µm) are rarely found in the reduce porosity area. The contribution of these precipitates to the total surface analyzed for the three zones of the sample is presented in **Figure II-68**. The surface contribution of the precipitates smaller than 25 µm in the agglomerates is twice higher than in the porous matrix and the reduce porosity area. Nevertheless, for precipitates larger than 25 µm, the surface contribution in the reduce porosity area is seven times higher than in the agglomerates.

[7] Ten images of 170 x 130 µm² of the three first zones were used to determine the number and surface contribution of the white inclusions.

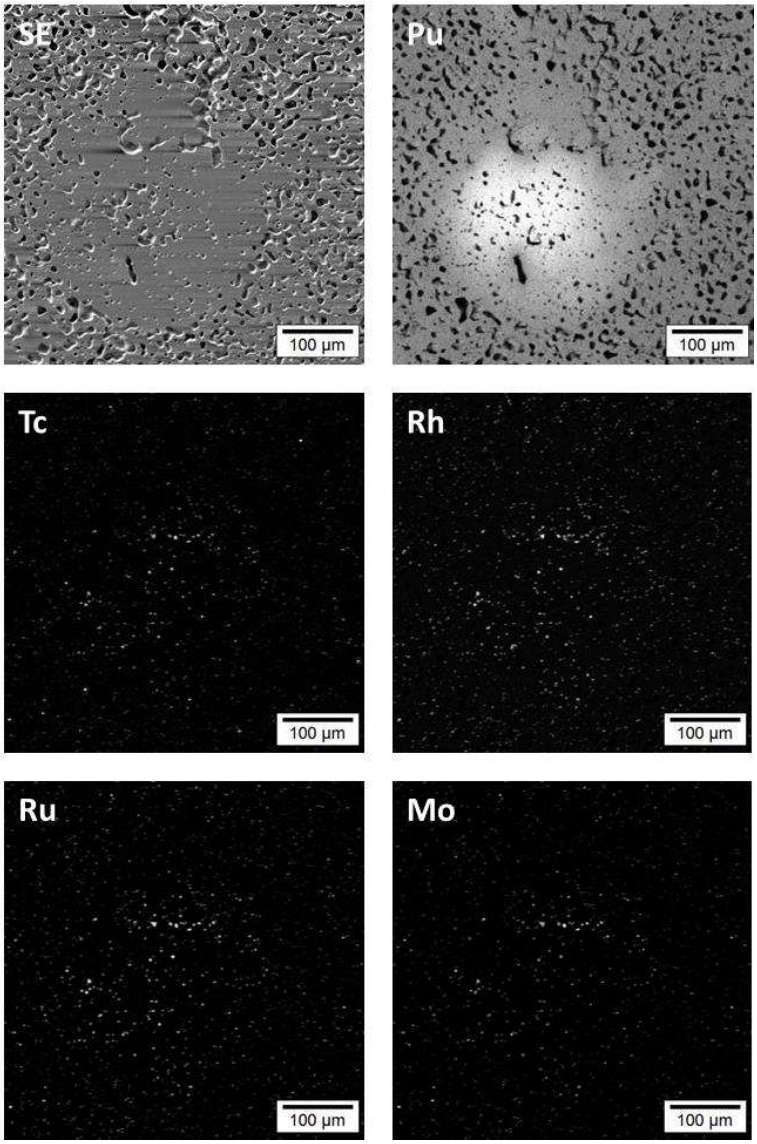

Figure II-66: SEM-SE and Pu, Tc, Rh , Ru and Mo X-ray maps acquired at 0.5R on sample V-4R

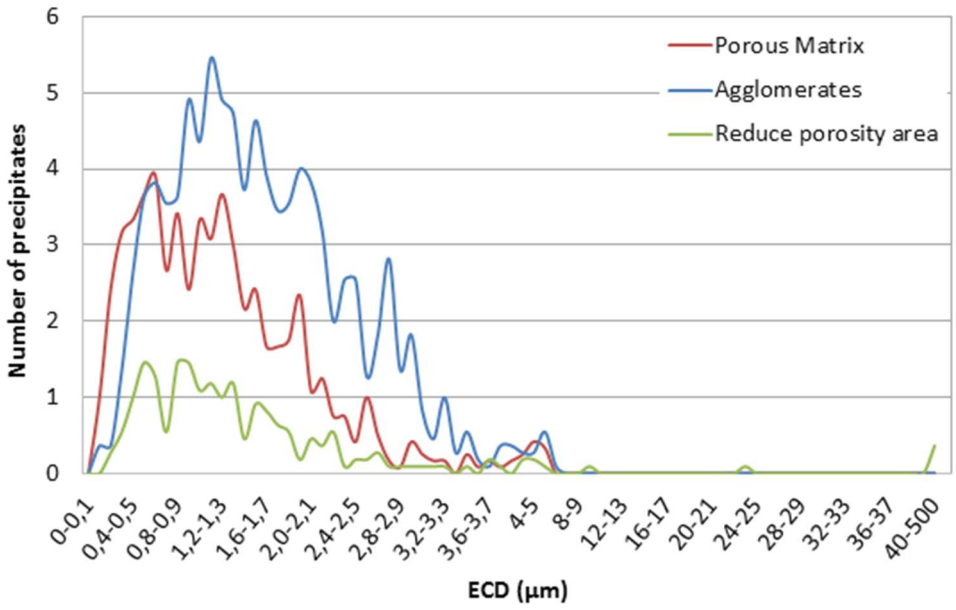

Figure II-67: Histogram of the white inclusions size distribution in the different zones of the V-4R sample

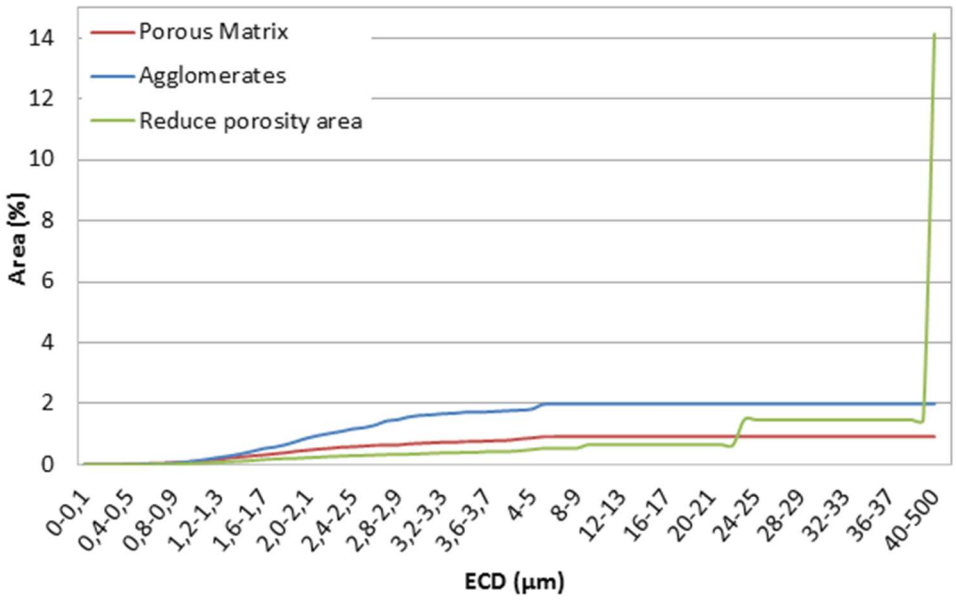

Figure II-68: Integrated white inclusions surface contribution in the different zones of the V-4R sample

II.3.3.2.2 Chemical analyses

As shown in **Figure II-69** and **Figure II-70**, the large metallic precipitates observed in the sample are composed of Ru, Rh, Tc and Mo. The mass spectrum corresponding to one of these precipitates is presented in **Figure II-71**. The isotopic distribution is consistent with the fission creation ratios for these four FP (Rh < Tc < Ru < Mo). The quantitative profiles of two large precipitates found at 1R (**Figure II-70**) and 1R' (**Figure II-51**), representative of the whole population analyzed are presented in **Figure II-72**. No correlation between the location of the precipitates and their composition could be made. The main components of these precipitates are Ru and Mo. Nevertheless, the ratio between Ru and Mo evolves from a precipitate to another. Indeed, at 1R the Ru and Mo contents are 43.4 at% and 41.8 at% respectively (Ru/Mo ≈ 1) whereas at 1R', the Ru content increases up to 52.4 at% and the Mo concentration decreases down to 28.1 at% (Ru/Mo ≈ 2). These two types of precipitates are

consistent with the white inclusions found in the B05 sample (initial state). However, in the B05 sample, the precipitates with a Ru/Mo ratio of 2 were located only in the Pu-agglomerates of the HBS region whereas the inclusions with Ru/Mo ≈ 1 were located in the center of the sample.

The Rh content remains constant in both cases with 9.6 at%. The ratio Ru/Rh ≈ 4.5 ± 0.1 in these precipitates is consistent with the one obtained in the B05 sample indicating that almost no release took place for these two FP during the test. Locally, the Rh content can increase up to 16.5 at% in the precipitate located at 1R corresponding to the brighter dots observed in **Figure II-70**.

Nb is also present with a concentration of 1.5 at% at 1R and 3.3 at% at 1R'. This is probably due to the location of the precipitates in the molten Zr-rich regions of the sample. Nb is thus observed to be preferably dissolved in the metallic phase than in the $U_yZr_{1-y}O_{2\pm x}$ liquid phase. No Pd could be detected as it was the case for the V-3M sample, indicating its total release during the VERDON-4 test. Once again, Tc could not be quantified due to the lack of standard.

Once molten, these precipitates probably coalesced at the periphery of the pellet. Their flat shape towards the edges of the pellet may indicate that they were probably trapped by the remaining cladding. This phenomenon could explain the composition of the two populations of metallic precipitates and their random location in the sample. Indeed, depending on their path to the edges of the pellets, the two types of precipitates coalesced in different proportions leading to an enrichment or a depletion in Mo.

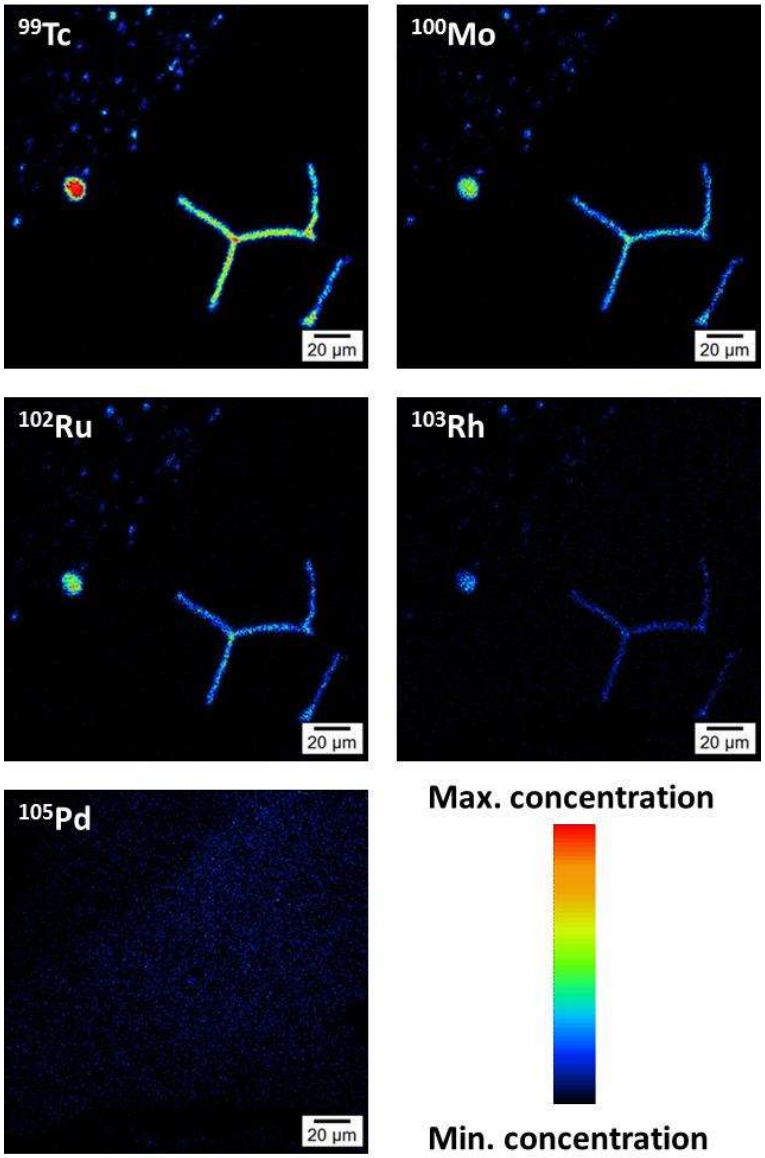

Figure II-69: SIMS isotope mapping performed at 99, 100, 102, 103 and 105 amu, acquired at 1R on sample V-4R. The black zones correspond to regions of the sample poor in the isotope measured whereas red areas are rich in this isotope.

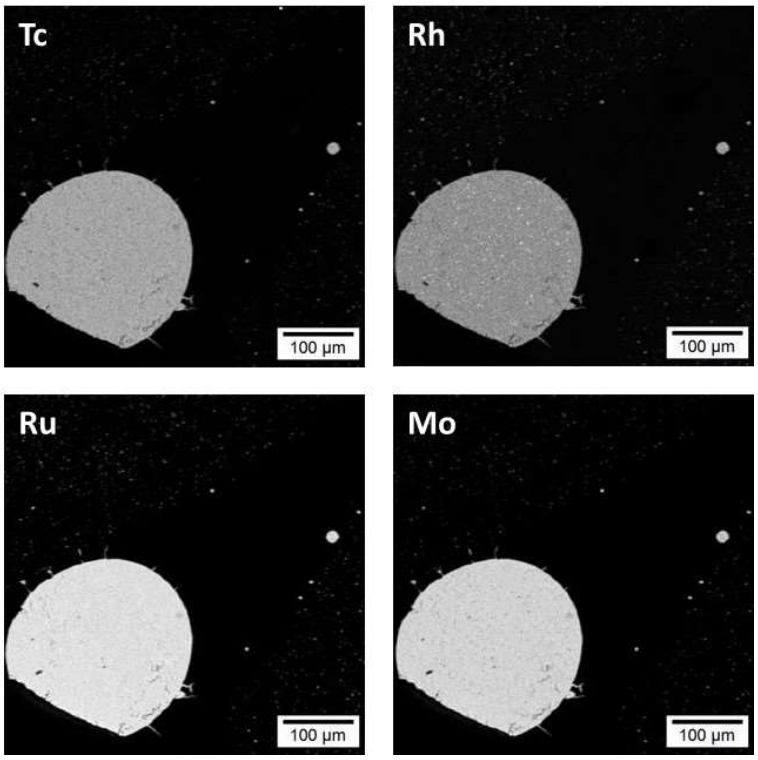

Figure II-70: SEM-SE and Tc, Rh , Ru and Mo X-ray maps acquired at 1R on sample V-4R

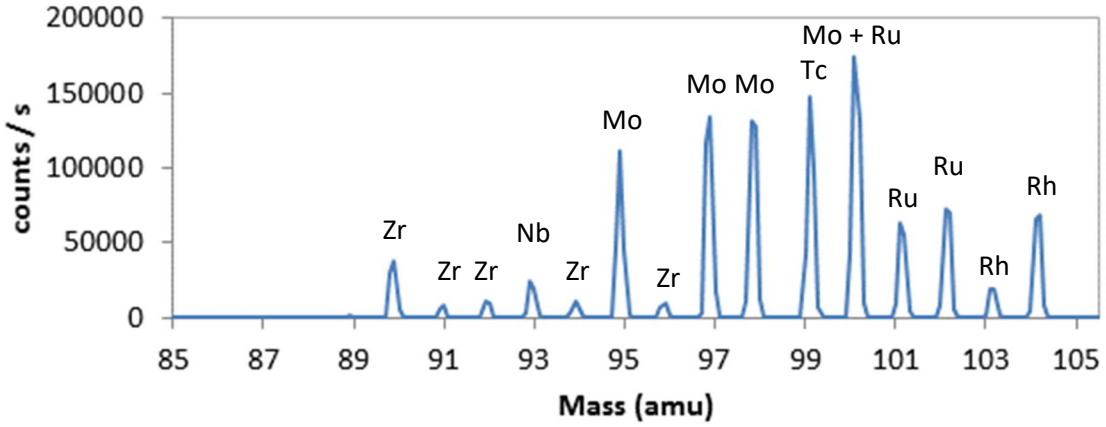

Figure II-71: Mass spectrum ranging from 85 to 105 amu acquired at 0.75R on a precipitate found in the sample V-4R

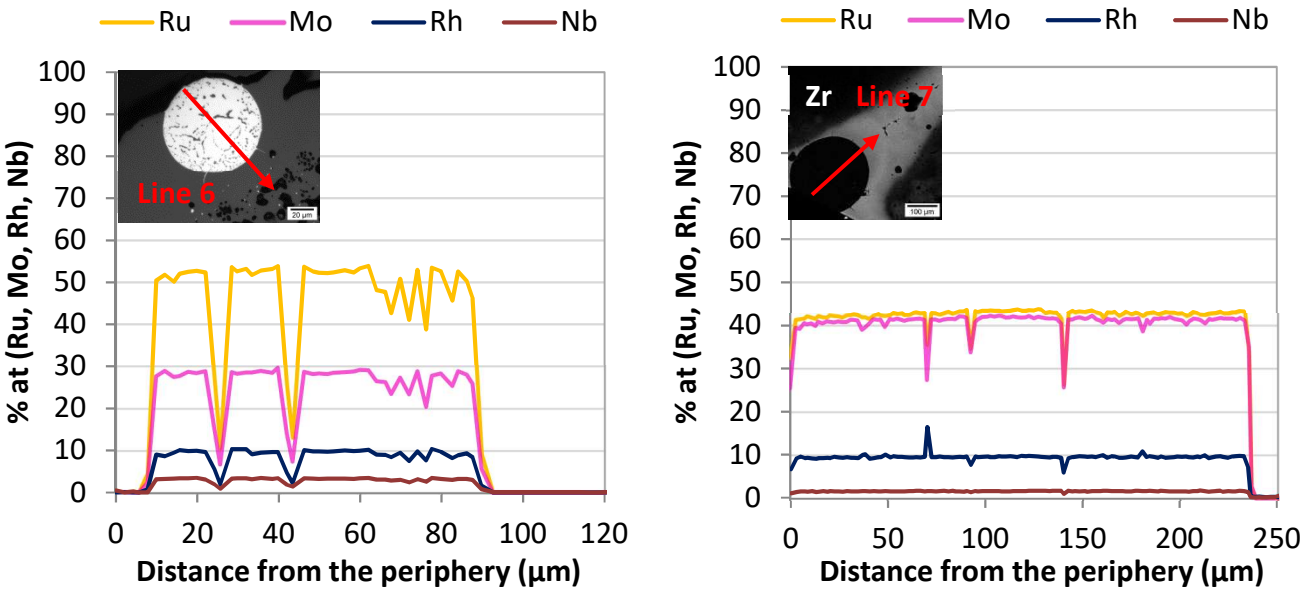

Figure II-72: Ru, Mo, Rh and Nb quantitative profiles along Line 6 (left) and line 7 (right), 1R' and 1R zones respectively on sample V-4R

II.3.3.2.3 Thermodynamic calculations

The calculated evolution of the metallic phases formed by the interactions between Mo, Ru, Rh, Pd and Tc is shown in **Figure II-73**. The oxygen potential of stages 2 and 3 have been calculated supposing thermodynamic equilibrium and by integration of the whole quantity of gas injected during the stage considered (**section II.2.2**). The transition between the two stages at 1500°C is thus discontinuous. An emphasis is made on the behavior of Mo in this part.

Initially, three types of metallic phases are present in the fuel: a fcc metallic phase, a hcp one both composed of Tc, Ru, Rh, Pd and Mo and $MoRh_3$. At around 940°C, the $MoRh_3$ phase is decomposed in fcc and hcp phases. At the end of stage 2, the only metallic precipitates present in the fuel have a hcp structure and contain no Mo (**Figure II-74**).

According to the calculations, during stage 3, the metallic precipitates remaining in the fuel would melt around 2200°C (Liquid Metal. in **Figure II-73**). Their final composition would be 54.0 % of Ru, 41.8 % of Tc and 3.0 % of Rh (Nb was not considered in the calculation) and only 4.2 % of Mo. The experimental compositions are not consistent with the results obtained through thermodynamic calculations which clearly underestimated the Mo content in the metallic phase.

Mo can be mainly found in Cs_2MoO_4, $BaMoO_4$, $MoRh_3$ and MoO_2 in stage 2, as shown in **Figure II-74**. Around 680°C, melting of the molybdate phases occurs. Massive $BaMoO_4$ melting occurs around 1000°C. A decomposition of the Cs_2MoO_4 and the vaporization of MoO_2 explain the presence of Mo in the gas phase from 800°C. The decomposition of $MoRh_3$ leads to an increase of Mo amount in the fcc and hcp phases. Around 1450°C, the whole amount of Mo contained in the fcc metallic phase passes in the hcp one.

As shown in **Figure II-74**, the switch of atmosphere between stage 2 and 3 leads to a brutal increase of the Mo content in the metallic precipitates. Indeed, the Mo amount contained in the gas phase (mainly as MoO_2) and in the liquid molybdate phase (Liquid#2) at the end of stage 2, is condensed in the hcp metallic phase at the beginning of stage 3. Around 2 % of Mo is also present in the perovskite

phase at the beginning of stage 3. This phase disappears around 2000°C leading to Mo vaporization. The amount of Mo contained in the hcp metallic phase decreases until its melting. The decomposition of this phase is associated with Mo vaporization. At the end of the test, the total amount of Mo in the system would be found in the liquid $U_yZr_{1-y}O_{2\pm x}$ phase (**Figure II-74**).

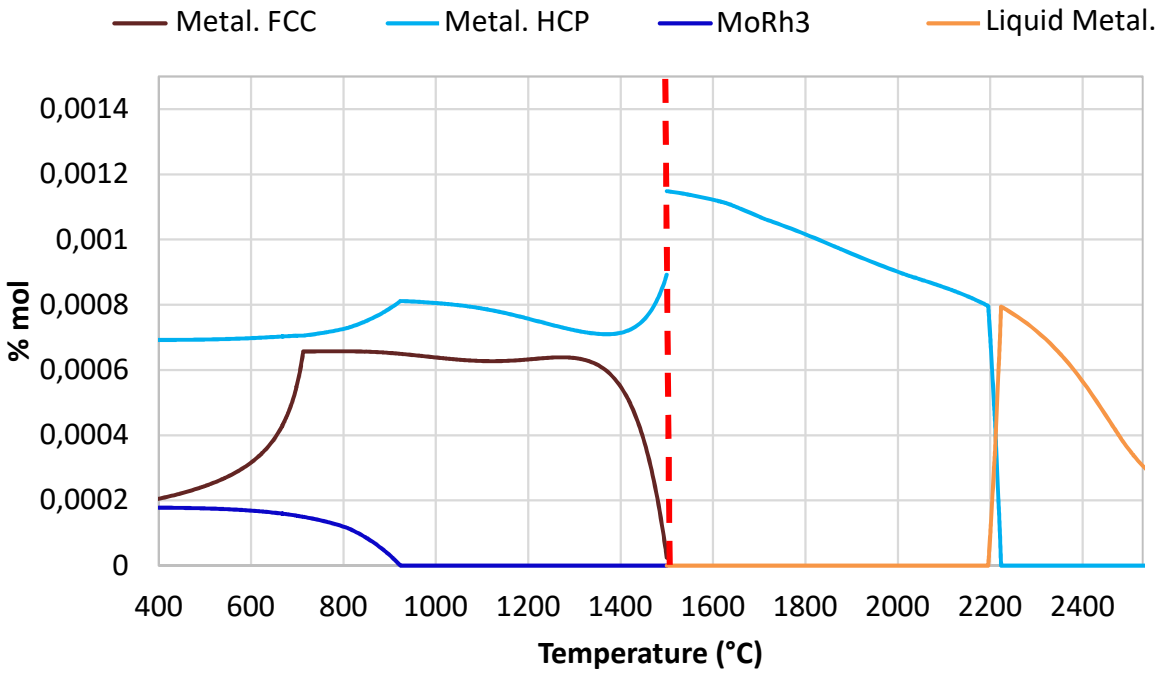

Figure II-73: Evolution of the metallic FP phases during the stages 2 and 3 of the VERDON-4 test, calculated using Thermo-Calc [7] coupled with the TAF-ID [8]

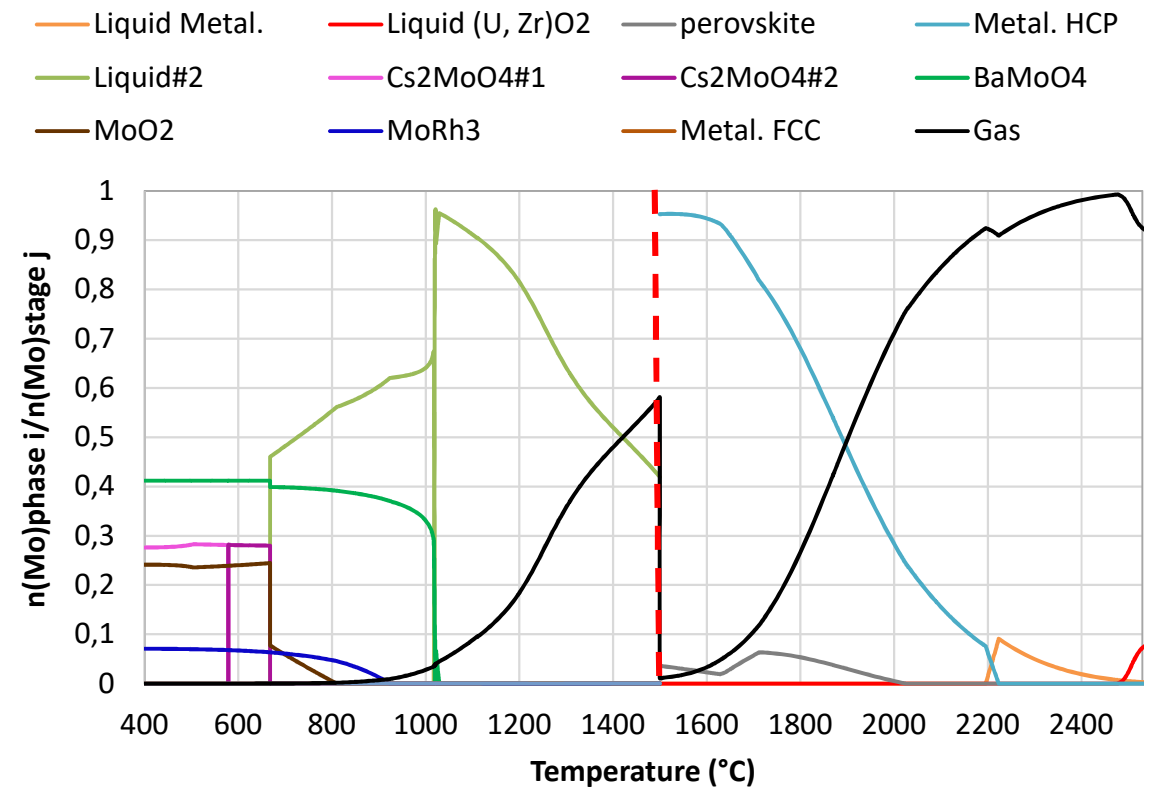

Figure II-74: Mo behavior during the stages 2 and 3 of the VERDON-4 test, calculated using Thermo-Calc [7] coupled with the TAF-ID [8]

II.3.3.3 Dissolved FP: special emphasis on Cs and Ba behavior

II.3.3.3.1 Chemical analyses

As shown in **Figure II-75**, the Zr and Ce contents are increasing respectively from 0.3 at% and 0.2 at% in the matrix to 0.8 at% and 0.4 at% in the Pu agglomerates, consistently with the observations made on the B05 sample.

However the amount of Ba varies between 0.1 and 0.2 at% in the whole sample. The quantitative profile performed along Line 5 (**Figure II-76**) indicates that the amount of Ba decreases between the porous matrix (around 0.1 at%) and the molten Zr-rich zone (0.04 at%).

Several precipitates containing both Ba and Ce can be observed at the interface between the Zr-rich area (reduce porosity zone) and the Zr-depleted one (porous matrix) as shown in **Figure II-77**. None of these precipitates has been observed at 1R.

Some of these precipitates containing also Pu and U have been identified in the porous matrix at 0R (**Figure II-78**) and thanks to the quantitative profiles. The isotopic distribution of Zr observed in **Figure II-79** is consistent with the fission creation ratios calculated by the CESAR code [13] (^{90}Zr < ^{91}Zr < ^{92}Zr < ^{93}Zr < ^{94}Zr < ^{96}Zr). It was thus produced by fission and not provided by the cladding as in the molten region of the fuel.

Some precipitates containing Ba, Cs and Ce and others containing only Ba or Cs are observed at 16 µm, 252 µm and 286 µm in **Figure II-76**. As for the V-3M sample, these precipitates could correspond to a rest of perovskite phase which is supposed to be decomposed at 2020°C (**Figure II-80**).

Some rare Cs precipitates or bubbles are detected. This indicates that almost all the Cs was volatilized.

Concerning Xe, rare bubbles containing up to 0.1 at% of Xe can be observed around 20 µm in **Figure II-76**, corresponding also to higher concentrations of Cs. The association between Xe and Cs probably means that Cs is located in the gas bubbles. The rest of the signal is inferior to the detection limit of EPMA meaning that Xe has been totally released from the fuel.

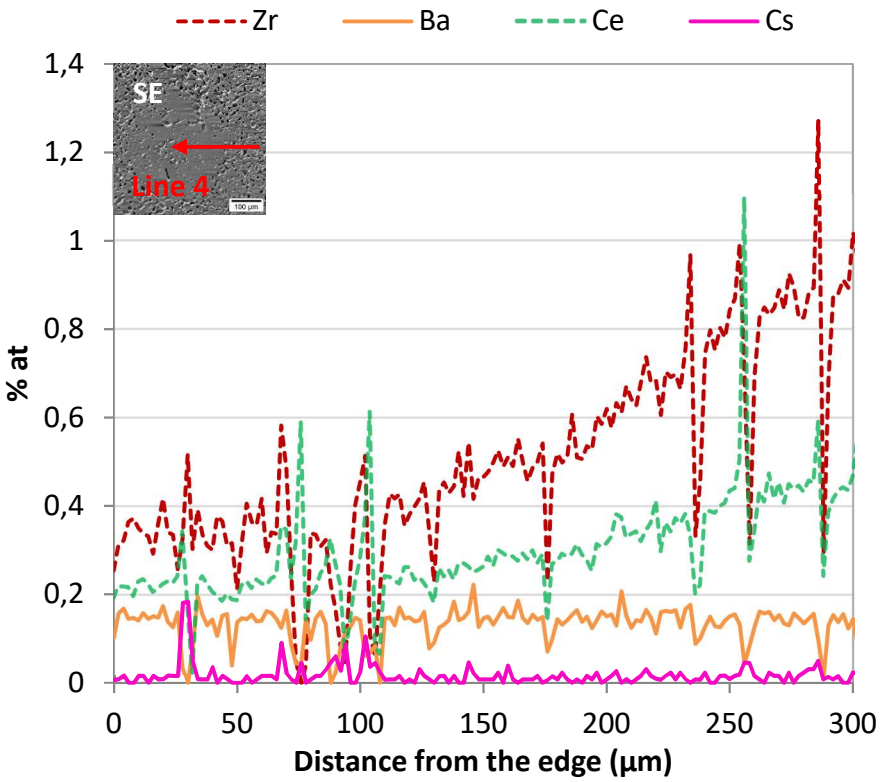

Figure II-75: Zr, Ba, Ce and Cs quantitative profiles along Line 4, 0.5R on sample V-4R

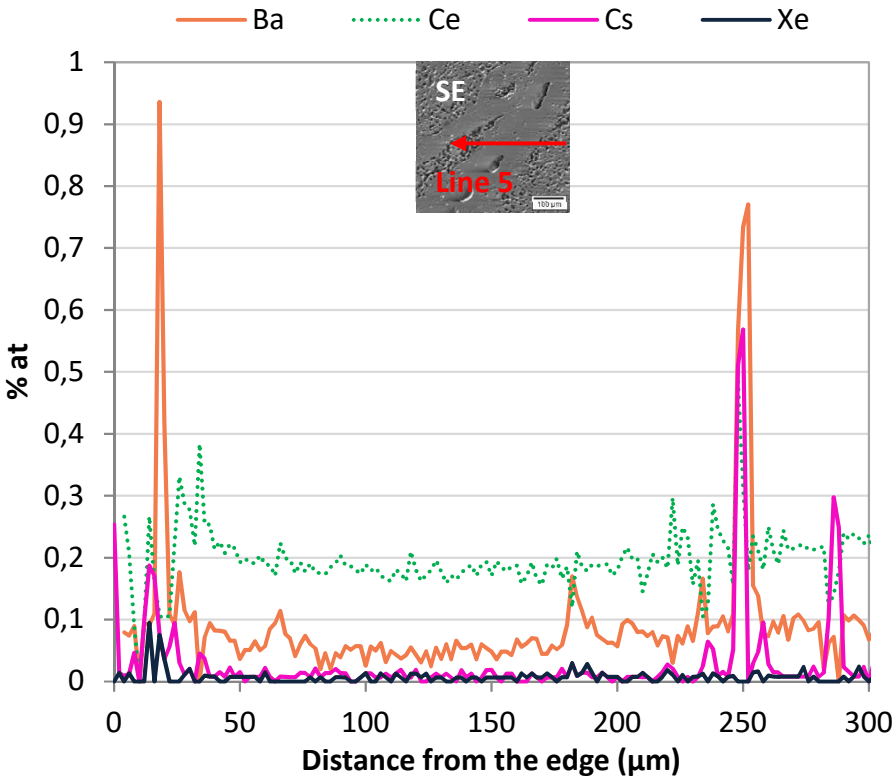

Figure II-76: Ba, Ce, Cs, Xe quantitative profiles along Line 5, 0.75R on sample V-4R

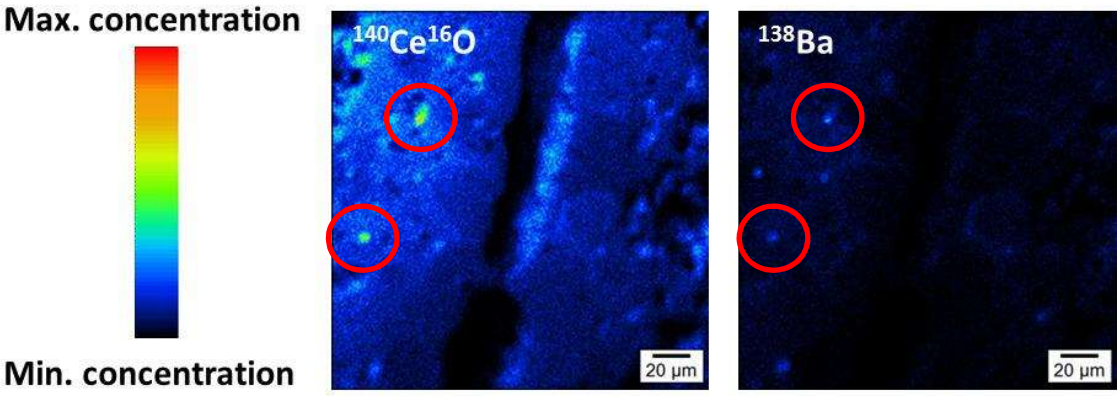

Figure II-77: SIMS isotope mapping performed at 138 and 156 amu, acquired at 0.75R on sample V-4R. The black zones correspond to regions of the sample poor in the isotope measured whereas red areas are rich in this isotope.

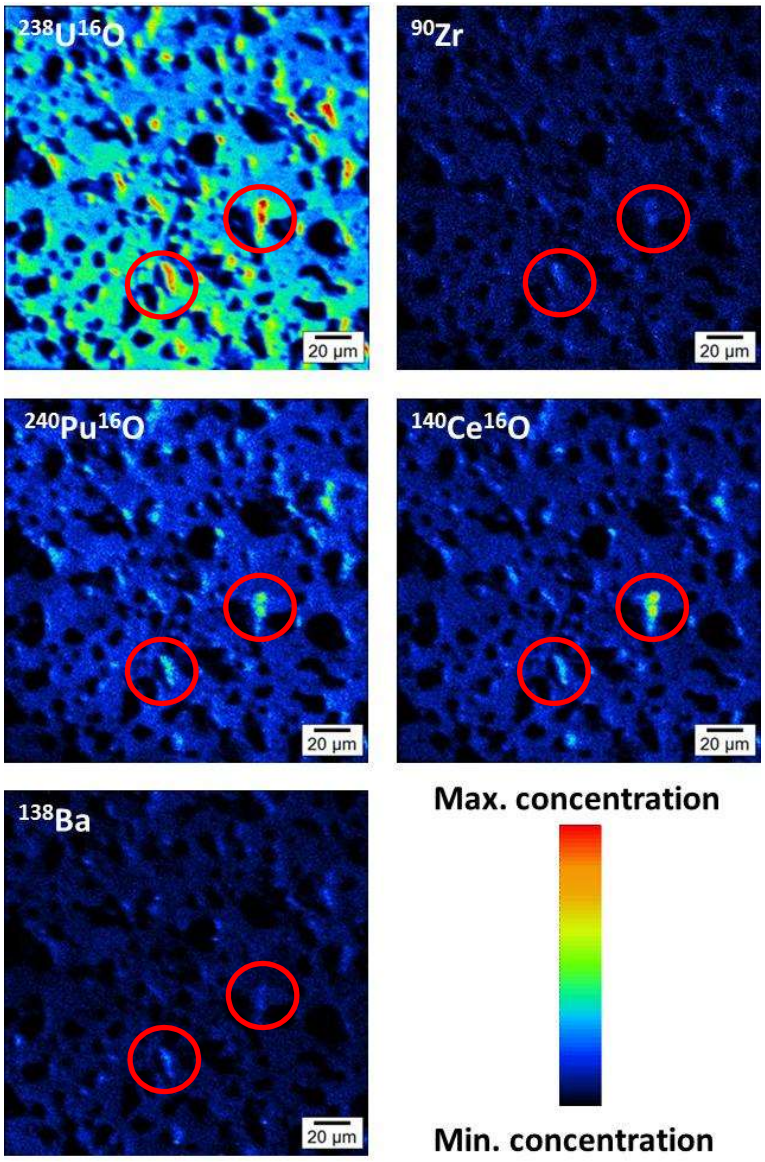

Figure II-78: SIMS isotope mapping performed at 254, 90, 256, 138 and 156 amu acquired at 0R on sample V-4R. The black zones correspond to regions of the sample poor in the isotope measured whereas red areas are rich in this isotope.

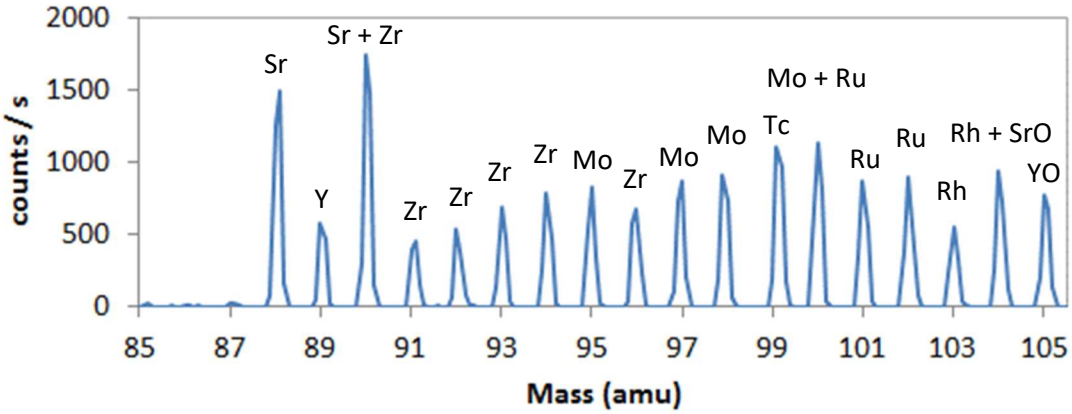

Figure II-79: Mass spectrum ranging from 85 to 105 amu acquired at 0R on sample V-4R, the peaks intensities are typical of Zr produced by fission

II.3.3.3.2 Thermodynamic calculations

The calculated evolution of the phases containing Ba and Cs is shown in **Figure II-80**. The oxygen potential of stages 2 and 3 have been calculated supposing thermodynamic equilibrium and by integration of the whole quantity of gas injected during the stage considered (**section II.2.2**). The transition between the two stages at 1500°C is thus discontinuous. An emphasis is made on the behavior of Mo in this part.

Initially, four phases are calculated to be present in the sample: CsI, MoO_2, Cs2MoO_4 and $BaMoO_4$.

- CsI is totally vaporized at 500°C leading to an increase of the Cs amount in the gas phase, as shown in **Figure II-81**.
- Cs_2MoO_4 melts around 680°C leading to the vaporization of Cs and Mo as Cs_2MoO_4, as shown in **Figure II-81**.
- BaMoO4 also melts in the same time. As soon as the phase transition from monoclinic to tetragonal ZrO_2 appears, part of $BaMoO_4$ is decomposed leading to Ba dissolution in the tetragonal ZrO_2 phase (**Figure II-82**) and MoO_2 vaporization (**Figure II-74**).

As shown in **Figure II-80**, at the beginning of stage 3, the perovskite phase containing Ba, Mo, Zr, Ce, Sr etc. is present. This could explain the presence of very rare precipitates containing Cs, Ba, Ce and Zr observed in the samples. This phase is calculated to disappear at 2050°C.

As shown in **Figure II-81**, Cs is totally vaporized at the beginning of the stage 3.

Concerning Ba, at the beginning of stage 3 (**Figure II-82**), half of it is found in the perovskite phase and the other half is dissolved in the tetragonal ZrO_2. Around 1650°C, Ba contained in the tetragonal ZrO_2 goes in the perovskite phase. At 2000°C, Ba the perovskite phase is vaporized and 1.4 % passes in the (U, Zr)O_2 phase. At the end of the sequence, gaseous Ba is condensed in the liquid (U, Zr)O_2. This was not observed experimentally (Ba amount decreased in the molten (U, Zr)O_2 phase). Above 2000°C, the perovskite phase is totally decomposed in ZrO_2 and gaseous BaO, which would have diffused through the cladding until melting happened. Ba would thus have been trapped in the liquid cladding external part that disappeared during sample preparation. An explanation could be that the Ba released before melting of the fuel was chemically trapped in the cladding, probably as $BaZrO_3$ (Perovskite phase in **Figure II-82**). This physical trapping effect of the cladding was already observed in [28], [29], [34].

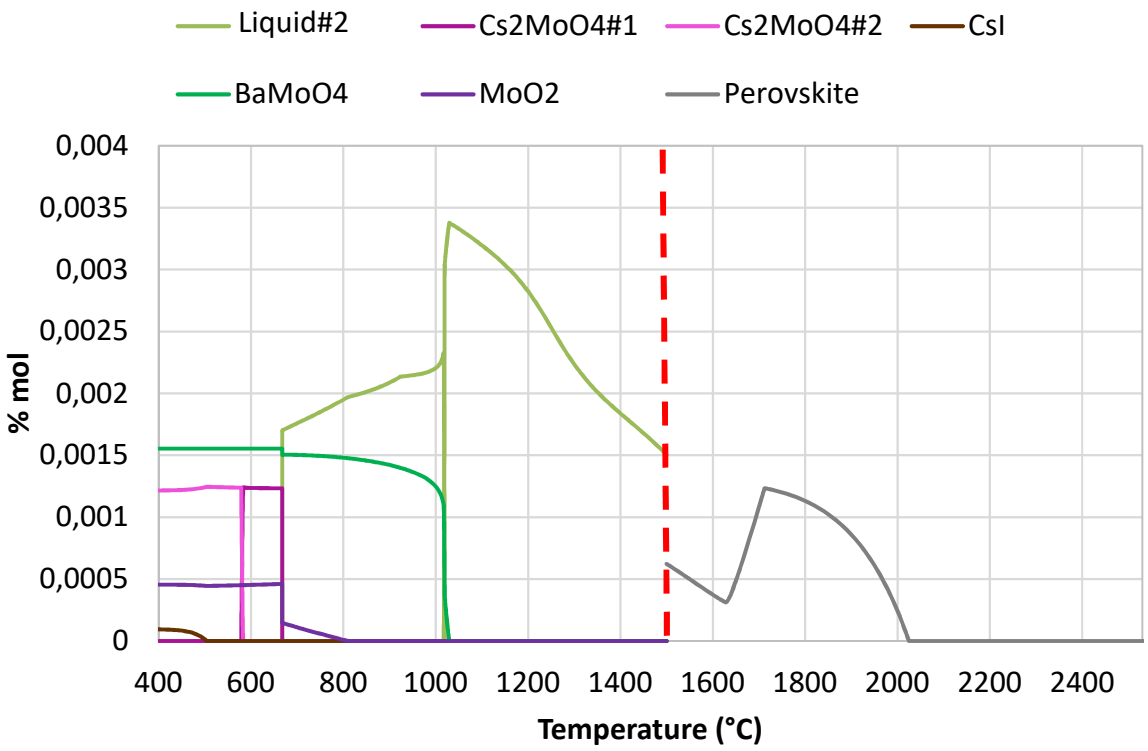

Figure II-80: Evolution of the oxide FP phases during the stages 2 and 3 of the VERDON-4 test, calculated using Thermo-Calc [7] coupled with the TAF-ID [8]

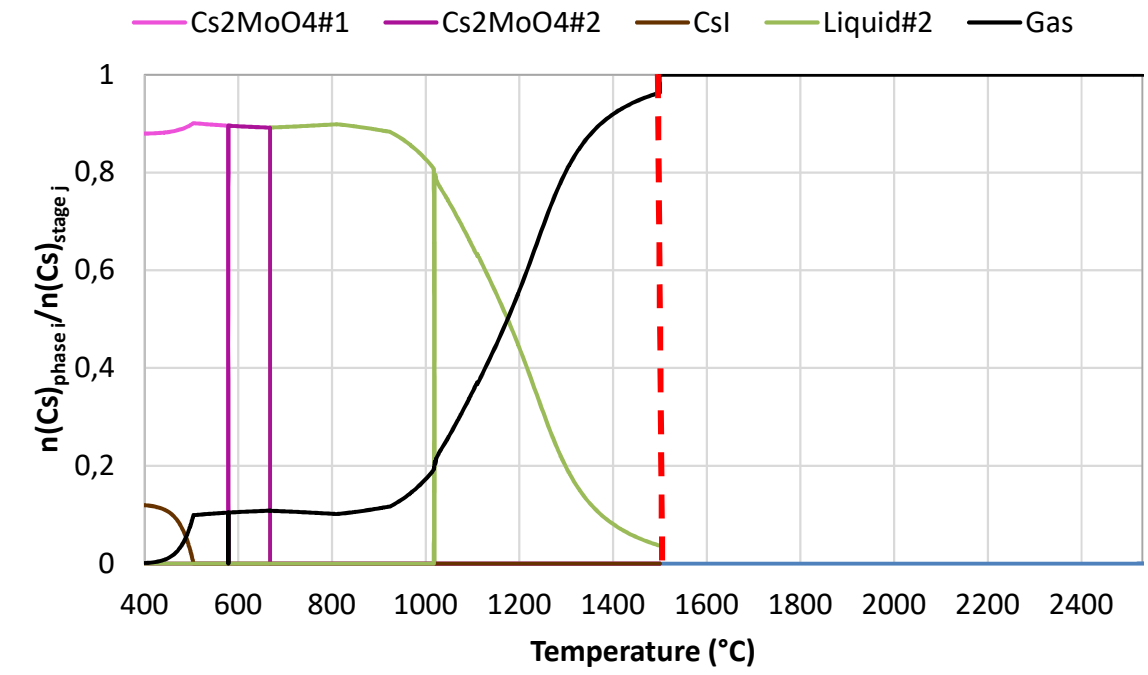

Figure II-81: Cs behavior during the stages 2 and 3 of the VERDON-4 test, calculated using Thermo-Calc [7] coupled with the TAF-ID [8]

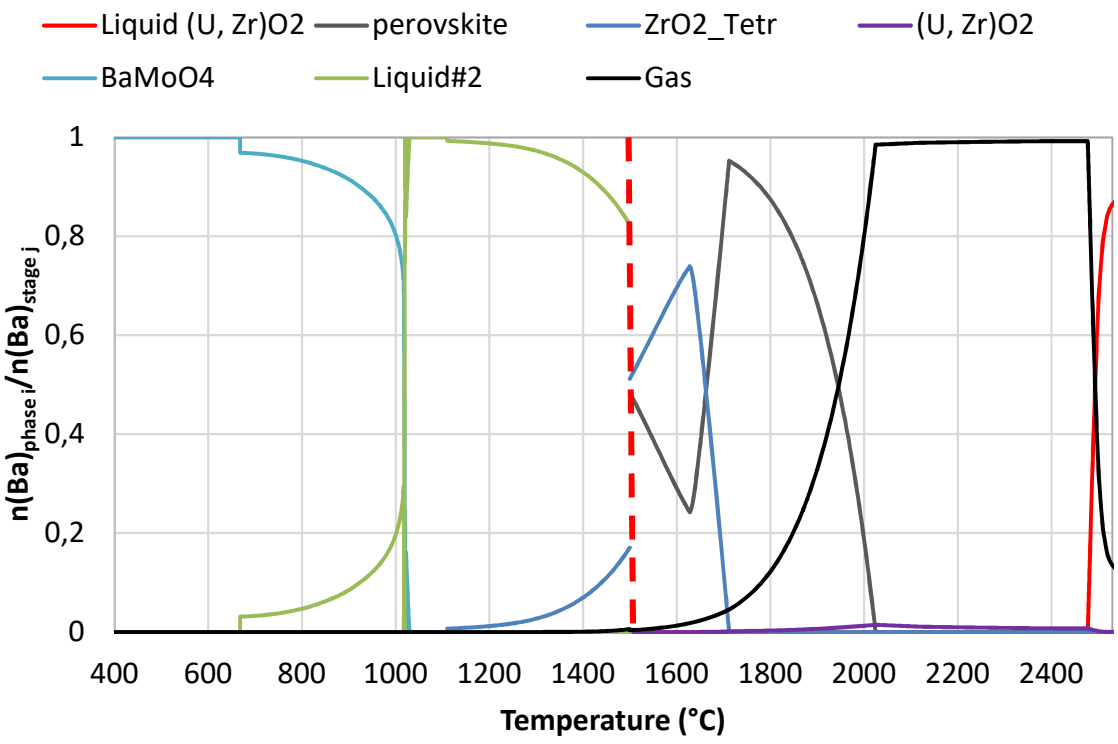

Figure II-82: Ba behavior during the stages 2 and 3 of the VERDON-4 test, calculated using Thermo-Calc [7] coupled with the TAF-ID [8]

II.3.3.4 Summary of the observations made in the VERDON-4 sample

A summary of the results obtained through experimental characterizations of the VERDON-4 sample and thermodynamic calculations is given in **Table II.3**.

Table II-3: Summary of the phases observed experimentally and calculated using Thermo-Calc [7] coupled with the TAF-ID [8] after the VERDON-4 test, and their main characteristics

	Experimentations	Calculations
Fuel-cladding interaction	Presence of a molten $U_yZr_{1-y}O_{2\pm x}$ phase ($0.43 \leq y \leq 0.50$) starting from the periphery of the pellet towards its center $1.50 \pm 0.10 \leq O/M \leq 1.60 \pm 0.10$	Presence of a molten $U_yZr_{1-y}O_{2\pm x}$ phase ($y = 0.43$) at 2530°C The formation of this phase is predicted to start at 2480°C $O/M \approx 2.03$
Metallic precipitates	Total amount of Mo measured in the sample is located in the metallic precipitates Two types of precipitates with $Mo/Ru \approx 1$ or 2 Very large precipitates observed in the periphery of the pellet and in the molten $U_yZr_{1-y}O_{2\pm x}$ phase Small precipitates in the rest of the sample mainly located in the Pu agglomerates	Total amount of condensed Mo is located in the molten $U_yZr_{1-y}O_{2\pm x}$ phase at 2530°C Melting of the metallic inclusion predicted at 2200°C
Dissolved phases (Ba and Cs)	Ba homogeneously distributed all over the sample, its concentration decreases in the molten $U_yZr_{1-y}O_{2\pm x}$ phase Very few Cs bubbles observed	Ba located in the $U_yZr_{1-y}O_{2\pm x}$ phase Total volatilization of Cs predicted

III.3.3.4.1 Fuel-cladding interaction

The thermodynamic calculations performed in this part enable a global understanding of the local fuel-cladding interaction phenomenon that takes place in the fuel pellet during the VERDON-4 sample. This interaction took place at the periphery of the pellet and led to the melting of a $U_yZr_{1-y}O_{2\pm x}$ phase, which penetrated through the cracks of the fuel dissolving it on its way to the center of the pellet. This phase was predicted to extend all over the pellet in the thermodynamic calculations. As already explained in **section III.3.2.4**, this is due to the hypotheses made in the calculations:

- All the initial input species are mixed and considered as a homogeneous mixture composed of (U, Pu)O_2, Zr and FP. Thus, the heterogeneity of the initial fuel sample (Pu agglomerates, UO_2 matrix, coating phase or cladding at the periphery) is not taken into account.
- Thermodynamic equilibrium is supposed.

According to thermodynamic, the melting of the $U_yZr_{1-y}O_{2\pm x}$ phase would have taken place at 2480°C in the case of VERDON-4 whereas it was predicted at 2420°C in VERDON-3. It thus appears that the atmosphere of the test does not seem to strongly impact the melting temperature of the fuel.

The composition of the molten $U_yZr_{1-y}O_{2\pm x}$ phase observed in the periphery of the VERDON-4 sample is in good agreement with the calculations. However, the O/M measured in the molten zones by EPMA is lower than that predicted by the calculations, which may be related to the uncertainty linked to O measurement by EPMA.

III.3.3.4.2 Metallic precipitates

The experimental composition of the metallic precipitates after the VERDON-4 test is not in agreement with the thermodynamic calculations. Indeed, the amount of Mo in the calculations has been highly underestimated (30 to 40 at% of Mo has been found experimentally in the precipitates compared to only 4.2 at% of Mo condensed in the system in the calculations). Moreover, at 2530°C, the total amount of Mo is found in the liquid $U_yZr_{1-y}O_{2\pm x}$ phase in the calculations whereas it is found in the precipitates experimentally.

Melting of these precipitates is predicted at 2200°C by thermodynamics. It is highly consistent with the presence of large rounded shaped precipitates in the molten zones of the VERDON-4 sample. It is inferred from these observations that melting of the metallic precipitates occurred before melting of the (U, Zr)O_2 mixed oxide. Once these precipitates were in contact with the molten $U_yZr_{1-y}O_{2\pm x}$ phase, they migrated more easily towards the periphery of the sample and coalesced.

III.3.3.4.3 Cs and Ba behavior

The experimental observations concerning Cs are in agreement with thermodynamic calculations, as Cs has been released from the sample during the test. Very few Cs is indeed observed in the VERDON-3 sample.

Concerning Ba, its concentration was measured to be constant all over the sample except in the fuel-cladding interaction zone, where it decreased. Some precipitates containing Ba have been found in the periphery of the molten areas of the fuel. This is not in agreement with the behavior of Ba predicted by thermodynamics. Indeed, Ba has been calculated to be located in the $U_yZr_{1-y}O_{2\pm x}$ phase. In this case again, this can due to the hypotheses of thermodynamic equilibrium and to the homogeneous mixture of (U, Pu)O_2, Zr and FP supposed in the calculations. However, Ba could also have returned to the (U, Pu)O_2 phase during the cooling stage of the VERDON-4 test.

Globally, the fuel heterogeneity has been conserved after the VERDON-4 test similarly to the as-irradiated father rod:

- **The fuel-cladding interaction zone which extended on 5 µm in the father rod melted and progressed through the cracks of the fuel sample during the VERDON-4 test.**
- **The Pu concentration has slightly decreased in the observed agglomerates down to 4.5 at% instead of 5 at% in the father rod. Reversely, it has increased up to 1.6 at% in the rest of the sample compared to 0.5 at % in the UO_2 matrix of the father rod and 1.3 at% in the coating phase.**
- **The metallic precipitates have been observed to be mainly located in the Pu agglomerates, consistently with their location in the father rod. Two kinds of precipitates with a Ru/Mo ratio of 1 or 2 have been observed randomly distributed in the samples. They were also observed in the father rod in the Pu agglomerate of the restructured area of the pellet with a Ru/Mo = 1.8 and in the rest of the sample with a Ru/Mo ≈ 1.**
- **The concentrations of other FP such as Ba have also been measured to be constant all over the VERDON-4 sample, whereas their concentrations were clearly higher in the Pu agglomerates in the father rod.**

II.4 CONCLUSION

The results of characterizations performed on irradiated fuels before and after the VERDON-3 and 4 tests have been detailed in this chapter. Three samples were extracted from the same PWR MOX father rod. One was kept as irradiated and the other two were submitted to a VERDON thermal sequence up to 2300°C in oxidizing conditions (VERDON-3) or 2530°C in reducing conditions (VERDON-4). A summary of the main experimental observations is given in **Table II-4**. The effect of the oxygen potential on the fuel and FP behavior was highlighted:

- Higher Pu mobility, and more generally of all the elements composing the fuel pellet, has been observed in oxidizing conditions consistently with [19], [20].

- An interaction between the fuel and the cladding occurred in both types of conditions by interdiffusion mainly between U and Zr. This phenomenon led to the formation of a $U_yZr_{1-y}O_{2\pm x}$ cubic phase at the periphery of the fuel pellet which melted in reducing conditions, penetrating through the cracks of the sample and dissolving the fuel matrix. No liquid was formed in oxidizing conditions despite a large fuel-cladding interaction zone. However, this is not surprising as the final VERDON-3 temperature was 230°C lower than in the case of the VERDON-4 test. The observations also showed that Pu did not play a major role in the melting of the fuel as hardly more than 2 at% of Pu was found in the fuel-cladding interaction zone and in the $U_yZr_{1-y}O_{2\pm x}$ liquid phase in both tests.

- Enhanced migration of the metallic precipitates was noted in oxidizing condition. No more Mo and Pd could be found in the sample after the VERDON-3 test. The metallic precipitates were only composed of Ru, Tc and Rh.

- Melting and coalescence of metallic precipitates occurred in reducing conditions of the VERDON-4 test most probably due to the higher final temperature compared to VERDON-3. The mobility of these precipitates may have then been encouraged by the melting of the $U_yZr_{1-y}O_{2\pm x}$ phase leading to the formation of very large precipitates in the edges of the pellets. Contrary to the VERDON-3 sample, Mo remaining in the sample after the VERDON-4 test was contained in the metallic precipitates along with Ru, Tc and Rh.
  The semi-volatile behavior of Mo which is known to be released in very high quantity in oxidizing atmosphere [35] was thus confirmed. Pd was completely released during both tests which indicates that Pd release does not depend on the atmosphere of the test. Thus, it could be classified in volatile FP instead of semi-volatile elements as was originally proposed in [26].

- Almost no Cs was observed in the samples after the VERDON-3 and 4 tests which is consistent with its volatile behavior [26], [35]. This was again well described in the two FP speciation mechanisms.

- Ba is known to be released in high quantity in reducing atmosphere [26], [28], [35]–[37]. However, Ba behavior was hard to assess in the case of the VERDON-3 and 4 tests. Indeed, the remaining amount of Ba dissolved in the fuel after the two tests is almost the same and

well inferior to its initial concentration in the B05 sample. This may indicate that important release took place in both cases.

Some rare precipitates containing Ba, Cs, Ce and sometimes Zr, Pu and U were observed in the samples treated in both oxidizing and reducing conditions. They may attest for the presence of the perovskite phase at some point of the tests.

Table II-4: Summary of the phases observed experimentally in the B05, VERDON-3 and VERDON-4 samples, and their main characteristics.

	B05 (father rod) **As-irradiated**	**VERDON-3** **2300°C, oxidizing**	**VERDON-4** **2530°C reducing**
Fuel composition	Pu agglomerates (5 at% Pu) Coating phase (3 at% Pu) UO_2 matrix (0.5 at% Pu) Restructured area from 0.4 to 1R Global O/M = 2.0 ± 0.1	Pu agglomerates (1.8 at% Pu) UO_2 matrix (1.3 at% Pu) Pu agglomerates densified and visible in the whole pellet Global O/M = 2.1 ± 0.4	Pu agglomerates (4.5 at% Pu) UO_2 matrix (1.6 at% Pu) Pu agglomerates densified and visible from 0.4 to 1R Global O/M = 1.6 ± 0.3
Fuel-cladding interaction	Observation of a $U_yZr_{1-y}O_{2\pm x}$ phase ($0 \leq y \leq 1$) on 5 µm at the pellet-cladding interface	Presence of a $U_yZr_{1-y}O_{2\pm x}$ phase on 70 µm at the interface of the fuel and cladding O/M ≈ 1.80 ± 0.20 No melting of the $U_yZr_{1-y}O_{2\pm x}$ phase observed at 2300°C	Presence of a molten $U_yZr_{1-y}O_{2\pm x}$ phase ($0.43 \leq y \leq 0.50$) starting from the periphery of the pellet towards its center $1.50 \pm 0.10 \leq O/M \leq 1.60 \pm 0.10$
Metallic precipitates	Metallic precipitates containing Mo-Ru-Rh-Pd-Tc observed mainly in the Pu agglomerates In the center of the pellet Ru/Mo = 0.9 in the precipitates In the Pu agglomerates of the restructured area Ru/Mo = 1.8 and in the UO_2 matrix Ru/Mo = 0.75	No Mo observed in the sample Ru/Rh = 3.5 ± 0.1 Rounded shaped precipitates observed all over the sample	Total amount of Mo measured in the sample is located in the metallic precipitates Two types of precipitates with Mo/Ru ≈ 1 or 2 Very large precipitates observed in the periphery of the pellet and in the molten $U_yZr_{1-y}O_{2\pm x}$ phase Small precipitates in the rest of the sample mainly located in the Pu agglomerates
Dissolved phases (Ba and Cs)	No particular association between Xe and Cs Cs and Ba contents increase in the Pu agglomerates in the same way as Ce and Zr	Few Cs bubbles observed (associated with Xe) Ba homogeneously distributed all over the sample, its concentration decrease in the $U_yZr_{1-y}O_{2\pm x}$ phase	Few Cs bubbles observed (associated with Xe) Ba homogeneously distributed all over the sample, its concentration decrease in the molten $U_yZr_{1-y}O_{2\pm x}$ phase

Thermodynamic calculations using the ThermoCalc software coupled with the TAF-ID were realized to interpret the chemical evolution of the different phases observed in the samples after the VERDON-3 and 4 sequences.

Some discrepancies between the calculations and experimental observations were found:

- The absence of Mo in the metallic precipitates calculated at the end of the test conducted in reducing conditions is in contradiction with experimental observations.
- Under both reducing and oxidizing conditions, Ba was calculated to be preferentially dissolved in the $U_yZr_{1-y}O_{2\pm x}$ phase which was not supported by the characterizations.

These differences may be explained by the initial hypotheses made in the calculations. Indeed, the fuel was considered to be a homogeneous mixture of (U, Pu)O_2, Zr and FP in the calculations and thermodynamic equilibrium was supposed. Thus, no kinetics effects such as the time needed for the elements to diffuse are taken into account. Moreover, the observations were performed after cooling down the sample. Phase separation could thus have occurred, as it is the case in the fuel-cladding interaction zone of the VERDON-3 sample.

The global approach adopted to perform these calculations, considering the whole irradiated fuel-FP-cladding systems, thus showed some limitations. Indeed, they enabled to better understand the fuel-cladding interaction phenomena as well as the global behavior of metallic precipitates (which do not interact with the fuel during the test) but the oxide phase behavior could not be reproduced in the fuel.

To improve their representativeness, these calculations should be made at a local scale. Thus, different regions of the fuel should be considered:

- *The evolution of the Pu-agglomerates in the case of MOX fuel, in the center and in the periphery of the pellets.*
- *The fuel matrix (mainly UO_2).*
- *The fuel-cladding interaction zone.*

Finally, the calculations coupled to the experimental data led to the proposition of a mechanism for FP speciation adapted to each test. The two mechanisms initially proposed in the literature were thus modified and is presented in **Figure II-83**. As the VERDON-3 and 4 tests were performed in similar conditions up to 2000°C, the chemical state of FP in the four first steps are identical. In the last two steps, the green arrows correspond to the evolution of FP in both oxidizing and reducing conditions, the red arrows correspond to FP chemical evolution in oxidizing conditions (i.e. during the VERDON-3 test) and the blue arrows in reducing conditions (i.e. during the VERDON-4 test). The purple boxes correspond to the phases observed experimentally; the orange ones correspond to phases that could not be clearly identified in the fuel samples. The blue boxes correspond to the steps resulting from MFPR calculations with adjustments made through Thermocalc coupled with the TAF-ID.

According to these mechanisms:

- Mo should be found at the initial state whether in metallic precipitates along with Ru, Pd, Rh and Tc or under MoO_2. The observations performed on the B05 sample showed that Mo is indeed present in the white inclusions. It was also observed to be “dissolved” preferentially in the Pu-rich regions of the sample, where the burn-up and temperature were higher than in the other parts of the sample. *Nevertheless, further characterizations, using TEM for example, would be necessary to conclude on the state of Mo outside the metallic precipitates.*

In the final stage, Mo should be totally released in oxidizing conditions whereas it is supposed to remain in the metallic precipitates under reducing conditions. As stated above, this was validated experimentally in the VERDON-3 and 4 samples.

- Ba should be found as BaO dissolved in the fuel, Zr as ZrO_2, and Cs should be found as uranate. The concentrations of Ba and Zr were indeed observed to increase in the Pu-agglomerates in the B05 sample. The same trend was observed for Cs. This indicates that these three FP may be dissolved in the agglomerates probably as oxides (like ZrO_2 or BaO). However, very locally, some submicronic oxide precipitates such as BaO, Cs_2O or even Cs_2UO_4 could have been formed. Ba and Zr speciation could not be confirmed experimentally as it would require to lower the scale of observations.
  In the final stage of the mechanism, Cs was totally released which is consistent with experimental observations. Ba and Zr should be found respectively as BaO and ZrO_2 dissolved in the fuel. These two elements were indeed observed dissolved in the fuel after the VERDON-3 and 4 tests but, again, their exact speciation could no be confirmed experimentally.

Globally, the post-tests analyses performed on the B05, V-3M and V-4R samples were consistent with the initial and final stages of the mechanism proposed in the literature for FP speciation. Nevertheless, some structural data about the phases observed in irradiated fuel are still missing and the validity of the intermediate steps of this mechanism could not be assessed experimentally in this work axis.

In order to fill these gaps, model materials called SIMFuels are used. These materials are made of depleted fresh UO_2 mixed with FP surrogates and sintered at high temperature. Given their low radioactivity, their transportation and handling are easier. This enables the access to a wide range of cutting edge characterization techniques towards FP speciation which are not yet available on irradiated fuels, such as X-ray Absorption Spectroscopy. The next chapter presents the fabrication process used to produce the SIMFuels, the thermal treatments performed and the results of characterizations obtained.

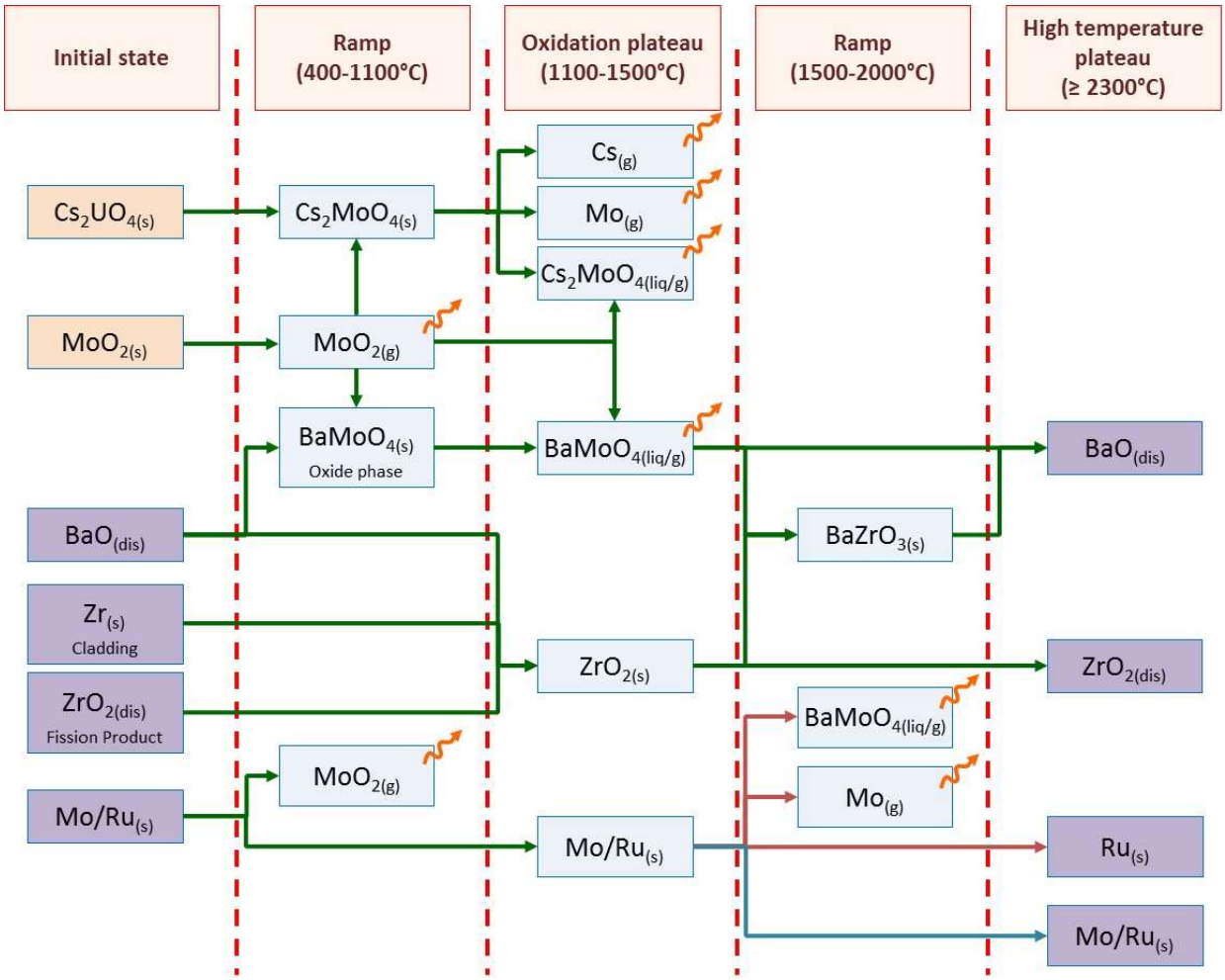

Figure II-83: FP speciation mechanism proposed for the VERDON-3 (oxidizing conditions) and 4 tests (reducing conditions), adapted from [3].

II.5 REFERENCES

[1] G. Nicaise, “Note Technique DPAM/SEMIC n° 2004/37 - Interprétation du relâchement de Cs, Mo, Ba, I, Ru dans les essais VERCORS, VERCORS HT et VERCORS RT.” 2004.

[2] G. Nicaise, R. Dubourg, and P. Taylor, “Analyse d’essais de séquences accidentales et interprétation du relâchement des produits de fission : interdépendance de relâchement du Cs, du Mo, et du Ba,” presented at the 11th Symposium on Thermodynamics of Nuclear Materials, Karlsruhe, Germany, 2004.

[3] E. Geiger, “Study of fission products (Cs, Ba, Mo, Ru) behaviour in irradiated and simulated nuclear fuels during severe accidents using X-ray absorption spectroscopy, SIMS and EPMA,” PhD Thesis, Paris-Saclay, CEA Cadarache, 2016.

[4] K. Hanifi, “Examens du combustible MOX-E MIMAS ADU/TU2 MELOX (campagne FM07) irradié dans CHINON B3,” CEA Cadarache, Note technique NT SA3C/L2EC 2009-021-0, 2009.

[5] K. Hanifi, “Examen Microsonde et SIMS du combustible MOX-E MIMAS ADU/TU2 MELOX (campagne FM07 - Assemblage FXP2CC-crayon B05) irradié 4 cycles dans CHINON B3,” CEA Cadarache, Note technique NT SA3C/LEMCI 10-009-0, 2010.

[6] A. Gallais-During *et al.*, “Performance and first results of fission product release and transport provided by the VERDON facility,” *Nucl. Eng. Des.*, vol. 277, pp. 117–123, 2014.

[7] J.-O. Andersson, T. Helander, L. Höglund, P. Shi, and B. Sundman, “Thermo-Calc & DICTRA, computational tools for materials science,” *Calphad*, vol. 26, no. 2, pp. 273–312, 2002.

[8] “OECD NEA/NSC: Thermodynamics of Advanced Fuels – International Database (TAF-ID) - working version of january 2018.” [Online]. Available: https://www.oecd-nea.org/science/taf-id/. [Accessed: 25-Aug-2016].

[9] J. Spino and D. Papaioannou, “Lattice parameter changes associated with the rim-structure formation in high burn-up UO2 fuels by micro X-ray diffraction,” *J. Nucl. Mater.*, vol. 281, no. 2–3, pp. 146–162, 2000.

[10] J. Noirot, L. Desgranges, and J. Lamontagne, “Detailed characterisations of high burn-up structures in oxide fuels,” *J. Nucl. Mater.*, vol. 372, no. 2–3, pp. 318–339, 2008.

[11] H. Kleykamp, “Post-irradiation studies on LWR-MOX fuel fabricated by the optimized co-milling process,” *J. Nucl. Mater.*, vol. 324, no. 2–3, pp. 198–202, 2004.

[12] C. Ciszak, “Etude de l’accrochage pastille/gaine des crayons combustibles des réacteurs à eau pressurisée,” thesis, Bourgogne Franche-Comté, 2017.

[13] “Cesar 5.1, developed by DEN/DER/SPRC,” CEA Cadarache.

[14] H. Kleykamp, “The solubility of selected fission products in UO2 and (U, Pu)O2,” *J. Nucl. Mater.*, vol. 206, no. 1, pp. 82–86, 1993.

[15] G. Giacchetti and C. Sari, “Behavior of Molybdenum in Mixed-Oxide Fuel,” *Nucl. Technol.*, vol. 31, no. 1, pp. 62–69, Oct. 1976.

[16] H. Kleykamp, “The chemical state of the fission products in oxide fuels,” *J. Nucl. Mater.*, vol. 131, no. 2–3, pp. 221–246, 1985.

[17] B. J. Lewis, W. T. Thompson, and F. C. Iglesias, “2.20 - Fission Product Chemistry in Oxide Fuels,” in *Comprehensive Nuclear Materials*, R. J. M. Konings, Ed. Oxford: Elsevier, 2012, pp. 515–546.

[18] C. Sari, C. T. Walker, and G. Schumacher, “Solubility and migration of fission product barium in oxide fuel,” *J. Nucl. Mater.*, vol. 79, no. 1, pp. 255–259, Jan. 1979.

[19] J.-P. Hiernaut *et al.*, “Fission product release and microstructure changes during laboratory annealing of a very high burn-up fuel specimen,” *J. Nucl. Mater.*, vol. 377, no. 2, pp. 313–324, Jul. 2008.

[20] J.-Y. Colle *et al.*, “Fission product release and microstructure changes of irradiated MOX fuel at high temperatures,” *J. Nucl. Mater.*, vol. 442, no. 1–3, pp. 330–340, Nov. 2013.

[21] D. R. O’boyle, F. L. Brown, and J. E. Sanecki, “Solid fission product behavior in uranium-plutonium oxide fuel irradiated in a fast neutron flux,” *J. Nucl. Mater.*, vol. 29, no. 1, pp. 27–42, Jan. 1969.

[22] J. P. Guha and D. Kolar, “Phase equilibria in the system BaO-CeO2,” *J. Mater. Sci.*, vol. 6, no. 9, pp. 1174–1177.
[23] B. Adroguer *et al.*, “Core loss during a severe accident (COLOSS),” *Nucl. Eng. Des.*, vol. 235, no. 2, pp. 173–198, Feb. 2005.
[24] J. P. Leveque, B. Andre, G. Ducros, G. Le Marois, and G. Lhiaubet, “The HEVA experimental program,” *Nucl. Technol.*, vol. 108, no. 1, pp. 33–44, 1994.
[25] G. Ducros, P. P. Malgouyres, M. Kissane, D. Boulaud, and M. Durin, “Fission product release under severe accidental conditions: general presentation of the program and synthesis of VERCORS 1–6 results,” *Nucl. Eng. Des.*, vol. 208, no. 2, pp. 191–203, 2001.
[26] Y. Pontillon, G. Ducros, and P. P. Malgouyres, “Behaviour of fission products under severe PWR accident conditions VERCORS experimental programme—Part 1: General description of the programme,” *Nucl. Eng. Des.*, vol. 240, no. 7, pp. 1843–1852, 2010.
[27] Y. Pontillon *et al.*, “Lessons learnt from VERCORS tests.: Study of the active role played by UO2–ZrO2–FP interactions on irradiated fuel collapse temperature,” *J. Nucl. Mater.*, vol. 344, no. 1–3, pp. 265–273, 2005.
[28] Y. Pontillon *et al.*, “Fission products and nuclear fuel behaviour under severe accident conditions part 1: Main lessons learnt from the first VERDON test,” *J. Nucl. Mater.*, vol. 495, no. Supplement C, pp. 363–384, 2017.
[29] E. Geiger *et al.*, “Fission products and nuclear fuel behaviour under severe accident conditions part 2: Fuel behaviour in the VERDON-1 sample,” *J. Nucl. Mater.*, vol. 495, no. Supplement C, pp. 49–57, 2017.
[30] B. Clément *et al.*, “LWR severe accident simulation: synthesis of the results and interpretation of the first Phebus FP experiment FPT0,” *Nucl. Eng. Des.*, vol. 226, no. 1, pp. 5–82, Nov. 2003.
[31] L. E. Herranz, M. Vela-García, J. Fontanet, and C. L. del Prá, “Experimental interpretation and code validation based on the PHEBUS-FP programme: Lessons learnt from the analysis of the containment scenario of FPT1 and FPT2 tests,” *Nucl. Eng. Des.*, vol. 237, no. 23, pp. 2210–2218, Dec. 2007.
[32] B. Clément and R. Zeyen, “The objectives of the Phébus FP experimental programme and main findings,” *Ann. Nucl. Energy*, vol. 61, pp. 4–10, Nov. 2013.
[33] P. Piluso, G. Trillon, and C. Journeau, “The UO2–ZrO2 system at high temperature (T > 2000 K): importance of the meta-stable phases under severe accident conditions,” *J. Nucl. Mater.*, vol. 344, no. 1–3, pp. 259–264, 2005.
[34] R. Dubourg and P. Taylor, “A qualitative comparison of barium behaviour in the PHEBUS FPT0 test and analytical tests,” *J. Nucl. Mater.*, vol. 294, no. 1, pp. 32–38, Apr. 2001.
[35] Y. Pontillon and G. Ducros, “Behaviour of fission products under severe PWR accident conditions: The VERCORS experimental programme—Part 2: Release and transport of fission gases and volatile fission products,” *Nucl. Eng. Des.*, vol. 240, no. 7, pp. 1853–1866, 2010.
[36] Z. Lui, D. S. Cox, R. S. Dickson, and P. Elder, “A summary of CRL fission product release measurements from UO2 samples during post-irradiation annealing (1983-1992),” COG-92-377, 1994.
[37] R. A. Lorenz and M. F. Osborne, “A summary of ORNL fission product release tests with recommended release rates and diffusion coefficients,” Nuclear Regulatory Commission, Oak Ridge National Lab., NUREG/CR--6261, 1995.

Chapter III:

STUDY OF SIMULATED FUELS TREATED IN INTERMEDIATE CONDITIONS OF A NUCLEAR SEVERE ACCIDENT

TABLE OF CONTENT

III.1 INTRODUCTION

The objective of this chapter is to provide experimental data on FP behavior in intermediate stages of a nuclear severe accident. More precisely, the effect of the oxygen potential on Mo and Ba speciation is investigated in a temperature range corresponding to the intermediary steps of a VERDON test, as described in **section I.4.1.4.2**.

To this end, thermal treatments are performed under controlled temperature and oxygen potential conditions on simulated high burn-up UO_2 fuels, called SIMFuels. These materials are composed of a powder mixture between UO_2 and several oxides used as FP surrogates, sintered under reducing atmosphere at high temperature. As proven in the study of Geiger [1], SIMFuel samples are powerful tools to study FP speciation in severe accident conditions. Indeed, the FP chemical behavior in these materials is representative of the one observed in irradiated fuels. Due to their lower radioactivity compared to irradiated fuels, they are easier to handle and enable to perform characterizations in several facilities such as synchrotron radiation ones.

The experimental method adopted in this work axis lies on the synthesis and detailed characterizations of SIMFuel samples. OM and SEM observations enabled to study the microstructure of the samples. Semi-quantitative EDX analyses and X-ray Absorption Near Edge Spectroscopy (XANES) analyses, carried thanks to synchrotron radiation facilities, enabled identifying precisely the phases formed by FP in the SIMFuel samples. XRD analyses were also performed.

Thermodynamic calculations helped determining the temperature and oxygen potential conditions of the different thermal treatments in order to observed chemical evolution in the phases containing Mo and Ba. Detailed post-tests characterizations were carried on and the results were compared to the as-sintered sample so as to conclude on the effect of oxygen potential on Mo and Ba behavior.

Finally, the results obtained were integrated to the corresponding steps of the mechanisms proposed for the VERDON-3 and 4 tests at the end of the previous chapter.

III.2 MATERIALS AND METHODS

III.2.1 Starting materials

The samples were synthesized with depleted UO_2 from batch TU2-792 (Areva NC) produced through wet route. The initial average stoichiometry of the powder was 2.20 (mixture of mainly $UO_{2.01}$ and U_4O_9). This powder is made of submicronic particles of approximately 150 to 300 nm in diameter which form agglomerates of 10 to 50 µm as shown in **Figure III-1**.

Eleven additives were used to simulate the major FP created in irradiated fuels except volatile FP. They were mainly added under oxide form or a carbonate form in the case of Ba. Commercial powders provided by different suppliers were used as received. Their characteristics are summarized in **Table III-1**. The Equivalent Circle Diameter (ECD) of the particles composing each type of powders was determined thanks to SEM-SE observations and image analysis (see **Appendix 2.1**).

Table III-1: Description of the additives used to synthesize the SIMFuel samples. The mean particles ECD were determined from 10 measurements.

Additives	**$BaCO_3$**	**CeO_2**	**La_2O_3**	**MoO_3**	**SrO**	**Y_2O_3**	**ZrO_2**	**Rh_2O_3**	**PdO**	**RuO_2**	**Nd_2O_3**
Provider	Alfa Aesar	Prolabo	Aldrich	Aldrich	Aldrich	Aldrich	CERAC	Aldrich	Aldrich	Aldrich	Aldrich
Mean particles size (µm)	1.7 ± 0.7	0.3 ± 0.1	3.0 ± 0.8	1.2 ± 0.3	1.5 ± 0.4	2.9 ± 0.9	0.5 ± 0.2	1.6 ± 0.4	0.1 ± 0.0	0.2 ± 0.1	0.5 ± 0.2

SEM-SE images of the eleven FP surrogates are shown in **Figure III-1**. The morphologies of the various powders are very different. For example, the CeO_2, PdO and RuO_2 powders consist in submicronic spherical particles of 0.3 ± 0.1 µm, 0.1 ± 0.1 µm and 0.2 ± 0.1 µm respectively which agglomerate. The $BaCO_3$ and ZrO_2 powders present similar morphologies with small spherical crystallites in the size range 1-5 µm organized in agglomerates from 10 to 60 µm in the case of ZrO_2. Concerning the Rh_2O_3 and MoO_3 powders, they are composed of platelets like particles of approximately 1.6 ± 0.4 µm and 1.2 ± 0.3 µm in length respectively. MoO_3 also presents elongated grains up to 70 µm. Both types of powders show agglomerate size of up to 200 µm. The La_2O_3, SrO and Nd_2O_3 powders are made of complex shaped crystallites in loose agglomerates up to a tens of micrometers. Finally, the Y_2O_3 powder consists in cracked agglomerates up to 20 µm in size made of flakes.

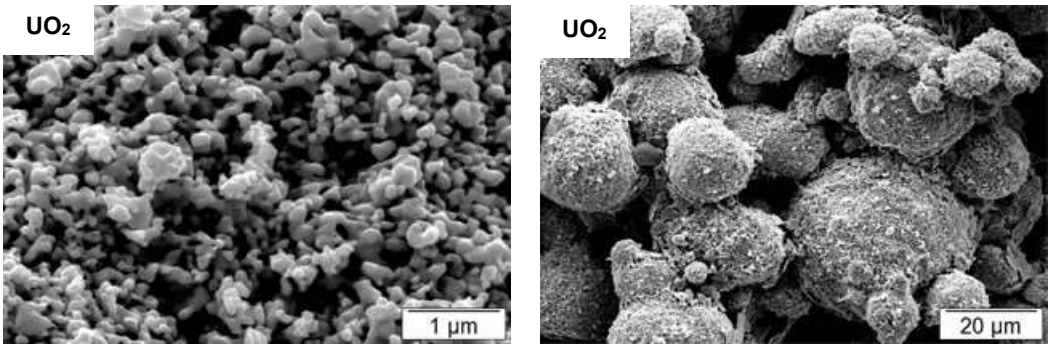

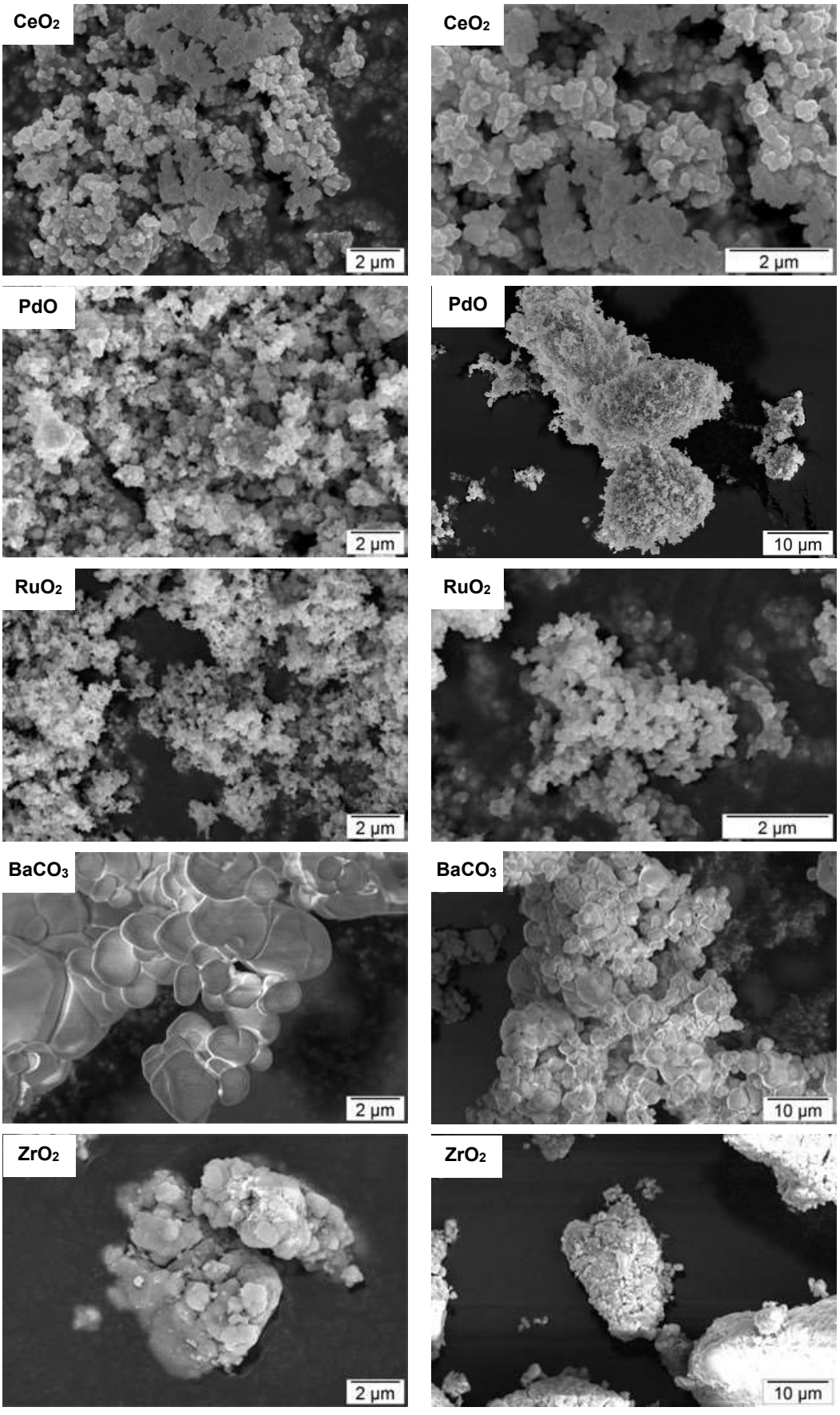
CeO2
2 µm
CeO2
2 µm
PdO
2 µm
PdO
10 µm
RuO2
2 µm
RuO2
2 µm
BaCO3
2 µm
BaCO3
10 µm
ZrO2
2 µm
ZrO2
10 µm

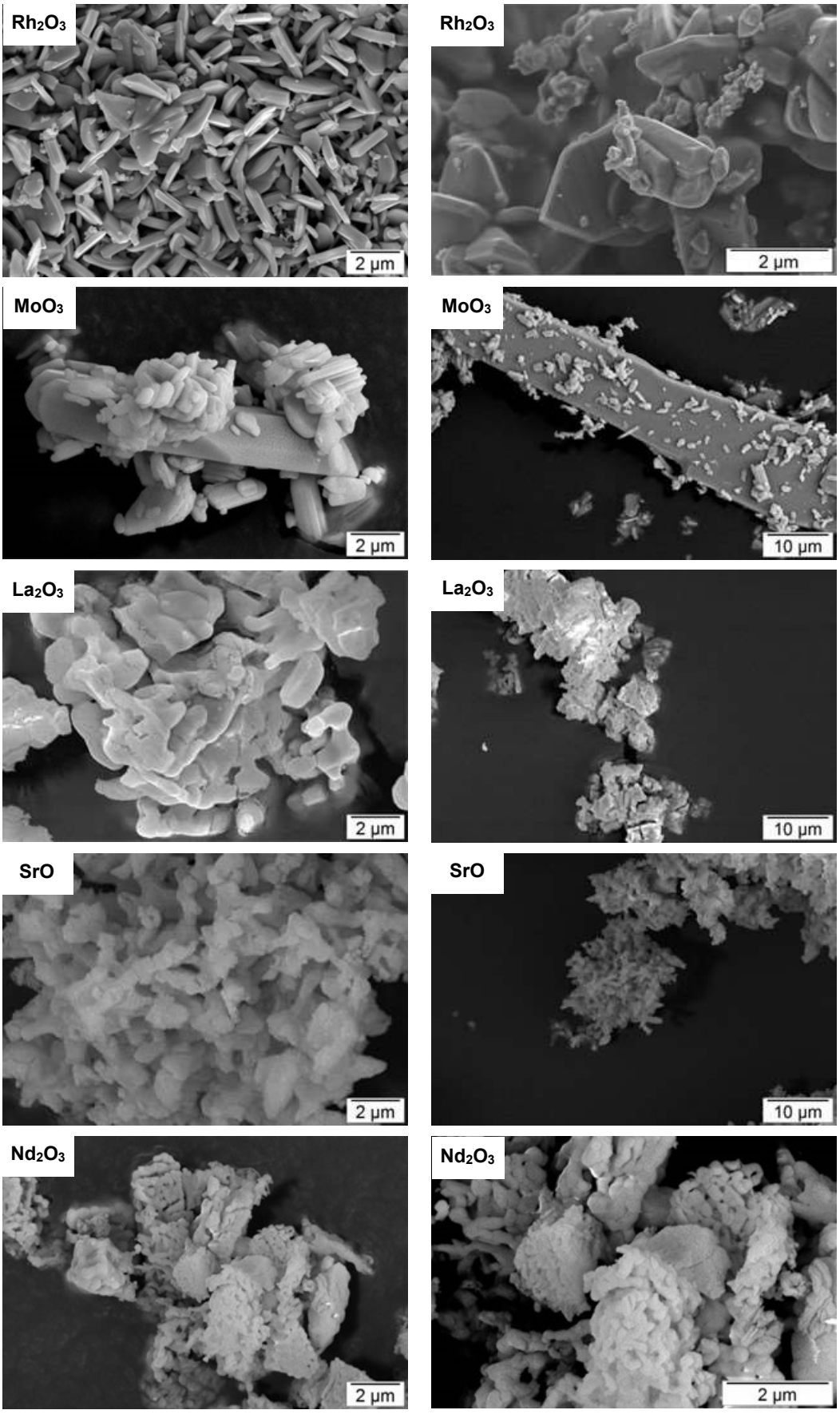
Rh2O3
2 µm
Rh2O3
2 µm
MoO3
2 µm
MoO3
10 µm
La2O3
2 µm
La2O3
10 µm
SrO
2 µm
SrO
10 µm
Nd2O3
2 µm
Nd2O3
2 µm

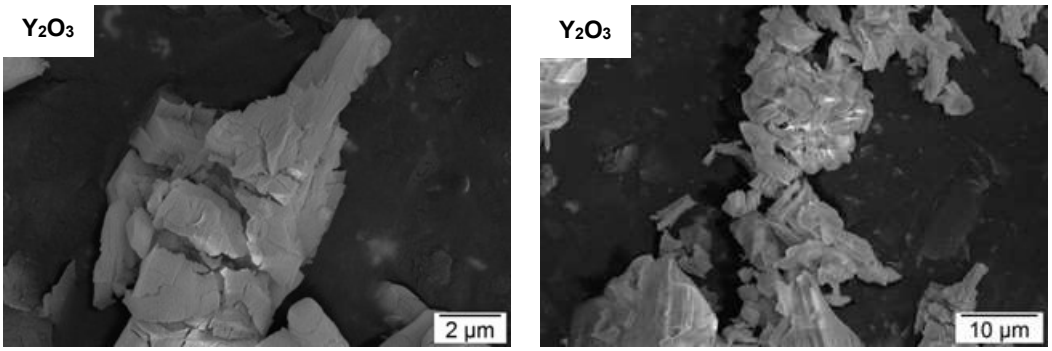

Figure III-1: SEM-SE images of starting powders. From top to bottom: UO_2, CeO_2, PdO, RuO_2, $BaCO_3$, ZrO_2, Rh_2O_3, MoO_3, La_2O_3, SrO, Nd_2O_3 and Y_2O_3

III.2.2 Sintering process

Sample preparation was carried out in a glovebox according to the procedure described in [2], [3]. The initial quantities of FP surrogates were weighted to correspond to the composition of a PWR UO_2 fuel with a burn-up of 76 $GWd.t_{HM}^{-1}$, calculated using the CESAR code [4] (**Table III-2**). The eleven FP surrogates were mixed together and added to UO_2. Planetary milling with Al_2O_3 balls was performed during 30 min in ethanol to achieve a well homogeneous dispersion of the additives in the matrix. The resulting slurry was dried in an oven and sieved first at 1000 µm and then at 160 µm. Pre-compaction (50 MPa), pressing (450 MPa) and sintering at 1650°C for 2h under flowing H_2 were then performed.

The sintering behavior of the SIMFuel mixture has been monitored by dilatometry on one pellet using a Setaram DHT 2050K device with Al_2O_3 sensors (**Figure III-2**). An Al_2O_3 pellet has been used as a reference in order to get rid of the thermal expansion of the device. Between 200°C and 950°C, swelling of the pellet occurs, which is not observed on the reference. This phenomenon could be due to the formation of H_2O vapors due to the reduction of MoO_3, RuO_2, PdO and Rh_2O_3 under flowing H_2 [3], [5]. Sintering occurs in three times with a first phase starting at 950°C, a second one at 1350°C and the last one at 1600°C. The maximum sintering rate is reached at 1450°C.

One batch of 31 pellets containing eleven FP surrogates in concentration representative of a pressurized water reactor fuel with a burn-up of 76 $GWd.t_U^{-1}$ was thus obtained (**Table III-2**).

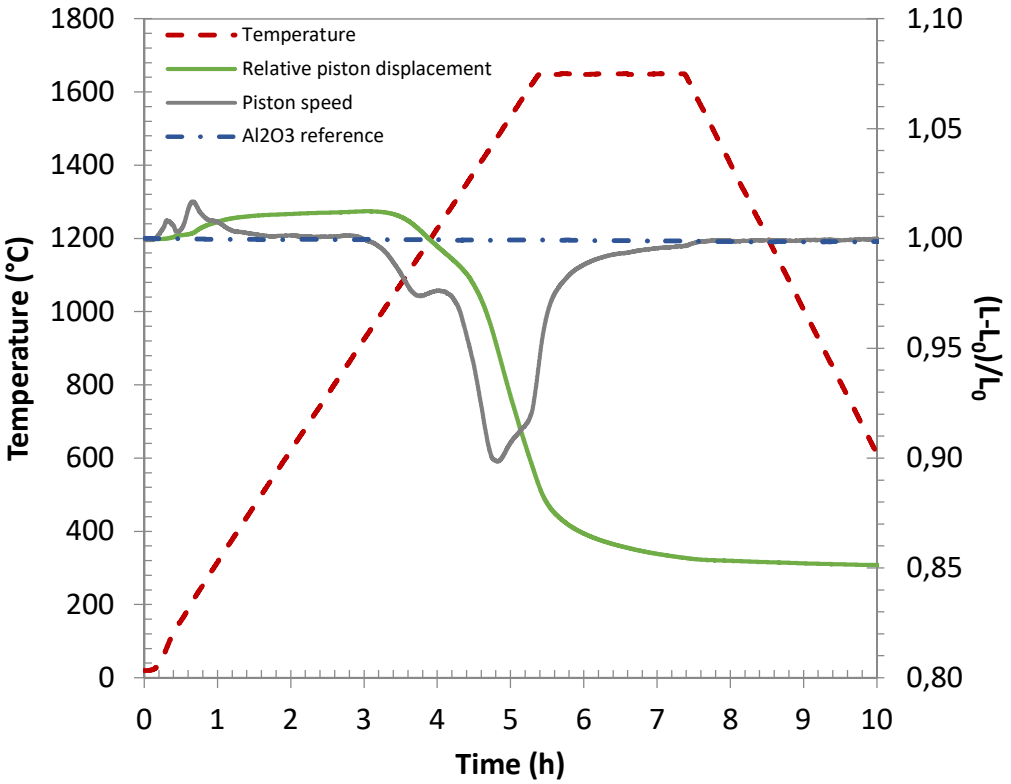

Figure III-2: Dilatometry curve and densification rate of the SIMFuel samples. The relative density and densification rate curves have been smoothed using a Savitzky-Golay filter [6] with 50 points.

Table III-2: Final composition of the SIMFuel samples (the difference to 100% is due to the O content)

Elements	U	Ba	Ce	La	Mo	Sr	Y	Zr	Rh	Pd	Ru	Nd
Content (wt%)	82.62	0.31	0.53	0.30	0.66	0.13	0.06	0.62	0.07	0.40	0.70	1.08
Content (at%)	29.60	0.19	0.32	0.18	0.59	0.13	0.06	0.58	0.06	0.32	0.59	0.64
Uncertainty (%)	0.00	0.11	0.07	0.13	0.05	0.30	0.51	0.06	0.58	0.10	0.05	0.04

III.2.3 Thermal treatment conditions

These thermal treatments were performed in the DURANCE experimental loop located in the UO_2 laboratory [7] (**Figure III-3**). The sample is a disk prepared by cutting and polishing SIMFuel pellets. It is then placed in a metallic W crucible within an induction furnace. Only one side of the disk is in contact with the atmosphere. The pO_2 in the inlet gas (Ar + 4% H_2) is controlled in input of the loop thanks to a zirconia oxygen pump. The pO_2 is also measured in input and output of the loop thanks to two MicroPoas probes (provided by Setnag) maintained at 650°C (Gen'air and Jok'air respectively). The temperature below the crucible is monitored by a thermocouple during the tests. A temperature calibration is done before each campaign of tests by measuring the melting point of standards.

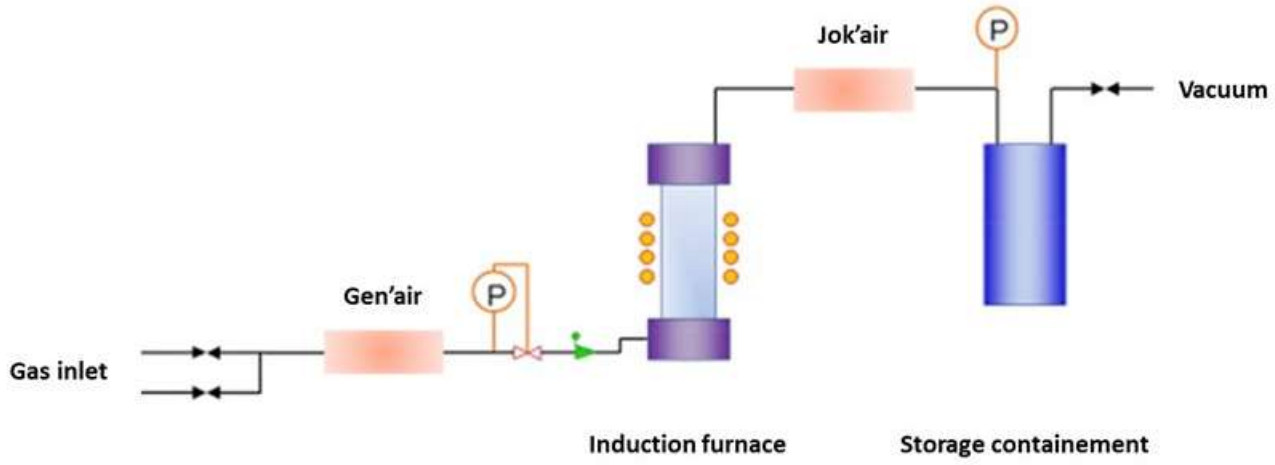

Figure III-3: DURANCE experimental loop

The objective of the thermal treatments was to investigate the effect of oxygen potential on Mo and Ba speciation in conditions representative of the early stages of a severe accident. The chemical evolution of Ba and Mo in these conditions was calculated using the FactSage™ 6.3 software coupled with the SGPS thermodynamic databases [8], [9] (**Figure III-4**). The appropriate temperature and oxygen potential values enabling to observe a chemical change of the phases containing Mo and Ba were then selected.

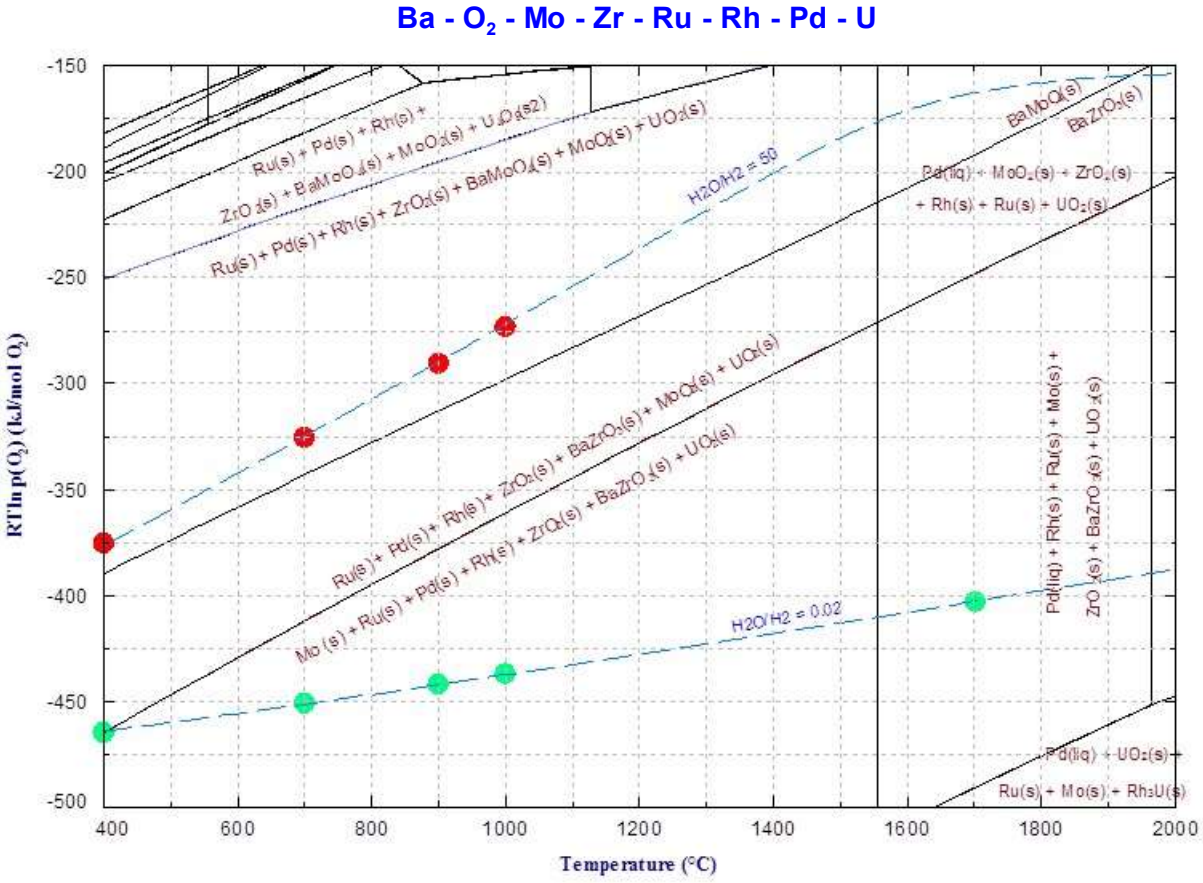

Figure III-4: Predominance diagram for the Ba-Zr-Mo-Ru-Rh-Pd-U-O_2 system obtained using the SGPS database of FactSage [8], [9]

Two campaigns of thermal treatments were thus performed as indicated by the points in **Figure III-4**. The corresponding experimental conditions are developed in **Table III-3**. The "R-" campaign was carried out under reducing conditions at 400°C, 700°C, 900°C, 1000°C and 1700°C (green points). The pO_2 on the Gen'air[1] (at 650°C) was maintained at $5.08x10^{-27}$ atm (H_2O/H_2 = 0.02). The "O-" one was performed under oxidizing conditions at 400°C, 700°C, 900°C and 1000°C (red points). The pO_2 in this series was maintained at $1.97x10^{-20}$ atm (H_2O/H_2 = 50) at 650°C. The evolution of the oxygen potential during the tests performed in oxidizing conditions is in the same range compared to the ones of the stage 2 ("oxidation plateau") of the VERDON-3 and 4 tests.

No tests could be performed at higher temperature in oxidizing conditions given the nature of the crucible used (metallic W).

Table III-3: Experimental conditions used to perform the different annealing tests

Sample	Temperature (°C)	Oxygen partial pressure (atm)	Oxygen potential ($kJ.mol^{-1}$)
O400	400	$8.78x10^{-31}$	-387.73
O700	700	$5.41x10^{-19}$	-340.30
O900	900	$1.89x10^{-14}$	-308.22
O1000	1000	$1.04x10^{-12}$	-292.05
R400	400	$2.26x10^{-37}$	-472.23
R700	700	$1.40x10^{-25}$	-463.05
R900	900	$4.87x10^{-21}$	-456.19
R1000	1000	$2.69x10^{-19}$	-452.63
R1700	1700	$5.17x10^{-12}$	-426.33

The tests consisted in a temperature ramp of $20°C.s^{-1}$ (except in the case of R1700 for which the ramp was set at $0.2°C.s^{-1}$) followed by a dwell time of 2h at the different temperatures under controlled pO_2 (**Figure III-5**). To cool down the sample, the high frequency generator was shut down. The atmosphere within the furnace was maintained until the sample has reached room temperature. The gas flow was set at 40 $mL.min^{-1}$. After each dwell in temperature, the SIMFuel disk was extracted and analyzed and another one was placed and treated up to the following temperature dwell.

[1] The operating temperature of the oxygen probe is 650°C.

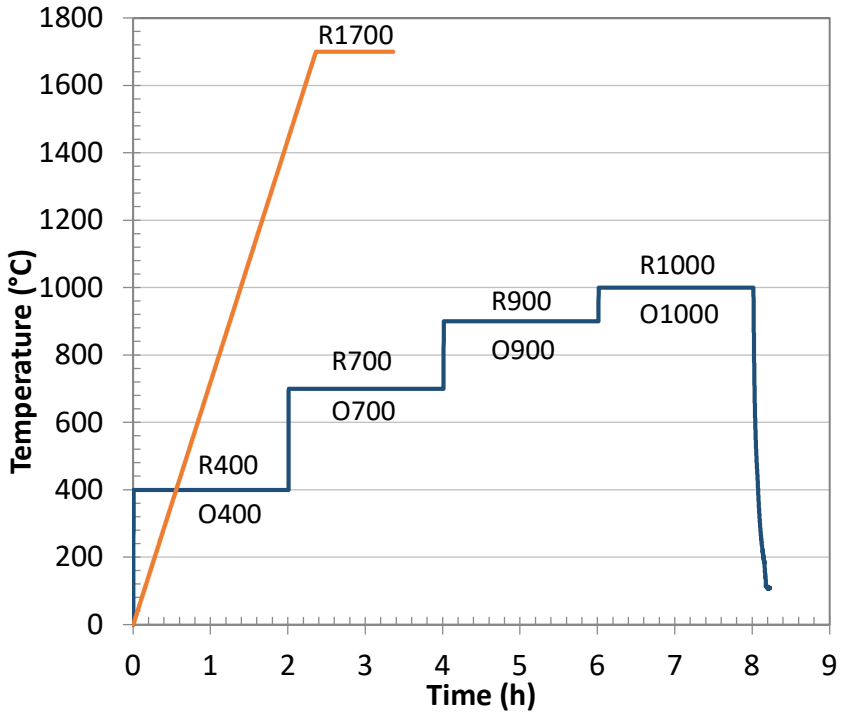

Figure III-5: Thermal sequences performed on the SIMFuel samples in the DURANCE loop

III.3 SAMPLES CHARACTERIZATION

Detailed characterizations were performed on the samples as-sintered and after the different thermal treatments to study the chemical evolution of the different phases observed in the SIMFuels. These characterizations included density measurements, OM and SEM observations that enabled describing the evolution of the microstructure after the different treatments.

X-ray maps and local EDX analyses were performed on the whole range of elements present in the SIMFuel samples but only the ones expected to compose the different phases of interest are shown (Mo, Ru, Rh, Pd, O and U in the case of metallic precipitates and Ba, Zr, Sr, Y, Ce, O and U in the case of the oxide precipitates). These analyses coupled to XANES measurements were performed in order to study the chemical evolution of the phases observed in the samples.

More specifically, XANES measurements allowed to study Mo and Ba speciation in the different samples. XANES calculations using the FDMNES software [10] were performed when some reference samples were missing, in order to interpret the experimental spectra.

The results were then compared with each other and with thermodynamic predictions in order to conclude on the effect of temperature and oxygen potential towards Mo and Ba speciation.

XRD analyses were also performed in two ways:

- Using an laboratory XRD device: through this approach, no phases containing FP could be detected, probably because of the small volume they occupy with the samples and the concentration of FP which is below the usual detection limit of this techniques (5 wt%).
- Using synchrotron radiation facility on the MARS beamline (SOLEIL, Saclay): this promising high-resolution approach enabled the detection of the different phases containing FP. However, the data could not be analyzed properly in the time of the PhD.

These results will thus not be presented in this manuscript.

The methods used to perform the characterizations as well as the experimental conditions are described in **Appendix 2.1**. FDMNES calculations are also described as well as the method to analyze experimental XANES spectra.

III.3.1 As-sintered samples

III.3.1.1 Physical characteristics of the samples

The density values obtained for the SIMFuel samples by geometrical and hydrostatic methods are summarized in **Table III-4**. Both types of measurements are consistent and give a final density of 92.09 ± 0.15 % d_{th} which is less than the expected value of 95-97 % d_{th} obtained in [2].

This is consistent with the remaining fraction of open porosity indicating that the sintering is not completed at the end of the thermal sequence. The remaining close porosity suggests that a phenomenon has hindered the sintering of the sample, as already seen in the dilatometry curve (**Figure III-2**). This could be due to the formation of H_2O vapors after reduction of some oxides or because of CO_2 production after the decomposition of $BaCO_3$ which starts below 810°C and would be complete around 1360°C under pure Ar [3], [5], [11].

Table III-4: Results of density measurements made on the SIMFuel samples by the geometric and the Archimedes methods (average values for the 31 pellets)

Green density (% d_{th})	Geometrical density (% d_{th})	Hydrostatic density (% d_{th})	Open porosity (%)	Closed porosity (%)
57.4 ± 0.3	91.7 ± 0.2	92.1 ± 0.2	2.4 ± 0.3	5.5 ± 0.3

III.3.1.2 Microstructure analysis

A typical macrograph of a SIMFuel sample is presented in **Figure III-6**. Some cracks can be observed starting from the edges of the pellets. The porosity is homogeneously distributed within the sample and some pores with a diameter larger than 10 µm, termed as voids, are visible. The mean pore size and area are given in **Table III-5** and the pore size distribution within the SIMFuel samples is given in **Figure III-7**.

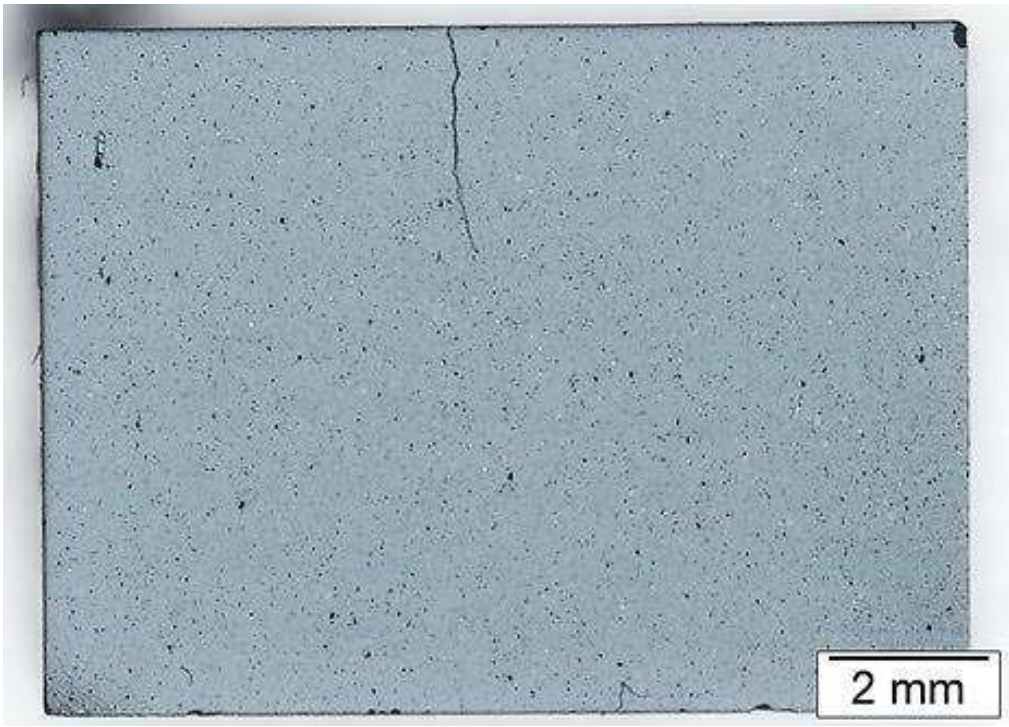

Figure III-6: Optical panorama micrograph of the polished surface of an axial cut of a pellet

Table III-5: Calculation of the contribution of porosity in the SIMFuel samples using AnalySIS

Mean void diameter (µm)	Mean pore diameter (µm)	Pore area (%)	Number of images used
16.9 ± 0.5	2.7 ± 0.0	8.4 ± 2.8	10

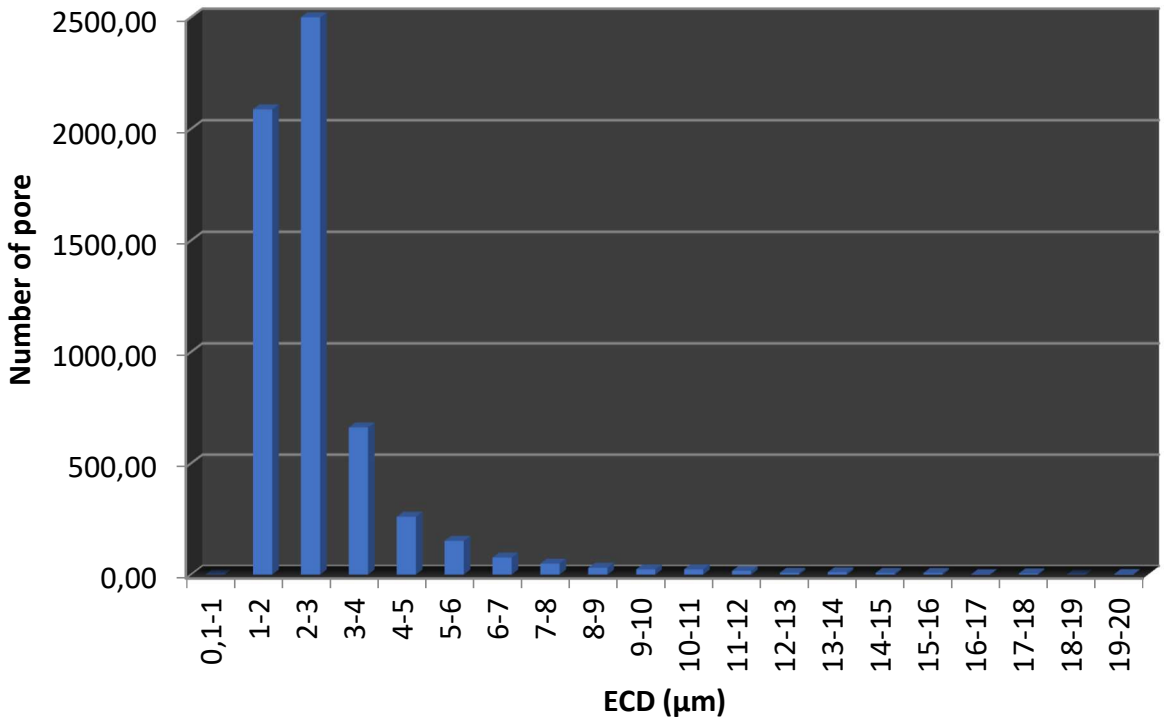

Figure III-7: Pore size distribution within the SIMFuel samples (ECD from 0.1 to 20 µm) calculated with AnalySIS

The high porosity observed within the samples could be due to the decomposition of carbonates or oxides during the high temperature sintering stage under pure H_2, leading to gas trapping into the matrix. The chemical composition of the matrix and the different types of precipitates has been determined by means of SEM-EDX analyses.

Figure III-8 shows the matrix of the SIMFuel samples. EDX measurements performed in these regions indicated that they mainly consist in UO_2 with dissolved elements such as Y, Ce, Nd and Zr. The concentrations of these FP are higher in some regions leading to darker areas observed in Back-Scattering Electrons (BSE) detection mode, as shown in **Figure III-8 right**. The amount of La was lower than the detection limit of EDX analysis in all the areas analyzed, which is no aberrant given the small amount (0.18 at%) added before sintering.

The average grain size in the bulk of the SIMFuel samples has been determined after thermal etching at 1700°C to be 6.8 ± 3.5 µm[2]. This is representative of the grain size measured in PWR irradiated fuel in normal operating conditions outside the HBS region. Indeed, it varies from 0.1-0.8 µm in the HBS region up to around 10 µm in the rest of the fuel [12]–[16].

[2] Average on 30 measurements.

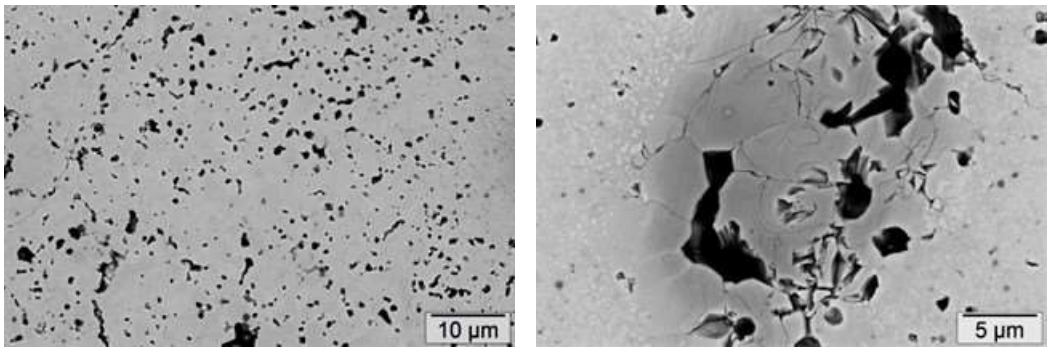

Figure III-8: SEM images obtained in Back-Scattering Electrons (BSE) detection mode of the UO_2 matrix in two regions of a polished SIMFuel sample. On the left, the UO_2 matrix containing dissolved Nd, Y, Ce and Zr can be seen and on the right, a Nd-rich area is observed.

Different types of secondary phases are homogeneously distributed within the SIMFuel matrix. These precipitates show various shapes, sizes and appear with different contrasts even during the OM observations. Two classes of precipitates were highlighted thanks to their colors as shown in **Figure III-9**: white precipitates which are metallic (orange frames) and grey precipitates which are made of a complex oxide phase (red frame).

III.3.1.3 Metallic precipitates

Three types of morphologies are observed in the metallic precipitates population:

- Some precipitates consist in large (few tens of micrometers) white precipitates with complex shapes sometimes containing darker inclusions. They are generally found in dense regions of the matrix.
- The smaller precipitates are forming clusters of several tenth of micrometers mainly located in areas with lower densities. They have a mean ECD of 0.6 ± 0.3 µm [3] but their size can vary between 0.2 and 5.0 µm.
- The third type of metallic precipitates consists in white elongated and rounded shaped phases of a few tens of micrometers in length, located in the porosity.

A detailed chemical analysis of these two types of precipitates is given hereafter.

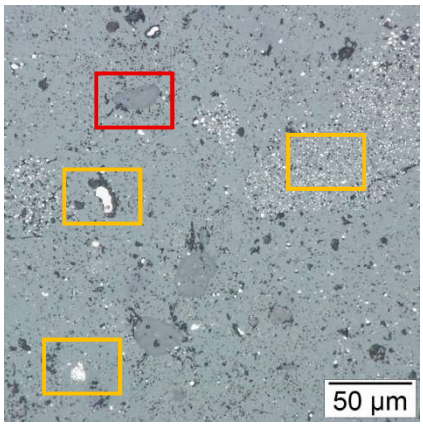

Figure III-9 : Optical micrograph of a SIMFuel sample showing the different classes of precipitates present in the UO_2 matrix

[3] Average on 30 measurements.

III.3.1.3.1 SEM-EDX analyses

Pd-Rh precipitates

Two precipitates belonging to the first type of metallic precipitates are shown in **Figure III-10**. They contain only Pd, Rh and sometimes U.

They exhibit a Rh-rich darker region containing and a brighter part rich in Pd with lower Rh content. The composition of these precipitates is given in **Appendix 2.2** (**Table B-2**). A high U content not associated with the presence of O has been detected in these precipitates. The ratio between (Rh+Pd) and U is around 3.3 ± 0.5. The amount of Rh and Pd differs depending on the region of the precipitates leading to two phases.

These kinds of biphasic inter-metallic compounds have also been observed in defective FBR irradiated fuels at very low oxygen potential and temperature above 1700°C [17]–[20]. Their composition was given to be $(U_xPu_{1-x})(Rh_yPd_{1-y})_3$ which is consistent with the present observations.

The observation of $U(Rh_{1-x}Pd_x)_3$ intermetallic compounds in the T_0 sample is consistent with the sintering conditions. As indicated by the predominance diagram in **Figure III-4**, the atmosphere of the sintering was below -500 $kJ.mol^{-1}$. The rounded shape of these precipitates indicates that the melting of at least one of the compounds, most probably that of Pd at 1555°C which occurred during sintering.

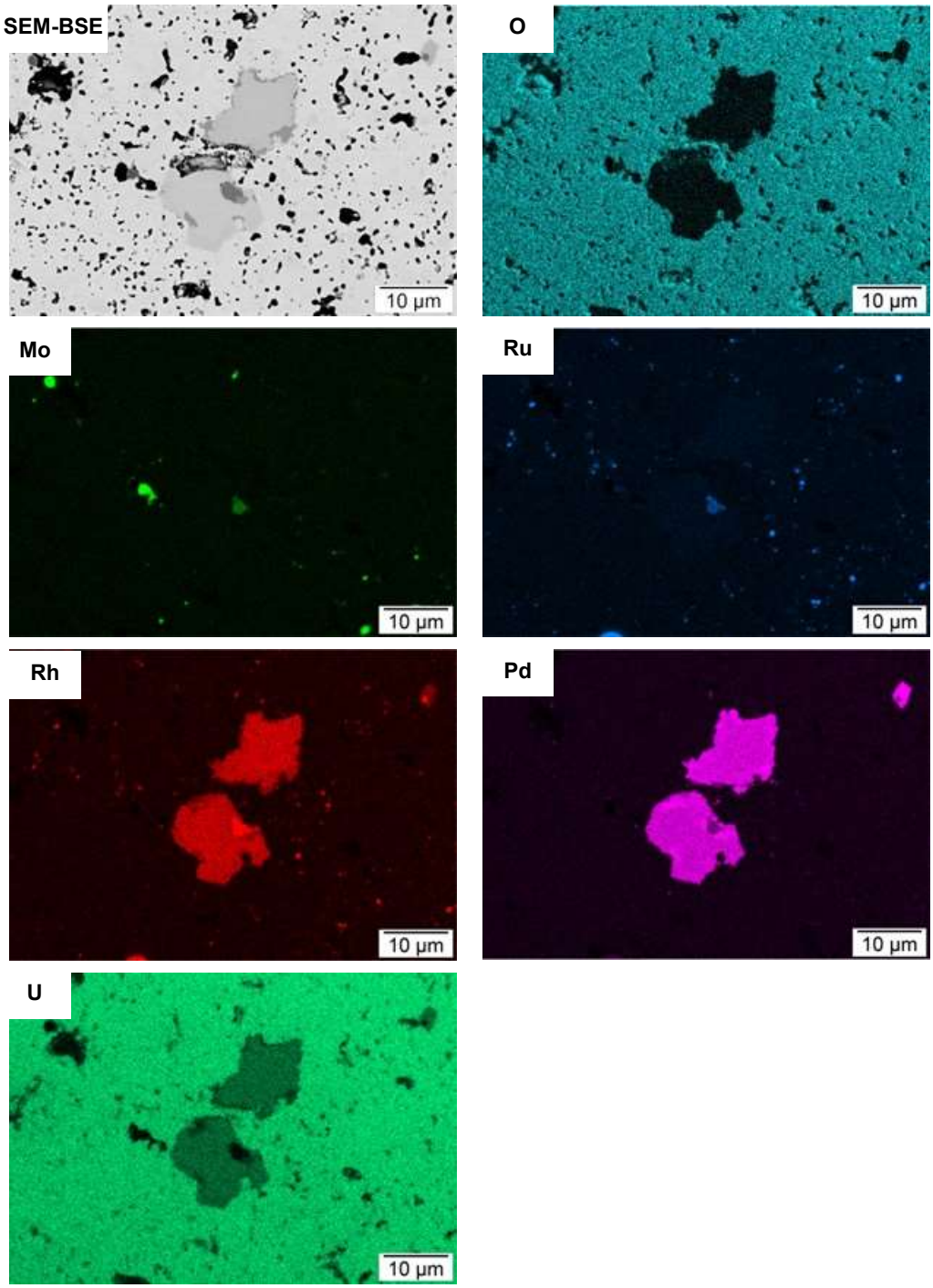

Figure III-10: SEM-SE image of typical Pd-Rh metallic precipitates (precipitates n°2 and 3 in Table B-2) found in the SIMFuel samples along with O, Mo, Ru, Rh, Pd and U X-ray maps (from top to bottom and left to right side).

Mo-Ru-Rh-Pd precipitates

The majority of the smaller precipitates mainly consist of Mo-Ru-Rh-Pd phases with a size below 5 µm (**Figure III-11**). The concentrations within these precipitates vary from one another. Some contain Ru as the major component whereas others are more concentrated in Mo (**Appendix 2.2**, **Table B-3**). The Ru/Mo ratio ranges from 0.3 to 16.4.

In most of the cases, no Rh could be detected by EDX probably because of an overlapping of Rh $L\alpha_{1,2}$ lines (2.697 and 2.692 keV) with Ru (2.558 and 2.554 keV) and Pd $L\alpha_{1,2}$ ones (2.838 and 2.833 keV).

Indeed, these lines are separated by less than the spectral resolution of the EDX Solid State Detector (SSD) given to be around 150 eV at Mn Kα. The U and O content detected in these precipitates are likely to belong to the surrounding UO_2 matrix as the interaction volume of X-rays with the samples is around 1 μm^3 which is in the range of the precipitates size.

According to the Mo-Ru-Pd ternary phase diagram shown in **Figure III-40**, these precipitates belong to the bcc (rich in Mo), bcc+hcp and hcp (rich in Ru) domains.

The composition and sizes of these precipitates are consistent with the experimental data on metallic precipitates reported in the literature in SIMFuel samples [1]–[3], [21]–[23] and also in both UO_2 and MOX irradiated fuels [17], [19], [24]–[27].

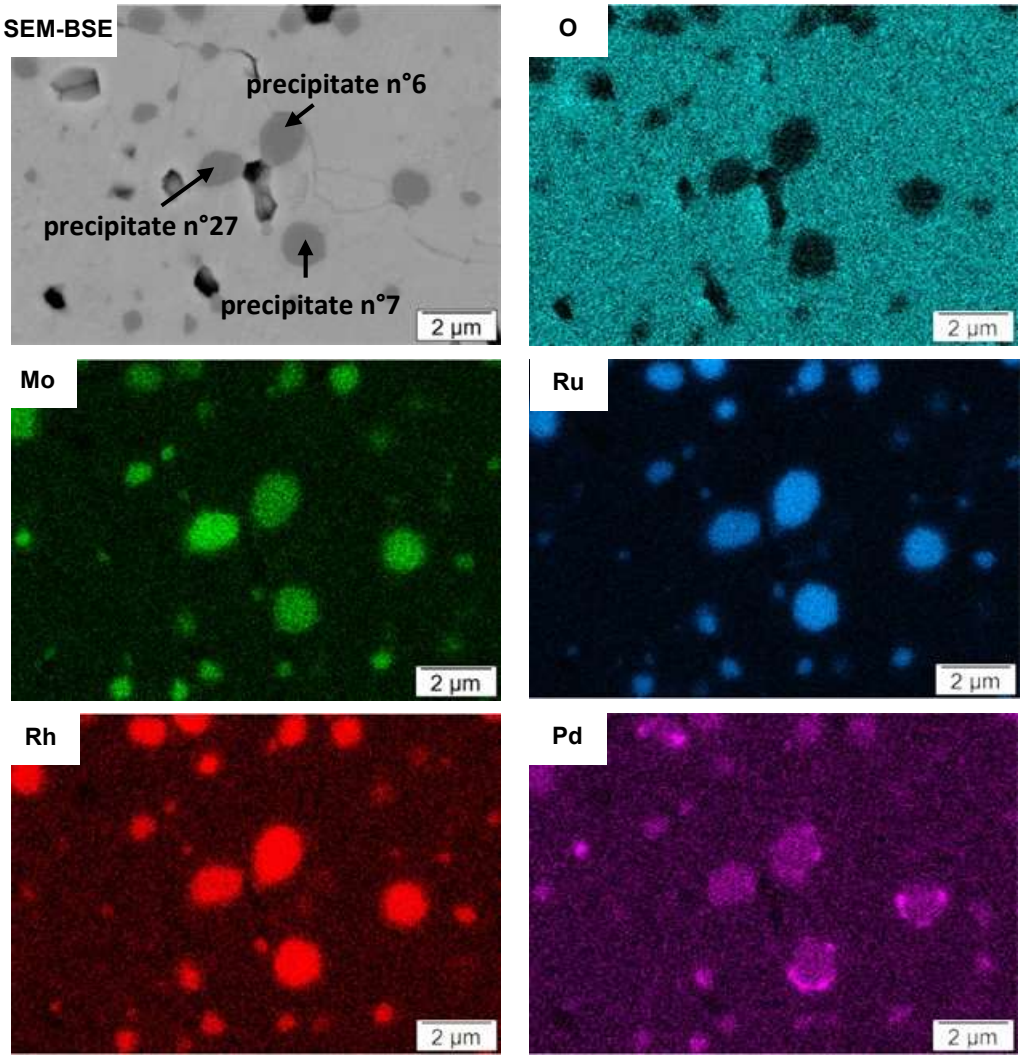

Figure III-11: SEM-SE images of typical Mo-Ru-Rh-Pd metallic precipitates (precipitates n° 6, 7 and 8 in Table B-3) found in the SIMFuel samples along with O, Mo, Ru, Rh and Pd X-ray maps (from top to bottom and left to right side).

Pure Mo precipitates

The chemical composition of the third type of white precipitates is shown in **Figure III-12** and given in **Appendix 2.2** (**Table B-4**). They contain only Mo and a trace of Pd, Rh and Ru. They belong to the bcc domain of the Mo-Ru-Pd phase diagram.

Once again, the amount of U and O found in these precipitate is due to the surrounding UO_2 matrix indicating that these precipitates are metallic. They are most of the time located in the pores and have a rounded shape. This is probably due to the melting of MoO_3 (around 800°C) well below the sintering temperature. MoO_3 would then have been reduced to metallic Mo under the reducing sintering atmosphere (pure H_2) inducing a shrinkage of the phase. This shrinkage would represent 36 to 54 % of the initial volume of the molten phase whether the reduction of MoO_2 (dth = 6.5 $g.cm^{-3}$) or MoO_3 (d_{th} = 4.7 $g.cm^{-3}$) into Mo (d_{th} = 10.2 $g.cm^{-3}$) is considered. The ratio between the voids and pure-Mo precipitates volumes, considering they are perfectly spherical, ranges around 51 %. This is perfectly consistent with the reduction of MoO_3 into Mo.

This kind of precipitates can also be observed in irradiated fuels [17], [18], [28]–[30].

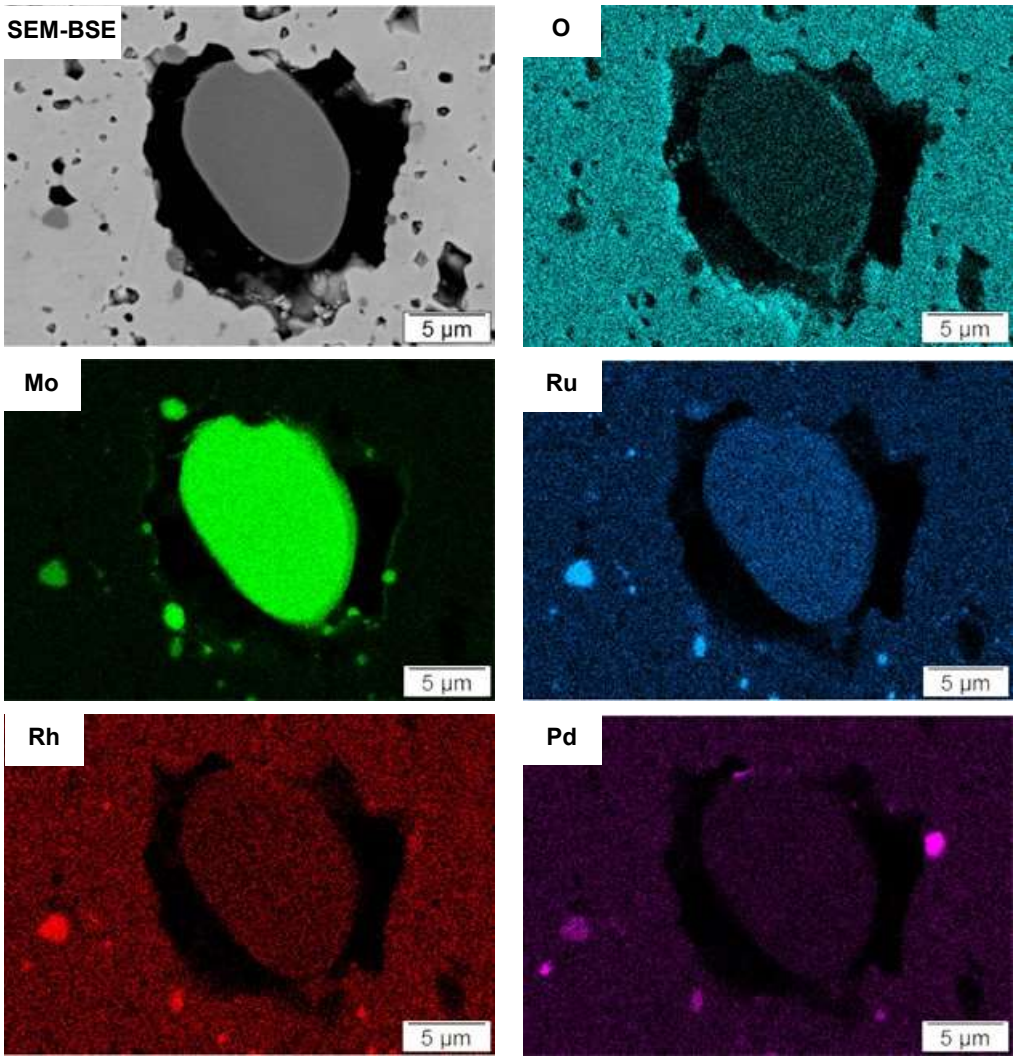

Figure III-12 : SEM-SE image of typical Mo metallic precipitates (precipitate n°10 in Table B-4) found in the SIMFuel samples along with O, Mo, Ru, Rh and Pd X-ray maps (from top to bottom and left to right side).

III.3.1.3.2 XANES analyses

In this section, the speciation of Mo has been investigated through XANES measurements.

SEM-EDX analyses tend to indicate that Mo is only present under metallic precipitates with a bcc or hcp structure, in association with Ru or alone in the T_0 sample. Thus, the normalized experimental

XANES spectra obtained at Mo K-edge on the T_0 sample will be compared to experimental bcc-metallic Mo and calculated hcp-metallic Mo spectra (**Figure III-13**). The feature observed on the calculated hcp-Mo spectrum at 20.009 keV is an artefact attributed to the automatic positioning of the Fermi level during the calculation.

The shape of the T_0 spectrum is very similar to that of bcc-metallic Mo. Nevertheless, the feature observed at 20.028 keV on the bcc-Mo spectrum is flattened on the T_0 spectrum (red dashed line in **Figure III-13**) and is not present on the hcp-Mo spectrum. The shoulder at 20.047 keV on the bcc-Mo spectrum is also slightly shifted to lower energies (20.044 keV) in the T_0 sample (blue dashed line in **Figure III-13**). This phenomenon is even more dramatic in the hcp-Mo spectrum as the second shoulder appeared at 20.037 keV.

The E_0 value measured for the T_0 sample is 20.001 keV which is very similar to the one of metallic Mo (20.000 keV) confirming that Mo has an oxidation state of 0.

The results of the linear combination fitting of the T_0 XANES spectrum using the bcc and hcp- metallic Mo spectra (**Figure III-14**) show that 82% of Mo may be present in the sample in bcc structure and 18% in hcp structure. The discrepancies between the fit and the experimental data shown in **Appendix 2.5** (**Figure B-1**) may be due to the presence of Ru in the metallic precipitates analyzed in the T_0 sample. Indeed, Ru has a lower atomic radius than Mo and has an impact on the structural parameters of pure metallic Mo. As indicated in [18], the structural parameters of the hcp-metallic precipitates decrease when increasing the amount of Ru. This has not be taken into account in the calculation of the hcp-Mo XANES spectrum. In the same way, the T_0 experimental XANES spectrum has been compared to pure bcc-metallic Mo, which did not account for Ru effect on the structure.

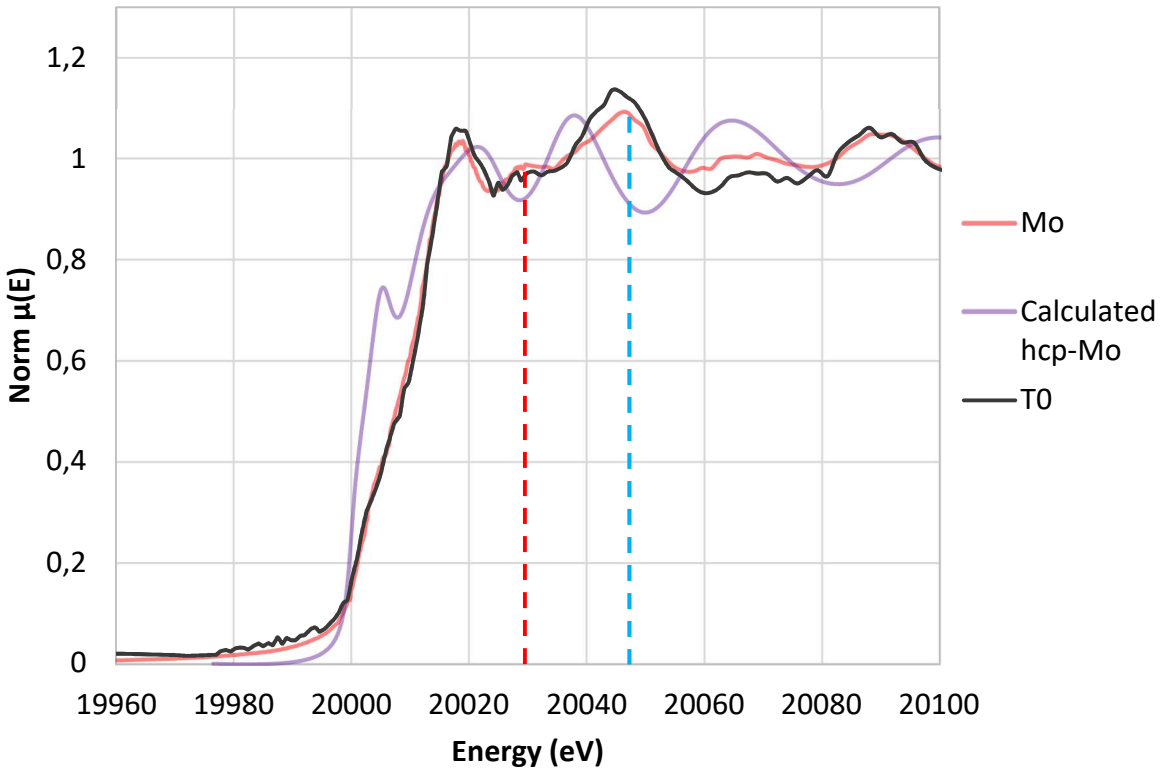

Figure III-13: Experimental XANES spectra of the as-sintered sample and metallic Mo (bcc) obtained at the Mo K-edge on the MARS beamline (SOLEIL) and calculated XANES spectrum of metallic Mo (hcp)

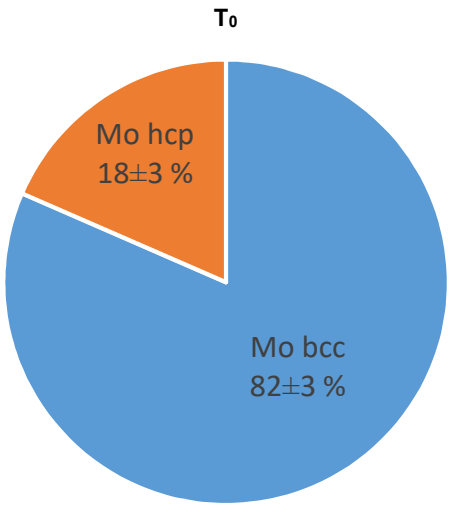

Figure III-14: Linear combination fitting results performed between -20 and +60 eV around the Mo K-absorption edge of the sample T_0 (R factor = 0.005496)

III.3.1.4 Oxide precipitates

III.3.1.4.1 SEM-EDX analyses

The oxide precipitates are composed of dark-grey core-shell feature when observed by OM or SEM. The average ECD of these precipitates is 12.2 ± 7.1 µm[4] but precipitates as large as 40 µm can be found. SEM-BSE image and X-ray maps of these precipitates are given in **Figure III-15**. The core-shell structure is mainly composed of three regions:

- A dark outer shell containing mainly Ba and Zr along with Sr and traces of Ce is observed for all the precipitates. The Ba/Zr, Sr/Zr and O/Zr ratios within this region have been determined through EDX analyses (**Appendix 2.2**, **Table B-5**) to be around 0.8, 0.2 and 2.5 respectively. This is consistent with the grey phase composition usually given as $(Ba_{1-x}Sr_x)(Zr,RE)O_3$ [1], [2], [17], [27], [31]–[33] where x turns out to be 0.2 in this case.
- The inner darker core of the precipitates is mainly composed of Zr. The O/Zr ratio is around 2, which is consistent with the formation of ZrO_2 (precipitates n°2, 3, 4, 6, 7, 9 and 10).
- A brighter U-rich layer is observed between the core and the outer shell in most of the precipitates (precipitates n°2, 3, 4, 5, 6, 7, 9 and 10). This region also exhibits a high Zr content and a lower amount of Ba. The O/(U+Zr) ratio is around 2 meaning that this layer may be composed of a solid solution with a composition $(Zr_{1-x}U_x)O_2$ where x has been measured to lay between 0.3 and 0.5.

Some rare very small oxide precipitates (e.g. precipitate n°1) exhibit a homogeneous $(Ba_{0.8}Sr_{0.2})ZrO_3$ composition within the whole particle.

[4] The size of the precipitates has been determined as the average of 100 measurements using the AnalySIS PRO software.

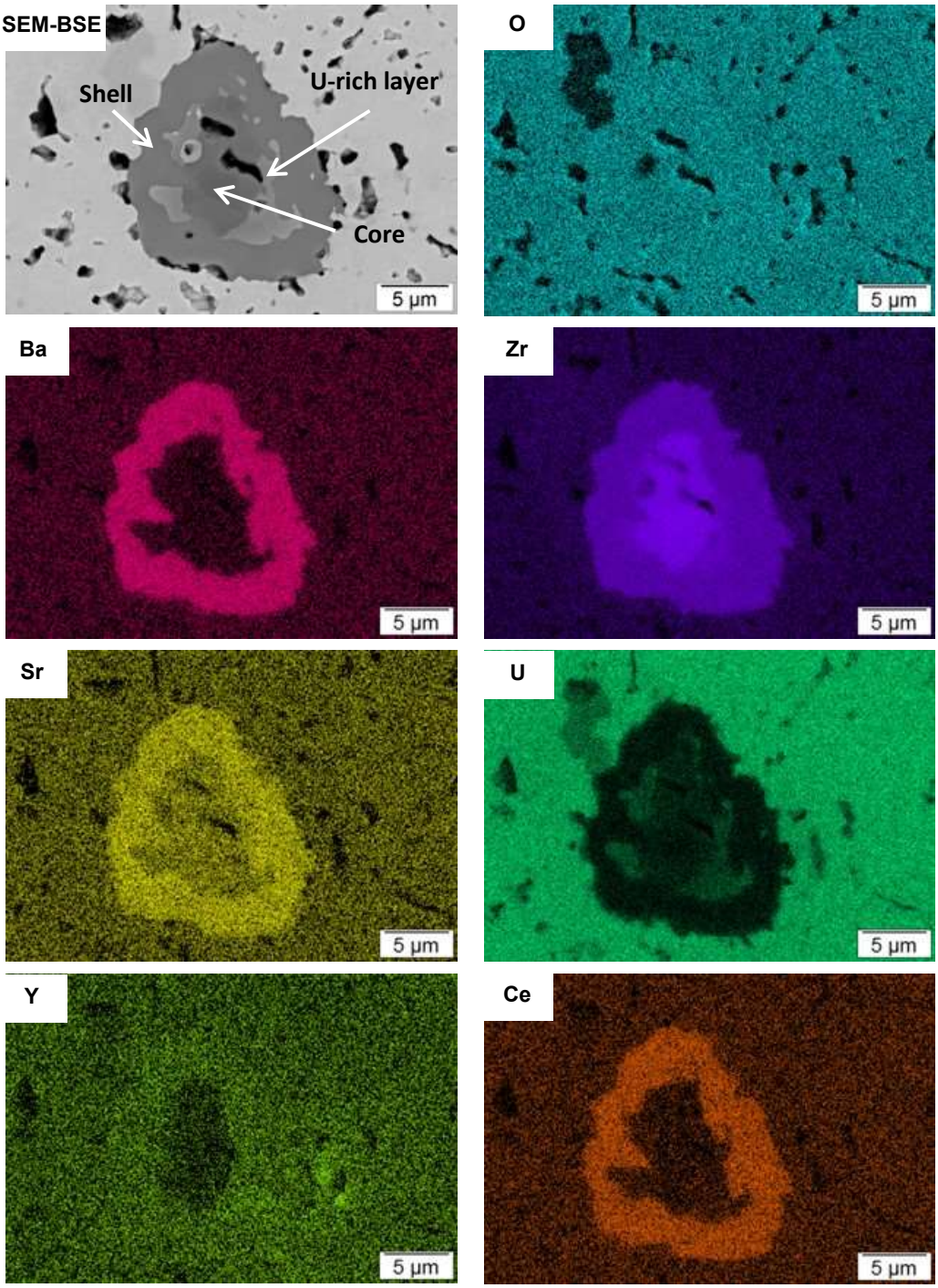

Figure III-15: SEM-SE images of a typical oxide precipitate (precipitate n°2 in Table B-5) found in a SIMFuel sample along with O, Ba, Zr, Sr, U, Y and Ce X-ray maps (from top to bottom and left to right hand side).

III.3.1.4.2 XANES analyses

In this section, the speciation of Ba has been investigated through XANES measurements.

According to the SEM-EDX analyses, Ba would be present in the sample only as $BaZrO_3$. However, BaO is also miscible in ZrO_2 and $(Zr_{1-x}U_x)O_2$. Thus, the normalized HERFD-XANES spectrum of the T_0 sample is compared to both $BaZrO_3$ and BaO experimental XANES spectra (**Figure III-16**). The features observed in the T_0 sample between 5.255 keV and 5.280 keV as well as the shape of the white line are very similar to those of $BaZrO_3$.

Complementary to Ba analyses, experimental XANES spectra were also recorded at the Zr K-edge on the T_0 sample and reference compounds of m-ZrO_2 and $BaZrO_3$. As observed by SEM-EDX, $SrZrO_3$ would also be present in the T_0 sample. Moreover, the composition of the $(Zr_{1-x}U_x)O_2$ with $0.3 \leq x \leq 0.5$ indicates that this solid solution was either tetragonal or cubic at 1650°C (**cf phase diagram of Fig. 64 chap. 2**). Thus, the XANES spectra of t-ZrO_2, c-ZrO_2, and $SrZrO_3$ were calculated using FDMNES and compared to the experimental spectra in **Figure III-17**.

The T_0 spectrum presents two peaks at 18.017 and 18.027 keV (blue dashed lines in **Figure III-17**) consistent with the ones observed on the $BaZrO_3$. The first of these two peaks is also observed on the c-ZrO_2 spectrum whereas the second one is observed on the $SrZrO_3$ spectrum. The small shoulder observed at 18.046 keV on the m-ZrO_2 and t-ZrO_2 spectra is also present on the one of the T_0 sample (red dashed line in **Figure III-17**).

The E_0 values obtained at both edges are summarized for each sample in **Table III-6**. The E_0 of the T_0 sample is similar to the references in both Ba and Zr cases confirming that:

- Ba presents the same oxidation state as the reference samples (+II) in the T_0 sample as expected for an alkaline earth element (i.e. this phase is of II-IV perovskite type).
- Zr has the same oxidation state in the T_0 sample and in the references (+IV).

According to the linear combination fitting results synthesized in **Figure III-18**, 83 ± 1 % of Ba would be present in the T_0 sample as $BaZrO_3$ (0.16 ± 0.01 at% considering the initial quantity of Ba in the SIMFuel samples given in **Table III-2**) and 17 ± 1 % of Ba would be found under the form of BaO (0.03 ± 0.01 at%).

Concerning Zr, 48% would be in the ZrO_2 form (47 ± 3 % as monoclinic zirconia and 1 ± 2 % as cubic zirconia). No Zr was found to be present under t-ZrO_2. 52% of Zr was found to be in zirconate form, with 33 ± 3 % of $BaZrO_3$ and 19 ± 3 % of $SrZrO_3$. This corresponds to 0.19 ± 0.03 at% of the initial amount of Zr in the SIMFuel samples found in $BaZrO_3$ and 0.11 ± 0.03 at% in $SrZrO_3$ which would lead to a composition for the oxide phase of $(Ba_{0.6}Sr_{0.4})ZrO_3$, not consistent with the one obtained through EDX. However, the Zr and Ba amount contained in the $BaZrO_3$, according to the XANES fits, are consistent within the uncertainties. This would tend to indicate that part of the Ba considered to be part of the $(Ba_{1-x}Sr_x)ZrO_3$ phase according to the EDX analyses would be in fact dissolved in the ZrO_2 as BaO.

Nevertheless, in the case of Zr, the fit does not very well reproduce the two peaks seen at 18.017 and 18.027 keV on the experimental signal. Indeed, as shown in **Appendix 2.5** (**Figure B-2**), the fit spectrum is flattened on the top of the white line. This could have led to an underestimation of the Zr

amount contained in $BaZrO_3$. A good agreement is obtained between the experimental T_0 spectrum and the fit signal in the case of Ba (**Appendix 2.5**, **Figure B-3**).

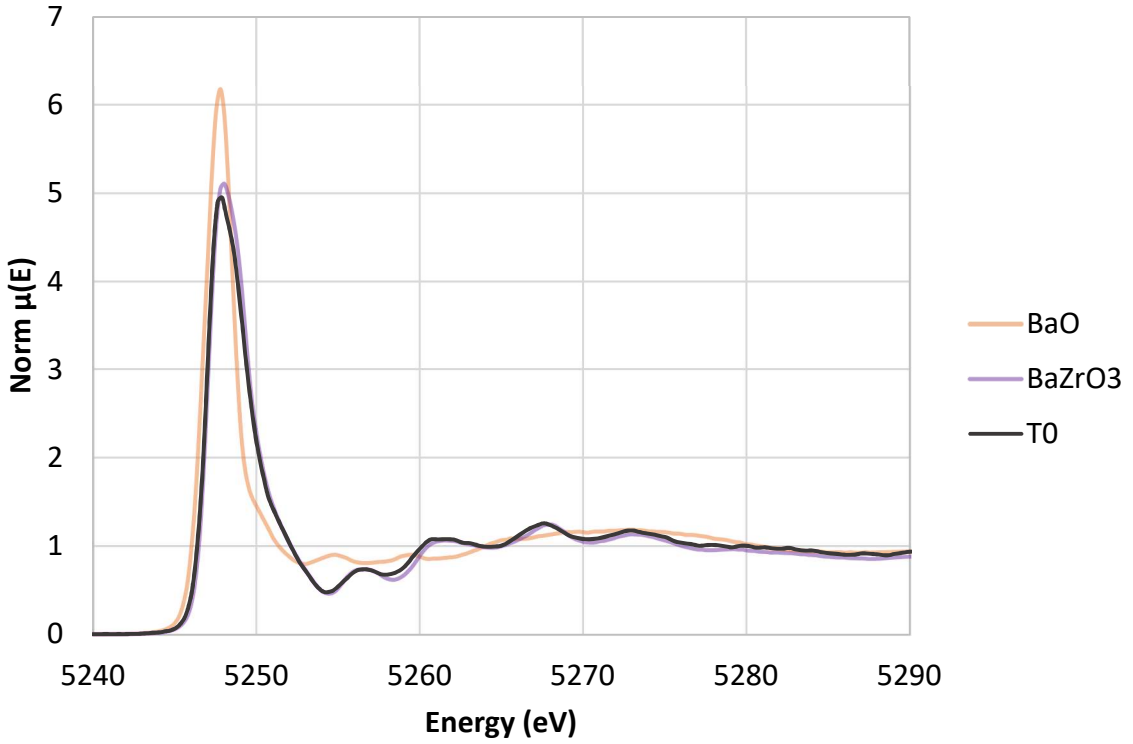

Figure III-16: Experimental XANES spectra of the as-sintered sample, $BaZrO_3$ and BaO obtained at the Ba L_3-edge on the FAME-UHD beamline (ESRF)

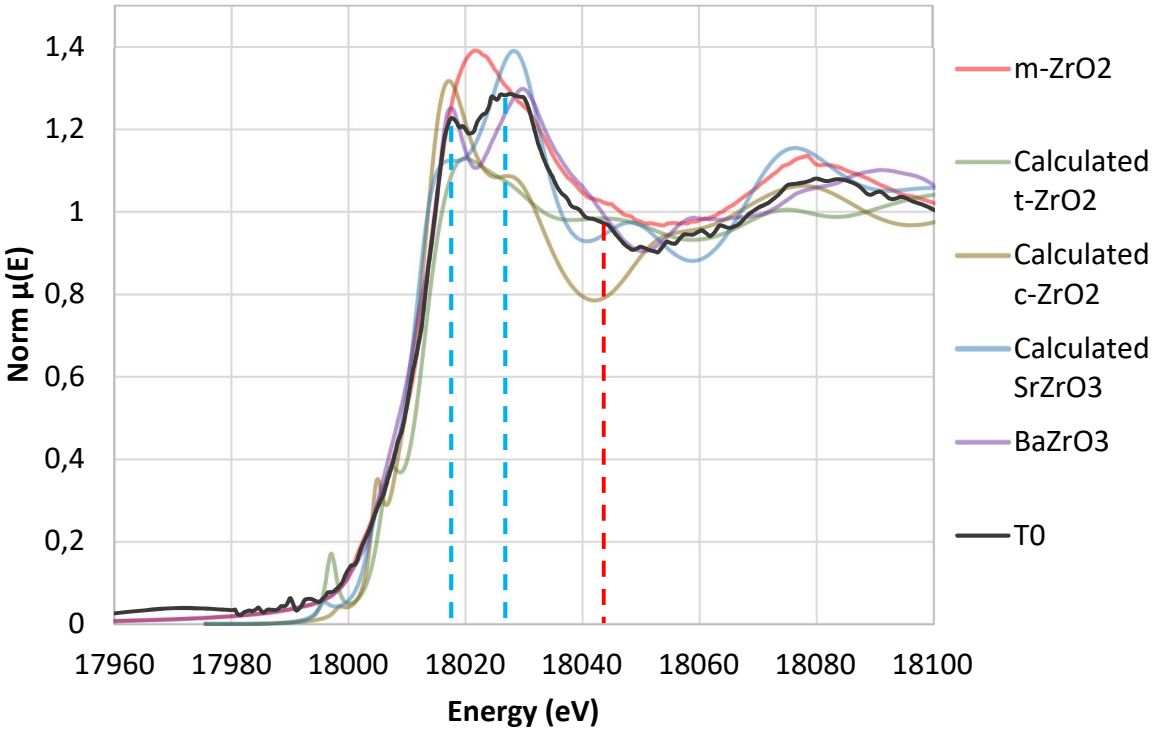

Figure III-17: Experimental XANES spectra of the as-sintered sample, m-ZrO_2 and $BaZrO_3$ obtained at the Zr K-edge on the MARS beamline (SOLEIL) and calculated XANES spectra of t-ZrO_2, c-ZrO_2 and $SrZrO_3$

Table III-6: E_0 position of the as-sintered sample and references spectra collected at the Ba L3-edge and Sr K-edge (the uncertainty on the energy is 0.6 eV)

	Ba L_3-edge	Zr K-edge
Sample	**E_0 (eV)**	**E_0 (eV)**
BaO	5248.1	-
BaZrO3	5247.9	18015.4
$SrZrO_3$	-	18015.4
m-ZrO_2	-	18013.5
c-ZrO_2	-	18013.5
T_0	5247.8	18014.1

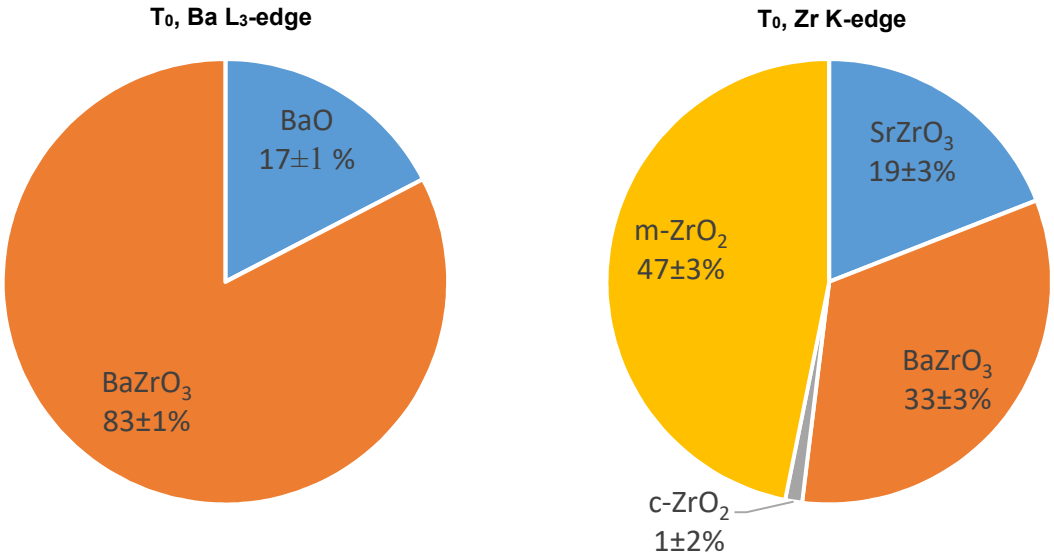

Figure III-18: Linear combination fitting results performed between -20 and +60 eV around the Ba L_3-absorption edge (left, R factor = 0.002758) and Zr K-absorption edge (right, R factor = 0.001996) in the sample T_0

III.3.1.5 Discussion on the observations made in the as-sintered sample

Mo speciation

In the SIMFuel samples synthesized in this study, Mo is only found in metallic precipitates, alone or in association with Ru, Pd and Rh. These precipitates have a bcc or hcp structure depending on their Ru content.

The variety of compositions obtained for the Mo-Ru-Rh-Pd metallic precipitates in the SIMFuel samples at the initial state are representative of the real white inclusions population found in irradiated fuels during normal operating conditions and the different stages of a severe accident. The size of these precipitates are also in the range of the ones found in PWR fuels (submicronic to 10 µm), except concerning the pure metallic Mo ones, which are larger.

Ba speciation

Concerning Ba, it is only found in oxide precipitates whether dissolved in (U, Zr)O_2 probably as BaO, or in association with Sr and Zr as $Ba_{0.8}Sr_{0.2}ZrO_3$. This last phase has a perovskite structure and is not usually observed in normal operating conditions in PWR fuels. It may be formed at higher temperature probably between 1000°C and 1500°C as observed in FBR fuels or in LWR irradiated fuels treated up to 1500°C [27].

Due to the size and morphology of the starting additives, the oxide precipitates observed in the SIMFuel samples synthesized in this study are way bigger than the ones which can be found in irradiated fuels (> 10 µm vs. < 1 µm). Moreover, the core-shell structure has not been observed in irradiated fuels [17], [27], [32], [33] and other SIMFuel samples [2], [21]–[23], [34], [35]. However, the core-shell composition of the oxide phase observed here is consistent with the study made in [3], [5].

These differences may be linked to the characteristics of the initial additives used to produce the SIMFuel samples and to the sintering conditions which did not enable to reach thermodynamic equilibrium. A mechanism, first proposed in [5] and adapted here to explain the formation of such precipitates is shown in **Figure III-19**. It is based on the inhomogeneity of the starting powder mixture with large ZrO_2 agglomerates distributed in the UO_2. As shown in **Figure III-1**, the initial ZrO_2 and $BaCO_3$ powders used to produce SIMFuel have a tendency to agglomerate. The size of the crystallites is 1-5 µm but the agglomerates can be as large as 60 µm. Even if the initial powder mixture has been ground, some agglomerates may have remained. The fact that the additives were first mixed together before being added to the UO_2, may have favored a contact between them which would have remained during the whole process.

When heating the compacted powder mixture, interdiffusion can take place between the ZrO_2 particle and the surrounding UO_2 matrix leading to the formation of a $(U_{1-x}Zr_x)O_2$ solid solution. This reaction takes place on the outer surface of the zirconia particle and consumes it from outside.

In contact with the t-ZrO_2 beyond 1200°C or with the tetragonal or cubic $(U_{1-x}Zr_x)O_2$ solid solution, BaO would have been dissolved. Then, given the strongly reducing atmosphere of the sintering, a transformation into an intermediary compound of $Ba(U_{1-x}Zr_x)O_3$, then into the most stable $BaZrO_3$ would have taken place. If the original ZrO_2 particle is small enough (< 5 µm), it reacts to form a homogeneous perovskite particle during the sintering process, but larger ZrO_2 particles (> 5 µm) remain partially unreacted. The results obtained through EDX and XANES analyses on the oxide precipitates of sample T_0 support this mechanism.

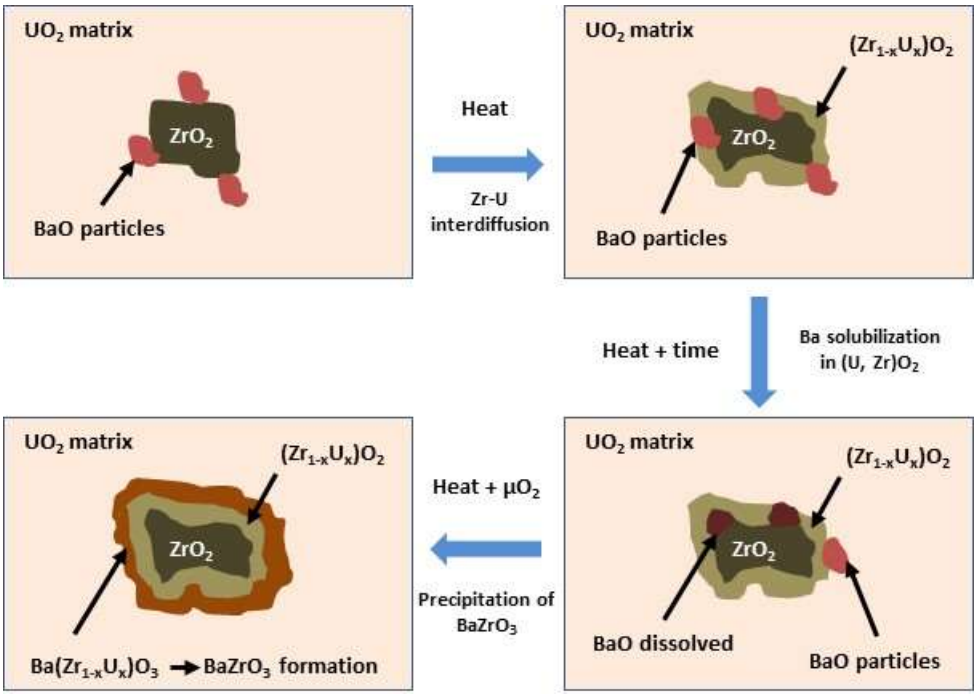

Figure III-19: Schematic mechanism for the formation of core-shell structured oxide precipitates during sintering adapted from [5]

Comparison between SIMFuels and PWR irradiated fuels

Finally, the main differences between FP speciation in normal operating PWR irradiated fuels and SIMFuel samples is due to the fabrication stage of the latter. Indeed, the FP surrogates have been brought as oxides and reduced in the strongly reducing atmosphere and high temperature of the sintering (pure H_2 at 1650°C). This leads to the formation of several phases that are not observed in PWR irradiated fuels under normal operating conditions. This is particularly the case of the $U(Rh_{1-x}Pd_x)_3$ intermetallic compounds which are not stable at the oxygen potentials considered in normal conditions in PWR and the oxide or grey phase, not usually observed in PWR irradiated fuels under normal operating conditions. However, these phases can be found in FBR fuels and are consistent with thermodynamic calculations.

III.3.2 Samples treated in oxidizing conditions

The samples considered in this part were submitted to temperatures between 400 and 1000°C and oxygen potentials ranging between -387 and -292 $kJ.mol_{O2}^{-1}$ as presented in **Section III.2.3** (**Table III-3**).

The different precipitates already observed in the T_0 sample are also found in the samples treated in oxidizing conditions whatever the temperature (**Figure III-20**). No evolution of the precipitates' size can be observed through OM, as shown in **Table 37** (the measurements performed on the pure metallic Mo and Pd-Rh precipitates are not presented as the size range is too broad). However, a change in the metallic Pd-Rh precipitates' morphology takes place at 700°C (red circles in **Figure III-20**) and a light purple layer appears at the edges of pure Mo metallic precipitates in OM is observed between 900°C and 1000°C (green circles in **Figure III-20**).

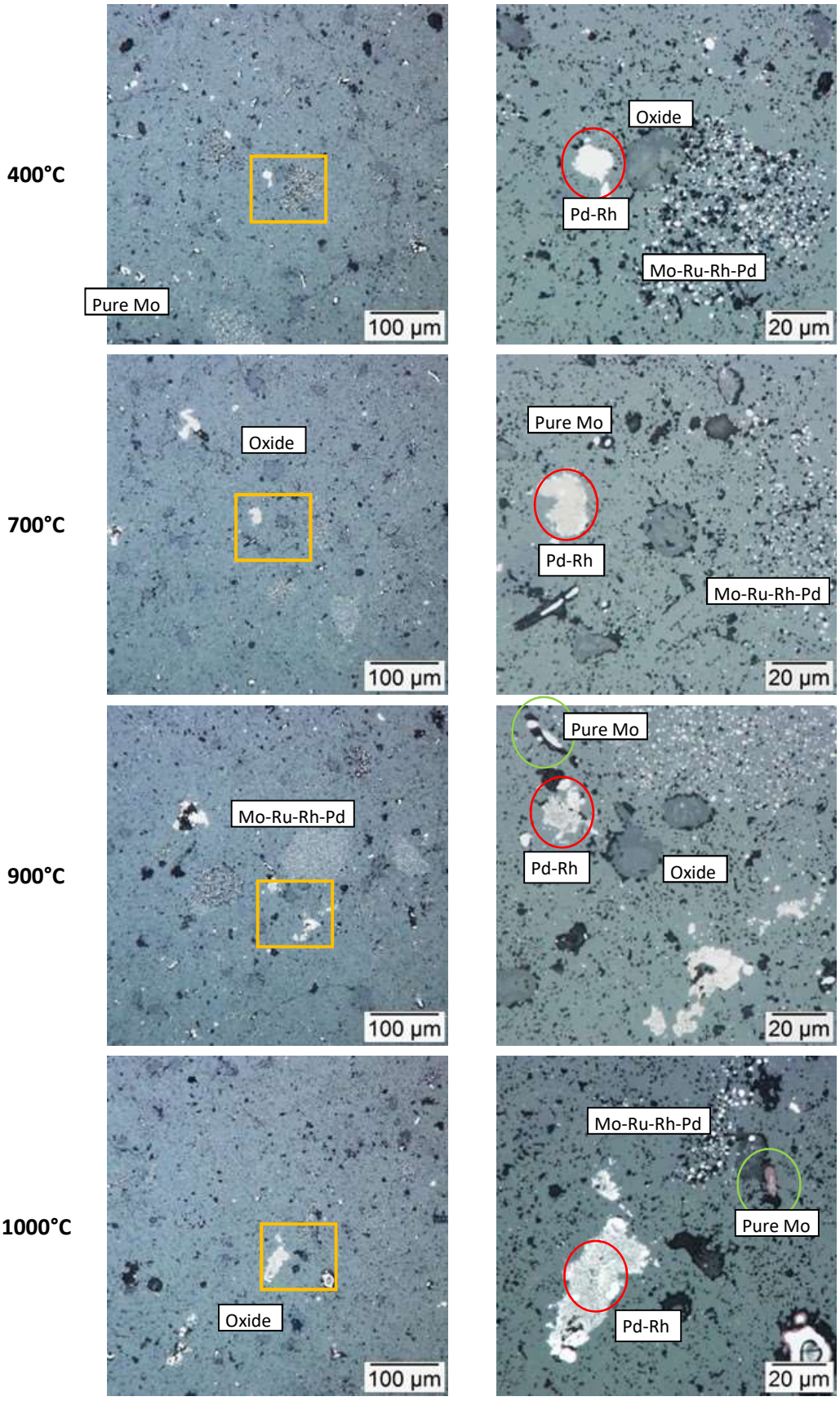

Figure III-20: Evolution of the different precipitates with the temperature under oxidizing atmosphere observed in OM (Pd-Rh precipitates in the red circles, Pure Mo precipitates in the green circles). The OM images on the right are taken at higher magnification in the yellow frames shown on the left images.

Table III-7: Summary of oxide and Mo-Ru-Rh-Pd metallic precipitates sizes (measurements on 30 precipitates of each type thanks to image analysis)

Temperature (°C)	Pecipitate size (µm)	
	Oxide precipitates	Mo-Ru-Rh-Pd metallic precipitates
O400	15.53 ± 9.11	0.94 ± 0.42
O700	14.40 ± 5.34	0.74 ± 0.42
O900	16.97 ± 6.99	0.76 ± 0.41
O1000	16.22 ± 5.79	0.97 ± 0.57

III.3.2.1 Metallic precipitates

III.3.2.1.1 SEM-EDX analyses

The SEM-BSE pictures of the different types of metallic precipitates are shown in **Figure III-21**.

Pd-Rh precipitates

Concerning the Pd-Rh precipitates, they are mainly composed of Pd and Rh and U up to 400°C (**Appendix 2.3**, **Table B-6**). Above 400°C, the U-content in the precipitate drops to traces: the U and O detected in the precipitates above 400°C are likely to come from the UO_2 matrix. Indeed, the O/U ratio is approximately 2 (notably in the case of precipitate n°2 in **Table B-7**). No evolution can be seen between 700°C and 1000°C as shown in **Figure III-21**, **Figure III-22** and in **Appendix 2.3** (**Table B-6, Table B-7, Table B-8** and **Table B-9**).

Thus, the morphological change of these precipitates is probably due to the oxidation of U in the two phases of the precipitates $U(Rh_{1-x}Pd_x)_3$ to UO_2. Indeed, the oxygen potential imposed during the annealing tests (**Table III-3**) is too oxidizing to stabilize these intermetallic phases according to the calculation presented in **Figure III-4** and the study made in [20], [36].

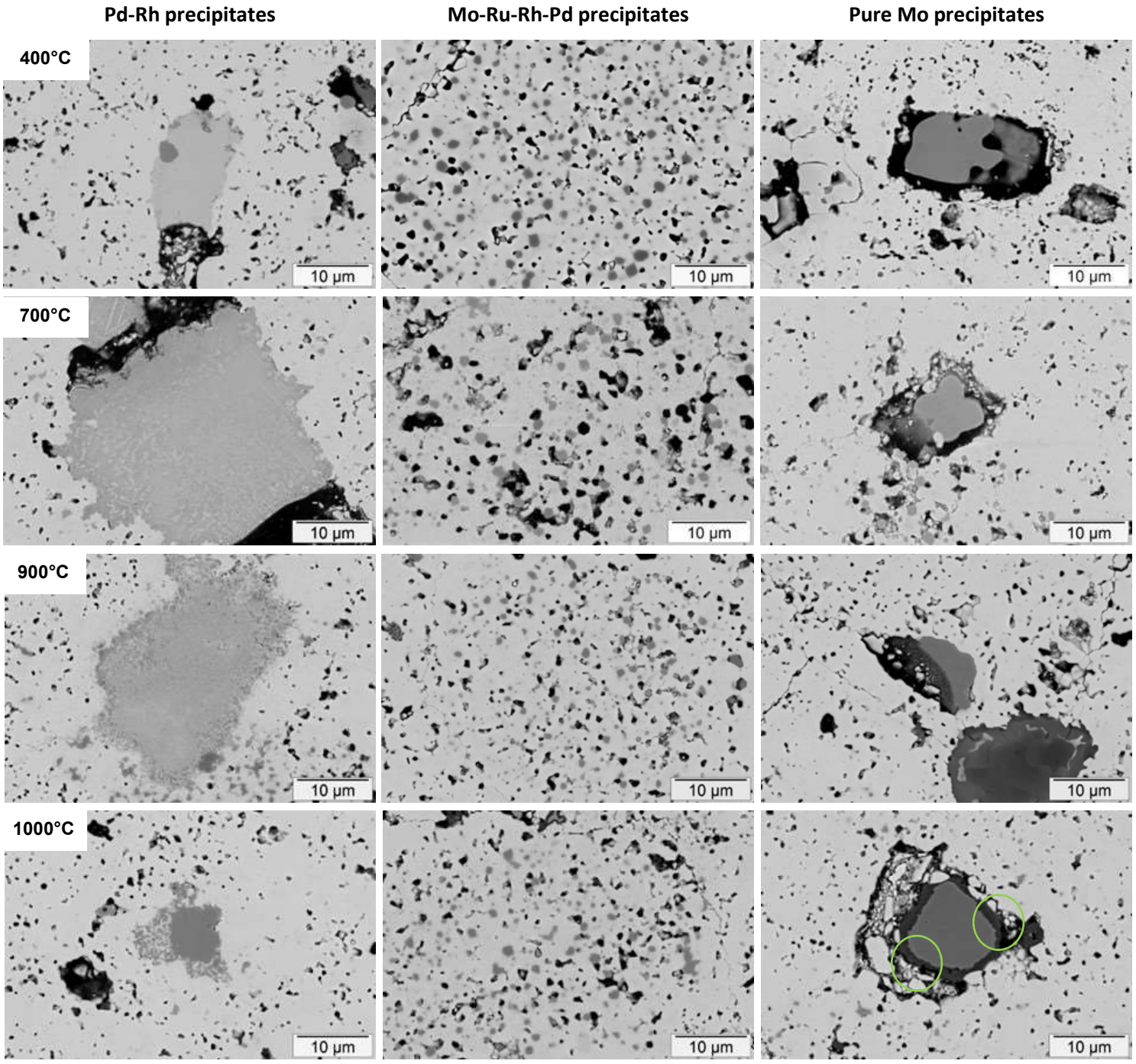

Figure III-21: SEM-BSE images of the different metallic precipitates in the SIMFuel samples annealed under oxidizing conditions

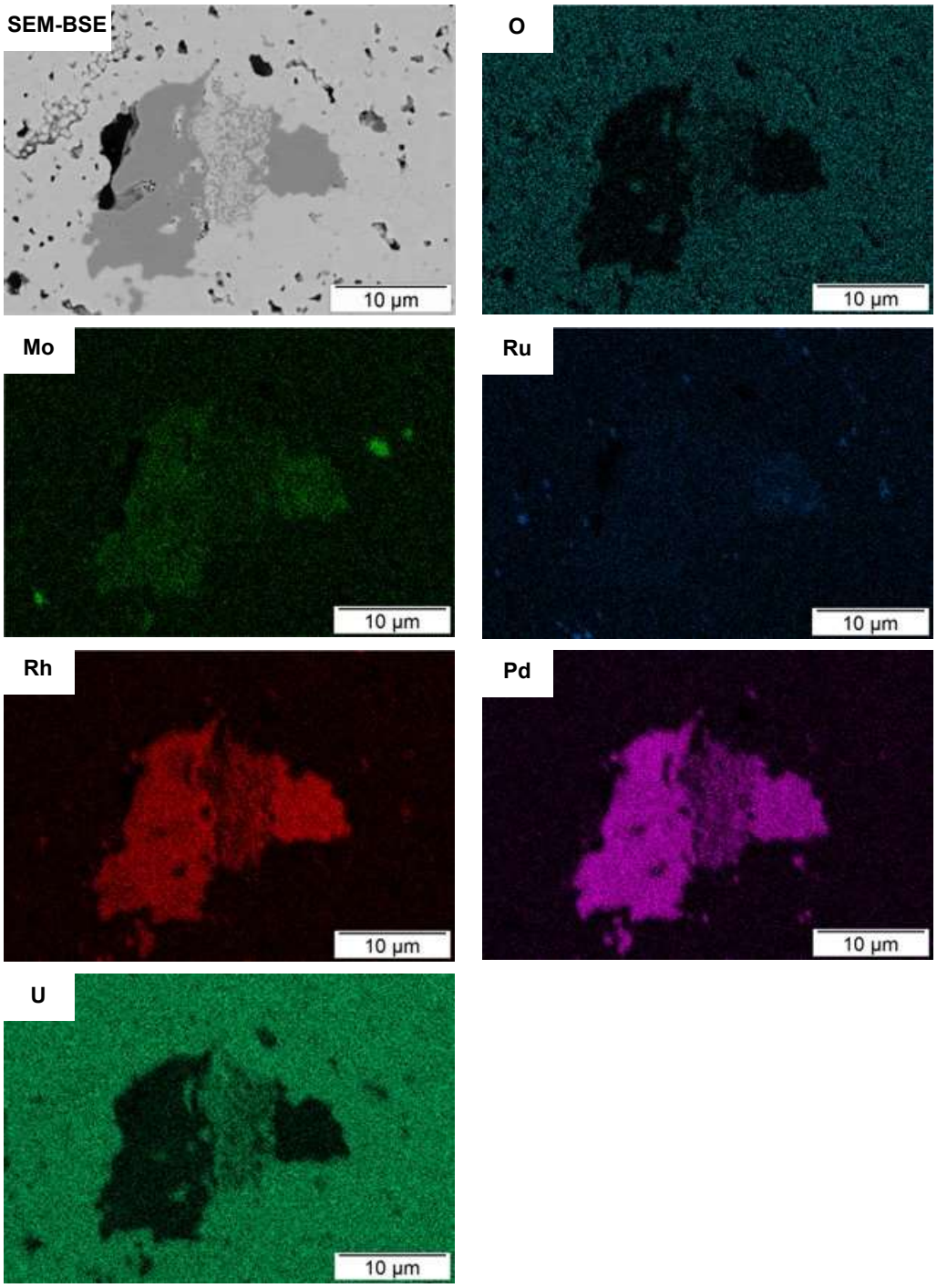

Figure III-22: SEM-SE image of typical Pd-Rh metallic precipitates (precipitates n°2 in Table B-9) found in the SIMFuel sample annealed up to 1000°C under oxidizing conditions, along with O, Mo, Ru, Rh, Pd and U X-ray maps (from top to bottom and left to right hand side).

Considering the Rh-Pd system in the samples above 400°C, two-phase precipitates are still observed in a wide range of composition due to the miscibility gap existing in the Pd-Rh binary diagram (**Figure III-23**) [37], [38]. Nevertheless, U and O are sometimes observed in these precipitates even at high temperature which does not enable to place the exact compositions of the precipitates on the Pd-Rh binary diagram.

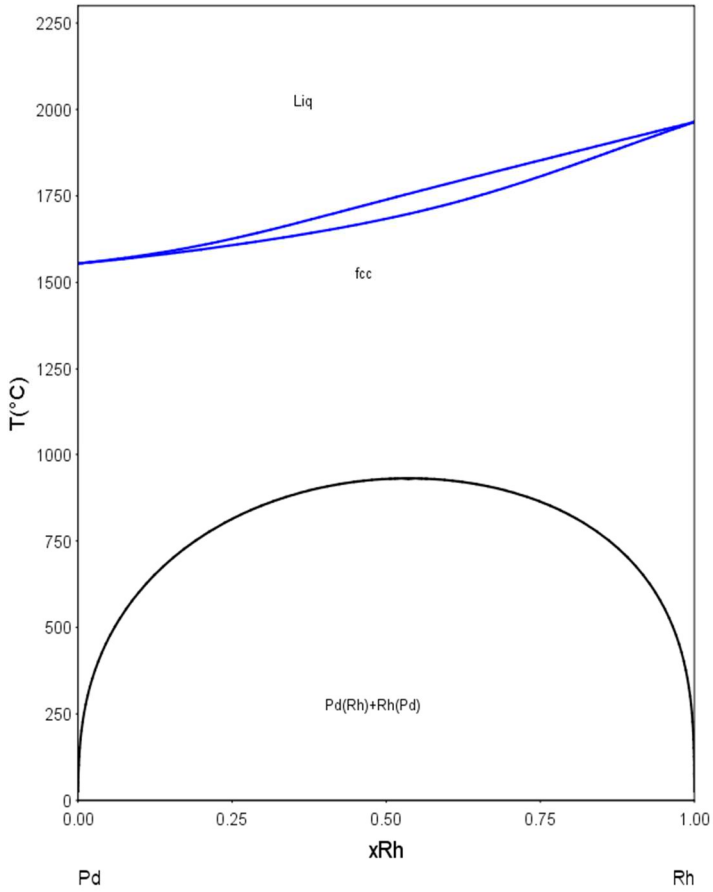

Figure III-23: Pd-Rh phase diagram calculated using Thermo-calc 4.1 softaware and the TAF-ID [39], [40]

Mo-Ru-Rh-Pd precipitates

As already observed through OM (**Figure III-20**), no evolution of the size and morphology of the Mo-Ru-Rh-Pd precipitates can be seen. Nevertheless, the EDX results obtained on the samples treated at 400°C, 700°C, 900°C and 1000°C given in **Appendix 2.3** (**Table B-10, Table B-11, Table B-12** and **Table B-13** respectively) indicate a decrease of the Mo amount in these precipitates, which contain almost exclusively Ru at 1000°C. As observed in the O1000 sample, all these precipitates are in the hcp domain of the Mo-Ru-Pd ternary diagram shown in **Figure III-24**.

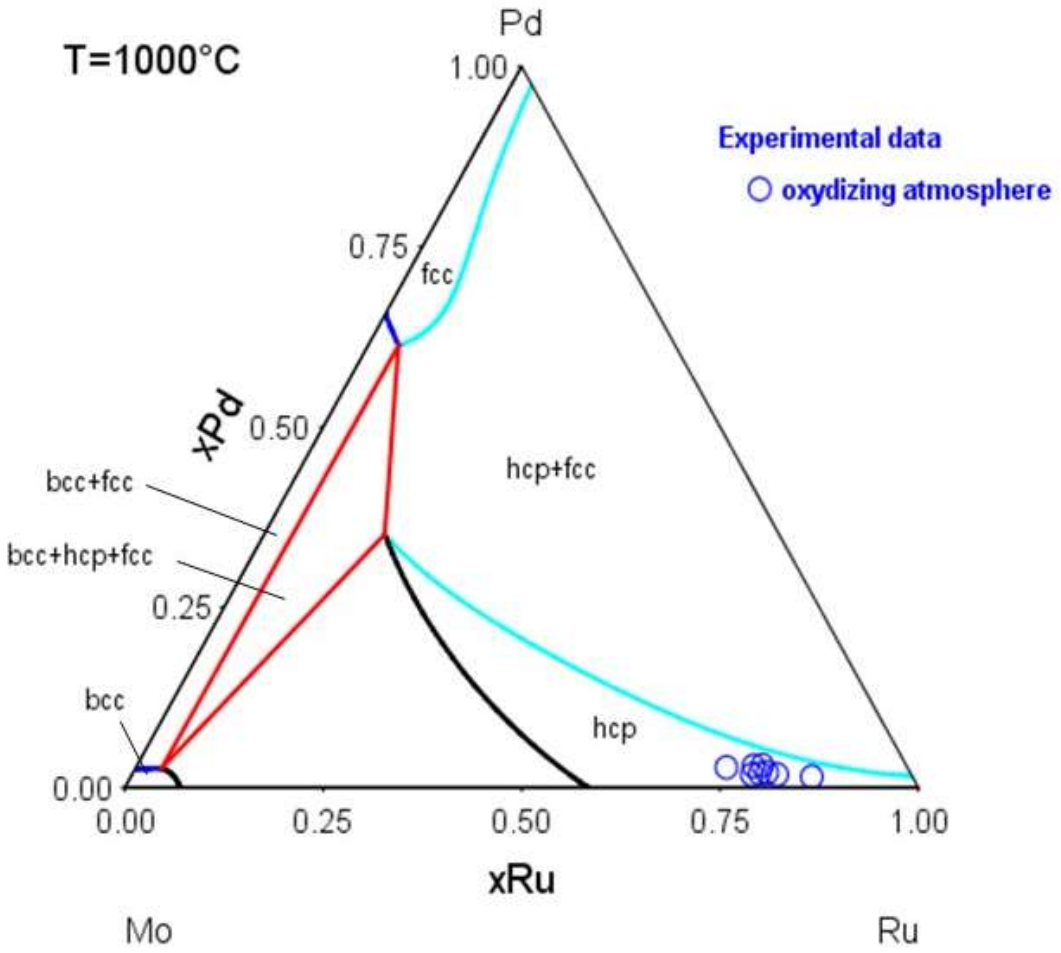

Figure III-24: Isothermal section of the ternary Mo-Ru-Pd system at 1000°C calculated using Thermo-Calc 4.1 software and the TAF-ID database [39], [40]

Pure Mo precipitates

According to the SEM-BSE pictures and the EDX results given in **Figure III-21** and **Appendix 2.3** (**Table B-14, Table B-15, Table B-16** and **Table B-17**) no change can be observed in the composition of the pure Mo metallic precipitates until 900°C. Between 900°C and 1000°C (green circles in **Figure III-21**), a darker layer forms on the edges of these precipitates on approximately 1.5 ± 0.8 µm. This layer corresponds to the purple layer observed with the OM (green circles in **Figure III-20**). According to the X-ray maps shown in **Figure III-25**, it is composed of Mo and O with an O/Mo ratio of 1.7 ± 0.1 determined by EDX (**Appendix 2.3**, **Table B-17**).

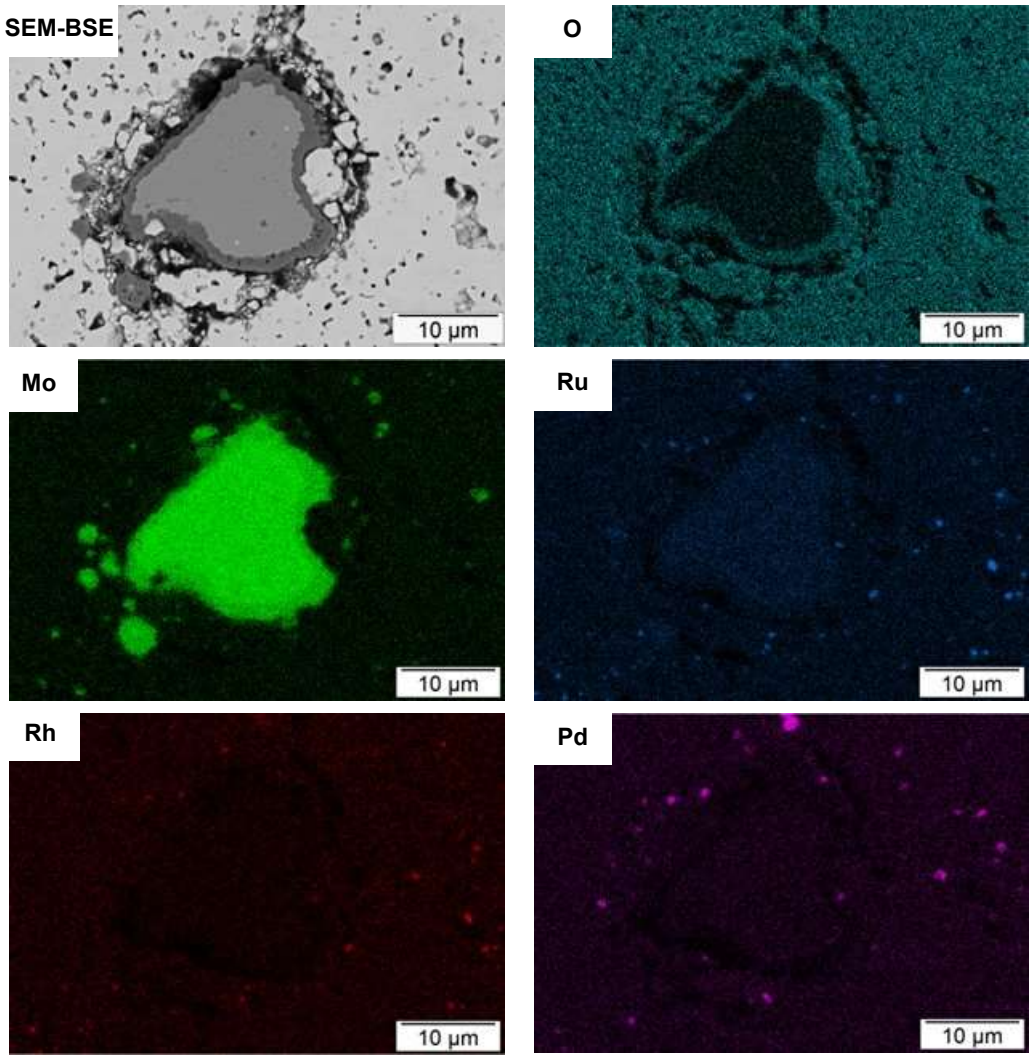

Figure III-25: SEM-SE image of typical Mo metallic precipitate (precipitate n°1 in Table B-17) found in the SIMFuel sample annealed up to 1000°C under oxidizing conditions, along with O, Mo, Ru, Rh and Pd X-ray maps (from top to bottom and left to right hand side).

III.3.2.1.2 XANES analyses

These observations are confirmed by the XANES analyses performed at Mo K-edge on the different samples. Indeed, as shown in **Figure III-26**, no evolution can be seen in the XANES spectra between the T_0 and the O700 samples. The XANES spectrum of the O1000 sample is very different from the others and the O900 one can be seen as an intermediate stage between the T_0 and O1000 spectra.

Indeed, the O900 XANES spectra is flattened compared to the T_0, O400 and O700 ones and the two peaks at 20.017 and 20.047 keV are not present anymore. The O1000 XANES spectrum is shrinked compared to the O900 one and a small prepic has appeared at 20.006 keV. The E_0 values of the O900 and O1000 samples are also higher compared to the E_0 of the other samples, indicating that at least part of Mo is oxidized in the O900 and O1000 samples (**Table III-8**).

The O1000 XANES spectrum was compared to the experimental spectra of bcc-metallic Mo, $BaMoO_4$, MoO_2 and to the calculated hcp-Mo and $BaMoO_3$, which are the main component suspected to form in this sample given the EDX results. As shown in **Figure III-27**, the overall shape of the O1000 spectrum is very close to that of MoO_2. The prepic at 20.006 keV is also present in the $BaMoO_4$ spectrum and is typical of Mo at an oxidation state of +VI (red dashed line in **Figure III-27**).

The results of the linear combination fitting (**Figure III-28**) indicate that 28 ± 2 % of Mo is present in the form of MoO_2 in the O900 sample. This part increases in the O1000 sample up to 84 ± 1 %. The part of Mo in the $BaMoO_4$ phase also increases from 2 ± 2% (1.2 at% considering the initial quantity of Mo in the SIMFuel samples given in **Table III-2**) at 900°C up to 11 ± 1 % (6.5 ± 1 at%) at 1000°C whereas the metallic Mo amount would decrease from 70 % (53 ± 2 % in bcc-Mo and 17 ± 2 % in hcp-Mo) down to 5 ± 1 % (bcc-Mo) in the metallic phase. According to the fit, no Mo would be present as $BaMoO_3$. The residual signal after the fit can be seen in **Figure B-4** (**Appendix 2.6**).

This tends to indicate that Mo would be oxidized further as the temperature is rising and would leave the Mo-Ru-Rh-Pd metallic precipitates as was indeed observed through SEM-EDX.

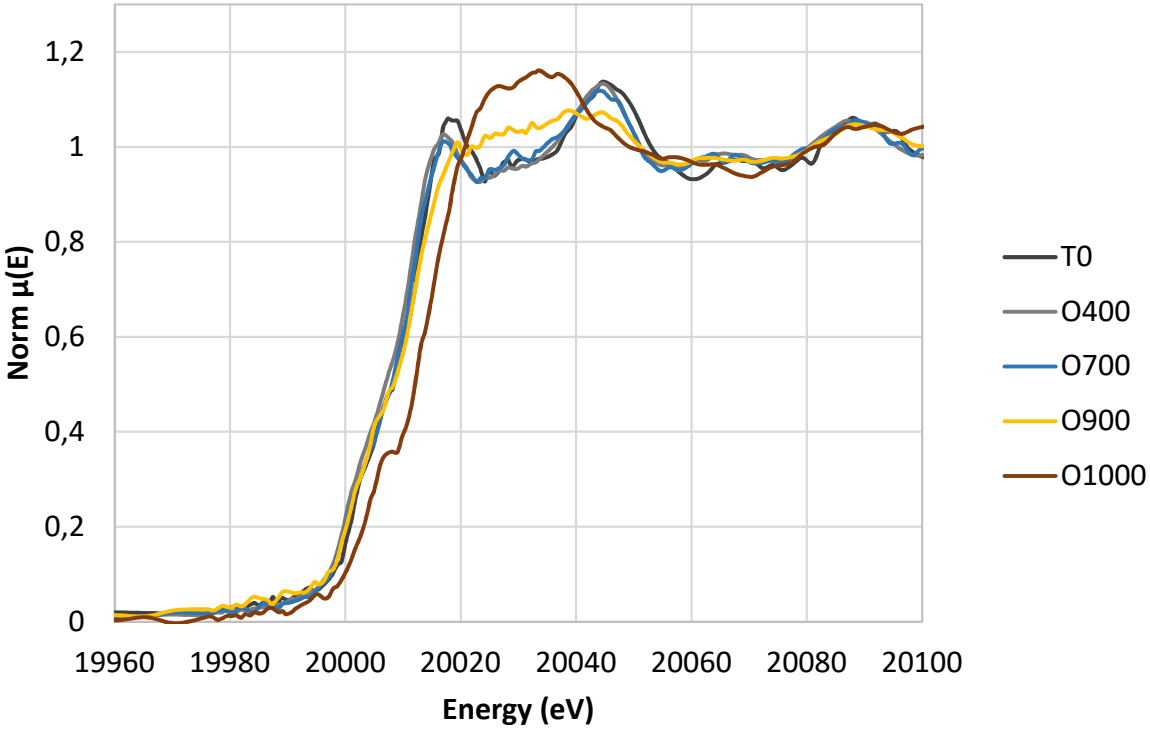

Figure III-26: Experimental XANES spectra of the samples as-sintered and treated at 400°C, 700°C, 900°C and 1000°C under oxidizing conditions obtained at the Mo K-edge on the MARS beamline (SOLEIL)

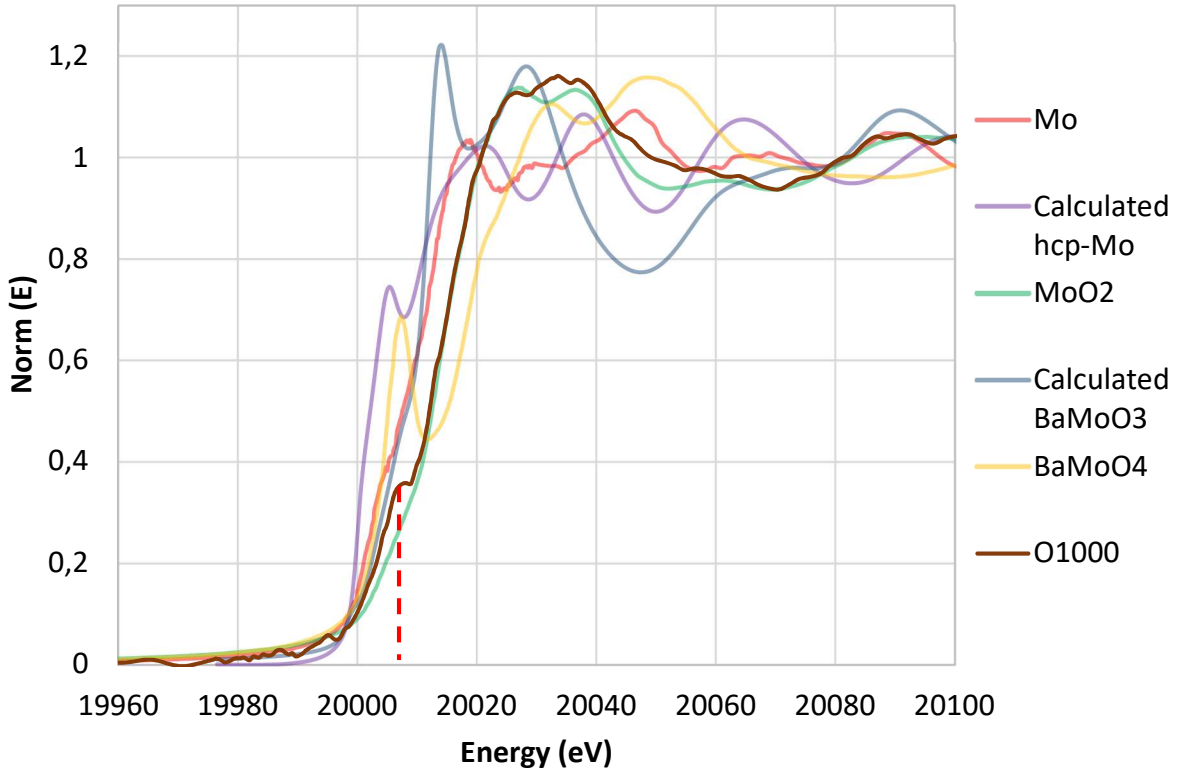

Figure III-27: Experimental XANES spectra of the sample treated up to 1000°C under oxidizing atmosphere, metallic Mo (bcc), MoO_2, $BaMoO_4$ obtained at the Mo K-edge on the MARS beamline (SOLEIL) and calculated XANES spectra of metallic Mo (hcp) and $BaMoO_3$

Table III-8: E_0 position of the samples treated under oxidizing conditions and references spectra collected at the Mo K-edge (the uncertainty on the energy is 0.6 eV)

	Mo K-edge
Sample	**E_0 (eV)**
$BaMoO_4$	20019.4
MoO_2	20013.3
Mo (bcc, hcp)	20000.0
T_0	20001.0
O400	20000.0
O700	20000.0
O900	20011.8
O1000	20012.3

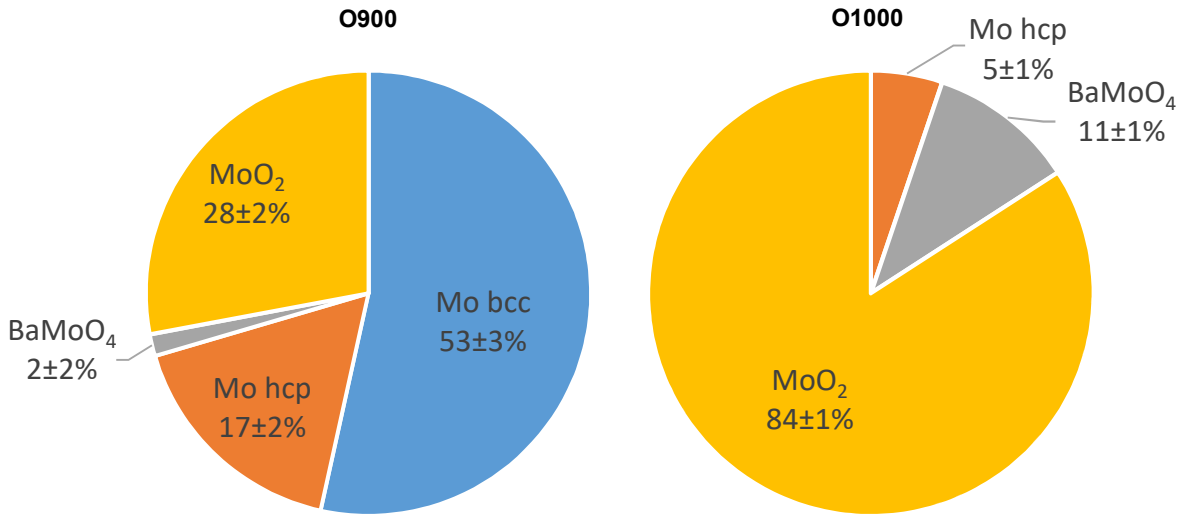

Figure III-28: Linear combination fitting results performed between -20 and +60 eV around Mo absorption edge of the samples O900 (left, R factor = 0.003374) and O1000 (right, R factor = 0.001380)

III.3.2.2 Oxide precipitates

III.3.2.2.1 SEM-EDX analyses

In the T_0 sample, Ba was found in oxide precipitates with a core-shell morphology. It was whether dissolved in the (U, Zr)O_2 areas of these precipitates or in the shell, as $Ba_{0.8}Sr_{0.2}ZrO_3$. The core of the precipitates was composed of ZrO_2.

SEM-BSE pictures of the evolution of the oxide precipitates under oxidizing conditions are shown in **Figure III-29**. In the sample annealed at 900°C a darker area corresponding to a Mo-rich zone can be observed starting from the edges of few oxide precipitates (blue circles in **Figure III-29**). The quantity of Mo present in the oxide precipitates increases in the O1000 sample (**Figure III-30**).

The compositions of the oxide precipitates after annealing under oxidizing conditions are given in **Appendix 2.3** (**Table B-18, Table B-19, Table B-20** and **Table B-21**). The results are consistent with the previous observations: the composition remains unchanged until 700°C. Between 700°C and 900°C Mo starts to migrate toward the oxide precipitates leading to the formation of a phase containing Ba, Sr, Mo, Zr and O with a Ba/Mo ratio of 0.9 ± 0.1, a Ba/Zr ratio approximately equal to 0.5 ± 0.1 and an increased amount of oxygen (O/Zr of 3.4 ± 0.5). The Ba/Mo ratio is consistent with one of the phases observed by Geiger [1], [21], [22] in its SIMFuel samples treated in oxidizing conditions at 1200°C, and identified as $BaMoO_4$.

400°C

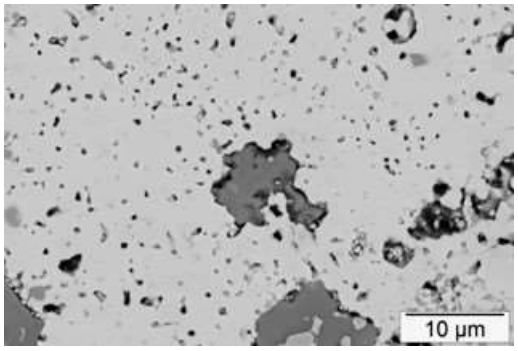

700°C

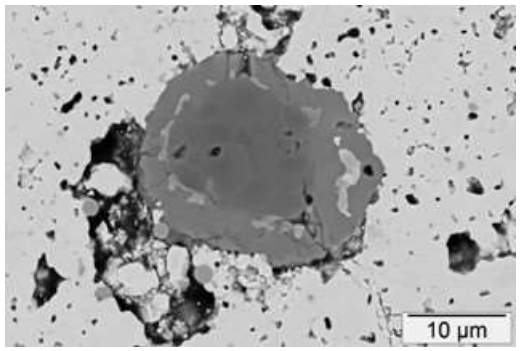

900°C

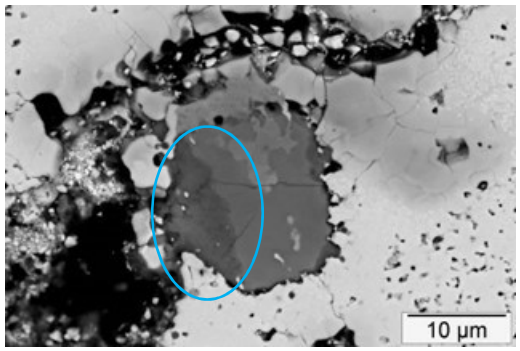

1000°C

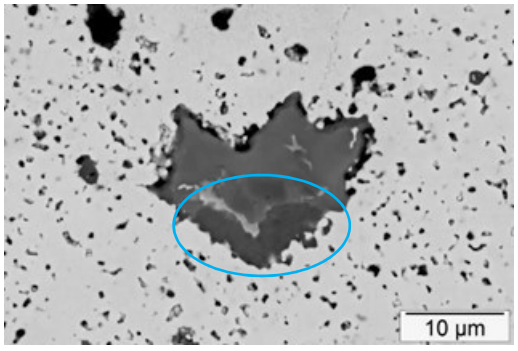

Figure III-29: SEM-BSE images of the oxide precipitates in the SIMFuel samples annealed under oxidizing conditions

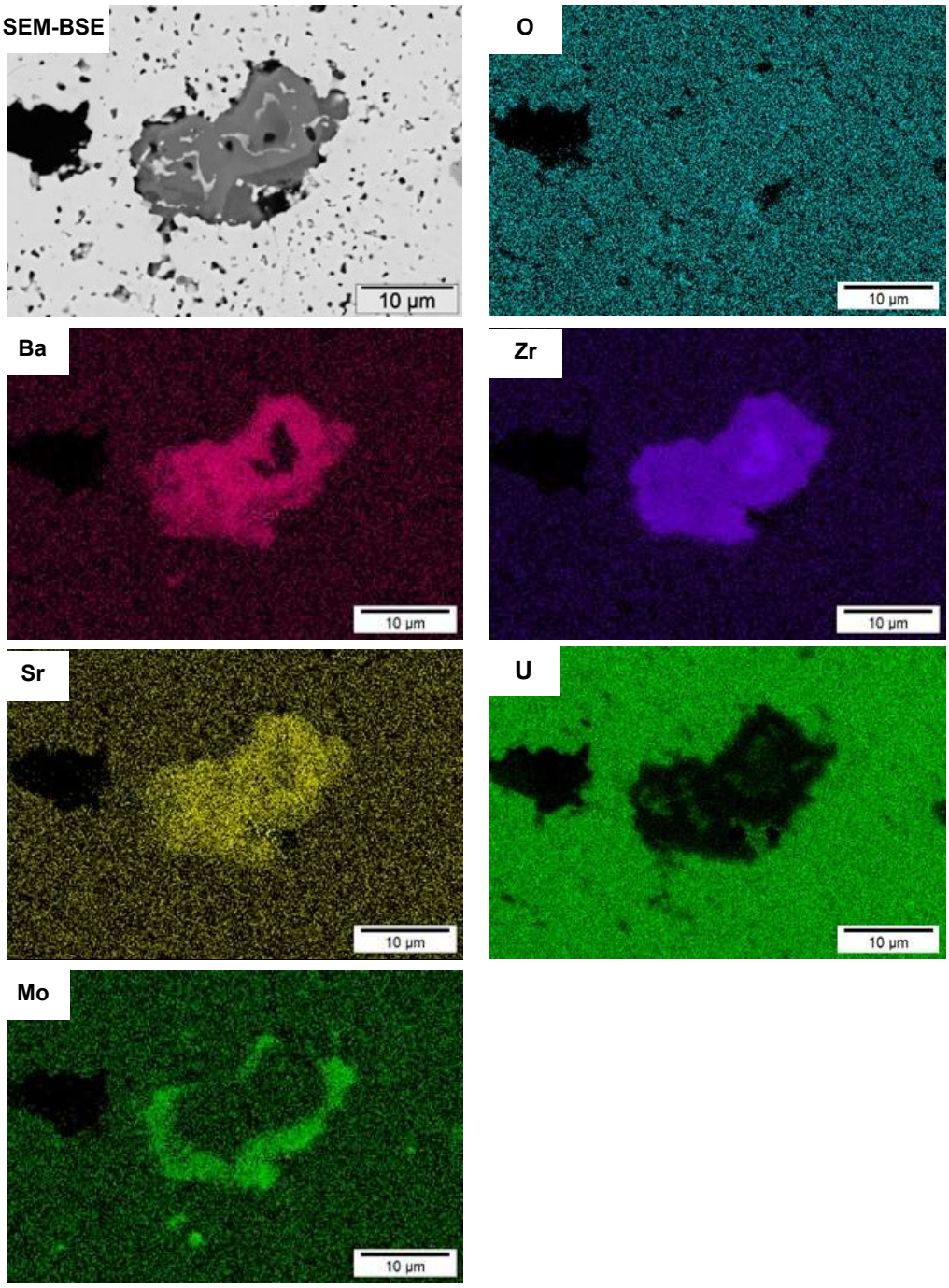

Figure III-30: SEM-SE image of typical oxide precipitate (precipitate n°5 in Table B-21) found in the SIMFuel sample annealed up to 1000°C under oxidizing conditions, along with O, Ba, Zr, Sr, U and Mo X-ray maps (from top to bottom and left to right side).

III.3.2.2.2 XANES analyses

In order to conclude on the nature of this phase, HERFD-XANES analyses were performed at Ba L_3-edge on both O900 and O1000 samples and compared to the T_0 spectrum as shown in **Figure III-31**. A broadening of the white line is seen in the O1000 spectrum and the oscillations observed between 5.255 and 5.280 keV are flattened.

Given the results of EDX measurements, the O900 and O1000 XANES spectra have been fitted using the experimental HERFD-XANES spectra of BaO, $BaZrO_3$, $BaMoO_4$ and the calculated spectrum of $BaMoO_3$ (**Figure III-32**). The results of the fit are given in **Appendix 2.6** (**Figure B-6** and **Figure B-8**

respectively) and synthesized in **Figure III-33**. The amount of Ba found in the $BaZrO_3$ and BaO phases would decrease from 71 ± 1 % (13.5 at% in the whole sample) and 15 ± 1% respectively in the O900 sample down to 51 ± 1 % (9.7 at% in the whole sample) and 9 ± 1 % in O1000. On the contrary, the Ba content in $BaMoO_4$ rises from 10 ± 1 % (1.9 at%) in O900 up to 37 ± 1 % (7.0 at%) in the O1000 sample. These values are very consistent with the quantity of Mo calculated to be present in the $BaMoO_4$ phase thanks to the fit results, within the uncertainties (Ba/Mo = 1.1 in the O1000 sample). Ba contained in $BaMoO_3$ is almost constant in both samples (4 ± 1 % in O900 compared to 3 ± 1 % in O1000) but no Mo was found to be present in the $BaMoO_3$ phase in the fit.

XANES experiments were performed at Zr K-edge on all the samples treated in oxidizing conditions (**Figure III-34**). Again, an evolution is observed at 900°C. Indeed, the peaks present at 18.017 and 18.027 keV in the T_0 spectrum progressively disappear and the white line tends to shrink.

Figure III-35 shows the O1000 spectrum compared to the experimental m-ZrO_2, $BaZrO_3$ and the calculated c-ZrO_2 and $SrZrO_3$ spectra. The results of the fit of the O900 and O1000 spectra using these references are shown in **Appendix 2.6** (**Figure B-5** and **Figure B-7** respectively). They indicate that the quantity of Zr in the zirconate phase decreases for the benefit of zirconia. Indeed as shown in **Figure III-36**, the amount of Zr contained in the zirconate phase decreases from 37 % in O900 down to 18 % in O1000 when the Zr amount in the zirconia phase increases from 63 to 80 %. Within the zirconate phase, 27 ± 2 % (15.7 at% considering the initial quantity of Zr in the SIMFuel samples given in **Table III-2**) of the Zr is in the $BaZrO_3$ and 10 ± 2 % (5.8 at%) is in the $SrZrO_3$ at 900°C towards 11 ± 3 % (4.1 at%) and 7 ± 2 % (6.8 at%) respectively at 1000°C. The amount of Zr present in the $BaZrO_3$ phase is almost 2 times lower than the amount of Ba in the same phase which is consistent with the residual signal obtained after the fit of the O1000 sample (**Figure B-7**). Indeed, once again, the shape of the white line has not been correctly reproduced (the two peaks also present at 18.017 and 18.027 keV on the $BaZrO_3$ spectrum, highlighted with the red dashed lines in **Figure III-35**, have been flattened) probably leading to an underestimation of the Zr amount in $BaZrO_3$.

The E_0 values for each sample are given in **Table III-9** along with the references ones. They remain unchanged for both Ba and Zr, even at 1000°C confirming that these elements are not further oxidized compared to the T_0. Thus, Ba remains in an oxidation state of +II and Zr has probably an oxidation state of +IV.

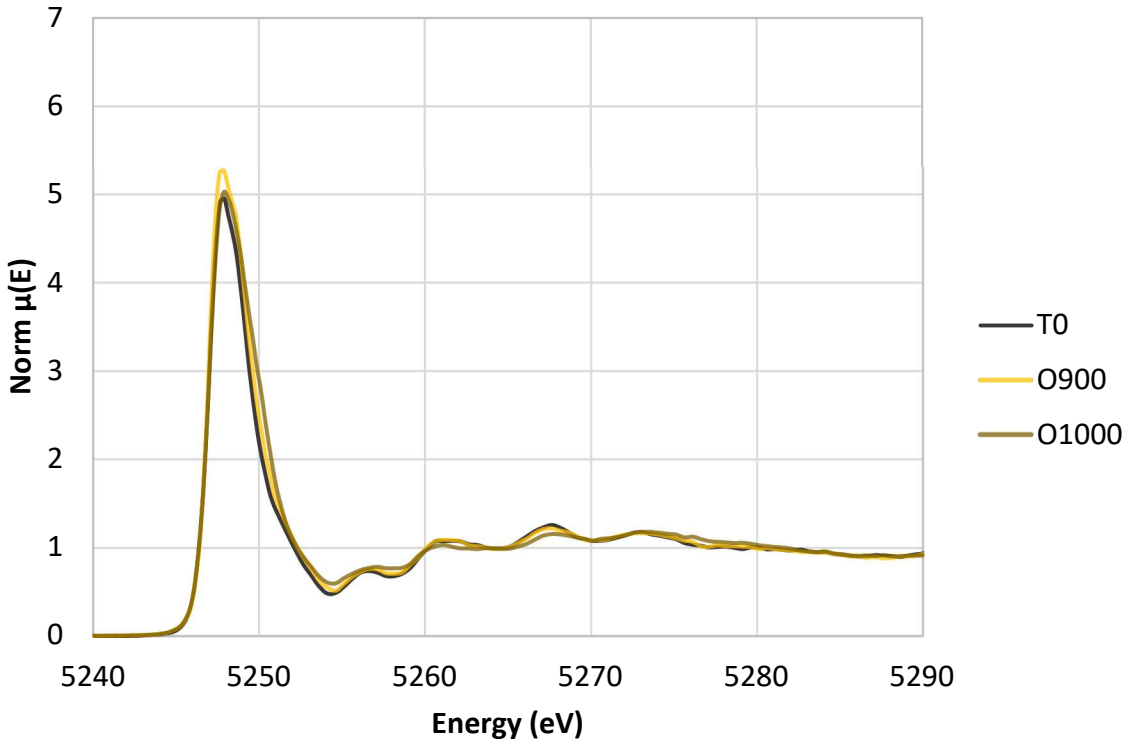

Figure III-31: Experimental HERFD-XANES spectra of the samples as-sintered and treated at 900°C and 1000°C under oxidizing conditions obtained at the Ba L_3-edge on the FAME-UHD beamline (ESRF)

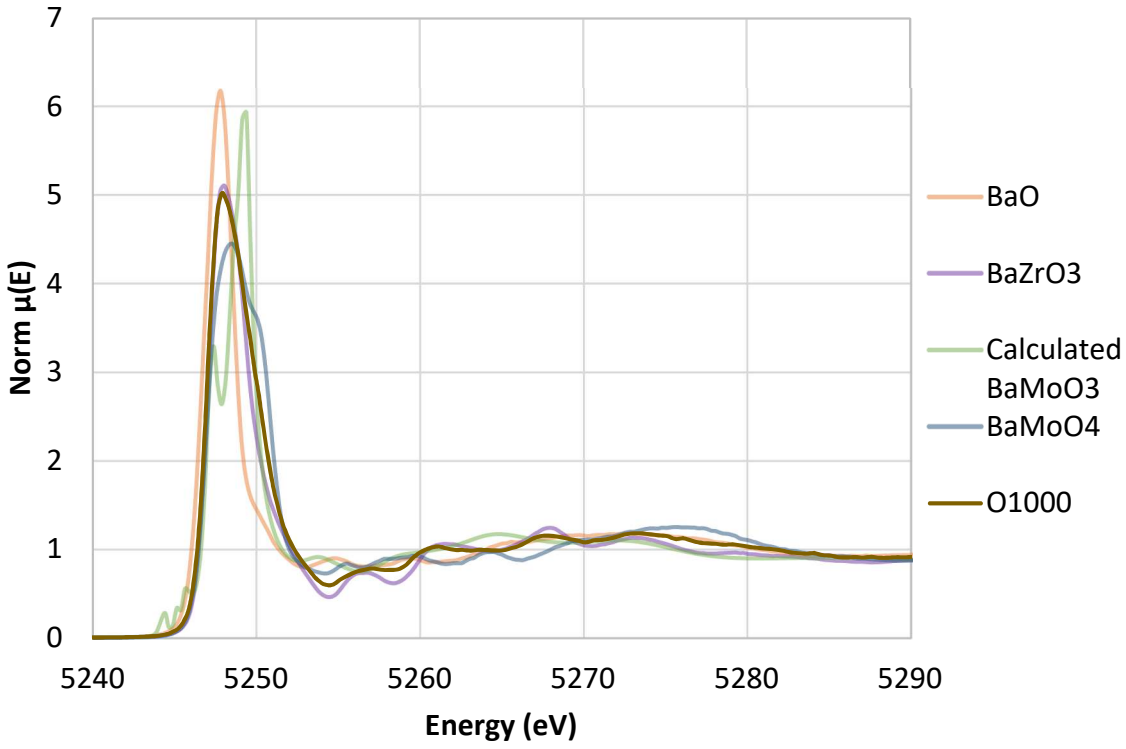

Figure III-32: Experimental XANES spectra of the sample treated up to 1000°C under oxidizing conditions, BaO, $BaZrO_3$ and $BaMoO_4$ obtained at the Ba L_3-edge on the FAME-UHD beamline (ESRF) and calculated XANES spectrum of $BaMoO_3$

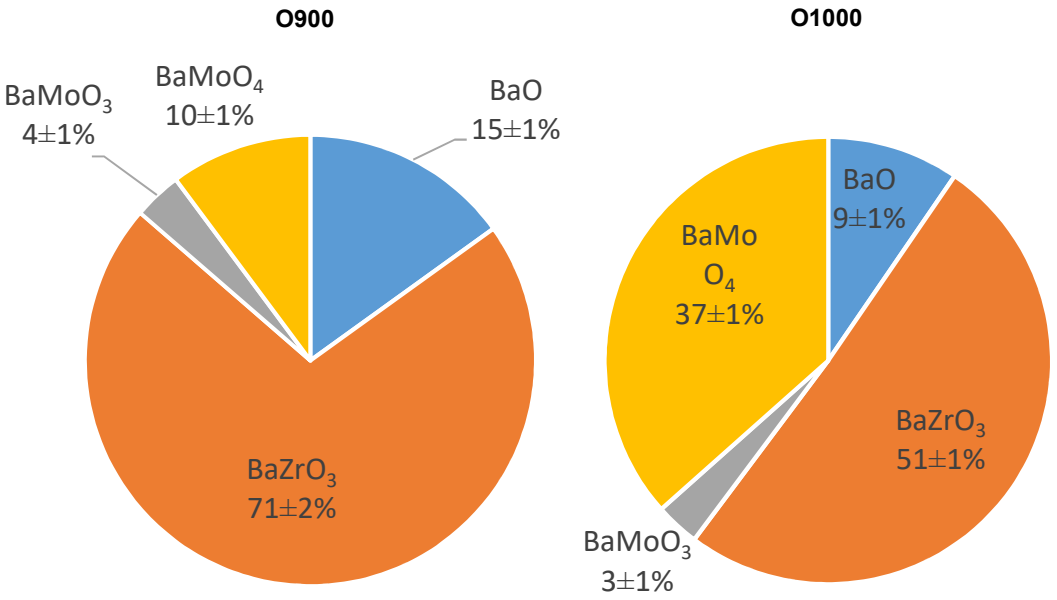

Figure III-33: Linear combination fitting results performed between -20 and +60 eV around Ba L_3-absorption edge of the samples O900 (left, R factor = 0.001869) and O1000 (right, R factor = 0.001056)

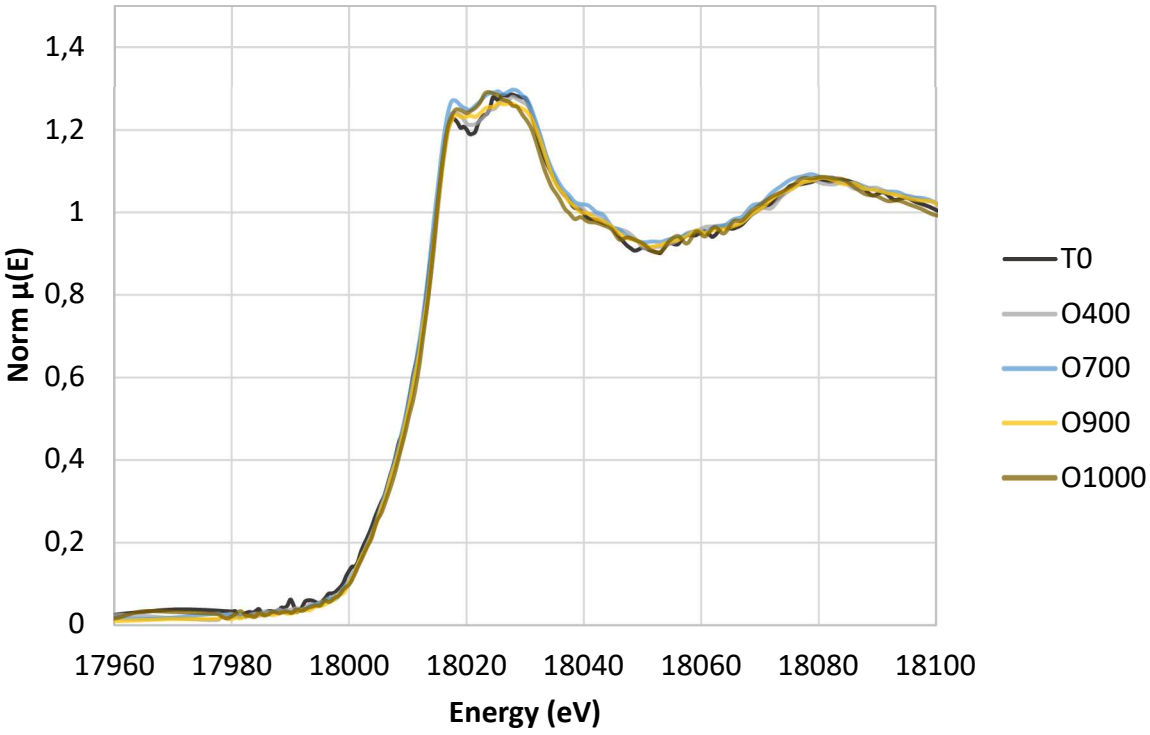

Figure III-34: Experimental XANES spectra of the samples as-sintered and treated at 400°C, 700°C, 900°C and 1000°C under oxidizing atmosphere obtained at the Zr K-edge on the MARS beamline (SOLEIL)

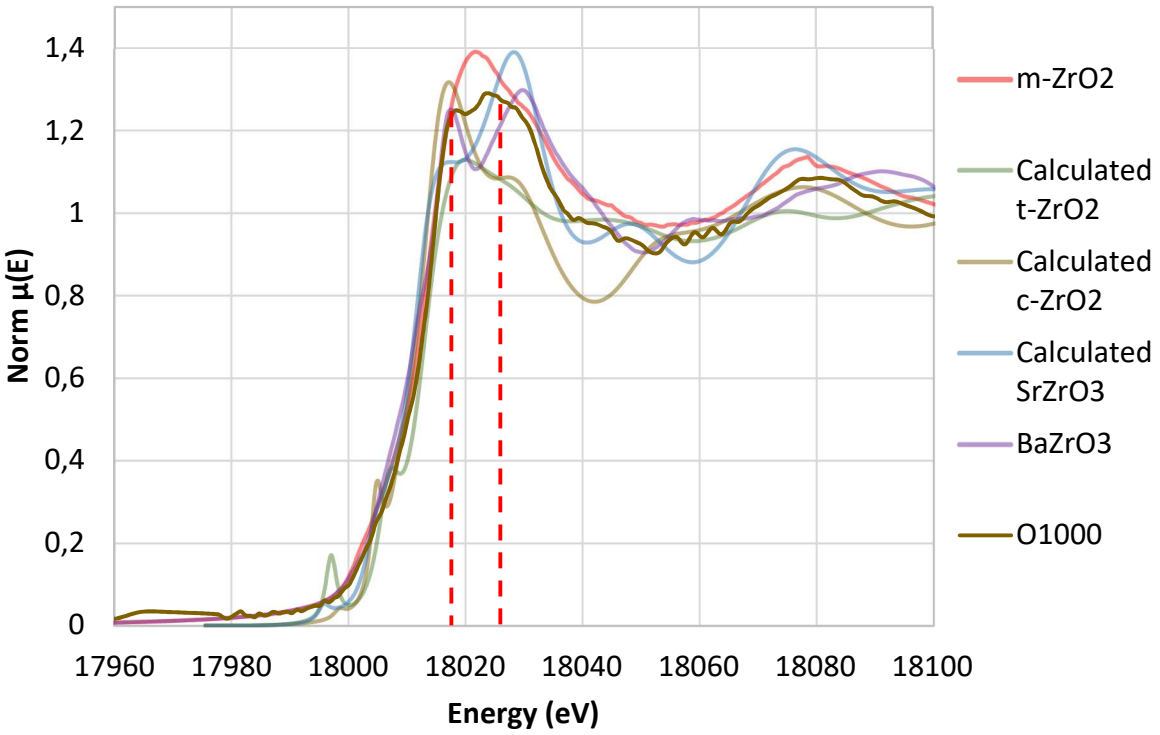

Figure III-35: Experimental XANES spectra of the sample treated up to 1000°C under oxidizing conditions, m-ZrO_2 and $BaZrO_3$ obtained at the Zr K-edge on the MARS beamline (SOLEIL) and calculated XANES spectra of t-ZrO_2, c-ZrO_2 and $SrZrO_3$

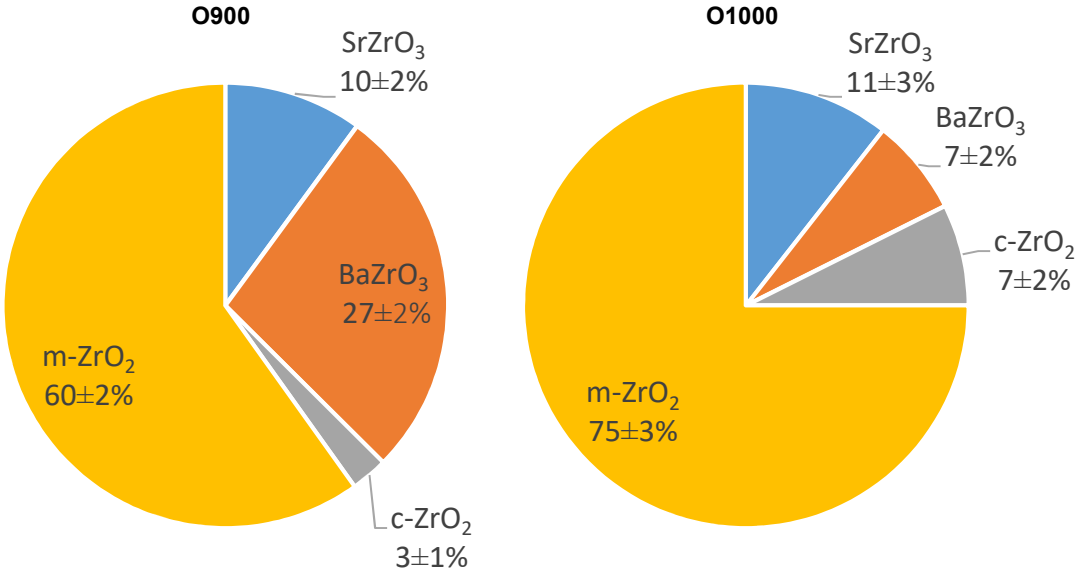

Figure III-36: Linear combination fitting results performed between -20 and +60 eV around Zr K-absorption edge of the samples O900 (left, R factor = 0.001147) and O1000 (right, R factor = 0.002769)

Table III-9: E_0 of the samples treated under oxidizing conditions and references spectra collected at Ba L_3-edge and Zr and K-edge (the uncertainty on the energy is 0.6 eV)

	Ba L_3-edge	Zr K-edge
Sample	**E_0 (eV)**	**E_0 (eV)**
BaO	5248.1	-
$BaZrO_3$	5247.9	18015.4
$BaMoO_3$	5247.9	-
$BaMoO_4$	5247.7	-
$SrZrO_3$	-	18015.4
ZrO_2 (c and m)	-	18013.5
T_0	5247.8	18014.1
O400	-	18015.0
O700	-	18014.1
O900	5247.9	18014.7
O1000	5247.9	18014.7

III.3.2.3 Discussion on the observations made in the samples treated in oxidizing conditions

All these results seem to show that between 900°C and 1000°C in oxidizing conditions, oxygen diffusion takes place from the UO_{2+x} matrix to the metallic precipitates leading to the formation of MoO_2. In the very small precipitates present in the SIMFuel samples (Mo-Ru-Rh-Pd ones), the whole Mo content would thus be oxidized at 1000°C whereas in the bigger ones (pure Mo ones), only the periphery reacted, due to the limited duration of the thermal treatments.

This buffer effect of the Mo/MoO_2 redox couple is well known in the PWR fuels [17], [41]–[43] and predicted by thermodynamic calculation (**Figure III-4**). Moreover, early Mo release probably takes place as MoO_2 (which is gaseous around 1100°C).

Then, MoO_2 would first dissolve in the UO_{2+x} matrix allowing Mo to migrate to the periphery of the oxide precipitates driven by the excess of oxygen in the $(Ba_{1-x}Sr_x)ZrO_3$ phase. It would then react with the Ba contained in $BaZrO_3$ probably forming $BaMoO_3$ which would be dissolved in $BaZrO_3$ until its solubility limit is reached [17], [18], [31]. Finally, $BaMoO_4$ would start to precipitate consuming the remaining BaO amount dissolved in the ZrO_2 phase and Ba present in $BaZrO_3$. This would thus lead to the formation of more ZrO_2 through the decomposition of $BaZrO_3$.

The observation of metallic precipitates partially oxidized and a Ba, Mo, Zr and O phase, instead of separate $BaMoO_4$ and ZrO_2 phases may be explained by kinetics. Indeed, the duration of the test was 2h at 1000°C which might not have allowed thermodynamic equilibrium to take place. A mechanism is proposed in **Figure III-37** to explain the formation of the molybdate phase at the periphery of the oxide precipitates.

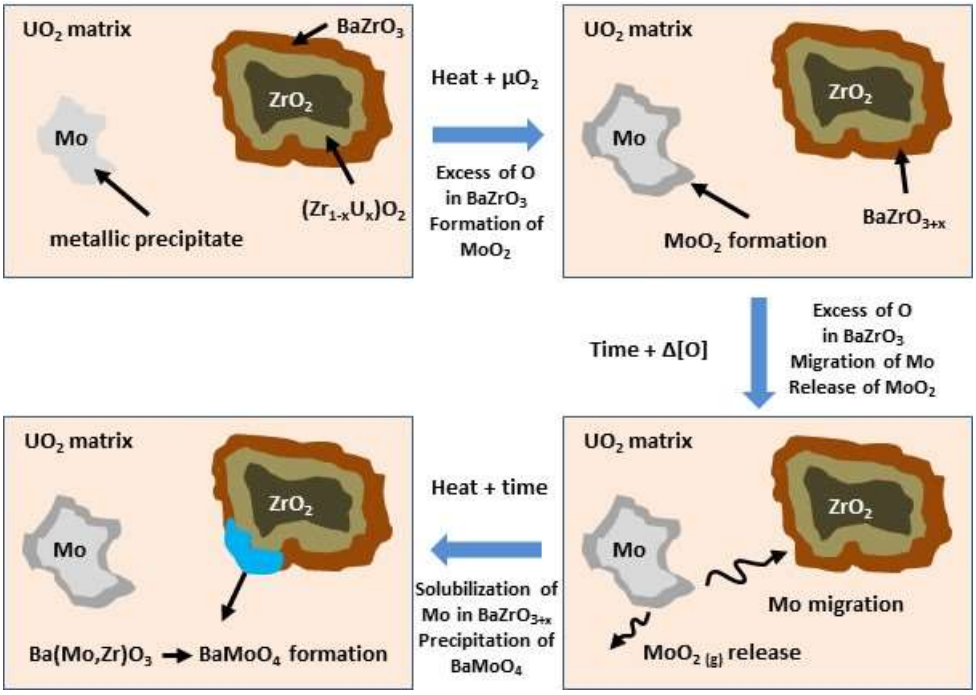

Figure III-37: Schematic mechanism for the evolution of the metallic and oxide precipitates in oxidizing atmosphere

III.3.3 Samples treated in reducing conditions

Under reducing conditions, the different types of precipitates are still observed in the SIMFuel samples, even after annealing at 1700°C (**Figure III-38**). The size and morphologies of the oxide precipitates and pure Mo ones are not modified until 1700°C (**Table III-10**) whereas the precipitates composed of Pd-Rh exhibit a change in their morphology, forming smaller precipitates at 700°C (red circles) as already noticed in the O700 sample. At 1700°C, most of the oxide precipitates do not exhibit a core-shell structure anymore.

400°C

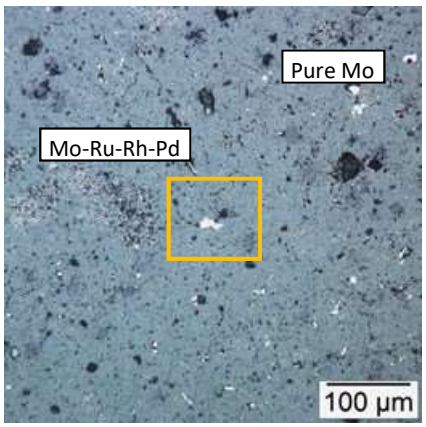

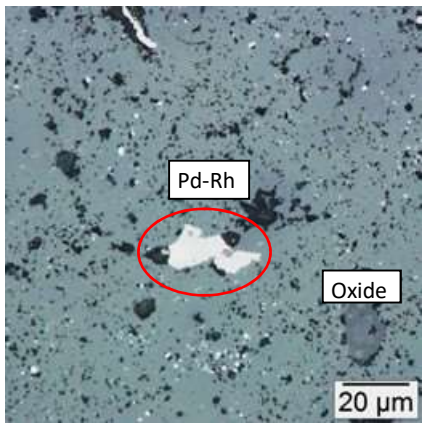

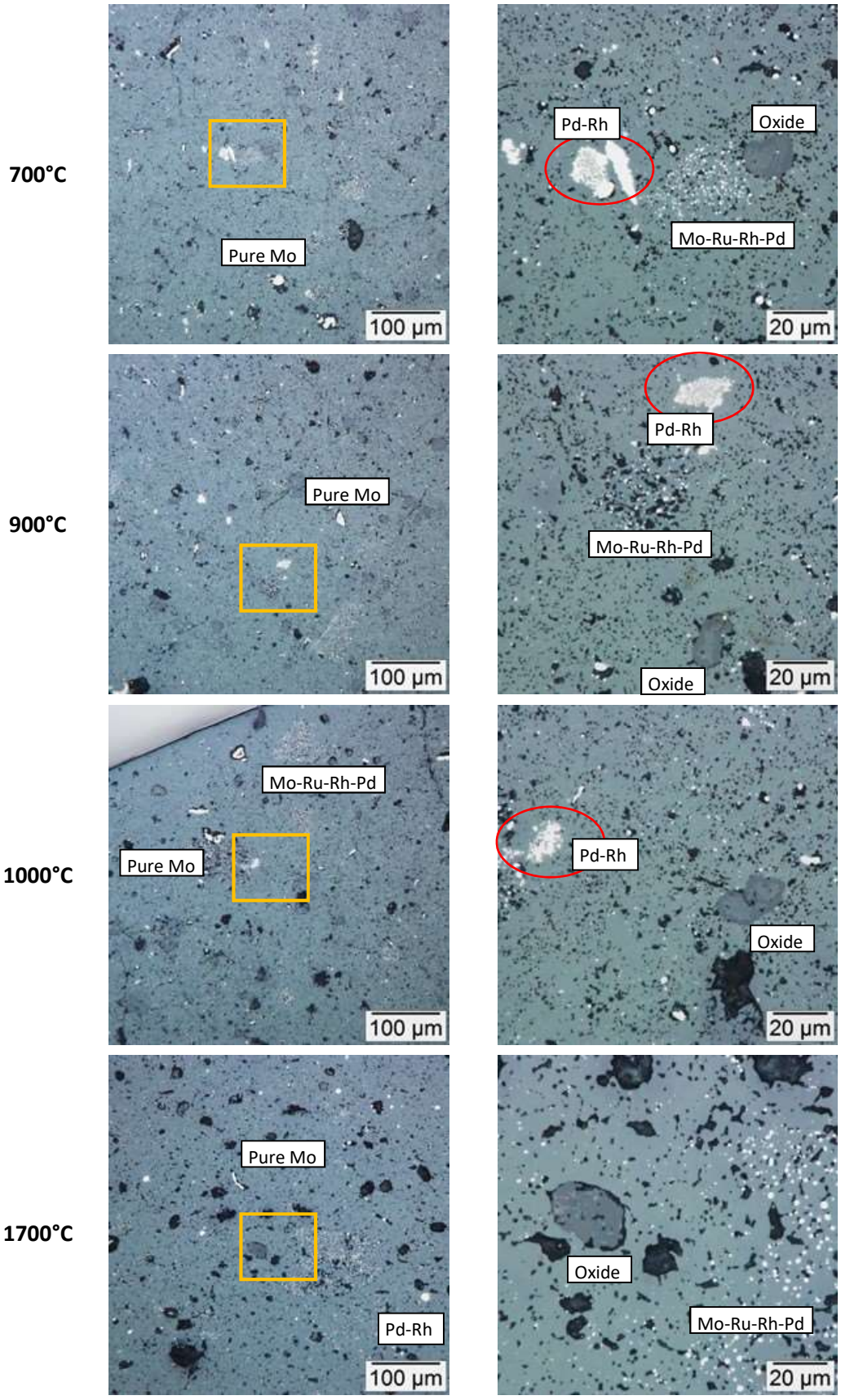

Figure III-38: Evolution of the different precipitates with temperature under reducing atmosphere observed through OM (Pd-Rh precipitates in the red circles). The OM images on the right are taken at higher magnification in the yellow frames shown on the left images.

Table III-10: Summary of oxide and Mo-Ru-Rh-Pd metallic precipitates sizes (average on 30 measurements)

Temperature (°C)	Precipitate size (µm)	
	Oxide precipitates	Mo-Ru-Rh-Pd precipitates
R400	17.0 ± 6.5	0.7 ± 0.3
R700	14.7 ± 4.4	0.9 ± 0.4
R900	15.9 ± 6.5	0.9 ± 0.4
R1000	19.7 ± 10.1	0.7 ± 0.4
R1700	19.5 ± 6.2	0.8 ± 0.4

III.3.3.1 Metallic precipitates

III.3.3.1.1 SEM-EDX analyses

SEM-BSE pictures of the evolution of the different metallic precipitates after annealing in reducing conditions are shown in **Figure III-39**. As already observed through OM, the morphology of these phases remains unchanged until 1700°C, except for precipitates composed of Mo-Ru-Rh-Pd which become more spherical, and the one composed of Pd-Rh. The morphology of these precipitates changes at 700°C and the amount of U decreases, just as what was observed in the O700 sample. However at 1700°C, larger two-phase precipitates are found.

Pd-Rh precipitates

The compositions of the Pd-Rh precipitates are given after annealing in **Appendix 2.4** (**Table B-22, Table B-23, Table B-24, Table B-25** and **Table B-26**). A phase rich in Pd and another one rich in Rh are still observed after annealing at different temperature as already observed in oxidizing conditions.

The morphological change of these intermetallic precipitates happens above 400°C in both reducing and oxidizing atmospheres due to the high enough oxygen potential that favors the oxidation of the U contained in these precipitates into UO_2 [17], [19], [20], [36]. Indeed, the O/U ratio is approximately 2 (notably in the case of precipitate n°5 in **Table B-23** or n°2 in **Table B-24**).

On the last SEM image of **Figure III-39**, a typical biphasic precipitate found in the sample R1700 can be observed (precipitate n°1 in **Table B-26**). The light grey region corresponds to the Pd-rich phase whereas the Rh-rich one appears in a darker shade of grey. According to **Figure III-23**, at 1700°C the Pd-Rh precipitates should exhibit a single composition and be in a liquid state or in a solid fcc phase partly molten depending on their initial composition in Pd. Thus, a demixion of these precipitates may have taken place during the cooling stage resulting in a Rh-rich and a Pd-rich phases as soon as the miscibility gap region of the Pd-Rh binary phase diagram was reached.

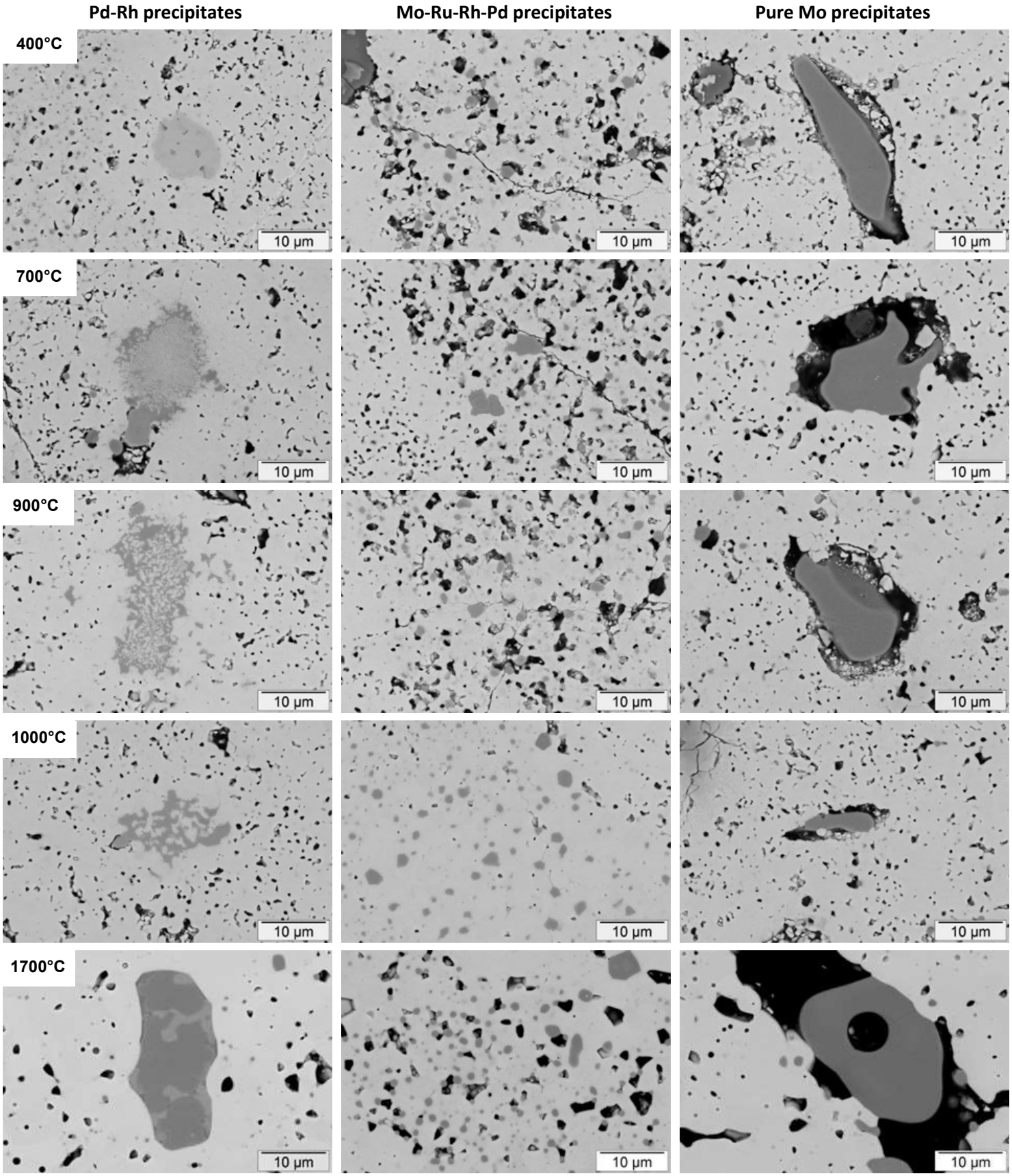

Figure III-39 : SEM-BSE images of the different types of metallic precipitates in the SIMFuel samples annealed under reducing conditions

Mo-Ru-Rh-Pd precipitates

The compositions of the Mo-Ru-Rh-Pd metallic precipitates in the samples treated at 400°C, 700°C, 900°C, 1000°C and 1700°C are given in **Appendix 2.4** (**Table B-27, Table B-28, Table B-29, Table B-30** and **Table B-31** respectively). At 1700°C the majority of the precipitates exhibit the same Ru/Mo ratio of around 1.67. The major part of the Mo-Ru-Rh-Pd precipitates is found in the hcp domain but one is in the bcc+hcp domain (**Figure III-40**).

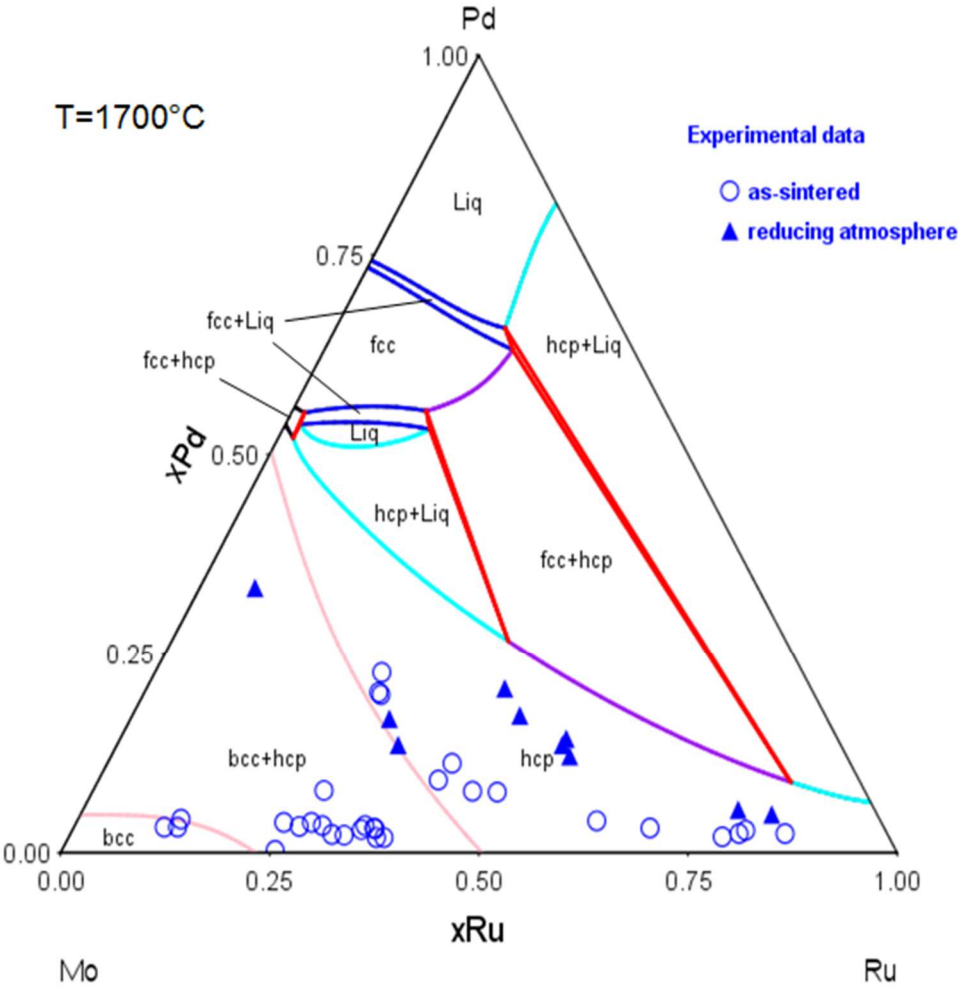

Figure III-40: Isothermal section of the ternary Mo-Ru-Pd system at 1700°C calculated using Thermo-Calc 4.1 software and the TAF-ID database [39], [40]. The experimental data obtained on the samples T_0 and R1700 have been reported on this diagram.

Pure Mo precipitates

Concerning the pure Mo metallic precipitates, their composition remains unchanged even at 1700°C as shown in **Appendix 2.4** (**Table B-32, Table B-33, Table B-34, Table B-35** and **Table B-36**).

III.3.3.1.2 XANES analyses

The normalized XANES spectra collected at the Mo K-edge on the samples T_0, R400, R700, R900, R1000 and R1700 are presented in **Figure III-41**. No strong evolution can be observed on the different samples' spectra except concerning the small oscillation at 20.029 keV which disappears completely in the R1700 spectrum. This oscillation is typical for the bcc-metallic Mo and is not observed on the hcp-Mo XANES spectrum as shown in **Figure III-42** (blue dashed line). Finally, the R1700 spectrum is also narrower compared to the bcc-Mo one. The oscillation observed at 20.065

keV is also flattened in the R1700 sample (red dashed line). However, the intensity of this oscillation is enhanced in the Mo-hcp compared to the bcc spectrum, which is consistent with a smaller contribution of the hcp-Mo in the experimental R1700 spectrum.

The E_0 values of the different samples are similar to that of metallic Mo within the uncertainties meaning that the oxidation state of Mo in all the samples remains 0. This is consistent with the EDX measurements.

The results of the XANES fit performed on the R1700 sample with both bcc and hcp-metallic Mo are summarized on the diagram in **Figure III-43**. The amount of Mo in the bcc and hcp-metallic Mo is exactly the same as that of the T_0 sample. This is not consistent with the EDX measurements performed on the R1700 sample, which indicated that the majority of the Mo-Ru-Rh-Pd precipitates were found in the hcp domain of the Mo-Ru-Pd ternary phase diagram, contrary to the T_0 sample. Thus, the hcp-metallic Mo contribution should be higher than in the T_0 sample.

As shown in **Appendix 2.7** (**Figure B-10**), the fit signal does not account for the disappearance of the oscillations at 20.029 keV nor for the contraction of the whole spectrum. These two phenomena are consistent with the hcp-metallic Mo XANES signal. The discrepancies could be explained by the calculated hcp-Mo spectrum which does not account for the effect of Ru, Rh and Pd on the structure (contraction of the lattice parameters as their atomic radius are smaller than Mo's one).

However, the flattening of the oscillation seen at 20.065 keV in the R1700 sample is more consistent with the presence of bcc-metallic Mo than with hcp-Mo. This can be inferred to the contribution of the pure Mo metallic precipitates to the R1700 XANES signal.

Another explanation to these differences could lie in the structural disorder occurring during the thermal treatment at 1700°C.

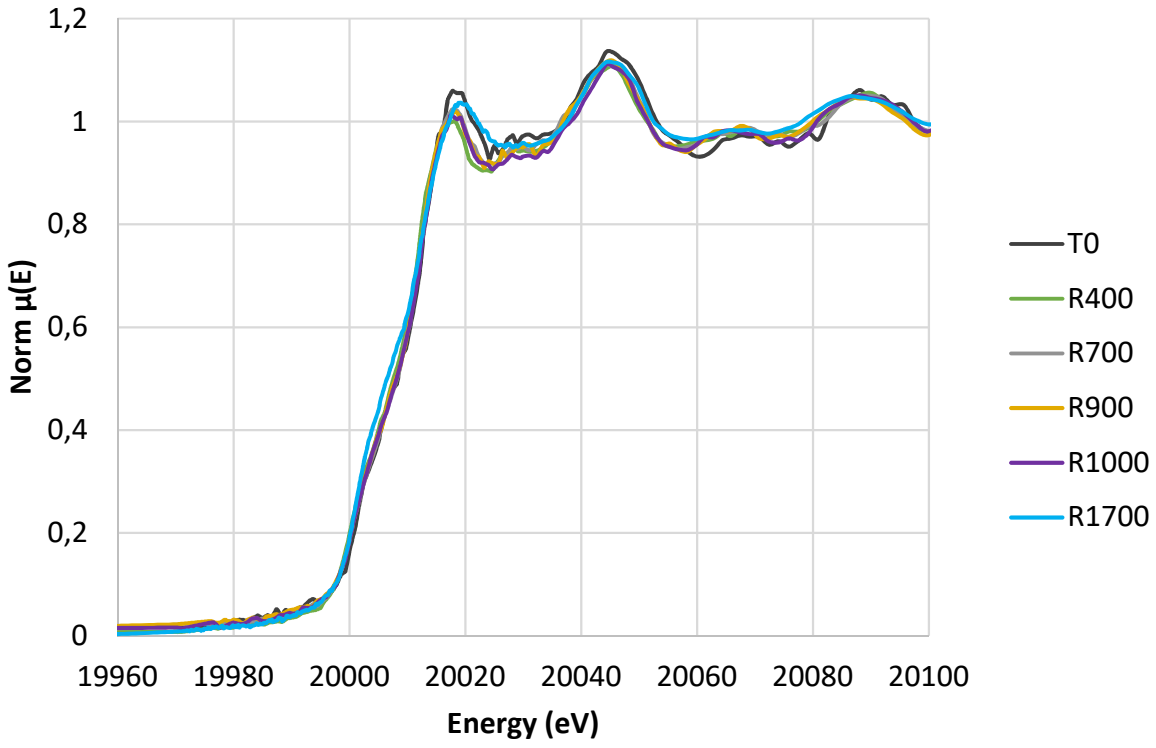

Figure III-41: Experimental XANES spectra of the samples as-sintered and treated at 400°C, 700°C, 900°C, 1000°C and 1700°C under reducing atmosphere obtained at the Mo K-edge on the MARS beamline (SOLEIL)

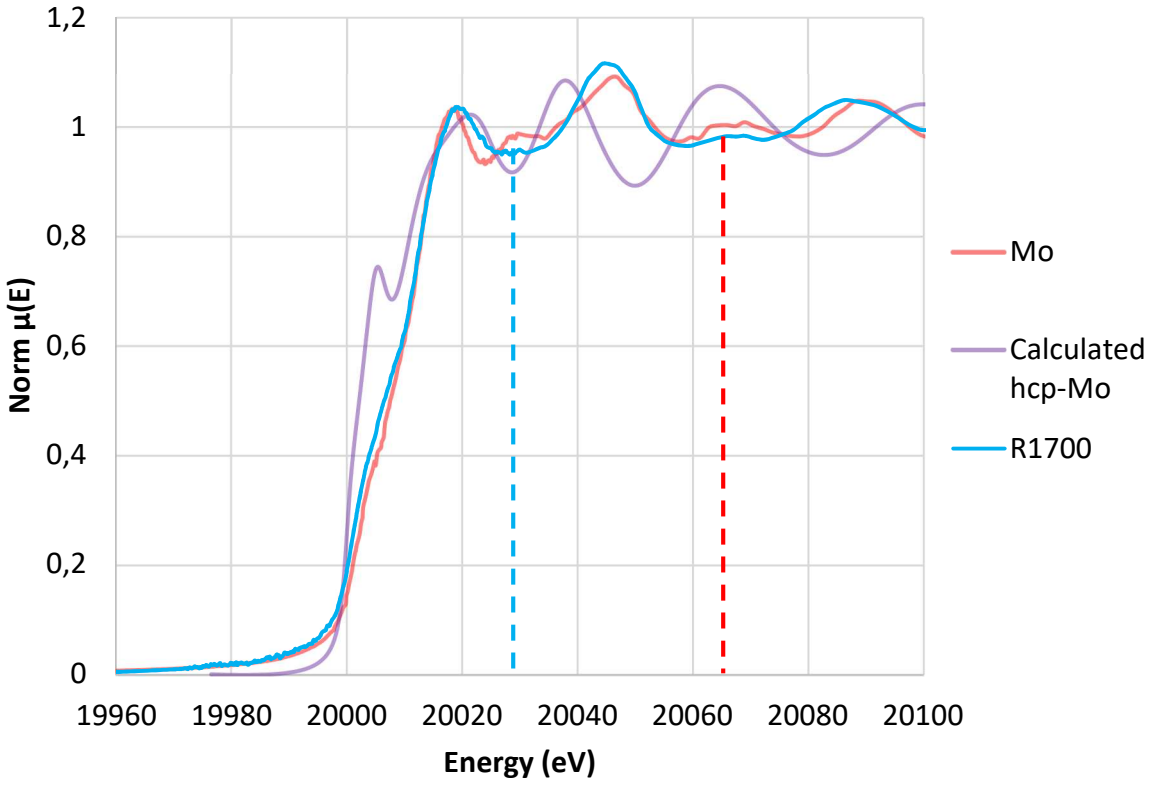

Figure III-42 : Experimental XANES spectra of the sample up to 1700°C under reducing atmosphere and metallic Mo (bcc) obtained at the Mo K-edge on the MARS beamline (SOLEIL) and calculated XANES spectrum of metallic Mo (hcp)

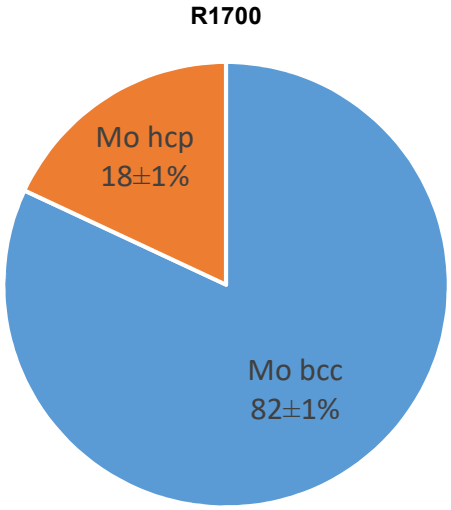

Figure III-43: Linear combination fitting results performed between -20 and +60 eV around Mo K-absorption edge of the sample R1700 (R factor = 0.002029)

III.3.3.2 Oxide precipitates

III.3.3.2.1 SEM-EDX analyses

SEM-BSE pictures of the oxide precipitates in the samples annealed under reducing conditions are shown in **Figure III-44**. Their size does not evolve much until 1700°C but the core-shell structure has disappeared in most of the cases.

This is confirmed by the chemical compositions of the oxide precipitates treated at 400°C, 700°C, 900°C, 1000°C and 1700°C, given in **Appendix 2.4** (**Table B-37, Table B-38, Table B-39, Table B-40** and **Table B-41** respectively). No chemical evolution can be observed under reducing conditions up to 1700°C. At 1700°C, most of the precipitates' composition has become more homogeneous. The ratio between Ba, Sr, Zr and O indicates the presence of $Ba_{0.9}Sr_{0.1}ZrO_3$. Depletion in Sr can thus be noticed compared to the samples treated up to 1000°C whose oxide precipitates had a composition $Ba_{0.8}Sr_{0.2}ZrO_3$.

Brighter inner regions depleted in Ba, but rich in U still exist at 1700°C within the grey phases. Based on the pseudo-binary phase diagram of **Figure I-25**, it is likely to be t-(U, Zr)O_2 or c-(U, Zr)O_2, depending on U content.

400°C

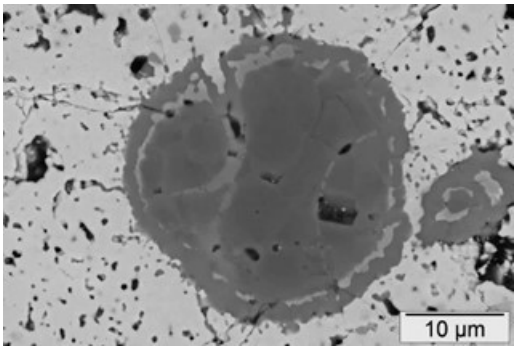

700°C

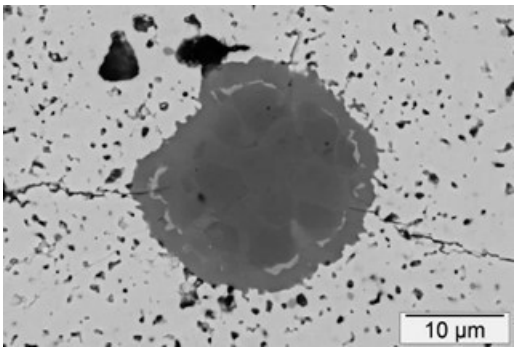

900°C

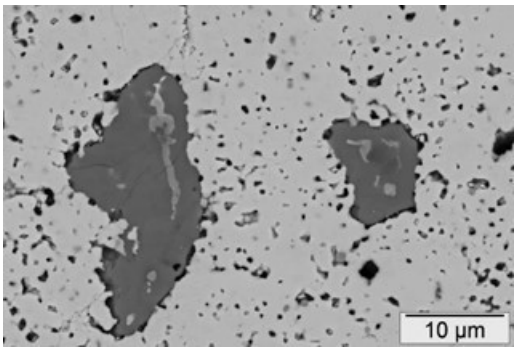

1000°C

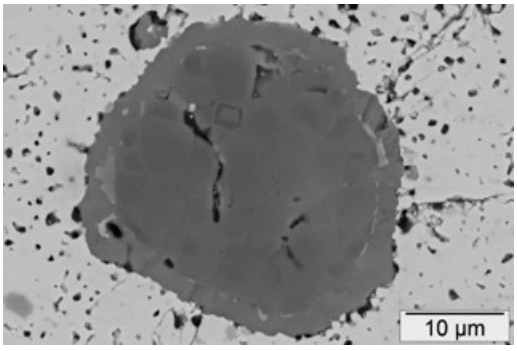

1700°C

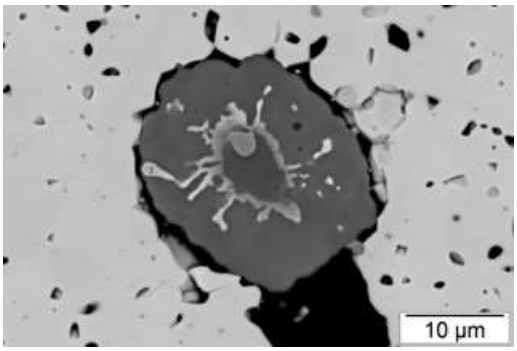

Figure III-44: SEM-BSE images of the oxide precipitates in the SIMFuel samples annealed under reducing conditions

III.3.3.2.2 XANES analyses

The HERFD-XANES analyses performed at Ba L_3-edge show that no change can be observed between the T_0 and R1700 spectra (**Figure III-45**) which are very similar to the $BaZrO_3$ one (**Figure III-46**). Concerning Zr, a shrinkage of the white line can be noticed between the T_0 and R1700 spectra (**Figure III-47**). The feature at 18.017 keV also present on the c-ZrO_2 and $BaZrO_3$ spectra (**Figure III-48**), is also more intense on the R1700 spectrum.

The E_0 values are reported in **Table III-11** and are similar for all the samples at both Ba L_3 and Zr K edges. No change can be observed between the T_0 and the sample treated at 1700°C meaning that no Ba and Zr reduction or further oxidation occurred in the samples.

The results of linear combination fitting of the sample R1700 performed for both Zr and Ba are shown in **Appendix 2.7** (**Figure B-11** and **Figure B-12**) and synthesized in **Figure III-49**. According to these results, the amount of Ba in the $BaZrO_3$ (83 ± 1 %) and BaO (17 ± 1 %) phases are strictly identical to those measured in the T_0 sample.

The amount of Zr contained in the zirconate phase decreases from 52 ± 3 % in the T_0 sample down to 37 ± 3 % in the R1700 sample. Within this phase, the amount of Zr in $SrZrO_3$ slightly decreases from 19 ± 3 % in T_0 down to 17 ± 3 % in R1700 whereas the Zr content in $BaZrO_3$ drops from 33 ± 3 % to 20 ± 3 % respectively. Alternatively, the amount of Zr in the zirconia increases from 48 ± 3 % to 63 ± 3 %. The amount of Zr in the c-ZrO_2 phase increases also up to 15 ± 2 % in the R1700 sample.

Considering the initial quantities of Ba and Zr in the samples (**Table III-2**), 15.8 ± 3 at% of Ba is calculated to be in the $BaZrO_3$ phase compared to only 11.6 ± 3 at% of Zr. This difference could be explained by the discrepancies observed between the fit signal and the experimental R1700 spectrum. Indeed, the two oscillations present at 18.017 and 18.027 keV (red dashed lines in **Figure III-48**) also present on the $BaZrO_3$ spectrum, are totally flattened. This could have led to an underestimation of the quantity of Zr in $BaZrO_3$. A qualitative comparison of the reference spectra and the R1700 spectrum gives the following information:

- The main contribution to the first oscillation occurring at 18.017 keV in the R1700 spectrum seems to come from c-ZrO_2 with a small contribution of $BaZrO_3$,
- The oscillation seen at 18.027 keV is more likely to be due to the presence of $SrZrO_3$ and $BaZrO_3$ in the sample.

However, this argumentation is only valid if no Ba release took place at 1700°C. Indeed, if Ba has been released during the thermal treatments, its distribution between $BaZrO_3$ and BaO could have remained unchanged whereas the Zr initially contained in $BaZrO_3$ would have transformed to ZrO_2. However, this is not in agreement with the SEM-EDX observations which seemed to show a homogenization of the oxide precipitates composition in $BaZrO_3$ and a depletion in Sr.

In order to conclude on this point, chemical analyses of the samples using total chemical analyses on the samples recovered after the different thermal treatments (e.g. ICP-MS or ICP-AES) or on-line analyses (e.g. gas chromatography) should be performed to determine the exact quantity of FP released.

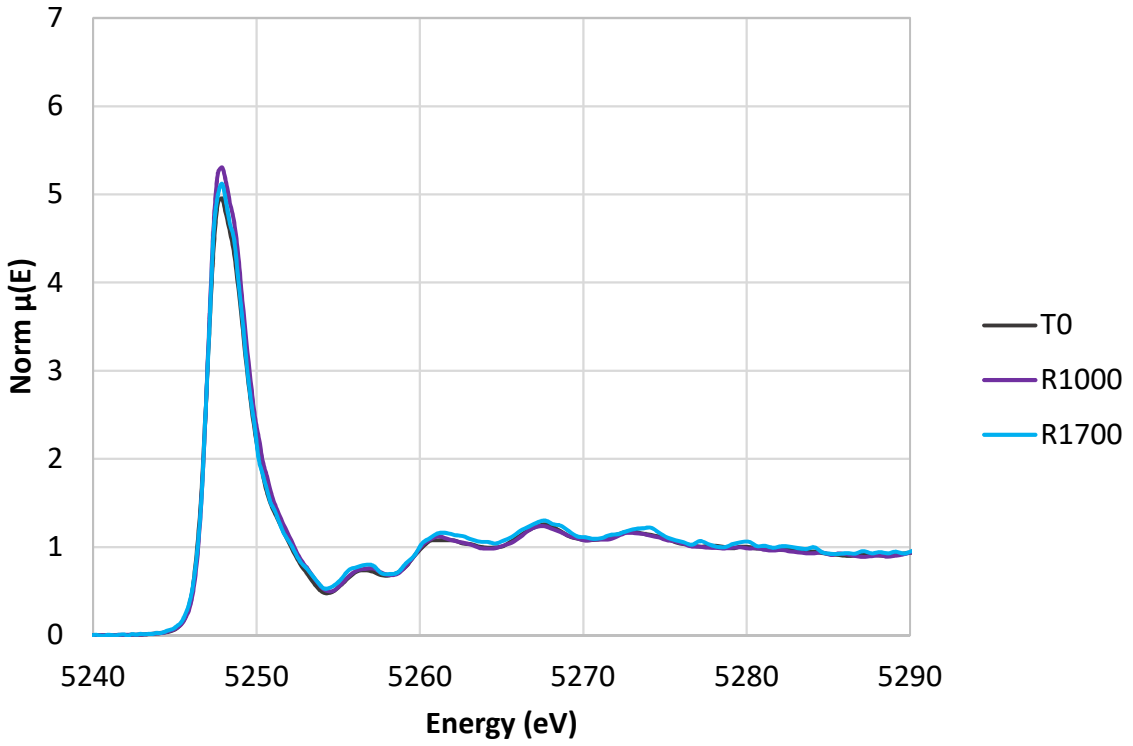

Figure III-45: XANES spectra of the samples as-sintered and treated at 1000°C and 1700°C under reducing conditions obtained at the Ba L_3-edge on the FAME-UHD beamline (ESRF)

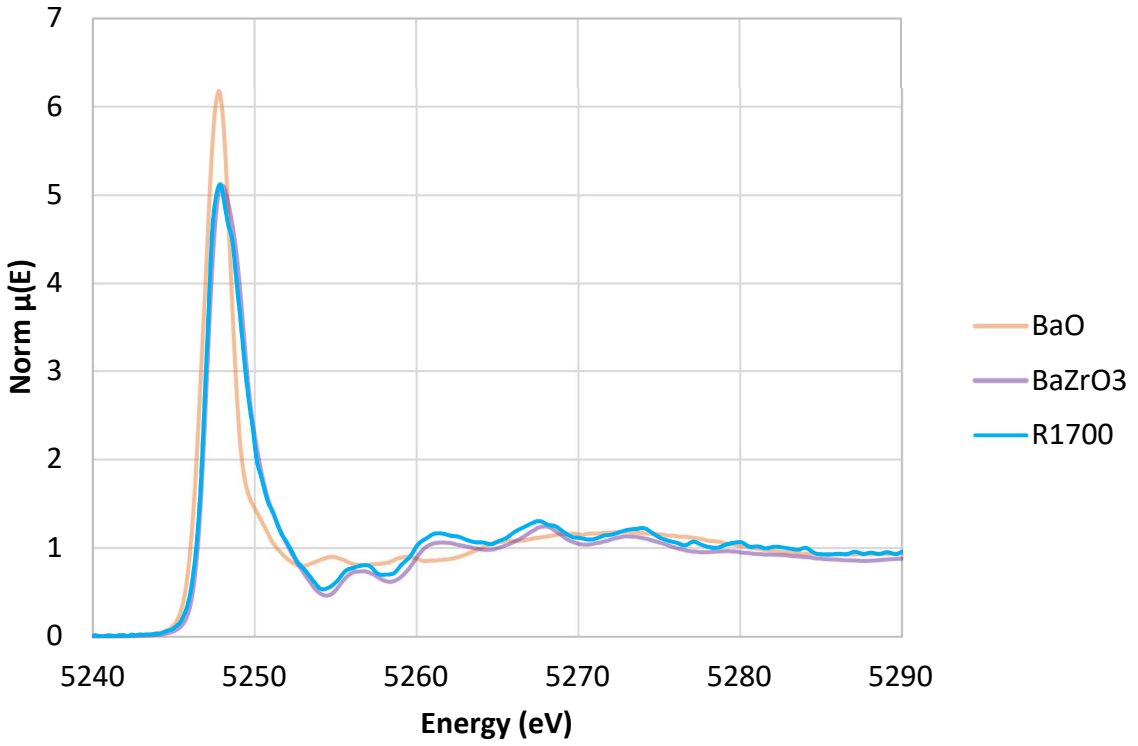

Figure III-46: Experimental XANES spectra of the sample treated up to 1700°C under reducing conditions, $BaZrO_3$ and BaO obtained at the Ba L_3-edge on the FAME-UHD beamline (ESRF)

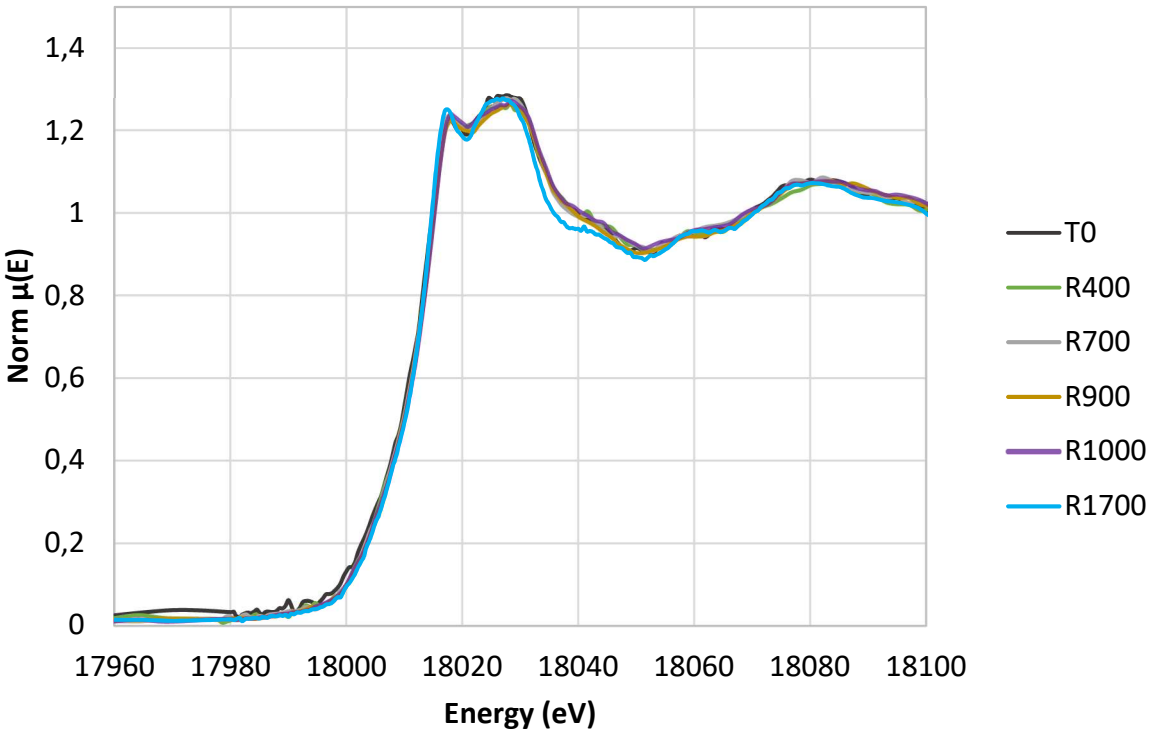

Figure III-47: Experimental XANES spectra of the sample as-sintered and treated at 400°C, 700°C, 900°C, 1000°C and 1700°C under reducing atmosphere obtained at the Zr K-edge on the MARS beamline (SOLEIL)

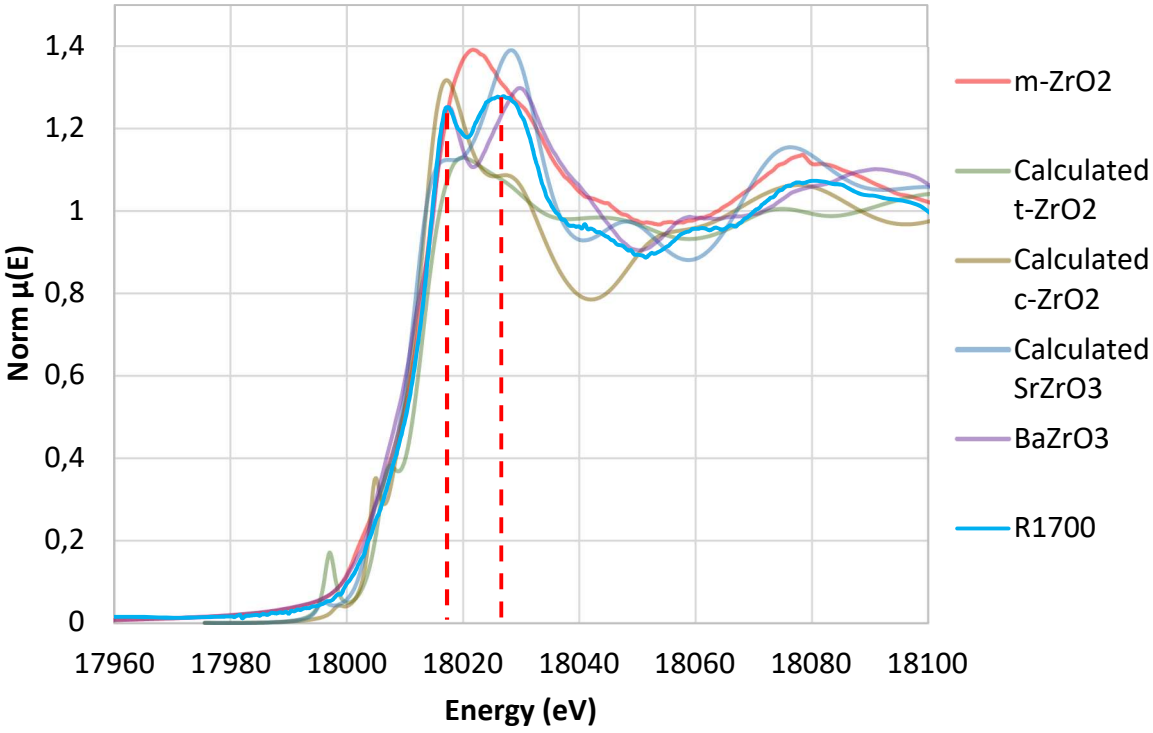

Figure III-48: Experimental XANES spectra of the sample treated up to 1700°C under reducing atmosphere, m-ZrO_2, $BaZrO_3$ obtained at the Zr K-edge on the MARS beamline (SOLEIL) and calculated XANES spectra of t-ZrO_2, c-ZrO_2 and $SrZrO_3$

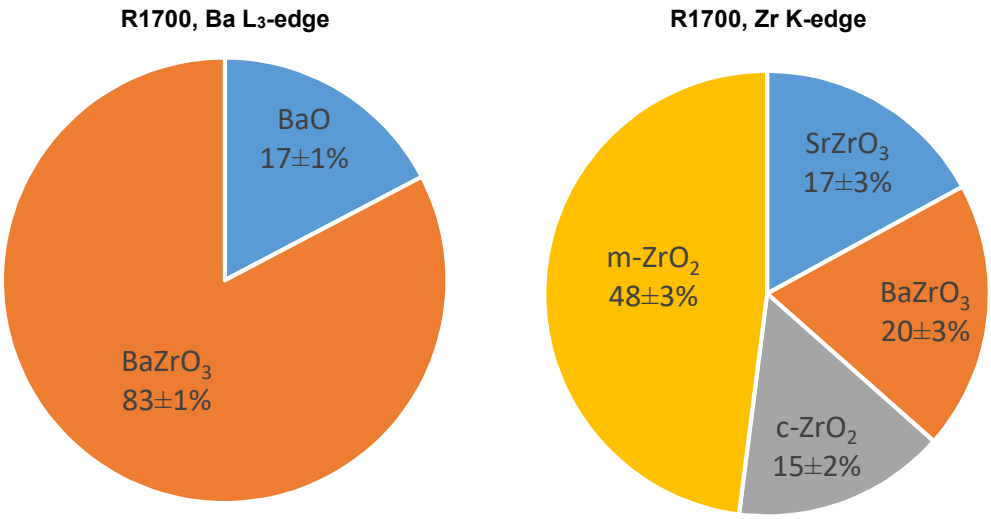

Figure III-49: Linear combination fitting results performed between -20 and +60 eV around Ba L_3-absorption edge (left, R factor = 0.003375) and the Zr K-edge (right, R factor = 0.004878) of the sample R1700

Table III-11: E_0 and white line position of the samples treated under reducing and references spectra collected at the Ba L3-edge and Sr K-edge (the uncertainty on the energy is 0.6 eV)

	Ba L_3-edge	Zr K-edge
Sample	**E_0 (eV)**	**E_0 (eV)**
BaO	5248.1	-
$BaZrO_3$	5247.9	18015.4
$BaMoO_3$	5247.9	-
$BaMoO_4$	5247.7	-
$SrZrO_3$	-	18015.4
ZrO_2 (c and m)	-	18013.5
T_0	5247.8	18014.1
R400	-	18015.0
R700	-	18014.7
R900	-	18014.7
R1000	5247.9	18015.2
R1700	5247.8	18014.5

III.3.3.3 Discussion on the observations made in the samples treated in reducing conditions

The evolution of the precipitates observed in reducing conditions is consistent with thermodynamic predictions (**Figure III-4**). Indeed, the oxide precipitates are still present in the samples, as well as metallic phases containing Mo, Ru, Rh and Pd. The phase transition from bcc to hcp observed in the metallic precipitates mainly composed of Mo and Ru is also consistent with the phase diagrams and with the thermochemistry calculations performed in **Chapter II**.

An evolution of the (Ba, Sr)ZrO_3 phase has been observed at 1700°C. Indeed, its composition appears more homogeneous through SEM-EDX analyses but depleted in Ba compared to the T_0 sample. XANES measurements would also tend to indicate that the amount of ZrO_2 increased at 1700°C, which is consistent with a decomposition of (Ba, Sr)ZrO_3 into ZrO_2, $SrZrO_3$ and BaO or Ba dissolved in ZrO_2 or partially released at 1700°C.

III.4 CONCLUSION

The objective of this chapter was to investigate the effect of the oxygen potential on FP speciation in intermediate stages of a nuclear severe accident. More precisely, a focus has been made on Mo and Ba behavior in a temperature range corresponding to the intermediary steps of a VERDON test (described in **Chapter I** and **II**).

To this end, SIMFuel samples containing 11 FP surrogates in concentrations representative of a PWR UO_2 fuel with a burn-up of 76 $GWd.t_{HM}^{-1}$ were synthesized. The different phases observed in the sample after sintering at 1650°C under H_2 during 2h were finely characterized and identified through OM, SEM-EDX and XANES analyses. *Complementary to these measurements, HR-XRD analyses using synchrotron radiation were also performed. The results have to be analyzed and should enable to go further in the identification and understanding of FP speciation.*

Ba and Mo were initially found in two types of phases in the samples consistently with the literature [17]:

- Mo was found in metallic precipitates alone or with Ru, Rh and Pd. These precipitates are also observed in PWR irradiated fuels in normal operating conditions. No MoO_2 has been detected at the initial state in the SIMFuel samples, which is consistent with the strongly reducing atmosphere of the sintering.
- Ba was found in oxide precipitates mainly whether as a simple oxide BaO or as $(Ba, Sr)(Zr, U, RE)O_3$. The latter is not observed under PWR normal operating conditions but usually found at higher temperatures. It was thus inferred that the high temperature sintering stage underwent by the SIMFuel samples enabled the formation of this complex oxide phase.

Two campaigns of thermal treatments were performed under controlled temperature and oxygen potentials, in order to study the evolution of these phases in conditions representative of intermediate stages of a VERDON test. Thermodynamic calculations performed using the SGPS database of the FactSage software enabled to determine these conditions: a first series of test was thus performed in oxidizing conditions and a second one in reducing conditions. Due to technical limitations encountered with the DURANCE experimental loop, the maximum temperature was limited to 1000°C in oxidizing conditions and to 1700°C in reducing conditions.

Detailed post-tests characterizations were carried on the different samples and the results were compared to the as-sintered sample. This approach enabled to conclude about the effect of oxygen potential on Mo and Ba behavior:

- No strong evolution of Ba and Mo speciation was observed in reducing conditions up to 1700°C, consistently with the observations performed in [17]–[19], [21], [25]–[27].
- However, between 900°C and 1000°C under oxidizing conditions, Mo starts to oxidize to form MoO_2. Mo depletion is also observed at temperature as low as 900°C in the Mo-Ru-Rh-Pd precipitates, which is in agreement with Mo behavior calculated by thermodynamics and observed in the studies of Kleykamp et al. [17], [18], [28], Bramman et. al [19] or Geiger [1].
  In the same range of temperature, a reaction between Mo and Ba at the periphery of the oxide precipitates led to partial decomposition of $(Ba, Sr)ZrO_3$ into ZrO_2 and $BaMoO_4$. This

behavior is in agreement with the calculated phases thanks to Factsage and with the experimental observations performed by Kleykamp et al. [17], [18], Paschoal et al. [31], Geiger et al. [21], [22], [27] and in the frame of the PHEBUS-FP integral tests [44], [45].
This reaction has been inferred to an enhanced diffusion of Mo in oxidizing conditions: Mo would first dissolved as MoO_2 in the UO_{2+x} matrix, and might have migrated from the metallic to the oxide precipitates driven by a gradient of O concentration.

Finally, the results obtained were integrated to the corresponding steps of the mechanisms proposed for the VERDON-3 and 4 tests at the end of **Chapter 2**. These two mechanisms were thus slightly adapted to account for the experimental observations made on SIMFuel samples in oxidizing conditions up to 1000°C and in reducing conditions up to 1700°C. One mechanism is thus presented in **Figure III-50**, where:

- The blue boxes correspond to the steps resulting from MFPR calculations with adjustments made through Thermocalc to account for the experimental observations made on the VERDON samples (**Chapter II**).
- The purple boxes correspond to the steps observed experimentally on PWR irradiated fuels, and notably on the VERDON-3 and 4 samples (**Chapter II**).
- The yellow boxes correspond to the compounds observed experimentally on the SIMFuel samples studied in this chapter.
- The red boxes correspond to the species that were not detected in the samples.

A very good agreement is found between the experimental observations described in this chapter and the mechanisms proposed for Mo and Ba speciation in intermediate conditions of a VERDON test. This would tend to indicate that:

- UO_2-based SIMFuel samples are suitable to study FP speciation in the case of both UO_2 and MOX fuels,
- Even if the ratios between FP slightly vary from UO_2 to MOX PWR fuels, FP chemistry is not strongly modified and seems to be mainly driven by thermodynamics (temperature and oxygen potential) and kinetics (diffusion).

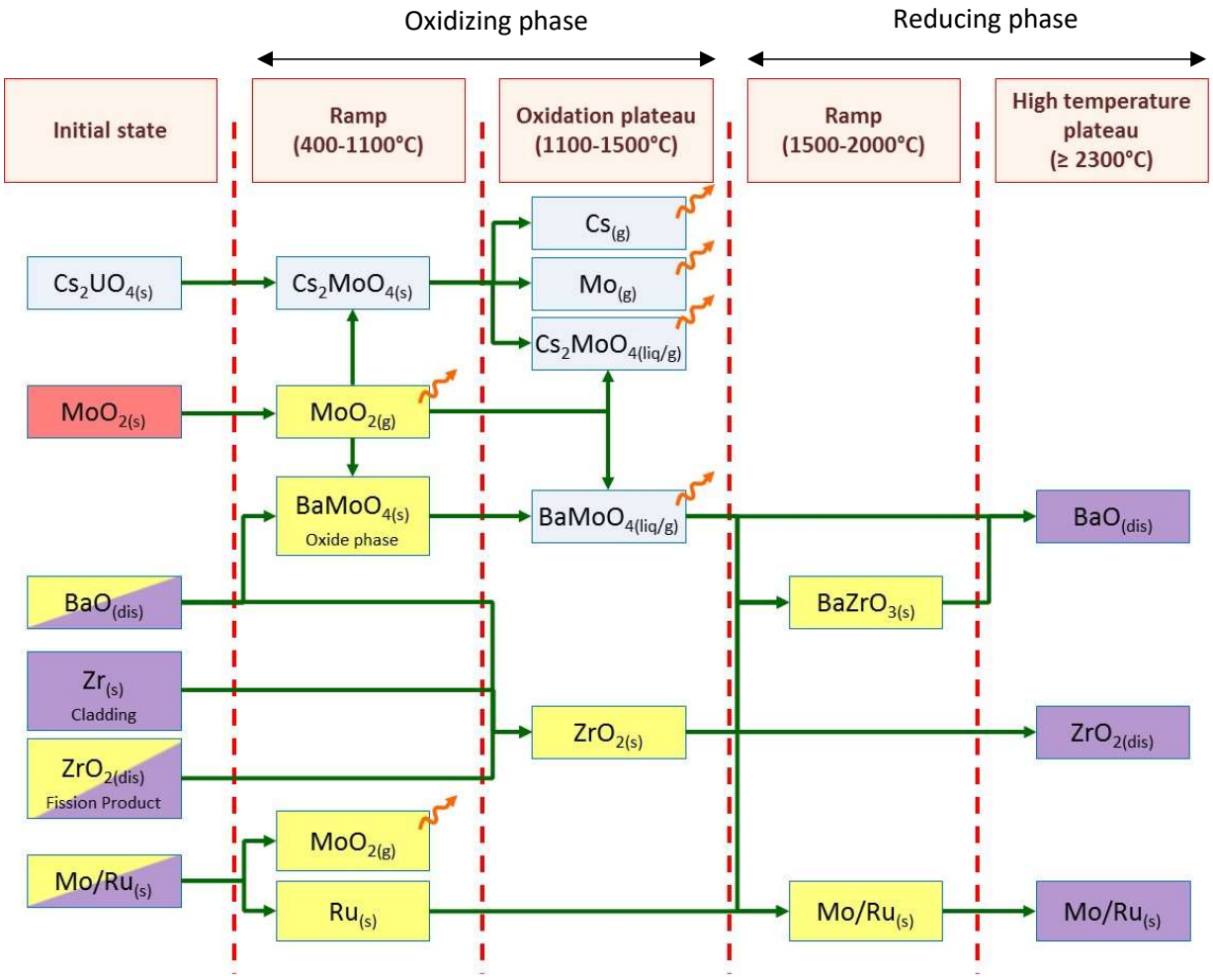

Figure III-50: FP speciation mechanism proposed for the VERDON-4 test (two last stages in reducing conditions)

As already demonstrated by Geiger in [1], SIMFuels are a good alternative to irradiated fuels studies as far as the behavior of FP at intermediate temperatures is concerned. As they are easily transportable, they give access to a wide range of techniques enabling to study FP speciation at a crystallographic level.

However, given the simulated nature of the SIMFuels, several parameters, beyond irradiation, are neglected. Among others, temperature gradients within the fuel in reactor are not reproduced during thermal treatments. Temperature and concentration gradients between Pu-agglomerates and U-matrix as it is the case in MOX fuels are not accounted either. All these parameters can play an important role on kinetics of reactions in the early stages of a severe accident.

The main drawback of SIMFuel samples when it comes to FP speciation lies in the high temperature sintering stage (1650°C) needed to produce them, which limit their representativeness towards PWR irradiated fuels. Indeed, it leads to the formation of species that are not present in PWR irradiated fuel under normal operating conditions (400 to 1500°C). This explains the discrepancies between the initial stage predicted in the mechanism and the phases observed in the as-sintered SIMFuel samples. Moreover, this fabrication route leads to the total release of highly volatile FP such as Cs. Studies of Cs speciation is thus impossible in these materials.

Thus, an innovative method to produce SIMFuel samples at rather low temperature has been developed through Spark Plasma Sintering. The next chapter describes in details the fabrication process of such materials as well as the characterizations performed on the as-sintered samples.

III.5 REFERENCES

[1] E. Geiger, “Study of fission products (Cs, Ba, Mo, Ru) behaviour in irradiated and simulated nuclear fuels during severe accidents using X-ray absorption spectroscopy, SIMS and EPMA,” PhD Thesis, Paris-Saclay, CEA Cadarache, 2016.

[2] P. G. Lucuta, R. A. Verrall, H. Matzke, and B. J. Palmer, “Microstructural features of SIMFUEL — Simulated high-burnup UO2-based nuclear fuel,” *J. Nucl. Mater.*, vol. 178, no. 1, pp. 48–60, 1991.

[3] Z. Hiezl, “Processing and microstructural characterisation of UO2-based simulated spent nuclear fuel ceramics for the UK’s advanced gas-cooled reactors,” Ph.D., Imperial College London, 2015.

[4] “Cesar 5.1, developed by DEN/DER/SPRC,” CEA Cadarache.

[5] Z. Hiezl, D. I. Hambley, C. Padovani, and W. E. Lee, “Processing and microstructural characterisation of a UO2-based ceramic for disposal studies on spent AGR fuel,” *J. Nucl. Mater.*, vol. 456, pp. 74–84, Jan. 2015.

[6] A. Savitzky and M. J. E. Golay, “Smoothing and differentiation of data by simplified least squares procedures,” *Anal. Chem.*, vol. 36, pp. 1627–1639, 1964.

[7] Y. Pontillon *et al.*, “Fission gas release under normal and off-normal conditions: New analytical device implemented at the CEA Cadarache,” presented at the European Working Group “Hot Laboratories and Remote handling” Plenary Meeting, Petten, Netherlands, 2005.

[8] C. W. Bale *et al.*, “FactSage thermochemical software and databases,” *Calphad*, vol. 26, no. 2, pp. 189–228, 2002.

[9] C. W. Bale *et al.*, “FactSage thermochemical software and databases — recent developments,” *Calphad*, vol. 33, no. 2, pp. 295–311, 2009.

[10] Y. Joly, “X-ray absorption near-edge structure calculations beyond the muffin-tin approximation,” *Phys. Rev. B*, vol. 63, no. 12, p. 125120, Mar. 2001.

[11] I. Arvanitidis, D. Siche, and S. Seetharaman, “A study of the thermal decomposition of BaCO<Subscript>3</Subscript>,” *Metall. Mater. Trans. B*, vol. 27, no. 3, pp. 409–416, Jun. 1996.

[12] J. Spino, K. Vennix, and M. Coquerelle, “Detailed characterisation of the rim microstructure in PWR fuels in the burn-up range 40–67 GWd/tM,” *J. Nucl. Mater.*, vol. 231, no. 3, pp. 179–190, 1996.

[13] H. Matzke and J. Spino, “Formation of the rim structure in high burnup fuel,” *J. Nucl. Mater.*, vol. 248, pp. 170–179, 1997.

[14] N. Lozano, L. Desgranges, D. Aymes, and J. C. Niepce, “High magnification SEM observations for two types of granularity in a high burnup PWR fuel rim,” *J. Nucl. Mater.*, vol. 257, no. 1, pp. 78–87, Sep. 1998.

[15] J. Noirot, L. Desgranges, and J. Lamontagne, “Detailed characterisations of high burn-up structures in oxide fuels,” *J. Nucl. Mater.*, vol. 372, no. 2–3, pp. 318–339, 2008.

[16] J. Noirot, I. Zacharie-Aubrun, and T. Blay, “FIB/SEM Examination of High Burn-Up UO2 in the Center of a Pellet,” *Nucl. Eng. Technol.*

[17] H. Kleykamp, “The chemical state of the fission products in oxide fuels,” *J. Nucl. Mater.*, vol. 131, no. 2–3, pp. 221–246, 1985.

[18] H. Kleykamp, J. O. Paschoal, R. Pejsa, and F. Thümmler, “Composition and structure of fission product precipitates in irradiated oxide fuels: Correlation with phase studies in the Mo-Ru-Rh-Pd and BaO-UO2-ZrO2-MoO2 Systems,” *J. Nucl. Mater.*, vol. 130, pp. 426–433, 1985.

[19] J. I. Bramman, R. M. Sharpe, D. Thom, and G. Yates, “Metallic fission-product inclusions in irradiated oxide fuels,” *J. Nucl. Mater.*, vol. 25, no. 2, pp. 201–215, Feb. 1968.

[20] M. H. Kaye, B. J. Lewis, and W. T. Thompson, “Thermodynamic treatment of noble metal fission products in nuclear fuel,” *J. Nucl. Mater.*, vol. 366, no. 1, pp. 8–27, Jun. 2007.

[21] E. Geiger, R. Bès, P. Martin, Y. Pontillon, G. Ducros, and P. L. Solari, “Insights on fission products behaviour in nuclear severe accident conditions by X-ray absorption spectroscopy,” *J. Nucl. Mater.*, vol. 471, pp. 25–33, 2016.

[22] E. Geiger, R. Bès, P. Martin, Y. Pontillon, P. L. Solari, and M. Salome, “Fission products behaviour in UO 2 submitted to nuclear severe accident conditions,” *J. Phys. Conf. Ser.*, vol. 712, no. 1, p. 012098, 2016.
[23] J. Cobos, D. Papaioannou, J. Spino, and M. Coquerelle, “Phase characterisation of simulated high burn-up UO2 fuel,” *J. Alloys Compd.*, vol. 271–273, pp. 610–615, Jun. 1998.
[24] G. Giacchetti and C. Sari, “Behavior of Molybdenum in Mixed-Oxide Fuel,” *Nucl. Technol.*, vol. 31, no. 1, pp. 62–69, Oct. 1976.
[25] B. M. Jeffery, “Microanalysis of inclusions in irradiated UO2,” *J. Nucl. Mater.*, vol. 22, no. 1, pp. 33–40, Apr. 1967.
[26] B. T. Bradbury, J. T. Demant, P. M. Martin, and D. M. Poole, “Electron probe micro-analysis of irradiated UO2,” *J. Nucl. Mater.*, vol. 17, no. 3, pp. 227–236, Nov. 1965.
[27] E. Geiger *et al.*, “Fission products and nuclear fuel behaviour under severe accident conditions part 2: Fuel behaviour in the VERDON-1 sample,” *J. Nucl. Mater.*, vol. 495, no. Supplement C, pp. 49–57, 2017.
[28] H. Kleykamp, “Constitution and thermodynamics of the Mo-Ru, Mo-Pd, Ru-Pd and Mo-Ru-Pd systems,” *J. Nucl. Mater.*, vol. 167, pp. 49–63, Sep. 1989.
[29] H. Kleykamp, “Thermodynamics of the Mo□Ru system,” *J. Common Met.*, vol. 144, no. 1, pp. 79–86, Nov. 1988.
[30] S. Yamanaka and K. Kurosaki, “Thermophysical properties of Mo–Ru–Rh–Pd alloys,” *J. Alloys Compd.*, vol. 353, no. 1–2, pp. 269–273, 2003.
[31] J. O. A. Paschoal, H. Kleykamp, and F. Thümmler, “Phase equilibria in the pseudoquaternary BaO-UO2-ZrO2-MoO2 system,” *J. Nucl. Mater.*, vol. 151, no. 1, pp. 10–21, 1987.
[32] K. Masumichi, S. Masakazu, and N. Kenji, “Phase study on solid fission products, Ba, Sr and Zr in oxide fuel,” *J. Nucl. Mater.*, vol. 51, no. 1, pp. 90–94, 1974.
[33] I. Sato, H. FURUYA, T. ARIMA, K. IDEMITSU, and K. YAMAMOTO, “Behavior of Fission Products Zirconium and Barium in Fast Reactor Fuel Irradiated to High Burnup,” *J. Nucl. Sci. Technol.*, vol. 36, no. 9, pp. 775–780, Sep. 1999.
[34] V. G. Baranov, A. V. Lunev, V. F. Reutov, A. V. Tenishev, M. G. Isaenkova, and A. V. Khlunov, “An attempt to reproduce high burn-up structure by ion irradiation of SIMFUEL,” *J. Nucl. Mater.*, vol. 452, no. 1–3, pp. 147–157, Sep. 2014.
[35] K. Ollila, “SIMFUEL dissolution studies in granitic groundwater,” *J. Nucl. Mater.*, vol. 190, pp. 70–77, Aug. 1992.
[36] M. Kaye and L. Wang, “U-Ru-Rh-Pd QUATERNARY SYSTEM: THERMODYNAMIC CALCULATIONS AND EXPERIMENTAL EXPLORATIONS,” 2016.
[37] S. N. Tripathi and S. R. Bharadwaj, “The Pd-Rh System,” *J. Phase Equilibria*, vol. 15, no. 2, pp. 208–212, 1994.
[38] Y. V. Shubin, P. E. Plyusnin, and S. V. Korenev, “Determination of the equilibrium miscibility gap in the Pd–Rh alloy system using metal nanopowders obtained by decomposition of coordination compounds,” *J. Alloys Compd.*, vol. 622, no. Supplement C, pp. 1055–1060, Feb. 2015.
[39] J.-O. Andersson, T. Helander, L. Höglund, P. Shi, and B. Sundman, “Thermo-Calc & DICTRA, computational tools for materials science,” *Calphad*, vol. 26, no. 2, pp. 273–312, 2002.
[40] “OECD NEA/NSC: Thermodynamics of Advanced Fuels – International Database (TAF-ID) - working version of january 2018.” [Online]. Available: https://www.oecd-nea.org/science/taf-id/. [Accessed: 25-Aug-2016].
[41] H. Matzke, “Oxygen potential in the rim region of high burnup UO2 fuel,” *J. Nucl. Mater.*, vol. 208, no. 1, pp. 18–26, Jan. 1994.
[42] H. Matzke, “Oxygen potential measurements in high burnup LWR U02 fuel,” *J. Nucl. Mater.*, vol. 223, no. 1, pp. 1–5, May 1995.

[43] P. Martin, M. Ripert, G. Carlot, P. Parent, and C. Laffon, “A study of molybdenum behaviour in UO2 by X-ray absorption spectroscopy,” *J. Nucl. Mater.*, vol. 326, no. 2, pp. 132–143, Mar. 2004.
[44] M. Barrachin, D. Gavillet, R. Dubourg, and A. De Bremaecker, “Fuel and fission product behaviour in early phases of a severe accident. Part I: Experimental results of the PHEBUS FPT2 test,” *J. Nucl. Mater.*, vol. 453, no. 1, pp. 340–354, Oct. 2014.
[45] R. Dubourg, M. Barrachin, R. Ducher, D. Gavillet, and A. De Bremaecker, “Fuel and fission product behaviour in early phases of a severe accident. Part II: Interpretation of the experimental results of the PHEBUS FPT2 test,” *J. Nucl. Mater.*, vol. 453, no. 1, pp. 355–374, Oct. 2014.

Chapter IV:

DEVELOPMENT OF A SPARK PLASMA SINTERING ROUTE TO SYNTHESIZE SIMFUEL SAMPLES TO STUDY VOLATILE FP BEHAVIOR

TABLE OF CONTENT

IV.1 INTRODUCTION

Despite the great advantages of SIMFuel samples described in the previous chapter, the high temperature sintering stage required for their production makes it impossible to confine volatile compounds such as Cs in a UO_2 matrix. Implantation has thus been widely used to study the behavior of gases [1]–[3] and volatile compounds such as Mo [4], Cs [5] and I [6], [7]. However, the presence of the implanted atoms is limited to the very surface of the samples (up to 250 nm depending on the size of the implanted atoms, the incident energy of the beam…) in the case of implantation processes [5]. The absence of volatile species in the bulk may thus induce their early release during thermal treatments without any chemical reactions with the other additives present in the samples, linked to thermodynamic equilibrium.

Another drawback of the high temperature sintering stage is that the chemical state of FP surrogates in SIMFuels is not representative of that observed in PWR irradiated fuels in normal operation conditions. Indeed, the normal operating temperature of a PWR fuel varies from 500°C at the periphery of the pellets up to 1300°C in their center [8] which is much lower than the SIMFuels sintering temperature of 1650°C.

Recently, SPS was successfully used to synthesize dense UO_2 pellets containing CsI at 1000°C [9]. This promising result was the starting point of a collaboration between the CEA Cadarache and the JRC Karlsruhe. The aim was to synthesize SIMFuel samples through SPS in order to study Cs behavior in the fuel and its interactions with other fission products such as Mo and Ba during a nuclear severe accident. Several objectives were set regarding the syntheses of the samples by SPS:

- The first one was to **embed Cs in the SIMFuel pellets as well as Mo and Ba** in order to study their interactions in severe accident conditions. Indeed, as shown in **Figure I-32** and **Figure I-33** (**Chapter I**), Cs is able to interact with Mo to form Cs_2MoO_4. This reaction might enter in competition with the formation of $BaMoO_4$ occurring in the same range of temperature. Numerous analytical tests performed on irradiated fuels treated at high temperature showed that at 1500°C almost 50% of the initial Cs amount was released from the fuel [5], [10]–[17]. In order to keep at least half of the initial Cs quantity added in the SIMFuel samples, the maximum sintering temperature was first set to 1500°C.
- The second objective was to obtain samples in which FP surrogates speciation is representative of that observed in PWR irradiated fuels in normal operation conditions. To this end, the sintering temperature has to lie in the range of the irradiated fuel rods in a PWR. For this reason, **the maximum sintering temperature was finally set to 1300°C**.
- The third objective was to **reach a final density of at least 90 % of the theoretical density of the mixture** in order to enable easy characterizations of the samples. Powders containing UO_2 are indeed much more complicated to handle and transport than bulk materials and prevent the use of some characterization techniques.

The fabrication process is described in detail in the first part of this chapter. Post-sintering characterizations results constitute the second part of this chapter. They included density measurements, chemical analyses by ICP-AES and ICP-MS to quantify the release of FP surrogates during sintering. SEM-EDX and HERFD-XANES analyses were then performed to study the FP surrogates speciation in the samples after sintering.

Another part of the innovative method proposed in this chapter to study volatile FP speciation consists in the development of an in-situ HERFD-XANES experiment, set-up in collaboration with the ESRF. The objective of this kind of analyses was to study Cs speciation in temperature and oxygen potential conditions representative of a severe accident. The experimental set-up as well as the results of the first experiment are described in the last part of this chapter.

IV.2 SYNTHESES

IV.2.1 Method

Two series of samples were produced at the JRC. The first one (SPS-1) was prepared with additives at concentrations around 1 wt% in order to respect the range of FP concentrations in PWR irradiated fuels. The objective of this series of materials was to check if the different additives could be detected with our set of characterization means. The second series of samples (SPS-2) was prepared in frame of Pierre Taupin's internship, with additives concentrations close to 4 wt% to make the characterizations easier.

In each series, several batches of samples containing FP surrogates under different chemical forms have been prepared and sintered. Only those fulfilling the objectives stated in the introduction (final sintering temperature < 1300°C and final density > 90 % d_{th}) are presented in this chapter. The initial composition of the different batches prepared is given in **Table IV-1** and the corresponding amounts of Cs, Mo, Ba and U are given in **Table IV-2**.

The first batch was synthesized using pure UO_2 in order to check its behavior before adding FP additives. Then, one additive containing Cs, Mo or Ba was added to UO_2 and sintered to study separately the behavior of each additive in UO_2 (batches 2, 3, 5 and 6).

Finally, the most complex systems were sintered. Batch 4, initially containing cesium uranate and molybdenum oxide in UO_2, was synthesized to study the interaction between Cs, Mo and U. Batches 7 and 8 were produced using different additives containing Cs, Mo and Ba in UO_2 in order to study the interactions between these three elements and U.

As shown by the color code used in **Table IV-1**, the observations performed on the systems containing UO_2 and one additive were used to study the behavior of the systems composed of UO_2 and two additives. Thus, batches 2 and 5 were used to explain the behavior of the system composing batch 7. In the same way, batch 3 and 6 were used to discuss the results obtained on batch 8. Batch 3 was also used to interpret the behavior of batch 4.

Table IV-1: Initial composition of the different batches synthesized through a SPS route (concentration in wt%)

Series	Batch	UO_2	Cs_2MoO_4	$Cs_2U_xO_y$	$BaCO_3$	$BaMoO_4$	MoO_3
SPS-1	1	100.00	-	-	-	-	-
	2	99.10	0.90	-	-	-	-
	3	98.80	-	1.20	-	-	-
	4	98.46	-	1.19	-	-	0.34
SPS-2	5	95.90	-	-	4.40	-	-
	6	95.60	-	-	-	4.10	-
	7	92.00	4.00	-	4.00	-	-
	8	92.00	-	4.00	-	4.00	-

Table IV-2: Initial elemental composition in wt% of the different batches of SIMFuel samples produced by a SPS route (the difference to 100% is due to the O content)

Batch	U	Cs	Mo	Ba
2	87.36	0.56	0.20	-
3	87.09	0.56	-	-
4	86.80	0.56	0.23	-
5	84.27	-	-	3.06
6	84.54	-	1.32	1.89
7	81.10	2.78	0.90	2.50
8	81.10	1.87	1.29	1.85

IV.2.2 Starting materials

Commercial depleted UO_2 (Cogema) was first pre-reduced at 800°C during 4h under Ar + 6.5% H_2 in order to avoid a stoichiometry gradient in the pellets after sintering and to limit the deviation from stoichiometry of the as-sintered pellets [18]. The lattice parameter (a) of the powder was determined through powder XRD and the final O/M was calculated according to equation (1) where x represents the deviation from stoichiometry [19]. The powder was thus reduced from 2.16 to 2.01.

$$a = 5.4705 - 0.132x \qquad (1)$$

Figure IV-1 shows that pre-reduced UO_2 powder exhibit some tiny crystallites of 100 to 200 nm in size which are found in agglomerates of up to 30 µm in diameter.

Commercial MoO_3 (99.5% purity, MERCK) was used as received. This powder was made of platelets of approximately 13 µm in size as shown in **Figure IV-1**. Commercial $BaCO_3$ from the same batch as the one used for the production of SIMFuel samples by high temperature sintering (already presented in **Figure III-1**, **Chapter III**) as well as commercial $BaMoO_4$ (ALFA AESAR) and Cs_2MoO_4 (MERCK) were used. Concerning $BaMoO_4$, it is composed of round particles of around 1 µm which form agglomerates of a few tens of microns in size. As shown in **Figure IV-1**, Cs_2MoO_4 is composed of submicronic spherical particles and pyramidal shaped ones with a size around 10 µm.

Cesium uranate was synthesized according to the protocol described in [20]. Thus, $CsNO_3$ (MERCK) and depleted $UO_{2.16}$ (Cogema) were mixed in an agate mortar by manual grinding and placed in a calcination furnace. The initial molar ratio between Cs and U was 2. The temperature was increased gradually and held at 700°C under static air during 24h. As shown in **Figure IV-1**, two types of particles can be observed in the final powder: large rounded shaped ones with a size of around 200 µm and smaller ones with a size ranging from 1 to 10 µm. The small particles, which correspond to Cs uranate, are agglomerated around the bigger ones composed of $CsNO_3$. The transformation of $CsNO_3$ was thus not complete at the end of the sequence, so the heating process was repeated a second time up to 800°C. The composition of the final orange powder was characterized through XRD to be a mixture between Cs_2UO_4 (22 %), $Cs_2U_2O_7$ (75 %) and Cs_2O (3 %). The final Cs/U molar ratio is calculated to be 1.28 which is lower than the initial ratio of 2, indicating that almost 36 % of Cs has been lost.

According to the phase diagram taken from [21], these two uranate compounds coexist up to 650°C. Beyond this temperature, only β-$Cs_2U_2O_7$ is supposed to be stable. However, the study performed in

[22] demonstrated that under dry air or argon, the decomposition of Cs_2UO_4 appears at higher temperature, around 950°C. Indeed, Cs uranates are highly hygroscopic and the water adsorbed could be responsible for the early decomposition observed in the study made in [21]. This could be an explanation for the presence of both Cs_2UO_4 and $Cs_2U_2O_7$ in the powder after calcination.

In this study, the air used to synthesize Cs uranates was probably not dried. It was also observed that the relative amount of Cs_2UO_4 and $Cs_2U_2O_7$ varied between two syntheses apparently performed in the same conditions. These observations thus go in the same direction as the study carried by [22]: depending on the humidity of the gas used during the synthesis, a varying quantity of Cs_2UO_4 is yielded.

As shown in the phase diagram presented in **Figure IV-2**, the appearance of Cs_2O at 800°C may be the result of the decomposition of a small unreacted amount of Cs_2NO_3 into $Cs_2O_{(l)}$ and $N_{2(g)}$.

For the sake of clarity, in the following chapter, the Cs uranates will be termed as $Cs_2U_xO_y$.

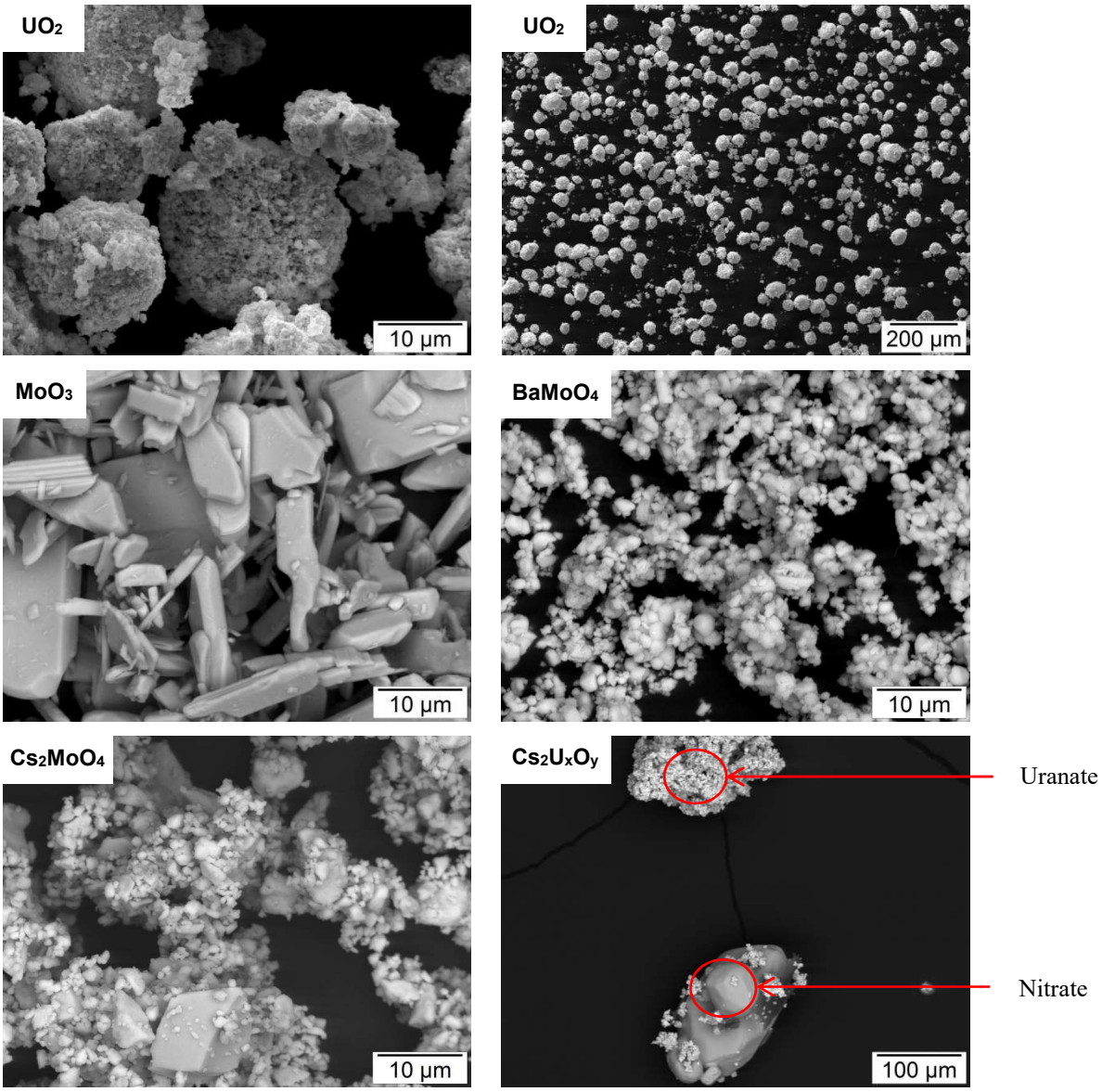

Figure IV-1: SEM-SE images of the starting powders. From top to bottom and left to right hand sides: pre-reduced UO_2, as-received MoO_3, as-received $BaMoO_4$, as-received Cs_2MoO_4 and $Cs_2U_xO_y$ obtained after 24h at 700°C under air.

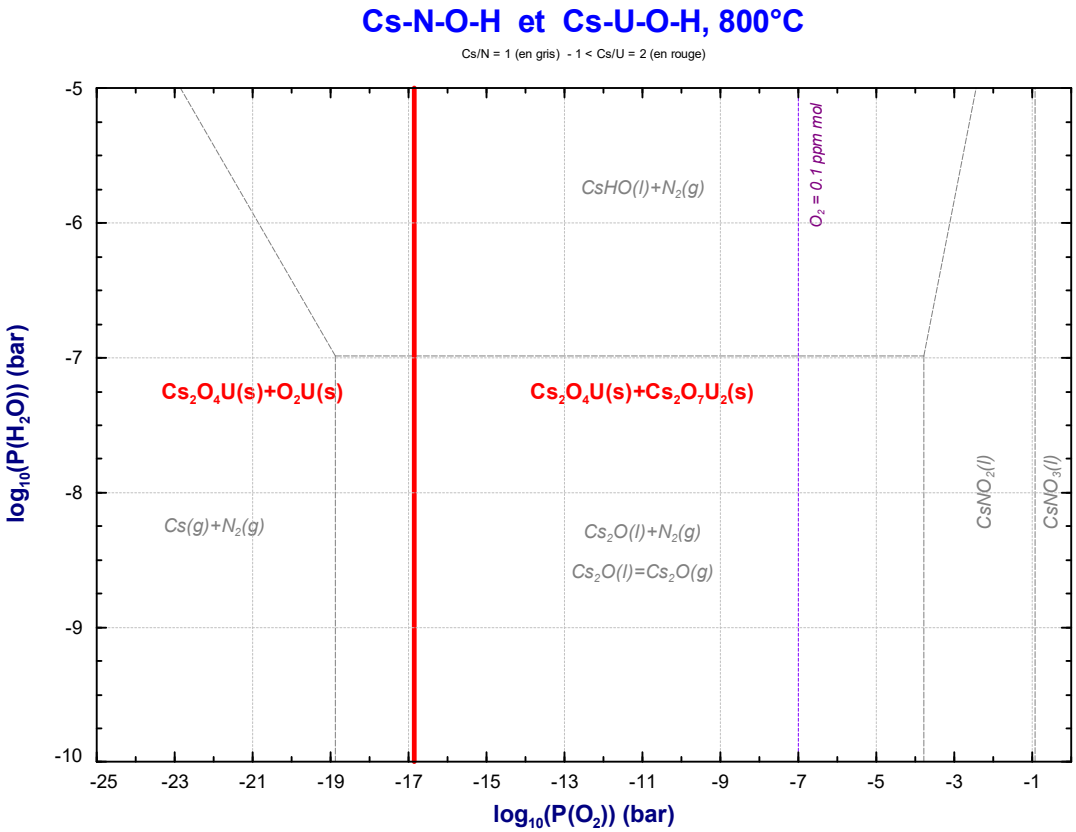

Figure IV-2: Predominance diagram for the C-N-O-H and Cs-U-O-H systems at 800°C, considering the quantities of elements determined through XRD, obtained using the SGPS database of FactSage [23], [24]. The dashed blue line corresponds to the maximum amount of O_2 in ultra-pure Ar.

IV.2.3 Fabrication process: determination of the sintering conditions

Sample preparation was carried out in a glovebox under Ar atmosphere. The additives powders were first ground separately in an agate mortar. The pre-reduced UO_2 was then added to the mixture which was ground again manually. The powder was finally poured into a 6 mm diameter SPS matrix made out of graphite and containing a graphite foil to ease the extraction of the pellet after sintering. Graphite disks were also placed between the pistons and the powder to prevent the pellet from being stuck to the pistons. A pre-compaction step was performed at 500 N (~17.7 MPa) and the following cycle was run:

- Gas evacuation to <10 Pa
- Pressing up to 2.5 kN (~88 MPa) and fill the chamber with Ar
- Heating up to the final temperature at 200°C/min
- Holding at the final temperature for 5 min
- Cooling down at 200°C/min
- Releasing the pressure

In order to optimize the sintering temperature, 0.5 g of pure pre-reduced UO_2 was first sintered at 1500°C. The sintering behavior of UO_2 can be seen in **Figure IV-3**. The onset of sintering takes place around 700°C and a maximum shrinkage is reached at 850°C. The speed of the piston displacement is back to 0 at 1215°C meaning that sintering has ended.

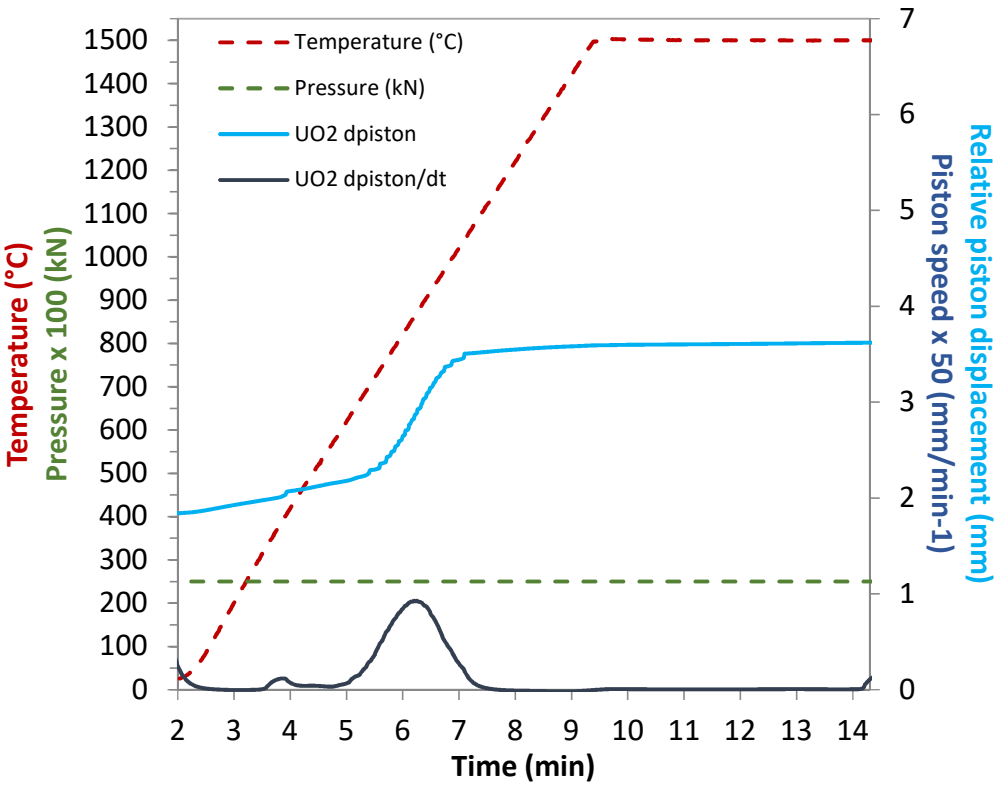

Figure IV-3: Relative piston displacement and piston speed during the sintering of pure pre-reduced UO_2 up to 1500°C during 5 min. The relative piston displacement and piston speed curves have been smoothed using a Savitzky-Golay filter [25] with 20 points.

The sintering temperature was thus set to 1200°C for all the mixtures studied in order to guarantee both the sintering of the different pellets and a limited release of FP surrogates. Sintering took place under Ar and the holding time at 1200°C was kept to 5 minutes.

IV.3 AS-SINTERED SAMPLES CHARACTERIZATION

The samples of the SPS-1 series were transported to Cadarache after a first series of characterization at the JRC Karlsruhe. They were then polished and analyzed in the UO_2 laboratory as well as in synchrotron radiation facilities. However, the samples of the SPS-2 series could not be transported within the time of the thesis. Thus, only the first results obtained on this series at the JRC are presented in this chapter (sintering behavior and SEM-EDX analyses on fractured samples). The experimental conditions in which the characterizations were performed are described in **Appendix 3.1**.

Thermodynamic calculations using the FactSage 7.0 software were performed in order to go further in the interpretation of the experimental data. Thus predominance diagrams were established using the species involved in the different systems considered. The main hypotheses made in the calculations are described in **Appendix 3.2**.

IV.3.1 Study of pure UO_2 (batch 1)

IV.3.1.1 Sintering behavior

1 g of pure pre-reduced UO_2 sintered at 1200°C was first studied. Its sintering behavior is given in **Figure IV-4**. As already observed during the sintering of UO_2 at 1500°C, the onset of the densification takes place around 600°C. Then the piston speed (which represents the derivative of the relative piston displacement) reaches a maximum at 750°C before going back to 0 during the sintering plateau.

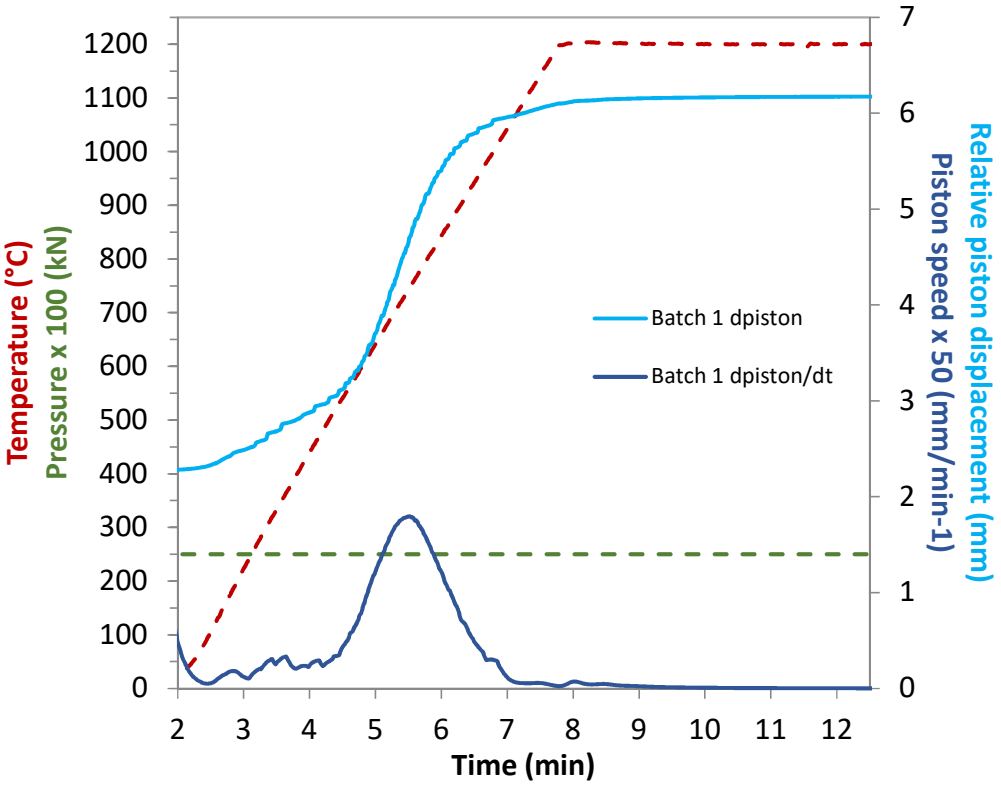

Figure IV-4: Relative piston displacement and piston speed during the sintering of Batch 1 (pure pre-reduced UO_2) at 1200°C during 5 min. The relative piston displacement and piston speed curves have been smoothed using a Savitzky-Golay filter [25] with 20 points.

IV.3.1.2 Density measurements

The five pellets of this batch were recovered and roughly polished to remove the graphite layer created during sintering. Their final density was measured thanks to the geometrical method and He pycnometry as shown in **Table IV-3**. The discrepancies between the two measurements are mainly due to the approximations taken to calculate the geometrical density and the fact that He pycnometry enables to deduce only closed porosity whereas the geometrical density takes into account the total porosity. Indeed, the pellet is considered as a cylinder in the calculation whereas its shape after sintering and polishing is not perfectly cylindrical. Moreover, the graphite remaining on the pellet is not taken into account in the theoretical density of the mixture and given the size of the final pellet (6 mm of diameter and 3 mm high), the graphite may represent a non-negligible part of it. Considering that the graphite (d_{th} = 2.23 g.cm^{-3}) represents 1 to 5 % of the whole pellet and forms a homogeneous layer around it (thickness from 0.9 to 2.01 mm which is consistent with the observations performed on the samples), the final geometrical density would range from 93.4 to 96.5 % $d_{th(UO2)}$. The error on the geometrical density would roughly range from 1 to 5 %.

Nevertheless, both values are higher than 90% $d_{th\ (UO2)}$ confirming that the pellets have been densified according to our initial objective on the final density.

Table IV-3: Results of density measurements made on pure pre-reduced UO_2 samples produced by SPS thanks to the geometric method and He pycnometry (average values on the batch)

Batch	Geometrical density (% d_{th})	He pycnometry (% d_{th})
1 (pre-reduced UO_2)	92.2 ± 0.7	98.2 ± 0.4

IV.3.1.3 SEM observations

Finally, the pellets were characterized thanks to SEM. As observed in **Figure IV-5**, some small intergranular pores ranging from 2 µm in the center of the pellets to 0.4 µm in the periphery, are still observed all over the pellets along with submicronic intragranular porosity.

The grain size is also higher in the center of the pellets (6.5 ± 0.9 µm) compared to the periphery (2.1 ± 0.3 µm). This phenomenon has already been observed in the study by [18]. UO_{2+x} pellets were sintered at 1200°C during five minutes which resulted in higher grain size in the center of the pellets compared to the one observed in the surfaces. This microstructure gradient was attributed to a higher oxidation state in the bulk of the samples compared to the surfaces due to a probable interaction between UO_{2+x} (where x = 0.01 in the study by [18]) and the graphite matrix according to reaction (2):

$$UO_{2+x} + xC \rightarrow UO_2 + xCO \qquad (2)$$

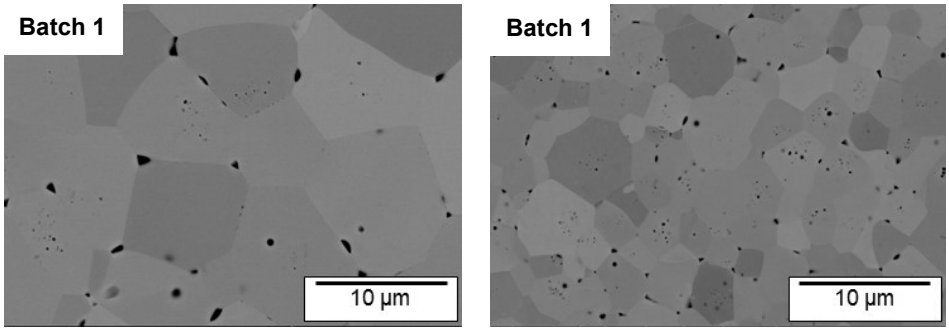

Figure IV-5: SEM-BSE images showing the morphology of the grains in the center (left hand-side) and the periphery (right hand-side) of a pre-reduced UO_2 pellet sintered at 1200°C during 5 minutes.

IV.3.2 Study of the system UO_2 / $Cs_2U_xO_y$ / MoO_3 (batches 1, 3 and 4)

IV.3.2.1 Sintering behavior

The sintering behavior of batch 4 (UO_2 + 1.2 % $Cs_2U_xO_y$ + 0.3 % MoO_3) can be observed in **Figure IV-6** along with batch 3 (UO_2 + 1.2 % $Cs_2U_xO_y$) and pure UO_2 (batch 1). 1 g of each mixture was sintered.

The sintering of the pellet of batch 4 occurs in two stages, which can be clearly identified, as two peaks are present in the piston speed curve (purple curve on the bottom of the graph). The first densification stage can be attributed to UO_2. Indeed, the beginning of the piston displacement curve of UO_2 and batch 4 are superimposed up to 650°C. However, in the case of batch 4, the sintering of UO_2 has been limited. This can be attributed to the presence of additives in between the UO_2 grains, limiting the contact surfaces.

The second densification stage begins around 650°C and the maximum sintering speed is reached at 880°C. This step is probably due to the impact of the two additives. Indeed, as observed in the red curves, the addition of $Cs_2U_xO_y$ to UO_2 implies a shift of almost 200°C in the beginning of the sintering compared to pure UO_2. The onset of sintering thus occurs at the same temperature than the second densification stage of batch 4. However, the maximum sintering speed of batch 3 is reached at 950°C which is higher compared to batch 4 (880°C). A second phenomenon occurs in this range of temperature which is the melting of MoO_3 at 795°C. This could explain the acceleration of the densification in the second sintering phase of batch 4 compared to batch 3. Indeed, as shown in [26] in the case of UO_2 + Cr_2O_3, a liquid phase can enhance the sintering speed if it can dissolve part of the matrix.

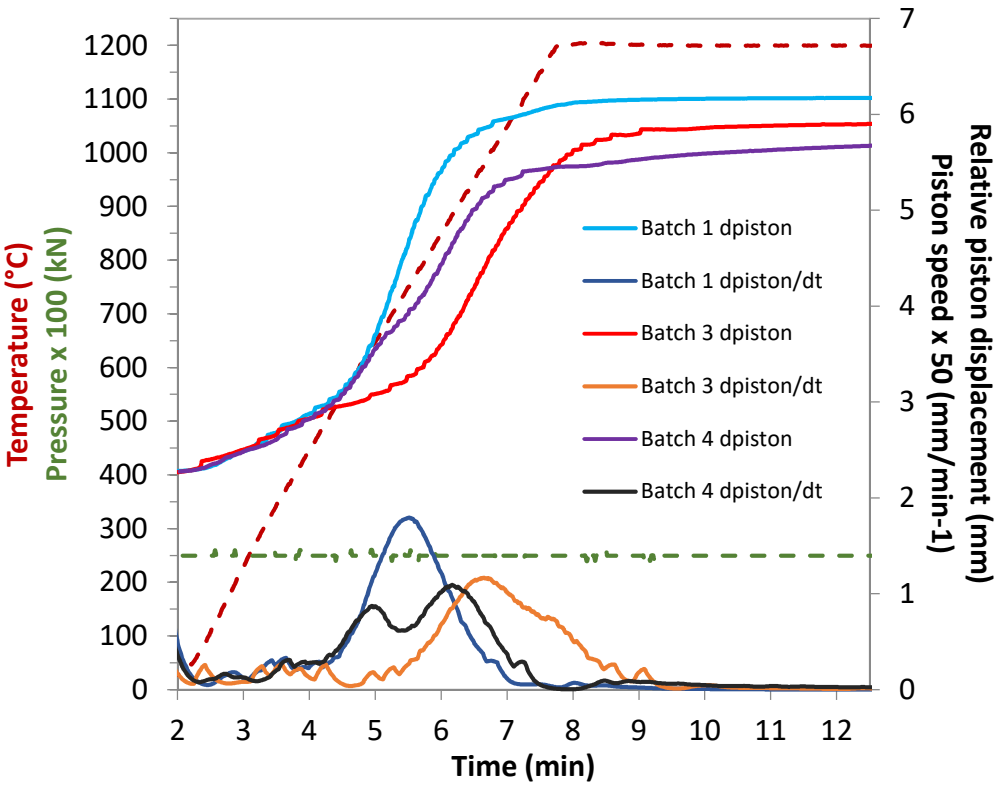

Figure IV-6: Relative piston displacement and piston speed during the sintering of pure pre-reduced UO_2, mixtures of batch 3 (UO_2 + 1.2 % $Cs_2U_xO_y$), batch 4 (UO_2 + 1.2 % $Cs_2U_xO_y$ + 0.3 % MoO_3) at 1200°C during 5 min. The relative piston displacement and piston speed curves have been smoothed using a Savitzky-Golay filter [25] with 20 points.

According to the piston displacement at the end of the SPS sequence for the three batches (**Figure IV-6**) and given the fact that the same mass (1 g) of mixtures was sintered in each case, the final density of batch 4 should be a little smaller than the ones of batch 1 and 2. This is globally the case as shown in **Table IV-4**.

IV.3.2.2 Density measurements

The final densities of five pellets composed of UO_2 + 1.2 % $Cs_2U_xO_y$ and three pellets composed of UO_2 + 1.2 % $Cs_2U_xO_y$ + MoO_3 were measured by three different methods (**Table IV-4**). The values obtained through He pycnometry and the Archimedes method (termed as hydrostatic density) are in good agreement whereas the geometrical density values are lower. As already discussed in the case of pure UO_2, this is probably due to the shape of the pellets, which are not exactly cylindrical, the contribution of graphite and the type of porosity taken into account during the different measurements. In the case of the Archimedes method, both the closed and the open porosity are taken into account as shown in **Appendix 3.1**. However, the determination of the humid mass in this method is the main source of error. This could explain why the hydrostatic density values are in between that of the geometrical and that of the He pycnometry.

Table IV-4: Results of density measurements made on SIMFuel samples from batches 3 and 4 produced by SPS thanks to the geometric method, the Archimedes one and He pycnometry (average values on each batch)

Batch	Geometrical density (% d_{th})	Hydrostatic density (% d_{th})	He pycnometry (% d_{th})
3 (UO_2 + 1.2 % $Cs_2U_xO_y$)	87.6 ± 1.4	95.9 ± 2.5	97.4 ± 0.4
4 (UO_2 + 1.2 % $Cs_2U_xO_y$ + 0.3% MoO_3)	86.1 ± 4.8	93.8 ± 4.2	96.9 ± 0.6

IV.3.2.3 Chemical analyses

The amount of Cs and Mo contained in three samples of batches 3 and 4 was measured through ICP-MS and ICP-AES. The uncertainty given on the analysis is ± 10 %. The results are presented in **Table IV-5**. The percentage of each element contained in the samples was determined considering the initial composition of the batch, assuming that it was homogeneous between each pellet of the same batch.

The difference in the concentration of Cs and Mo arising in the pellets before and after sintering can be attributed to the partial release of these elements during sintering. However, this does not explain the difference observed in the pellets of the same batch. The inhomogeneity of the initial powder mixtures could have led to different initial concentrations in Cs and Mo between the different pellets of the same batch. This would thus have implied an inaccurate estimation of the final amount of elements remaining in the pellets.

Indeed in the same batch, the amount of Mo and Cs remaining in the samples after sintering varies a lot. As a matter of fact, around 30 to 70 % of the initial Cs amount added to UO_2 is still present in the sample after sintering in the case of batch 3. In the case of batch 4, 6 to 16 % of Mo and 40 to 50 % of Cs remained. According to the results, the error brought by the inhomogeneity of the mix would be the main source of uncertainties and would be superior to 10 %.

Table IV-5: Concentration in U, Mo and Cs remaining in the samples of batches 3 and 4 after sintering at 1200°C during 5 min, obtained through ICP-MS and ICP-AES

Batch	Sample	U concentration (mg/g_{sample})	Mo concentration (mg/g_{sample})	% Mo remaining in the sample	Cs concentration (mg/g_{sample})	% Cs remaining in the sample
3 (UO_2 + 1.2 % $Cs_2U_xO_y$)	A	830.3 ± 16.6	-	-	2.680 ± 0.268	69 ± 7
	B	870.9 ± 17.4	-	-	2.706 ± 0.271	55 ± 6
	C	863.0 ± 17.3	-	-	1.506 ± 0.151	31 ± 3
4 (UO_2 + 1.2 % $Cs_2U_xO_y$ + 0.3% MoO_3)	D	848.5 ± 17.0	0.348 ± 0.035	16 ± 2	2.125 ± 0.213	54 ± 5
	E	858.2 ± 17.2	0.122 ± 0.012	6 ± 1	1.579 ± 0.158	40 ± 4
	F	816.7 ± 16.6	0.154 ± 0.015	7 ± 1	1.510 ± 0.151	40 ± 4

IV.3.2.4 SEM observations

Pellets of batches 3 and 4 were polished and observed by means of SEM (**Figure IV-7**). Similarly to the pure UO_2 samples, larger grains are observed in the center compared to the periphery. The grain size is globally higher in the center of the samples of batch 3 (2.45 ± 0.77 µm) compared to batch 4 (1.35 ± 0.31 µm). However, grains are smaller in the periphery of samples of batch 3 compared to batch 4 (respectively 0.62 ± 0.13 µm and 0.93 ± 0.27 µm). For both batches, the global grain size is smaller than for pure UO_2. An explanation can be find in the sintering behavior of these three batches. While the sintering of UO_2 has already ended at the beginning of the 1200°C dwell, the sintering of batch 3 and 4 is not completed yet. Thus, the thermal energy brought to the UO_2 during the 1200°C plateau may have been used for grain growth whereas in the case of batches 3 and 4 it was also used for sintering. Nevertheless, statistical microstructure analysis of several pellets of the same batch should be carried in order to conclude on this point.

Many grains were pulled-out during the polishing phase which resulted in highly porous samples at their surface contrary to what was observed in the case of pure UO_2 samples. Furthermore, the grain boundaries are most of the time clearly identified in the SEM pictures. This may indicate that grain boundaries have not the same nature as UO_2 and would have trapped FP during sintering.

No Cs nor Mo were detected by EDX in the polished samples. However, Cs was found in a fractured sample of batch 3. As shown in the SEM-BSE image of **Figure IV-8**, no chemical contrast could be noticed through BSE mode, which could indicate that Cs is maybe present as uranates, deposited at the surface of some grains or at the grain boundaries.

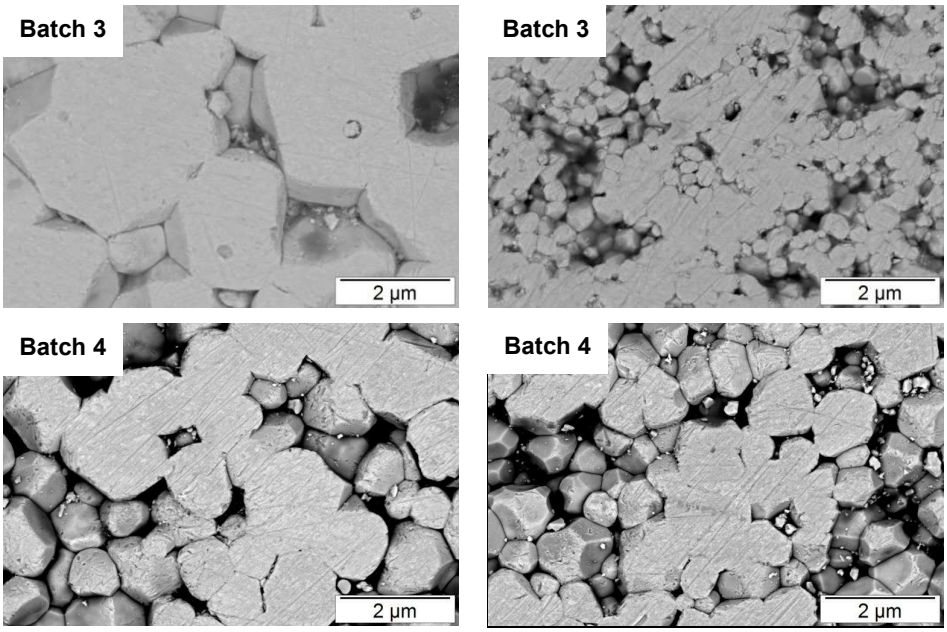

Figure IV-7: SEM-BSE images showing the morphology of the grains in the center (left) and the periphery (right) of the pellets of the SPS-1 series. From the top to bottom: UO_2 + 1.2 % $Cs_2U_xO_y$ and UO_2 + 1.2 % $Cs_2U_xO_y$ + 0.3 % MoO_3.

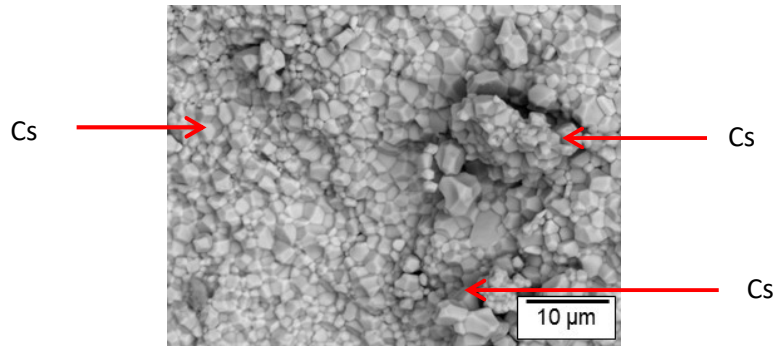

Figure IV-8: SEM-BSE image of fractured surface from a sample of batch 3 (UO_2 + 0.9 % $Cs_2U_xO_y$)

IV.3.2.5 XANES analyses

HERFD mode was used to probe the speciation of Cs at L_2-edge on the same samples. As shown in **Figure IV-9**, the shape of the Cs spectra of samples of batch 3 and 4 are very similar.

This is also the case of the spectra of Cs_2MoO_4 and $Cs_2U_xO_y$ standards as shown in **Figure IV-10**. This can be explained by the fact that even $Cs_2U_xO_y$ and Cs_2MoO_4 do not have the same crystallographic structure, Cs local environment is very similar. Indeed, Cs_2UO_4 is tetragonal, $Cs_2U_2O_7$ is monoclinic and Cs_2MoO_4 can be orthorhombic or monoclinic beyond 568°C [27]. However, in these four types of structures, Cs is surrounded by oxygen atoms (whether in -MoO_4 or -UO_4 tetrahedra or -UO_6 octahedra). The Cs-O distances are also very close in the two compounds.

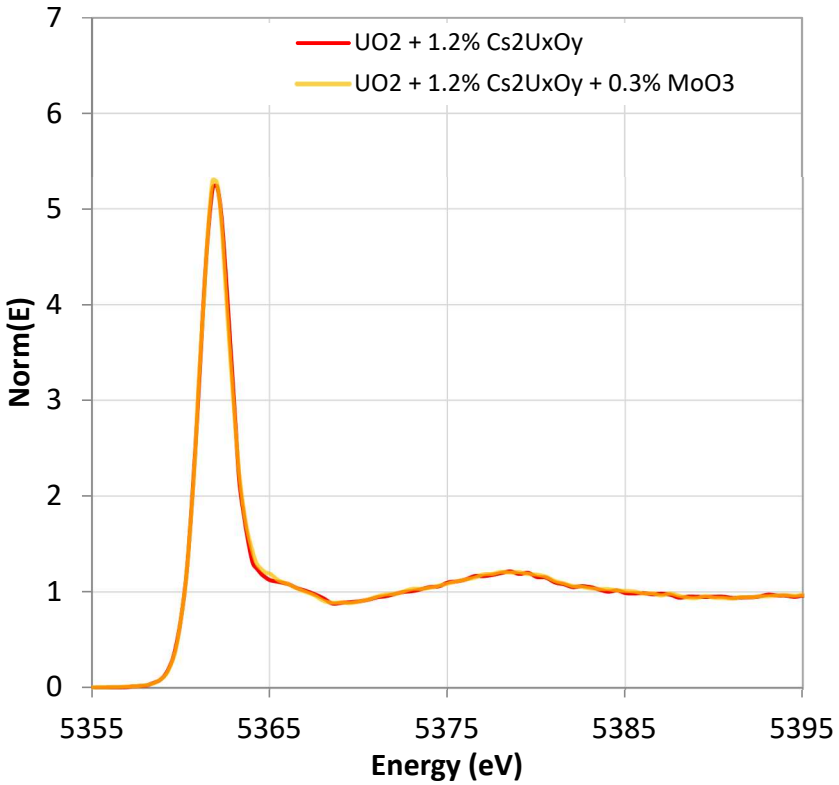

Figure IV-9: Experimental HERFD-XANES spectra of a sample of batch 3 and batch 4 as-sintered acquired on the FAME-UHD beamline (ESRF)

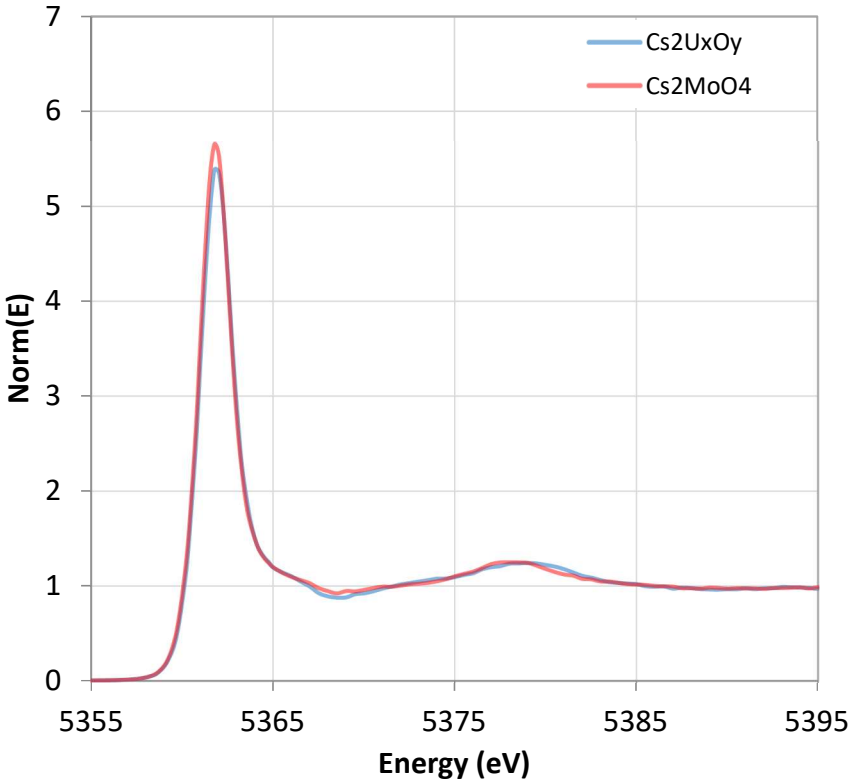

Figure IV-10: Experimental HERFD-XANES spectra of $Cs_2U_xO_y$ and Cs_2MoO_4 standards acquired on the FAME-UHD beamline (ESRF)

IV.3.2.6 Thermodynamic calculations

Thermodynamic calculations using the FactSage 7.0 software were performed in order to go further in the interpretation of the experimental data obtained in the previous sections. The predominance diagrams of the phases involved in the systems considered in batches 3 and 4 are shown in **Figure IV-11** and **Figure IV-12** respectively. These diagrams have been performed accounting for the amount of Cs and Mo remaining in the samples after sintering, measured by chemical analyses (**Table IV-5**). As the initial stoichiometry of the UO_2 powder used was 2.01 and considering that an interaction between UO_2 and the graphite die took place during sintering, some redox indicators have been added to the diagrams:

- The equilibrium $C_{(s)}/CO_{(g)}$ at 0.1 and 1 bar.
- The equilibrium $CO_{(g)}/CO_{2(g)}$ at 1 bar.
- The oxygen potential corresponding to stoichiometric UO_2 in the calculation range of temperature.
- The oxygen potential corresponding to $UO_{2.01}$ in the calculation range of temperature.

According to the HERFD-XANES measurements performed in the samples of batch 3, the local environment of Cs is very similar to that of $Cs_2U_xO_y$. Chemical analyses indicated that around half of the initial Cs amount has been released from the sample.

According to **Figure IV-11**, at 1200°C Cs can be present as free Cs (gaseous in these conditions) or under uranate condensed forms. These phases are both consistent with the experimental

observations. The release of Cs at 1200°C results from the decomposition of uranates to form free Cs according to $Cs_2UO_4 \rightarrow 2\ Cs + O_2 + UO_2$.

Considering the experimental data, Cs and Cs_2UO_4 coexist in the samples of batch 3. As shown in **Figure IV-11**, the oxygen potential range during sintering is thus probably located around the limit between the $UO_2 + Cs_2UO_4$ and $UO_2 + Cs_{(l)}$ domains, which also corresponds to the area between the $C_{(s)}/CO_{(g)}$ equilibrium at 1 bar and the oxygen potential corresponding to $UO_{2.00}$. This domain is pointed out thanks to the grey circle on **Figure IV-11**, and extends from -550 $kJ.mol_{(O2)}^{-1}$ to -475 $kJ.mol_{(O2)}^{-1}$.

Following these assumptions, Cs should be found in the samples of batch 4 as Cs_2UO_4, Cs_2MoO_4 and free Cs while Mo should be found as Cs_2MoO_4 or metallic Mo (**Figure IV-12**). However, the experimental data available on this batch do not enable to conclude.

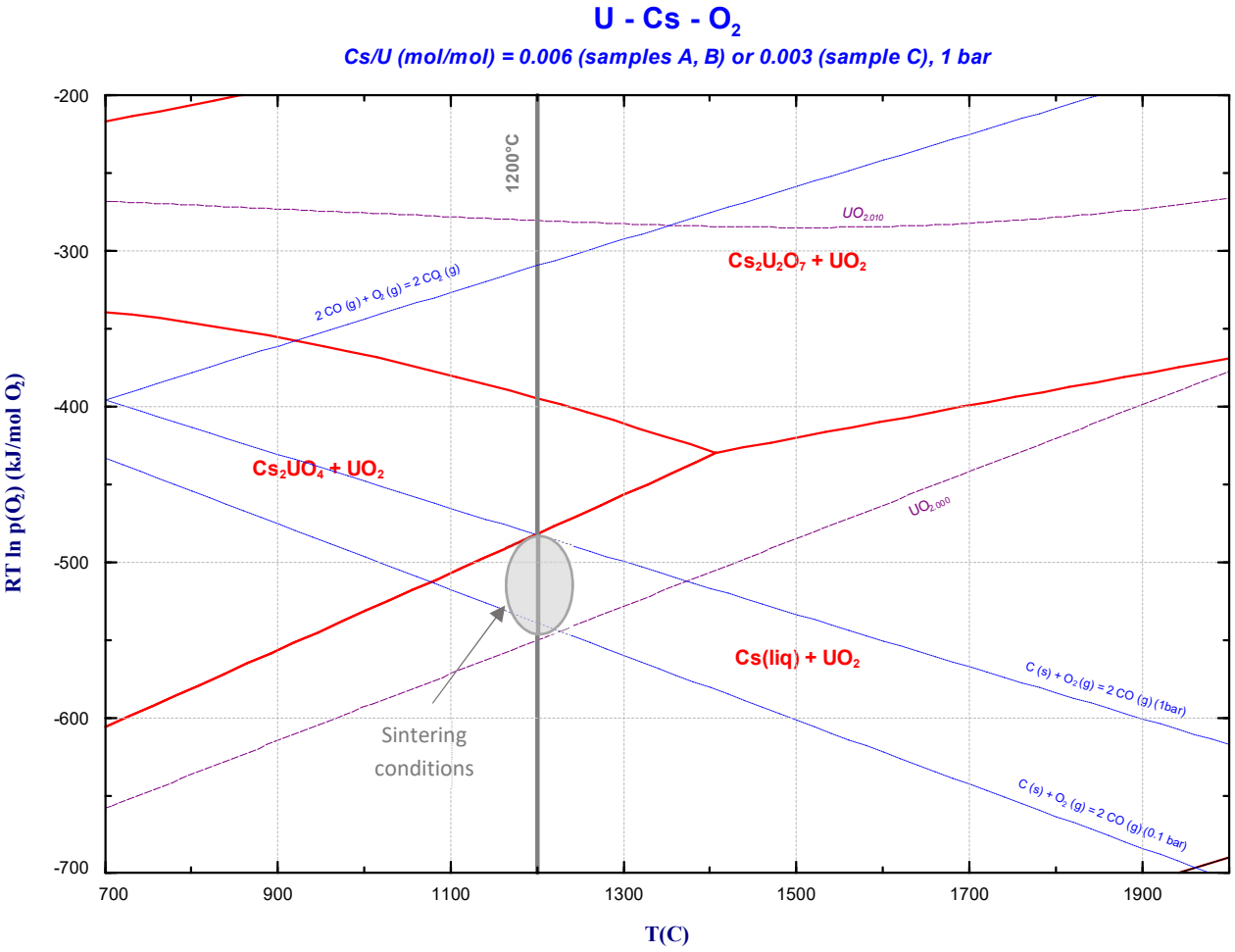

Figure IV-11: Predominance diagram for the Cs-U-O_2 system (Batch 3), considering the quantities of elements remaining in the system after sintering (the diagram is equivalent for samples A, B and C in Table IV-5), obtained using the SGPS database of FactSage [23], [24]. The grey line corresponds to the sintering temperature, the blue dashed lines correspond to the equilibrium $C_{(s)}/CO_{(g)}$ and $CO_{(g)}/CO_{2(g)}$ at 0.1 and 1 bar and the purple lines correspond to stoichiometric $UO_{2.000}$ and hyperstoichiometric $UO_{2.010}$.

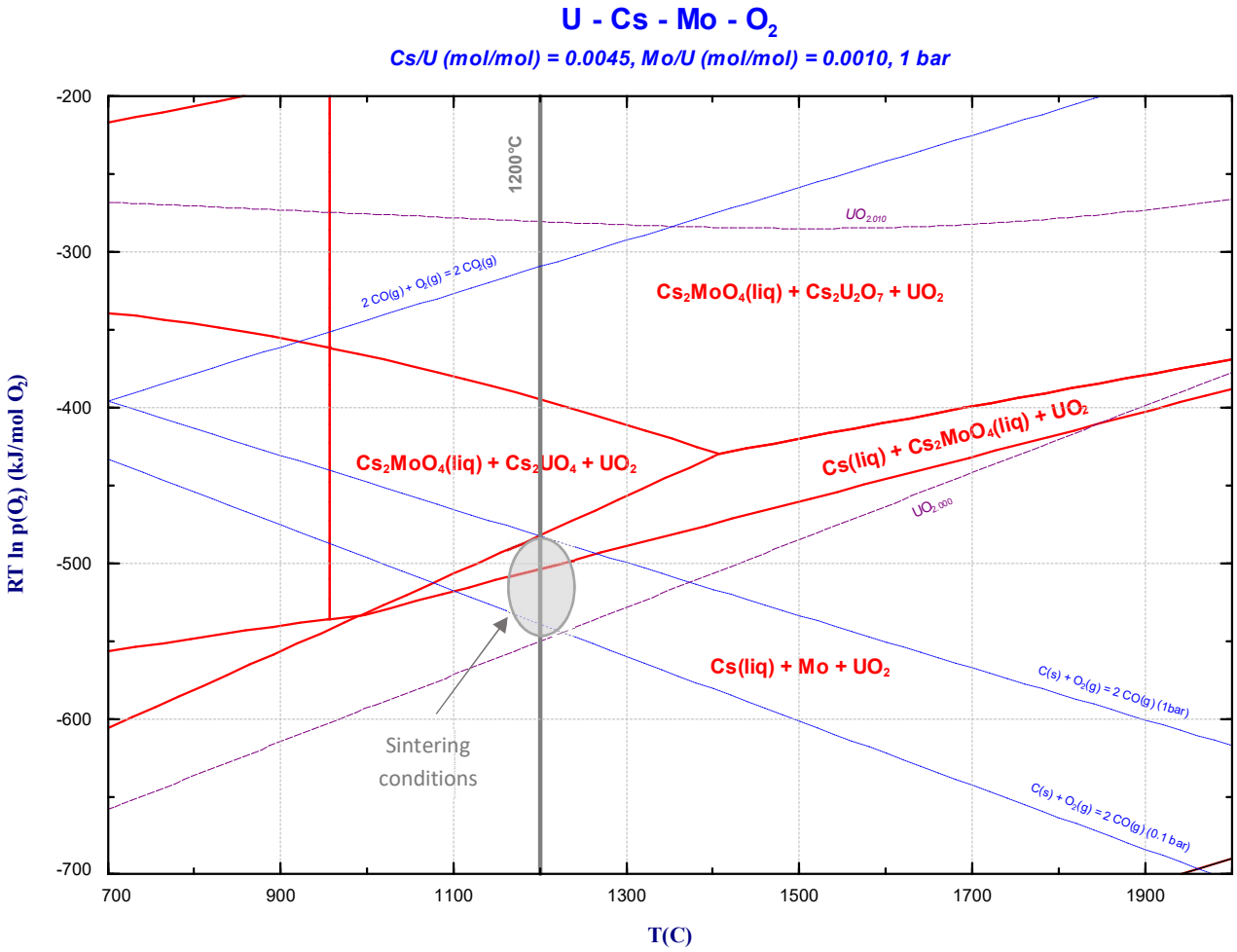

Figure IV-12: Predominance diagram for the Cs-Mo-U-O_2 system (Batch 4), considering the quantities of elements remaining in the system after sintering (the diagram is equivalent for samples D, E and F in Table IV-5), obtained using the SGPS database of FactSage [23], [24]. The grey line corresponds to the sintering temperature, the blue dashed lines correspond to the equilibrium $C_{(s)}/CO_{(g)}$ and $CO_{(g)}/CO_{2(g)}$ at 0.1 and 1 bar and the purple lines correspond to stoichiometric $UO_{2.000}$ and hyperstoichiometric $UO_{2.010}$.

IV.3.3 Study of the system UO_2 / Cs_2MoO_4 / $BaCO_3$ (batches 1, 2, 5 and 7)

IV.3.3.1 Sintering behavior

Figure IV-13 presents the sintering behavior of 1 g of pure UO_2, of 1 g of batch 2 (UO_2 + 0.9 % Cs_2MoO_4), 0.7 g of batch 5 (UO_2 + 4.4 % $BaCO_3$) and 0.5 g of batch 7 (UO_2 + 4.0 % Cs_2MoO_4 + 4.0 % $BaCO_3$).

The sintering of the mixture composed of UO_2 + 4.0 % Cs_2MoO_4 + 4.0 % $BaCO_3$ presents a single densification phase starting around 1000°C. The maximum sintering speed is reached at 1110°C but sintering has been interrupted on the temperature plateau (1200°C). The melting of Cs_2MoO_4 occurring at 956°C [28] could explain the later sintering of samples of batch 7. However, in the case of samples composed of UO_2 + Cs_2MoO_4 sintering starts around 700°C with a maximum speed reached at 850°C which is in contradiction with the previous hypothesis. In the case of batch 5, sintering happens in two times. A first phase starting at 550°C may be attributed to UO_2 whereas the second one occurring at 1005°C is most probably due to $BaCO_3$. According to the predominance diagram shown in **Figure IV-21**, $BaCO_3$ is decomposed in Ba_3UO_6 and CO around 950°C. Gaseous CO could thus be trapped in the closed porosity and create pressure which would work against sintering.

Given that none of the sintering temperatures of samples of batch 2 or 5 are consistent with that of batch 7, an interaction between the additives and UO_2 may probably have occurred. This interaction would then have delayed the sintering of sample of batch 7.

The piston displacement at the end of the SPS sequence is very dependent on the mass of powder initially introduced in the graphite matrix as a relative piston displacement is measured. It is thus logical to observe a longer piston travel in the case of pure UO_2 and batch 2 (1 g each) than in the case of batch 5 (0.7 g) and 7 (0.5 g).

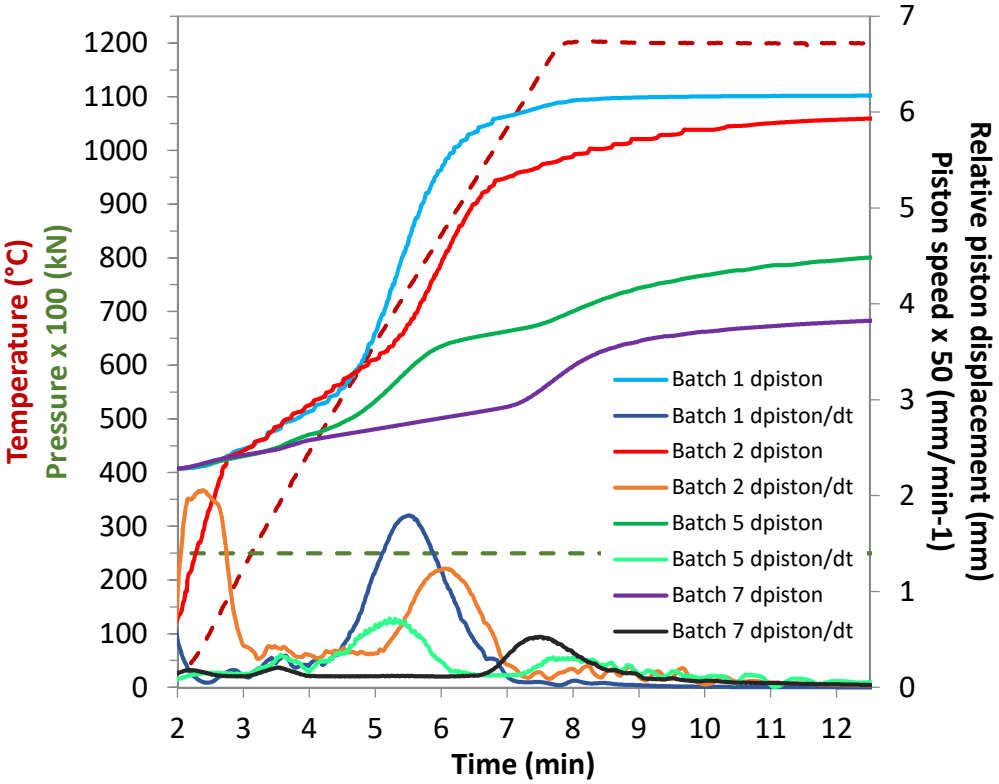

Figure IV-13: Relative piston displacement and piston speed during the sintering of pure pre-reduced UO_2, mixtures of batch 2 (UO_2 + 0.9 % Cs_2MoO_4), batch 5 (UO_2 + 4.4 % $BaCO_3$) and batch 7 (UO_2 + 4.0 % Cs_2MoO_4 + 4.0 % $BaCO_3$) at 1200°C during 5 min. The relative piston displacement and piston speed curves have been smoothed using a Savitzky-Golay filter [25] with 20 points.

IV.3.3.2 Density measurements

The pellets were removed from the furnace and roughly polished to remove the graphite layer. In the case of the samples containing $BaCO_3$, the graphite foil and disks used to facilitate the retrieving of the pellets from the graphite matrix were removed very easily. This may indicate that weak interactions took place between the graphite and the sample during sintering. Thus, these samples were not polished, reducing the error on the geometrical density measurement (no contribution of graphite).

The final density of the three types of samples has been measured and turns out to be higher than 90 $\%d_{th(mixture)}$ considering the values obtained by the Archimedes method (hydrostatic density), as shown in **Table IV-6**. The values are nonetheless lower than for pure UO_2, confirming the impact of additives on the sintering behavior of UO_2 and on the final density.

The discrepancies between the geometrical density measurements and the hydrostatic ones in the case of batches 5 and 7 are surprisingly high. Moreover, the evolution of the hydrostatic density is not consistent with the geometrical one. This can be due to the open porosity which could have been underestimated for these two batches. Complementary measurements should thus be carried out in order to conclude on the "real" density of samples of batches 5 and 7.

Table IV-6: Results of density measurements made on SIMFuel samples from batches 2, 5 and 7 produced by SPS thanks to the geometric method, the Archimedes one and He pycnometry (average values over the batch)

Batch	Geometrical density (% d_{th})	Hydrostatic density (% d_{th})	He pycnometry (% d_{th})
2 (UO_2 + 0.9 % Cs_2MoO_4)	86.1 ± 3.1	91.2 ± 2.3	93.3 ± 0.6
5 (UO_2 + 4.4 % $BaCO_3$)	74.4 ± 4.2	93.0 ± 2.4	-
7 (UO_2 + 4.0 % Cs_2MoO_4 + 4.0 % $BaCO_3$)	64.3 ± 6.3	92.0 ± 2.3	-

IV.3.3.3 Chemical analyses

The amount of Cs and Mo remaining in three pellets sintered from batch 2 was determined through ICP-MS and ICP-AES as shown in **Table IV-7**. Batches 5 and 7 could not be analyzed through these techniques because of the amount of pellets available (only 2 per batch). Indeed, before performing destructive chemical analyses, the pellets were planned to be transported back to Cadarache and fully characterized, which could not be done within the time of the Ph.D.

Huge differences can be noticed concerning the final Mo and Cs quantities remaining in the samples after sintering. Indeed, 5 to 56 % of the initial amount of Mo and 21 to 47 % of Cs have remained in the pellets which were made out of the same batch of powder.

One can notice that Cs and Mo releases were not identical in the case of sample G and H. The more Mo remaining in the sample, the less Cs has been retained. This indicates that Cs_2MoO_4 may have been decomposed prior to its evaporation which is supposed to be congruent [29], [30]. The molar Cs/Mo ratio calculated using the data presented in **Table IV-7**, is 2.13 for sample H and 0.76 for sample G. This would indicate that Cs and Mo may have been released as Cs_2MoO_4 in sample H whereas a decomposition of Cs_2MoO_4 appeared in sample G.

Nevertheless, the discrepancies between the amounts of Mo released from sample I compared to sample G and H cannot be explained. An error during the preparation of the solutions used to determine Mo concentration has been disregarded as two different and independent ways of measuring this concentration have been used (ICP-AES and ICP-MS, see **Appendix 3.1**).

Table IV-7: Concentration in U, Mo and Cs remaining in the samples from batch 2 after sintering at 1200°C during 5 min, obtained through ICP-MS and ICP-AES

Batch	Sample	U concentration (mg/g_{sample})	Mo concentration (mg/g_{sample})	% Mo remaining in the sample	Cs concentration (mg/g_{sample})	% Cs remaining in the sample
2 (UO_2 + 0.9 % Cs_2MoO_4)	G	860.1 ± 17.2	1.144 ± 0.114	56 ± 6	1.196 ± 0.120	21 ± 2
	H	850.2 ± 17.0	0.694 ± 0.069	34 ± 3	2.043 ± 0.204	36 ± 4
	I	862.7 ± 17.3	0.141 ± 0.014	5 ± 1	3.941 ± 0.394	47 ± 5

IV.3.3.4 SEM observations

These chemical analyses are consistent with SEM-SE image of a fractured sample from batch 1 (**Figure IV-14**) showing a melted phase composed of Mo without Cs as determined through EDX analyses.

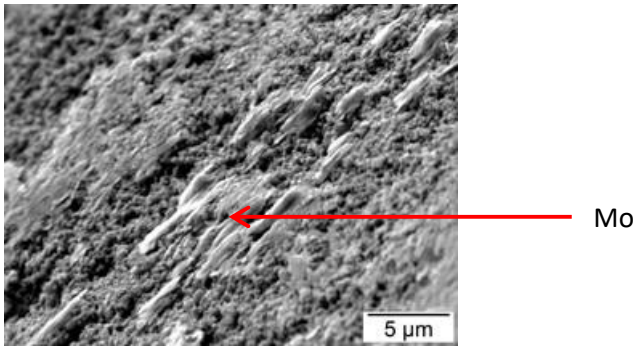

Figure IV-14: SEM-SE image of fractured surface from a sample of batch 2 (UO_2 + 0.9 % Cs_2MoO_4)

Pellets of batch 2 (UO_2+Cs_2MoO_4) were polished and observed through SEM. Similarly to the samples composed of pure UO_2, UO_2 + $Cs_2U_xO_y$ and UO_2 + $Cs_2U_xO_y$ + MoO_3, grains are smaller at the periphery of the pellets (0.44 ± 0.10 µm) compared to the center (1.36 ± 0.27 µm, **Figure IV-15**). Once again, several grains were pulled-out during the polishing phase and no Cs nor Mo could be detected through EDX analyses after polishing. The red circles seen in **Figure IV-15** point out what is probably polishing debris.

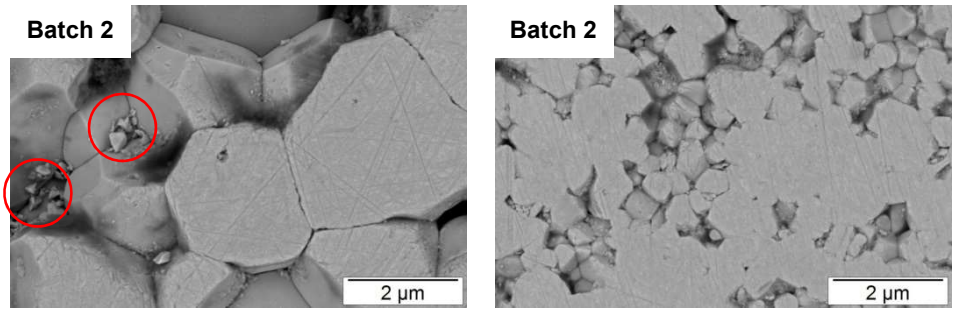

Figure IV-15: SEM-BSE images showing the morphology of the grains in the center (left hand side) and the periphery (right hand side) of the pellet composed of UO_2 + 0.9 % Cs_2MoO_4.

Fractured pellets obtained from the sintering of batches 5 and 7 were also observed. Huge agglomerates of several hundreds of microns containing Ba and oxygen without U or C have been

seen all over the sample composed of UO_2 + $BaCO_3$, as shown in **Figure IV-16**. Some Ba was also observed associated with U but in smaller precipitates.

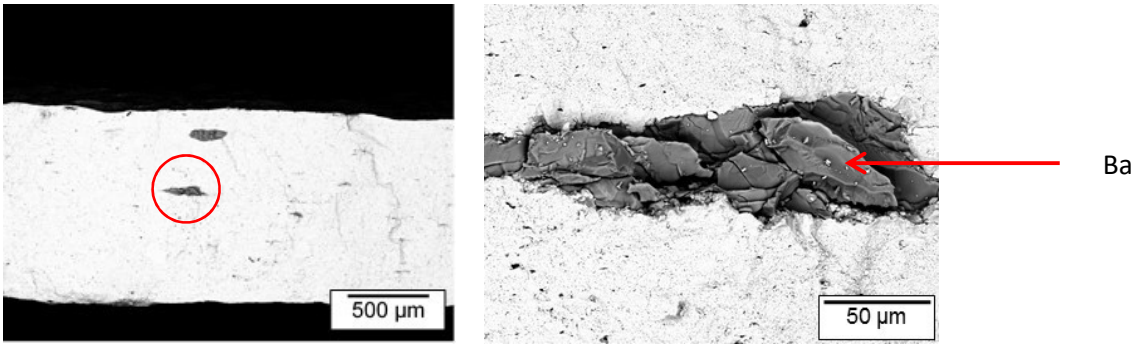

Figure IV-16: SEM-BSE images of fractured surface from a sample of batch 5 (left hand side, UO_2 + 4.4 % $BaCO_3$) and focus on the phase observed in the red circle (right hand side)

As observed in the blue circles in **Figure IV-17**, several phases containing Cs, Ba or Mo are observed all over the sample. Thanks to EDX analyses, some associations between Cs and Ba were noticed (purple circles) as well as regions containing only Ba (orange circles) or Cs (red circles) with U. Mo was rarely observed and most of the time alone or in association with Cs. These observations indicate that reactions may have occurred during sintering, which have led to the decomposition of part of the Cs_2MoO_4 along with some Cs and Mo release.

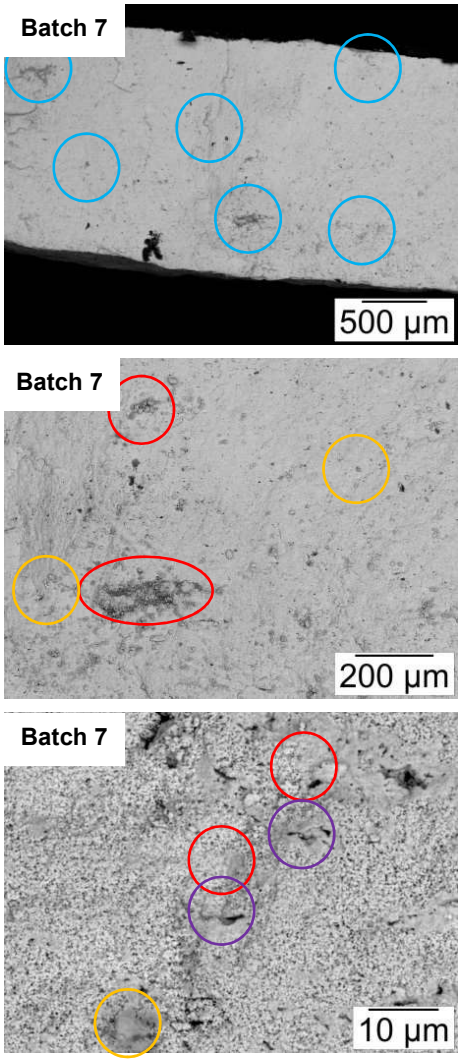

Figure IV-17: SEM-BSE images of fractured surfaces of a sample of batch 7 (UO_2 + 4.0 % Cs_2MoO_4 + 4.0 % $BaCO_3$) of the SPS-2 series. The blue circles correspond to regions where Cs, Mo or Ba were detected, the red circles correspond to regions where Cs was detected by EDX, orange circles correspond to areas containing Ba and purple circles correspond to areas where both Cs and Ba were detected.

IV.3.3.5 XANES analyses

HERFD-XANES experiments carried out on a sample from batch 2 at Cs L_2-edge (**Figure IV-18**), confirmed that Cs was still present in the sample whether under molybdate or uranate form. The white line of the sample of batch 2 is narrower than those of Cs_2MoO_4 and $Cs_2U_xO_y$, which is particularly visible at 5.365 keV. However, considering the similarities between the spectra of Cs_2MoO_4 and $Cs_2U_xO_y$ standards, it was impossible to discriminate both species in this sample.

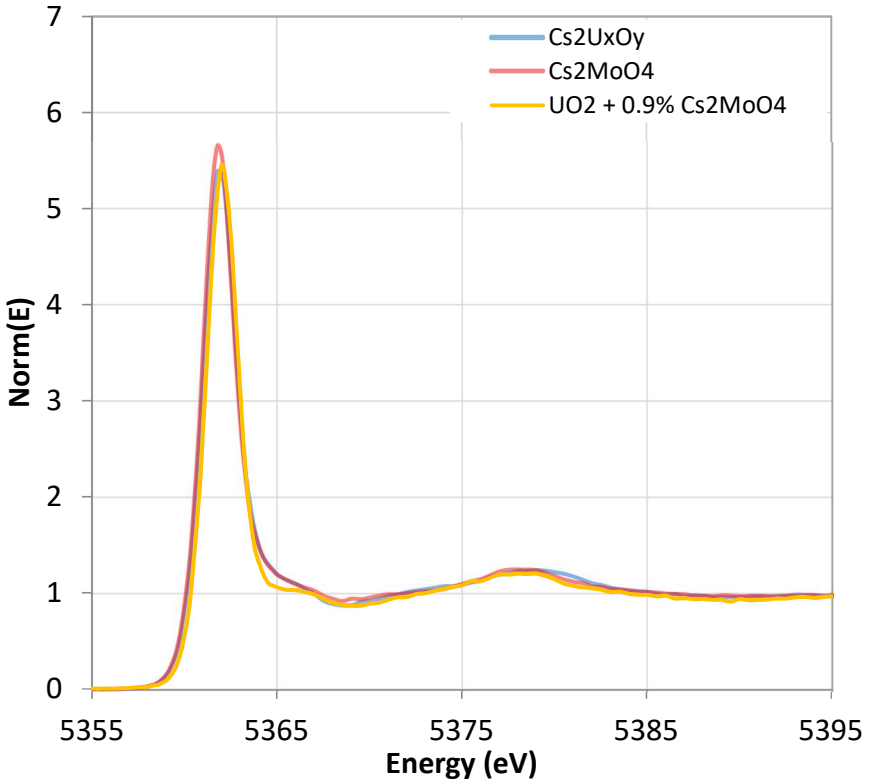

Figure IV-18: Experimental HERFD-XANES spectra of a sample of batch 2 as-sintered, $Cs_2U_xO_y$ and Cs_2MoO_4 standards acquired on the FAME-UHD beamline (ESRF)

IV.3.3.6 Thermodynamic calculations

Mo was observed to be present alone in the samples through SEM-EDX. According to the the HERFD-XANES measurements performed in the samples of batch 2, the local environment of Cs is very similar to that of $Cs_2U_xO_y$ or Cs_2MoO_4. Finally, chemical analyses indicated that the molar Cs/Mo ratio in sample H is 2.13 which is very close from 2.00 as in the Cs_2MoO_4 phase. In sample G, this ratio is lower (0.76), indicating that Cs was released in higher quantity than Mo, which would be consistent with the decomposition of the initial Cs_2MoO_4 additive according to $Cs_2MoO_4 \rightarrow 2Cs(g) + Mo(s) + 2O_2$.

The predominance diagrams corresponding to the system considered in batch 2 considering the amount of Cs and Mo in samples G and H are presented in **Figure IV-19** and **Figure IV-20** respectively.

In **Figure IV-19**, Mo can be present as Mo, MoO_2 or Cs_2MoO_4 at 1200°C and Cs as free Cs or Cs_2MoO_4. According to this, the only way to explain the decomposition of Cs_2MoO_4 in sample G is to consider the formation of free Cs and solid Mo. In consistency with the XANES results, the oxygen potential during sintering must be defined as in **section IV.3.2.6** (grey circle). Mo should thus be present as metallic Mo when not associated with Cs.

This is in agreement with other studies performed on samples containing pre-reduced UO_2 and Mo introduced as MoO_2 and metallic Mo [31]. The samples were sintered in the same conditions as the pellets studied in the present work. The final state of Mo ended up to be metallic, which indicates that the atmosphere during the sintering is reducing compared to the equilibrium Mo/MoO_2. Thus, the oxygen potential in the pellets during sintering at 1200°C may not exceed - 350 $kJ.mol_{(O2)}^{-1}$ and is thus probably highly influenced by the $C_{(s)}/CO_{(g)}$ equilibrium, provided by the interaction of the graphite SPS die and UO_{2+x}.

In sample H, Cs may be present as free Cs or Cs_2MoO_4 and Mo respectively as metallic Mo or Cs_2MoO_4 in the conditions indicated in the domain contained in the grey circle in **Figure IV-20**. This is perfectly consistent with the experimental observations.

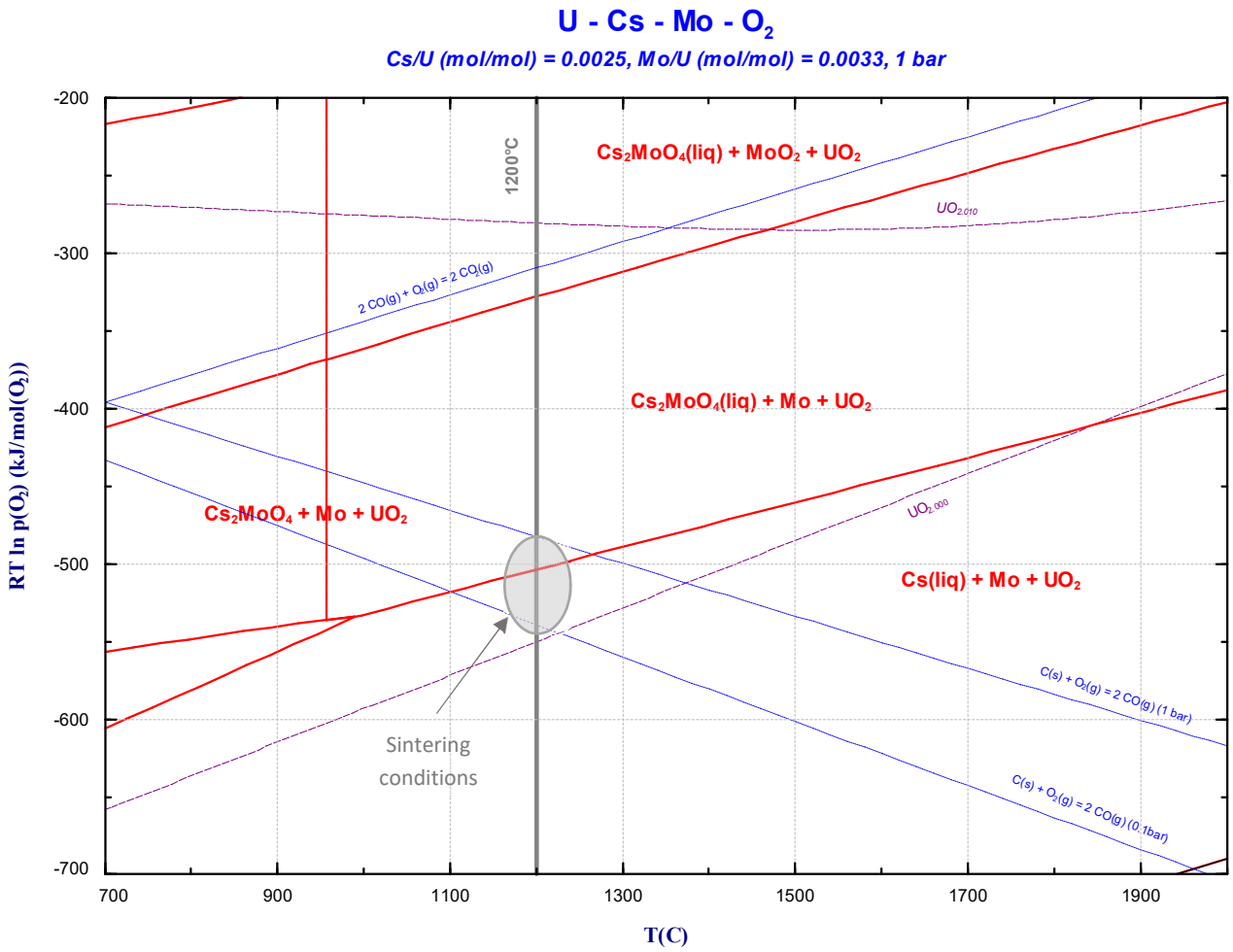

Figure IV-19: Predominance diagram for the Cs-Mo-U-O_2 system (Batch 2), considering the quantities of elements remaining in the system after sintering (sample G in Table IV-7), obtained using the SGPS database of FactSage [23], [24]. The grey line corresponds to the sintering temperature, the blue dashed lines correspond to the equilibrium $C_{(s)}/CO_{(g)}$ and $CO_{(g)}/CO_{2(g)}$ at 0.1 and 1 bar and the purple lines correspond to stoichiometric $UO_{2.000}$ and hyperstoichiometric $UO_{2.010}$.

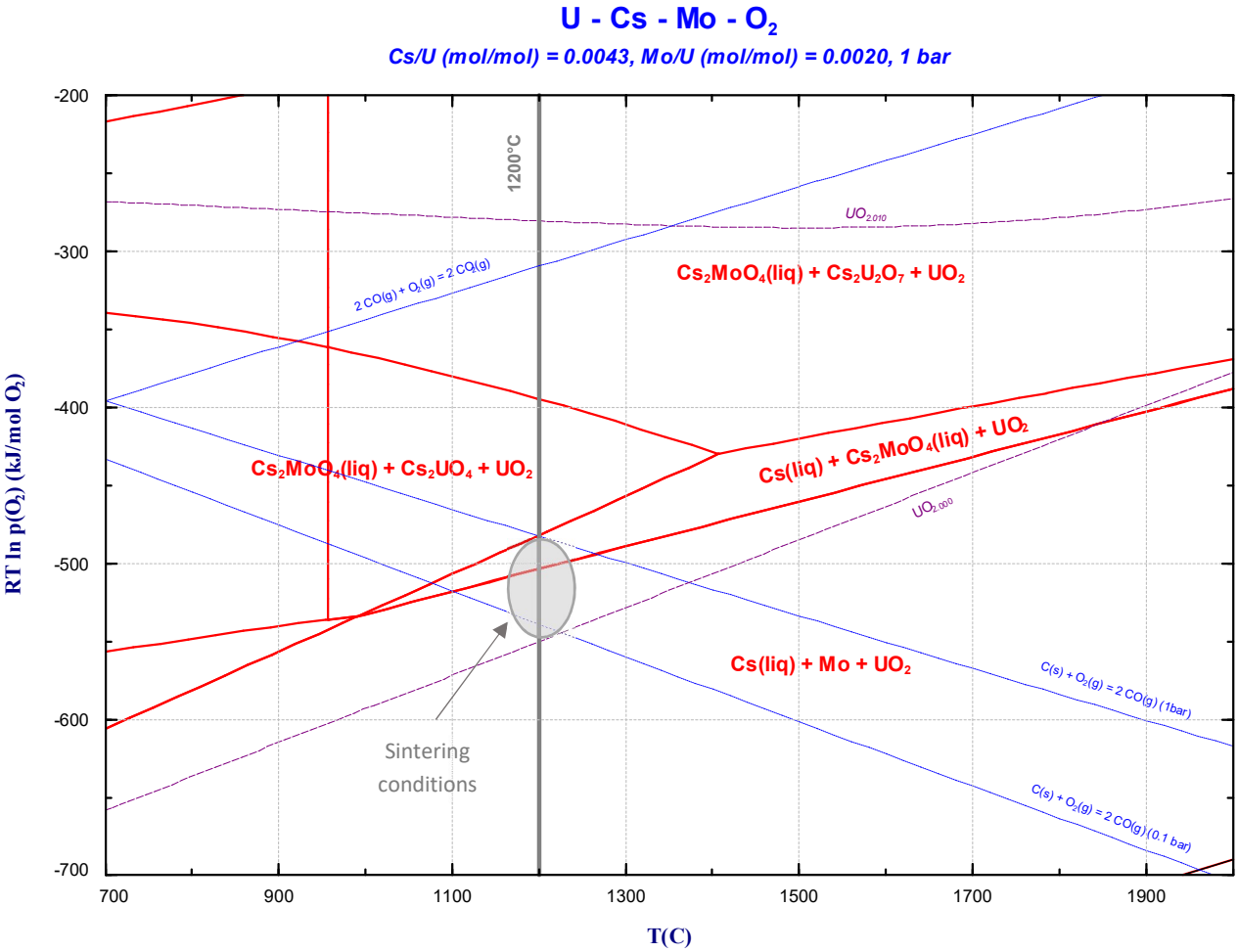

Figure IV-20: Predominance diagram for the Cs-Mo-U-O_2 system (Batch 2), considering the quantities of elements remaining in the system after sintering (sample H in Table IV-7), obtained using the SGPS database of FactSage [23], [24]. The grey line corresponds to the sintering temperature, the blue dashed lines correspond to the equilibrium $C_{(s)}/CO_{(g)}$ and $CO_{(g)}/CO2_{(g)}$ at 0.1 and 1 bar and the purple lines correspond to stoichiometric $UO_{2.000}$ and hyperstoichiometric $UO_{2.010}$.

The predominance diagrams related to batches 5 and 7 (**Figure IV-21** and **Figure IV-23** respectively) were established assuming that no Cs, Mo and Ba releases took place, as no quantitative chemical analyses could be performed on these samples. Thus, the initial concentrations in additive were used.

According to these calculations, Ba is always found as uranate ($BaUO_3$) at 1200°C in the oxygen potential domain supposed. This is consistent with the observations performed on the sample of batch 5, where part of Ba was associated to U, except in the large agglomerates containing Ba and O without U. This may be explained by the decomposition of unreacted $BaCO_3$ into BaO and C in these agglomerates. No reaction with U took place because of their size (kinetics limitation). This hypothesis agrees with the evolution of $BaCO_3$ calculated thermodynamically and given in **Figure IV-22**.

As shown in **Figure IV-23**, the existence of $BaUO_3$ in the sintering conditions is also consistent with the observations made on the samples of batch 7, where Ba was found with U in the sample. Regarding Cs, it can be found as free Cs or Cs_2MoO_4 and Mo as metallic Mo or Cs_2MoO_4. These results are perfectly consistent with the observations made in the samples of batch 7, as Cs and Ba were observed through SEM-EDX to be alone or associated with Mo for part of the Cs.

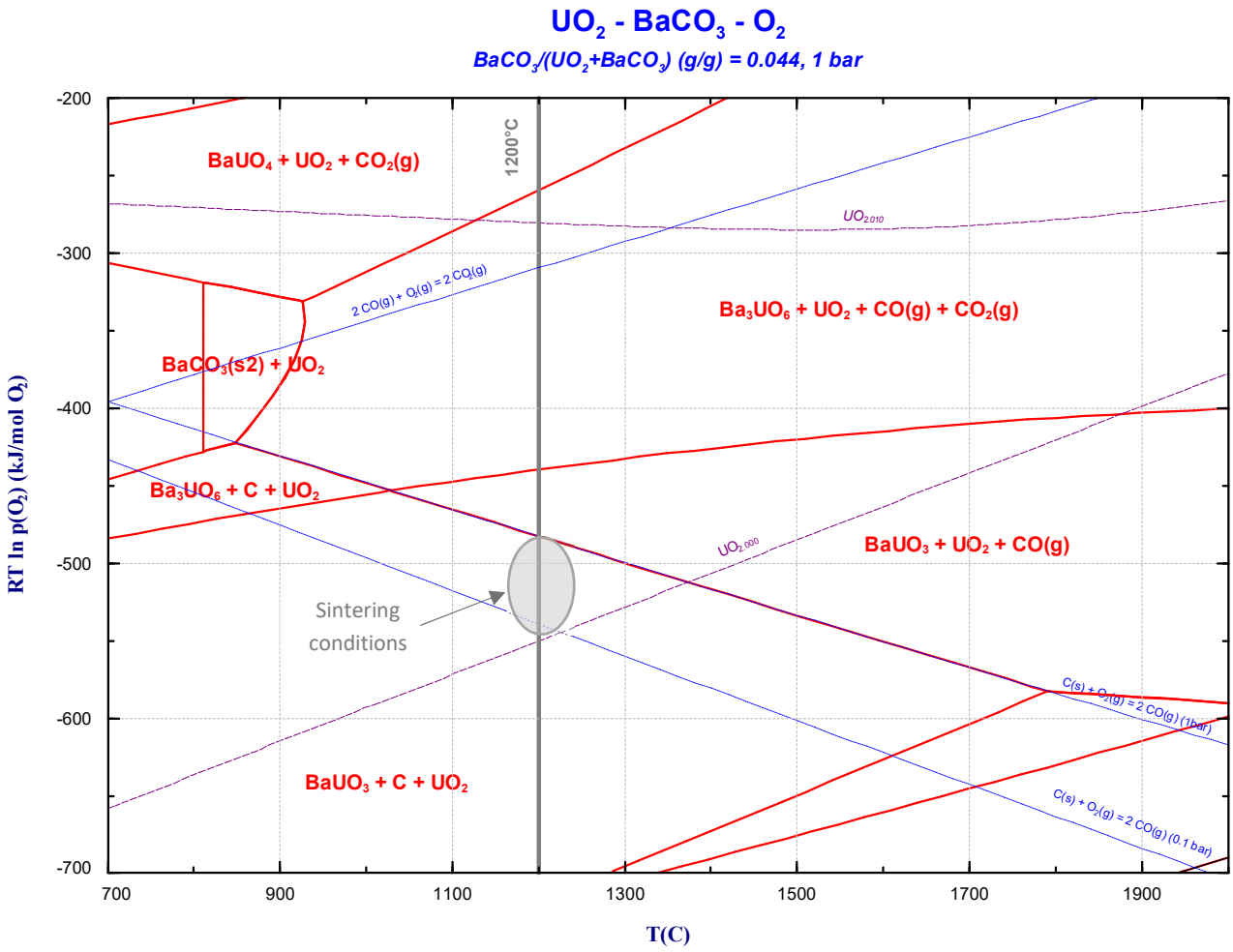

Figure IV-21: Predominance diagram for the UO_2-$BaCO_3$-O_2 system (Batch 5), considering the quantities of elements added before sintering, obtained using the SGPS database of FactSage [23], [24]. The grey line corresponds to the sintering temperature, the blue dashed lines correspond to the equilibrium $C_{(s)}/CO_{(g)}$ and $CO_{(g)}/CO_{2(g)}$ at 0.1 and 1 bar and the purple lines correspond to stoichiometric $UO_{2.000}$ and hyperstoichiometric $UO_{2.010}$.

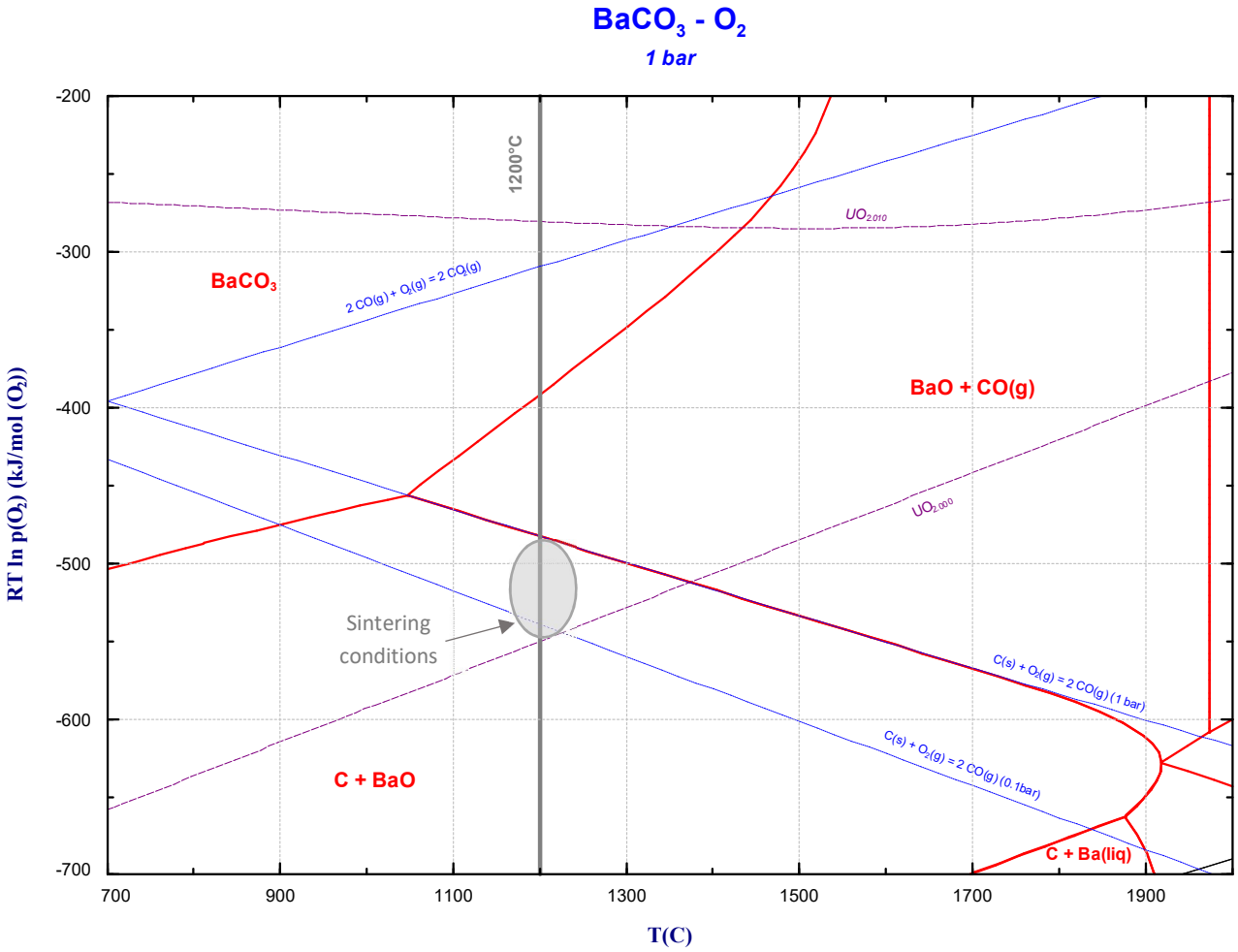

Figure IV-22: Predominance diagram for the $BaCO_3$-O_2 system obtained using the SGPS database of FactSage [23], [24]. The grey line corresponds to the sintering temperature, the blue dashed lines correspond to the equilibrium $C_{(s)}/CO_{(g)}$ and $CO_{(g)}/CO_{2(g)}$ at 0.1 and 1 bar and the purple lines correspond to stoichiometric $UO_{2.000}$ and hyperstoichiometric $UO_{2.010}$.

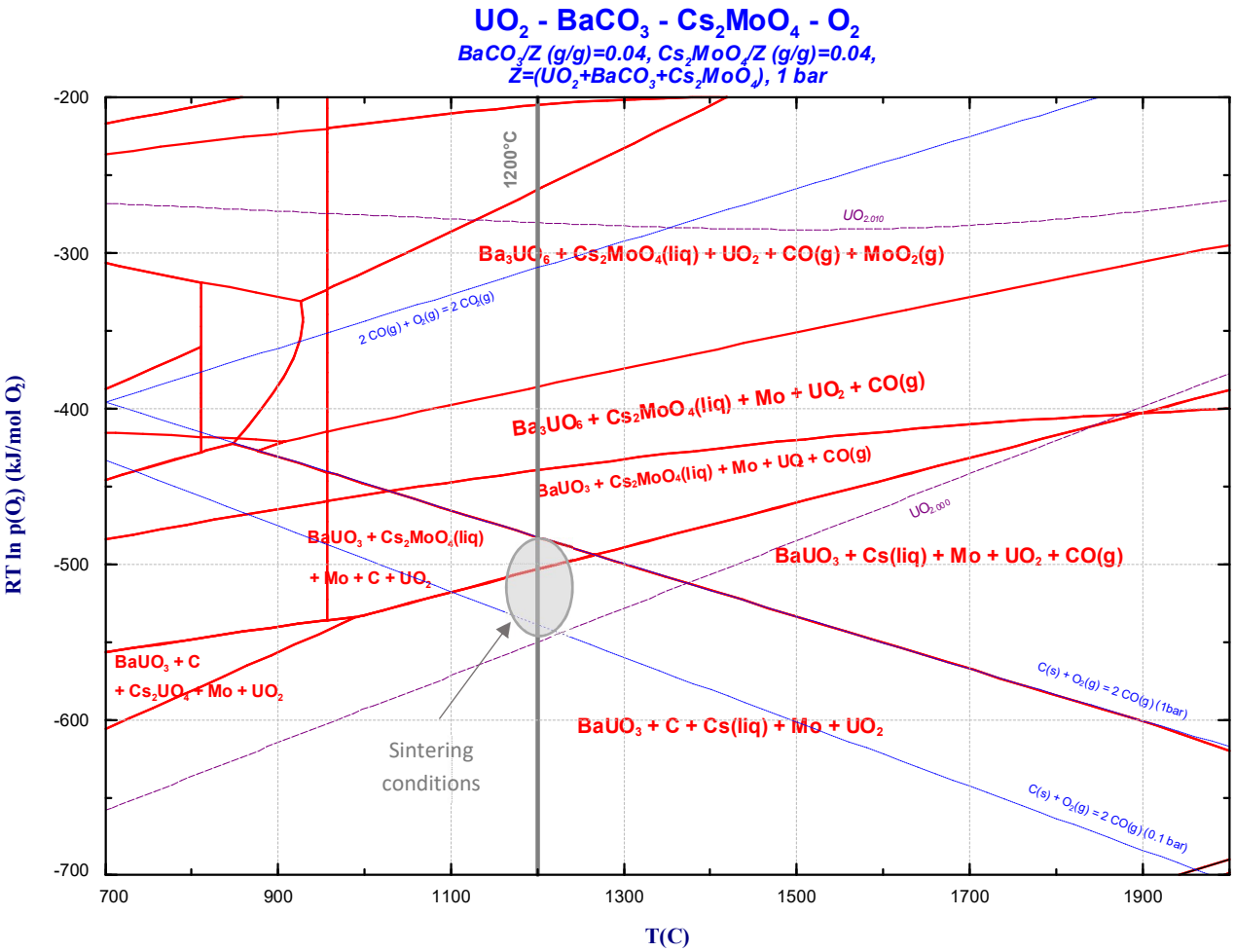

Figure IV-23: Predominance diagram for the UO_2-$BaCO_3$-Cs_2MoO_4-O_2 system (Batch 7), considering the quantities of elements added before sintering, obtained using the SGPS database of FactSage [23], [24]. The grey line corresponds to the sintering temperature, the blue dashed lines correspond to the equilibrium $C_{(s)}/CO_{(g)}$ and $CO_{(g)}/CO_{2(g)}$ at 0.1 and 1 bar and the purple lines correspond to stoichiometric $UO_{2.000}$ and hyperstoichiometric $UO_{2.010}$.

IV.3.4 Study of the system UO_2 / $Cs_2U_xO_y$ / $BaMoO_4$ (batches 1, 3, 6 and 8)

IV.3.4.1 Sintering behavior

The sintering behavior of 1 g of pure UO_2 and samples of 1 g of batch 3 (UO_2 + 1.2 % $Cs_2U_xO_y$), 0.3 g of batch 6 (UO_2 + 4.1 % $BaMoO_4$) and 0.7 g of batch 8 (UO_2 + 4.0 % $Cs_2U_xO_y$ + 4.0 % $BaMoO_4$) can be seen in **Figure IV-24**.

The sintering of batch 8 occurs in several steps. A first phase is observed to start around 550°C with a maximum sintering speed reached at 600°C. This phase is probably related to the sintering of the part of UO_2 matrix and to the effect of $BaMoO_4$. Indeed, the sintering of the mixture UO_2 + $BaMoO_4$ starts around 550°C and reaches a maximum at 750°C. A second densification stage starting around 750°C with a maximum speed reached at 1000°C, may be related to the sintering of $Cs_2U_xO_y$. The third and last step occurs slightly before 1200°C (at 1175°C) and could be attributed to a reaction between UO_2, $BaMoO_4$ and $Cs_2U_xO_y$.

The huge differences observed between the piston stroke for batches 6 and 8 and for pure UO_2 and batch 3 is mainly due to the lower amounts of mixtures used in the first two cases.

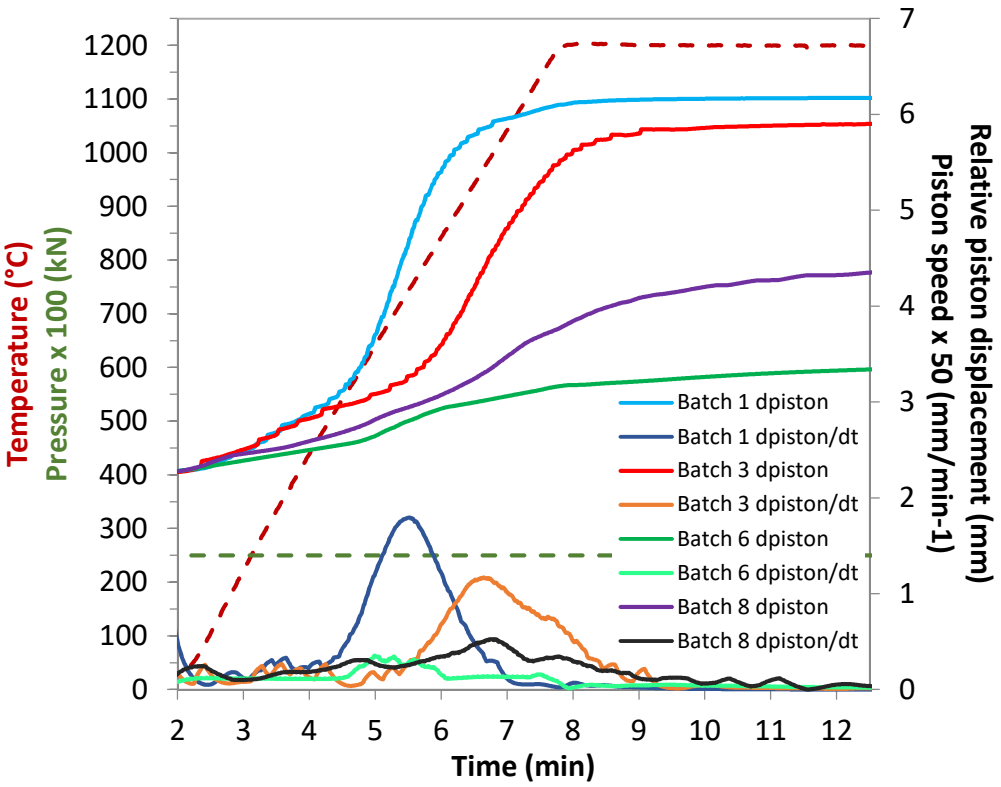

Figure IV-24: Relative piston displacement and piston speed during the sintering of pure pre-reduced UO_2, mixtures of batch 3 (UO_2 + 1.2 % $Cs_2U_xO_y$), batch 6 (UO_2 + 4.1 % $BaMoO_4$) and batch 8 (UO_2 + 4.0 % $Cs_2U_xO_y$ + 4.0 % $BaMoO_4$) at 1200°C during 5 min. The relative piston displacement and piston speed curves have been smoothed using a Savitzky-Golay filter [25] with 20 points.

IV.3.4.2 Density measurements

The densities of the pellets of batches 6 and 8 recovered after sintering were measured by the geometrical and Archimedes methods (**Table IV-8**). According to the hydrostatic value, the pellets obtained fulfill the objective set on the final density (> 90 $d_{th(mixture)}$). As already observed in the previous section, the geometrical values of the final density of batch 6 and 8 are much smaller than the hydrostatic values (gap of 20 to 30 %).

In this case also, complementary measurements should thus be done in order to conclude on the "real" density of samples of batches 6 and 8.

Table IV-8: Results of density measurements made on SIMFuel samples from batches 3, 6 and 7 produced by SPS thanks to the geometric method, the Archimedes one and He pycnometry (average values on each batch)

Batch	Geometrical density (% d_{th})	Hydrostatic density (% d_{th})	He pycnometry (% d_{th})
3 (UO_2 + 1.2 % $Cs_2U_xO_y$)	87.6 ± 1.4	95.9 ± 2.5	97.4 ± 0.4
6 (UO_2 + 4.1 % $BaMoO_4$)	72.6 ± 3.5	93.0 ± 2.5	-
8 (UO_2 + 4.0 % $Cs_2U_xO_y$ + 4.0 % $BaMoO_4$)	62.0 ± 6.5	91.0 ± 2.1	-

IV.3.4.3 SEM observations

EDX analyses were performed at several spots on a fractured surface of the sample of batch 6 (**Figure IV-25**) and confirmed the presence of Ba and Mo. These two elements were mostly found together but some inclusions containing only Mo and white phases containing small quantities of Ba were also found. This would indicate that partial decomposition of $BaMoO_4$ took place during the sintering.

In this picture, the area observed seems to have melted at some point of the SPS thermal sequence. This is not consistent with the melting of $BaMoO_4$ which occurs around 1600°C [32], well over the sintering temperature (1200°C). However, if partial decomposition happened, MoO_3 could have been formed and melted over 795°C.

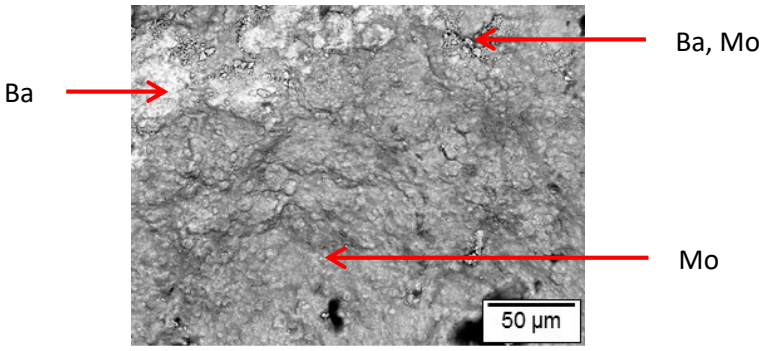

Figure IV-25: SEM-BSE image of fractured surface from a sample of batch 6 (UO_2 + 4.1 % $BaMoO_4$)

Concerning the sample of batch 8, Ba and Cs were often found together but no chemical contrast could be observed in BSE mode (purple circles in **Figure IV-26**). This is probably because Ba and Cs are associated to U which prevents contrast to be observed between the UO_2 matrix and potential Ba or Cs uranates. Some Mo is observed alone as shown in the green circle in **Figure IV-26**, as well as some Cs (red circle) and Ba (not shown here). These analyses did not enable to obtain more information on the speciation of these three elements in the samples.

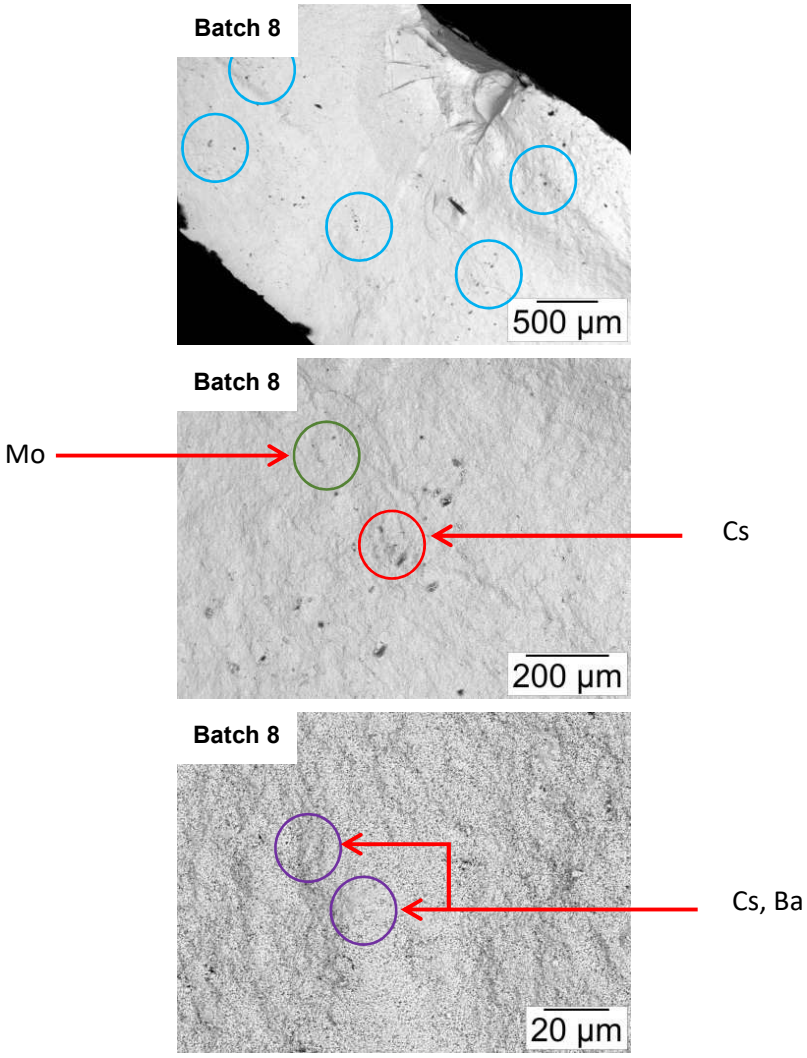

Figure IV-26: SEM-BSE images of fractured surfaces of a sample of batch 8 (UO_2 + 4.0 % $Cs_2U_xO_y$ + 4.0 % $BaMoO_4$) of the SPS-2 series. The blue circles correspond to areas where Cs, Mo or Ba were detected, the red circles correspond to regions where Cs was detected by EDX, green circles to area containing Mo and purple circles correspond to areas where both Cs and Ba were detected.

IV.3.4.4 Thermodynamic calculations

The predominance diagram related to batches 6 and 8 are shown in **Figure IV-27** and **Figure IV-28** respectively. They were established assuming that no Cs, Mo and Ba releases took place, as no quantitative chemical analyses could be performed on these samples. Thus, the initial concentrations in additive were used.

As shown in these predominance diagrams, $BaMoO_4$ is decomposed in reducing conditions and react with UO_2 to form $BaUO_3$ and metallic Mo. This is in agreement with the experimental observations performed by SEM-EDX showing most of Mo and Ba in separated phases. However, some Ba and Mo are still observed associated but the analyses did not enable to conclude on the nature of this phase. Assuming that sintering took place in the oxygen potential range defined previously, this could mean that the sample did not reach thermodynamic equilibrium during sintering.

The decomposition of $BaMoO_4$ is also consistent with the observations performed by SEM-EDX on the samples of batch 8. Concerning Cs, it is calculated to be present either as free Cs or Cs_2MoO_4 at thermodynamic equilibrium in the sintering conditions determined in the previous sections (**Figure**

IV-28). Mo is calculated to be present either as Cs_2MoO_4 or metallic Mo in these conditions. This agrees partly with the experimental observations performed on batch 8 as Cs and Mo were not found associated.

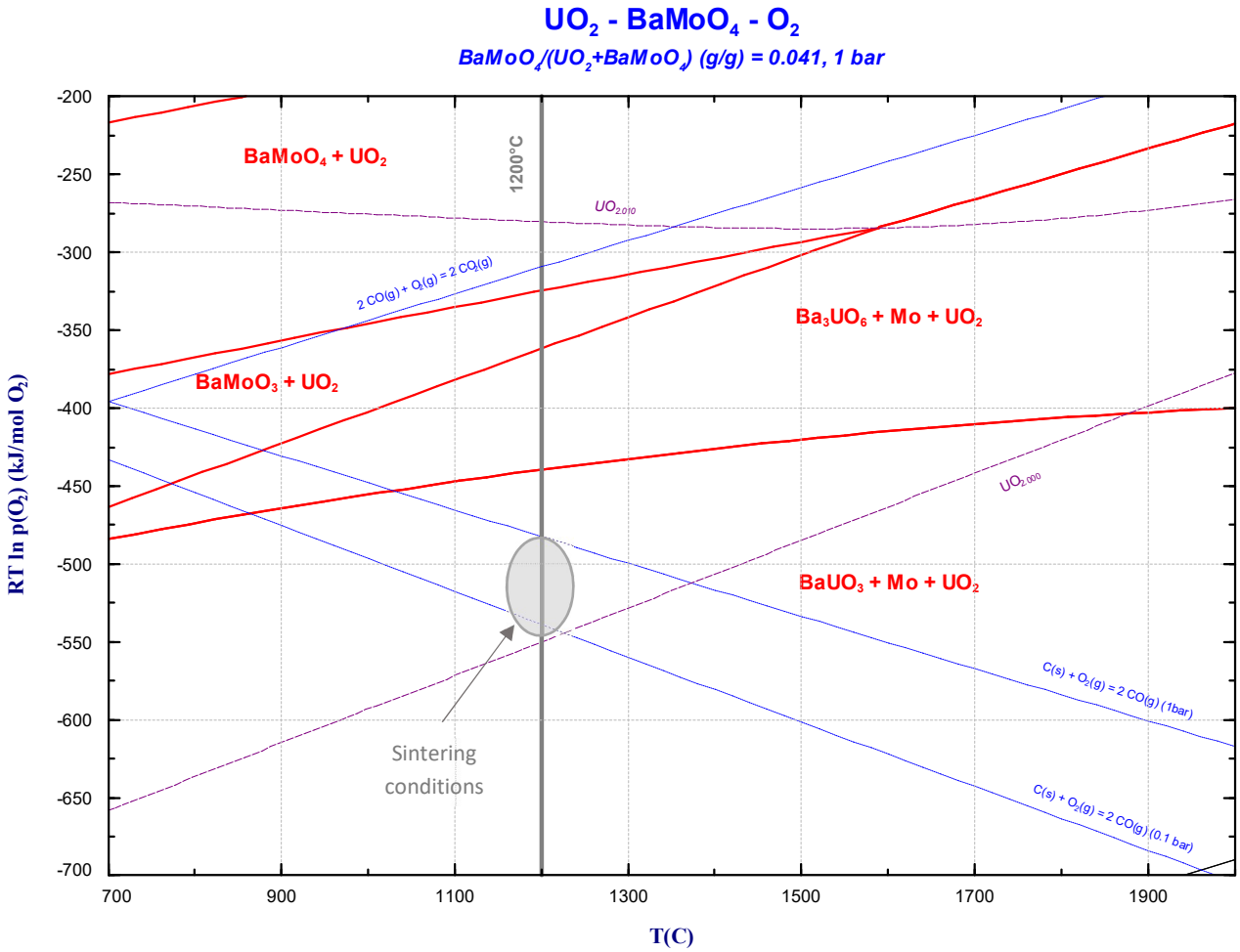

Figure IV-27: Predominance diagram for the UO_2-$BaMoO_4$-O_2 system (Batch 6), considering the quantities of elements added before sintering, obtained using the SGPS database of FactSage [23], [24]. The grey line corresponds to the sintering temperature, the blue dashed lines correspond to the equilibrium $C_{(s)}/CO_{(g)}$ and $CO_{(g)}/CO_{2(g)}$ at 0.1 and 1 bar and the purple lines correspond to stoichiometric $UO_{2.000}$ and hyperstoichiometric $UO_{2.010}$.

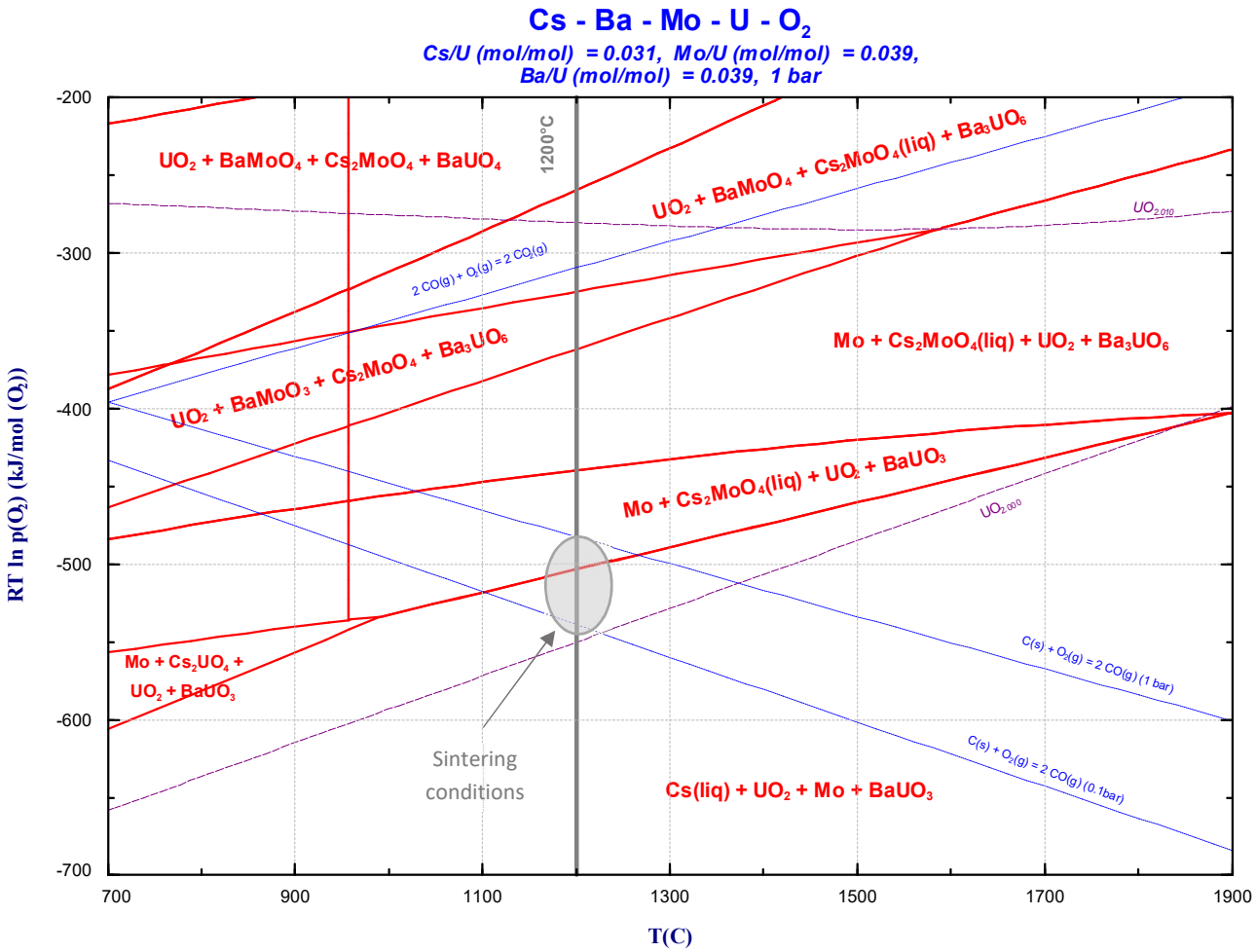

Figure IV-28: Predominance diagram for the U-Cs-Ba-Mo-O_2 system (Batch 8), considering the quantities of elements added before sintering, obtained using the SGPS database of FactSage [23], [24]. The grey line corresponds to the sintering temperature, the blue dashed lines correspond to the equilibrium $C_{(s)}/CO_{(g)}$ and $CO_{(g)}/CO_{2(g)}$ at 0.1 and 1 bar and the purple lines correspond to stoichiometric $UO_{2.000}$ and hyperstoichiometric $UO_{2.010}$.

IV.3.5 Summary of the results obtained from the post-sintering characterizations

Even at low concentration, the additives have a strong impact on the sintering behavior of UO_2. Indeed, the sintering of UO_2 occurs at higher temperatures after the addition of FP surrogates which can also provoke two-stage sintering. Some additives can also hinder sintering by forming agglomerates, which may be explained by the inhomogeneity of the mixtures prepared by grinding powders in a mortar.

FP surrogates impact the final density of the pellets by lowering it compared to pure UO_2. According to He pycnometry and the Archimedes method, the pellets obtained after sintering have a density higher than 90 % $d_{th(mixture)}$ which was the original goal to produce easily characterizable samples. However, the geometrical density is always lower and not in agreement with the previous values. This cannot be only explained by the uncertainties linked to the shape of the sintered pellets or the remaining graphite layer and should be investigated more in detail. Notably, the determination of the open porosity during the Archimedes measurements could be looked closer.

Post-sintering characterizations of fractured samples showed that the additives were dispersed in the whole pellets. However, segregation occurred and very large precipitates containing the FP

surrogates were observed within the pellets. The additives play a role on the the general grain size in the pellets, which is smaller compared to pure UO_2.

Chemical quantitative analyses of the composition of the sintered pellets could only be done on the SPS-1 series of samples. A low concentration of Cs and Mo remained which makes it difficult to characterize their chemical state with conventional techniques (SEM-EDX, XANES). Indeed, 20 to 70 % of the Cs amount added before sintering and 5 to 56 % of Mo remained in the pellets.

Cs and Mo were most of the time observed alone in the samples but some rare associations between these two FP were also found. None of the FP was observed after polishing of the samples by SEM-EDX. Only Cs could thus be characterized thanks to HERFD-XANES analyses performed at Cs L_2-edge on the FAME-UHD beamline of the ESRF. Nevertheless, the standards available did not enable the determination of Cs speciation for sure. Coupling the HERFD-XANES studies of Mo, Ba and Cs as well as high resolution XRD using a synchrotron radiation are necessary to be able to conclude on the speciation of each element.

The presence of a liquid phase observed through SEM in the sample composed of UO_2 + Cs_2MoO_4 is consistent with the formation of liquid Cs_2MoO_4. However, the experimental observations showed that this liquid phase contained only Mo. A decomposition of liquid Cs_2MoO_4 may thus have occurred leading to huge Cs release probably under Cs(g) according to the thermodynamic calculations performed using the Factsage 7.0 software coupled with the SGPS database. The remaining Cs is believed to be present as Cs_2UO_4 or Cs_2MoO_4 according to the experimental results and the thermodynamic calculations.

In the samples of SPS-2 series, the concentration of additives was set to 4 wt% to ease the characterizations. Cs and Ba were often found together but almost always without Mo, which tends to indicate that they are probably under free Cs (baking effect) and Ba uranate according to the thermodynamic calculations performed. Very few Mo was observed and it is often found alone in the samples probably as metallic Mo. Complementary characterizations using SEM-EDX on polished samples, HERFD-XANES and high resolution XRD should be carried in order to conclude on FP speciation in these samples.

The predominance diagrams established through this study coupled with the experimental observations enabled to define a probable range of oxygen potential conditions that were set during sintering at 1200°C. This domain extends roughly around -550 $kJ.mol_{(O2)}^{-1}$ and -475 $kJ.mol_{(O2)}^{-1}$ and corresponds to the domain located in between $UO_{2.00}$ and the $C_{(s)}/CO_{(g)}$ equilibrium at 1 bar. This implies that the graphite environment of the SPS device controls the oxygen potential during sintering and imposes reducing conditions with respect to the initial $UO_{2.01}$ conditions. This phenomenon has been clearly evidenced by the microstructure of the samples which exhibited smaller grains at their periphery (in contact with graphite) than in their center.

IV.4 In-situ HERFD-XANES experiments

The development of an in-temperature HERFD-XANES experiment is presented in this part. The objective was to be able to study the behavior of FP until their release being free from hypothetical reversible reactions that could distort the interpretation of FP speciation observed after cooling down the samples. This is of main importance in the case of Cs which is more volatile than Mo or Ba.

IV.4.1 Description of the experimental set-up

The device designed to perform the experiment has been extensively described in [33]–[35] and used to carry out in-situ XAS analyses on radioactive materials at the INE beamline (ANKA synchrotron radiation facility, Germany) [36]. However, this beamline was not equipped with HERFD-XANES set-up, which is mandatory to be able to detect the FP present in the SPS samples as stated above. Thus, a collaboration with the beamline FAME-UHD and the Safety staff of the ESRF was launched.

The design of a HERFD-XANES experiment is based the Johann's geometry, as shown in **Figure IV-29**. The sample, the detector and the Crystal Analyzer Spectrometer (CAS) are located on the Rowland circle. The first and last crystals composing the five CAS are separated with an angle of 120° [37], [38].

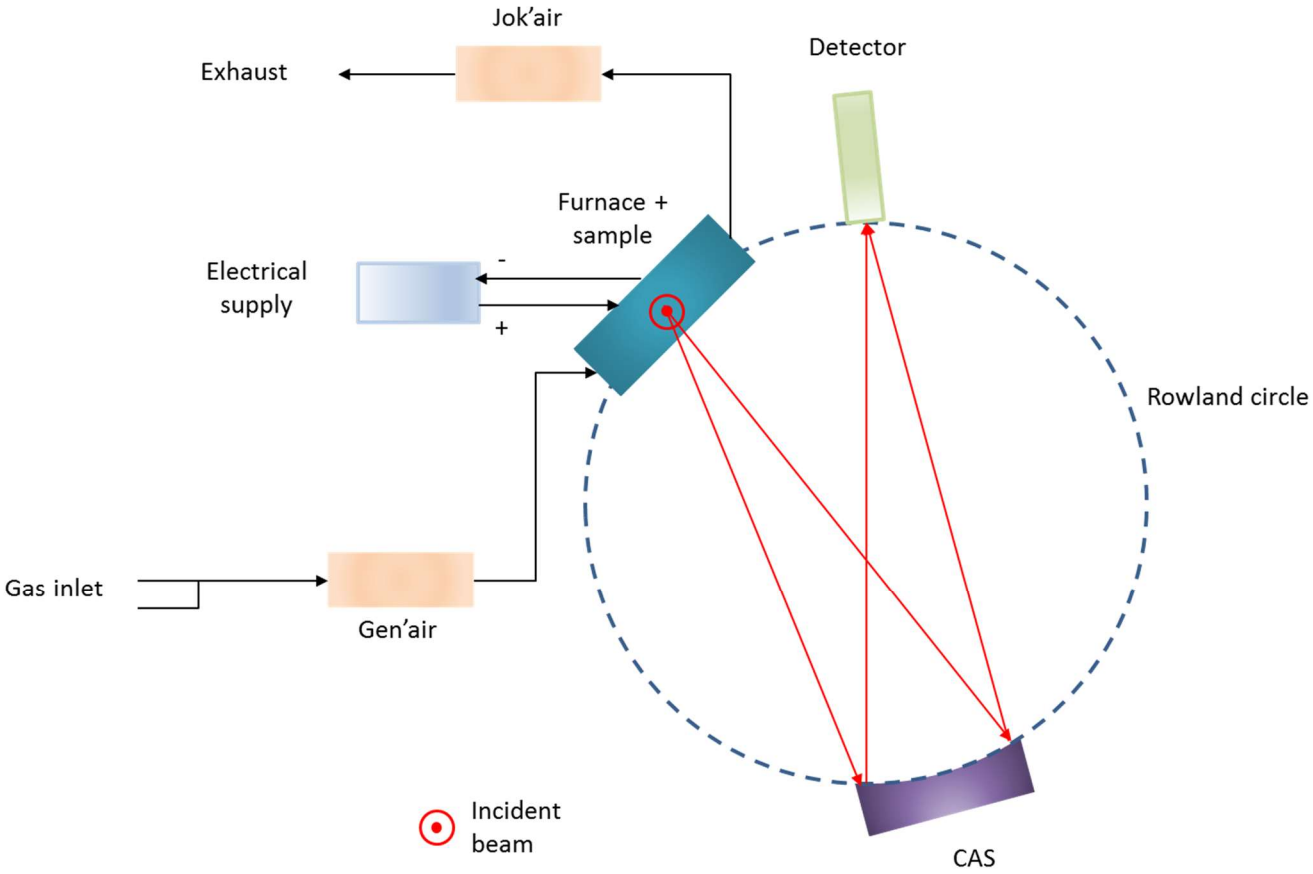

Figure IV-29: In-situ HERFD-XANES experimental loop. The beam is travelling through a He bag placed between the glovebox containing the furnace, the CAS and the detector.

In order to be able to perform this experiment, two requirements had to be fulfilled. The first one concerned the activity of the samples that could be heated on FAME-UHD which had to be less than 14 Bq, so that they could not be considered as radioactive. Thus, a sample of 1 mg, which

corresponds to a small piece of 1 x 1 x 0.1 mm^3 of SIMFuel, had to be prepared. The sample holder was modified in order to handle and confine this type of samples on a W-5 % Re wire heated by Joule effect (**Figure IV-30**, left). In the new sample holder (**Figure IV-30**, right), the sample is maintained thanks to two crimped W-5 % Re nuts. A hole in the center of one nut enables the X-ray beam to interact with the sample. This hole was machined to be a cone of 120° in order to recover the fluorescence signal on the five crystals of the CAS.

A support made of Al_2O_3 was designed in order to prevent any deformation of the wire downward at high temperature. The temperature was monitored during the test thanks to a thermocouple placed as close as possible to the sample and to a pyrometer measuring the temperature on the wire.

The atmosphere inside the furnace was set thanks to a zirconia oxygen pump (GEN'AIR) controlling the amount of O in a flowing gas mixture (Ar + 4 % H_2). The O partial pressure was measured after the furnace thanks to a MicroPoas probe (JOK'AIR) as shown in **Figure IV-29**.

The second requirement concerned the double confinement during every step of the experiment. This was ensured by the furnace, which is tight and a glovebox filled with He, designed to fit on the beamline.

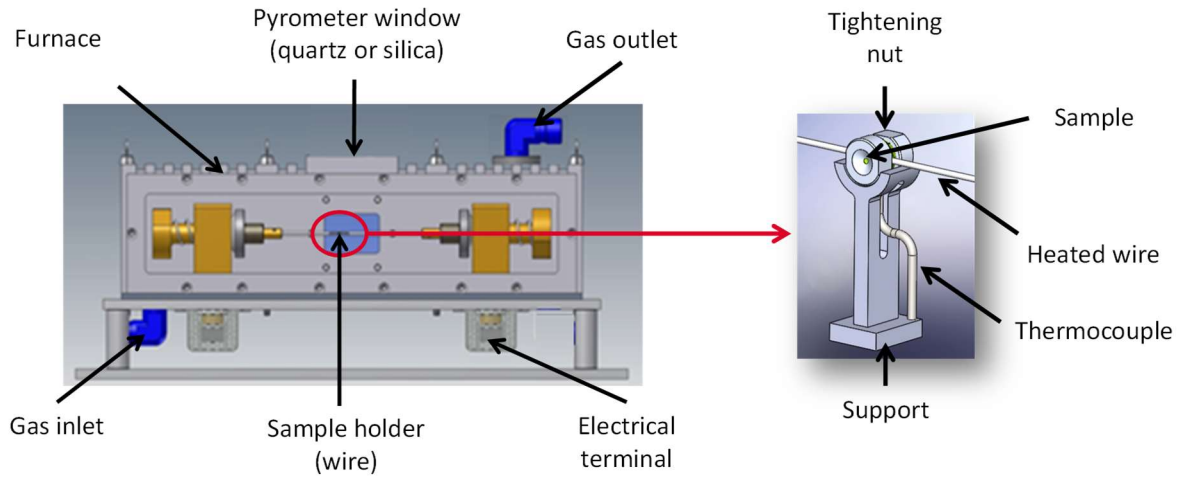

Figure IV-30: Schematic view of the in-temperature XAS furnace (left) and newly designed sample holder (right)

IV.4.2 Qualification of the experimental set-up

A first qualification phase consisted in preparing 1 x 1 x 0.1 mm^3 samples from inactive materials and trying to place them in the sample holder within the glovebox. Pellets composed of CeO_2 were thus produced by the LFC of the CEA Marcoule and sent to Cadarache where they were cut using a wire saw and polished at the right dimensions. Once the protocol validated, the whole set-up was tested in real conditions on the FAME-UHD beamline at Ba L_3-edge (**Figure IV-32** and **Figure IV-33**), using the SIMFuel samples described in **Chapter 3**. As shown in **Figure IV-31**, a 1 x 1 x 0.1 mm^3 SIMFuel sample was characterized through optical microscopy and SEM and the presence of Ba and Mo was confirmed, which is necessary to study their interactions in temperature. Two samples as-sintered (T_0) were heated in the same oxidizing and reducing atmosphere as described in **Chapter 3** up to 400 and 700°C during 20h.

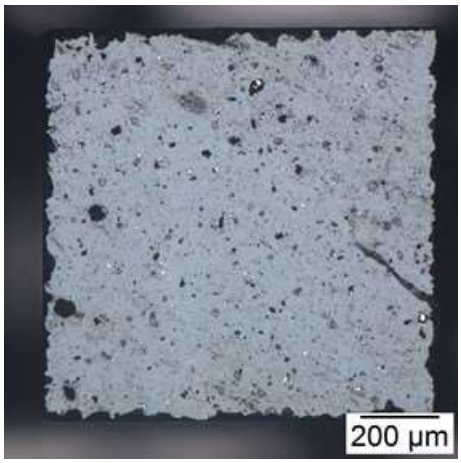

Figure IV-31: Micrograph of a 1 x 1 x 0.1 mm³ as-sintered sample prepared from the SIMFuel batch described in Chapter 3

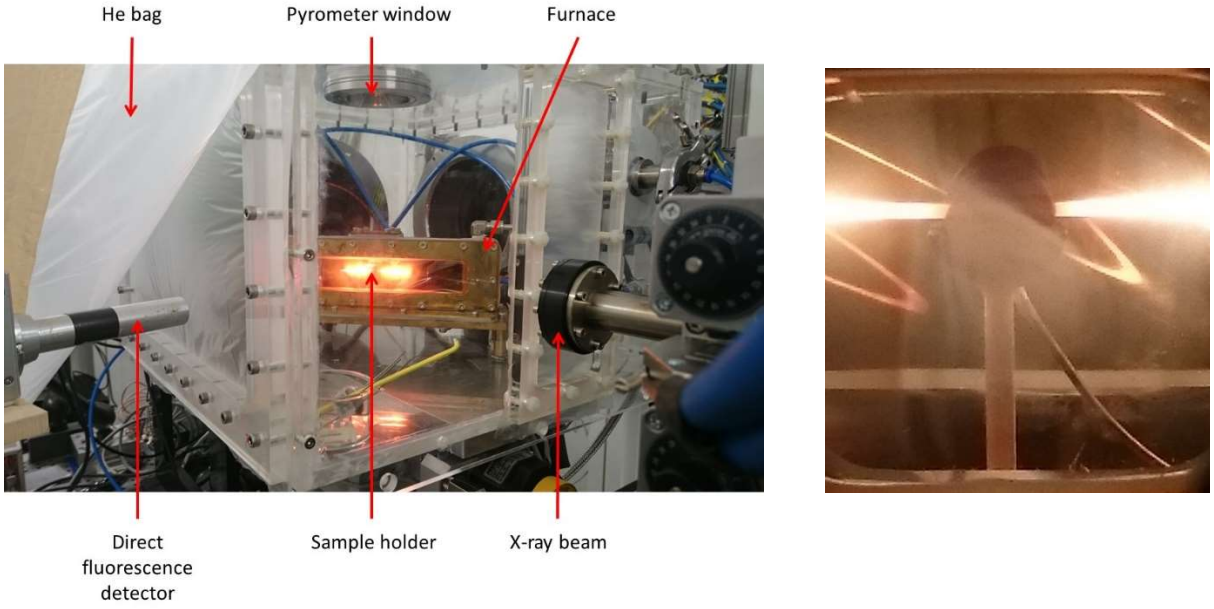

Figure IV-32: Experimental set-up showing the furnace in a glovebox filled-in with He (left) and the sample holder with its thermocouple (right) during the qualification phase

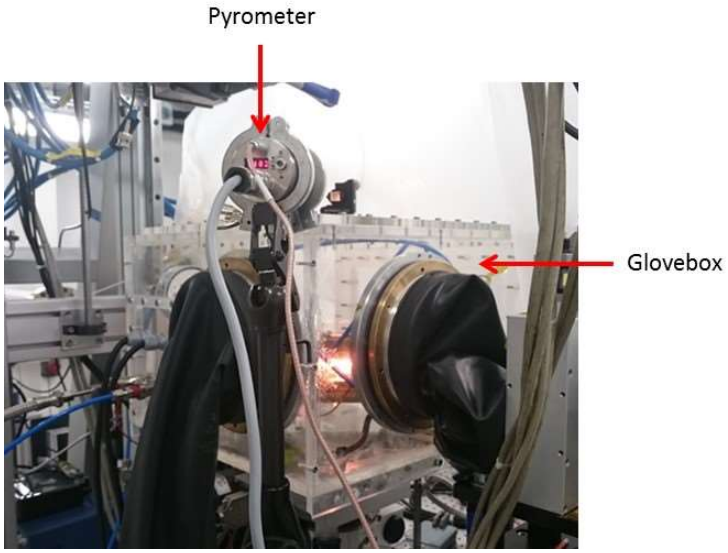

Figure IV-33: Experimental set-up showing the pyrometer and the glovebox during the qualification phases

The temperature and pO_2 were successfully controlled during the experiment and Ba was detected. The experimental HERFD-XANES spectra obtained on the T_0, O400 and R400 samples are presented in **Figure IV-34**. The global shape of the T_0 spectrum is preserved at 400°C. Nevertheless, the intensity of the white line decreases as well as the oscillation present at 5.268 keV. This phenomenon is further observed at 700°C in both oxidizing and reducing conditions as shown in **Figure IV-35**. Indeed, the width of the white line increases and the four oscillations observed between 5.255 and 5.280 keV flatten. These observations may be due to the disordering effect caused by the increase in temperature. This is also confirmed by the spectrum of the sample O700 recorded after cooling down the sample: its shape is identical to that of the T_0 sample (**Figure IV-36**).

As already shown in **Chapter 3**, no evolution of Ba speciation can be observed up to 700°C in reducing or oxidizing conditions, probably because the thermal treatments are not long enough to reach thermodynamic equilibrium.

However, during the tests, the sample's temperature was limited to 750°C while the temperature at both ends of the heated wire was 1600°C. Indeed, the sample holder designed to prevent the samples from falling in the furnace had a huge impact on the final temperature achievable during the experiment. Thus, a new heating device should thus be developed in order to conduct these tests at higher temperature on the FAME-UHD beamline.

Another issue was raised as far as the samples produced by SPS were concerned. Indeed, the very low concentrations of additives found in these samples did not allow the identification of a 1 x 1 mm^2 square containing Cs, Mo and Ba thanks to SEM. Furthermore, given the inhomogeneity of the pellets obtained by SPS, it was impossible to sample a 1 mg chip containing these three elements at the same time. Being able to heat larger samples or synthesizing more homogeneous samples through SPS could be solutions to trigger these issues.

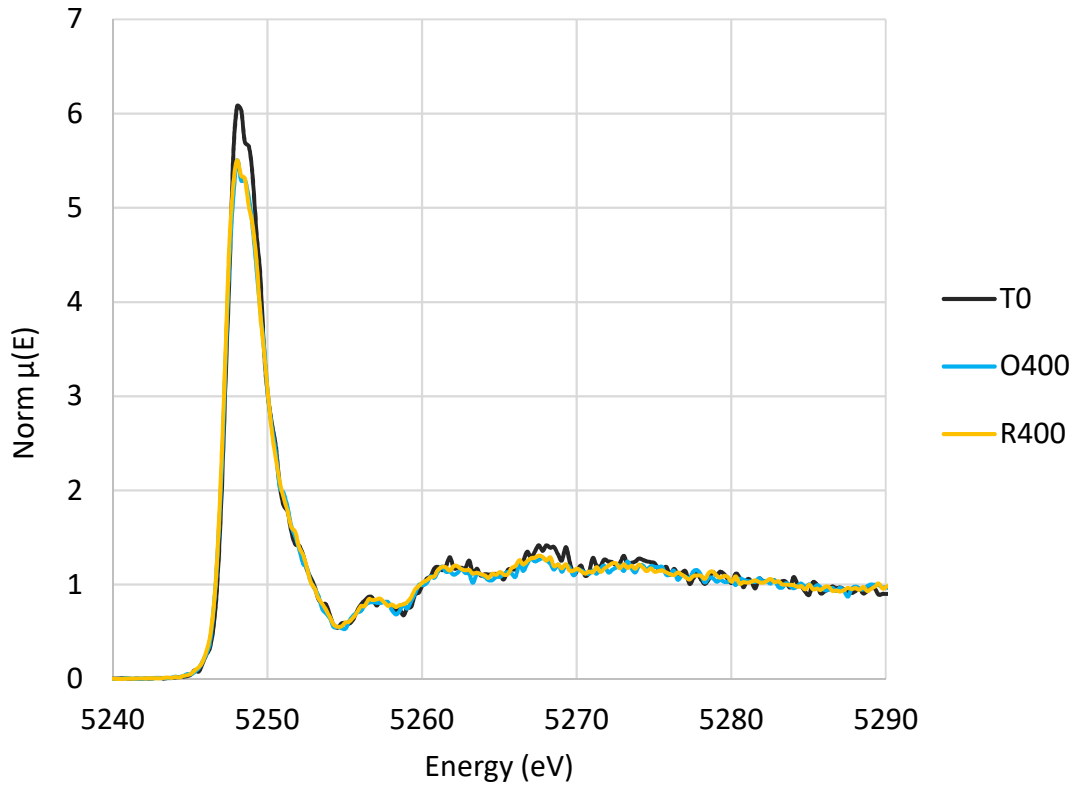

Figure IV-34: Experimental HERFD-XANES spectra of the samples as-sintered and heated up to 400°C under reducing and oxidizing conditions obtained in temperature at Ba L_3-edge on the FAME-UHD beamline (ESRF)

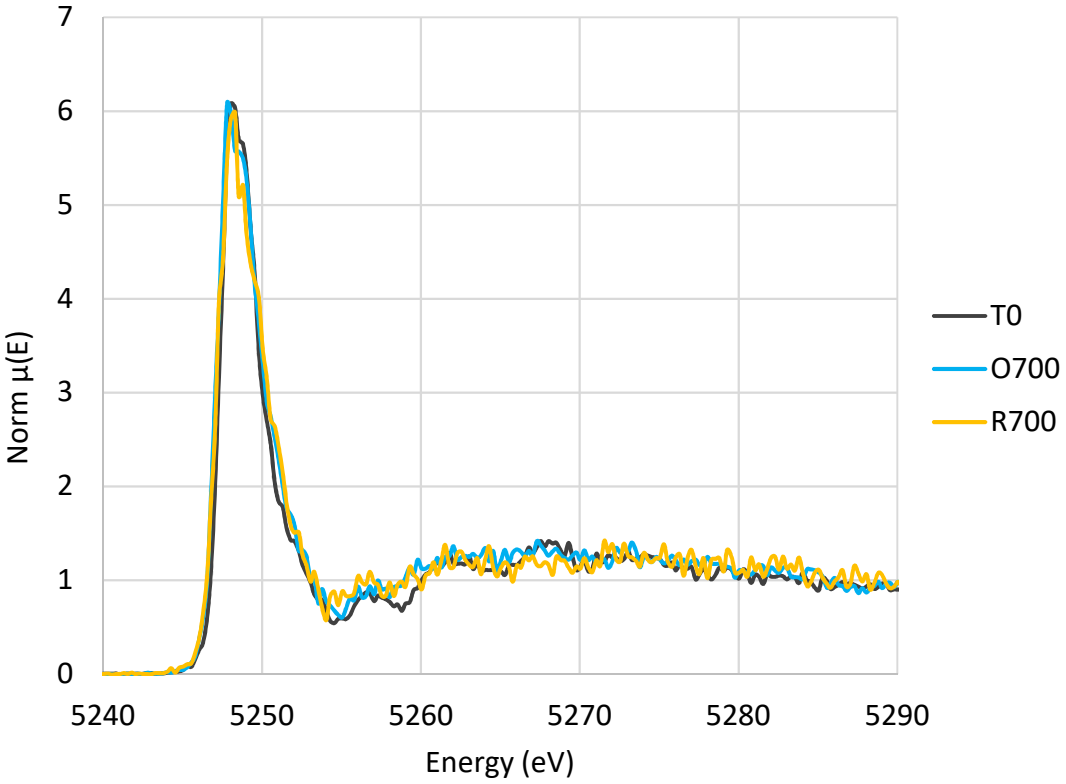

Figure IV-35: Experimental HERFD-XANES spectra of the samples as-sintered and heated up to 700°C under reducing and oxidizing conditions obtained in temperature at Ba L_3-edge on the FAME-UHD beamline (ESRF)

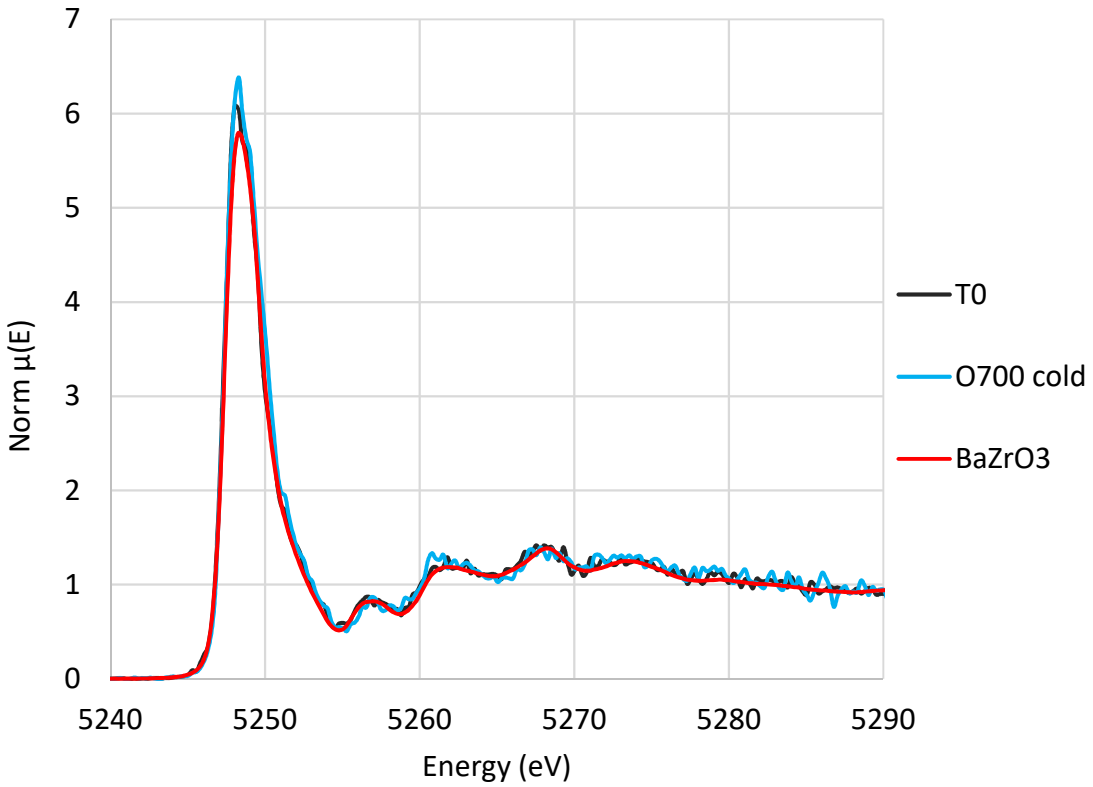

Figure IV-36: Experimental HERFD-XANES spectra of the samples as-sintered, O700 after cooling and $BaZrO_3$ obtained at Ba L_3-edge on the FAME-UHD beamline (ESRF)

IV.5 CONCLUSION

A method was developed to be able to study the behavior of volatile FP such as Cs in severe accident conditions. It first lies on the production of dense SIMFuel samples containing Cs, Mo and Ba in UO_2 thanks to SPS. The second axis of this method consists in performing thermal treatments under controlled atmosphere representative of a severe accident and study FP speciation in-situ. Thus, an in-temperature HERFD-XANES experiment was developed in collaboration with the ESRF.

The main challenge of this work axis was to synthesize the samples thanks to SPS. Three objectives were set on the final samples:

- The first objective concerned the **presence of the three FP (Cs, Mo and Ba) in the UO_2 after sintering**, to be able to study their interactions in severe accident conditions.
  This objective was indeed fulfilled: post-sintering characterizations of the samples indicated the presence of these three FP. However, Cs and Mo release took place during the sintering thermal sequence leading to 20 to 70 % of Cs and 5 to 56 % of Mo remaining in the final pellets.
- The second objective concerned **the maximum temperature of sintering set at 1300°C** in order to obtain pellets containing Cs and representative of PWR fuels state under normal operating conditions.
  This objective was also reached: sintering was performed at 1200°C, with a dwell time of 5 minutes.
- The third objective was about the final density of the pellets, which **had to be higher than 90 %d_{th}** in order to avoid the handling and transportation of powders.
  According to the hydrostatic and He-pycnometry measurements, this objective was achieved. However, the discrepancies between these values of density and the geometrical density measurements (much lower) could not be explained and would require more investigations.

Different initial compositions were used to produce the samples in order to study the behavior of different phases containing Cs, Ba and Mo during the sintering. The addition of FP surrogates had a strong impact on the sintering behavior of UO_2, the final density and the microstructure of the pellets obtained through SPS. The experimental observations performed in the as-sintered samples clearly indicated that:

- The dispersion of the additives in the UO_2 matrix after sintering is not uniform in the pellets. Indeed, some large agglomerates were observed which may indicate that the initial mixing of the different powder has not been effective. This was also confirmed by the chemical quantitative analyses performed on several pellets of the same initial batch which showed that the final amount of additives varied a lot from a sample to another.

- The oxygen potential was most likely imposed by the $C_{(s)}/CO_{(g)}$ equilibrium during sintering, as a result of the interaction between the graphite environment of the SPS furnace and the samples. This imposed reducing sintering conditions (oxygen potential range between -550

$kJ.mol_{(O2)}^{-1}$ and -475 $kJ.mol_{(O2)}^{-1}$). Therefore, **the SPS experimental device has a strong impact on FP speciation.**

- Interactions between the different additives and the UO_2 matrix indeed took place during this phase despite the very short holding time at 1200°C. Ba is mainly found alone in the samples, probably as uranate as predicted by thermodynamics. Cs can be found in association with Mo or alone which is explained through thermodynamics by the decomposition of Cs_2MoO_4 into Cs uranate or gaseous Cs condensed on the surface of the samples. Mo is most of the time observed in precipitates probably as a metal according to thermodynamic calculations. No experimental information could be obtained on its exact chemical state in this study. *Further investigation on the initial state of FP should be carried on in order to determine the speciation of Cs, Ba and Mo using high resolution XRD and HERFD-XANES on Mo and Ba. A measurement of the UO_2 matrix stoichiometry in the periphery and in the center after sintering could also help understanding the range on which graphite acts as oxygen potential buffer. This could be performed by RAMAN spectroscopy.*

SPS is thus a very useful and suitable tool to study volatile FP speciation in UO_2. *Nevertheless, further developments are needed to improve the synthesis process so as to obtain pellets with uniform distribution of additives and better controlled final compositions. Several paths to improve these points are proposed here after:*

- *Impregnation of the UO_2 powder by a solution containing FP surrogates with the desired concentrations. After evaporation of the solvent, the additives would be homogeneously present in the batch.*
- *Mixing the UO_2 powder with FP surrogates thanks to planetary milling in ethanol just like conventional SIMFuel samples. However, this method implies working with a large quantity of powder.*
- *Use a different kind of matrix to perform sintering in order to prevent an interaction between UO_2 and C.*
- *Being able to control or at least monitor the oxygen potential in the SPS furnace during sintering could help improving the amount of additives remaining in the samples after sintering. In addition, controlling the oxygen potential while sintering is essential to control the speciation of the additives.*

IV.6 REFERENCES

[1] H. Matzke and A. Turos, “Ion implantation studies of UO2 and UN,” in *Nuclear Materials for Fission Reactors*, H. Matzke and G. Schumacher, Eds. Oxford: Elsevier, 1992, pp. 285–292.

[2] S. Guilbert *et al.*, “He migration in implanted UO2 sintered disks,” presented at the ATALANTE 2004, Nîmes, France, 2004.

[3] N. Djourelov and H. Marinov, “Xe Bubbles Formation in Materials for use in Nuclear Reactors Studied by low Positrons,” *Bulg. J. Phys.*, no. 40, pp. 289–293, 2013.

[4] P. Martin, M. Ripert, G. Carlot, P. Parent, and C. Laffon, “A study of molybdenum behaviour in UO2 by X-ray absorption spectroscopy,” *J. Nucl. Mater.*, vol. 326, no. 2, pp. 132–143, Mar. 2004.

[5] E. Geiger, “Study of fission products (Cs, Ba, Mo, Ru) behaviour in irradiated and simulated nuclear fuels during severe accidents using X-ray absorption spectroscopy, SIMS and EPMA,” PhD Thesis, Paris-Saclay, CEA Cadarache, 2016.

[6] W. H. Hocking, A. M. Duclos, and L. H. Johnson, “Study of fission-product segregation in used CANDU fuel by X-ray photoelectron spectroscopy (XPS) II,” *J. Nucl. Mater.*, vol. 209, no. 1, pp. 1–26, 1994.

[7] W. H. Hocking, R. A. Verrall, and I. J. Muir, “Migration behaviour of iodine in nuclear fuel,” *J. Nucl. Mater.*, vol. 294, no. 1–2, pp. 45–52, 2001.

[8] C. Lemaignan, *Science des matériaux pour le nucléaire*. EDP Sciences, 2004.

[9] T. Wangle, V. Tyrpekl, M. Cologna, and J. Somers, “Simulated UO2 fuel containing CsI by spark plasma sintering,” *J. Nucl. Mater.*, vol. 466, pp. 150–153, 2015.

[10] S. Gamaury Dubois, “Amélioration de la rétention du césium dans le dioxyde d’uranium au moyen de phases exogènes,” Institut National Polytechnique de Grenoble, CEA Grenoble, 1995.

[11] J. P. Leveque, B. Andre, G. Ducros, G. Le Marois, and G. Lhiaubet, “The HEVA experimental program,” *Nucl. Technol.*, vol. 108, no. 1, pp. 33–44, 1994.

[12] Y. Pontillon *et al.*, “Lessons learnt from VERCORS tests.: Study of the active role played by UO2–ZrO2–FP interactions on irradiated fuel collapse temperature,” *J. Nucl. Mater.*, vol. 344, no. 1–3, pp. 265–273, 2005.

[13] M. D. Allen, H. W. Stockman, K. O. Reil, A. J. Grimley, and W. J. Camp, “ACRR Fission Product Release Tests ST-1 and ST-2,” in *Proceedings*, Avignon, France, 1988.

[14] M. F. Osborne, R. A. Lorenz, and J. L. Collins, “ORNL studies of fission product release under LWR accident conditions,” presented at the 2nd Workshop on LWR Severe Accident Research, Tokyo, Japan, 1991.

[15] R. A. Lorenz and M. F. Osborne, “A summary of ORNL fission product release tests with recommended release rates and diffusion coefficients,” Nuclear Regulatory Commission, Oak Ridge National Lab., NUREG/CR--6261, 1995.

[16] Y. Pontillon and G. Ducros, “Behaviour of fission products under severe PWR accident conditions: The VERCORS experimental programme—Part 2: Release and transport of fission gases and volatile fission products,” *Nucl. Eng. Des.*, vol. 240, no. 7, pp. 1853–1866, 2010.

[17] Y. Pontillon *et al.*, “Fission products and nuclear fuel behaviour under severe accident conditions part 1: Main lessons learnt from the first VERDON test,” *J. Nucl. Mater.*, vol. 495, no. Supplement C, pp. 363–384, 2017.

[18] V. Tyrpekl *et al.*, “On the Role of the Electrical Field in Spark Plasma Sintering of UO_{2+x},” *Sci. Rep.*, vol. 7, p. srep46625, Apr. 2017.

[19] K. Teske, H. Ullmann, and D. Rettig, “Investigation of the oxygen activity of oxide fuels and fuel-fission product systems by solid electrolyte techniques. Part I: Qualification and limitations of the method,” *J. Nucl. Mater.*, vol. 116, pp. 260–266, 1983.

[20] D. W. Osborne, P. A. Brletic, H. R. Hoekstra, and H. E. Flotow, “Cesium uranate, Cs2UO4: heat capacity and entropy from 5 to 350 K and standard Gibbs energy of formation at 298.15 K,” *Journal of Chemical Thermodynamics*, pp. 361–365, 1976.

[21] E. H. P. Cordfunke, A. B. Van Egmond, and G. Van Voorst, “Investigations on cesium uranates—I: Characterization of the phases in the Cs□U□O system,” *J. Inorg. Nucl. Chem.*, vol. 37, no. 6, pp. 1433–1436, Jun. 1975.
[22] S. R. Dharwadkar, M. Shyamala, G. Chattopadhyay, and M. S. Chandrasekharaiah, “Thermal stability of Cs2UO4 phase at high temperature,” *Trans. Indian Inst. Met.*, vol. 36, pp. 295–297, 1983.
[23] C. W. Bale *et al.*, “FactSage thermochemical software and databases,” *Calphad*, vol. 26, no. 2, pp. 189–228, 2002.
[24] C. W. Bale *et al.*, “FactSage thermochemical software and databases — recent developments,” *Calphad*, vol. 33, no. 2, pp. 295–311, 2009.
[25] A. Savitzky and M. J. E. Golay, “Smoothing and differentiation of data by simplified least squares procedures,” *Anal. Chem.*, vol. 36, pp. 1627–1639, 1964.
[26] V. Peres *et al.*, “High temperature chromium volatilization from Cr2O3 powder and Cr2O3-doped UO2 pellets in reducing atmospheres,” *J. Nucl. Mater.*, vol. 423, no. 1, pp. 93–101, Apr. 2012.
[27] G. Wallez, P. E. Raison, A. L. Smith, N. Clavier, and N. Dacheux, “High-temperature behavior of dicesium molybdate Cs2MoO4: Implications for fast neutron reactors,” *J. Solid State Chem.*, vol. 215, pp. 225–230, Jul. 2014.
[28] R. J. M. Konings and E. H. P. Cordfunke, “The thermochemical properties of cesium molybdate, CS2MoO4, from 298.15 to 1500 K,” *Thermochim. Acta*, vol. 124, pp. 157–162, 1988.
[29] M. Yamawaki, T. Oka, M. Yasumoto, and H. Sakurai, “Thermodynamics of vaporization of cesium molybdate by means of mass spectrometry,” *J. Nucl. Mater.*, vol. 201, pp. 257–260, 1993.
[30] I. Johnson, “Mass spectrometric study of the vaporization of cesium and sodium molybdates,” *J. Phys. Chem.*, vol. 79, no. 7, pp. 722–726, 1975.
[31] M. Khair, “Personal Communication,” CEA Cadarache, mai-2018.
[32] C. Pupp, R. Yamdagni, and R. F. Porter, “Mass spectrometric study of the evaporation of BaMoO4 and BaWO4,” *J. Inorg. Nucl. Chem.*, vol. 31, no. 7, pp. 2021–2029, Jul. 1969.
[33] P. Richet, P. Gillet, A. Pierre, M. Bouhifd, I. Daniel, and G. Fiquet, “Raman spectroscopy, X-ray diffraction and phase relationship determinations with a versatile heating cell for measurements up to 3600 K (or 2700 K in air),” *J Appl Phys*, vol. 54, pp. 5451–5456, 1993.
[34] P. Richet, B. O. Mysen, and J. Ingrin, “High-temperature X-ray diffraction and Raman spectroscopy of diopside and pseudowollastonite,” *Phys. Chem. Miner.*, vol. 25, no. 6, pp. 401–414.
[35] D. R. Neuville, L. Hennet, P. Florian, and D. de Ligny, “In situ High-Temperature Experiments,” *Rev. Mineral. Geochem.*, vol. 78, no. 1, pp. 779–800, 2014.
[36] M. Caisso *et al.*, “In situ characterization of uranium and americium oxide solid solution formation for CRMP process: First combination of in situ XRD and XANES measurements,” *Dalton Trans.*, vol. 44, pp. 6391–6399, 2015.
[37] J.-L. Hazemann *et al.*, “High Resolution Spectroscopy on an X-ray Absorption Beamline,” *J. Synchrotron Radiat.*, vol. 16, no. 2, pp. 283–292, 2008.
[38] O. Proux *et al.*, “High-Energy Resolution Fluorescence Detected X-Ray Absorption Spectroscopy: A Powerful New Structural Tool in Environmental Biogeochemistry Sciences,” *J. Environ. Qual.*, vol. 0, no. 0, Apr. 2017.

CONCLUSIONS AND FUTURE PROSPECTS

The objective of this work was to experimentally investigate the effect of the oxygen potential on the fuel and FP chemical behavior in conditions representative of a severe accident. More specifically, the speciation of Cs, Mo and Ba was investigated. These three highly reactive FP are among the most abundant elements produced through ^{235}U and ^{239}Pu thermal fission and may have a significant impact on human health and environmental contamination in case of a PWR severe accident.

This work has set out to contribute to the following three fields:

- Experimental data on PWR MOX fuel behavior submitted to severe accident conditions and related FP speciation

- Effect of oxygen potential on FP speciation at different stages of a severe accident thermal sequence

- Development of a method to study volatile FP behavior, involving the investigation of SIMFuel samples manufactured at low temperature through SPS.

Two types of samples have been studied in detail in this thesis report: irradiated MOX fuels and simulated high burn-up UO_2 fuels produced through sintering at high temperature (1650°C, 2h, H_2 atmosphere). The samples were submitted to thermal treatments in conditions representative of a PWR severe accident. This approach made it possible to cover a temperature range from 400°C up to 2530°C and oxygen potentials from -470 $kJ.mol_{(O2)}^{-1}$ to -100 $kJ.mol_{(O2)}^{-1}$. The samples were characterized before and after each test using complementary techniques like OM, SEM, EPMA and SIMS in the case of irradiated fuels. XANES measurements using synchrotron radiation facilities were also performed on model materials and produced valuable results on FP speciation (oxidation state, crystallographic structures, etc.).

The experimental observations were compared with a speciation mechanism based on mechanistic calculations, which made it possible to validate and enabled validating several of the mechanism's steps. This mechanism is based on a specific accident sequence representative of the VERCORS and VERDON analytical tests. A first stage was considered up to 400°C in a neutral He atmosphere, corresponding to normal PWR operating conditions. The second stage corresponded to the cladding oxidation and ranged from 400°C up to 1500°C under an oxidizing H_2O/H_2 atmosphere. A final stage ranging from 1500°C up to more than 2300°C was performed in a varying atmosphere (reducing or oxidizing H_2O/H_2 ratios or air). This phase is representative of a severe accident scenario, whether it involves core reflooding, massive H_2 production and starvation after cladding oxidation, or air ingress into the reactor.

The main phenomena assessed in the scope of this work were:

- Interactions between Mo and the oxide phase containing Ba. These interactions were shown to occur at temperatures as low as 1000°C under oxidizing conditions. The formation of MoO_2 and its reaction with $BaZrO_3$ results in the breakdown of this phase into $BaMoO_4$ and ZrO_2

- Effect of fuel melting, which tends to limit Ba releases in reducing conditions

- Effect of fuel-cladding interactions on the fuel's melting temperature. It seems that the role of the oxygen potential in this phenomenon is to enhance the diffusion of species in oxidizing conditions. The $U_{1-x}Zr_xO_{2\pm x}$ composition for which the melting temperature is minimal is thus reached earlier than in the case of a reducing atmosphere

- The composition and behavior of metallic phases in severe accident conditions. Mo depletion of the Mo-Ru-Rh-Pd-Tc inclusions was observed to take place around 1000°C in oxidizing conditions because of the oxidation of Mo into MoO_2. In reducing conditions, no major composition changes were observed.

In addition to the current approach which combines studies on irradiated and simulated fuels, working on simplified systems should also provide us with a better understanding of the chemical interactions between FP in the fuel. For example, a study of $BaZrO_3$/Mo diffusion in the atmosphere range investigated in the present work would allow us to progress on the Mo and Ba speciation mechanisms.

Some difficulties have arisen in assessing the speciation of FP in irradiated fuels. The characterization techniques currently available for this type of material give information on the association between the different elements and their distribution, but not on the nature of the compounds they form. Despite the use of SIMFuel samples, the data could not be obtained at high temperature (> 1700°C) given the temperature range accessible in the DURANCE loop.

Performing HR-XRD analyses on irradiated fuels will be possible in 2019 using the MARS beamline (SOLEIL synchrotron, Saclay). The set-up and the experimental procedure are currently being qualified within the scope of a collaboration agreement between the CEA/DEN/DEC and the MARS beamline. These analyses would definitely allow us to improve our understanding of FP speciation in normal PWR operating conditions and at the end of a VERDON test.

In the framework of this work, such analyses were initiated on SIMFuel samples produced at high temperature using the MARS beamline. The measurements produced promising results which unfortunately are not discussed herein as they remain to be fully analyzed.

More generally, the principal limitation of the approach adopted in this work lies in the behavior of volatile FP such as Cs. These FP are released relatively quickly during a severe accident and are totally released from the fuel above 2300°C. Thus, any characterizations performed on irradiated fuels before and after a full accident sequence provide very little information on volatile FP speciation. Much in the same way, volatile FP are volatilised during the sintering stage of the SIMFuel fabrication process produced at high temperature, thus preventing their study at intermediate temperature levels.

Thus, **low-temperature sintering was investigated for the production of SIMFuel samples containing Cs, Mo and Ba.** Cs proved to remain in the samples obtained through SPS (1200°C, 5 min, Ar atmosphere). Moreover, the chemical state of these three FP in the pellets is representative of that in the center of PWR fuels under normal operating conditions. Despite these promising results, large Cs and Mo releases occurred during sintering and the additives in the pellets were not distributed homogeneously. These issues brought us to consider further development of this production route.

In order to enhance the fabrication of SIMFuels using SPS, efforts should be made to improve the homogeneity of the powder mixtures and to better control FP speciation during sintering. This could be achieved by:

- *Mixing the UO_2 powder with FP surrogates thanks to planetary milling in ethanol much like conventional SIMFuel samples.*

- *Impregnating the UO_2 powder with a solution containing FP surrogates with the desired concentrations. After evaporation of the solvent, the additives would be homogeneously distributed in the batch.*

- *Using a different kind of matrix to perform sintering. This would prevent interactions between UO_2 and graphite, and would provide access to another oxygen potential range during sintering.*

- *Controlling or at least measuring the oxygen potential in the SPS furnace during sintering. This could help improve the amount of additives remaining in the samples after sintering. It could also help control the speciation of additives.*

These samples could then be fully characterized (HR-XANES, HR-XRD, SEM-EDX, etc.) to provide experimental data on the behavior of Cs in severe accident conditions.

Throughout this study, thermodynamic calculations were performed to assess the FP and fuel chemical state in the different conditions and materials in question. These calculations proved to be a necessary tool to interpret the experimental data obtained. The key contributions of thermodynamics in this work are:

- Interpretation of the VERDON-3 and 4 scenarios in term of FP speciation and fuel behavior. The calculations coupled with the experimental data led to the proposal of a mechanism for FP speciation adapted to each test. However, the assumptions used in these calculations (considering the whole irradiated fuel-FP-cladding systems) showed some limitations.
  To improve their representativeness, these calculations should be performed on a local scale. Thus, different regions of the fuel should be considered:
  - *Changes in the Pu-agglomerates in the case of MOX fuel, in the centre and on the periphery of the pellets*
  - *Fuel matrix (mainly UO_2)*
  - *Fuel-cladding interaction area.*

- Choice of the experimental conditions in which thermal treatments were led on SIMFuels so as to observe a chemical evolution of Ba and Mo in the samples.

- Determination of the oxygen potential range within which the SIMFuels were manufactured in the SPS furnace. The sintering range was defined between -550 $kJ.mol_{(O2)}^{-1}$ to -475 $kJ.mol_{(O2)}^{-1}$ at 1200°C.

The experimental data provided throughout this thesis could be supplemented by improving the representativeness of the tests performed on SIMFuels compared to those carried on irradiated samples.

Thus, thermal treatments should be performed at high temperature (above 2000°C) on SIMFuel samples in VERDON reducing and oxidizing oxidising conditions. Release measurements during these tests should also provide important, complementary experimental data to better understand the release mechanisms of FP from nuclear fuels. The representativeness of SIMFuels could also be improved by placing them in Zr cladding, which would make it possible to perform a detailed study of the suspected trapping effect of cladding on Ba or Cs during a severe accident.

In the same way, thermal treatments at intermediate temperature levels under conditions representative of a severe accident should be carried out on irradiated fuels. More specifically, we recommend performing a test under the conditions reached during the oxidation plateau in the VERCORS or VERDON tests (1500°C under an oxidizing H_2O/H_2 atmosphere). This test would provide valuable information on the fuel state and FP speciation (notably Cs) during cladding oxidation, providing a better understanding of the changes occurring during the accident scenario.

APPENDICES

TABLE OF CONTENT

A) APPENDIX 1: IRRADIATED FUEL SAMPLES

Appendix 1.1: Experimental conditions

Microscopy

OM observations were performed using a LEICA DM RXA2 device adapted for hot cell work. Image acquisition was done with a LEICA DFC 320 camera on the SIS acquisition system. Image analysis was performed using the AnalySIS pro software v 5.0 provided by Olympus.

SEM observations were performed using a field electron gun Carl Zeiss Auriga 40 device equipped with a Crytur YAG crystal based scintillator backscattering electron detector, a SE and energy selective BSE inlens detector (ESB) [36]. The accelerating voltage was set at 20 kV. Large-field acquisitions were performed using the ADDA SIS system and the AnalySIS software was used for image analysis.

SIMS analyses

SIMS analyses were performed using a shielded CAMECA IMS 6f [37]. Oxygen was used as primary ion source. The focused O_2^+ beam was accelerated to 12.5 kV and 15 kV and the secondary ions were extracted at +5 kV and –5 kV for the measurement of positive and negative secondary ions, respectively. A current beam of about 0.1 nA was used for analyses. Isotope mapping was performed on 250 x 250 µm² areas after systematic pre-puttering to clean the sample surface. In the case of the V-4R sample that was embedded in a non-conductive epoxy resin during the preparation, an electron flood gun needed to be use for charge compensation during analyses. Due to a contamination of the surface of the sample during its storage, a polishing was performed before the SIMS analyses.

EPMA

A shielded CAMECA SX100R device was used to perform X-ray mapping and quantitative profiles through EPMA. X-ray mapping was performed with the incident electron beam voltage set at 30 kV the filament current at 200 nA. Quantitative profiles were also acquired with a beam voltage of 20 kV. Generally, the total amount of elements measured during quantitative analyses was around 95 to 99 wt%. This is due to the limited number of elements analyzed in this study compared to the wide range of species created during Pu or U fission.

Appendix 1.2: Thermochemistry calculations

The Thermo-Calc software enables performing calculations of stable phase equilibria, of the amount of phases, their compositions and transformation in multicomponent systems [38].

The calculations performed within the frame of this study were based on thermodynamic data supplied by the Thermodynamics of Advanced Fuels – International Database (TAF-ID version of the 01/2018) currently developed by the OECD-NEA [20]. This project aims at providing a complete database of phase diagrams and thermodynamic properties of advanced nuclear fuels, which will be used and recognized internationally. The main objectives are to predict the evolution of the chemical composition of the fuel in different operation conditions as well as the different phases formed during fuel-cladding interaction. The following elements are taken into account in the TAF-ID but only the bold ones were used in this study : Ag, Al, Am, Ar, B, **Ba**, C, Ca, **Ce**, Cr, **Cs**, Fe, Gd, H, He, **I**, **La**, Mg, **Mo**, N, Nb, **Nd**, Ni, Np, **O**, **Pd**, **Pu**, Re, **Rh**, **Ru**, Si, **Sr**, Ta, **Tc**, **Te**, Th, Ti, **U**, V, W, **Zr**.

The TAF-ID is developed using the CALPHAD (CALculation of PHAse Diagrams) method which consists in collecting and assessing experimental and theoretical data available on the systems considered. The Gibbs free energy is modelled in order to describe the thermodynamic properties of each phase of a multicomponent system using its physical and chemical characteristics (crystallography, type of bonding, phase diagram, oxygen potential…) [39].

Calculations of the FP and fuel behavior during the VERDON-3 and 4 tests were performed using these tools. Different hypotheses were made in order to simplify the calculation:

- The initial quantity of Zr was calculated as the sum between the Zr coming from fission (given in the initial inventory) and the Zr coming from the cladding. The later was estimated by the geometric characteristics of the cladding tube (**Table II.1**) considering that all the cladding was metallic at the beginning of the test.
- The fuel in the calculation is considered as a homogeneous mixture of (U, Pu)O_2 and Zr.
- The initial O amount was calculated using the geometric characteristics of the pellets (**Table II.1**) considering it to be composed of (U, Pu)O_2. The average Pu amount talen for the calculation was 7.247 wt%. At the end of stage 2, the oxygen present in the condensed phases is reinjected in stage 3.
- The ratio between H_2O and H_2 has been estimated multiplying the time of the step by the gas flow rate.
- At the end of stage 2, the fraction of the different elements in the gas phase is not reinjected in stage 3.
- The calculation is performed at thermodynamic equilibrium.

Appendix 1.3: Macro files used to calculate the VERDON-3 and 4 tests

@@VERDON-3; stage 2

```
@@duration stage 2: 7000s
@@Flow H2O= 25 mg/s so b(H2O)= 175000 mg; Flow H2= 0.45 mg/s so b(H2)= 3150 mg
@@Zr from cladding 0.05703 mol ; Zr from FP 0.00054
go data
sw u
define-sys ba sr cs ce zr mo pu u ru rh pd tc i te la nd y h o
get
go poly
s-c t=1273 p=1e5
s-c n(sr)=8.59E-5 n(zr)=0.0576 n(mo)=6.36e-4 n(tc)=1.50e-4 n(rh)=1.35e-4 n(pd)=5.51e-4
s-c n(te)=9.95e-5 n(i)=4.83e-5 n(cs)=4.04e-4  n(ba)=2.57e-4 n(pu)=2.03e-3
s-c n(la)=1.71e-4 n(ce)=3.09e-4 n(nd)=4.95e-4 n(ru)=5.55e-4 n(u)=6.81e-2
s-i-a b(h2o)=175.00 b(h2)=3.15 b(o)=2.366
s-r-s o gas * 1E5
set-num-lim 1000 1E-06 1E-12 Y
adv glo Y 10000
c-e
s-a-v 1 t 673 1773 10
step
NORMAL
Set-int
```

@@VERDON-3; stage 3

```
@@duration stage 3: 7000s
@@Flow H2O= 2.5 mg/s so b(H2O)= 17500 mg; Flow H2= 0 mg/s
go data
sw u
define-sys ba sr cs ce zr mo pu u ru rh pd tc la nd h o
get
go poly
s-c t=2173 p=1e5
s-c n(sr)=8.60e-5 n(zr)=5.76e-2 n(mo)=3.28e-4 n(tc)=1.50e-4 n(pu)=2.03e-3
s-c n(cs)=1.10e-5 n(ba)=2.55e-4 n(la)=1.71e-4 n(ce)=3.09e-4 n(u)=6.81e-2
s-c n(nd)=4.95e-4 n(ru)=5.55e-4 n(rh)=1.35e-4 n(pd)=1.19e-4
s-i-a b(h2o)=17.50 b(h2)=0 b(o)=3.784
s-r-s o gas * 1E5
set-num-lim 1000 1E-06 1E-12 Y
adv glo Y 10000
c-e
s-a-v 1 t 1773 2573 20
step
NORMAL
set-int
```

@@VERDON-4; stage 2

```
@@duration stage 2: 7000s
@@Flow H2O= 25 mg/s so b(H2O)= 175000 mg; Flow H2= 0 mg/s
@@Zr from cladding 0.05703 mol ; Zr from FP 0.00054
go data
sw u
define-sys ba sr cs ce zr mo pu u ru rh pd tc i te la nd y h o
get
go poly
s-c t=1273 p=1e5
s-c n(sr)=8.34e-5 n(zr)=0.0576 n(mo)=6.29e-4 n(tc)=1.49e-4 n(pu)=2.03e-3
s-c n(te)=9.86e-5 n(i)=4.78e-5 n(cs)=3.95e-4 n(ba)=2.59e-4 n(u)=6.82e-2 n(rh)=1.34e-4
s-c n(la)=1.69e-4 n(ce)=3.06e-4 n(nd)=4.90e-4 n(ru)=5.48e-4 n(pd)=5.45e-4
s-i-a b(o)=2.360 b(h2o)=175.00 b(h2)=0
s-r-s o gas * 1E5
set-num-lim 1000 1E-06 1E-12 Y
adv glo Y 10000
c-e
s-a-v 1 t 673 1773 5
step
NORMAL
set-int
```

@@VERDON-4; stage 3

```
@@duration stage 2: 9350s
@@Flow H2O= 0 mg/s; Flow H2= 0.4 mg/s so b(H2)= 3740 mg
go data
sw u
define-sys ba sr cs ce zr mo pu u ru rh pd tc la nd h o
get
go poly
s-c t=2323 p=1e5
s-c n(sr)=8.3e-5 n(zr)=5.76e-2 n(mo)=2.64e-4 n(tc)=1.49e-4
s-c n(cs)=1.40e-5 n(ba)=2.57e-4 n(la)=1.69e-4  n(ce)=3.06e-4 n(pu)=2.03e-3
s-c n(nd)=4.90e-4 n(ru)=5.47e-4 n(rh)=1.34e-4  n(pd)=8.60e-5 n(u)=6.81e-2
s-i-a b(h2)=3.740 b(o)=21.40
s-r-s o gas * 1E5
set-num-lim 1000 1E-06 1E-12 Y
adv glo Y 10000
c-e
s-a-v 1 t 1773 2873,,,
step
NORMAL
set-int
```

B) APPENDIX 2: SIMFUEL SAMPLES SINTERED AT HIGH TEMPERATURE

Appendix 2.1: Experimental method

Density measurements

The theoretical density for the different mixtures has been calculated taking into account the quantity of additives (C_i) and their theoretical density (d_{thi}) into the UO_2 matrix as follows [46]:

$$d_{th} = \sum_i^n \frac{C_i d_{thi}}{100} \qquad (2)$$

The geometric density of a pellet-type sample is given by the ratio of its mass over its volume in air considering that the sample as a cylinder (equation (3)). The mass is measured on a METTLER Toledo XS205 balance. The height and the diameter are measured thanks to an ABSOLUTE micrometer and are used to determine the volume of the sample.

$$d_g = \frac{m}{V} \qquad (3)$$

The mean diameter of the pellet has been calculated according to equation (4). D_u and D_l are taken at 1 mm from the upper and lower surfaces of the pellet respectively. D_h is the diameter at half the height of the pellet.

$$D_m = \frac{D_u + 4D_h + D_l}{6} \qquad (4)$$

In the case of SPS samples, the pellets were recovered and roughly polished before measuring their dimensions in order to remove the graphite deposit on their surface. The diameter and the height of the pellets were calculated as the average of three measurements.

The hydrostatic method enables a more precise determination of the density as it does not take into account the geometry of the pellet. It enables also to determine the nature of the porosity.

The pellets are first placed in vacuum in order to remove all traces of water. The dry mass (m_d) is weighed on a METTLER Toledo XP205 balance. Then, the pellets are immersed in Bromobenzene (purity $\geq$ 99%) under vacuum during 45 min at a controlled temperature to enable all the porosity to be filled with liquid. The immersed mass is measured by weighing the sample in Bromobenzene (m_{im}). Finally, the samples are wiped rapidly on a tissue until the surface of the pellet is slightly humid. The humid mass (m_h) is weighed under air. The hydrostatic density is then calculated as follow:

$$d_h = \frac{d_{solvent}\, m_d}{m_h - m_{im}} \qquad (5)$$

The volume fractions of open and closed porosities are given by the following formulas:

$$P_{op} = 100\, \frac{m_h - m_d}{m_h - m_{im}} \qquad (6)$$

$$P_{cl} = 100 - d_h - P_{op} \qquad (7)$$

A standard is weighed in the same conditions as the samples every 8 measurements. This enables the determination of the Bromobenzene density and prevents the drift of the balance. The temperature of Bromobenzene is monitored with a thermometer during the measurements.

Sample preparation

The samples are first stuck onto a cylinder thanks to wax and cut whether axially or radially with a wire saw (the thickness of the wire is 0.2 mm) [47]. Slices or disks are thus obtained. They are then polished on a Buehler Vector grinding device using several SiC grinding foils from the thickest (grain size of 6.5 µm) to the finest (grain size of 2.5 µm) during 10 s and 1 min respectively. During these steps, the force applied on the surface of the sample is set to 5 N and the rotating speed is set at 150 rpm. An optical polishing is finally obtained thanks to a diamond polishing suspension with a grain size of 1 µm. The force is set to 10 N during minimum 10 min. The samples are placed in ethanol and cleaned with ultrasounds between each polishing step [48].

Microscopy

The pellets are then observed with an OLYMPUS DSX-500 optical microscope. These observations enable the study of the macro-structure of the samples, notably the determination of pores and precipitates sizes.

The microstructure and the chemical composition of the different SIMFuel samples were analyzed thanks to a FEI Nova Nano SEM 450 coupled with FEI SE and BSE detectors and an Oxford Instruments EDX detector. Polished samples were observed with an accelerating voltage set to 15 kV. Quantitative analyses have been performed for all the additives with a typical detection limit of 1 wt%. X-ray maps were recorded using the $L_{\alpha 1}$ lines of every FP surrogates. The $M_{\alpha 1}$ and $K_{\alpha 1}$ lines were used respectively in the case of U and O.

Image analysis was performed using the analySIS pro software v.5.0 from Olympus Soft Imaging Solutions. This software enabled the determination of the ECD of particles or precipitates and the grain size within the matrix.

X-Ray Absorption Spectroscopy

XANES measurements were performed in HERFD at the FAME-UHD beamline of the ESRF at the L_3-edge of Ba [49], [50]. The photon energy was scanned from 5.150 to 5.553 keV using a Si(220) double crystal monochromator. A helium bag was used between the sample, the CAS and the detector in order to avoid beam absorption by the air. The signal was recorded with a five Ge(400) crystal analyzer and a Vortex-EX SII detector. The beamsize was 300 x 200 µm² (Horizontal x Vertical Full Width at Half Maximum). The energy calibration was done using $BaZrO_3$ spectrum.

XANES and EXAFS measurements were carried out at the MARS beamline of the SOLEIL synchrotron facility [51] at the K-edges of Zr and Mo. The photon energy was scanned from 17.70 to 18.97 keV in the case of Zr and from 19.70 to 20.38 keV in the case of Mo using a Si(220) double crystal monochromator. The signal was recorded using a twelve elements Ge detector (ORTEC). The beamsize was 300 x 140 µm² (Horizontal x Vertical Full Width at Half Maximum). Calibration was done using the K-edge excitation energies of Zr (17.998 keV) and Mo (20.000 keV) metallic foils.

The ATHENA software [52] was used to normalize the XAS spectra: pre-edge removal and normalization was achieved using linear functions. The E_0 values of each spectrum were taken as the first zero-crossing of its second derivative respectively. Mo and Zr references spectra were acquired on pure metallic foils. The algorithm Fluo of ATHENA has thus been used to correct them for self-absorption.

Linear combination fitting was performed on ATHENA using XANES spectra acquired experimentally on several reference samples and calculated using the FDMNES software. This helped determining the amount of FP involved in the different compounds taken as reference samples.

XANES spectra of some reference samples (c-ZrO_2, t-ZrO_2, $SrZrO_3$ and $BaMoO_3$) which were unavailable at the time of the experiments were calculated using the FDMNES software [10]. The crystallographic structures were described using "crystal" and "Spgroup" keywords. The cluster radius taken for the calculations was 5.0 Å. All the calculations were performed in "Green" mode which implies the muffin-tin approximation of spherical atoms in a constant interstitial potential. The absorber atoms were considered as initially excited. The keyword "Spinorbite" was also used in order to account for relativistic effects (as heavy atoms are considered). The spectra calculated at Mo and Zr K-edges were convoluted with a width of 2 eV whereas the convolution width of those calculated at Ba L_3-edge was 0.2 eV. The crystallographic data extracted from the literature and used to calculate the XANES spectra of the different reference samples are described in **Table B-1**.

The hcp-metallic Mo XANES spectrum was calculated considering an atomic radius (r_{at}) of 145 pm [53]. The α = β and γ angles were taken respectively as 90° and 120°. The structural parameters were calculated geometrically to be:

$$a = b = 2\,r_{at} = 290\,pm$$

$$c = 4\,r_{at}\sqrt{\frac{2}{3}} = 473.6\,pm$$

The calculated spectra were calibrated in energy using experimental spectra with the same oxidation state of the absorber atom. Linear combination fittings could then be performed using both experimental and calculated XANES spectra.

Table B-1: Crystallographic data used in FDMNES calculations of c-ZrO_2, t-ZrO_2, $SrZrO_3$ and $BaMoO_3$ XANES spectra

Phase	Space group	Atom	Atomic positions	a (Å)	b (Å)	c (Å)	α (°)	β (°)	γ (°)	Ref.
c-ZrO_2	215	Zr	0.000;0.000;0.000	5.170	5.170	5.170	90	90	90	[54]
		O	0.250;0.250;0.250							
t-ZrO_2	137:1	Zr(1)	0.000;0.000;0.000	3.640	3.640	5.270	90	90	90	[55]
		Zr(2)	0.500;0.500;0.500							
		O(1)	0.000;0.500;0.185							
		O(2)	0.000;0.500;-0.185							
		O(3)	0.500;0.000;0.315							
$SrZrO_3$	62:cab	Zr	0.000;0.000;0.000	5.792	5.813	8.196	90	90	90	[56]
		Sr	0.001;0.525;0.250							
		O(1)	-0.073;-0.015;0.250							
		O(2)	0.216;0.285;0.035							
$BaMoO_3$	221	Mo	0.000;0.000;0.000	4.040	4.040	4.040	90	90	90	[57]
		Ba	0.500;0.500;0.500							
		O	0.500;0.000;0.000							

Appendix 2.2: EDX analyses performed on the as-sintered sample

Table B-2: Composition of 10 Pd-Rh metallic precipitates analyzed in the SIMFuel samples

N°	Element composition (at.%)						(Rh+Pd)/U	Rh/Pd
	Mo	Ru	Rh	Pd	U	O		
1	0.2 ± 0.0	0.8 ± 0.1	36.5 ± 0.8	30.8 ± 1.2	22.7 ± 0.9	7.8 ± 2.7	3.0	1.2
	0.1 ± 0.1	1.9 ± 2.0	0.3 ± 0.2	67.8 ± 0.1	12.7 ± 3.1	16.6 ± 3.5	-	-
2	0.4 ± 0.1	1.0 ± 0.2	41.9 ± 0.5	24.7 ± 0.3	22.0 ± 0.3	9.4 ± 0.8	3.0	1.7
	0.2 ± 0.2	0.6 ± 0.3	37.7 ± 0.5	54.4 ± 0.7	0.7 ± 0.4	5.4 ± 0.9	-	0.7
3	0.3 ± 0.2	0.4 ± 0.3	33.9 ± 0.4	35.1 ± 0.5	22.7 ± 0.5	7.6 ± 0.3	3.0	1.0
	0.2 ± 0.2	0.5 ± 0.2	26.3 ± 1.0	43.6 ± 0.4	21.4 ± 0.9	7.0 ± 1.5	3.3	0.6
4	0.0 ± 0.0	1.1 ± 0.2	43.7 ± 1.0	24.7 ± 1.1	22.3 ± 0.8	6.3 ± 2.6	3.1	1.8
	0.5 ± 0.2	1.2 ± 0.3	49.4 ± 0.6	37.7 ± 0.6	2.6 ± 0.4	6.9 ± 0.4	-	1.3
5	0.2 ± 0.2	0.8 ± 0.5	40.3 ± 1.1	26.9 ± 0.6	22.9 ± 0.6	8.2 ± 2.8	2.9	1.5
	0.2 ± 0.2	0.6 ± 0.3	40.7 ± 0.5	37.9 ± 0.5	12.4 ± 0.5	7.9 ± 0.3	-	1.1
6	0.1 ± 0.1	0.4 ± 0.2	0.5 ± 0.2	75.8 ± 1.5	14.7 ± 0.6	7.0 ± 1.2	-	-
7	0.2 ± 0.2	0.6 ± 0.2	23.7 ± 0.3	44.9 ± 0.7	21.9 ± 0.1	7.9 ± 0.7	3.1	0.5
8	0.1 ± 0.1	0.9 ± 0.2	35.1 ± 2.6	31.4 ± 2.1	21.6 ± 0.7	9.8 ± 3.0	3.1	1.1
	0.0 ± 0.2	0.9 ± 0.3	41.8 ± 0.5	40.0 ± 0.5	11.4 ± 0.5	5.6 ± 0.3	-	1.1
9	0.1 ± 0.1	0.4 ± 0.2	11.7 ± 0.9	61.7 ± 1.2	18.0 ± 0.6	6.9 ± 0.8	4.1	0.2
	0.1 ± 0.2	0.4 ± 0.2	11.5 ± 1.1	63.5 ± 2.0	16.9 ± 2.6	6.9 ± 1.0	4.4	0.2
10	0.1 ± 0.1	0.4 ± 0.1	0.4 ± 0.2	77.2 ± 0.8	14.7 ± 0.7	6.4 ± 1.2	-	-

Table B-3: Composition of 30 Mo-Ru-Rh-Pd metallic precipitates analyzed in the SIMFuel samples

N°	Element composition (at.%)						Ru/Mo
	Mo	Ru	Rh	Pd	U	O	
1	4.9 ± 0.3	80.5 ± 0.7	0.0 ± 0.0	2.8 ± 0.4	1.7 ± 0.3	9.8 ± 0.4	16.4
2	6.1 ± 0.3	85.4 ± 0.8	0.0 ± 0.0	2.4 ± 0.4	0.8 ± 0.3	4.7 ± 0.4	14.0
3	8.8 ± 0.3	79.9 ± 0.7	0.0 ± 0.0	2.4 ± 0.4	2.2 ± 0.3	9.3 ± 0.4	9.1
4	9.3 ± 0.3	78.1 ± 0.7	0.0 ± 0.0	2.0 ± 0.4	0.7 ± 0.3	9.8 ± 0.4	8.4
5	9.6 ± 0.3	45.4 ± 0.5	27.8 ± 0.50	7.7 ± 0.5	4.7 ± 0.4	4.1 ± 0.3	4.7
6	15.9 ± 0.4	68.9 ± 0.7	0.0 ± 0.0	3.1 ± 0.4	2.2 ± 0.4	9.7 ± 0.4	4.3
7	22.9 ± 0.4	62.1 ± 0.6	0.0 ± 0.0	4.0 ± 0.4	1.6 ± 0.3	9.3 ± 0.4	2.7
8	14.4 ± 0.3	34.7 ± 0.6	40.6 ± 0.6	3.4 ± 0.5	1.1 ± 0.4	5.2 ± 0.4	2.4
9	18.9 ± 0.4	36.8 ± 0.5	35.9 ± 0.5	1.9 ± 0.5	0.5 ± 0.4	5.2 ± 0.4	1.9
10	20.7 ± 0.4	37.7 ± 0.6	36.2 ± 0.6	1.9 ± 0.5	0.4 ± 0.4	2.9 ± 0.4	1.8
11	20.2 ± 0.4	35.9 ± 0.5	32.3 ± 0.5	3.1 ± 0.5	1.8 ± 0.4	6.2 ± 0.3	1.8
12	20.4 ± 0.4	36.1 ± 0.5	33.7 ± 0.5	3.0 ± 0.5	0.5 ± 0.4	6.3 ± 0.4	1.8
13	17.7 ± 0.4	27.6 ± 0.5	36.0 ± 0.6	7.8 ± 0.5	3.9 ± 0.4	6.2 ± 0.3	1.6
14	16.9 ± 0.4	25.5 ± 0.5	4.1 ± 0.6	0.3 ± 0.5	3.4 ± 0.4	3.4 ± 0.4	1.5
15	23.3 ± 0.4	34.5 ± 0.5	35.4 ± 0.5	2.9 ± 0.5	0.8 ± 0.4	2.9 ± 0.4	1.5
16	34.6 ± 0.8	48.4 ± 0.4	0.0 ± 0.0	7.6 ± 0.3	4.2 ± 0.4	4.5 ± 0.4	1.4
17	24.9 ± 0.4	32.8 ± 0.5	37.8 ± 0.6	2.2 ± 0.5	0.7 ± 0.4	1.2 ± 0.4	1.3
18	24.2 ± 0.4	31.3 ± 0.5	35.9 ± 0.6	2.3 ± 0.5	0.7 ± 0.3	5.2 ± 0.3	1.3
19	35.2 ± 0.4	40.6 ± 0.5	0.0 ± 0.0	9.1 ± 0.4	4.7 ± 0.4	9.7 ± 0.4	1.2
20	26.2 ± 0.4	29.6 ± 0.5	34.1 ± 0.5	3.4 ± 0.5	0.5 ± 0.3	6.1 ± 0.3	1.1
21	25.7 ± 0.4	26.9 ± 0.5	38.4 ± 0.6	3.3 ± 0.5	0.9 ± 0.3	4.2 ± 0.3	1.0
22	27.0 ± 0.4	28.1 ± 0.5	35.5 ± 0.6	3.8 ± 0.5	0.3 ± 0.4	5.0 ± 0.4	1.0
23	39.9 ± 0.5	41.2 ± 0.5	0.0 ± 0.0	11.2 ± 0.4	1.4 ± 0.3	5.8 ± 0.4	1.0
24	28.4 ± 0.5	24.8 ± 0.5	37.3 ± 0.6	3.8 ± 0.5	0.2 ± 0.4	5.1 ± 0.3	0.9
25	44.7 ± 0.5	28.4 ± 0.5	0.0 ± 0.4	19.8 ± 0.4	0.5 ± 0.3	5.9 ± 0.3	0.6
26	44.4 ± 0.5	28.0 ± 0.5	0.0 ± 0.5	20.1 ± 0.4	0.5 ± 0.3	6.9 ± 0.3	0.6
27	43.4 ± 0.5	27.1 ± 0.5	0.0 ± 0.4	22.6 ± 0.4	0.6 ± 0.3	6.1 ± 0.3	0.6
28	31.2 ± 0.4	12.4 ± 0.4	47.5 ± 0.6	3.2 ± 0.5	0.8 ± 0.3	4.6 ± 0.3	0.4
29	31.6 ± 0.5	12.3 ± 0.4	48.5 ± 0.6	4.2 ± 0.5	0.4 ± 0.4	2.9 ± 0.4	0.4
30	31.0 ± 0.5	10.8 ± 0.4	47.9 ± 0.6	3.2 ± 0.5	0.6 ± 0.4	6.3 ± 0.3	0.3

Table B-4: Composition of 10 pure Mo metallic precipitates analyzed in the SIMFuel samples

N°	Element composition (at.%)					
	Mo	Ru	Rh	Pd	U	O
1	86.8 ± 0.9	0.7 ± 0.4	0.1 ± 0.3	0.8 ± 0.2	1.2 ± 0.3	10.1 ± 0.4
2	79.0 ± 0.8	2.2 ± 0.4	0.0 ± 0.3	1.2 ± 0.2	0.3 ± 0.3	7.4 ± 0.3
3	88.7 ± 0.7	0.0 ± 0.0	0.0 ± 0.0	1.3 ± 0.2	0.5 ± 0.3	8.7 ± 0.3
4	91.3 ± 0.4	0.0 ± 0.2	0.0 ± 0.1	1.4 ± 0.1	0.6 ± 0.2	6.0 ± 0.1
5	87.7 ± 2.1	2.4 ± 0.1	0.0 ± 0.2	1.7 ± 0.1	0.5 ± 0.0	8.5 ± 1.3
6	71.6 ± 0.9	9.7 ± 0.5	2.5 ± 0.4	3.2 ± 0.3	2.0 ± 0.3	10.5 ± 0.3
7	80.5 ± 0.9	4.4 ± 0.5	2.3 ± 0.3	2.8 ± 0.3	0.1 ± 0.3	9.5 ± 0.3
8	89.2 ± 0.8	2.1 ± 0.5	0.0 ± 0.0	1.2 ± 0.2	1.4 ± 0.3	6.0 ± 0.4
9	90.7 ± 2.1	0.1 ± 0.2	0.0 ± 0.0	1.6 ± 0.3	0.4 ± 0.1	6.7 ± 2.1
10	77.3 ± 0.8	0.5 ± 0.4	0.0 ± 0.0	1.6 ± 0.3	2.2 ± 0.0	17.7 ± 0.8

Table B-5: Composition of the different zones (shell, U-rich layer and core) of 10 oxide precipitates analyzed in the SIMFuel samples

N°	Zone	Element composition (at.%)						Ba/Zr	Sr/Zr	O/Zr
		Ba	Zr	Sr	Ce	U	O			
1	-	18.4 ± 1.4	22.2 ± 0.9	3.9 ± 0.6	0.1 ± 0.0	0.9 ± 0.7	54.3 ± 1.1	0.8	0.18	2.44
2	shell	18.1 ± 1.7	21.8 ± 2.7	4.0 ± 0.8	0.1 ± 0.2	2.3 ± 4.2	53.9 ± 1.0	0.8	0.2	2.5
	U	2.1 ± 1.2	20.7 ± 2.4	1.2 ± 0.4	0.7 ±0.5	11.7 ± 1.0	62.2 ± 0.3	0.1	0.1	3.0
	core	0.0 ± 0.1	33.2 ± 1.0	0.2 ± 0.1	0.0 ± 0.1	1.0 ± 0.6	63.8 ± 1.6	0.0	0.0	1.9
3	shell	17.0 ± 0.6	21.1 ± 1.1	4.6 ± 0.4	0.3 ± 1.4	7.3 ± 0.6	55.5 ± 0.7	0.8	0.2	2.6
	U	5.2 ± 3.9	14.9 ± 2.3	1.7 ± 1.0	2.6 ± 1.1	10.2 ± 3.6	56.9 ± 8.6	0.4	0.1	3.8
4	shell	18.0 ± 1.5	20.6 ± 1.3	3.3 ± 0.6	0.1 ± 0.1	1.3 ± 0.7	55.6 ± 0.4	0.9	0.2	2.7
	U	2.5 ± 2.6	23.1 ± 4.2	1.0 ± 0.4	0.5 ± 0.1	8.8 ± 1.5	62.0 ± 0.6	0.1	0.0	2.7
	core	0.3 ± 0.4	35.4 ± 0.5	0.3 ± 0.2	0.0 ± 0.0	1.4 ± 0.6	62.3 ± 1.2	0.0	0.0	1.8
5	shell	15.8 ± 0.6	20.6 ± 0.8	4.3 ± 0.6	0.0 ± 0.0	1.5 ± 1.2	57.2 ± 0.9	0.8	0.2	2.8
	U	0.6 ± 0.6	11.8 ± 5.3	0.5 ± 0.2	0.4 ± 0.2	19.2 ± 3.7	65.3 ± 0.2	0.1	0.0	5.5
6	shell	18.5 ± 0.8	22.1 ± 1.6	2.8 ± 0.6	0.2 ± 0.2	1.0 ± 1.0	54.9 ± 0.9	0.8	0.1	2.5
	U	1.0 ± 1.0	24.6 ± 2.2	0.7 ± 0.1	0.6 ± 0.1	6.9 ± 0.7	62.9 ± 2.0	0.0	0.0	2.6
	core	0.3 ± 0.5	35.3 ± 0.7	0.3 ± 0.0	0.1 ± 0.0	0.8 ± 0.7	62.7 ± 0.7	0.0	0.0	1.8
7	shell	18.6 ± 0.6	21.6 ± 1.0	3.2 ± 0.9	0.1 ± 0.1	0.6 ± 0.6	55.3 ± 0.9	0.9	0.2	2.6
	U	1.1 ± 0.3	24.3 ± 0.5	0.7 ± 0.2	0.3 ± 0.2	9.0 ± 0.5	63.7 ± 0.4	0.1	0.0	2.6
	core	0.1 ± 0.1	34.7 ± 0.9	0.3 ± 0.1	0.1 ± 0.0	0.8 ± 0.1	63.7 ± 1.0	0.0	0.0	1.8
8	shell	20.1 ± 0.4	21.2 ± 0.3	2.4 ± 0.1	0.1 ± 0.1	0.7 ±0.3	55.0 ± 0.4	1.0	0.1	2.6
	U	11.8 ± 0.4	13.4 ± 0.4	1.6 ± 0.2	0.3 ± 0.3	10.0 ± 0.5	61.6 ± 0.4	0.9	0.1	4.6
9	shell	19.0 ± 0.7	22.4 ± 0.5	3.8 ± 0.4	0.1 ± 0.1	0.3 ± 0.1	54.0 ± 0.5	0.9	0.2	2.4
	core	0.0 ± 0.0	35.6 ± 0.8	0.2 ± 0.0	0.0 ± 0.0	0.5 ± 0.3	63.3 ± 0.7	0.0	0.0	1.8
10	shell	19.6 ± 0.7	22.3 ± 0.6	3.4 ± 0.5	0.1 ± 0.1	0.5 ± 0.2	53.7 ± 0.5	0.9	0.2	2.4
	U	3.6 ± 2.7	21.3 ± 1.5	1.2 ± 0.4	0.5 ± 0.1	10.4 ± 0.4	61.7 ± 0.8	0.2	0.1	2.9
	core	1.1 ± 1.1	33.2 ± 0.8	0.4 ± 0.1	0.1 ± 0.0	2.6 ± 0.6	62.1 ± 0.8	0.0	0.0	1.9

Appendix 2.3: EDX analyses performed on the samples treated in oxidizing conditions

Table B-6: Composition of the Pd-Rh metallic precipitates analyzed in the SIMFuel samples annealed at 400°C under oxidizing conditions.

N°	Element composition (at.%)						(Rh+Pd)/U	Rh/Pd
	Mo	Ru	Rh	Pd	U	O		
1	0.0 ± 0.2	0.1 ± 0.3	19.7 ± 0.4	58.1 ± 0.6	12.4 ± 0.5	9.7 ± 0.3	-	0.3
	0.1 ± 0.1	0.7 ± 0.1	35.6 ± 1.0	32.8 ± 0.9	22.2 ± 0.7	8.0 ± 1.8	3.1	1.1
2	0.1 ± 0.0	0.4 ± 0.1	8.5 ± 0.2	74.0 ± 1.3	9.5 ± 0.2	6.5 ± 1.7	-	0.1
3	0.0 ± 0.2	0.4 ± 0.3	22.7 ± 0.4	61.0 ± 0.6	8.4 ± 0.5	7.5 ± 0.3	-	0.4
	0.3 ± 0.1	0.5 ± 0.3	38.2 ± 0.6	30.4 ± 0.9	22.2 ± 0.3	7.9 ± 0.7	3.1	1.3
4	0.4 ± 0.4	0.7 ± 0.1	29.3 ± 0.7	53.2 ± 0.8	9.1 ± 0.2	7.2 ± 0.2	-	0.6
	0.1 ± 0.1	0.6 ± 0.2	39.7 ± 0.9	30.3 ± 0.5	22.9 ± 0.6	6.0 ± 1.5	3.1	1.3
5	0.1 ± 0.1	0.4 ± 0.2	20.8 ± 2.1	61.5 ± 3.5	12.1 ± 1.2	4.8 ± 0.9	-	0.3
	0.0 ± 0.0	0.6 ± 0.3	26.0 ± 2.7	50.6 ± 3.4	15.8 ± 1.5	6.3 ± 1.1	4.8	0.5

Table B-7: Composition of the Pd-Rh metallic precipitates analyzed in the SIMFuel samples annealed at 700°C under oxidizing conditions

N°	Element composition (at.%)						(Rh+Pd)/U	Rh/Pd
	Mo	Ru	Rh	Pd	U	O		
1	0.3 ± 0.2	0.2 ± 0.2	0.4 ± 0.3	88.8 ± 0.8	4.6 ± 0.4	4.9 ± 0.2	-	-
2	0.1 ± 0.2	0.5 ± 0.2	17.4 ± 0.4	63.0 ± 0.4	5.4 ± 0.5	13.0 ± 0.4	-	0.3
	0.2 ± 0.2	0.5 ± 0.3	26.3 ± 0.4	15.4 ± 0.7	15.8 ± 0.4	41.5 ± 0.4	-	1.7
3	0.2 ± 0.2	0.3 ± 0.2	0.3 ± 0.3	83.1 ± 0.7	9.1 ± 0.4	6.6 ± 0.3	-	-
4	0.0 ± 0.2	0.5 ± 0.2	0.5 ± 0.3	86.5 ± 0.7	7.0 ± 0.4	5.5 ± 0.4	-	-
5	0.1 ± 0.2	0.5 ± 0.2	4.7 ± 0.3	79.4 ± 0.6	4.3 ± 0.4	10.5 ± 0.4	-	0.1

Table B-8: Composition of the Pd-Rh metallic precipitates analyzed in the SIMFuel samples annealed at 900°C under oxidizing conditions

N°	Element composition (at.%)						(Rh+Pd)/U	Rh/Pd
	Mo	Ru	Rh	Pd	U	O		
1	6.4 ± 1.6	6.9 ± 2.5	21.3 ± 3.4	56.8 ± 3.3	1.0 ± 0.7	7.5 ± 4.9	-	0.4
2	0.7 ± 0.2	1.0 ± 0.2	28.1 ± 2.0	28.2 ± 0.7	15.5 ± 2.4	26.0 ± 0.9	-	1.0
	6.6 ± 0.3	12.1 ± 0.4	58.4 ± 0.7	15.8 ± 0.5	1.5 ± 0.4	5.3 ± 0.4	-	3.7
3	7.0 ± 0.3	4.8 ± 0.3	51.6 ± 0.6	27.2 ± 0.5	0.7 ± 0.4	8.5 ± 0.4	-	1.9
	1.0 ± 0.1	0.9 ± 0.4	22.4 ± 2.8	17.6 ± 1.0	15.1 ± 0.3	42.2 ± 3.1	-	1.3
4	6.2 ± 0.3	4.5 ± 0.4	58.9 ± 0.7	19.8 ± 0.5	0.7 ± 0.4	9.5 ± 0.4	-	3.0
	0.5 ± 0.2	0.6 ± 0.3	26.7 ± 0.4	13.9 ± 0.4	15.5 ± 0.4	42.8 ± 0.4	-	1.9
5	6.3 ± 0.3	1.8 ± 0.3	12.7 ± 0.5	55.8 ± 0.6	1.3 ± 0.4	6.7 ± 0.4	-	0.2

Table B-9: Composition of the Pd-Rh metallic precipitates analyzed in the SIMFuel samples annealed at 1000°C under oxidizing conditions

N°	Element composition (at.%)						(Rh+Pd)/U	Rh/Pd
	Mo	Ru	Rh	Pd	U	O		
1	0.8 ± 0.2	0.7 ± 0.3	20.8 ± 0.4	73.4 ± 0.7	0.7 ± 0.4	3.10 ± 0.4	-	0.3
	2.6 ± 0.2	1.0 ± 0.1	16.7 ± 1.5	22.9 ± 1.2	15.7 ± 0.8	40.85 ± 3.0	-	0.7
2	5.2 ± 0.1	0.9 ± 0.3	31.3 ± 0.1	41.5 ± 0.3	1.5 ± 0.0	19.15 ± 0.9	-	0.8
	4.7 ± 0.2	2.5 ± 0.3	42.6 ± 0.6	28.8 ± 0.5	1.5 ± 0.4	19.30 ± 0.3	-	1.5
3	1.7 ± 0.2	3.5 ± 0.2	6.4 ± 0.2	73.0 ± 0.4	2.9 ± 0.6	12.48 ± 0.4	-	0.1
	0.3 ± 0.2	1.5 ± 0.3	2.0 ± 0.4	27.9 ± 0.7	22.7 ± 0.4	43.07 ± 0.4	-	0.1
4	4.3 ± 2.7	3.3 ± 1.5	12.7 ± 2.7	67.5 ± 2.3	3.5 ± 3.0	8.48 ± 4.0	-	0.2
	2.2 ± 1.1	5.7 ± 1.6	21.5 ± 1.9	62.1 ± 2.6	1.1 ± 0.3	6.75 ± 1.1	-	0.4
5	4.0 ± 1.0	4.0 ± 0.3	2.0 ± 0.4	81.8 ± 1.7	1.7 ± 0.2	6.06 ± 2.0	-	0.0

Table B-10: Composition of 10 Mo-Ru-Rh-Pd metallic precipitates analyzed in the SIMFuel samples annealed at 400°C under oxidizing conditions

N°	Element composition (at.%)						Ru/Mo
	Mo	Ru	Rh	Pd	U	O	
1	2.5 ± 0.3	84.4 ± 0.8	0.0 ± 0.5	1.6 ± 0.5	0.9 ± 0.3	10.0 ± 0.4	33.8
2	3.5 ± 0.3	89.3 ± 0.7	0.0 ± 0.6	1.8 ± 0.4	0.5 ± 0.3	4.9 ± 0.3	25.5
5	3.2 ± 0.3	89.4 ± 0.8	0.0 ± 0.5	1.1 ± 0.4	1.0 ± 0.3	4.9 ± 0.3	27.9
4	6.4 ± 0.3	83.6 ± 0.7	0.0 ± 0.5	1.6 ± 0.4	1.0 ± 0.3	7.4 ± 0.3	13.1
3	8.8 ± 0.3	82.7 ± 0.7	0.0 ± 0.5	2.6 ± 0.4	0.9 ± 0.3	4.7 ± 0.3	9.4
7	19.1 ± 0.4	27.9 ± 0.5	42.3 ± 0.6	2.8 ± 0.5	0.6 ± 0.4	7.3 ± 0.4	1.5
6	21.2 ± 0.4	24.7 ± 0.5	47.0 ± 0.6	2.9 ± 0.5	0.7 ± 0.4	3.2 ± 0.4	1.2
8	34.2 ± 0.5	2.9 ± 0.4	49.7 ± 0.6	7.0 ± 0.5	0.3 ± 0.4	5.8 ± 0.3	0.1
9	35.5 ± 0.5	2.7 ± 0.4	49.6 ± 0.6	7.4 ± 0.5	0.7 ± 0.4	3.8 ± 0.3	0.1
10	35.3 ± 0.5	2.7 ± 0.4	47.8 ± 0.6	7.9 ± 0.5	0.6 ± 0.4	5.6 ± 0.3	0.1

Table B-11: Composition of 10 Mo-Ru-Rh-Pd metallic precipitates analyzed in the SIMFuel samples annealed at 700°C under oxidizing conditions

N°	Element composition (at.%)						Ru/Mo
	Mo	Ru	Rh	Pd	U	O	
1	3.5 ± 0.3	81.1 ± 0.8	0.0 ± 0.6	5.9 ± 0.4	1.4 ± 0.4	7.4 ± 0.3	23.2
2	6.5 ± 0.3	77.2 ± 0.7	0.0 ± 0.5	4.9 ± 0.4	2.6 ± 0.4	8.5 ± 0.4	11.9
3	9.4 ± 0.3	81.0 ± 0.7	0.0 ± 0.6	1.9 ± 0.4	1.0 ± 0.3	6.5 ± 0.3	8.6
4	12.9 ± 0.3	70.5 ± 0.6	0.0 ± 0.5	2.6 ± 0.4	4.0 ± 0.4	9.9 ± 0.4	5.5
5	14.6 ± 0.3	77.0 ± 0.6	0.0 ± 0.5	3.0 ± 0.4	0.7 ± 0.3	4.7 ± 0.4	5.3
6	16.4 ± 0.3	73.7 ± 0.7	0.0 ± 0.5	3.0 ± 0.4	0.9 ± 0.3	5.9 ± 0.4	4.5
7	26.5 ± 0.4	62.0 ± 0.6	0.0 ± 0.5	5.4 ± 0.4	0.6 ± 0.3	5.4 ± 0.3	2.3
8	36.8 ± 0.5	40.2 ± 0.5	0.0 ± 0.5	16.2 ± 0.4	1.0 ± 0.3	5.1 ± 0.3	1.1
9	40.8 ± 0.5	34.3 ± 0.5	0.0 ± 0.5	19.3 ± 0.4	0.7 ± 0.4	4.1 ± 0.3	0.8
10	41.1 ± 0.5	20.1 ± 0.4	0.0 ± 0.4	32.5 ± 0.5	0.9 ± 0.4	5.1 ± 0.3	0.5

Table B-12: Composition of 10 Mo-Ru-Rh-Pd metallic precipitates analyzed in the SIMFuel samples annealed at 900°C under oxidizing conditions

N°	Element composition (at.%)						Ru/Mo
	Mo	Ru	Rh	Pd	U	O	
1	6.0 ± 0.3	83.8 ± 0.7	0.0 ± 0.5	2.5 ± 0.4	1.5 ± 0.3	6.0 ± 0.4	14.0
2	6.1 ± 0.3	84.9 ± 0.7	0.0 ± 0.5	1.6 ± 0.4	1.2 ± 0.3	6.2 ± 0.4	13.9
3	6.0 ± 0.3	81.5 ± 0.7	0.0 ± 0.5	3.0 ± 0.4	1.3 ± 0.3	8.0 ± 0.4	13.6
4	16.6 ± 0.3	16.2 ± 0.4	29.9 ± 0.5	27.3 ± 0.5	0.6 ± 0.4	8.6 ± 0.4	1.0
5	21.6 ± 0.4	19.3 ± 0.5	41.4 ± 0.6	9.6 ± 0.5	0.5 ± 0.4	7.0 ± 0.4	0.9
6	7.1 ± 0.3	4.8 ± 0.3	57.8 ± 0.7	19.6 ± 0.5	1.9 ± 0.4	8.5 ± 0.4	0.7
7	20.4 ± 0.4	11.7 ± 0.4	51.9 ± 0.7	6.0 ± 0.5	1.2 ± 0.4	8.5 ± 0.4	0.6
8	11.0 ± 0.3	5.6 ± 0.4	58.3 ± 0.6	19.2 ± 0.5	0.4 ± 0.4	5.5 ± 0.4	0.5
9	15.1 ± 0.3	5.6 ± 0.4	55.3 ± 0.6	15.0 ± 0.5	0.5 ± 0.4	8.0 ± 0.4	0.4
10	30.4 ± 0.5	8.3 ± 0.4	50.4 ± 0.6	3.1 ± 0.5	0.6 ± 0.4	7.0 ± 0.4	0.3

Table B-13: Composition of 10 Mo-Ru-Rh-Pd metallic precipitates analyzed in the SIMFuel samples annealed at 1000°C under oxidizing conditions

N°	Element composition (at.%)						Ru/Mo
	Mo	Ru	Rh	Pd	U	O	
1	3.0 ± 0.3	85.8 ± 0.8	0.0 ± 0.5	1.5 ± 0.4	1.5 ± 0.3	7.9 ± 0.4	28.6
2	4.0 ± 0.3	81.3 ± 0.7	0.0 ± 0.5	1.8 ± 0.4	3.7 ± 0.4	8.6 ± 0.4	20.3
3	5.3 ± 0.3	79.9 ± 0.7	0.0 ± 0.5	2.1 ± 0.4	5.0 ± 0.4	7.5 ± 0.4	15.1
4	6.6 ± 0.3	78.1 ± 0.7	0.0 ± 0.5	1.8 ± 0.4	4.1 ± 0.4	9.1 ± 0.4	11.8
5	6.7 ± 0.3	82.5 ± 0.8	0.0 ± 0.5	2.4 ± 0.3	1.1 ± 0.3	6.6 ± 0.4	12.3
6	6.6 ± 0.3	80.6 ± 0.8	0.0 ± 0.5	2.2 ± 0.3	2.1 ± 0.3	8.1 ± 0.4	12.2
7	7.6 ± 0.3	79.0 ± 0.7	0.0 ± 0.4	2.0 ± 0.4	2.2 ±0.4	9.0 ± 0.4	10.4
8	9.9 ± 0.3	74.4 ± 0.8	0.0 ± 0.5	2.8 ± 0.4	2.3 ± 0.3	9.6 ± 0.4	7.5
9	10.9 ± 0.3	78.8 ± 0.7	0.0 ± 0.5	3.1 ± 0.4	1.3 ± 0.3	5.7 ± 0.4	7.2
10	11.5 ± 0.3	77.7 ± 0.7	0.0 ± 0.5	3.0 ± 0.4	1.3 ± 0.3	6.3 ± 0.4	6.8

Table B-14: Composition of the pure Mo metallic precipitates analyzed in the SIMFuel samples annealed at 400°C under oxidizing conditions

N°	Element composition (at.%)					
	Mo	Ru	Rh	Pd	U	O
1	77.2 ± 0.9	1.6 ± 0.5	4.2 ± 0.4	2.4 ± 0.3	0.5 ± 0.3	13.5 ± 0.4
2	89.8 ± 1.3	0.1 ± 0.2	0.0 ± 0.1	1.8 ± 0.1	0.1 ± 0.1	7.8 ± 1.2
3	84.6 ± 0.7	2.5 ± 0.4	0.0 ± 0.3	2.3 ± 0.3	1.9 ± 0.4	8.7 ± 0.4
4	80.3 ± 0.8	7.6 ± 0.5	0.4 ± 0.4	1.5 ± 0.3	2.1 ± 0.4	7.5 ± 0.3
5	90.0 ± 0.5	0.3 ± 0.1	0.0 ± 0.1	1.5 ± 0.2	0.3 ± 0.1	7.3 ± 0.8

Table B-15: Composition of the pure Mo metallic precipitates analyzed in the SIMFuel samples annealed at 700°C under oxidizing conditions

N°	Element composition (at.%)					
	Mo	Ru	Rh	Pd	U	O
1	92.0 ± 2.7	1.3 ± 0.4	0.0 ± 0.0	1.55 ± 0.4	0.1 ± 0.0	4.9 ± 3.3
2	84.7 ± 0.8	4.5 ± 0.4	0.0 ± 0.3	2.00 ± 0.3	0.4 ± 0.3	8.1 ± 0.3
3	78.3 ± 0.8	6.9 ± 0.5	0.0 ± 0.3	2.00 ± 0.3	0.7 ± 0.3	11.8 ± 0.3
4	84.4 ± 0.5	5.5 ± 1.3	0.0 ± 0.0	1.98 ± 0.1	0.7 ± 0.4	7.3 ± 1.1
5	92.0 ± 2.6	1.3 ± 0.4	0.0 ± 0.0	1.54 ± 0.4	0.1 ± 0.0	4.9 ± 3.2

Table B-16: Composition of the pure Mo metallic precipitates analyzed in the SIMFuel samples annealed at 900°C under oxidizing conditions

N°	Element composition (at.%)					
	Mo	Ru	Rh	Pd	U	O
1	85.4 ± 0.8	0.4 ± 0.5	0.0 ± 0.0	1.3 ± 0.2	1.3 ± 0.3	11.0 ± 0.4
2	86.5 ± 0.9	0.4 ± 0.2	1.2 ± 0.3	2.0 ± 0.2	0.3 ± 0.1	8.6 ± 0.8
3	89.3 ± 0.2	0.4 ± 0.3	0.1 ± 0.2	1.7 ± 0.1	0.4 ± 0.2	7.9 ± 0.5
4	89.2 ± 0.9	0.8 ± 0.5	0.0 ± 0.3	1.6 ± 0.2	0.4 ± 0.3	7.9 ± 0.4
5	87.3 ± 0.9	0.6 ± 0.4	0.1 ± 0.3	1.3 ± 0.2	0.5 ± 0.3	9.5 ± 0.4

Table B-17: Composition of the pure Mo metallic precipitates analyzed in the SIMFuel samples annealed at 1000°C under oxidizing conditions

N°	Element composition (at.%)					
	Mo	Ru	Rh	Pd	U	O
1	79.6 ± 0.2	0.2 ± 0.2	0.0 ± 0.0	1.6 ± 0.0	1.3 ± 0.1	17.0 ± 0.2
	35.6 ± 0.6	0.2 ± 0.1	0.0 ± 0.0	0.2 ± 0.1	0.8 ± 0.2	63.2 ± 0.5
2	92.9 ± 1.5	0.4 ± 0.4	0.0 ± 0.0	1.8 ± 0.0	0.2 ± 0.1	4.7 ± 0.9
3	36.3 ±1.9	0.6 ± 0.5	0.0 ± 0.0	0.5 ± 0.3	1.6 ± 1.3	60.9 ± 1.7
	86.9 ± 1.2	16.7 ± 0.2	0.1 ± 0.1	2.6 ± 0.5	0.2 ± 0.1	8.2 ± 1.4
4	81.2 ± 0.6	0.8 ± 0.4	0.0 ± 0.3	1.6 ± 0.3	0.1 ± 0.3	16.3 ± 0.3
5	35.3 ± 1.3	0.5 ± 0.4	0.0 ± 0.0	0.6 ± 0.5	0.8 ± 0.8	62.6 ± 1.5
	59.8 ± 0.7	3.8 ± 0.4	0.0 ± 0.3	7.7 ± 0.3	0.4 ± 0.3	27.8 ± 0.4

Table B-18: Composition of the different zones (shell, U-rich layer, core) of 5 oxide precipitates analyzed in the SIMFuel samples annealed at 400°C under oxidizing conditions

N°	Zone	Element composition (at.%)						Ba/Zr	Sr/Zr	O/Zr
		Ba	Zr	Sr	Mo	U	O			
1	-	15.9 ± 0.7	21.0 ± 1.5	5.9 ± 0.6	0.6 ± 1.1	0.6 ± 0.3	54.7 ± 0.4	0.8	0.3	2.6
2	shell	18.9 ± 1.0	22.4 ± 0.2	3.5 ± 0.5	0.0 ± 0.0	0.2 ± 0.1	54.3 ± 0.4	0.9	0.2	2.4
	core	0.4 ± 0.8	33.5 ± 3.7	0.3 ± 0.2	0.0 ± 0.0	1.3 ± 1.3	62.4 ± 1.3	0.0	0.0	1.9
3	shell	19.1 ± 0.5	22.4 ± 0.4	3.6 ± 0.6	0.0 ± 0.0	0.5 ± 0.3	54.0 ± 0.3	0.9	0.2	2.4
	core	0.1 ± 0.1	35.9 ± 0.7	0.3 ± 0.1	0.0 ± 0.0	1.2 ± 0.5	62.1 ± 0.4	0.0	0.0	1.7
4	shell	19.1 ± 1.0	22.2 ± 0.8	3.6 ± 0.8	0.2 ± 0.1	0.9 ± 0.6	53.9 ± 0.6	0.9	0.2	2.4
	core	0.9 ± 0.5	34.1 ± 1.8	0.4 ± 0.1	0.1 ± 0.1	2.4 ± 0.7	61.6 ± 0.8	0.0	0.0	1.8
5	shell	19.0 ± 1.5	22.7 ± 1.0	3.1 ± 0.8	0.3 ± 0.1	0.6 ± 0.6	54.0 ± 0.4	0.8	0.1	2.4
	core	0.0 ± 0.0	37.4 ± 0.2	0.3 ± 0.1	0.0 ± 0.1	0.6 ± 0.4	61.3 ± 0.3	0.0	0.0	1.6

Table B-19: Composition of the different zones (shell, core) of 5 oxide precipitates analyzed in the SIMFuel samples annealed at 700°C under oxidizing conditions

N°	Zone	Element composition (at.%)						Ba/Zr	Sr/Zr	O/Zr
		Ba	Zr	Sr	Mo	U	O			
1	shell	18.6 ± 0.0	22.2 ± 2.1	5.5 ± 1.5	0.0 ± 0.0	2.2 ± 2.3	51.3 ± 1.2	0.8	0.3	2.3
	core	0.0 ± 0.1	37.7 ± 0.7	0.3 ± 0.0	0.0 ± 0.0	0.8 ± 0.3	60.8 ± 0.5	0.0	0.0	1.6
2	shell	18.6 ± 0.0	22.2 ± 2.0	5.4 ± 1.5	0.0 ± 0.0	2.2 ± 2.3	51.3 ± 1.3	0.8	0.2	2.3
	core	0.1 ± 0.1	37.7 ± 0.7	0.3 ± 0.0	0.0 ± 0.0	0.8 ± 0.3	60.8 ± 0.4	0.0	0.0	1.6
3	shell	18.6 ± 0.6	21.8 ± 0.5	4.0 ± 0.1	0.2 ± 0.1	1.0 ± 0.8	54.2 ± 0.6	0.9	0.2	2.5
	core	0.2 ± 0.1	36.7 ± 0.7	0.2 ± 0.1	0.0 ± 0.0	0.9 ± 0.4	61.7 ± 0.6	0.0	0.0	1.7
4	shell	17.1 ± 0.3	21.9 ± 0.1	4.6 ± 0.5	0.2 ± 0.1	0.6 ± 0.1	55.0 ± 0.3	0.8	0.2	2.5
	core	0.1 ± 0.0	34.7 ± 3.7	0.3 ± 0.2	0.1 ± 0.1	1.7 ± 2.2	61.9 ± 0.6	0.0	0.0	1.8
5	-	18.3 ± 1.0	22.1 ± 0.3	4.4 ± 0.7	0.1 ± 0.1	0.5 ± 0.4	54.1 ± 0.5	0.8	0.2	2.5

Table B-20: Composition of the different zones (shell, U-rich layer, Mo-rich layer, core) of 5 oxide precipitates analyzed in the SIMFuel samples annealed at 900°C under oxidizing conditions

N°	Zone	Element composition (at.%)						Ba/Zr	Sr/Zr	O/Zr
		Ba	Zr	Sr	Mo	U	O			
1	shell	16.6 ± 0.9	21.2 ± 0.7	4.6 ± 0.5	0.3 ± 0.4	1.4 ± 1.0	55.3 ± 0.5	0.8	0.2	2.6
	U	3.6 ± 0.6	24.3 ± 0.1	1.4 ± 0.2	0.0 ± 0.0	7.3 ± 0.2	61.1 ± 1.1	0.2	0.1	2.5
	core	0.5 ± 0.3	34.4 ± 1.2	0.4 ± 0.1	0.0 ± 0.0	2.0 ± 0.6	62.0 ± 0.7	0.0	0.0	1.8
2	-	16.8 ± 0.5	20.6 ± 0.5	4.5 ± 0.3	0.0 ± 0.2	1.0 ± 0.3	56.5 ± 0.4	0.8	0.2	2.7
3	-	18.5 ± 0.3	21.8 ± 0.3	3.7 ± 0.3	0.0 ± 0.0	0.5 ± 0.4	54.8 ± 0.1	0.9	0.2	2.5
4	shell	17.5 ± 0.8	22.3 ± 0.5	5.1 ± 0.5	0.0 ± 0.0	0.5 ± 0.1	54.3 ± 0.7	0.8	0.2	2.4
	Mo	8.0 ± 0.3	18.4 ± 1.4	2.2 ± 0.0	8.0 ± 0.3	1.6 ± 0.4	61.0 ± 1.6	0.4	0.1	3.3
5	shell	19.1 ± 0.9	22.1 ± 0.1	3.3 ± 0.7	0.0 ± 0.0	0.2 ± 0.1	54.6 ± 0.2	0.9	0.2	2.5
	Mo	8.1 ± 1.1	21.1 ± 1.3	1.4 ± 0.4	8.4 ± 1.4	0.4 ± 0.2	60.0 ± 1.9	0.4	0.1	2.8
	U	0.6 ± 0.4	17.7 ± 1.8	0.6 ± 0.3	0.0 ± 0.0	3.5 ± 0.3	60.6 ± 0.6	0.0	0.0	3.4

Table B-21: Composition of the different zones (shell, Mo-rich layer, core) of 5 oxide precipitates analyzed in the SIMFuel samples annealed at 1000°C under oxidizing conditions

N°	Zone	Element composition (at.%)						Ba/Zr	Sr/Zr	O/Zr
		Ba	Zr	Sr	Mo	U	O			
1	shell	18.1 ± 0.5	22.1 ± 0.5	3.9 ± 0.3	0.0 ± 0.2	0.2 ± 0.2	55.3 ± 0.3	0.8	0.2	2.5
	Mo	10.6 ± 0.4	17.8 ± 0.5	1.8 ± 0.2	11.8 ± 0.4	0.6 ± 0.3	56.5 ± 0.3	0.6	0.1	3.2
	core	0.5 ± 0.7	32.3 ± 5.1	0.4 ± 0.3	0.0 ± 0.0	1.5 ± 1.7	62.9 ± 1.8	0.0	0.0	1.9
2	shell	17.5 ± 1.8	23.0 ± 2.3	3.7 ± 0.3	0.1 ± 0.2	0.4 ± 0.2	54.7 ± 0.6	0.8	0.2	2.4
	Mo	10.8 ± 0.4	18.2 ± 0.4	2.1 ± 0.2	4.8 ± 0.3	4.3 ± 0.3	59.0 ± 0.4	0.6	0.1	3.2
3	shell	15.3 ± 0.5	20.2 ± 0.5	4.0 ± 0.3	0.9 ± 0.3	2.1 ± 0.3	56.9 ± 0.4	0.8	0.2	2.8
	Mo	8.1 ± 0.4	18.6 ± 1.2	1.8 ± 0.2	8.1 ± 0.8	2.2 ± 0.8	60.7 ± 1.7	0.4	0.1	3.3
4	shell	19.0 ± 0.5	22.1 ± 0.5	3.6 ± 0.3	0.0 ± 0.2	0.3 ± 0.2	55.0 ± 0.3	0.9	0.2	2.5
	Mo	6.8 ± 1.5	14.8 ± 1.6	1.6 ± 0.3	7.2 ± 2.0	5.3 ± 1.6	63.4 ± 4.5	0.6	0.1	4.3
5	shell	18.3 ± 0.4	21.9 ± 0.4	3.9 ± 0.6	0.0 ± 0.0	0.3 ± 0.1	54.9 ± 0.5	0.8	0.2	2.5
	Mo	6.6 ± 0.3	20.9 ± 0.4	1.6 ± 0.1	7.8 ± 0.3	1.2 ± 0.4	61.5 ± 0.8	0.3	0.1	2.9
	core	3.3 ± 2.2	32.8 ± 1.6	0.8 ± 0.4	0.1 ± 0.1	1.5 ± 0.2	61.1 ± 1.2	0.1	0.0	1.9

Appendix 2.4: EDX analyses performed on the samples treated in reducing conditions

Table B-22: Composition of the Pd-Rh metallic precipitates analyzed in the SIMFuel samples annealed at 400°C under reducing conditions

N°	Element composition (at.%)						(Rh+Pd)/U	Rh/Pd
	Mo	Ru	Rh	Pd	U	O		
1	0.3 ± 0.2	0.5 ± 0.2	0.3 ± 0.3	80.0 ± 0.7	10.7 ± 0.4	7.6 ± 0.3	-	-
2	0.0 ± 0.1	0.7 ± 0.0	17.5 ± 0.2	55.4 ± 1.2	17.3 ± 1.0	7.8 ± 0.6	4.2	0.3
3	0.0 ± 0.0	0.4 ± 0.2	17.7 ± 1.2	53.8 ± 2.9	18.1 ± 0.4	9.1 ± 1.7	3.9	0.3
4	0.2 ± 0.2	0.3 ± 0.1	32.0 ± 0.2	36.4 ± 1.6	21.5 ± 0.9	8.2 ± 2.4	3.2	0.9
5	0.2 ± 0.2	0.5 ± 0.3	37.8 ± 0.4	28.9 ± 0.4	21.7 ± 0.5	9.7 ± 0.4	3.1	1.3

Table B-23: Composition of the Pd-Rh metallic precipitates analyzed in the SIMFuel samples annealed at 700°C under reducing conditions

N°	Element composition (at.%)						(Rh+Pd)/U	Rh/Pd
	Mo	Ru	Rh	Pd	U	O		
1	0.0 ± 0.2	0.4 ± 0.3	5.9 ± 0.3	84.3 ± 0.7	3.3 ± 0.4	6.0 ± 0.4	-	0.1
2	0.0 ± 0.2	0.6 ± 0.2	10.9 ± 0.3	76.6 ± 0.6	5.2 ± 0.4	6.5 ± 0.4	-	0.1
	0.1 ± 0.2	0.9 ± 0.3	68.7 ± 0.8	19.6 ± 0.5	0.7 ± 0.4	9.4 ± 0.4	-	3.5
3	0.2 ± 0.2	0.7 ± 0.2	14.8 ± 0.4	73.4 ± 0.8	3.1 ± 0.4	7.1 ± 0.4	-	0.2
4	0.2 ± 0.2	0.2 ± 0.2	6.0 ± 0.3	80.9 ± 0.7	3.5 ± 0.4	8.9 ± 0.4	-	0.1
5	0.2 ± 0.2	0.6 ± 0.3	32.9 ± 0.5	12.3 ± 0.4	16.1 ± 0.5	37.2 ± 0.4	2.8	2.7

Table B-24: Composition of the Pd-Rh metallic precipitates analyzed in the SIMFuel samples annealed at 900°C under reducing conditions

N°	Element composition (at.%)						(Rh+Pd)/U	Rh/Pd
	Mo	Ru	Rh	Pd	U	O		
1	0.2 ± 0.1	0.5 ± 0.0	0.4 ± 0.1	86.8 ± 1.8	4.4 ± 0.8	7.1 ± 2.6	-	-
2	0.1 ± 0.0	0.4 ± 0.2	10.9 ± 0.7	80.1 ± 0.5	2.6 ± 0.0	5.9 ± 0.2	-	0.1
3	0.1 ± 0.2	0.4 ± 0.3	25.6 ± 0.4	66.2 ± 0.6	0.8 ± 0.4	6.9 ± 0.4	-	0.4
4	5.7 ± 0.2	4.7 ± 0.3	54.5 ± 0.6	27.3 ± 0.6	1.0 ± 0.4	6.1 ± 0.4	-	2.0
5	0.4 ± 0.2	1.0 ± 0.3	35.0 ± 0.5	16.5 ± 0.4	15.5 ± 0.5	30.9 ± 0.4	3.3	2.1

Table B-25: Composition of the Pd-Rh metallic precipitates analyzed in the SIMFuel samples annealed at 1000°C under reducing conditions

N°	Element composition (at.%)						(Rh+Pd)/U	Rh/Pd
	Mo	Ru	Rh	Pd	U	O		
1	0.7 ± 0.3	0.9 ± 0.2	0.4 ± 0.3	87.8 ± 1.0	3.3 ± 0.2	6.1 ± 1.0	-	-
2	0.3 ± 0.2	1.0 ± 0.3	7.9 ± 0.3	82.0 ± 1.2	3.3 ± 0.3	5.2 ± 0.8	-	0.1
3	0.3 ± 0.2	1.0 ± 0.3	16.7 ± 0.4	74.5 ± 0.7	2.5 ± 0.4	5.0 ± 0.4	-	0.2
4	0.2 ± 0.0	1.2 ± 0.1	27.2 ± 0.3	63.6 ± 0.5	2.7 ± 1.0	4.8 ± 1.0	-	0.4
5	3.7 ± 0.7	1.4 ± 0.1	61.8 ± 0.4	27.5 ± 1.5	0.7 ± 0.2	4.7 ± 1.3	-	2.2

Table B-26: Composition of the Pd-Rh metallic precipitates analyzed in the SIMFuel samples annealed at 1700°C under reducing conditions

N°	Element composition (at.%)						(Rh+Pd)/U	Rh/Pd
	Mo	Ru	Rh	Pd	U	O		
1	0.4 ± 0.3	0.8 ± 0.2	11.9 ± 2.2	66.5 ± 3.7	4.4 ± 1.1	15.7 ± 2.3	-	0.2
	5.1 ± 0.7	6.7 ± 1.5	51.4 ± 1.7	23.1 ± 0.1	0.7 ± 1.5	12.7 ± 0.1	-	2.2
2	3.9 ± 0.2	2.9 ± 0.3	61.7 ± 1.6	23.1 ± 0.4	0.7 ± 0.1	7.5 ± 1.8	-	2.7
	1.0 ± 0.2	7.5 ± 3.7	3.2 ± 0.2	1.5 ± 0.2	32.6 ± 2.1	54.0 ± 1.7	-	-
3	1.0 ± 1.0	0.8 ± 0.3	11.3 ± 5.7	71.8 ± 4.7	4.3 ± 2.9	10.5 ± 2.3	-	0.2
	7.3 ± 0.4	6.7 ± 1.0	50.0 ± 0.9	25.4 ± 2.0	0.5 ± 0.1	9.8 ± 1.6	-	2.0

Table B-27: Composition of 10 Mo-Ru-Rh-Pd metallic precipitates analyzed in the SIMFuel samples annealed at 400°C under reducing conditions

N°	Element composition (at.%)						Ru/Mo
	Mo	Ru	Rh	Pd	U	O	
1	4.1 ± 0.3	85.2 ± 0.8	0.0 ± 0.5	1.7 ± 0.4	0.4 ± 0.3	8.0 ± 0.4	20.8
2	32.0 ± 0.4	31.8 ± 0.5	0.0 ± 0.5	28.0 ± 0.4	0.9 ± 0.3	7.2 ± 0.3	1.0
3	18.1 ± 0.4	16.9 ± 0.4	43.0 ± 0.6	11.5 ± 0.5	3.5 ± 0.4	6.5 ± 0.4	0.9
4	37.5 ± 0.4	31.2 ± 0.5	0.0 ± 0.5	24.1 ± 0.4	0.6 ± 0.3	6.5 ± 0.4	0.8
5	41.0 ± 0.5	31.0 ± 0.5	0.0 ± 0.4	22.1 ± 0.4	1.0 ± 0.3	4.3 ± 0.4	0.8
6	43.4 ± 0.5	24.7 ± 0.4	0.0 ± 0.4	25.8 ± 0.4	0.8 ± 0.3	5.1 ± 0.3	0.6
7	41.0 ± 0.5	23.0 ± 0.4	1.0 ± 0.4	23.7 ± 0.4	2.4 ± 0.4	8.9 ± 0.4	0.6
8	40.4 ± 0.5	20.2 ± 0.4	0.0 ± 0.4	27.3 ± 0.4	4.5 ± 0.4	6.7 ± 0.3	0.5
9	41.4 ± 0.5	23.4 ± 0.4	0.0 ± 0.4	26.4 ± 0.4	0.7 ± 0.3	7.4 ± 0.3	0.6
10	79.8 ± 0.8	7.8 ± 0.5	0.0 ± 0.3	3.4 ± 0.3	0.4 ± 0.3	8.3 ± 0.4	0.1

Table B-28: Composition of 10 Mo-Ru-Rh-Pd metallic precipitates analyzed in the SIMFuel samples annealed at 700°C under reducing conditions

N°	Element composition (at.%)						Ru/Mo
	Mo	Ru	Rh	Pd	U	O	
1	1.7 ± 0.2	50.1 ± 0.5	0.0 ± 0.5	39.2 ± 0.5	2.1 ± 0.4	6.8 ± 0.4	29.5
2	4.5 ± 0.3	87.3 ± 0.7	0.0 ± 0.5	1.9 ± 0.4	0.7 ± 0.3	5.6 ± 0.4	19.4
3	12.6 ± 0.3	73.9 ± 0.6	0.0 ± 0.5	3.0 ± 0.4	3.9 ± 0.4	6.3 ± 0.4	5.9
4	0.4 ± 0.2	0.9 ± 0.2	1.9 ± 0.3	90.4 ± 0.8	1.2 ± 0.4	4.4 ± 0.4	2.3
5	23.7 ± 0.4	50.9 ± 0.7	15.8 ± 0.5	3.8 ± 0.4	0.6 ± 0.3	5.1 ± 0.4	2.1
6	0.3 ± 0.2	0.4 ± 0.2	6.0 ± 0.3	85.2 ± 0.8	1.0 ± 0.4	6.8 ± 0.4	1.3
7	33.5 ± 0.5	20.3 ± 0.5	35.5 ± 0.5	4.5 ± 0.5	0.6 ± 0.3	5.5 ± 0.4	0.6
8	26.2 ± 0.4	15.6 ± 0.4	49.2 ± 0.6	3.4 ± 0.5	0.6 ± 0.4	4.5 ± 0.4	0.6
9	23.1 ± 0.4	10.7 ± 0.4	53.1 ± 0.6	4.1 ± 0.5	1.0 ± 0.4	7.9 ± 0.4	0.5
10	27.9 ± 0.4	10.5 ± 0.4	53.8 ± 0.7	3.8 ± 0.5	0.8 ± 0.4	2.4 ± 0.4	0.4

Table B-29: Composition of 10 Mo-Ru-Rh-Pd metallic precipitates analyzed in the SIMFuel samples annealed at 900°C under reducing conditions

N°	Element composition (at.%)						Ru/Mo
	Mo	Ru	Rh	Pd	U	O	
1	4.5 ± 0.3	86.2 ± 0.8	0.0 ± 0.5	2.2 ± 0.4	0.9 ± 0.3	5.5 ± 0.4	19.2
2	6.0 ± 0.3	81.8 ± 0.8	0.0 ± 0.5	1.7 ± 0.4	2.4 ± 0.4	7.5 ± 0.4	13.6
3	11.9 ± 0.3	78.3 ± 0.7	0.0 ± 0.5	2.8 ± 0.4	0.9 ± 0.3	5.9 ± 0.4	6.6
4	14.1 ± 0.3	17.2 ± 0.4	48.0 ± 0.6	13.6 ± 0.5	1.0 ± 0.4	5.7 ± 0.4	1.2
5	38.5 ± 0.5	29.6 ± 0.5	0.0 ± 0.4	22.1 ± 0.4	1.6 ± 0.4	8.0 ± 0.3	0.8
6	41.4 ± 0.5	29.7 ± 0.5	0.0 ± 0.4	19.6 ± 0.4	1.6 ± 0.4	7.5 ± 0.4	0.7
7	23.4 ± 0.4	16.0 ± 0.4	47.9 ± 0.6	4.0 ± 0.5	0.9 ± 0.4	7.5 ± 0.4	0.7
8	41.2 ± 0.5	22.5 ± 0.5	0.0 ± 0.5	26.3 ± 0.4	0.8 ± 0.3	8.8 ± 0.4	0.5
9	72.9 ± 0.6	10.2 ± 0.4	0.0 ± 0.3	3.3 ± 0.3	4.3 ± 0.4	8.7 ± 0.4	0.1
10	74.5 ± 0.7	12.2 ± 0.5	0.0 ± 0.4	3.5 ± 0.3	2.8 ± 0.4	6.6 ± 0.4	0.2

Table B-30: Composition of 10 Mo-Ru-Rh-Pd metallic precipitates analyzed in the SIMFuel samples annealed at 1000°C under reducing conditions

N°	Element composition (at.%)						Ru/Mo
	Mo	Ru	Rh	Pd	U	O	
1	3.8 ± 0.3	86.1 ± 0.7	0.0 ± 0.5	5.0 ± 0.4	2.0 ± 0.3	2.9 ± 0.3	22.7
2	5.0 ± 0.3	80.8 ± 0.8	0.0 ± 0.5	5.7 ± 0.4	1.2 ± 0.3	6.8 ± 0.4	16.2
3	5.3 ± 0.3	83.7 ± 0.7	0.0 ± 0.5	2.4 ± 0.4	1.0 ± 0.3	7.0 ± 0.4	15.8
4	5.8 ± 0.3	82.7 ± 0.7	0.0 ± 0.5	3.1 ± 0.4	1.00 ± 0.3	7.2 ± 0.4	14.3
5	6.2 ± 0.3	87.1 ± 0.8	0.0 ± 0.5	1.9 ± 0.4	0.4 ± 0.3	4.1 ± 0.4	14.0
6	6.9 ± 0.3	85.4 ± 0.7	0.0 ± 0.5	2.3 ± 0.4	1.3 ± 0.3	3.6 ± 0.4	12.4
7	6.7 ± 0.3	83.0 ± 0.7	0.0 ± 0.5	1.6 ± 0.4	0.6 ± 0.3	8.0 ± 0.4	12.4
8	7.0 ± 0.3	81.6 ± 0.8	0.0 ± 0.5	2.0 ± 0.4	1.6 ± 0.3	7.4 ± 0.4	11.7
9	10.6 ± 0.3	71.9 ± 0.7	11.0 ± 0.5	1.2 ± 0.5	0.6 ± 0.3	4.8 ± 0.4	6.8
10	33.8 ± 0.4	51.8 ± 0.5	0.0 ± 0.5	9.0 ± 0.4	0.6 ± 0.3	4.5 ± 0.3	1.5

Table B-31: Composition of 10 Mo-Ru-Rh-Pd metallic precipitates analyzed in the SIMFuel samples annealed at 1700°C under reducing conditions

N°	Element composition (at.%)						Ru/Mo
	Mo	Ru	Rh	Pd	U	O	
1	9.4 ± 0.3	82.6 ± 0.7	0.0 ± 0.5	4.8 ± 0.40	1.0 ± 0.3	2.1 ± 0.4	8.8
2	9.6 ± 0.3	78.3 ± 0.7	0.0 ± 0.5	5.4 ± 0.40	1.0 ± 0.3	5.4 ± 0.4	8.2
3	23.2 ± 0.4	54.8 ± 0.6	0.0 ± 0.5	12.1 ± 0.40	0.8 ± 0.3	8.8 ± 0.4	2.4
4	24.0 ± 0.4	53.2 ± 0.5	0.0 ± 0.5	13.5 ± 0.40	0.6 ± 0.3	8.5 ± 0.4	2.2
5	24.9 ± 0.4	53.3 ± 0.6	0.0 ± 0.5	14.3 ± 0.40	0.6 ± 0.3	6.4 ± 0.4	2.1
6	25.2 ± 0.4	46.3 ± 0.6	0.0 ± 0.5	17.2 ± 0.40	0.8 ± 0.3	9.7 ± 0.4	1.8
7	28.0 ± 0.4	42.8 ± 0.5	0.0 ± 0.5	20.6 ± 0.40	0.5 ± 0.3	7.6 ± 0.4	1.5
8	21.4 ± 0.4	33.6 ± 0.5	20.4 ± 0.5	13.5 ± 0.50	1.6 ± 0.4	9.1 ± 0.4	1.6
9	23.9 ± 0.4	30.9 ± 0.5	19.6 ± 0.5	16.8 ± 0.50	0.9 ± 0.3	7.6 ± 0.4	1.3
10	49.8 ± 0.6	6.6 ± 0.4	0.0 ± 0.4	33.3 ± 0.50	0.4 ± 0.4	9.5 ± 0.4	0.1

Table B-32: Composition of the pure Mo metallic precipitates analyzed in the SIMFuel samples annealed at 400°C under reducing conditions

N°	Element composition (at.%)					
	Mo	Ru	Rh	Pd	U	O
1	90.5 ± 0.1	0.0 ± 0.0	0.0 ± 0.0	2.1 ± 0.6	6.9 ± 0.5	0.0 ± 0.0
2	92.0 ± 0.6	0.0 ± 0.5	0.0 ± 0.3	1.6 ± 0.3	0.2 ± 0.3	6.1 ± 0.4
3	89.1 ± 0.2	0.6 ± 0.4	0.0 ± 0.0	2.3 ± 0.4	0.1 ± 0.1	7.6 ± 0.3
4	86.2 ± 0.9	2.3 ± 0.5	0.0 ± 0.3	1.8 ± 0.3	0.4 ± 0.3	8.8 ± 0.4
5	85.7 ± 0.9	0.6 ± 0.5	0.0 ± 0.3	1.9 ± 0.2	0.1 ± 0.3	11.0 ± 0.4

Table B-33: Composition of the pure Mo metallic precipitates analyzed in the SIMFuel samples annealed at 700°C under reducing conditions

N°	Element composition (at.%)					
	Mo	Ru	Rh	Pd	U	O
1	90.1 ± 0.4	0.2 ± 0.2	0.3 ± 0.1	1.9 ± 0.0	0.1 ± 0.1	7.2 ± 0.5
2	89.9 ± 0.8	0.4 ± 0.5	0.0 ± 0.3	1.2 ± 0.2	0.2 ± 0.3	7.9 ± 0.4
3	88.3 ± 0.9	0.8 ± 0.5	0.1 ± 0.3	1.3 ± 0.2	0.2 ± 0.3	8.4 ± 0.4
4	89.5 ± 1.6	0.2 ± 0.3	0.0 ± 0.0	0.8 ± 0.1	0.3 ± 0.0	8.8 ± 1.5
5	88.3 ± 0.3	0.5 ± 0.0	0.0 ± 0.0	1.9 ± 0.3	0.3 ± 0.0	8.8 ± 0.3

Table B-34: Composition of the pure Mo metallic precipitates analyzed in the SIMFuel samples annealed at 900°C under reducing conditions

N°	Element composition (at.%)					
	Mo	Ru	Rh	Pd	U	O
1	87.4 ± 0.3	2.4 ± 0.1	1.5 ± 0.2	2.6 ± 0.2	0.4 ± 0.3	5.5 ± 0.3
2	91.7 ± 1.2	0.2 ± 0.1	0.0 ± 0.0	1.7 ± 0.5	0.2 ± 0.0	5.7 ± 1.0
3	88.9 ± 1.8	0.9 ± 0.4	0.0 ± 0.0	1.8 ± 0.2	0.3 ± 0.0	6.9 ± 0.9
4	89.3 ± 0.9	0.1 ± 0.1	0.0 ± 0.0	1.9 ± 0.5	0.2 ± 0.1	8.2 ± 1.4
5	87.9 ± 0.3	0.4 ± 0.1	0.0 ± 0.0	1.5 ± 0.2	1.1 ± 1.2	8.7 ± 1.4

Table B-35: Composition of the pure Mo metallic precipitates analyzed in the SIMFuel samples annealed at 1000°C under reducing conditions

N°	Element composition (at.%)					
	Mo	Ru	Rh	Pd	U	O
1	91.8 ± 2.0	0.4 ± 0.5	0.0 ± 0.0	1.2 ± 0.3	0.2 ± 0.2	6.1 ± 2.0
2	88.5 ± 1.3	0.4 ± 0.0	0.1 ± 0.0	2.1 ± 0.1	0.2 ± 0.0	8.0 ± 1.0
3	88.1 ± 2.2	0.3 ± 0.1	0.2 ± 0.1	2.3 ± 0.4	0.1 ± 0.0	8.9 ± 2.8
4	87.7 ± 2.3	0.5 ± 0.1	0.1 ± 0.1	1.6 ± 0.1	0.2 ± 0.0	9.8 ± 2.0
5	86.9 ± 1.7	0.5 ± 0.5	0.0 ± 0.0	1.5 ± 0.3	0.2 ± 0.1	10.6 ± 2.2

Table B-36: Composition of the pure Mo metallic precipitates analyzed in the SIMFuel samples annealed at 1700°C under reducing conditions

N°	Element composition (at.%)					
	Mo	Ru	Rh	Pd	U	O
1	86.3 ± 0.8	1.8 ± 0.5	0.0 ± 0.3	4.5 ± 0.3	0.1 ± 0.3	6.7 ± 0.4
2	81.8 ± 0.8	4.1 ± 0.5	0.0 ± 0.3	5.4 ± 0.3	0.5 ± 0.3	7.8 ± 0.4
3	85.6 ± 1.4	0.6 ± 0.2	0.0 ± 0.0	5.5 ± 0.1	0.2 ± 0.0	7.9 ± 1.4
4	83.7 ± 0.9	2.7 ± 0.5	0.2 ± 0.3	4.4 ± 0.3	0.3 ± 0.3	8.4 ± 0.4
5	83.5 ± 0.7	2.7 ± 0.5	0.0 ± 0.3	4.7 ± 0.3	0.6 ± 0.3	8.4 ± 0.4

Table B-37: Composition of the different zones (shell, core) of 5 oxide precipitates analyzed in the SIMFuel samples annealed at 400°C under reducing conditions

N°	Zone	Element composition (at.%)						Ba/Zr	Sr/Zr	O/Zr
		Ba	Zr	Sr	Ce	U	O			
1	shell	16.7 ± 0.3	20.5 ± 1.6	4.4 ± 0.6	0.1 ± 0.0	2.5 ± 1.8	55.3 ± 0.8	0.8	0.2	2.7
	core	0.2 ± 0.1	33.8 ± 1.6	0.3 ± 0.1	0.1 ± 0.1	2.4 ± 1.3	62.5 ± 0.3	0.0	0.0	1.9
2	shell	17.0 ± 1.0	22.4 ± 1.2	3.0 ± 1.5	0.2 ± 0.0	0.5 ± 0.4	56.5 ± 1.9	0.8	0.1	2.5
	core	0.1 ± 0.1	35.6 ± 0.2	0.3 ± 0.1	0.0 ± 0.0	0.2 ± 0.1	63.3 ± 0.2	0.0	0.0	1.8
3	shell	17.6 ± 0.7	22.2 ± 0.3	4.2 ± 0.8	0.1 ± 0.1	0.3 ± 0.1	55.3 ± 0.3	0.8	0.2	2.5
	core	0.0 ± 0.1	35.1 ± 0.1	0.3 ± 0.0	0.1 ± 0.1	0.8 ± 0.1	63.1 ± 0.6	0.0	0.0	1.8
4	shell	17.6 ± 1.1	22.1 ± 0.1	3.8 ± 0.5	0.1 ± 0.1	0.3 ± 0.0	55.9 ± 0.7	0.8	0.2	2.5
	core	0.1 ± 0.0	32.9 ± 3.7	0.3 ± 0.1	0.1 ± 0.1	1.6 ± 1.7	62.9 ± 1.1	0.0	0.0	1.9
5	shell	18.1 ± 1.2	22.2 ± 0.2	3.7 ± 0.5	0.3 ± 0.2	0.3 ± 0.1	55.2 ± 0.8	0.8	0.2	2.5
	core	0.6 ± 0.6	34.7 ± 0.1	0.2 ± 0.0	0.0 ± 0.0	0.8 ± 0.4	64.0 ± 0.2	0.0	0.0	1.9

Table B-38: Composition of the different zones (shell, core) of 5 oxide precipitates analyzed in the SIMFuel samples annealed at 700°C under reducing conditions

N°	Zone	Element composition (at.%)						Ba/Zr	Sr/Zr	O/Zr
		Ba	Zr	Sr	Ce	U	O			
1	shell	16.0 ± 0.3	19.9 ± 0.4	4.6 ± 0.2	0.1 ± 0.0	3.4 ± 0.3	55.1 ± 0.4	0.8	0.2	2.8
	core	0.3 ± 0.3	32.9 ± 4.2	0.5 ± 0.3	0.3 ± 0.3	1.8 ± 1.5	61.2 ± 1.4	0.0	0.0	1.9
2	shell	16.8 ± 0.6	22.0 ± 0.1	5.1 ± 0.2	0.1 ± 0.0	0.1 ± 0.4	54.4 ± 0.0	0.8	0.2	2.5
	core	0.8 ± 0.9	35.7 ± 0.0	0.4 ± 0.2	0.1 ± 0.1	1.3 ± 0.1	61.5 ± 1.4	0.0	0.0	1.7
3	shell	17.9 ± 1.6	20.9 ± 1.7	3.7 ± 1.0	0.1 ± 0.2	2.0 ± 1.3	54.9 ± 0.4	0.9	0.2	2.6
	core	0.1 ± 0.0	36.5 ± 0.5	0.2 ± 0.0	0.0 ± 0.0	0.6 ± 0.6	62.3 ± 0.1	0.0	0.0	1.7
4	shell	18.5 ± 0.3	21.6 ± 0.3	3.4 ± 0.0	0.1 ± 0.1	0.6 ± 0.2	55.5 ± 0.5	0.9	0.2	2.6
	core	4.8 ± 0.3	31.8 ± 0.6	0.9 ± 0.2	0.0 ± 0.3	2.4 ± 0.3	59.4 ± 0.4	0.2	0.0	1.9
5	-	17.4 ± 1.7	21.8 ± 0.7	3.9 ± 0.4	0.2 ± 0.2	1.3 ± 0.4	55.0 ± 1.1	0.8	0.2	2.5

Table B-39: Composition of the different zones (shell, core) of 5 oxide precipitates analyzed in the SIMFuel samples annealed at 900°C under reducing conditions

N°	Zone	Element composition (at.%)						Ba/Zr	Sr/Zr	O/Zr
		Ba	Zr	Sr	Ce	U	O			
1	-	18.1 ± 1.5	23.0 ± 1.1	4.0 ± 0.4	0.1 ± 0.1	0.4 ± 0.1	53.9 ± 0.7	0.8	0.2	2.3
2	shell	19.1 ± 0.4	22.8 ± 0.5	4.6 ± 0.3	0.1 ± 0.4	0.4 ± 0.2	53.1 ± 0.3	0.8	0.2	2.3
	core	0.3 ± 0.2	35.6 ± 0.7	0.4 ± 0.2	0.1 ± 0.2	1.9 ± 0.3	61.2 ± 0.5	0.0	0.0	1.7
3	shell	19.5 ± 0.5	22.5 ± 0.5	3.7 ± 0.6	0.2 ± 0.1	0.4 ± 0.4	53.5 ± 0.4	0.9	0.2	2.4
	core	0.1 ± 0.1	36.9 ± 0.3	0.3 ± 0.1	0.1 ± 0.1	0.3 ± 0.3	61.9 ± 0.4	0.0	0.0	1.7
4	shell	18.5 ± 0.5	22.3 ± 0.5	4.4 ± 0.3	0.2 ± 0.3	0.2 ± 0.2	54.3 ± 0.3	0.8	0.2	2.4
	core	0.3 ± 0.1	36.0 ± 0.3	0.3 ± 0.0	0.1 ± 0.0	1.1 ± 0.3	61.6 ± 0.2	0.0	0.0	1.7
5	shell	17.6 ± 0.4	23.0 ± 0.9	3.7 ± 0.1	0.1 ± 0.0	0.6 ± 0.3	54.4 ± 0.4	0.8	0.2	2.4
	core	0.4 ± 0.4	35.7 ± 1.4	0.2 ± 0.0	0.0 ± 0.0	0.6 ± 0.5	62.9 ± 0.8	0.0	0.0	1.8

Table B-40: Composition of the different zones (shell, core) of 5 oxide precipitates analyzed in the SIMFuel samples annealed at 1000°C under reducing conditions

N°	Zone	Element composition (at.%)						Ba/Zr	Sr/Zr	O/Zr
		Ba	Zr	Sr	Ce	U	O			
1	shell	16.8 ± 0.8	24.2 ± 2.8	4.0 ± 0.3	0.2 ± 0.1	1.0 ± 0.9	53.4 ± 1.2	0.7	0.2	2.2
	core	0.0 ± 0.0	35.9 ± 0.4	0.2 ±0.0	0.1 ± 0.1	1.1 ± 0.4	62.3 ± 0.2	0.0	0.0	1.7
2	shell	19.0 ± 1.2	22.1 ± 0.2	3.6 ± 1.0	0.1 ± 0.1	0.3 ± 0.2	54.5 ± 0.1	0.9	0.2	2.5
	core	0.0 ± 0.0	36.1 ± 0.7	0.2 ± 0.0	0.1 ± 0.1	0.6 ± 0.3	62.7 ± 0.7	0.0	0.0	1.7
3	shell	18.1 ± 0.2	22.0 ± 0.1	4.0 ± 0.1	0.2 ± 0.1	0.4 ± 0.0	55.1 ± 0.4	0.8	0.2	2.5
	core	0.1 ± 0.1	35.0 ± 0.6	0.3 ± 0.1	0.0 ± 0.0	1.7 ± 0.7	62.4 ± 0.2	0.0	0.0	1.8
4	shell	18.3 ± 0.0	22.4 ± 0.2	4.4 ± 0.0	0.1 ± 0.1	0.4 ± 0.2	54.0 ± 0.6	0.8	0.2	2.4
	core	0.0 ± 0.0	34.9 ± 0.6	0.2 ± 0.1	0.0 ± 0.0	0.2 ± 0.2	64.5 ± 0.4	0.0	0.0	1.9
5	-	19.4 ± 0.8	21.9 ± 0.4	3.0 ± 0.8	0.1 ± 0.1	0.3 ± 0.0	55.2 ± 0.7	0.9	0.1	2.5

Table B-41: Composition of the different zones (shell, U-rich layer, core) of 5 oxide precipitates analyzed in the SIMFuel samples annealed at 1700°C under reducing conditions

N°	Zone	Element composition (at.%)						Ba/Zr	Sr/Zr	O/Zr
		Ba	Zr	Sr	Ce	U	O			
1	-	16.7 ± 0.1	20.0 ± 0.2	1.7 ± 0.2	0.1 ± 0.1	1.6 ± 0.1	56.7 ± 0.2	0.8	0.1	2.8
2	shell	20.9 ± 0.4	21.0 ± 0.3	2.1 ± 0.3	0.1 ± 0.1	0.8 ± 0.1	55.1 ± 0.3	1.0	0.1	2.6
	core	0.2 ± 0.3	32.8 ± 0.7	0.2 ± 0.1	0.0 ± 0.0	3.3 ± 0.0	63.2 ± 0.6	0.0	0.0	1.9
3	-	19.9 ± 0.3	20.8 ± 0.5	2.1 ± 0.3	0.1 ± 0.1	1.6 ± 0.6	55.1 ± 0.6	1.0	0.1	2.7
4	shell	31.3 ± 0.3	21.0 ± 0.3	1.6 ± 0.3	0.1 ± 0.2	0.9 ± 0.2	54.8 ± 0.2	1.5	0.1	2.6
	U	1.5 ± 0.3	21.0 ± 0.5	0.6 ± 0.2	0.2 ± 0.3	12.8 ± 0.5	63.2 ± 0.4	0.1	0.0	3.0
	core	0.1 ± 0.1	32.5 ± 0.5	0.2 ± 0.0	0.0 ± 0.0	4.1 ± 0.4	62.4 ± 0.4	0.0	0.0	1.9
5	-	20.0 ± 0.7	21.1 ± 0.1	2.3 ± 0.6	0.1 ± 0.1	0.8 ± 0.2	55.5 ± 0.5	1.0	0.1	2.6

Appendix 2.5: XAS linear combination fitting performed on the T_0 sample

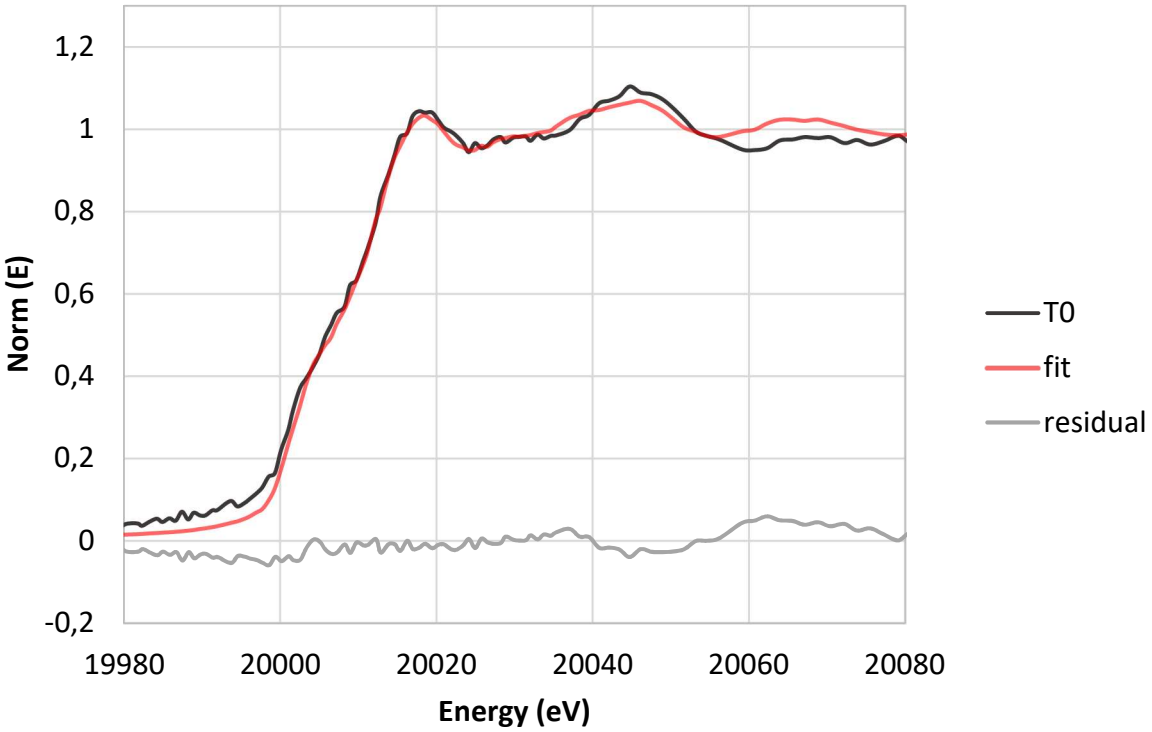

Figure B-1:Result of the linear combination fitting performed on the experimental XANES spectrum of the T_0 sample using the experimental XANES spectrum of metallic Mo (bcc) and calculated XANES spectrum of metallic Mo (hcp)

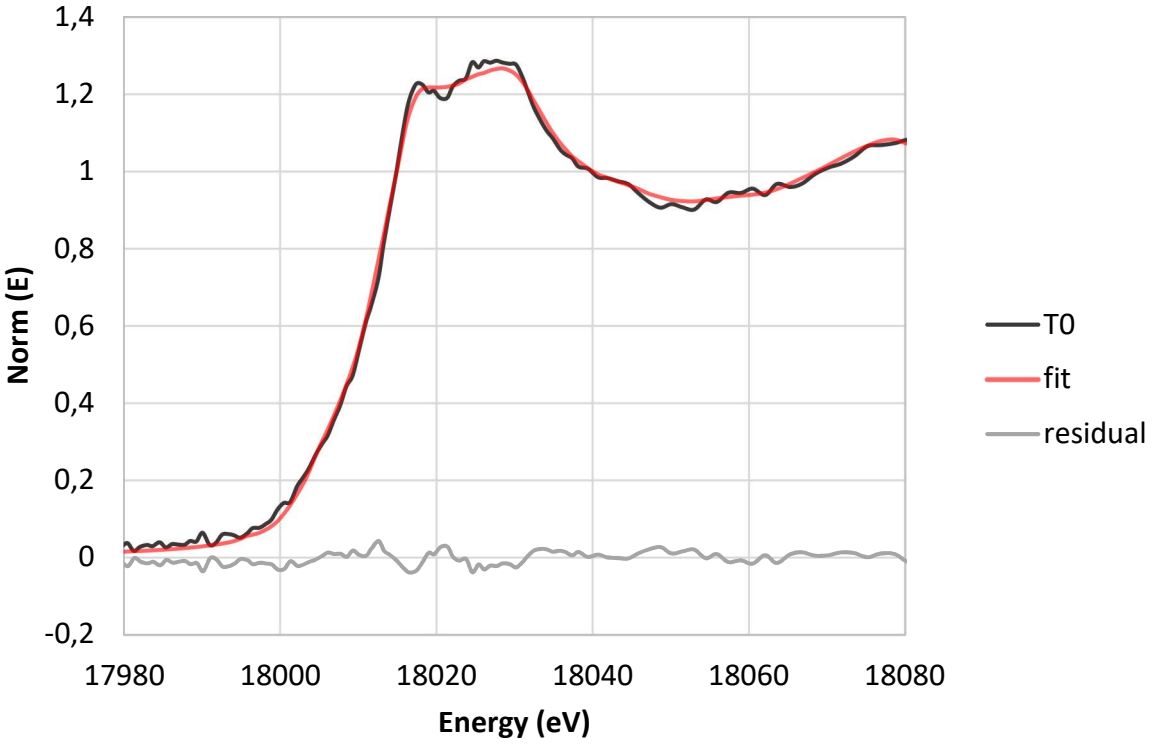

Figure B-2: Result of the linear combination fitting performed on the experimental XANES spectrum of the T_0 sample using the experimental XANES spectrum of m-ZrO_2, $BaZrO_3$ and calculated XANES spectrum of c-ZrO_2 and $SrZrO_3$

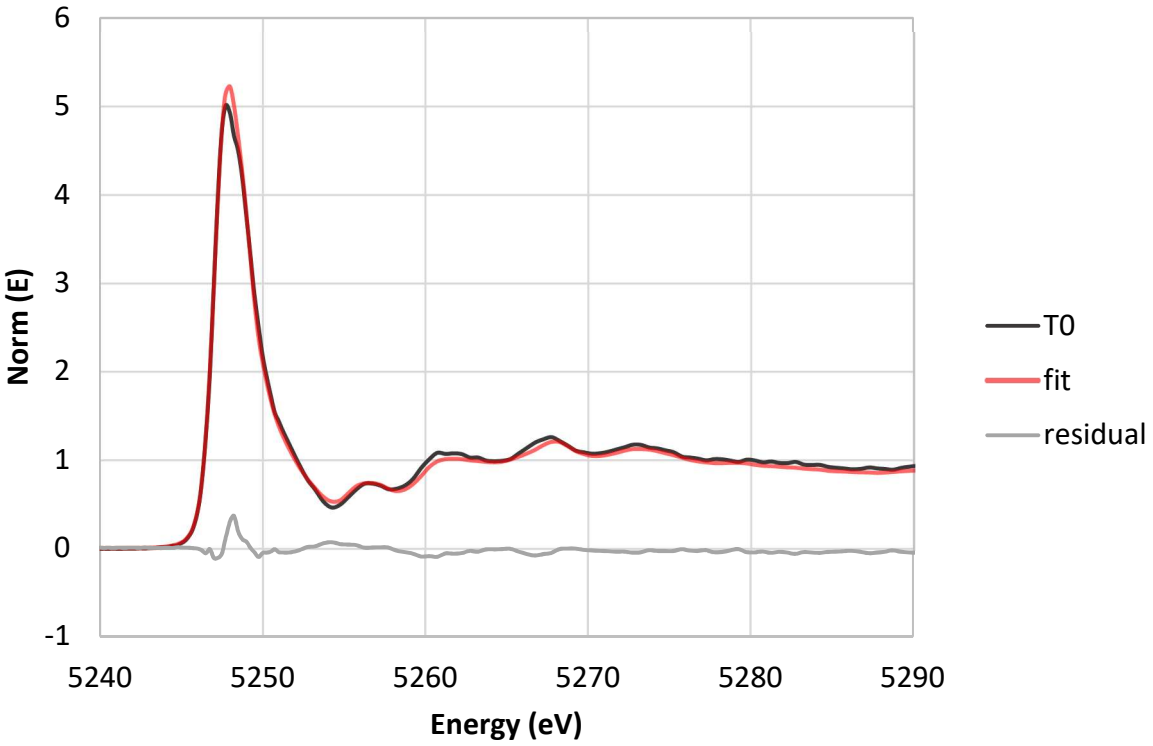

Figure B-3: Result of the linear combination fitting performed on the experimental XANES spectrum of the T_0 sample using the experimental XANES spectrum of BaO and $BaZrO_3$

Appendix 2.6: XAS linear combination fitting performed on the O900 and O1000 samples

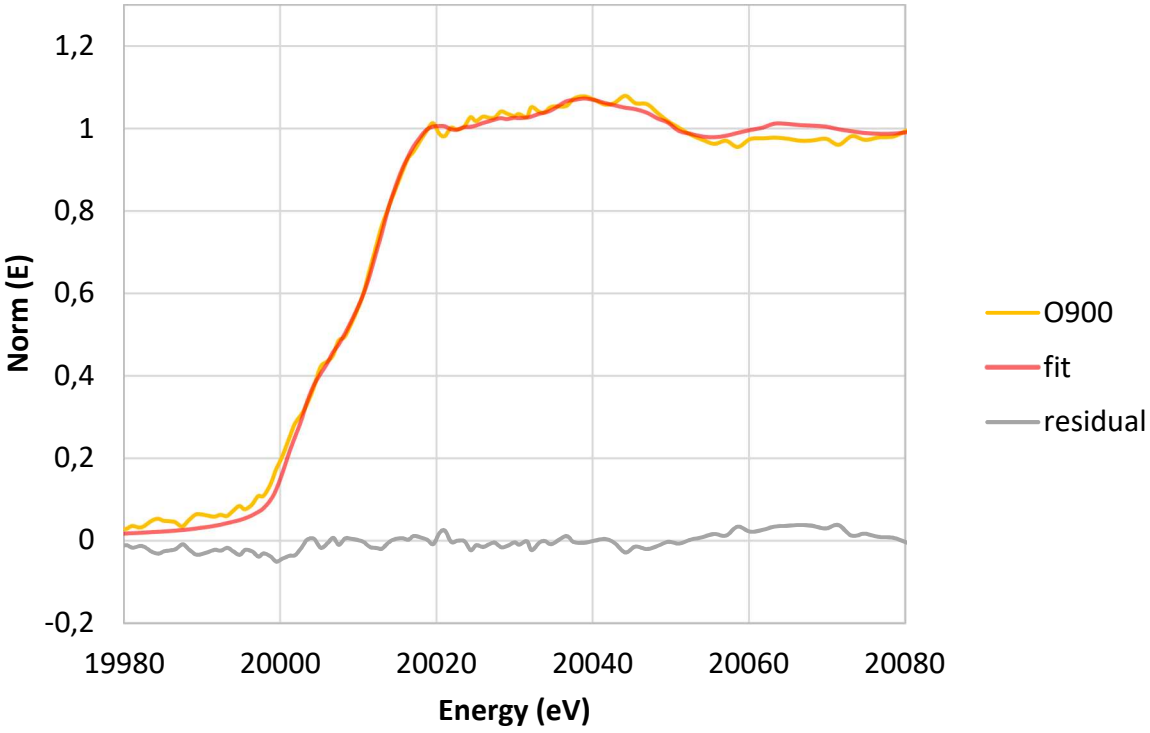

Figure B-4: Result of the linear combination fitting performed on the experimental XANES spectrum of the O900 sample using the experimental XANES spectrum of metallic Mo (bcc), MoO_2, $BaMoO_4$ and calculated XANES spectrum of metallic Mo (hcp)

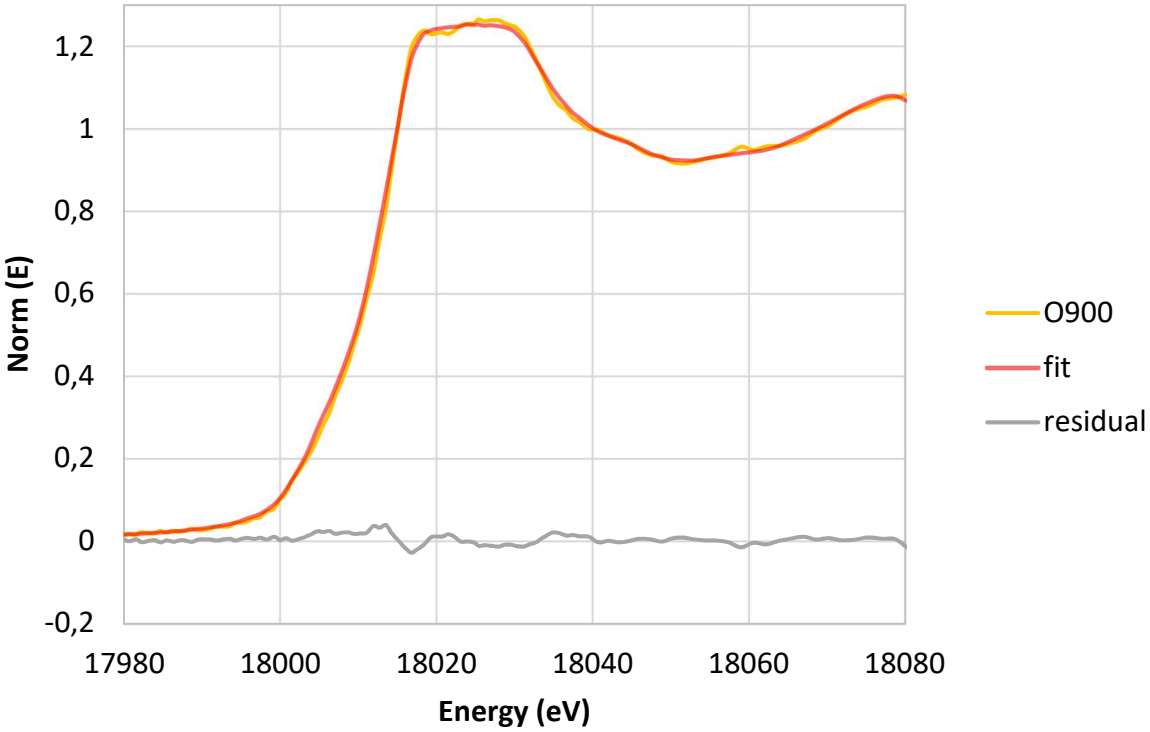

Figure B-5: Result of the linear combination fitting performed on the experimental XANES spectrum of the O900 sample using the experimental XANES spectrum of m-ZrO_2, $BaZrO_3$ and calculated XANES spectrum of c-ZrO_2 and $SrZrO_3$

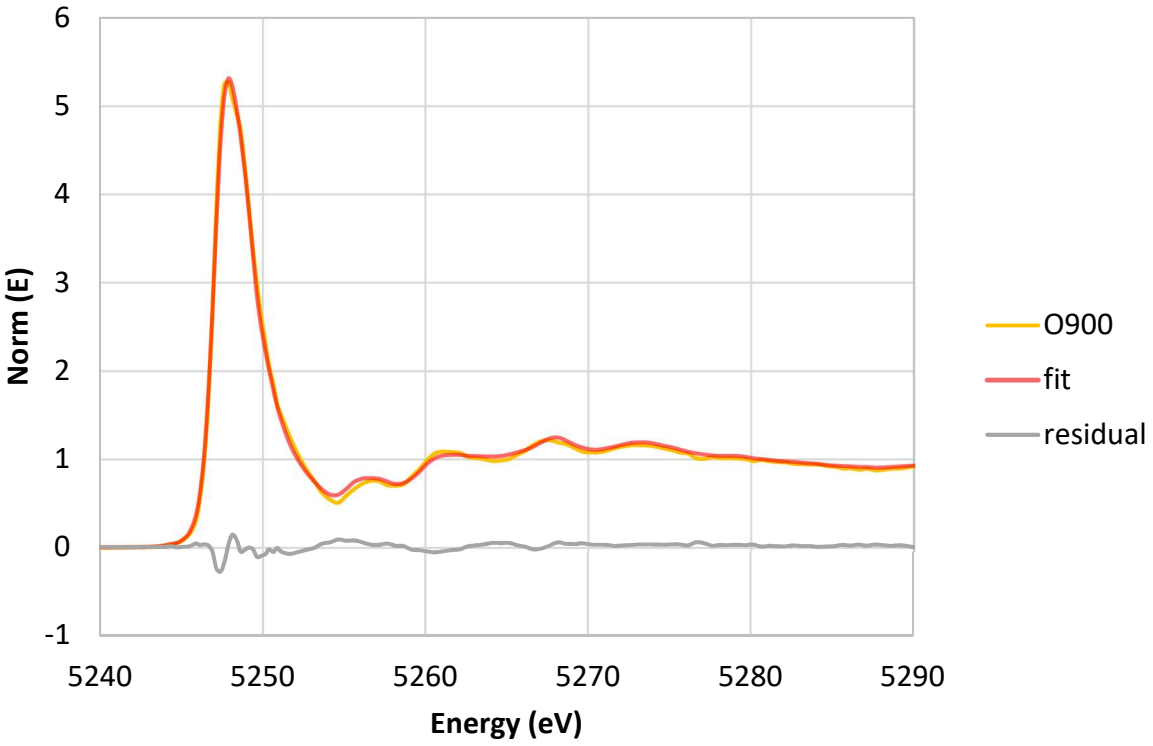

Figure B-6: Result of the linear combination fitting performed on the experimental XANES spectrum of the O900 sample using the experimental XANES spectrum of BaO, $BaZrO3_3$, $BaMoO_4$ and calculated XANES spectrum of $BaMoO_3$

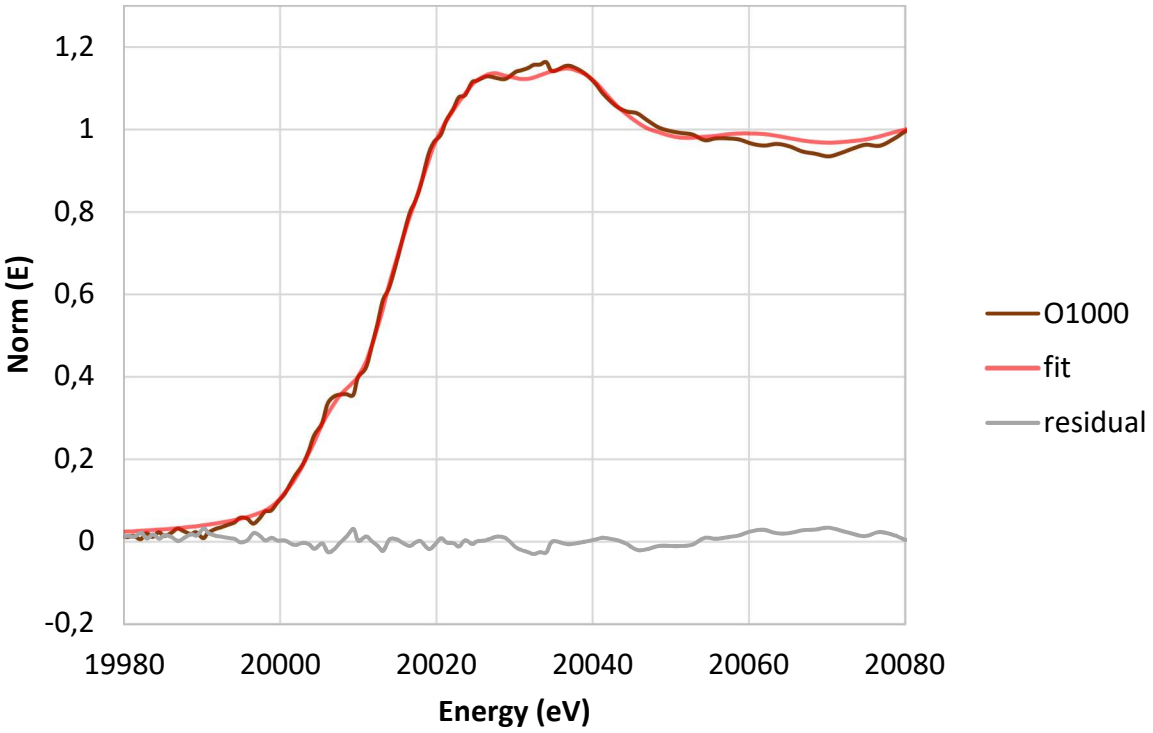

Figure B-7: Result of the linear combination fitting performed on the experimental XANES spectrum of the O1000 sample using the experimental XANES spectrum of metallic Mo (bcc), MoO_2, $BaMoO_4$ and calculated XANES spectrum of metallic Mo (hcp)

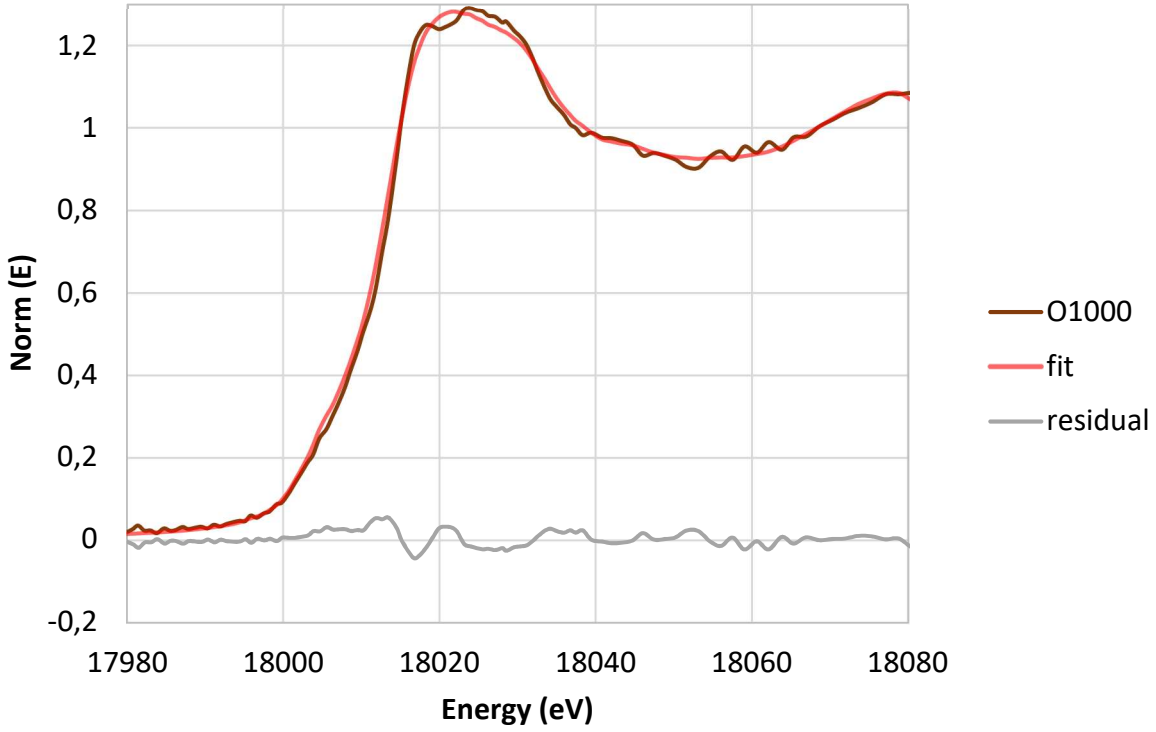

Figure B-8: Result of the linear combination fitting performed on the experimental XANES spectrum of the O1000 sample using the experimental XANES spectrum of m-ZrO_2, $BaZrO_3$ and calculated XANES spectrum of c-ZrO_2 and $SrZrO_3$

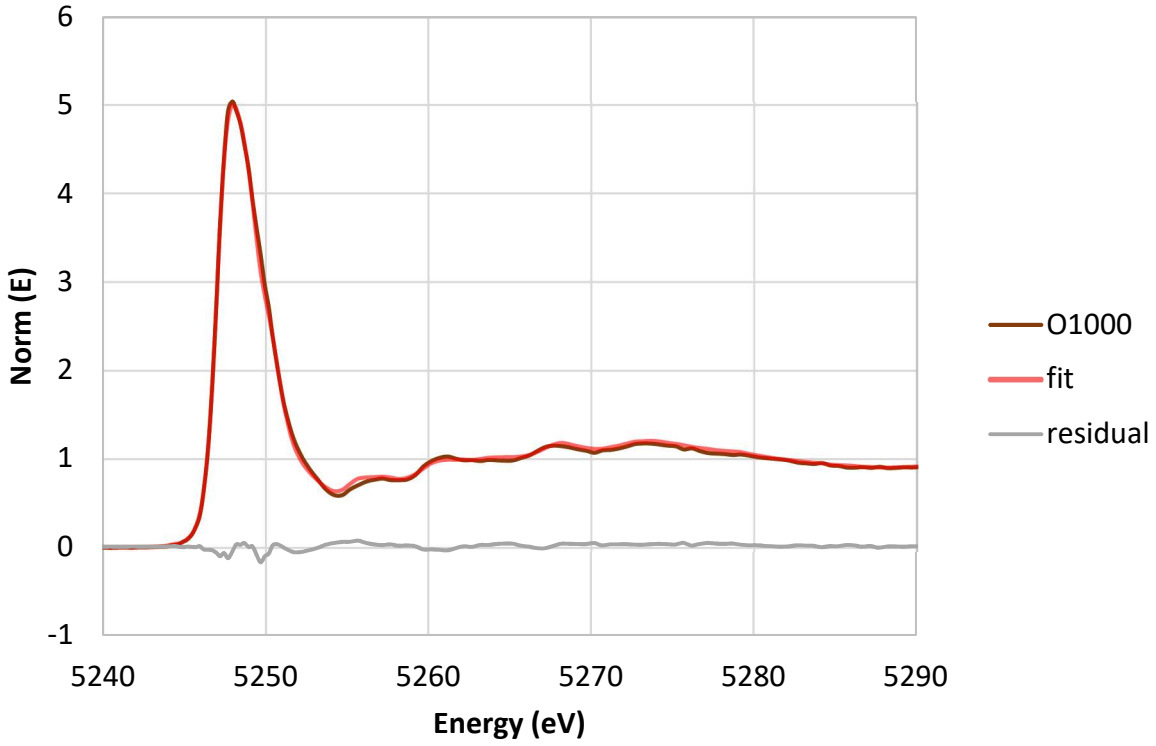

Figure B-9: Result of the linear combination fitting performed on the experimental XANES spectrum of the O1000 sample using the experimental XANES spectrum of BaO, $BaZrO3_3$, $BaMoO_4$ and calculated XANES spectrum of $BaMoO_3$

Appendix 2.7: XAS linear combination fitting performed on the R1700 sample

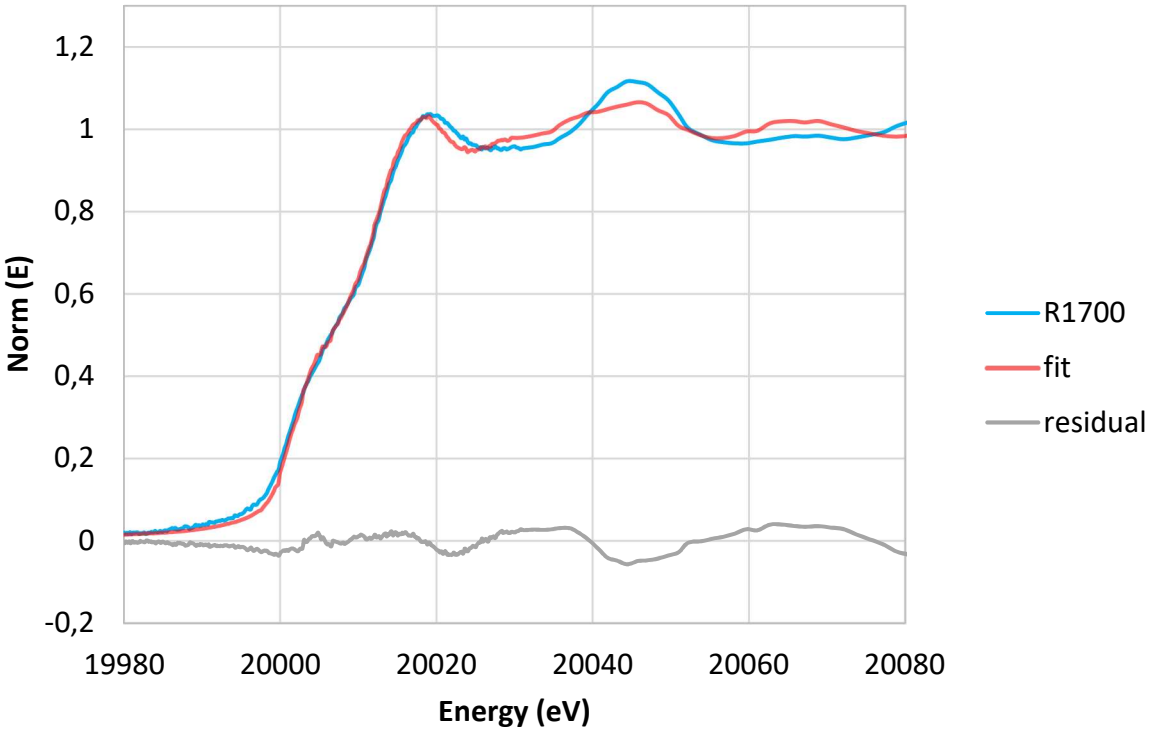

Figure B-10: Result of the linear combination fitting performed on the experimental XANES spectrum of the R1700 sample using the experimental XANES spectrum of metallic Mo (bcc) and calculated XANES spectrum of metallic Mo (hcp)

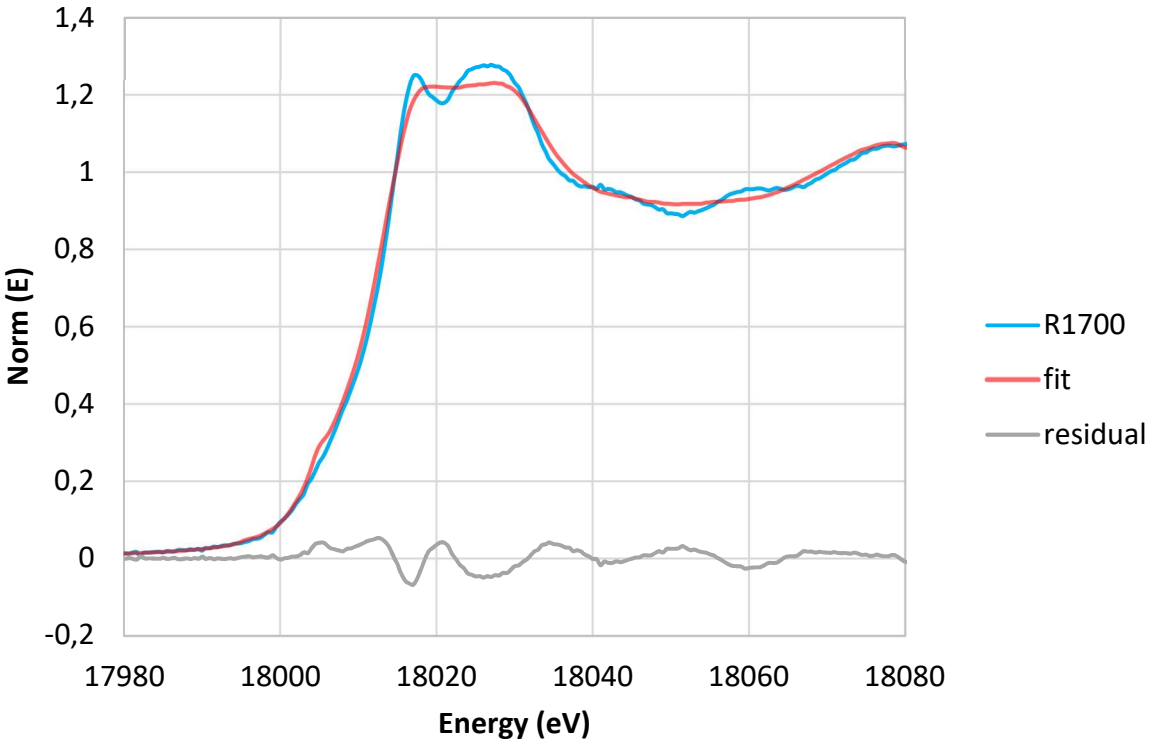

Figure B-11: Result of the linear combination fitting performed on the experimental XANES spectrum of the T_0 sample using the experimental XANES spectrum of m-ZrO_2, $BaZrO_3$ and calculated XANES spectrum of c-ZrO_2 and $SrZrO_3$

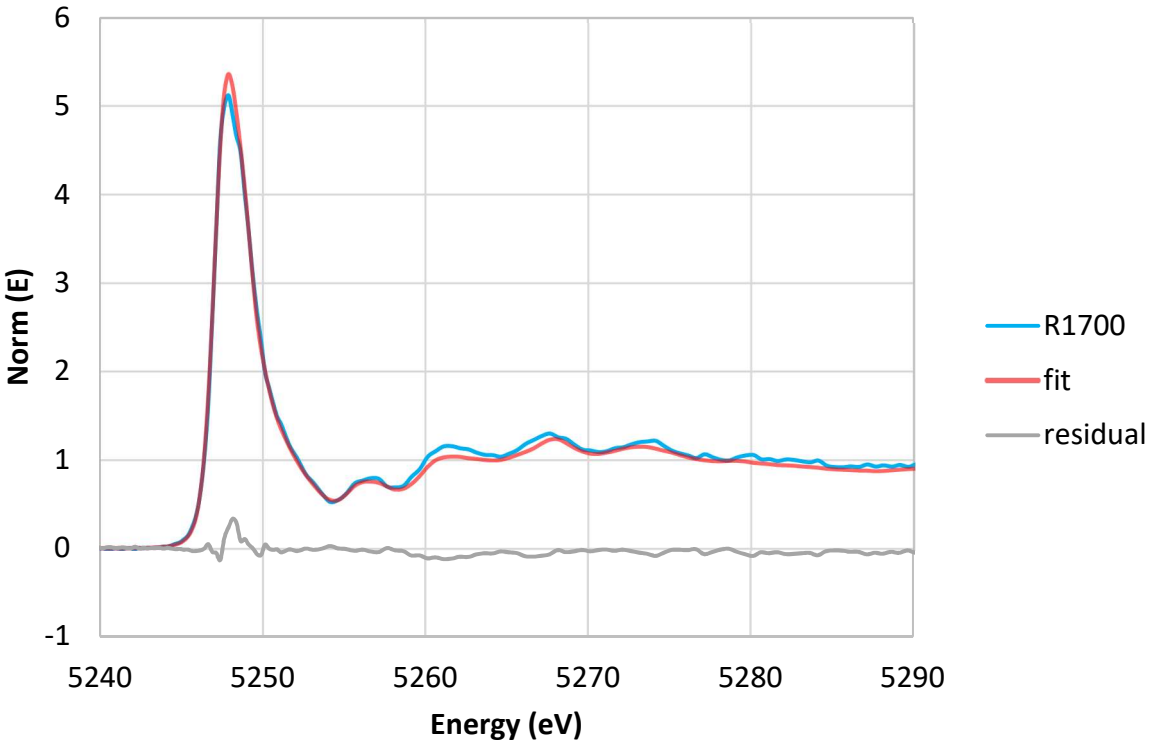

Figure B-12: Result of the linear combination fitting performed on the experimental XANES spectrum of the R1700 sample using the experimental XANES spectrum of BaO and $BaZrO_3$

C) APPENDIX 3: SIMFUEL SAMPLES SINTERED BY SPS

Appendix 3.1: Experimental method

Spark Plasma Sintering

Spark Plasma Sintering is a Field Assisted Sintering Technique (FAST) [39]–[41], which uses an electrical field to facilitate sintering. As shown in **Figure C-1**, the SPS set-up is composed of a graphite matrix consisting in a uniaxial hydraulic press with graphite pistons and dye. The powder is compacted by the pistons with a pressure of up to 100 MPa during the sintering. A pulsed direct current up to 10V and 10 kA is applied between the two pistons and goes through the powder and dye [9], [42]–[44].

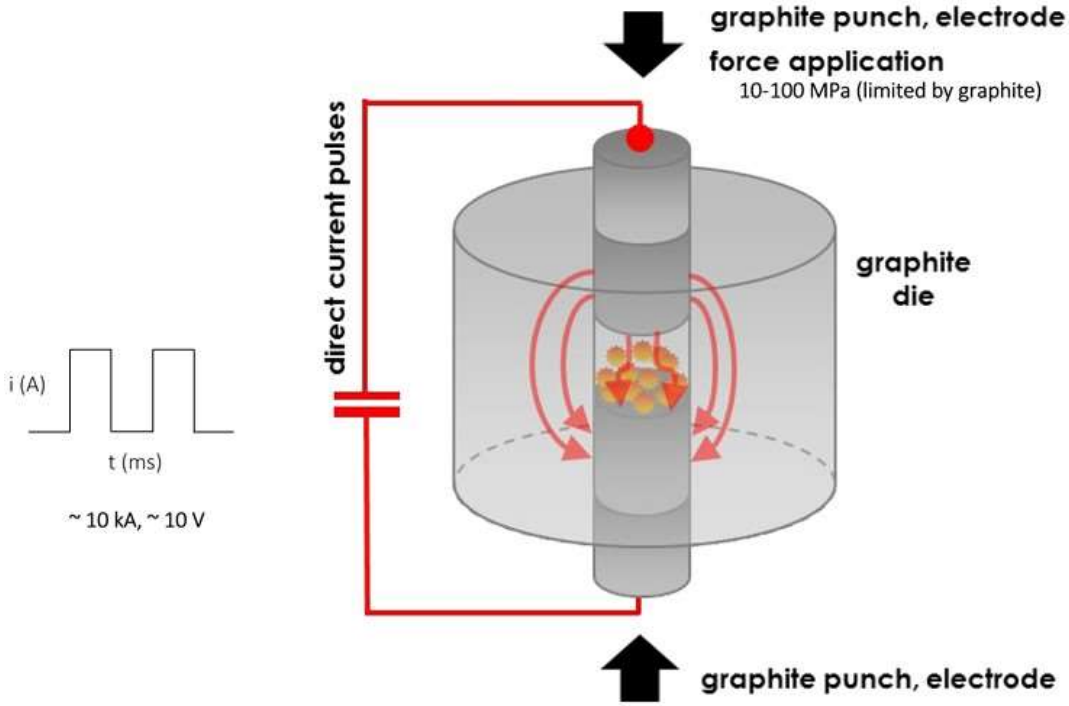

Figure C-1: Schematic principle of SPS extracted from [45]

Density measurement by He pycnometry

Density measurement were also performed thanks to He pycnometry in the case of the SIMFuel samples produced by SPS using a AccuPyc II 1340 pycnometer from Micromeritics. The pellets were placed in a sample chamber with a volume V_0 which was pressurized with He. The pressure is measured at equilibrium both before and after expansion (P_0 and P_{ech} respectively). The apparent density was thus determined using the mass of the samples (m_{ech}) on its volume (V_{ech}) which is calculated as follow:

$$\rho = \frac{m_{ech}}{V_{ec}} = m_{ech}\, x\, \frac{P_{ech}}{P_{ec}\ V_0 - P_0 V_0}$$

Chemical analyses

Mo, Ba and U concentrations in the different samples were determined through Inductively Coupled Plasma-Atomic Emission Spectroscopy and Mass Spectrometry (ICP-AES and ICP-MS). The Cs content was only measured thanks to ICP-MS.

The interest of coupling these two techniques is to get rid of the numerous spectral (mass effect) and non-spectral (matrix effect) interferences between the different additives.

The samples were composed of a whole pellet of SIMFuel (around 500 mg). They were first polished to remove the graphite layer formed during the sintering. The samples were then dissolved in a mixture of HNO_3 and HCl and the solution was evaporated almost to dryness (≈ 150°C during 3h). These two steps were repeated until full dissolution of the samples has been reached. Then, a dissolution in HNO_3 (3M) is performed in a final volume V_f calculated using the mass of the sample (m_{sample}), the percentage of U in UO_2 (U%) and the estimated amount of U in the sample ($[U]_{sample}$) [46]:

$$V_f = 1000\ x\ \frac{m_{sample}\ U\%}{[U]_{sample}}$$

Part of this stock solution was used to determine the U concentration. Two dilutions were realized in HNO_3 2% and U was measured thanks to three of its emission lines (**Table C-1**) by ICP-AES on an AGILENT Technologies 5100 device [46], [47].

Another part of the solution underwent a separation stage in order to avoid any matrix effect or spectral interferences between U and the additives. This step was done by liquid chromatography using a TRISKEM-UTEVA resin which will retain U. The final solution free from U was then diluted in HNO_3 and the Mo and Ba concentrations were determined by ICP-AES on an AGILENT Technologies 5100 device [48]. The wavelengths used to measure the amount of U, Mo and Ba are indicated in **Table C-1**. Cs could not be analyzed through this technique because its emission lines are too weak to be detected by the ICP-AES technique.

Finally, a third part of the stock solution was diluted in HNO_3 and was then analyzed by ICP-MS on a VARIAN 820 MS and an ANALYTIK JENA PQMS Elite [48]. For the quantification of Cs and Ba, a collision-reaction interface was used. Indeed, numerous polyatomic interferences due to interactions between Mo and Ar contained in the plasma or with Cl contained in the HCl solution used to dissolve the samples took place during the analyses. The isotopes used to measure the amount of U, Cs, Mo and Ba are indicated in **Table C-1**.

.

Table C-1: Wavelength and isotopes used to quantify U, Cs, Mo and Ba in the SIMFuel samples produced by SPS

Wavelength (nm)	367.007 385.957	-	202.032 203.846	455.403 493.408

	409.013		204.598	614.171
Isotopes	234 235 238	133	95 97 98 100	134 135 136 137 138

SEM-EDX analyses

The microstructure and the chemical composition of the different SIMFuel samples were analyzed thanks to a FEI Nova Nano SEM 450 coupled with FEI SE and BSE detectors and an Oxford Instruments EDX detector. Polished samples were observed with an accelerating voltage set to 15 kV. Quantitative analyses have been performed for all the additives with a typical detection limit of 1 wt%. X-ray maps were recorded using the $L_{\alpha 1}$ lines of every FP surrogates. The $M_{\alpha 1}$ and $K_{\alpha 1}$ lines were used respectively in the case of U and O.

Observations of fractured surfaces were performed on a Tescan Vega LSH device equipped with an Oxford EDX detector. Fractured samples were used in order to get rid of the graphite layer on their surface. Accelerating voltage was set to 20 kV. Semi-quantitative analyses have been performed for U, O, Mo and Cs.

Image analysis was performed using the analySIS pro software v.5.0 from Olympus Soft Imaging Solutions. This software enabled the determination of the ECD of particles or precipitates and the grain size within the matrix.

XRD

A Rigaken MiniFlux 600 diffractometer was used in Bragg-Brentano geometry (θ/2θ) to determine the composition of cesium uranate and the lattice parameter of the UO_2 powder used to synthesize the SPS samples. Measurements were recorded in the 2θ range of 15-120° with steps of 0.05°. The detection limit of this technique is typically around 5 wt%.

HERFD-XANES experiments

HERFD-XANES measurements were carried out at the FAME-UHD beamline of the European Synchrotron Radiation Facility at the L_2-edge of Cs. The photon energy was scanned from 5.26 to 5.70 keV using a Si(220) double crystal monochromator. He atmosphere was set between the sample, the CAS and the detector in order to avoid beam absorption by the air at such a low energy. The signal of the $L_{\beta 1}$ emission line was recorded with a five Ge(400) crystal analyzer and a Vortex-EX SII detector. The beamsize was 220 x 250 µm² (Horizontal x Vertical Full Width at Half Maximum). The energy calibration was done using a CsI reference sample.

In-temperature HERFD-XANES measurements were performed at the FAME-UHD beamline of the ESRF at the L_3-edge of Ba. The photon energy was scanned from 5.150 to 5.500 keV using a Si(220) double crystal monochromator. A helium bag was used between the sample, the CAS and the detector in order to avoid beam absorption by the air. The signal was recorded with a two Ge(400)

crystal analyzer and a Vortex-EX SII detector. The beamsize was 300 x 200 µm² (Horizontal x Vertical Full Width at Half Maximum). The energy calibration was done using $BaZrO_3$ spectrum.

The ATHENA software [49] was used to normalize the XAS spectra: pre-edge removal and normalization was achieved using linear functions. The E_0 values of each spectrum were taken as the first zero-crossing of its second derivative.

Appendix 3.2: Thermodynamic calculations

The predominance diagrams presented in this study were performed using the Phase Diagram module of the FactSage 7.0 software coupled to the SGPS database [23], [24]. The calculations were performed under constant total pressure (1 Bar). The initial elemental composition was set according to that of the various batached under study. Only temperature and oxygen potential were set as variables. These calculations are made assuming that the system is at thermodynamic equilibrium by minimization of the Gibbs free energy.

The elemental concentrations were determined using the results of chemical analyses performed on the samples from the different batches, when available. The calculation performed on batches 5, 6, 7 and 8 were performed using the initial amount of additives mixed to UO_2, assuming no release took place during sintering.

The calculations were performed by removing the gaseous phases in order to have access to the speciation of the different element in that phase. As no carbide phases involving Cs, Mo or Ba were observed to be formed, they were also removed from the calculation (in the case of batches 5 and 7).

D) REFERENCES

[1] J. Noirot, I. Zacharie-Aubrun, and T. Blay, “FIB/SEM Examination of High Burn-Up UO2 in the Center of a Pellet,” *Nucl. Eng. Technol.*

[2] B. Rasser, L. Desgranges, and B. Pasquet, “A new shielded SIMS instrument for analysis of highly radioactive materials,” *Appl. Surf. Sci.*, vol. 203–204, pp. 673–678, 2003.

[3] B. Sundman, B. Jansson, and J.-O. Andersson, “The Thermo-Calc databank system,” *Calphad*, vol. 9, no. 2, pp. 153–190, Apr. 1985.

[4] “OECD NEA/NSC: Thermodynamics of Advanced Fuels – International Database (TAF-ID) - working version of january 2018.” [Online]. Available: https://www.oecd-nea.org/science/taf-id/. [Accessed: 25-Aug-2016].

[5] H. Lukas, S. G. Fries, and B. Sundman, *Computational Thermodynamics: The Calphad Method*, 1st ed. New York, NY, USA: Cambridge University Press, 2007.

[6] F. Garel, C. Le Gall, P. Matheron, F. Audubert, and A. C. Robisson, “Procédé de fabrication d’UO2 avec 11 oxydes simulant des produits de fission,” CEA Cadarache, Note technique SFER/LCU/NT DO 2016-007, 2016.

[7] J. Da Rold, “Préparation métallographique des échantillons - opération de découpe à la scie à fil,” Mode opératoire SPUA/LCU CAR/MO 074 ind. 0.

[8] J. Da Rold, “Préparation métallographique des échantillons - Polissage,” SPUA/LCU CAR/MO 076 ind.0.

[9] I. Llorens *et al.*, “High energy resolution five-crystal spectrometer for high quality fluorescence and absorption measurements on an X-ray Absorption Spectroscopy beamline,” *Rev. Sci. Instrum.*, vol. 83, no. 6, p. 063104, 2012.

[10] O. Proux *et al.*, “High-Energy Resolution Fluorescence Detected X-Ray Absorption Spectroscopy: A Powerful New Structural Tool in Environmental Biogeochemistry Sciences,” *J. Environ. Qual.*, vol. 0, no. 0, Apr. 2017.

[11] I. LLorens *et al.*, “X-ray absorption spectroscopy investigations on radioactive matter using MARS beamline at SOLEIL synchrotron,” *Radiochim. Acta*, vol. 102, no. 11, pp. 957–972, 2014.

[12] B. Ravel and M. Newville, “ATHENA, ARTEMIS, HEPHAESTUS: data analysis for X-ray absorption spectroscopy using IFEFFIT,” *J. Synchrotron Radiat.*, vol. 12, no. 4, pp. 537–541, Jul. 2005.

[13] Y. Joly, “X-ray absorption near-edge structure calculations beyond the muffin-tin approximation,” *Phys. Rev. B*, vol. 63, no. 12, p. 125120, Mar. 2001.

[14] D. W. Smith, *Inorganic Substances: A Prelude to the Study of Descriptive Inorganic Chemistry*. Cambridge University Press, 1990.

[15] J. C. Garcia *et al.*, “Structural, electronic, and optical properties of ZrO2 from ab initio calculations,” *J. Appl. Phys.*, vol. 100, no. 10, p. 104103, Nov. 2006.

[16] G. Teufer, “The crystal structure of tetragonal ZrO2,” *Acta Crystallogr.*, vol. 15, no. 11, pp. 1187–1187, Nov. 1962.

[17] B. J. Kennedy, C. J. Howard, and B. C. Chakoumakos, “High temperature phase transitions in SrZrO3,” *Phys. Rev. B*, vol. 59, no. 6, 1999.

[18] V. Nassif, R. E. Carbonio, and J. A. Alonso, “Neutron Diffraction Study of the Crystal Structure of BaMoO4: A Suitable Precursor for Metallic BaMoO3 Perovskite,” *J. Solid State Chem.*, vol. 146, no. 1, pp. 266–270, Aug. 1999.

[19] J. R. Groza and A. Zavaliangos, “Sintering activation by external electrical field,” *Mater. Sci. Eng. A*, vol. 287, no. 2, pp. 171–177, Aug. 2000.

[20] R. Raj, M. Cologna, and J. S. C. Francis, “Influence of Externally Imposed and Internally Generated Electrical Fields on Grain Growth, Diffusional Creep, Sintering and Related Phenomena in Ceramics,” *J. Am. Ceram. Soc.*, vol. 94, no. 7, pp. 1941–1965, Jul. 2011.

[21] O. Guillon *et al.*, “Field-Assisted Sintering Technology/Spark Plasma Sintering: Mechanisms, Materials, and Technology Developments,” *Adv. Eng. Mater.*, vol. 16, no. 7, pp. 830–849, Jul. 2014.

[22] W. Chen, U. Anselmi-Tamburini, J. E. Garay, J. R. Groza, and Z. A. Munir, “Fundamental investigations on the spark plasma sintering/synthesis process: I. Effect of dc pulsing on reactivity,” *Mater. Sci. Eng. A*, vol. 394, no. 1, pp. 132–138, Mar. 2005.
[23] Z. A. Munir, U. Anselmi-Tamburini, and M. Ohyanagi, “The effect of electric field and pressure on the synthesis and consolidation of materials: A review of the spark plasma sintering method,” *J. Mater. Sci.*, vol. 41, no. 3, pp. 763–777, Feb. 2006.
[24] U. Anselmi-Tamburini, G. Spinolo, F. Maglia, I. Tredici, T. B. Holland, and A. K. Mukherjee, “Field Assisted Sintering Mechanisms,” in *Sintering*, R. Castro and K. van Benthem, Eds. Springer Berlin Heidelberg, 2012, pp. 159–193.
[25] T. Wangle, V. Tyrpekl, M. Cologna, and J. Somers, “Simulated UO2 fuel containing CsI by spark plasma sintering,” *J. Nucl. Mater.*, vol. 466, pp. 150–153, 2015.
[26] V. Tyrpekl *et al.*, “Implementation of a spark plasma sintering facility in a hermetic glovebox for compaction of toxic, radiotoxic, and air sensitive materials,” *Rev. Sci. Instrum.*, vol. 86, no. 2, p. 023904, 2015.
[27] F. Adam, “Préparation des échantillon d’oxyde d’uranium ou d’uraniul métal en vue de la mesure des impuretés,” CEA Cadarache, Méthode d’analyse LARC MA 083, 2005.
[28] N. Delteil and N. Arnal, “Dosage des métaux par spectrométrie d’émission atomique à couplage plasma - Norme NF EN ISO 11885 adaptée,” CEA Cadarache, Méthode d’analyse LARC MA 015, 1997.
[29] S. Pontremolli, “Extraction de l’uranium en vue du dosage des impuretés en matrice uranium par ICP-AES,” CEA Cadarache, Mode opératoire LARC MO 044, 2017.
[30] C. W. Bale *et al.*, “FactSage thermochemical software and databases,” *Calphad*, vol. 26, no. 2, pp. 189–228, 2002.
[31] C. W. Bale *et al.*, “FactSage thermochemical software and databases — recent developments,” *Calphad*, vol. 33, no. 2, pp. 295–311, 2009.

LIST OF FIGURES

LIST OF TABLES

ABSTRACT

In the nuclear community, it is a top priority to gain in-depth understanding of fission product (FP) speciation mechanisms occurring in nuclear fuel in order to precisely estimate the source term of a severe accident. Among the FP produced, some are highly reactive and may have a strong radiological impact if released into the environment. This is particularly the case of cesium (Cs), molybdenum (Mo) and barium (Ba). In this context, the objective of this study is to provide experimental data on the effect of the oxygen potential on Cs, Mo and Ba speciation in nuclear fuels at different stages of a severe accident.

A thermodynamic approach was coupled with the experimental work to support the interpretation of experimental data. Two types of samples were studied in detail: irradiated MOX fuels and simulated high burn-up UO_2 fuels produced through sintering at high temperature (SIMFuel). The samples were submitted to thermal treatments in conditions representative of a pressurised water reactor (PWR) severe accident. This approach made it possible to cover a temperature range from 400°C up to 2530°C and oxygen potentials from -470 $kJ.mol_{(O2)}^{-1}$ to -100 $kJ.mol_{(O2)}^{-1}$. The samples were characterized before and after each test using complementary techniques like OM, SEM, EPMA and SIMS in the case of irradiated fuels. XANES measurements using synchrotron radiation facilities were performed on SIMFuels and provided valuable results on FP speciation. Moreover, spark plasma sintering (SPS) was successfully investigated for the production of SIMFuel samples containing Cs, Mo and Ba in a chemical state representative of PWR fuel in normal operating conditions.

This work highlighted the effect of oxidizing severe accident conditions on the fuel and FP behavior. Oxidation of Mo initially contained in the fuel's metallic inclusions into MoO_2 was observed to take place around 1000°C in oxidizing conditions. An interaction between MoO_2 and the oxide phase containing Ba took place in the same conditions, leading to the formation of $BaMoO_4$. The oxygen potential also plays an important role in fuel-cladding interactions, enhancing the diffusion of species in oxidizing conditions and lowering the temperature at which fuel melting occurs.

RESUME

Comprendre les mécanismes de spéciation des Produits de Fission (PF) dans le combustible nucléaire est un enjeu majeur pour pouvoir estimer précisément le terme source d'un accident grave. Parmi les nombreux PF créés, certains sont très réactifs et peuvent avoir un impact radiologique important en cas de relâchement dans l'atmosphère. C'est notamment le cas du césium (Cs), du molybdène (Mo) et du baryum (Ba). C'est dans ce contexte que s'inscrit le travail de thèse qui propose d'apporter des données expérimentales sur l'effet du potentiel oxygène sur la spéciation du Cs, du Mo et du Ba dans des combustibles nucléaires, à différents stades d'un accident grave.

Une approche thermodynamique a été utilisée en support à l'interprétation des données expérimentales obtenues dans le cadre de ce travail. Deux types d'échantillons ont été étudiés: des combustibles MOX irradiés et des matériaux simulant un combustible UO_2 à fort taux de combustion, obtenus par frittage à haute température (SIMFuel). Les échantillons ont été traités thermiquement dans des conditions représentatives d'un accident grave survenant dans un Réacteur à Eau Pressurisée (REP). Les conditions expérimentales ont couvert une gamme de température allant de 400°C à 2530°C et des potentiels oxygène situés entre -470 $kJ.mol_{(O2)}^{-1}$ et -100 $kJ.mol_{(O2)}^{-1}$. Les échantillons ont été caractérisés finement avant et après chaque traitement à l'aide de techniques complémentaires comme la microscopie optique et électronique, la microsonde et le SIMS dans le cas de l'irradié. Des mesures de XANES sur synchrotron ont été réalisées sur SIMFuel et ont conduit à des résultats importants en termes de spéciation des PF. Enfin, la technique de Spark Plasma Sintering (SPS) a été explorée avec succès pour la fabrication de SIMFuel contenant du Cs, du Mo et du Ba sous des formes chimiques représentatives d'un combustible REP en fonctionnement nominal.

Ce travail a permis de mettre en évidence l'effet de la température en conditions oxydantes sur le comportement du combustible et des PF. Une oxydation du Mo, initialement présent sous forme métallique dans les inclusions blanches du combustible, en MoO_2 a été observée dès 1000°C en conditions oxydantes. Une interaction entre le MoO_2 formé et le Ba contenu dans la phase oxyde a eu lieu dans les mêmes conditions, menant à la formation de $BaMoO_4$. Le potentiel oxygène joue aussi un rôle important dans le phénomène d'interaction pastille-gaine, en favorisant la diffusion des espèces en conditions oxydantes, diminuant ainsi la température de fusion du combustible.